



Production of Rosmarinic Acid Nanoparticles, and Investigation of Anti-Oxidation Effects on Salmon Fish Meat

Zafer CEYLAN¹ , Yasemin BUDAMA KILINC² , Azime YILMAZ² , Kubra UNAL^{*3} ,
Burak OZDEMIR⁴ 

¹ Van Yüzüncü Yil University, Faculty of Tourism, Department of Gastronomy and Culinary Arts, Tuşba, Van, Turkey

²Yildiz Technical University, Department of Bioengineering, Istanbul, Turkey

³Selcuk University, Department of Food Engineering, Konya, Turkey

⁴Yildiz Technical University, Department of Bioengineering, Istanbul, Turkey

Abstract: In this study, an anti-oxidant nanoformulation to prevent the oxidation of salmon was developed using rosmarinic acid (RA). Minced salmon samples (MSs) were treated with 8.10^{-3} g (RAT1) and 16.10^{-3} g (RAT2) RA-loaded nanoparticles for 100 g MS rosmarinic acid, separately. The thiobarbituric acid (TBA) values of control (C), RAT1, and RAT2 samples stored at 4 °C were found as 2.995, 1.350, and 0.994 mg MDA/kg; respectively, after 9 days. While the initial free fatty acid (FFA) value of C samples was 2.011%, RAT1 and RAT2 were found as 2.765% and 2.494%, respectively. The 2,2-diphenylpicrylhydrazyl (DPPH) values of MSs treated with RAT1 and RAT2 were observed to be higher than that of C samples. C samples were evaluated as unfit for human consumption on the 5th day of the storage, it was revealed that but the sensory scores of MSs treated with RAT1 and RAT2 were still acceptable for human consumption.

Keywords: Nanotechnology application, nanoparticle, oxidation, rosmarinic acid, salmon quality.

Submitted: November 15, 2021. **Accepted:** February 03, 2022.

Cite this: Ceylan Z, Budama Kilinc Y, Yilmaz A, Unal K, Ozdemir B. Production of Rosmarinic Acid Nanoparticles, and Investigation of Anti-Oxidation Effects on Salmon Fish Meat. JOTCSA. 2022;9(2):311-20.

DOI: <https://doi.org/10.18596/jotcsa.1022787>.

***Corresponding author. E-mail:** ulusoy_kubra@hotmail.com, tel: +903322232936.

INTRODUCTION

Well-balanced nutrition is a very crucial issue for consumers. In this respect, fish is a unique essential nutrient source for human (1). However, as soon as fish samples are caught, they must be protected by using appropriate food preservation methods. Therefore, different conventional food preservation methods are already used to delay the rapid deterioration in fish meat after harvesting. Ionizing irradiation treatment, packaging treatments, food additives, chilling, and freezing technology are widely used to limit the rapid deterioration in fish all over the world (2-4). Yet, food additives are applied to processed, lightly processed, or raw fish samples.

Furthermore, most of the food additives used in the fish processing industry are based on chemical origin. Since natural or organic-based food additives are highly expensive, they are not preferred by the fish processing industry. Also, some of the micro or macro natural-based food additives may have a lower antioxidant or bactericidal effect on fish fillets/samples. In this regard, cost-effective food preservation methods having stronger antimicrobial and antioxidant properties are currently being tried, particularly in the scientific area. For example, in the last decade, there has been a significant increase in microencapsulation methods. Moreover, food nanotechnology applications such as nanoencapsulation, nanocoating, nanoemulsions,

nanoparticles, nanofibers recently take a great deal of attention in the food industry and scientific area. Ceylan, Sengor (5) revealed that nanofibers could be used as a nanocoating material for delaying the chemical deterioration in fish fillets. Özogul, Durmus (6) noted that nanoemulsions could be utilized to limit the rapid deterioration of fish samples. Osheba, Sorour (7) revealed that chitosan nanoparticle application successfully limited the rapid increase in chemical deteriorations parameters such as total volatile nitrogen, trimethylamine, and thiobarbituric acid in fish fingers. Ceylan, Sengor (8) reported that nano-thymol and the liquid smoke application delayed the rapid microbial spoilage in fish fillets during cold storage conditions. Also, the encapsulation of bio-based materials and functional ingredients are important and promising approaches for food nanotechnology applications. In this respect, encapsulations of nisin (9), rosehip seed oil (10), α -tocopherol (11), and zinc oxide (12) were successfully carried out, as can be seen from previous literature studies, as well. Additionally, nanomats that integrated with curcumin and nisin (13) or pomegranate seed oil (14), grape seed oil-loaded nanofibers (15) and zein nanofibers (16) effectively improved the acceptability of fish meats during cold storage.

In this study, rosmarinic acid (RA), which is one of the polyphenolic substances contained in culinary herbs such as perilla, rosemary, sage, mint, and basil, was used. Therefore, there are many studies in which rosmarinic acid is provided with effective antioxidants and other quality properties. To the best of our knowledge, the number of antioxidant and lipid oxidation studies about RA-loaded nanoparticles of the salmon fish is limited. In this sense, the initial aim of the study was to encapsulate RA and characterize RA nanoparticles, such as average particle size and in vitro release profile. Also, the main aim of the present study was to investigate the potential antioxidative effect of RA-loaded nanoparticles on the salmon fish mince stored under 4 °C, and its effects on its shelf life.

MATERIALS AND METHOD

Materials

Salmon fish samples were obtained from an international supermarket in Konya, Turkey. The fish samples were immediately transferred to the food processing laboratory. RA (96%, Mw=360.31 g/mol), polycaprolactone (PCL) (Mn=80,000), and polyvinyl alcohol (PVA) (Mw = 31,000–50,000, 87–89%) were purchased from Sigma-Aldrich (USA).

Treatment with Nanoparticles of Fish Samples

The samples were grouped as control (C), RAT1 (8.10⁻³ g RA-loaded nanoparticle/ 100 g minced fish), and RAT2 (16.10⁻³ g RA-loaded nanoparticle/ 100 g of minced fish), as compared to RAT1). 100 g of fish samples were separated as C, RAT1, and

RAT2, respectively. Following the nano treatment, the minced fish samples were placed into the locked plastic pouch and then stored at 4 °C for 9 days.

Calibration Process

The calibration curve of RA was obtained using UV-Vis Spectrophotometer (Shimadzu, Japan). Standard solutions of RA were prepared to give final concentrations of 1.5625, 3.125, 6.25, 12.5, and 25 μ g/ mL. Then the absorbance values of these samples were measured by UV-Vis Spectrophotometer at 324 nm, and the calibration curve was plotted.

Preparation of RA-Loaded PCL-Based Nanoparticles

The double-emission precipitation method was used to prepare the RA-loaded PCL nanoparticles. 10 mg of RA was dissolved in 1 mL of distilled water, 30 mg of PCL was dissolved in dichloromethane, and then the PCL solution was added to the RA solution, respectively. All solutions were mixed and sonicated for 10 minutes using an ultrasonicator at 55 W. This solution was placed into a syringe and then added dropwise into 4 mL of 5% PVA solution under continuous stirring. Following these first step procedures, the solution was sonicated again for ten minutes. After that, the mixture was left overnight under continuous stirring in the sonicator. Finally, the obtained RA-loaded nanoparticles were isolated by centrifugation (at 10,000 rpm for 30 min). The samples were washed three times to remove the organic solvent and freeze-dried for further characterization analysis and food nanotechnology applications.

Zeta Size (ZS) of Nanoparticles

The average size distribution of RA-loaded nanoparticles was obtained using a Zeta-Sizer Nano ZS (Malvern Instruments, Malvern, UK) instrument equipped with a 4.0 mV He-Ne laser.

Encapsulation Efficiency

The loading capacity (LC) and encapsulation efficiency (EE) of RA-loaded PCL nanoparticles were measured by separating the nanoparticles from the aqueous nanoparticle suspension via centrifugation. In this respect, the concentration of free RA in the supernatant was determined using a UV-visible Spectrophotometer via the RA standard curve. The loading capacity and encapsulation efficiency of RA-loaded PCL nanoparticles were respectively calculated by the formulas given below. Encapsulated RA amount was calculated by UV-vis absorbance value of supernatant which was obtained after centrifugation of the RA loaded PCL nanoparticles. The UV-vis absorbance value of supernatant put the formula which was obtained from the calibration curve.

$$EE = ((\text{Total RA Amount} - \text{Free RA Amount}) / \text{Total RA Amount}) \times 100 \quad (\text{Eq. 1})$$

$$LC = \left(\frac{\text{Encapsulated RA}}{\text{Total Nanoparticles Weight}} \right) \times 100 \quad (\text{Eq. 2})$$

The Amount of Released RA

To determine the in vitro release profile, the release study experiment was conducted at the optimum storage temperature (+4 °C) for meat products. 1 mg of RA-loaded PCL nanoparticles was dissolved in 2 mL distilled water and placed in a dialysis capsule. 100 mL PBS media at pH = 7.2 phosphate buffer solution was used as release medium. At designated time intervals, 1 mL of the release medium was taken and replaced by an equal volume of fresh pre-warmed release medium. The amount of released RA in samples was analyzed by UV-Vis spectrometer at 324 nm wavelength. The amount of RA released at the end of 144 h was evaluated from Equation 3, and the % amount released over time is plotted.

$$\text{Release Amount (\%)} = \left(\frac{\text{Released Amount of RA}}{\text{Total Amount of RA}} \right) \times 100 \quad (\text{Eq. 3})$$

Thermogravimetric Analysis (TGA) of Nano-Scale Material

Thermal behaviors of PCL nanoparticles and RA-loaded PCL nanoparticles were determined using Thermogravimetric Analyzer, TGA (SDT Q600, TA Instruments, and Newcastle, DE USA). As stated by Ceylan, Meral (17) continuous nitrogen flow at a rate of 20 mL/min in the temperature range of 25 °C to 800 °C at a rate of 10 °C min⁻¹ was applied.

Thiobarbituric Acid (TBA) Analysis

10 g of minced salmon fish samples, 4 N HCl (2.5 mL), and 97.5 mL of distilled water were added into the flask and then heated for distillation. After the distillation, 5 mL from the distillate sample was taken and added to the test tubes. All tubes were heated in hot water at 85°C for 30 min. Absorbance values of C, RAT1, and RAT2 were measured at 530 nm using a spectrophotometer (Shimadzu-UV mini 1240, Kyoto-Japan). Finally, TBA results of the samples were calculated as mg malondialdehyde per kg (mg MDA kg⁻¹) according to Tarladgis, Watts (18).

Antioxidant Activity Measurement by DPPH

The antioxidant capacity of the minced salmon samples was determined using a modified method as described by Brand-Williams, Cuvelier (19). Salmon fish samples, 5 g per sample, were mixed with 25 ml of methanol in ice Polytron homogenizer, centrifuged at 7000 × g for 10 min, and filtered by using Whatman No. 1. The supernatant was mixed with methanol to a volume of 25 mL, and then 50 µL was added to 2950 µL of 100 µM DPPH in methanol solution in a test tube. Methanol, 50 µL, and 2950 µL DPPH solution were used to be a blank.

The tubes were covered with parafilm, vortexed, and kept in the dark at room temperature. The absorbance value of the solution was obtained at 517 nm. The standard curve was developed with ascorbic acid and DPPH.

Free Fatty Acid (FFA)

FFA value as an index of fish fat hydrolyzes was determined according to Egan, Kirk (20). The samples were extracted and then 25 mL of the extract was mixed with 25 mL of ethyl alcohol (95%). The mixture was titrated against 0.1 N NaOH using an indicator (phenolphthalein). The percentages of FFAs in C, RAT1, and RAT2 samples were calculated as oleic acid by using the formula below.

$$\text{FFA} = \left(\frac{V \times N \times 2.82}{W} \right) \quad (\text{Eq. 4})$$

V: Volume of NaOH

N: Normality of NaOH

W: Weight of Lipid in Extractions

Sensory Evaluation

Sensory deteriorations in C, RAT1, and RAT2 groups were evaluated by trained sensory panelists as stated by Fan, Sun (21) (n=10). The samples were presented to the trained panelists in a room under well-ventilated and lighted conditions every analysis day. A 10-point hedonic scale was used to evaluate the samples in terms of the overall sensory score (SOVS; obtaining from odor, texture, and color parameters). Score 5.0 was considered as the borderline of all minced fish samples (C, RAT1, and RAT2) acceptability.

Statistical Analysis

All measurements were repeated twice with three replications. Collected data were subjected to analysis of variance (ANOVA) to evaluate the TBA, DPPH, FFA, and SOVS in all groups. Graphpad Prism software Version 5.00 (California Corporation, CA) was used to reveal significant differences between C, RAT1, and RAT2, and also comparisons of all differences among them were evaluated by the Tukey's Multiple Range Test (p<0.05).

RESULTS AND DISCUSSION

Particle Distribution of Nanoparticles

RA solutions were prepared with different concentrations (1.5625, 3.125, 6.25, 12.5, and 25 µg/mL). Then the absorbance values of these samples were measured by UV-Vis Spectrophotometer at 324 nm, and the calibration curve was plotted (Figure 1).

Zeta Size values of PCL and RAT-loaded PCL nanoparticles were determined to be 213.9±3.52 and 235.8±2.98 nm, respectively Figure 2A and 2B (Table 1).

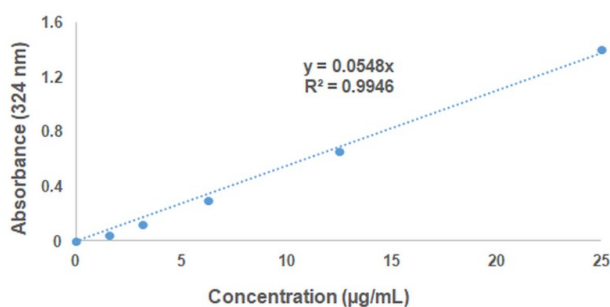


Figure 1: The calibration curve.

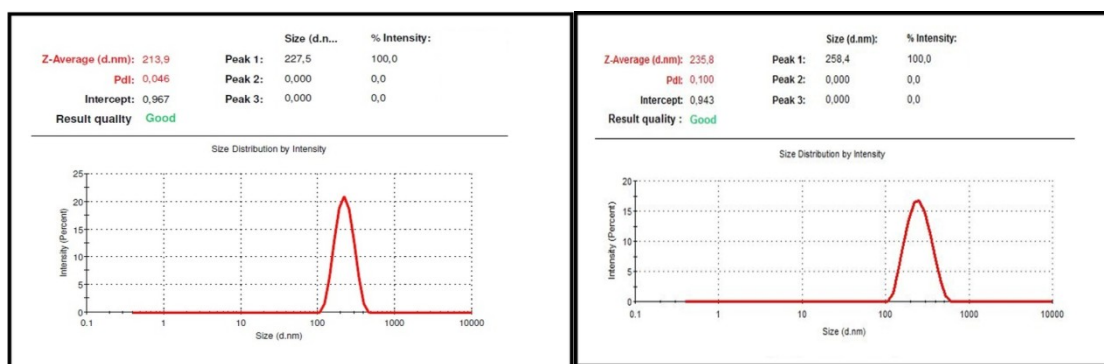


Figure 2: Zeta Size result of (A) blank and (B) RA PCL nanoparticles.

Table 1: Average particle size of nanoparticles.

Samples	Average Particle Size (nm)
PCL NP	213.9±3.52
RAT NP	235.8±2.98

PCL and RAT NPs define poly(ε-caprolactone) and rosmarinic acid-loaded poly(ε-caprolactone), respectively.

The in vitro release study was performed and the release profile graph was drawn based on time and cumulative RA release (%) (Figure 3) by using calibration curve data of RA. It was determined that RA was released 58.46% in the first 24 h. Moreover,

93.85% of RA was released from the RA-loaded PCL nanoparticles end of the 144 th hour. According to the results of in vitro release study, we concluded that the active ingredient (RA) has a controlled manner and slow-release rate over time.

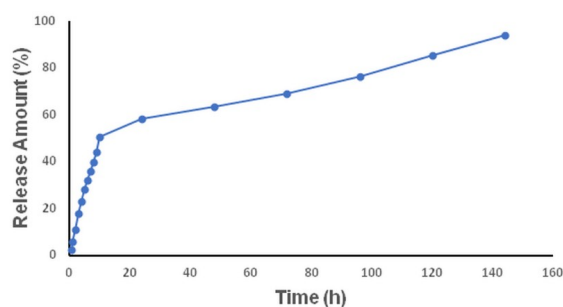


Figure 3: The cumulative RA release.

Loading of RA into PCL increased the average diameter of the RA-loaded nanoparticle according to the results of zeta size. Also, the biggest RA-

loaded nanoparticle detected by TEM analysis was given in Figure 4.

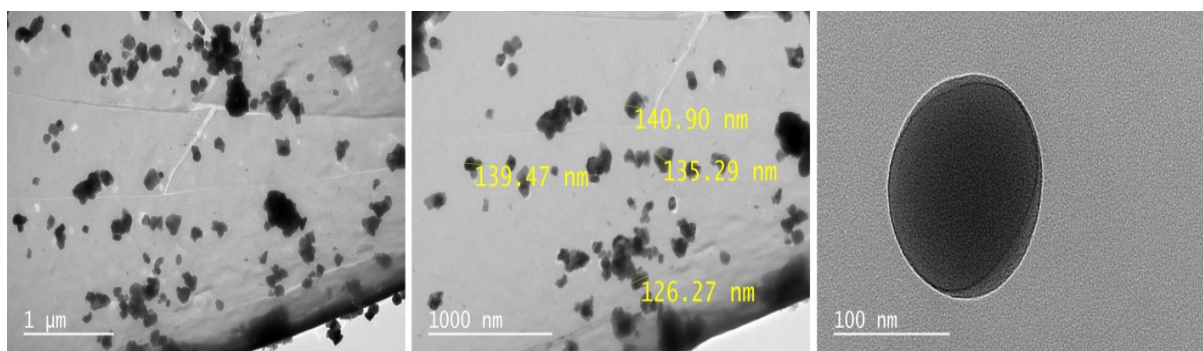


Figure 4: TEM image of RA-loaded nanoparticle.

PCL was used as a nanocarrier in the present study, the antioxidant activity of RA-loaded PCL nanoparticles on the minced salmon samples was revealed. In any nanotechnology application, the diameter of the nanomaterial can play a key role in food applications. Loading of RA into PCL provided an antioxidant effect on the minced salmon samples for 9 days, although RA did not significantly increase the diameter of the nanoparticle ($p < 0.05$). On the other hand, as can be seen from the previous study (8), loading of thymol and liquid smoke into chitosan nanofiber increased the average diameter of the chitosan-based nanofiber. Also, according to Merrell, McLaughlin (22), the diameter of PCL nanofibers fabricated by the electrospinning technique was found to be between 300 and 400 nm. da Silva, Ferreira (23) reported that RA encapsulated chitosan nanoparticles could have a diameter ranging from 200 to 300 nm. In this respect, the loading of RA possessing 235.8 ± 2.98 nm diameter provided a larger surface area to prevent the rapid oxidation of the minced salmon for 9 days.

Loading Efficiency and Encapsulation of RA-loaded PCL Nanoparticles

The encapsulation efficiency of the RA was found to be $99.0 \pm 0.35\%$. This ratio revealed that the RA was highly successfully encapsulated and also effective RA-loaded PCL nanoparticles were obtained. The loading efficiency of the RA-loaded PCL nanoparticles for each 10 mg was found as 9.2 mg of RA. For this study, loading and encapsulation efficiency are important to reveal the effectiveness of RA nanoparticles. Also, the results revealed that the high loading and encapsulation efficiency of RA known as an antioxidant may affect the stability of TBA, DPPH, FFA, and SOVS parameters obtained from the minced salmon samples. In the previous study, Snehalatha, Venugopal (24) reported that encapsulation and loading efficiency of etoposide (into PCL) were found to be 80.15% and 28.8%, respectively. In another study, the loading capacity

of RA in chitosan nanoparticles was defined to be lower as compared to our study results (25). As can be also seen from the previous study results, the nanocarrier and loading material play an important role to obtain effective productivity from the nanomaterials.

Thermal Decomposition of the Nanoparticles

The loss mass of the RA-loaded PCL nanoparticles and PCL nanoparticles was detected by the TGA analysis, as can be seen from Figures 5 and 6. Cold storage, especially at about 4 °C, is important in the fish processing industry. Therefore, revealing the nanoparticle's thermal decomposition in all mentioned temperature ranges (e.g. 60 °C - 80 °C, 121 °C) is much more important for further food nanotechnology studies as well. In this respect, there was no remarkable mass loss for PCL and RA nanoparticle samples in the range of cold storage temperatures. However, a mass reduction < 0.1328 mg (5.662%) and < 0.04301 mg (2.970%) was recorded respectively for PCL and RA nanoparticle samples at about in the range of 65 and 80 °C. As compared to 80°C, there was no remarkable mass reduction for both nanoparticle samples at 121 °C.

Thermal decomposition started at 250 °C for PCL nanoparticles with above 15%, but at the same temperature, loss in mass was found about 8.5% for the RA nanoparticles. Previous study results indicated that the type of the used material (probiotic bacteria or polymer etc.) play an important role to determine the thermal behavior of the nanoparticles. Ceylan, Meral (17) defined that the lost weight in nanofibers obtained from *L. rhamnosus* was found to be $\geq 5\%$ up to 200 °C degrees. However, Zhao, Li (26) reported that thermal decomposition of chitosan-based nanofibers started at 240°C and was completed at 650 °C. Therefore, the thermal behavior of obtained nanomaterials should be revealed for further studies related to food nanotechnology.

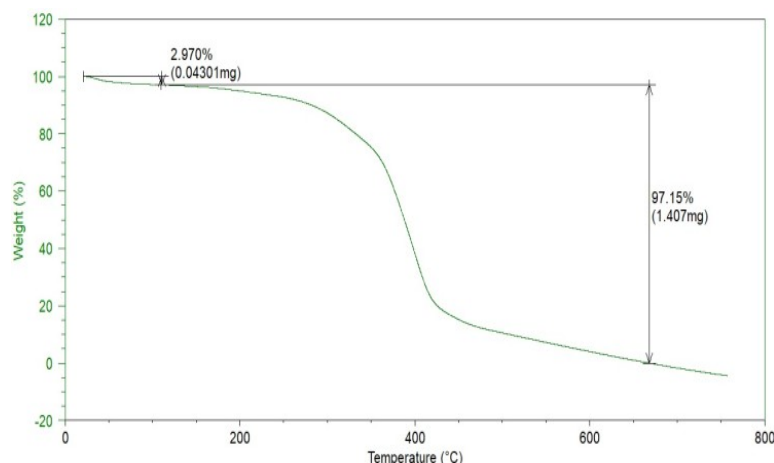


Figure 5: Thermal decomposition of rosmarinic acid-loaded PCL-based nanoparticles.

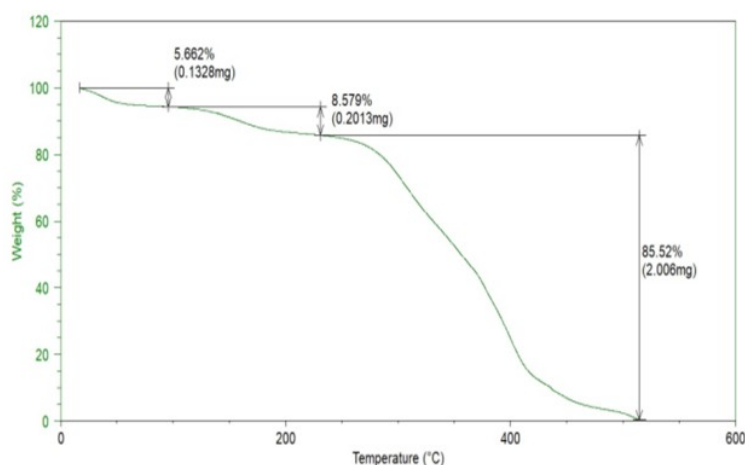


Figure 6: Thermal decomposition of PCL nanoparticles.

The Role of RA Nanoparticles in Lipid Oxidation and Antioxidant Activity (TBA)

The TBA results of processed and untreated minced salmon samples are given in Table 2. The TBA values of untreated minced salmon were higher than those of RA nanoparticles with different ratios ($p < 0.05$). While the TBA value of untreated samples was measured to be $0.51 \text{ mg MDA kg}^{-1}$ fish meat on the first day of the cold storage period, TBA values of RAT1 and RAT2 were found to be 0.18 and $0.155 \text{ mg MDA kg}^{-1}$, respectively. In another word, as compared to the control group samples, the increase in TBA of RAT1 and RAT2 samples was limited by 64.7 and 69.6% , respectively. As stated by Khalafalla, Ali (27), TBA value is evaluated to be an indicator of secondary lipid oxidation products. Therefore, in terms of revealing the lipid oxidation in fish products, it could play a key role. TBA value in fish samples, depending on the increase in storage period, can increase. With the increase of the storage period, the TBA level in C samples rapidly has increased as compared to the samples treated with nanomaterials (RAT1 and RAT2). In this

respect, on the 5th day of the cold storage, TBA values of C, RAT1, and RAT2 samples were defined as 1.12 , 0.4 (64.28% decrease), and $0.175 \text{ mg MDA kg}^{-1}$ (84.37% decrease), respectively ($p < 0.05$). At the end of the cold storage period, the TBA value of C samples reached $2.995 \text{ mg MDA kg}^{-1}$ when the TBA values of RAT1 and RAT2 samples could reach 1.35 and $0.994 \text{ mg MDA kg}^{-1}$. In addition, RA nanoparticles treatments have provided the limitation in the range of 54.92% and 84.37% for 9 days ($p < 0.05$). Roomiani, Ghaeni (28) reported that rosemary essential oils at 0.2% and 0.4% were effective in controlling lipids of fish fillets stored at -18°C for 6 months. Li, Mei (29) reported that the treatment of 1% chitosan coating incorporated with 20 , 30 , or 40 mg/L RA to delay the increase in TBA value of rainbow trout samples was successfully applied. When compared to the previous literature studies, it is seen that nanotechnology applications with 8.10^{-3} g and 16.10^{-3} g provided a big advantage to limit the rapid increase in the TBA value of minced fish products. Because nanomaterials could provide a larger contact area as compared to

microsized materials (5) and they can more successfully limit the penetration of oxygen that may cause the oxidation in fatty fish.

There is a linear correlation between the total phenolic substance amount and total antioxidant, which can be defined by the DPPH method (30). DPPH is one of the organic nitrogen radicals, also RA has phenolic compounds and fish meat has nitrogen, therefore some phenolic compounds could react with DPPH radicals. The amino acid composition, the abundance of free amino acids, peptide size, and solubility may have a key role in defining the DPPH radical scavenging capacity (31-34). The results of the DPPH (%) analysis are presented in Table 2. According to these results, the DPPH values of control group samples ranged from 1.184% to 1.669%. On the other hand, the DPPH values of the minced fish treated with RA nanoparticles rapidly increased as compared to those of the control group samples. On the 1st day of the cold storage, the DPPH value of RAT1 samples (2.843%) was found to be lower than those of the minced salmon samples treated with RAT2 samples (3.757%) ($p < 0.05$). Depending on the increase of the storage period, DPPH values of RAT1 and RAT2 samples highly increased because the release profile of RA may

begin to increase as can be seen from Figure 2. During the storage period, the DPPH value in C samples can increase because of nitrogen compounds, peptide structure in fish meat. However, DPPH values of RAT1 and RAT2 samples can more rapidly increase because they may have an interaction between the phenolic compound and nitrogen compounds in fish meat. Ceylan, Uslu (35) reported that the DPPH activity of the rainbow trout fillets treated with nanoencapsulated *L. reuteri* significantly was increased (up to 100%). Similarly, Hu, Wang (36), and Badawy, Lotfy (37) indicated that chitosan nanoparticles showed an excellent antioxidant effect for the meat samples during refrigerated storage. They also reported that the antioxidant activity significantly reduced with the storage time increase. Morsy, Mekawi (38) claimed that lyophilized pomegranate peel nanoparticles had a high phenolic content and antioxidant capacity. Meral and Köse (39) revealed that there is a good relationship between the total phenolic compounds and antioxidant activity in foods. Moreover, Meral (40) noted that antioxidant activity may be affected by different factors such as food composition, the amount of the food components, the interaction of food components, and technological processes.

Table 2: Oxidation parameters, antioxidant activity, and sensory analysis results of the minced salmon samples treated with nanoparticles and untreated samples.

Storage days	Parameters	Groups		
		C	RAT1	RAT2
1	TBA	0.510±0.000 ^A	0.180±0.000 ^B	0.155±0.000 ^C
	DPPH	1.184±0.335 ^C	2.843±0.191 ^B	3.757±0.430 ^A
	FFA	2.011±0.020 ^A	1.399±0.014 ^B	0.964±0.023 ^C
	SOVS	9.666±0.516 ^A	9.165±0.752 ^A	8.650±1.032 ^A
5	TBA	1.120±0.009 ^A	0.400±0.019 ^B	0.175±0.000 ^C
	DPPH	1.202±0.680 ^C	2.646±0.113 ^B	3.568±0.170 ^A
	FFA	2.507±0.205 ^A	2.029±0.405 ^A	2.101±0.072 ^A
	SOVS	4.660±0.816 ^C	7.500±0.547 ^B	7.600±0.547 ^A
9	TBA	2.995±0.064 ^A	1.350±0.044 ^B	0.994±0.004 ^C
	DPPH	1.669±1.331 ^C	5.282±0.073 ^B	7.112±0.443 ^A
	FFA	4.338±0.390 ^A	2.765±0.076 ^B	2.494±0.153 ^C
	SOVS	1.600±1.032 ^A	3.500±1.366 ^A	2.833±0.410 ^A

A-C Within each row, different superscript lowercase letters show differences between treatment groups for the same analysis group ($p < 0.05$). C: Minced salmon fish samples untreated, RAT1 and RAT2: Salmon fish samples treated with 8.10^{-3} g and 16.10^{-3} g RA nanoparticles, respectively. TBA: mg MDA kg^{-1} , DPPH: %, FFA: %

The Effect of RA Nanoparticles in Free Fatty Acid Levels (FFA)

The results of the FFA analysis are indicated in Table 2. The FFA values in the minced salmon samples (C, RAT1, and RAT2) increased with storage time. The FFA values of C group samples were found to be

higher when compared with those of RAT1 and RAT2 samples. Also, for 9 days, the FFA value of the minced salmon fish samples treated with RAT2 nanoparticles was determined to be lower than that of RAT1 samples. During 9 days, there were also statistical differences among all groups ($p < 0.05$).

Moreover, the initial FFA value of C samples was 2.011%, but at the end of the cold storage, this value reached 4.338% while FFA values of RAT1 and RAT2 samples were found to be 2.765% and 2.494%, respectively. A high-level FFA value can be defined by an undesirable aroma. Fish oil contains a great deal of PUFAs that can easily lead to the initiation of oxidation reactions and the formation of hydroperoxides of fatty acids. Also, bacterial activity plays a key role in the increase of FFA value in fish meat (41, 42). In addition, FFA values are used as a quality indicator of fish oils (43). Bimbo (44) reported that the FFA values of food-grade fish oil were found to be higher at the end of nine days of storage. The recommended FFA value is determined in the range of 1 and 7%. In this respect, as can be seen from the results of the study, nano-application in the present study provided a higher quality for minced salmon samples at 4 °C. In this respect, rosmarinic nanoparticle applications (8.10^{-3} and 16.10^{-3} g) with a larger contact area property successfully limited the rapid increase in the FFA value of fish meat.

The Role of RA Nanoparticles in Sensory Quality

Overall sensory scores of the minced salmon fish samples treated with RA nanoparticles, and without RA nanoparticles samples are shown in Table 2. Once the sensory score of all samples reached the point of minimum acceptability (5) grades, the samples were evaluated to be unfit for human consumption. All sensory attributes of every sample showed a declining trend for 9 days. After 5 days of refrigerated storage, putrid and fishy odor in untreated (C) samples was determined. On the 5th day of the refrigerated storage period, the FFA value of C samples reached 2.507, but, on the 9th day of the refrigerated storage, RAT2 samples could be measured as 2.494. The sensory quality of the samples treated with 8.10^{-3} and 16.10^{-3} g RA nanoparticles delayed the oxidation by four days when compared to the control samples. Tsai, Su (45) defined that the shelf life of salmon loins that were dipped into chitosan solution (1%) could be prolonged by four days as compared to control group samples stored at 4 °C. When compared to the amount of the used substance, in the present study better quality was provided with highly less nanomaterial.

CONCLUSION

The RA-loaded PCL nanoparticles were obtained with 235.8 ± 2.98 nm average particle size. The oxidation in the minced salmon fish samples was effectively limited using RA-loaded PCL nanoparticles for 9 days under cold storage conditions. The rapid changes in TBA, FFA values, and overall sensory score were limited although DPPH values of the minced salmon samples increased with time. Per 100 g minced salmon fish sample, especially, the

use of 8.10^{-3} and 16.10^{-3} g nanoform of RA provided well preservation for the limitation of the rapid increase in the tested oxidation parameters. It was revealed that the high loading and encapsulation efficiency of RA, in this respect especially RAT2 application, had an important effect on the oxidative stability of minced salmon samples. The nano-application presented a larger contact area on the surface of the minced fish. In this sense, the present study revealed that the use of RA in a nanotechnology application could be a promising approach, especially for fatty and minced food products.

CONFLICT OF INTEREST

Authors have no conflict of interest.

REFERENCES

1. Thilsted S, James D, Toppe J, Subasinghe R, Karunasagar I. Maximizing the contribution of fish to human nutrition. In FAO; 2014. <URL>.
2. Altan CO, Turan H. Synergistic Effect of Freezing and Irradiation on Bonito Fish (*Sarda sarda* Bloch, 1793). Journal of Food Protection. 2016 Dec 1;79(12):2136–42. <DOI>.
3. Das P, Ganguly S. Chilling and freezing techniques for fish preservation and maintenance of quality parameters: A Review. Ind J Sci Res and Tech. 2014;2(6):3–5.
4. Khanipour A, Mirzakhani N. Effect of different packaging methods on shelf life of hot smoked rainbow trout (*Oncorhynchus mykiss*) during storage at 0-2°C. Iranian Journal of Fisheries Science. 2013;12(3):620–8. <URL>.
5. Ceylan Z, Sengor GFU, Yilmaz MT. A Novel Approach to Limit Chemical Deterioration of Gilthead Sea Bream (*Sparus aurata*) Fillets: Coating with Electrospun Nanofibers as Characterized by Molecular, Thermal, and Microstructural Properties: Coating with electrospun nanofiber... Journal of Food Science. 2017 May;82(5):1163–70. <DOI>.
6. Özogul Y, Durmus M, Ucar Y, Özogul F, Regenstein JM. Comparative study of nanoemulsions based on commercial oils (sunflower, canola, corn, olive, soybean, and hazelnut oils): Effect on microbial, sensory, and chemical qualities of refrigerated farmed sea bass. Innovative Food Science & Emerging Technologies. 2016 Feb;33:422–30. <DOI>.
7. Osheba A, Sorour M, Abdou E. Effect of chitosan nanoparticles as active coating on chemical quality and oil uptake of fish fingers. Journal of Agriculture and Environmental Sciences. 2013;2(1):1–14.
8. Ceylan Z, Unal Sengor GF, Yilmaz MT. Nanoencapsulation of liquid smoke/thymol combination in chitosan nanofibers to delay microbiological spoilage of sea bass (*Dicentrarchus labrax*) fillets. Journal of Food Engineering. 2018 Jul;229:43–9. <DOI>.
9. Oner B, Meral R, Ceylan Z. Determination of some quality indices of rainbow trout fillets treated with nisin-loaded polyvinylalcohol-based nanofiber and packed with

- polyethylene package. LWT. 2021 Sep;149:111854. [<DOI>](#).
10. Yao Z-C, Chang M-W, Ahmad Z, Li J-S. Encapsulation of rose hip seed oil into fibrous zein films for ambient and on demand food preservation via coaxial electrospinning. Journal of Food Engineering. 2016 Dec;191:115–23. [<DOI>](#).
11. Fabra MJ, López-Rubio A, Lagaron JM. Use of the electrohydrodynamic process to develop active/bioactive bilayer films for food packaging applications. Food Hydrocolloids. 2016 Apr;55:11–8. [<DOI>](#).
12. Castro-Mayorga JL, Fabra MJ, Pourrahimi AM, Olsson RT, Lagaron JM. The impact of zinc oxide particle morphology as an antimicrobial and when incorporated in poly(3-hydroxybutyrate-co-3-hydroxyvalerate) films for food packaging and food contact surfaces applications. Food and Bioprocess Processing. 2017 Jan;101:32–44. [<DOI>](#).
13. Meral R, Alav A, Karakas C, Dertli E, Yilmaz MT, Ceylan Z. Effect of electrospun nisin and curcumin loaded nanomats on the microbial quality, hardness and sensory characteristics of rainbow trout fillet. LWT. 2019 Oct;113:108292. [<DOI>](#).
14. Kutlu N, Meral R, Ekin MM, Erim Kose Y, Ceylan Z. A new application for the valorisation of pomegranate seed oil: nanoencapsulation of pomegranate seed oil into electrospun nanomats for food preservation. Int J of Food Sci Tech. 2022 Feb;57(2):1074–82. [<DOI>](#).
15. Ceylan Z, Kutlu N, Meral R, Ekin MM, Kose YE. Protective effect of grape seed oil-loaded nanofibers: Limitation of microbial growth and lipid oxidation in kashar cheese and fish meat samples. Food Bioscience. 2021 Aug;42:101076. [<DOI>](#).
16. Cetinkaya T, Wijaya W, Altay F, Ceylan Z. Fabrication and characterization of zein nanofibers integrated with gold nanospheres. LWT. 2022 Feb;155:112976. [<DOI>](#).
17. Ceylan Z, Meral R, Karakaş CY, Dertli E, Yilmaz MT. A novel strategy for probiotic bacteria: Ensuring microbial stability of fish fillets using characterized probiotic bacteria-loaded nanofibers. Innovative Food Science & Emerging Technologies. 2018 Aug;48:212–8. [<DOI>](#).
18. Tarladgis BG, Watts BM, Younathan MT, Dugan L. A distillation method for the quantitative determination of malonaldehyde in rancid foods. J Am Oil Chem Soc. 1960 Jan;37(1):44–8. [<DOI>](#).
19. Brand-Williams W, Cuvelier ME, Berset C. Use of a free radical method to evaluate antioxidant activity. LWT - Food Science and Technology. 1995;28(1):25–30. [<DOI>](#).
20. Egan H, Kirk R, Sawyer R, editors. Pearson's Chemical Analysis of Food. In: 8th edition. Sussex, UK: Langnan Scientific and Technical; 1987.
21. Fan W, Sun J, Chen Y, Qiu J, Zhang Y, Chi Y. Effects of chitosan coating on quality and shelf life of silver carp during frozen storage. Food Chemistry. 2009 Jul;115(1):66–70. [<DOI>](#).
22. Merrell JG, McLaughlin SW, Tie L, Laurencin CT, Chen AF, Nair LS. Curcumin-loaded poly(ϵ -caprolactone) nanofibres: Diabetic wound dressing with anti-oxidant and anti-inflammatory properties. Clinical and Experimental Pharmacology and Physiology. 2009 Dec;36(12):1149–56. [<DOI>](#).
23. da Silva SB, Ferreira D, Pintado M, Sarmento B. Chitosan-based nanoparticles for rosmarinic acid ocular delivery—In vitro tests. International Journal of Biological Macromolecules. 2016 Mar;84:112–20. [<DOI>](#).
24. Snehath M, Venugopal K, Saha RN. Etoposide-Loaded PLGA and PCL Nanoparticles I: Preparation and Effect of Formulation Variables. Drug Delivery. 2008 Jan;15(5):267–75. [<DOI>](#).
25. Darwish Y, Abd-Elhakeem M, El-Maksod A, Sabit H, El-Zawahri M. Antitumor Activity of Rosmarinic Acid Encapsulated in Chitosan Nanoparticles. Acad J Cancer Res. 2018;11:1–8.
26. Zhao R, Li X, Sun B, Zhang Y, Zhang D, Tang Z, et al. Electrospun chitosan/sericin composite nanofibers with antibacterial property as potential wound dressings. International Journal of Biological Macromolecules. 2014 Jul;68:92–7. [<DOI>](#).
27. Khalafalla FA, Ali FHM, Hassan A-RHA. Quality improvement and shelf-life extension of refrigerated Nile tilapia (*Oreochromis niloticus*) fillets using natural herbs. Beni-Suef University Journal of Basic and Applied Sciences. 2015 Mar;4(1):33–40. [<DOI>](#).
28. Roomiani L, Ghaeni M, Moarref M, Fallahi R, Lakzaie F. The effects of Rosmarinus officinalis essential oil on the quality changes and fatty acids of *Ctenopharyngodon idella*. Iranian Journal of Fisheries Sciences [Internet]. 2018 [<DOI>](#)
29. Li N, Mei J, Shen Y, Xie J. Quality improvement of half-smooth tongue sole (*Cynoglossus Semilaevis*) fillets by chitosan coatings containing rosmarinic acid during storage. CyTA - Journal of Food. 2018 Jan;16(1):1018–29. [<DOI>](#).
30. Huang D, Ou B, Prior RL. The Chemistry behind Antioxidant Capacity Assays. J Agric Food Chem. 2005 Mar 1;53(6):1841–56. [<DOI>](#).
31. Ndhala A, Moyo M, Van Staden J. Natural Antioxidants: Fascinating or Mythical Biomolecules? Molecules. 2010 Oct 8;15(10):6905–30. [<DOI>](#).
32. Ryan JT, Ross RP, Bolton D, Fitzgerald GF, Stanton C. Bioactive Peptides from Muscle Sources: Meat and Fish. Nutrients. 2011 Aug 31;3(9):765–91. [<DOI>](#).
33. Samadi B, Ismail A. Antioxidative peptides from food Peptides Review. Peptides. 2010;31(10):1949–56.
34. Samaranyaka AGP, Li-Chan ECY. Food-derived peptidic antioxidants: A review of their production, assessment, and potential applications. Journal of Functional Foods. 2011 Oct;3(4):229–54. [<DOI>](#).
35. Ceylan Z, Uslu E, İspirli H, Meral R, Gavgalı M, Yilmaz MT, et al. A novel perspective for *Lactobacillus reuteri*: Nanoencapsulation to obtain functional fish fillets. LWT. 2019 Nov;115:108427. [<DOI>](#).

36. Hu J, Wang X, Xiao Z, Bi W. Effect of chitosan nanoparticles loaded with cinnamon essential oil on the quality of chilled pork. *LWT - Food Science and Technology*. 2015 Sep;63(1):519–26. [<DOI>](#).
37. Badawy MEI, Lotfy TMR, Shawir SMS. Facile synthesis and characterizations of antibacterial and antioxidant of chitosan monoterpene nanoparticles and their applications in preserving minced meat. *International Journal of Biological Macromolecules*. 2020 Aug;156:127–36. [<DOI>](#).
38. Morsy MK, Mekawi E, Elsabagh R. Impact of pomegranate peel nanoparticles on quality attributes of meatballs during refrigerated storage. *LWT*. 2018 Mar;89:489–95. [<DOI>](#).
39. Meral R, Köse YE. The effect of bread-making process on the antioxidant activity and phenolic profile of enriched breads. *Quality Assurance and Safety of Crops & Foods*. 2019 Apr 9;11(2):171–81. [<DOI>](#).
40. Meral R. The effect of different temperatures on antioxidant activity and phenolic profile of the Rheum ribes. *YYU Journal of Agricultural Science*. 2017;27:88–94.
41. Ježek F, Buchtová H. Monitoring of Physicochemical Changes in Frozen Fish Muscle Tissue. *Agriculturae Conspectus Scientificus*. 2011;76(3):201–4. [<URL>](#).
42. Milijašević M, Milijašević JB, Djinović-Stojanović J, Moračanin SV, Lilić S. Changes of pH and peroxide value in carp (*Cyprinus carpio*) cuts packaged in modified atmosphere. *IOP Conference Series: Earth and Environmental Science*. 2017 Sep;85:012041. [<DOI>](#).
43. Wu TH, Bechtel PJ. Salmon by-product storage and oil extraction. *Food Chemistry*. 2008 Dec 15;111(4):868–71. [<DOI>](#).
44. Bimbo AP. Guidelines for characterizing food-grade fish oils. *Inform [Internet]*. 1998;9(5). Available from: [<URL>](#).
45. Tsai G-J, Su W-H, Chen H-C, Pan C-L. Antimicrobial activity of shrimp chitin and chitosan from different treatments and applications of fish preservation. *Fisheries Sci*. 2002 Feb;68(1):170–7. [<DOI>](#).



Exposure Analysis at the Territory of Nevşehir (Cappadocia) due to Additive Gamma-rays in Air, Turkey

Muttalip Ergun TURGAY¹, Merve CİCEKFİDAN², Nursel SEZGİN³

¹Yalova University, Yalova, Turkey

²Yildiz Technical University, İstanbul, Turkey

³Van Yuzuncu Yil University, Van, Turkey

Abstract: Radioactivity measurements for water, soil, and air have been completed in national and international regions. The radioactivity process is randomized and occurs naturally by primordial nuclides. Another case is hand-made reactions which realized by artificial reactions. The high rate of the total dose of radiation, whichever is exposed to humans, originates as Natural Radioactivity. In this case, environmental radioactivity measurements are important to investigate the background radiation level, especially for primordial radioactive sources. This radiation which measured outdoor gamma dose includes both cosmic rays and terrestrial elements. Terrestrial radiation can be measured via gamma-ray spectroscopy separately. By the way, cosmic effects would be calculated by subtracting terrestrial from measured outdoor gamma dose. Scientific Committee (UNSCEAR, 2000) declares the annual dose for humans as 2.4 mSv. The radionuclides present in soil samples (terrestrial components) are considered responsible for a portion of this amount (1). Rest amounts are originated water (2) and air, too.

Submitted: March 04, 2021. **Accepted:** February 08, 2022.

Cite this: Turgay M, Cicekfidan M, Sezgin N. Exposure Analysis at the Territory of Nevşehir (Cappadocia) due to Additive Gamma-rays in Air, Turkey. JOTCSA. 2022;9(2):321-30.

DOI: <https://doi.org/10.18596/jotcsa.891062>.

***Corresponding author. E-mail:** eturgay20@hotmail.com.

INTRODUCTION

Literature Survey

Over the past two decades, a few results about radioactivity levels have been published in some papers related to gamma dose rates in the air for Turkish provinces (3-14). There is no study specifically for the Nevşehir region in the literature. Therefore, the purpose of our effort is to measure dose rates in the air from different locations throughout the city and, in this way, to determine the cancer risk. The human population in this city is up to one million, and this study will be the baseline for subsequent studies about environmental radioactivity measurements. By the way, there are also stated worldwide studies in the literature. For example, Licínio MV and friends have evaluated in 2013 for Brazil (15). Another study by Ghiassi-Nejad and Mortavazi in 2002 indicates the absorbed dose rates in air (ADRA) values concerning the Ramsar region of Persia. They studied the effects of radiation on human life. The annual dose was also calculated (260 mSv), and found higher than the

stipulated annual limit of 20 mSv in North Persia. Cytogenetic studies show no significant differences between people in the high background compared to people in normal background areas (16). The third study with Arnedo MA and coworkers reported the natural radioactivity of soils in the eastern Canary islands (17).

MATERIAL AND METHODS

Airborne Radiation and its Reading

Airborne radioactivity could be assigned on the spectrum on the spectrum peaks' one by one, showing the related nuclides. Radionuclides will very rapidly appear in ground-level air, and air samples can give the first indication on the nature of the contamination. Radioactive elements in the air could reduce due to human inhalation. Gamma dose rates were measured using a counter (reader: Eberline, ESP-2) as a mobile device and connected to the detector as a SPA-6 model plastic scintillator. The instrument was kept up to 1 m from the soil surface, and at the sampling point, the

measurement duration was 60 seconds. Then the average dose rates were recorded. The main instrument is ESP-2.

The detector is connected through a coaxial type MHV series. The readout function has been shown in 2×16 alphanumeric display-LCD. This ratemeter is operated by the CPU@ Intel_80C31 processor family and has external RAM- 8 KB and EPROM is 16 KB. The scintillation detector body, SPA-6, which is connected to the counter (ESP-2), was selected to optimize its output for the radiation of interest. It provides the pulse signal to the electronics in order

to the readout. On the detector side, the pulse rate is proportional to the intensity of radiation. The high voltage supply offers the required bias potential to the detector. This voltage is keyboard adjustable, and it controls the correct operating voltages for different detectors. The low voltage supply regulates the operating voltage for the ESP-2 electronics, as shown in Figure 1 (18). The amplifier is linear and amplifies the probe's signal to a functional level at the amplifier output. The discriminator provides a signal on its output only if the amplifier's signal exceeds the adjustable threshold. It provides rejecting for noise and unwanted signal.



Figure 1: ESP-2 Rate meter and SPA-6 scintillation detector, Eberline (18).

Measuring Area

Cappadocia (Nevşehir), one of Turkey's central regions, is a neighbor to the capital city of Ankara. Its coordinates are between 38.154 to 38.9428 N as latitude and 34.1747 to 34.9038 E as longitude. The highest point is Ercas (1982 m), and other points are Hodul (1949 m) and Kızıldağ (1768 m). The province of Nevşehir is surrounded by 18% mountain, 25% plain, 57% plateau, and hillside. The province was settled on the west side of a large plateau formed by ash and volcanoes, in the Anatolian span. River Kızılırmak is separated into two all city of Nevşehir. The climate is terrestrial, like cold-dry winters and hot, dry summers. The region's area is 5467 km² (19), and its population is 0.16 million (19). Nevşehir's map is shown in Figure 2.

RESULTS

Outdoor Dose Rates as Additive (Terrestrial and Cosmic Ray Effects)

Absorbed gamma doses are originated from terrestrial and cosmic rays together. In order to obtain the absorbed gamma dose rates in the air, the instrument was kept about 1 meter upperside from ground level. It is important to know how much exposure in the air to human gonads is about this level. The human gonad is the most vulnerable organ to radiation damage. Annual doses in the air were also calculated by using the gamma dose rates. In this case, measurements were perfected for a total of 45 different points. Dose rate map was shown in Figure 3.

Table 1: Dose rates, coordinates, and altitudes of Cappadocia's sampling points.

Name of measuring district	Dose Rate [nGy h⁻¹]	Latitude (pointed)	Longitude (pointed)	Altitude (meter)
Ihlara Valley	192.06	38.1540	34.1747	1180
Derinkuyu1	157.14	38.3735	34.7354	1350
Derinkuyu2	165.87	38.3737	34.7344	1350
Uçhisar1 (center)	200.79	38.6205	34.8049	1340
Uçhisar2 (center)	192.06	38.6314	34.7972	1310
Uçhisar3 (center)	165.87	38.6291	34.8070	1300
Paşabağları (Ürgüp)	192.06	38.6773	34.8560	1020
Çavuşin (Avanos)	183.33	38.6767	34.8575	1050
Göreme1 (center)	130.95	38.7274	34.8214	940
Göreme (Open air museum1)	165.87	38.6386	34.8451	1140
Göreme (Open air museum2)	192.06	38.6384	34.8453	1140
Göreme (Open air museum3)	183.33	38.6385	34.8455	1150
Göreme (Open air museum4)	200.79	38.6382	34.8457	1140
Göreme (Open air museum5)	192.06	38.6384	34.8458	1150
Göreme (Open air museum6)	226.98	38.6389	34.8461	1140
Göreme (Open air museum7)	139.68	38.6432	34.8366	1130
Göreme (Open air museum8)	157.14	38.6403	34.8450	1120
Göreme (Open air museum9)	192.06	38.6411	34.8440	1100
Göreme (Open air museum10)	174.60	38.6397	34.8448	1130
Cappadocia (central1)	174.60	38.6288	34.7158	1190
Cappadocia (central2)	183.33	38.6289	34.7228	1190
Cappadocia (central3)	392.85	38.6282	34.7240	1200
Cappadocia (central4)	157.14	38.6281	34.7245	1200
Cappadocia (central5)	192.06	38.6277	34.7256	1210
Cappadocia (central6)	200.79	38.6280	34.7264	1210
Cappadocia (central7)	174.60	38.6282	34.7268	1210
Cappadocia (central8)	157.14	38.6278	34.7271	1220
Cappadocia (central9)	139.68	38.6279	34.7275	1220
Cappadocia (central10)	200.79	38.6278	34.7281	1230
Cappadocia (central11)	139.68	38.6274	34.7281	1230
Cappadocia (central12)	158.89	38.6279	34.7273	1230
Cappadocia (central13)	185.08	38.6275	34.7264	1220
Cappadocia (central14)	107.38	38.6265	34.7250	1210
Cappadocia (central15)	139.68	38.6276	34.7241	1210
Cappadocia (central16)	200.79	38.6278	34.7223	1190
Cappadocia (central17)	157.14	38.6271	34.7203	1190
Avanos1	192.06	38.6876	34.8329	950
Avanos2	148.41	38.7017	34.8417	950
Avanos3	134.44	38.7013	34.8421	930
Avanos4	192.06	38.7027	34.8403	950
Ürgüp (Üç Güzeller)	165.87	38.6411	34.8440	1170
Ürgüp (Turasan1)	157.14	38.6329	34.9038	1130
Ürgüp (Turasan2)	183.33	38.6373	34.8446	1130
Ortahisar (Derbent)	192.06	38.6725	34.8855	1070
Hacıbektaş	209.52	38.9428	34.5625	1300
Nevşehir (45)	178.69 nGy/h	Average value of ADRA		

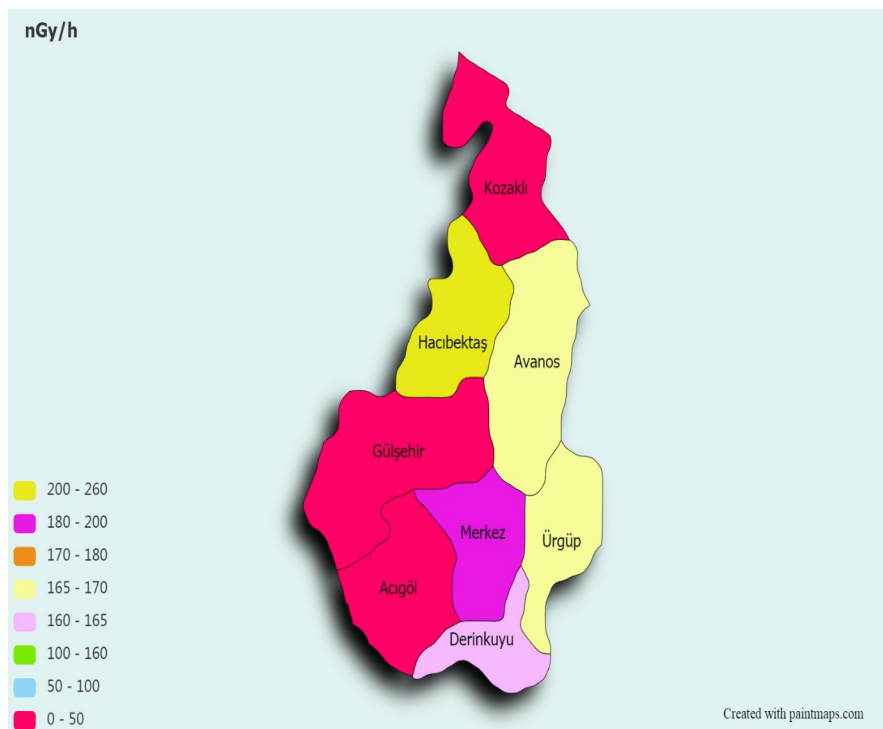


Figure 3: Outdoor Gamma Dose Rate map for Cappadocia district (Nevşehir)(21).

Calculations

Annual Effective Dose Equivalent (AEDE) and Excess Lifetime Cancer Risk (ELCR) were calculated in the literature using ADRA (1):

$$AEDE = ADRA * DCF * OF * T \quad (Eq. 1)$$

$$ELCR = AEDE * DL * RF \quad (Eq. 2)$$

DCF signs the dose conversion factor (0.7 Sv Gy^{-1}), OF is outdoor occupancy factor (0.2), T is the

exposure time (8760 h y^{-1}). DL is the duration of life (70 years), RF is a risk factor (Sv^{-1}) as fatal cancer risk per Sv [calculate to stochastic effects; ICRP 60 (22)] uses the value of 0.05 for the public (ICRP, 2007).

ADRA values were handled from Table 1 and applied upper formulas. Calculated values for AEDE and also ELCR are shown in Table 2 with average altitudes as regionally.

Table 2: AEDE and ELCR values for Cappadocia.

Name of measuring district [number of m. point]	Av. ADRA [nGy h ⁻¹]	Av. AEDE [μSv]	Av. ELCR [(x10 ⁻⁴)]	Av. Altitude (meter)
Ihlara Valley [1]	192.06	235.47	8.24	1180
Derinkuyu [2]	161.51	198.01	6.93	1350
Uçhisar [3]	186.24	228.33	7.99	1316
Paşabağları [1]	192.06	235.47	8.24	1020
Çavuşin [1]	183.33	224.76	7.87	1050
Göreme [11]	177.78	217.96	7.63	1116
Cappadocia- central [17]	180.10	220.80	7.73	1209
Avanos [4]	166.74	204.42	7.16	945
Ürgüp [3]	168.78	206.92	7.24	1143
Ortahisar [1]	192.06	235.47	8.24	1070
Hacibektaş [1]	209.52	256.87	8.99	1300
Nevşehir [45]	178.69	219.07	7.67	1162

The frequency distribution of annual gamma doses is shown in the figure below (4.a.) by the related linear fitting curve and its R² equation. Another

graphic (figure 4.b) shows the ELCR values with a logarithmic curve and its R² equation.

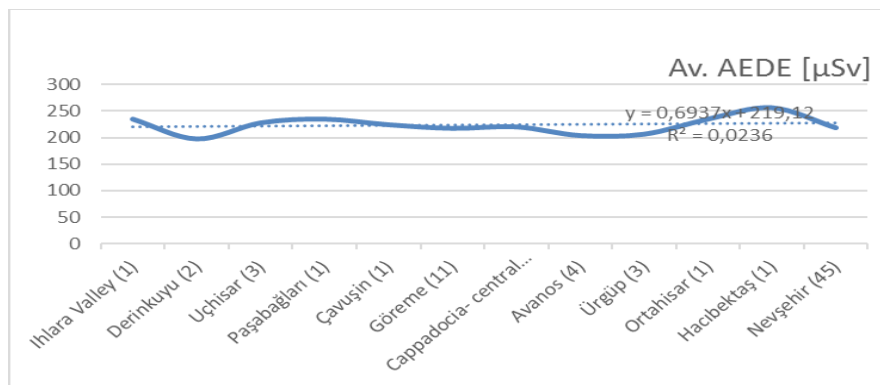


Figure 4.a.: Frequency Distribution of AEDE for Cappadocia (Nevşehir) district.

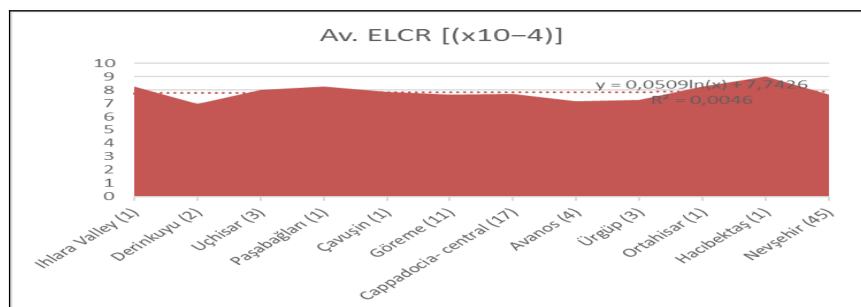


Figure 4.b.: Frequency Distribution of ELCR for Cappadocia (Nevşehir) district.

Statistics

Standard deviations

Using the group data such as AEDE and ELCR values of districts (Table 2), it is easy to calculate standard deviations. The standard deviation of AEDE is 10.31

and for ELCR is 0.36. The deviation rate is not as low as 4.7% for both AEDE and ELCR values. annual critical values are $219.07 \pm 10.31 \mu\text{Sv}$ and $7.67 \pm 0.36 (x10^{-4})$. Related bar charts are shown in Figure 5.

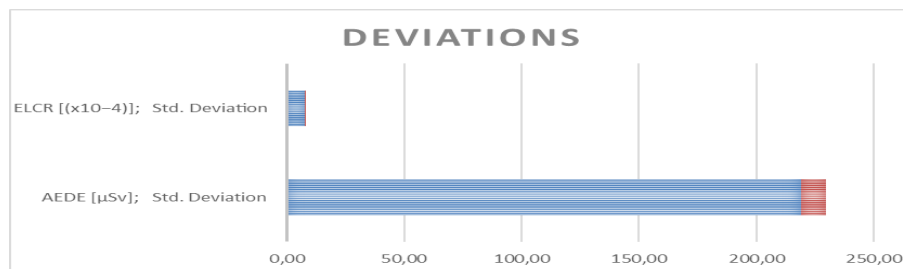


Figure 5: Bar chart for both AEDE and ELCR values and their deviations.

Comparison with literature

The data in Table 4 pertain to the Figure 6 distribution of Excess Life Time Cancer Risk

corresponding to the Annual Effective Dose Equivalent.

Table 4: Comparison for AEDE and ELCR values regarding gamma dose rates.

(ref no), Region, [nm of samplings]	(AEDE) [μSv], average	ELCR [(x10 ⁻⁴), average	Reference
(02) Hatay [39]	7.50 (only alpha)	0.26	(2)
(03) Adana	82.00	2.87	(3)
(04) Ankara [341]	71.83	2.69	(4)
(05) Artvin [204]	214.50	7.50	(5)

(06) Balıkesir [92]	156.30	6.30	(6)
(07) Bolu [74]	27.23	0.95	(7)
(08) Çanakkale [379]	81.40	2.85	(8)
(09) Edirne [14]	47.30	1.66	(9)
Kocaeli [35]	29.31	1.02	(np)
Hatay [215]	63.93	2.24	(np)
(10) IDA [75]	198.66	6.95	(10)
(11) İstanbul [105]	79.72	2.79	(11)
(12) Kastamonu [60]	58.88	2.06	(12)
(13) Şanlıurfa	74.70	2.62	(13)
(14) Van	142.59	4.99	(14)
This work [45]	219.07	7.67	(tw)
(23) Nevşehir [RESA]	306.50	10.73	(23)
(1) World	73.60	2.58	(1)
(15) R. D. J.- Brazil	90.00	3.15	(15)
(16) Ramsar- IRAN	105.00	3.68	(16)
(17) Canary I- Spain	91.95	3.22	(17)

(np): Not published yet. (tw): This work.

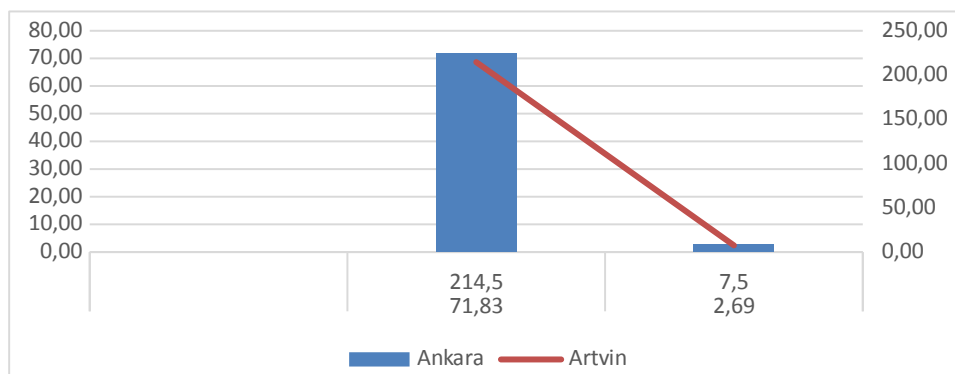


Figure 6: Graphical distribution of AEDE and ELCR [µSv; x10⁻⁴].

Comparison to RESA

TAEK, the Turkish Atomic Energy Agency, periodically measures the natural radiation in the air by RESA (23) system, consisting of a Geiger

detector and reader. Due to this system's locations, there is one measuring point referenced as the central county of Nevşehir province. Below pictures are referred the RESA system in Figure 7.



Figure 7: RESA; detector- counter and control center, TAEK (23).

RESA's online value was 175 nSv h⁻¹, which corresponds to 250 nGy h⁻¹. This dose rate indicates to AEDE value of 306.50 (µSv) and ELCR value as

8.75 (x10⁻⁴). The average of our measurements is 178.69 nGy h⁻¹. Due to our measurements, the minimum rate was 107.38, and the maximum rate

was 392.85 nGy⁻¹. There are a few possible reasons due to this difference. There are a few possible reasons for this difference. One of them is that our measurements are not for only one fixed point on the RESA system. Another reason could be

the measurement times. Our measurements are not conducted periodically as well as RESA's. Annual doses and cancer risks were compared by the below figure, too.

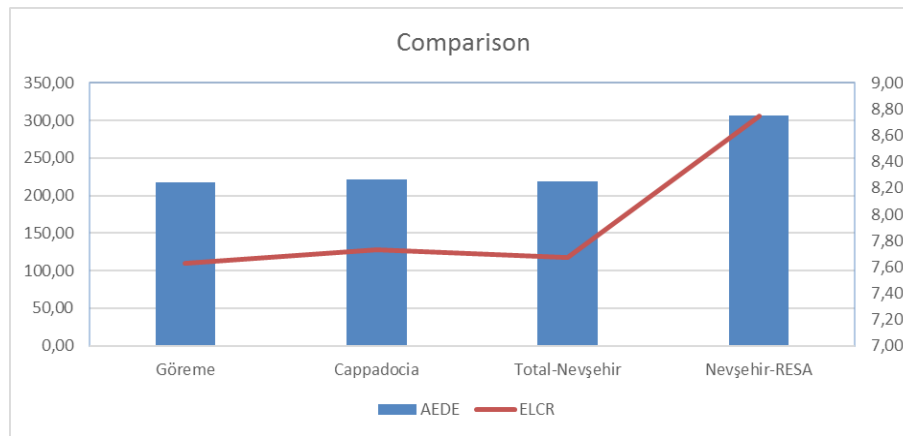


Figure 8: Horizontal Bar chart and line graphic [AEDE in μSv; ELCR, x10⁻⁴]

CONCLUSION

Due to the measurement results, minimum, maximum, and average dose rates in Cappadocia are 107.38, 392.85, and 180.10 nGy/h, respectively. For the other touristic destinations, namely Avanos and Ürgüp, average dose rates are so close to each other as 166.74 to 168.78 nGy/h, respectively. For Hacıbektaş county, in which the minimum population of Nevşehir lives, the dose rate is 209.52 nGy/h. The average dose rate of Nevşehir is 178.69 nGy/h, and this rate refers to 219.07 μSv as the annual dose. It also refers to 7.67 (x10⁻⁴) as a cancer risk. These values are a little higher than Artvin's values. They also refer to values three times higher than the world's references. Nevşehir is a well known tourist county without sea-sand-sun trio, so gamma-radiation levels are important for visitors as well. Nevşehir is in the middle of Anatolia, especially the north-south axis. Existing nuclear power reactor buildings in Mersin are less than 300 km away, and it is important to get setting parameters to compare after a possible radioactive fallout. The present study findings' serve as a reference for future studies.

REFERENCES

1. UNSCEAR. Report of the United Nations scientific committee on the effects of atomic radiation, sources, effects, and risks of ionizing radiation [Internet]. 2008 [cited 2022 Feb 14]. Available from: <https://www.unscear.org>
2. Turgay ME, Yazici AN, Taskin H, Kam E, Karahan G. Assessment of gross α and β radioactivity for drinking water in Hatay province, Turkey. *Desalination and Water Treatment*. 2016 Mar 2;57(11):4960–5.
3. Değerlier M. Annual Effective Dose of Natural Environmental Radioactivity Measurements for Adana region [PhD Thesis]. [Adana]: Çukurova University; 2007.
4. Turgay ME, Yazici AN, Taskin H, Kam E, Karahan G. Assessment of gross α and β radioactivity for drinking water in Hatay province, Turkey. *Desalination and Water Treatment*. 2016 Mar 2;57(11):4960–5.
5. Kobya Y, Taşkın H, Yeşilkanat CM, Çevik U. Evaluation of Outdoor Gamma Dose Rate and Cancer Risk in Artvin Province, Turkey. *Human and Ecological Risk Assessment: An International Journal*. 2015 Nov 17;21(8):2077–85.
6. Kapdan E, Varinlioglu A, Karahan G. Outdoor radioactivity and health risks in Balıkesir, northwestern Turkey. *Radiation Protection Dosimetry*. 2012 Feb 1;148(3):301–9.
7. Ateş NZ, Bayrak K, Turgay ME, Kam E. Evaluation of Excess Lifetime Cancer Risk Caused by External Exposure due to Natural Radioactivity in Bolu, Turkey. *Sigma Journal of Engineering and Natural Sciences*. 2020;38(2):945–54.
8. Kam E, Bozkurt A, Ilgar R. A study of background radioactivity level for Canakkale, Turkey. *Environ Monit Assess*. 2010 Sep;168(1–4):685–90.
9. Yümün ZÜ, Bayrak K, Aksoy H, Ayseli U. A Study of Background Radioactivity Level for Edirne, Turkey. *Journal of Engineering Technology and Applied Sciences*. 2018 Aug 30;3(2):135–9.
10. Turgay ME. Cancer Risk Determination for IDA villages by using Annual Gamma Doses in Air, around Edremit&Ayvack Districts;

Balikesir&Çanakale, TURKEY. European Journal of Science and Technology. 2019 Mar 31;433-9.

11. Karahan G, Bayulken A. Assessment of gamma dose rates around Istanbul (Turkey). Journal of Environmental Radioactivity. 2000 Jan;47(2):213-21.

12. Kam E, Bozkurt A. Environmental radioactivity measurements in Kastamonu region of northern Turkey. Applied Radiation and Isotopes. 2007 Apr;65(4):440-4.

13. Bozkurt A, Yorulmaz N, Kam E, Karahan G, Osmanlioglu AE. Assessment of environmental radioactivity for Sanliurfa region of southeastern Turkey. Radiation Measurements. 2007 Sep;42(8):1387-91.

14. Akan Z, Baskurt B, Asliyukse H, Kam E, Yilmaz A, Yuksel MB, et al. Environmental Radioactivity and High Incidence Rates of Stomach and Esophagus Cancer in the Van Lake Region: A Causal Relationship? Asian Pacific Journal of Cancer Prevention. 2014 Jan 15;15(1):375-80.

15. Licínio MV, Freitas AC, Evangelista H, Costa-Gonçalves A, Miranda M, Alencar AS. A high spatial resolution outdoor dose rate map of the Rio de Janeiro city, Brasil, risk assessment and urbanization effects. Journal of Environmental Radioactivity. 2013 Dec;126:32-9.

16. Ghiassi-nejad M, Mortazavi SMJ, Cameron JR, Niroomand-rad A, Karam PA. Very High Background Radiation Areas Of Ramsar, Iran: Preliminary Biological Studies. Health Physics [Internet]. 2002;82(1). <URL>.

17. Arnedo MA, Rubiano JG, Alonso H, Tejera A, González A, González J, et al. Mapping natural radioactivity of soils in the eastern Canary Islands. Journal of Environmental Radioactivity. 2017 Jan;166:242-58.

18. Eberline. Eberline esp2 technical manual [Internet]. <URL>.

19. Governorship of Nevşehir. 2020.

20. Kapadokya Rehberli Turlar. Kapadokya Rehberli Turlar [Internet]. [cited 2022 Feb 14]. <URL>.

21. Paintmaps.com. COLOR MAPs with STATISTICAL DATA. [Internet]. 2014 [cited 2022 Feb 14]. <URL>.

22. ICRP. Publication 103 recommendations of the ICRP: annals of the ICRP volume 37/2-4. Pergamon Press; 2007.

23. TAEK. Radiation Measurement Systems (RESA).



Angiotensin(1-7)-Stearic Acid Conjugate: Synthesis and Characterization

Tayfun ACAR^{1*} , Burcu UCAR^{1*} 

¹Yildiz Technical University, Faculty of Chemistry and Metallurgy Engineering, Department of Bioengineering, Istanbul, 34220, Turkey

Abstract: The novel coronavirus, SARS-CoV-2, broken out as the COVID-19 epidemic, is transported into the cytoplasm by angiotensin-converting enzyme-2 (ACE2), a key protein of the renin-angiotensin-system (RAS). ACE2 is a protective protein that reduces angiotensin (Ang) II, the bioactive component of RAS, by converting it to its potent antagonist, Ang-(1-7) peptide, in order to provide a pathophysiological response to stimuli. Although ACE-2 is upregulated especially in pulmonary endothelial cells and alveolar epithelial cells, downregulation of ACE-2 in the lung owing to loss of key regulatory factors explains the enzyme-dependent lethality of SARS-CoV-2. The N-terminal domain (NTD) of S1, one of the protein subunits of coronaviruses, is known to recognize acetylated sialic acids on glycosylated cell surface receptors. In this study, the stearic acid-peptide conjugate mimicking the sialic acid structure was synthesized, which will be able to balance uncontrolled inflammatory response and excessive cytokine production, and depending on these to suppress pneumonia and acute respiratory distress syndrome (ARDS), against SARS-CoV-2. It was expected that fatty acid acylation would greatly enhance cellular internalization and cytosolic distribution of the peptide through the cell membrane. Thus, we synthesized fatty acyl derivative of the N-Ac-Gly₄-Ang (1-7) peptide. The peptide was synthesized using Fmoc/tBu solid-phase peptide chemistry and characterized by FT-IR, Zetasizer, and LC-ESI-MS. This study provided more detailed insights into understanding and meeting the basic structural requirements for optimal cellular delivery and formulation of the stearyl Ang (1-7)-peptide conjugate.

Keywords: COVID-19, solid phase peptide synthesis, angiotensin (1-7), stearic acid, conjugation.

Submitted: December 13, 2021. **Accepted:** February 12, 2022.

Cite this: Acar T, Ucar B. Angiotensin(1-7)-Stearic Acid Conjugate: Synthesis and Characterization. JOTCSA. 2022;9(2):331-8.

DOI: <https://doi.org/10.18596/jotcsa.1032642>.

***Corresponding authors. E-mails:** acrtafun@gmail.com, brccr87@gmail.com

INTRODUCTION

Coronaviruses (CoVs), classified within the family *Coronaviridae*, subfamily *Orthocoronavirinae*, are positive-sense single-stranded, enveloped viruses that are found in birds and mammals, prone to crossover between host species. Four different genera have been identified: Alpha, Beta, Gamma, and Delta coronavirus. CoVs, which can cause disease by transmitting from animals to humans, pose a constant threat to public health. Deadly respiratory coronaviruses have emerged three times in this century. While one of them, SARS, emerged towards the end of 2002 and disappeared by 2004,

the second one, MERS, emerged in 2012. Lastly, COVID-19, which broke out on 31 December 2019 and still continues, was characterized as an epidemic (pandemic) by WHO on 11 March 2020 (1-3).

As comprehensive genetic researches covering COVID-19, the virus is phylogenetically related to SARS-like bat viruses. For this reason, bats can be estimated as a potential principal reservoir. Although the intermediate source and source of transfer to humans is unknown, person-to-person rapid virus transmission has been approved. The transmission occurs mainly through direct contact or

through droplets emitted from an infected person as a result of coughing or sneezing (4, 5).

CoVs have positive polarity, single-stranded enveloped RNA viruses (6). The key viral proteins are membrane glycoprotein (M), nucleocapsid protein (N), and spike glycoprotein (S). SARS-CoV-2 diverges from past CoVs by encoding an additional glycoprotein with acetyl esterase and hemagglutination (HE) features (7). Most of the drug and vaccine investigation studies against COVID-19 seem to target spike protein. The spike protein comprises two subunits, S1 and S2, which are responsible for the replication of the virus. The RBD (receptor binding domain) of the S1 subunit interacts with ACE2 followed by the S2 subunit mediating the fusion between virus and host cell membranes, allowing viral RNA to be transported into the cytoplasm (6). CoVs typically have two domains within S1 that can bind to host receptors, an amino (N)-terminal domain (NTD) and a carboxy (C)-terminal domain (CTD) (8, 9). Acetylated sialic acids on glycosylated cell surface receptors are recognized by S1 NTD (10). A docking study showed that resembling sialic acid, peptides mimicking the sialic acid structure are recognized by the receptor-binding site in Hemagglutinin (11). Therefore, it is important to modify the molecules to be developed with sialic acid or to combine them with structures that can mimic sialic acid.

The novel coronavirus that caused the COVID-19 epidemic enters human cells by binding to ACE2 like the SARS coronavirus (12). ACE2 is a protective protein of the RAS that converts angiotensin (Ang) II, the biologically active basic peptide of the RAS, to its physiological antagonist, Ang-(1-7). The binding of SARS-CoV-2 to the ACE2 catalytic site decreases ACE2 expression, resulting in an increase in Ang II (12). Although ACE-2 is upregulated especially in pulmonary endothelial cells and alveolar epithelial cells, downregulation of ACE-2 in the lung due to loss of key regulatory factors explains the enzyme-dependent lethality of SARS-CoV-2 (13, 14).

Ang-(1-7) inhibits alveolar type II cell apoptosis against the damage caused by the virus in its progression to the brain, and reduces the activation of endothelial cells lining blood vessels. Thus, it reduces the loss of blood-brain barrier function and edema. Ang-(1-7) plays a crucial role in protecting against the development of pulmonary inflammation and idiopathic pulmonary fibrosis (IPF) in the course of very severe recurrent illness. Pneumonia and ARDS in the illness are accompanied by an uncontrolled inflammatory response and excessive cytokine production due to immune response dysregulation caused by the virus. This heptapeptide balances the uncontrolled release and synthesis of proinflammatory and profibrotic cytokines due to epithelial damage (13).

In this study, it was suggested that the increase of Ang-(1-7) concentration during viral infection may be vital for protection from endothelial cellular activation and pulmonary damage. Among other strategies, the use of Ang-(1-7) or one of its mimetics was considered a promising step to prevent damage and reduce the severity of COVID-19 infection in high-risk patients.

Bioconjugation is a chemical method used to bring two molecules, at least one of which is a biomolecule (peptide, protein, etc.), together with a covalent bond. Bioconjugation is a tool at the interface between chemistry and biology. Bioconjugation reactions are critical in the modification of peptides. Due to recent advances in the study of biomolecules, peptides can be designed to perform a variety of functions such as cellular monitoring, imaging, and target drug delivery (15-20).

Because of the reasons mentioned above, Ang-(1-7) peptide was studied and the peptide was modified. During peptide synthesis, the N-terminal end of the sequence was acetylated to form a sialic acid-like structure. The sialic acid mimic peptide was obtained by binding the peptide with stearic acid from the side chain. In this way, it is aimed to see a dual effect for the fight against the virus. In a study similar to this hypothesis, stearic acid-peptide conjugates (N-Stearoyl Peptides) that can mimic sialic acid have been developed for influenza virus-caused disease. (11, 21, 22). In summary, we designed and synthesized a novel Ang-(1-7) peptidomimetic against COVID-19 via N-terminal acetylation modification, and conjugation with stearic acid.

MATERIAL AND METHODS

All L-amino acids, HCTU (o-(1H-6-chlorobenzotriazole-1-yl)-1,1,3,3-tetramethyluronium hexafluorophosphate), HOBt.H₂O (1-hydroxybenzotriazole hydrate), Wang resin LL, EDC (1-ethyl-3-(3-dimethylaminopropyl)carbodiimide hydrochloride), stearic acid as well as organic solvents such as DMF, DCM, ACN, etc. were commercially available from Sigma Aldrich (St. Louis) in the USA. Ultra-pure water was supplied from a Millipore Milli-Q system. Molecules were drawn using *ChemDraw Ultra 12.0*.

The FT-IR spectra were obtained from Thermo Scientific Nicolet iS10 in ATR mode. Analyses were performed at room temperature in the wavenumber range of 4,000-650 cm⁻¹ with a resolution of 4 cm⁻¹, and out of 32 scans. The background spectrum was obtained at ambient atmosphere before sample analysis (23).

The absorption spectra of each sample were monitored with a Shimadzu-2600 UV spectrophotometer within the wavelength range of 190-800 nm at 25 ± 1 °C (23).

LC-MS system with electrospray ionization (ESI) probe was used as the chromatographic system. 75 μ L sample was injected into Shim-Pack MRC-ODS-C18 LC column (25 cm X 6 mm). The wavelength of the PDA detector was set to 210 and 280 nm. RP-HPLC analysis was carried out at room temperature. A gradient was applied from eluent A (dH₂O, 0.1% (v/v) FA) to eluent B (ACN, 0.1% (v/v) FA). The flow rate of the eluent was 0.6 mL/min. The ESI was operated in positive ion mode in the 200-1500 m/z range. The capillary temperature was kept at 250 °C. The flow rate of the nebulizer gas (N₂) was set at 1.5 L/min (24, 25).

The mean size and zeta potential of the samples were determined by Zetasizer Nano ZS (Malvern). Samples were dissolved in PBS (pH 7.2). Samples were diluted to 1:2 for the analysis and injected into a disposable capillary cell DTS1070 (Malvern Instruments, MA) and loaded onto the analyzer. Measurements were performed at 25 ± 1 °C with a material refraction index of 1.33, and viscosity of 0.8872 cp. All measurements were performed in triplicate (26).

Peptide Synthesis and Characterization

Angiotensin (1-7) peptide with four glycine amino acids added to its N-terminal was synthesized by Fmoc/tBu solid-phase peptide chemistry. In addition, the N-terminal end of the sequence was modified by acetylation. The peptide sequence was as follows: N-Ac-GGGGDRVYIHP-COOH. First of all, the C-terminal of the peptide sequence was loaded onto unloaded Wang resin used as the solid phase. For this, 1 g of Wang resin LL (0.67 mmol/g) was swollen in 25 mL of DMF:DCM (1:9; v:v) for 30 minutes. According to the resin, 2 eq of Fmoc-Pro-OH and 2 eq of HOBt.H₂O were dissolved in a minimum amount of DMF and added to the resin mixture. According to the resin, 0.1 eq of DMAP (4-(Dimethylamino)pyridine) was dissolved in a minimum volume of DMF and added to the resin mixture simultaneously with 1 eq of DIC (N,N'-Diisopropylcarbodiimide) relative to the Fmoc-Pro-OH. Then, it was shaken at room temperature for six hours. The resin beads were washed three times with DMF, MeOH, DCM, and Et₂O, respectively. After the reaction, 2 eq of acetic anhydride and 2 eq of pyridine were added to the resin mixture according to the resin and shaken for 30 minutes to close the hydroxyl groups that remain unreacted on the resin beads. The resin beads were washed with DMF, MeOH, DCM, and Et₂O, respectively, three times, and dried under vacuum (27-29). The loading efficiency of the Wang resin was performed according to the literature based on the removal of

Fmoc groups and UV-Vis analysis of Fmoc with using Equation 1 (30).

$$L = \frac{A \cdot v}{\epsilon \cdot l \cdot m} \quad (\text{Eq. 1})$$

L: amino acid loading (mmol/g)

A: absorbance value at the 301 nm

v: dilution factor of solvent

ϵ : molar absorptivity of the Fmoc group at 301 nm (7800 L x mol⁻¹ x cm⁻¹)

l: light path length of the cell (1 cm)

m: weight of the loaded resin (mg)

For the synthesis of the peptide, 150 mg of the Fmoc-Pro-Wang resin was swollen in 25 mL of dry DMF: DCM (1:3, v/v) for 3 hours. After filter drying, a freshly prepared deprotection solution (20% piperidine in DMF) was added for removing Fmoc protecting groups. Washing was performed with an excess amount of DMF and DCM. The next amino acid solution, activator (HBTU (o-(Benzotriazol-1-yl)-N,N,N',N'-tetramethyluronium hexafluorophosphate), HOBt.H₂O), and activator base (NMP (N-methylpyrrolidone), DIEA (N,N-diisopropylethylamine)) solutions were added, respectively, and incubated for 1 hour. Then the above-mentioned washing process was done again. These processes (deprotection, activation, and coupling) were continued until all amino acids were added (26). The N-terminal end of the peptide was acetylated by adding 0.5M acetic anhydride solution together with 0.125 M DIEA and 0.015 M HOBt.H₂O in DMF. The resin was washed with MeOH, DCM and Et₂O, three times and dried under vacuum (19). The peptide was cleaved from the resin with a cleavage cocktail (trifluoroacetic acid (TFA, 94% v/v):1,2-ethanedithiol (EDT, 2.5% v/v):triisopropylsilane (TIS, 1% v/v):dH₂O (2.5%, v/v)). The solution including the desired peptide was concentrated, the peptide was precipitated with cold Et₂O and separated by centrifugation. It was dissolved in 1:1 H₂O:ACN at a concentration of 1 mg/mL and characterized by LC-ESI-MS (19).

Conjugation of the Peptide with Stearic Acid

The stearic acid molecule was conjugated with the synthesized and characterized peptide sequence from the amine group at the side chain of the Arginine residue of the peptide sequence in the presence of EDC. For this, 0.1 mmol stearic acid (SA) solution in 10 mL of EtOH was prepared. For the activation, relative to SA 10 equivalents of EDC in pure water was added. Stearic acid peptide conjugation was performed by adding 1 equivalent of the peptide in sodium acetate buffer (pH 4.5) after 1 hour of activation. The mixture was stirred intensively overnight at 25 °C under nitrogen gas. The organic solvent was evaporated under vacuum followed by lyophilization. The resulting product was further washed with EtOH to remove the unreacted SA. Finally, the peptide-SA conjugate was redispersed in dH₂O and lyophilized. The molecular

weight of the lyophilized conjugate was determined by LC-ESI-MS (31, 32).

RESULTS AND DISCUSSION

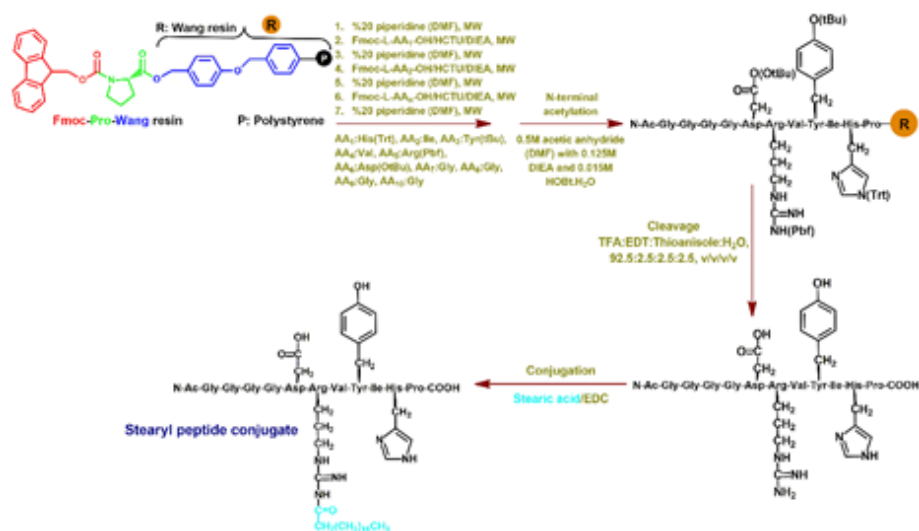
Scheme 1 demonstrated the synthesis of the designed peptide and the conjugation reaction with stearic acid of the synthesized peptide. The coupling of amino acids to the resin, N-terminal modification of peptidyl resin with acetylation, cleavage of the peptide, and conjugation of stearic acid to the peptide, and other respectively applied methods were shown schematically.

For the solid phase peptide synthesis, unloaded Wang resin was loaded with Fmoc-Pro-OH. The resin substitution was determined by the Fmoc removal process. This process was based on the spectroscopic determination of the Fmoc and its dibenzofulvene-piperidine derivatives after deprotection of the resin with a deprotection solution. 1 mL of freshly prepared 20% piperidine solution in DMF was added onto a certain amount of

the Fmoc-Pro-Wang resin in an Eppendorf tube. After 15 minutes of shaking in an incubator, a minute was kept on hold for the precipitation of resin beads. UV-Vis spectrum of the supernatant phase (diluted by 10 times with DMF) was recorded. The resin substitution of Fmoc-Pro-Wang was found as 0.33 mmol/g (Figure 1). The resin substitution for commercially available Fmoc-Pro-Wang resin produced by different companies ranges between 0.2-0.8 mmol/g (33, 34).

ESI-MS is often preferred both in determining the average molecular weight of degradation products of biomolecules such as proteins and enzymes and in verifying the molecular weights of materials with smaller molecular weights such as peptides (35, 36). In this study, we applied the ESI-MS method to verify the molecular weight of the peptide. The obtained spectrum of the peptide was given in Figure 2 and the mass of the peptide was calculated as follows:

$$[M + 3Na]^{3+} = 412.5 \text{ Da} \Rightarrow M_{\text{exp}} = 1168.5 \text{ Da} \quad M_{\text{calc}} = 1169.25 \text{ Da}$$



Scheme 1: Illustration of synthesis mechanism of the stearyl peptide conjugate.

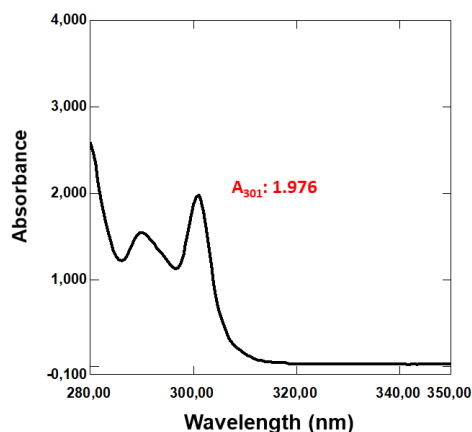


Figure 1: UV-Vis spectrum of dibenzofulvene-piperidine by-product formed after the removal of the Fmoc group ($A_{301}: 1.976$).

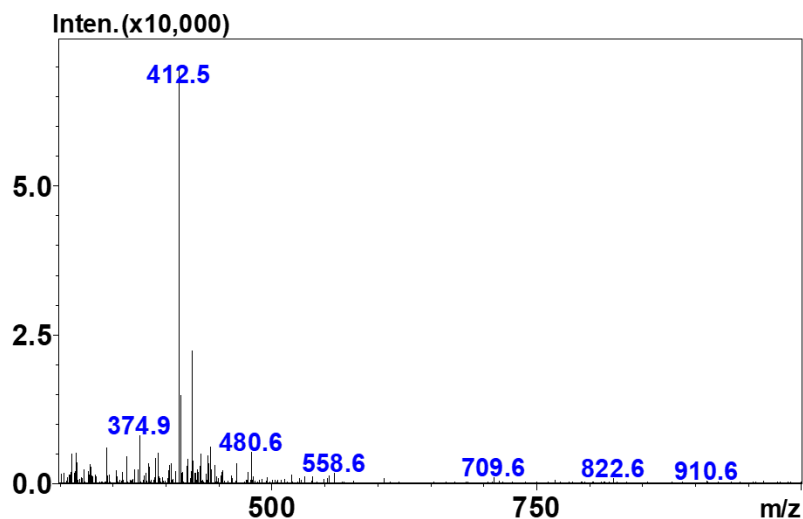


Figure 2: ESI-MS spectrum of the N-Ac-Gly₄-Ang (1-7) peptide.

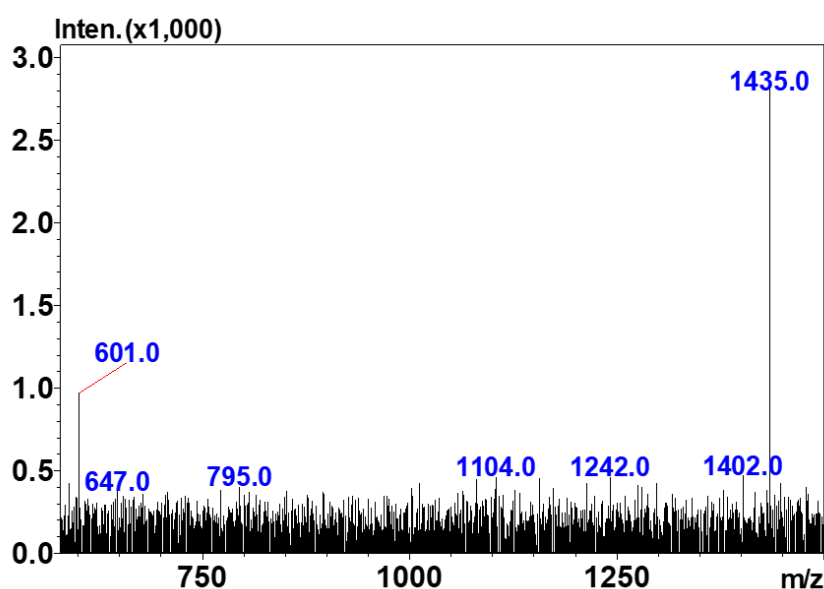


Figure 3: ESI-MS spectrum of the peptide-stearic acid conjugate.

The stearyl peptide conjugate of stearic acid and N-Ac-Gly₄-Ang (1-7) was synthesized by carbodiimide chemistry. Unreacted EDC and its *o*-acylisourea byproduct and unreacted stearic acid were removed from the environment with post-synthesis washing processes. The conjugate was characterized by LC-ESI-MS. As illustrated in Figure 3, ESI-MS ion peak at 1435.0 confirmed the formation of the conjugate. $[M] = 1435.0 \text{ Da} \Rightarrow M_{\text{exp}} = 1435.0 \text{ Da} \quad M_{\text{calc}} = 1435.73 \text{ Da}$

FT-IR analysis was performed to evaluate the changes of functional groups in peptide and stearic acid after conjugation reaction. The conjugation reaction was carried out between the -COOH groups of stearic acid and the amine group of the arginine residue of the peptide. Therefore, it is expected that there will be a change in the peaks of these groups.

FT-IR spectrum of the stearyl peptide conjugate was comparatively given with stearic acid and peptide in Figure 4. Some of the basic peaks of the peptide were N-H stretching at 3276.5 cm⁻¹, -CH₂ stretching at 2976.6 cm⁻¹, C=O (carboxylic acid) stretching 1734.7 cm⁻¹, C=O (amide I) stretching 1680.7 and 1628.6 cm⁻¹, and amide II band resulting from N-H bending and C-N stretching at 1548.1 cm⁻¹. It can be understood from the FT-IR spectrum of stearic acid that the band at 1629.6 cm⁻¹ was C=O stretching of carboxyl and the broad peaks at 2915.8 and 2848.8 cm⁻¹ were C-H stretching. The peak around 719.7 cm⁻¹ corresponded to the bending vibration of long (CH₂)_n chains of stearic acid. In the stearyl peptide spectrum, the presence of N-H stretching of the peptide at 3275.0 cm⁻¹, the presence of C-H bendings around 2900 cm⁻¹ of the stearic acid, and also the shifting of the carbonyl

peaks of the carboxylic acid and amide (seen at 1720.7 and 1641.1 cm^{-1}) supported the conjugation.

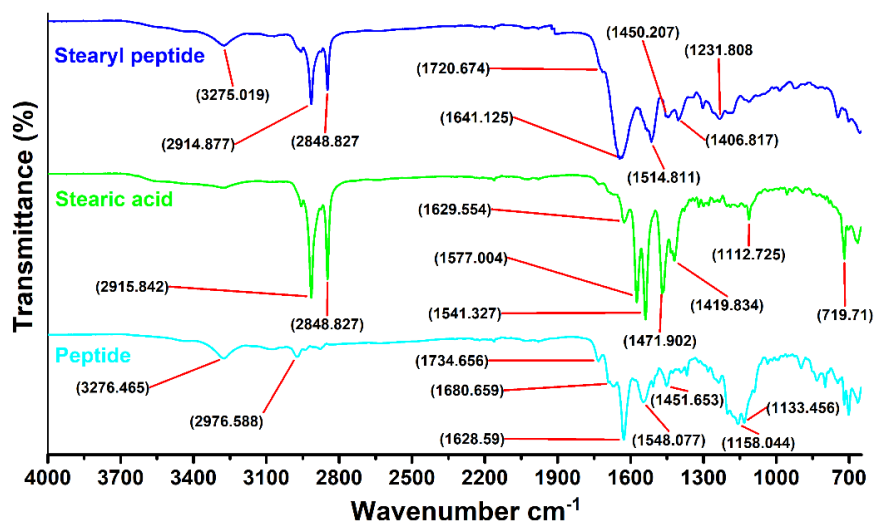


Figure 4: FT-IR spectrum of the stearyl peptide conjugate comparatively given with stearic acid and peptide.

Another methods we use to characterize the stearyl peptide conjugate were dynamic and electrophoretic light scattering measurements. The average size results obtained by the DLS method were given in Figure 5. The mean size of the peptide and stearic acid were 6.33 ± 0.996 and 8.55 ± 2.400 nm, respectively. The size of the obtained conjugate was measured as 25.92 ± 3.295 nm. With the combination of peptide and stearic acid after the conjugation reaction, the obtained structure got a little bigger and the average particle size increased (19).

Zeta potential values obtained from electrophoretic light scattering measurements for the peptide, stearic acid, and stearyl peptide conjugate were -6.20 ± 0.621 , -17.20 ± 1.96 , and -15.90 ± 1.53 mV, respectively (Figure 6). The zeta potential became more negative as a result of participating the amine groups of the peptide to the conjugation reaction and the C-terminal $-\text{COOH}$ groups making the environment negatively charged (shift from -6.20 to -15.90 mV). With the addition of stearic acid $-\text{COOH}$ groups to the reaction, the zeta potential value shifted slightly to positive (shift from -17.20 to -15.90 mV) (19).

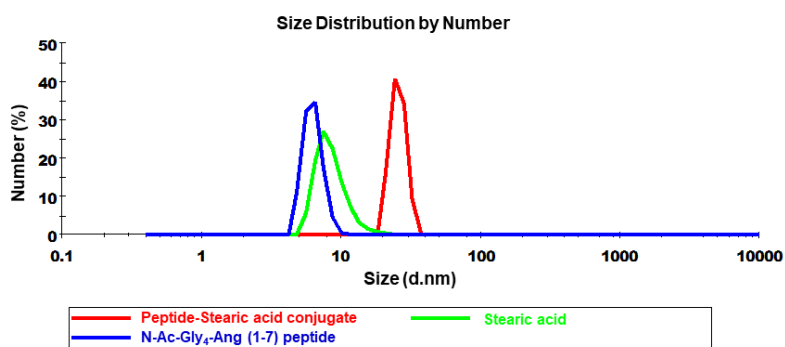


Figure 5: The particle size distribution of peptide, stearic acid, and stearyl peptide conjugate by number.

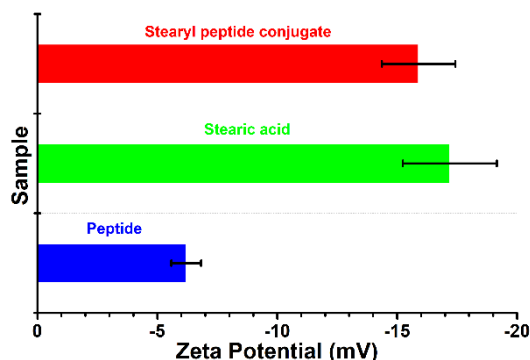


Figure 6: Zeta potential values of the peptide, stearic acid, and stearyl peptide conjugate.

CONCLUSION

Herein, modified angiotensin (1-7) peptide was synthesized by being N-terminal acetylation and four glycine adding. The molecular weight of the peptide was confirmed by LC-ESI-MS. The stearyl peptide conjugate of the N-Ac-Gly₄-Ang (1-7) with stearic acid was formed with carbodiimide chemistry using EDC. The characterization of the conjugate was performed by FT-IR, Zetasizer, and LC-ESI-MS methods. Changes in size, zeta potential values, FT-IR peaks of functional groups after conjugation and also mass analysis result supported the formation of the stearyl peptide conjugate. As future research, it is aimed to reveal more detailed information about the obtained conjugate by cellular studies.

REFERENCES

- Xu Z, Shi L, Wang Y, Zhang J, Huang L, Zhang C, et al. Pathological findings of COVID-19 associated with acute respiratory distress syndrome. *The Lancet Respiratory Medicine*. 2020 Apr;8(4):420–2. [<DOI>](#).
- Duan K, Liu B, Li C, Zhang H, Yu T, Qu J, et al. Effectiveness of convalescent plasma therapy in severe COVID-19 patients. *Proc Natl Acad Sci USA*. 2020 Apr 28;117(17):9490–6. [<DOI>](#).
- Chen H, Guo J, Wang C, Luo F, Yu X, Zhang W, et al. Clinical characteristics and intrauterine vertical transmission potential of COVID-19 infection in nine pregnant women: a retrospective review of medical records. *The Lancet*. 2020 Mar;395(10226):809–15. [<DOI>](#).
- Rothan HA, Byrareddy SN. The epidemiology and pathogenesis of coronavirus disease (COVID-19) outbreak. *Journal of Autoimmunity*. 2020 May;109:102433. [<DOI>](#).
- Shereen MA, Khan S, Kazmi A, Bashir N, Siddique R. COVID-19 infection: Emergence, transmission, and characteristics of human coronaviruses. *Journal of Advanced Research*. 2020 Jul;24:91–8. [<DOI>](#).
- Dhama K, Sharun K, Tiwari R, Dadar M, Malik YS, Singh KP, et al. COVID-19, an emerging coronavirus infection: advances and prospects in designing and developing vaccines, immunotherapeutics, and therapeutics. *Human Vaccines & Immunotherapeutics*. 2020 Jun 2;16(6):1232–8. [<DOI>](#).
- Kannan S, Shaik Syed Ali P, Sheeza A, Hemalatha K. COVID-19 (Novel Coronavirus 2019) – recent trends. *European Review for Medical and Pharmacological Sciences*. 2020 Feb;24(4):2006–11. [<DOI>](#).
- Hurdiss DL, Drulyte I, Lang Y, Shamorkina TM, Pronker MF, van Kuppeveld FJM, et al. Cryo-EM structure of coronavirus-HKU1 haemagglutinin esterase reveals architectural changes arising from prolonged circulation in humans. *Nat Commun*. 2020 Dec;11(1):4646. [<DOI>](#).
- Bakkers MJG, Lang Y, Feitsma LJ, Hulswit RJG, de Poot SAH, van Vliet ALW, et al. Betacoronavirus Adaptation to Humans Involved Progressive Loss of Hemagglutinin-Esterase Lectin Activity. *Cell Host & Microbe*. 2017 Mar;21(3):356–66. [<DOI>](#).
- Kirchdoerfer RN, Cottrell CA, Wang N, Pallesen J, Yasinine HM, Turner HL, et al. Pre-fusion structure of a human coronavirus spike protein. *Nature*. 2016 Mar;531(7592):118–21. [<DOI>](#).
- Matsubara T, Onishi A, Saito T, Shimada A, Inoue H, Taki T, et al. Sialic Acid-Mimic Peptides As Hemagglutinin Inhibitors for Anti-Influenza Therapy. *J Med Chem*. 2010 Jun 10;53(11):4441–9. [<DOI>](#).
- Zhang H, Penninger JM, Li Y, Zhong N, Slutsky AS. Angiotensin-converting enzyme 2 (ACE2) as a SARS-CoV-2 receptor: molecular mechanisms and potential therapeutic target. *Intensive Care Med*. 2020 Apr;46(4):586–90. [<DOI>](#).
- Santos RAS, Sampaio WO, Alzamora AC, Motta-Santos D, Alenina N, Bader M, et al. The ACE2/Angiotensin-(1-7)/MAS Axis of the Renin-Angiotensin System: Focus on Angiotensin-(1-7). *Physiological Reviews*. 2018 Jan 1;98(1):505–53. [<DOI>](#).
- Kuba K, Imai Y, Rao S, Gao H, Guo F, Guan B, et al. A crucial role of angiotensin converting enzyme 2 (ACE2) in SARS coronavirus-induced lung injury. *Nat Med*. 2005 Aug;11(8):875–9. [<DOI>](#).
- Amin HH, Meghani NM, Oh KT, Choi H, Lee B-J. A conjugation of stearic acid to apotransferrin, fattigation-platform, as a core to form self-assembled nanoparticles: Encapsulation of a hydrophobic paclitaxel and receptor-driven cancer targeting. *Journal of Drug Delivery Science and Technology*. 2017 Oct;41:222–30. [<DOI>](#).
- Khan AA, Alanazi AM, Jabeen M, Chauhan A, Abdelhameed AS. Design, synthesis and in vitro anticancer eval-

- uation of a stearic acid-based ester conjugate. *Anticancer research*. 2013;33(6):2517–24.
17. Wang Y, Cheetham AG, Angacian G, Su H, Xie L, Cui H. Peptide–drug conjugates as effective prodrug strategies for targeted delivery. *Advanced Drug Delivery Reviews*. 2017 Feb;110–111:112–26. [<DOI>](#).
18. Hoppenz P, Els-Heindl S, Beck-Sickinger AG. Peptide-Drug Conjugates and Their Targets in Advanced Cancer Therapies. *Front Chem*. 2020 Jul 7;8:571. [<DOI>](#).
19. Ucar B, Acar T, Pelit-Arayici P, Demirkol MO, Mustafaeva Z. A new radio-theranostic agent candidate: Synthesis and analysis of (ADH-1) c-EDTA conjugate. *Fre-senius Environmental Bulletin*. 2018;27(7):4751–8.
20. Ucar B, Acar T, Arayici PP, Sen M, Derman S, Mustafaeva Z. Synthesis and applications of synthetic peptides. In: *Peptide Synthesis*. IntechOpen; 2019.
21. Heerze LD, Smith RH, Wang N, Armstrong GD. Utilization of sialic acid-binding synthetic peptide sequences derived from pertussis toxin as novel anti-inflammatory agents. *Glycobiology*. 1995;5(4):427–33. [<DOI>](#).
22. Matsubara T. Potential of Peptides as Inhibitors and Mitotopes: Selection of Carbohydrate-Mimetic Peptides from Phage Display Libraries. *Journal of Nucleic Acids*. 2012;2012:1–15. [<DOI>](#).
23. Cebeci C, Ucar B, Acar T, Erden I. Colorimetric detection of hydrogen peroxide with gadolinium complex of phenylboronic acid functionalized 4,5-diazafluorene. *Inorganica Chimica Acta*. 2021 Jul;522:120386. [<DOI>](#).
24. Acar T, Pelit Arayıcı P, Ucar B, Karahan M, Mustafaeva Z. Synthesis, Characterization and Lipophilicity Study of Brucella abortus' Immunogenic Peptide Sequence That Can Be Used in the Future Vaccination Studies. *Int J Pept Res Ther*. 2019 Sep;25(3):911–8. [<DOI>](#).
25. Ucar B. Synthesis and characterization of natural lanthanum labelled DOTA-Peptides for simulating radioactive Ac-225 labeling. *Applied Radiation and Isotopes*. 2019 Nov;153:108816. [<DOI>](#).
26. Ucar B, Acar T, Arayici PP, Derman S. A nanotechnological approach in the current therapy of COVID-19: model drug oseltamivir-phosphate loaded PLGA nanoparticles targeted with spike protein binder peptide of SARS-CoV-2. *Nanotechnology*. 2021 Nov 26;32(48):485601. [<DOI>](#).
27. Guillier F, Orain D, Bradley M. Linkers and Cleavage Strategies in Solid-Phase Organic Synthesis and Combinatorial Chemistry. *Chem Rev*. 2000 Jun 1;100(6):2091–158. [<DOI>](#).
28. Chan W, White P, editors. *Fmoc Solid Phase Peptide Synthesis: A Practical Approach* [Internet]. Oxford University Press; 1999 [cited 2022 Feb 19]. [<URL>](#).
29. Atherton E, Logan CJ, Sheppard RC. Peptide synthesis. Part 2. Procedures for solid-phase synthesis using N^α-fluorenylmethoxycarbonylamino-acids on polyamide supports. Synthesis of substance P and of acyl carrier protein 65–74 decapeptide. *J Chem Soc, Perkin Trans 1*. 1981; (0):538–46. [<DOI>](#).
30. Al Musaimi O, Basso A, de la Torre BG, Albericio F. Calculating Resin Functionalization in Solid-Phase Peptide Synthesis Using a Standardized Method based on Fmoc Determination. *ACS Comb Sci*. 2019 Nov 11;21(11):717–21. [<DOI>](#).
31. Hu F-Q, Zhang, Du Y-Z, Yuan. Brain-targeting study of stearic acid–grafted chitosan micelle drug-delivery system. *IJN*. 2012 Jun;3235. [<DOI>](#).
32. Pereira P, Barreira M, Cruz C, Tomás J, Luís Â, Pedro AQ, et al. Brain-Targeted Delivery of Pre-miR-29b Using Lactoferrin-Stearic Acid-Modified-Chitosan/Polyethyleneimine Polyplexes. *Pharmaceuticals*. 2020 Oct 15;13(10):314. [<DOI>](#).
33. Anonymous. AAPPTec. Resins for Solid Phase Peptide Synthesis [Internet]. AAPPTec. Resins for Solid Phase Peptide Synthesis. 2021 [cited 2022 Feb 19]. [<URL>](#).
34. Anonymous. Sigma-Aldrich. Fmoc-Pro-Wang resin [Internet]. Sigma-Aldrich. Fmoc-Pro-Wang resin. 2021 [cited 2022 Feb 19]. [<URL>](#).
35. Banerjee S, Mazumdar S. Electrospray Ionization Mass Spectrometry: A Technique to Access the Information beyond the Molecular Weight of the Analyte. *International Journal of Analytical Chemistry*. 2012;2012:1–40. [<DOI>](#).
36. Zhang S (Weihua), Jian W. Recent advances in absolute quantification of peptides and proteins using LC-MS. *Reviews in Analytical Chemistry* [Internet]. 2014 Jan 1 [cited 2022 Feb 19];33(1). [<DOI>](#).



***Ricinus communis* Seed Oils as a Source of Biodiesel; A Renewable Form of Future Energy**

Hadush Gebrehiwot^{1*}  and Demis Zelelew² 

¹Wachemo University, Department of Chemistry, Hossana, P.O. Box 667, Ethiopia

²Adama Science and Technology University, Department of Applied Chemistry, Adama, P.O. Box: 1888, Ethiopia

Abstract: Diminishing supply and environmental pollution of fossil fuels are the vital factors leading to the search of alternative sources of energy like biodiesel. Biodiesel is one of the eco-friendly substitutes of energy which is mainly utilized in diesel engines. *Ricinus communis* (castor plant), which belongs to the family Euphorbiaceae yields an oil rich beans and plays important role in the production of biodiesel. Recently, the demand of castor oil and its products has been raised in the world market due to its versatility to use and simplicity to produce. Therefore, this study investigates the extraction of castor oil and its conversion in to biodiesel via alkali catalyzed transesterification. The seed oil of the plant was extracted using Soxhlet apparatus and the quality of the biodiesel was examined using the standard procedures of American standards for testing methods. Furthermore, the chemical composition of the extracted oil was examined using GC-MS. The seed oil was liquid at room temperature (25 °C), golden yellow in color with a nutty odor. The extraction processes yielded 324 g (9.25% w/w) and 78% of oil and biodiesel respectively. The density (0.86 g/mL), viscosity (5.42 mm²s⁻¹), flash point (87 °C), acid value (0.35 mg KOH/g), water content (0.80%), iodine value (108.60), and cetane number (58.00) were reported in this study and showed a good agreement with the standards of biodiesel. GC-MS analysis of the seed oil also showed the presence of 10 different fatty acids (9-Octadecenoic acid, 12-hydroxy-, methyl ester, [R-(Z)] took the highest composition) which plays significant role for the production of methyl esters. So, the study can assure that castor oil can be used for commercial production of biodiesel at cost effective scales.

Keywords: Biodiesel, GC-MS, Renewable energy, *Ricinus communis*, Transesterification

Submitted: November 12, 2021. Accepted: February 12, 2022.

Cite this: Hadush G, Demis Z. *Ricinus communis* Seed oils as a Source of Biodiesel; A Renewable Form of Future Energy. JOTCSA. 2022;9(2):339–54.

DOI: <https://doi.org/10.18596/jotcsa.1019969>.

***Corresponding Author. E-mail:** hadushgebrehiwot@yahoo.com.

INTRODUCTION

Today, one of the great problems of humanity is its dependence on non-renewable forms of energy which have a nature of depletion, economic disturbances, and negative environmental impacts (1). Currently, fossil fuels cover most of the energy used in the world. They are broadly used for cooking, generation of electricity, transportation, to heat environments, etc. However, a concern has been generated, that leads to the search and the study of new sources for the production of biofuels.

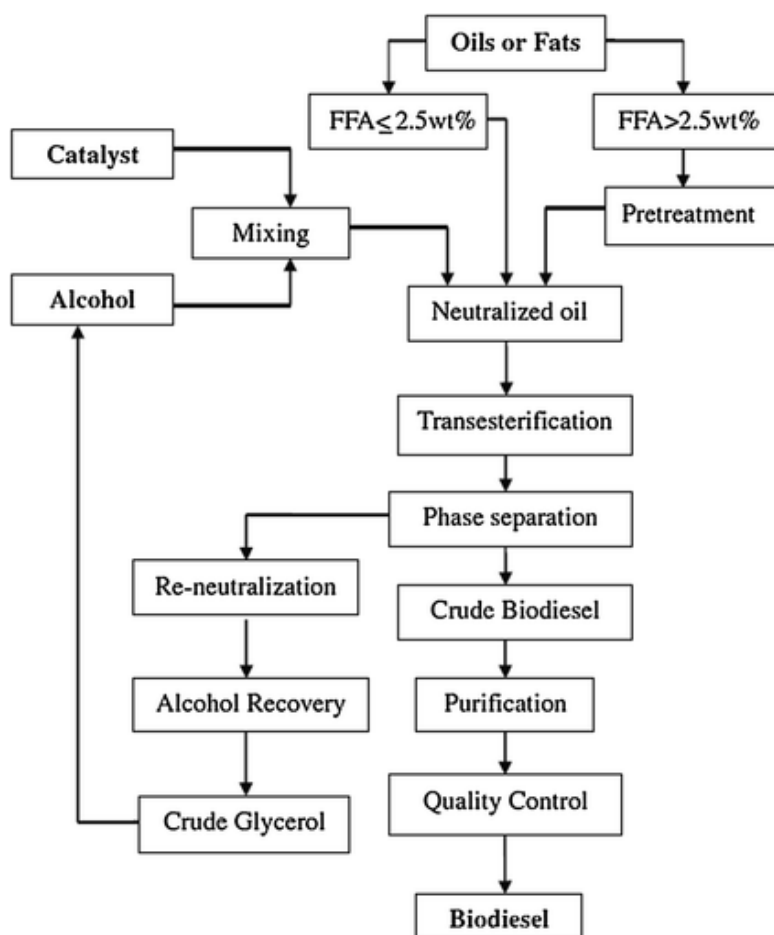
The challenge is to ensure that those energy sources are gradually replacing the fossil fuels (2).

The diminution of natural oil which leads to high oil price and emission of greenhouse gases make renewable energy sources more attractive. One of the best ways to reduce our dependence on petroleum reserves is to develop renewable fuels such as biodiesel (3). Recently, biodiesel is evolving to be one of the most employed biofuels for partial replacement of petroleum based diesel fuel (4). The demand and consumption of petroleum products are

increasing from time to time due to the increase in population, living standards, and urbanization. The use of diesel machineries has been banned in some cities of the world like in India for serious problems of air pollution due to higher emissions of poisonous gasses. Global warming, depletion of ozone layer, and acidic rain are some of the consequences of the toxic gases from petroleum fuels (5).

Methyl ester fatty acid (biodiesel) is one of the key solutions of the future threats of petroleum fuels

because of its renewability and friendship to the environmental. Surveys conducted by different researchers revealed that currently more than 95 percent of biodiesel is produced from edible oil sources (6, 7) (Scheme 1). Use of alternative non-edible oil sources such as castor oil, jatropha oil, algae oil, karanja (*Pongamia pinnata*), tobacco (*Nicotiana tabacum*), rubber plant (*Hevea brasiliensis*), waste cooking oil etc. are gaining increasing attention and are broadly under examination (8, 9).



Scheme 1: Production of biodiesel via transesterification process (10).

Ricinus communis (castor plant) belongs to the family Euphorbiaceae and grows in both domestic and wild climatic conditions (4, 11, 12). The plant produces castor beans that are rich of castor oil (up to 50% oil by weight). The oil can easily be produced from the seeds of the plant and is used in many sectors such as chemical industry, agriculture, medicine and other technologies (13). Nowadays, the demand for castor oil and its products has been on the steady increase in the world market due to its low costs, eco-friendliness, non-competition with food, renewable nature and biodegradability (2). The chemistry of *R. communis* oil is mainly aligned on ricinoleic acid which takes place in high content in the seed oil of the plant and possess three functional groups. These functional groups are

essential towards the versatility of the oil for the production of many castor oil based products (14, 15). The presence of carboxylic functional group, for example, can lead to a wide range of esterification products. Whereas, the presence of hydroxyl functional group, can be acetylated, alkoxyated, or removed by dehydration to increase the unsaturation of the oil (16-18).

R. communis (Figure 1) is locally called Gulo (Amharic name) and is one of the biodiesel feed stocks. The beans contain a toxin that makes the oil and cake inedible. It grows very well on marginal land, it is drought- and pest-resistant and is one of the highest viscosities among vegetable oils (19, 20). The oil extracted from the seed of castor plant

(*R. communis*) has stimulated some interests such as production of biodiesel. *R. communis* beans are non-edible biodiesel raw materials to substitute the consumption of fossil fuels. Furthermore, they are

widely available and has no any other commercial purpose, has high oil content, grows in marginal land and has a resistance for variable climatic and soil conditions (21).



Figure 1: Castor plant (left) and castor seeds (right).

Ethiopia is one of the most suitable nations in Africa for tapping renewable sources of energy because of its location and natural wealth. The country has been looking at enhancing its energy capacity, especially over the past twenty years (9). The government recently issued biofuel strategies to

encourage domestic biofuel production, with an objective of reducing the dependence on high-cost fossil oil. The plant possess high oil content (45%-55%) relative to other plants in the country and got a great attention by stakeholders (22) (Table 1).

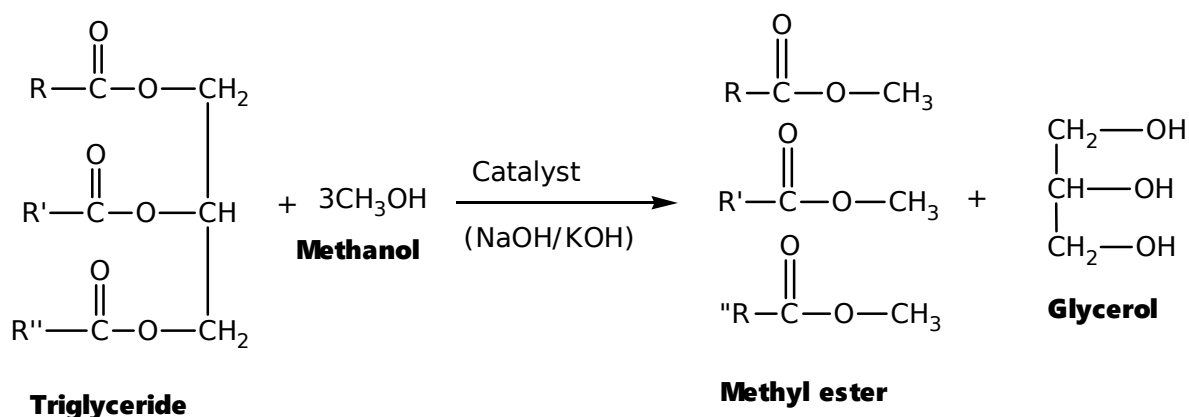
Table 1: Comparison of the most common biodiesel feed stocks.

Seed type	Oil content (%)	Advantage	Disadvantage	References
Castor bean	45-55	High flash point, high pour point, high cloud point, non-edible, miscible with alcohol	High viscosity, low cetane number	(23-29)
Rapeseed	38-46	Low cloud point, high flash point	High NOx emissions in most experiments	(24, 25, 27, 29, 30)
Mustard	28-32	Cheap feed stock, high cetane number	High cloud point, low heating value, high viscosity	(24, 27, 29, 31-34)
Palm	18-40	High flash point, cheap feed stock	Edible, high cloud point	(24, 25, 27-29, 35)
Sunflower	25-35	Low viscosity	Long term cultivation	(24, 25, 27-29, 35)
Soybean	15-20	High thermal stability, low viscosity	High acid value, long term cultivation, edible,	(24, 25, 27-29)

Biodiesel should be investigated for some important parameters to ensure its quality before it is used in different kinds of fuel machineries (36). Biodiesel density (the measure of the degree of combustion and atomization), viscosity (the property to resist the relative movement tendency), flash point (the minimum temperature at which the fuel will ignite), acid value (to quantify the acid moieties in the biodiesel), iodine value (the measure of the total unsaturation of fatty acids), water content and cetane number (the measure of ignition quality of biodiesel) are some substantial parameters of

biodiesel that should be taken in to consideration before application (37-42).

Transesterification is the displacement of alcohol from an ester by another in a process similar to hydrolysis, except alcohol is used instead of water. This process has been widely used to reduce the high viscosity of triglycerides. A catalyst is usually used to improve the reaction rate and yield (Scheme 2). Excess alcohol is used to shift the equilibrium toward the product because of reversible nature of the reaction (16, 37, 43).



Scheme 2: Transesterification process.

The production of biodiesel in Africa in general and in Ethiopia in particular is at its infant stage and has yet to mature. That is because much of the struggles in Africa so far have fixated on nurturing the feedstock market. Although many works have been performed on the transesterification of non-edible oils of many seed oils; few studies have been done on the optimization, oil characterization, and fuel analysis of the non-edible oil seeds particularly *R. communis*. So, the present work aimed to study the seed oil of *R. communis* as a source of future renewable energy. The study has a remarkable finding on the important aspects of the seed oil of *R. communis* as a feed stock for biodiesel production at global perspectives in general and in Ethiopia in particular.

EXPERIMENTAL

Plant Materials

The plant materials were collected from a farm land around Abiy Adi, central province, 95 km from the capital of Tigray, Ethiopia. After collection the seeds were allowed to air dry, washed first with tap water and then with distilled water. The air dried seeds were ground in to coarse powder using an electric blender (Panasonic, Japan). Finally, the sample materials were sealed in a polyethylene bag to prevent from certain environmental factors.

General Experimental Procedures

The seed oil of *R. communis* was extracted using Soxhlet extractor (Lab Tech Grey Soxhlet Apparatus, BST/SXM-1, India). The concentration/drying process of the oil was achieved using rotary evaporator (RV 3V, IKA, Germany). The biodiesel was produced by alkali-catalyzed transesterification method on a hot plate. The chemical composition of the seed oil was determined using Shimadzu QP2010 GC-MS (Shimadzu, Kyoto, Japan). Furthermore, the physico-chemical parameters of the biodiesel were tested and the instruments used are described under the procedure of each parameter.

Extraction Methods

Soxhlet extraction

About 3.5 kg of the powdered seeds of the plant were subjected to Soxhlet extraction (chemical method). 250 mL of n-hexane was poured into a round-bottomed flask and 100 g of the sample was placed in the thimble and extracted using Soxhlet extractor at 60 °C for 3 hrs. Distinct layers of oil and n-hexane appeared in the round-bottomed flask. The resulting mixture containing oil was concentrated using a rotary evaporator (RV 3V, IKA, Germany) to evaporate the solvent and weighed again to determine the amount of oil extracted. This procedure was repeated many times to generate sufficient oil (44).

Transesterification

An alkali-catalyzed transesterification method was used to produce the biodiesel. The crude oil was filtered by Whatman filter paper No 1 and the filtered oil was heated up to 125 °C on hot plate to decompose triglycerides into monoglycerides and diglycerides. Transesterification of 324 mL of oil was done for the production of methyl esters by using different alkaline catalysts (45).

3.5 g of NaOH was mixed with methanol (100 mL) to make alkali methoxide which was used as a catalyst in the reaction. The prepared methoxide was added to 324 mL of oil at 60 °C and stirred for 40 minutes at 600 rpm. After stirring the reaction mixture was kept overnight at room temperature to settle down distinct layers i.e. upper layer soap, middle layer of FAME (fatty acid methyl esters) and the bottom dense layer of glycerin. These layers were then separated through a glass separating funnel. The biodiesel was washed with ordinary tap water in order to remove impurities and suspended particles. Four washings were performed for complete clearance of the biodiesel. Few drops of acetic acid were also added and the residual water was eliminated by treatment with anhydrous sodium sulfate (Na₂SO₄) followed by filtration (44, 45).

Determination of Free Fatty Acid Number

The contents of free fatty acid were determined by aqueous acid-base titration method. Two types of titration i.e. blank titration and sample titration were performed. In case of blank titration, 1.4 g KOH were dissolved in 1000 mL of distilled water to prepare 0.025 M KOH solution and this solution were poured into a burette. 10 mL of isopropyl alcohol and 3 drops of phenolphthalein were mixed in an Erlenmeyer flask and titrated against 0.025 M KOH from the burette until the color of the solution became pink. The volume of KOH used was recorded

and this process was repeated three times to calculate the mean volume of KOH used for blank titration. While in the sample titration, 9 mL isopropyl alcohol, 1 mL of *R. communis* oil and 3 drops of phenolphthalein were taken into an Erlenmeyer flask and titrated against 0.025 M KOH from the burette until the end point. The volume of KOH used was recorded and three readings were taken by repeating the same experiment to calculate the mean volume of KOH used to titrate the sample (44). Finally, the value of acid number was calculated using (Equation 1).

$$\text{Acid number} = \frac{(A - B) \times C}{D} \quad (\text{Eq. 1})$$

Where, A = Volume used in sample (actual titration),
B = Volume used in blank titration,
C = Mass of catalyst in g/L,
D = Volume of oil used.

Physicochemical Characterization of the Biodiesel*Iodine value*

The iodine value was determined through the method described by Jessinta, et al., 2014 (46) with slight modifications. 0.1 g of the biodiesel was measured in to an Erlenmeyer flask and 20.0 mL of carbon tetrachloride was added and the flask was sealed until complete dissolution. 25.0 mL of Hanus'

solution (Iodine monobromide in glacial acetic acid, C=0.1 mol/L) was added into the previous solution, sealed and shaken for one minute. The sealed solution was left in a dark room (about 20 °C) for 30 minutes. Meanwhile 10.0 mL of 15% potassium iodide and 100 mL of water were added, sealed and shaken for 30 seconds. Finally the resulted solution was titrated with 0.1 mol/L sodium thiosulfate and the iodine value was calculated as follows (Equation 2) (46).

$$\text{Iodine value} = \frac{(BL1 - EP1) \times TF \times C1 \times K1}{S} \quad (\text{Eq. 2})$$

Where, EP1 = titration volume (mL),
BL1 = Blank level (47.074 mL),
TF = Factor of titrant (1.006),
C1 = Concentration conversion coefficient (1.269),
K1 = Unit conversion coefficient (1),
S = Sample size (g).

Biodiesel density

The density of the biodiesel was measured using a digital hydrometer (DA-130N, India). 20 mL of biodiesel sample was added in a graduate beaker, measuring room temperature using a thermometer. The hydrometer was dropped inside the beaker with biodiesel until the hydrometer stops and the density was read (25, 47, 48).

Cetane number

The Cetane number (CN) of the biodiesel was measured by using ignition quality tester (Advanced Engine Technology, India). This is a method that measures the time delay between the start of fuel injection and the start of significant combustion through auto-ignition of a pre-measured amount of diesel in a constant volume chamber. The time delay is used with a formula to calculate the Derived Cetane Number (DCN) which correlates to the D613 cetane engine (48, 49).

Flash point

The flash point of the biodiesel was measured by Pensky-Martens flash point tester (PMA 500, India). The flash point cup was filled with a biodiesel and was heated in the apparatus. It reads a point after the thermometer was put. The temperature at which the vapor reacted with the atmospheric air and gets ignited was recorded (50).

Viscosity

The viscosity of the biodiesel was calculated using Bitumen Dynamic Viscosity Apparatus (GD-0620A, China). The capillary viscometer was filled with the biodiesel. The sucker or filler of the viscometer was fixed to the upper part of the tube and then pumped till the fluid passes to the mouth of the tube. The time taken as the biodiesel moves down till it gets to the lower tube of the viscometer was recorded and multiplied by 0.01126 (51).

Water content

The water content (WC) was determined by the standard oven method, in which a sample is

weighed, dried in an oven at 105 °C for normally 12 hours and then weighed again (21) (Equation 3).

$$\text{Water content (\%)} = \frac{\text{Mass of water}}{\text{mass of biodiesel}} \times 100 \quad (\text{Eq. 3})$$

Acid value

The acid value was calculated by direct titration methods of oil against standard KOH in an alcoholic medium according to the method described by Jessinta et al., 2014 (46) with slight modifications. 0.5 g of oil was weighed into a 250 mL Erlenmeyer

flask and 50 mL of freshly neutralized hot ethyl alcohol and 1 mL of phenolphthalein indicator solution were added. The mixtures were boiled up to 5 minutes and titrated against standardized potassium hydroxide (0.24 M). The acid value was then calculated using (Equation 4).

$$\text{Acid Value} = \frac{[56.1][\text{titration of standard (mL)}][\text{molarity of standard (M)}]}{\text{weight of sample (g)}} \quad (\text{Eq. 4})$$

GC-MS Analysis of *R. communis* Seed Oil

The extracted oil was subjected to GC-MS analysis for its components using a Shimadzu QP2010 gas chromatograph coupled with mass spectroscopy detector (Shimadzu, Kyoto, Japan). A temperature range of 70 °C to 280 °C was set at and a carrier gas (helium) was used. The injection volume was set to be 2 µL at 250 °C with a flow rate of 1.80 mL/min. ACQ scanner having 30–700 amu range at speed of 1478 was operated for mass spectroscopy (Shimadzu, Kyoto, Japan). NIST05 mass spectral library (NIST, 2012) was used as a standard for comparison of spectral data obtained after the analysis (52).

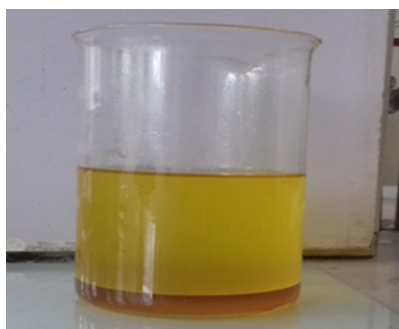
Data Analysis

Results were calculated using MS Excel (2013) and the physicochemical parameters of the biodiesel were determined using the standard procedures and compared with the standards of biodiesel (ASTM D 6751) and petrol diesel (ASTM D975) fuels described by ASTM. The compounds from GC-MS

were identified by means of their retention times, mass spectral fragmentation patterns and by comparing their mass spectra with the NIST 2012 library of mass spectra.

RESULTS AND DISCUSSION**Percentage Yield**

The extracted oil was liquid at room temperature (25 °C), golden yellow in color with a nutty odor. An alkali catalyzed transesterification technique was used for the production of the biodiesel and results revealed that three distinct layers (upper layer soap, middle layer biodiesel, and bottom layer glycerol) were formed after keeping the reaction mixtures overnight at room temperature. The extraction processes yielded 324 g (9.25% w/w) and 78% of seed oil and biodiesel respectively (figure 2). The harvesting time, method of extraction, growing region, damage caused by pests and maturity of the seeds were the main factors presented for the small yield of the seed oils.



Left, glycerin and biodiesel layers



Right, biodiesel and glycerin after separation

Figure 2: Transesterification of *R. communis* seed oils (upper layer; biodiesel and bottom layer; glycerol).

The yield of the biodiesel was good enough (78%) to substitute the regular diesel. The physicochemical properties of the biodiesel are given in Table 2 and the values are in close agreement with standards of ASTM. The standards also showed that the biodiesel

need to be purified before it is used as a fuel or blended with petroleum-based diesel fuel.

Physicochemical Results

The free fatty acid number of *R. communis* seed oils was determined to be 0.864% and the result was calculated from the following experimental values.

Experimental results

Volume used in Sample titration=3.2 mL

Volume used in Blank titration=1.2 mL

Volume of oil used=1 mL

Mass of Catalyst in g/L=1.4 g/1000 mL=1.4 g/L

$$\text{FFA number} = \frac{(A - B) \times C}{D} \quad (\text{Eq. 5})$$

Where A = Volume used in sample/actual titration,

B = Volume used in blank titration,

C = Mass of catalyst in g/L,

D = Volume of oil used.

$$\text{FFA number} = \frac{(3.2 \text{ mL} - 1.2 \text{ mL}) \times 1.4 \text{ g/L}}{1 \text{ mL}} = 2.8 \text{ g/L}$$

$$\% \text{FFA} = \frac{2.8 \text{ g}}{324 \text{ g}} \times 100 = 0.864\%$$

From Table 2 it can be seen that the density, viscosity, acid value, and water content of *R. communis* seed oil were found to be 0.887 g/mL, 35.5 mm²s⁻¹, 26.78 mg KOH/g, and 2.8% respectively, which are in large amounts. Therefore, it is not advisable to use *R. communis* seed oil directly as a fuel, because these are essential properties that have to be monitored in seed/vegetable oil to meet the biodiesel standards.

Evaluation of physicochemical parameters is vital to investigate the features of the biodiesel and results were determined according to the standard procedures described by ASTM. Figure 3 showed that the biodiesel has better cetane number than the seed oils and the acid value, kinematic viscosity, iodine value and water content of the seed oils were found to be higher than the biodiesel. The acid value of the biodiesel was 0.35 mg KOH/g (Table 2). According to the norms of the agency of national petroleum legislations, the established specification

showed that the acid value is between 0.1 and 0.5 mg KOH/g and the obtained result was within the interval of ASTM.

GC-MS analysis

A total of 10 different fatty acid methyl esters (Figure 5) were presented from the seed oil of the plant by GC-MS and include both saturated and unsaturated (Table 3). The Fatty acids were identified by means of their retention times, by comparison with the spectral data in the literature and mass spectral fragmentation patterns and by comparing their mass spectra with the NIST 2012 library of mass spectra. 9-Octadecenoic acid, 12-hydroxy-, methyl ester, [R-(Z)], 9,12-octadecadienoic acid (Z, Z)-, methyl ester and 6-octadecenoic acid, methyl ester, (Z)- were the major compounds presented from the oil sample (Figure 4).

Table 2: Physicochemical properties of castor oil and its biodiesel (min = minimum; max = maximum; HSD=high speed diesel).

Properties	Unit	Experimental results (oil)	Experimental results (biodiesel)	ASTM standard for biodiesel (ASTM D 6751)	ASTM standard for Petrol diesel (ASTM D975)
Density	g/mL	0.887	0.8571	0.87-0.90	0.95 max
Kinematic viscosity (40 °C)	mm ² s ⁻¹	35.5	5.42	1.9-6.0	1.9-4.1
Flash point	°C	-	87 relative to HSD	60-80	150 min
Acid value	mg KOH/g	26.78	0.35	0.5 max	-
Water content	%	2.8	0.8	0.05	-
Iodine value	I2 g/100 g	110.8	108.6	120 max	-
Cetane number (CN)	-	44	58.00	47 min	40 min

Table 3: Total Fatty acid methyl ester profile of *R. communis* seed oil.

No	Retention time (tR)	Compound Name	Molecular formula	Relative percentage (Area) in %	Abundance order
1	11.493	Hexadecanoic acid-methyl ester	C ₁₇ H ₃₄ O ₂	1.08	4
2	14.924	9,12-Octadecadienoic acid (Z, Z)- methyl ester	C ₁₉ H ₃₄ O ₂	4.74	2
3	15.073	6-Octadecenoic acid-methyl ester	C ₁₉ H ₃₆ O ₂	3.54	3
4	15.184	9-Octadecenoic acid (Z)-methyl ester	C ₁₉ H ₃₆ O ₂	0.48	7
5	15.618	Methyl stearate	C ₁₉ H ₃₈ O ₂	1.07	5
6	16.312	7-Hexadecenoic acid-methyl ester	C ₁₇ H ₃₂ O ₂	0.41	9
7	16.905	9,12-Octadecadienoic acid (Z, Z)	C ₁₈ H ₃₂ O ₂	0.05	10
8	19.214	9-Octadecenoic acid, 12-hydroxy-methyl ester-[R-(Z)]	C ₁₉ H ₃₆ O ₃	87.60	1
9	19.304	cis-Methyl 11-eicosenoate	C ₂₁ H ₄₀ O ₂	0.57	6
10	24.933	Octadecanoic acid, 9,10-dihydroxy-methyl ester	C ₁₉ H ₃₈ O ₄	0.43	8
Saturated			2.59		
Mono unsaturated			92.61		
Poly unsaturated			4.80		

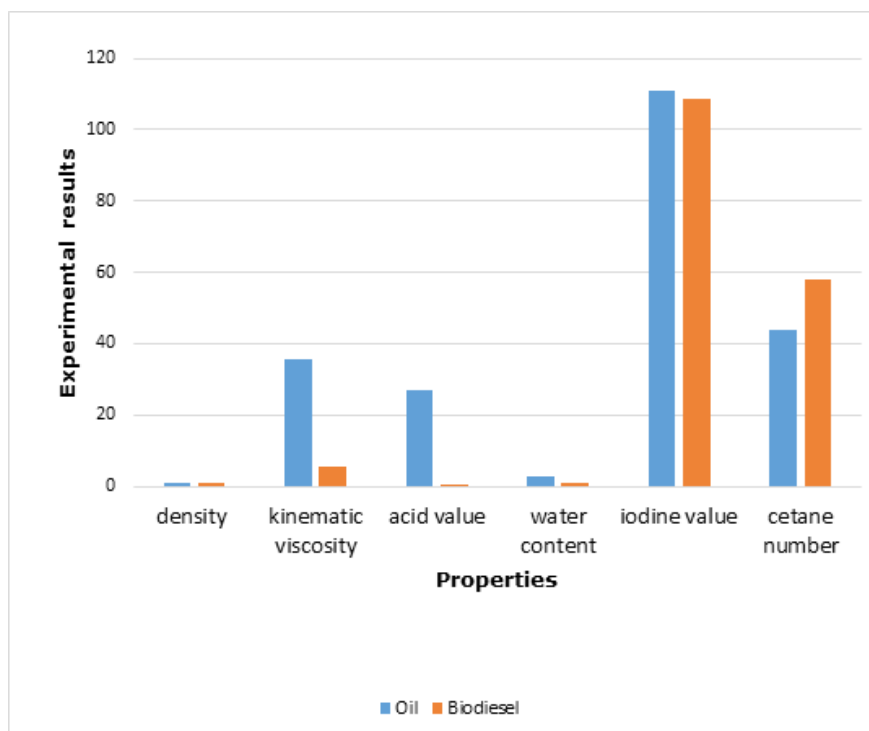


Figure 3: Comparison of the fuel properties of castor oil and its biodiesel.

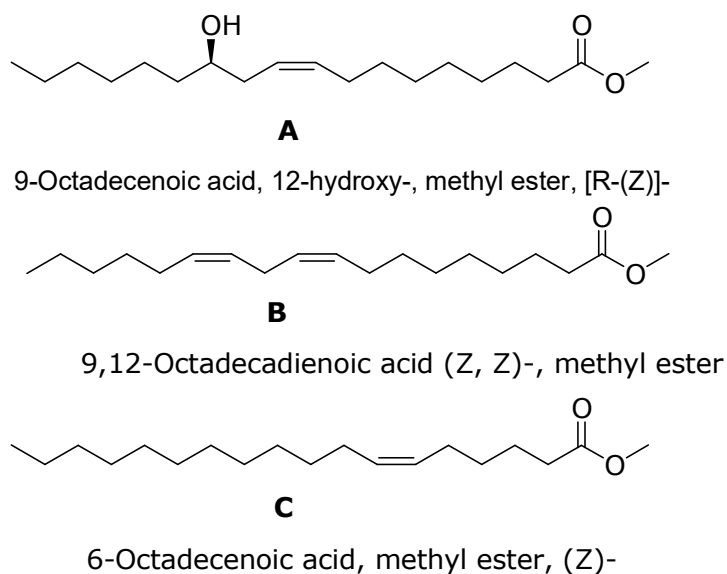


Figure 4: Proposed structures of the most abundant compounds from *R. communis* seed oil.

The total percentage of fatty acid methyl esters were 99.97% of which 9-octadecenoic acid, 12-hydroxy-methyl ester-[R-(Z)] took the maximum percentage (87.60 %). All the values are represented as the relative percentage area from the sum of all identified peaks. The overall results of

this analysis showed that the unsaturated fatty acids (UFA) make 97.31% of the compositions, whereby the monounsaturated fatty acids (MUFA) are 92.51%, polyunsaturated fatty acids (PUFA) are 4.80%; and the saturated fatty acids (SFA) are 2.59%, as shown in Table 3.

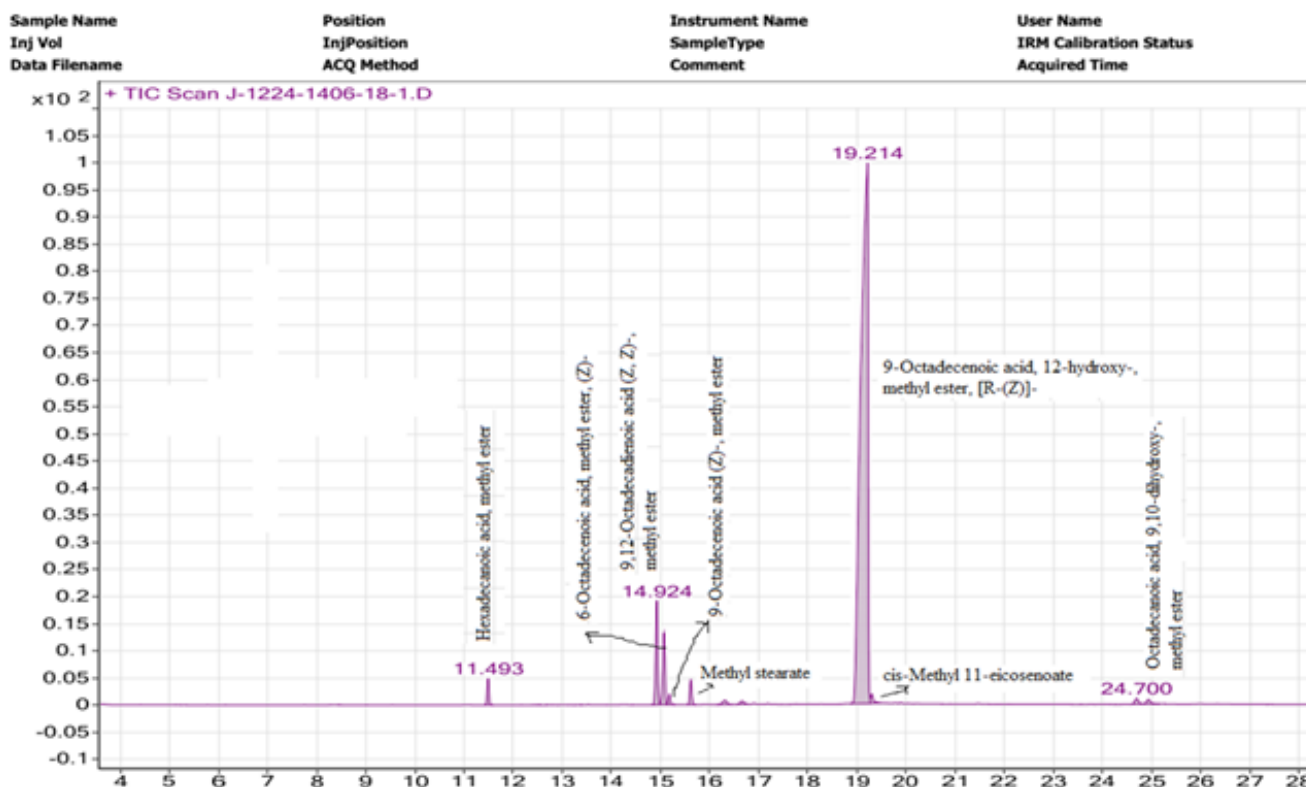
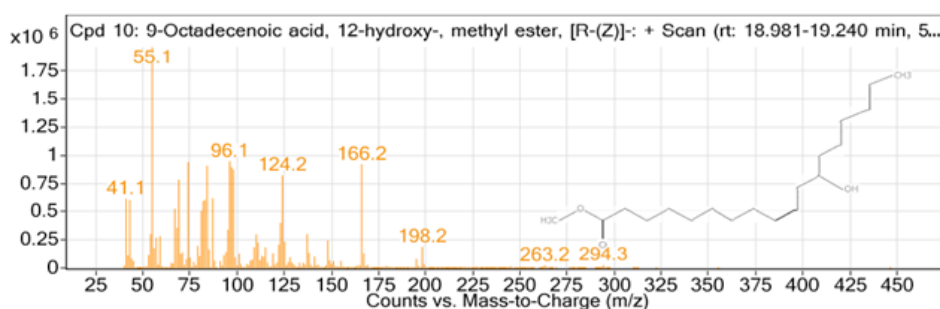


Figure 5: Gas chromatogram of *R. communis* seed oil with respect to its branded compounds.

The crude oil was evaluated by a means of gas chromatography and mass spectrometry (GC-MS) (Figures 5 and 6). The peaks were identified by the NIST 2012 library matching software. After evaluation, every single peak was matched with a single fatty acid methyl esters. The retention time (min) and position of the determined peaks are presented in Table 3. The GC-MS analysis was only towards the total fatty acid profile of the seed oil. As

a result, other organic compounds were not identified in the sample.

The mass spectra of the seed oil of the plant displayed some important fatty acid methyl esters that have a significant contribution for the production of the biodiesel by transesterification process and the fragmentation pattern of the GC-MS results of the seed oil is shown in Figure 6.



A) 9-Octadecenoic acid, 12-hydroxy-, methyl ester, [R-(Z)]-

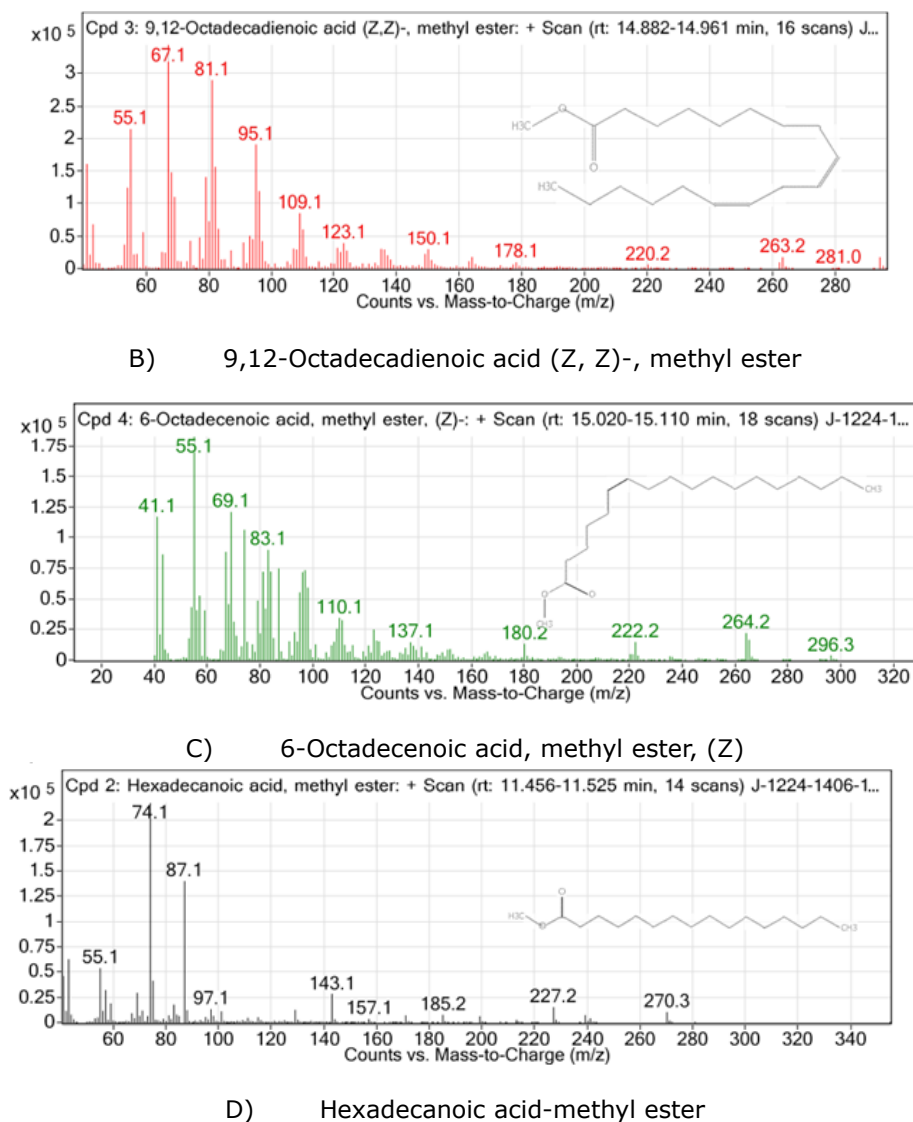


Figure 6: Mass spectra of the major components of *R. communis* seed oil.

Previous Reports

In general our results agreed to what were reported by Torrentes-Espinoza et al., 2017 (41) who presented the physico-chemical parameters of *R. communis* biodiesel that showed smooth relationships with ours'. In addition, the biodiesel properties of the plant showed a good correlation with Awais, et al., 2020 (53) but with slight differences. The GC-MS results of the seed oils reported by Khan et al., 2021 (54) that contains mainly methyl stearate, 9-octadecenoic acid (Z)-methyl ester, 9,12-octadecadienoic acid (Z, Z)-methyl ester and cis- 11- eicosenoic acid-methyl ester (54) confirmed the presences of similar fatty acid methyl esters with the results of this study. Moreover, the properties of the biodiesel reported by Khan et al., 2021 (54) (density; 0.924 g/mL, cetane number; 54.53, acid number; 1.19 mg KOH/g and water content; 0.31%) were very close to our finding (density; 0.857 g/mL, cetane number;

58.00, acid number; 0.35 mgKOH/g and water content; 0.8%).

The findings of this study are also in good agreement with the results obtained by Kiran and Prasad, 2017 (12), Zhang et al., 2015 (18), Yeboah et al., 2020 (36), Wara, 2015 (52), Anastasi et al., 2015 (55), Ramanjaneyulu et al., 2017 (56), Kondaiah et al., 2021 (57), Salihi et al., 2014 (58), Shombe et al., 2016 (59) and the seed oils were reported to possess an excellent energy substitute properties. The physicochemical results of the biodiesel showed that it can be used in any diesel engine (53). Many studies on the production of biodiesel from vegetable and seed oils were presented (5, 16, 43, 60-65) and the results are also in good agreement with the findings of this work.

In this study, the oil composition of the plant was reported to have a slight difference from some

recently published reports. This is due to the fact that the chemical composition of oils rely on certain environmental factors such as geographical location, harvesting time, temperature, extraction methods and genetic variation of the plant.

CONCLUSION

In this work, extraction with n-hexane proved to be good, since a yield of 9.25% oil was obtained in relation to the mass of the seeds used in the process. Based on the results of the study, the oil properties are interesting and promising for several applications. Biodiesel was produced through the transesterification process with a yield of 78% in relation to the *R. communis* oil mass. The combustibility of *R. communis* biodiesel was found to be better than petroleum diesel. The produced biodiesel meets the requirements of international standards of ASTM. The analysis of results by GC-MS strongly recommend that these crops are promising feed stocks for the production of biodiesel. So, *R. communis* seed oils could be used as future energy consumption replacing the current welfares of diesel and further studies are required to investigate its potential as feed stock for a new industrial products to intensify the future economic benefits of the plant.

ACKNOWLEDGEMENTS

The authors thanked to Wachemo University for the financial support and JIJE laboratory, Addis Ababa to cooperate in running the GC-MS results of the samples.

CONFLICT OF INTEREST

The authors declare that there is no conflict of interest for this manuscript.

REFERENCES

1. Tan X, Sudarsanam P, Tan J, Wang A, Zhang H, Li H, et al. Sulfonic acid-functionalized heterogeneous catalytic materials for efficient biodiesel production: a review. *Journal of Environmental Chemical Engineering*. 2021;9(1):104719. [<DOI>](#).
2. Mubofu EB. Castor oil as a potential renewable resource for the production of functional materials. *Sustainable Chemical Processes*. 2016;4(1):1-12. [<DOI>](#).
3. Hajlari SA, Najafi B, Ardabili SF. Castor oil, a source for biodiesel production and its impact on the diesel engine performance. *Renewable Energy Focus*. 2019;28:1-10. [<DOI>](#).
4. Keera S, El Sabagh S, Taman A. Castor oil biodiesel production and optimization. *Egyptian Journal of Petroleum*. 2018;27(4):979-84. [<DOI>](#).
5. Okechukwu R, Iwuchukwu A, Anuforo H. Production and characterization of biodiesel from *Ricinus communis* seeds. *Research Journal of Chemical Sciences*, ISSN. 2015;2231:606X.
6. Elango RK, Sathiasivan K, Muthukumaran C, Thangavelu V, Rajesh M, Tamilarasan K. Transesterification of castor oil for biodiesel production: Process optimization and characterization. *Microchemical Journal*. 2019;145:1162-8. [<DOI>](#).
7. Sánchez N, Encinar JM, Nogales S, González JF. Biodiesel production from castor oil by two-step catalytic transesterification: Optimization of the process and economic assessment. *Catalysts*. 2019;9(10):864. [<DOI>](#).
8. Banerjee A, Varshney D, Kumar S, Chaudhary P, Gupta V. Biodiesel production from castor oil: ANN modeling and kinetic parameter estimation. *International Journal of Industrial Chemistry*. 2017;8(3):253-62. [<DOI>](#).
9. Hailegiorgis SM, Hasraff MA, Khan SN, Ayoub M. Methanolysis of castor oil and parametric optimization. *Procedia engineering*. 2016;148:546-52. [<DOI>](#).
10. Pal A, Singh B, Mohan S. Waste Cooking Oil (WCO) Biodiesel Production Using Calcined Chalk as Heterogeneous Catalyst. *Biofuels and Bioenergy (BICE2016)*: Springer; 2017. p. 1-13. [<URL>](#).
11. Kaur R, Bhaskar T. Potential of castor plant (*Ricinus communis*) for production of biofuels, chemicals, and value-added products. *Waste biorefinery*: Elsevier; 2020. p. 269-310. ISBN: 978-0-12-818228-4.
12. Kiran BR, Prasad MNV. *Ricinus communis* L. (Castor bean), a potential multi-purpose environmental crop for improved and integrated phytoremediation. *The EuroBiotech Journal*. 2017;1(2):1-16.
13. Zhang A, Wang Q, He Y, Lai P, Miu Y, Xiao Z, editors. Preparation of Biodiesel Based on Alkaline Ionic Liquid [Bmim] OH Catalyzed Castor Oil. *IOP Conference Series: Materials Science and Engineering*; 2020: IOP Publishing. [<DOI>](#).
14. Alwaseem H, Donahue CJ, Marincean S. Catalytic transfer hydrogenation of castor oil. *Journal of Chemical Education*. 2014;91(4):575-8. [<DOI>](#).
15. Dasari SR, Goud VV. Comparative extraction of castor seed oil using polar and non polar solvents. *Int J Curr Eng Technol*. 2013;1:121-3.

16. Nakarmi A, Joshi S. A study on Castor Oil and its Conversion into Biodiesel by Transesterification Method. *Nepal Journal of Science and Technology*. 2014;15(1):45-52. [<DOI>](#).
17. Satpathy P, Thosar A, Rajan AP. Green technology for glycerol waste from biodiesel plant. *Int J Curr Microbiol App Sci*. 2014;3:730-9.
18. Zhang Q, Sun Y, Zhi L, Zhang Y, Di Serio M. Properties of ethoxylated castor oil acid methyl esters prepared by ethoxylation over an alkaline catalyst. *Journal of Surfactants and Detergents*. 2015;18(2):365-70. [<DOI>](#).
19. Gómez JJM, Saadaoui E, Cervantes E. Seed shape of castor bean (*Ricinus communis* L.) grown in different regions of Tunisia. *Journal of Agriculture and Ecology Research International*. 2016:1-11.
20. Velasco L, Fernández-Cuesta Á, Pascual-Villalobos MJ, Fernández-Martínez JM. Variability of seed quality traits in wild and semi-wild accessions of castor collected in Spain. *Industrial Crops and Products*. 2015;65:203-9. [<DOI>](#).
21. Asmare M, Gabbiye N. Synthesis and characterization of biodiesel from castor bean as alternative fuel for diesel engine. *American Journal of Energy Engineering*. 2014;2(1):1-15.
22. Gebreegziabher Z, Mekonnen A, Ferede T, Kohlin G. Profitability of bioethanol production: the case of Ethiopia. *Ethiopian Journal of Economics*. 2017;26(1):101-22. [<URL>](#).
23. Bateni H, Karimi K. Biodiesel production from castor plant integrating ethanol production via a biorefinery approach. *Chemical Engineering Research and Design*. 2016;107:4-12. [<DOI>](#).
24. Demirbas A, Bafail A, Ahmad W, Sheikh M. Biodiesel production from non-edible plant oils. *Energy Exploration & Exploitation*. 2016;34(2):290-318. [<DOI>](#).
25. Hoekman SK, Broch A, Robbins C, Cenicerros E, Natarajan M. Review of biodiesel composition, properties, and specifications. *Renewable and sustainable energy reviews*. 2012;16(1):143-69. [<DOI>](#).
26. Ijaz M, Bahtti KH, Anwar Z, Dogar UF, Irshad M. Production, optimization and quality assessment of biodiesel from *Ricinus communis* L. oil. *Journal of Radiation Research and Applied Sciences*. 2016;9(2):180-4. [<DOI>](#).
27. Issariyakul T, Dalai AK. Biodiesel from vegetable oils. *Renewable and Sustainable Energy Reviews*. 2014;31:446-71. [<DOI>](#).
28. Osorio-González CS, Gómez-Falcon N, Sandoval-Salas F, Saini R, Brar SK, Ramírez AA. Production of Biodiesel from Castor Oil: A Review. *Energies*. 2020;13(10):2467. [<DOI>](#).
29. Sajjadi B, Raman AAA, Arandiyani H. A comprehensive review on properties of edible and non-edible vegetable oil-based biodiesel: Composition, specifications and prediction models. *Renewable and Sustainable Energy Reviews*. 2016;63:62-92. [<DOI>](#).
30. Fagnano M, Visconti D, Fiorentino N. Agronomic approaches for characterization, remediation, and monitoring of contaminated sites. *Agronomy*. 2020;10(9):1335. [<DOI>](#).
31. Alam M, Rahman K. Biodiesel from mustard oil: a sustainable engine fuel substitute for Bangladesh. *International Journal of Renewable Energy Development*. 2013;2(3):141-9. [<DOI>](#).
32. Devarajan Y, Munuswamy DB, Nagappan B, Pandian AK. Performance, combustion and emission analysis of mustard oil biodiesel and octanol blends in diesel engine. *Heat and Mass Transfer*. 2018;54(6):1803-11. [<DOI>](#).
33. Sanjid A, Masjuki H, Kalam M, Abedin M, Rahman SA. Experimental investigation of mustard biodiesel blend properties, performance, exhaust emission and noise in an unmodified diesel engine. *APCBEE procedia*. 2014;10:149-53. [<DOI>](#).
34. Uyumaz A. Combustion, performance and emission characteristics of a DI diesel engine fueled with mustard oil biodiesel fuel blends at different engine loads. *Fuel*. 2018;212:256-67. [<DOI>](#).
35. Mekhilef S, Siga S, Saidur R. A review on palm oil biodiesel as a source of renewable fuel. *Renewable and Sustainable Energy Reviews*. 2011;15(4):1937-49. [<DOI>](#).
36. Yeboah A, Ying S, Lu J, Xie Y, Amoanimaa-Dede H, Boateng KGA, et al. Castor oil (*Ricinus communis*): a review on the chemical composition and physicochemical properties. *Food Science and Technology*. 2020. [<DOI>](#).
37. Barabas I, Todoruț A, Băldean D. Performance and emission characteristics of an CI engine fueled with diesel-biodiesel-bioethanol blends. *Fuel*. 2010;89(12):3827-32. [<DOI>](#).
38. Chaudhari B, Patel M, Dharajiya D, Patel A, Thakur M. Oil Content and Fatty Acid Composition in Castor (*Ricinus communis* L.) Genotypes. *International Journal of Agriculture, Environment and Biotechnology*. 2021;14(3):319-24.

39. Omotehinse S, Igboanugo A, Ikhuoria E, Ehigie C. Characterization of castor seed oil extracted from the seed species native to Edo State, Nigeria. *Journal of Science and Technology Research*. 2019;1(1):45-54.
40. Panhwar T, Mahesar SA, Mahesar AW, Kandhro AA, Talpur FN, Laghari ZH, et al. Characteristics and composition of a high oil yielding castor variety from Pakistan. *Journal of Oleo Science*. 2016;65(6):471-6. [<DOI>](#).
41. Torrentes-Espinoza G, Miranda B, Vega-Baudrit J, Mata-Segreda JF. Castor oil (*Ricinus communis*) supercritical methanolysis. *Energy*. 2017;140:426-35. [<DOI>](#).
42. Yusuf A, Mamza P, Ahmed A, Agunwa U. Extraction and characterization of castor seed oil from wild *Ricinus communis* Linn. *International Journal of Science, Environment and Technology*. 2015;4(5):1392-404.
43. Deshpande D, Urunkar Y, Thakare P. Production of biodiesel from castor oil using acid and base catalysts. *Research Journal of Chemical Sciences*, ISSN. 2012;2231:606X.
44. Ahmad M, Teong LK, Zafar M, Sultana S, Sadia H, Khan MA. Prospects and potential of green fuel from some non traditional seed oils used as biodiesel. *Biodiesel-feedstocks, production and applications*. 2012:104-26. ISBN: 978-953-51-0910-5.
45. Ahmad M, Ullah K, Khan M, Ali S, Zafar M, Sultana S. Quantitative and qualitative analysis of sesame oil biodiesel. *Energy sources, part A: Recovery, utilization, and environmental effects*. 2011;33(13):1239-49. [<DOI>](#).
46. Jessinta S, Azhari H, Saiful N, Abdurahman H. Impact of geographic variation on physicochemical properties of neem (*Azadirachta indica*) seed oil. *International Journal of Pharmaceutical Sciences and Research*. 2014;5(10):4406-13.
47. Saxena P, Jawale S, Joshipura MH. A review on prediction of properties of biodiesel and blends of biodiesel. *Procedia Engineering*. 2013;51:395-402. [<DOI>](#).
48. Thangaraj B, Solomon PR. Scope of biodiesel from oils of woody plants: a review. *Clean Energy*. 2020;4(2):89-106. [<DOI>](#).
49. Mishra VK, Goswami R. A review of production, properties and advantages of biodiesel. *Biofuels*. 2018;9(2):273-89. [<DOI>](#).
50. Fu J. Flash points measurements and prediction of biofuels and biofuel blends with aromatic fluids. *Fuel*. 2019;241:892-900. [<DOI>](#).
51. Yahya SI, Aghel B. Estimation of kinematic viscosity of biodiesel-diesel blends: Comparison among accuracy of intelligent and empirical paradigms. *Renewable Energy*. 2021;177:318-26. [<DOI>](#).
52. Warra A. Physico-chemical and GC/MS analysis of castor bean (*Ricinus communis* L.) seed oil. *Chem Mater Res*. 2015;7(2):2224-3224.
53. Awais M, Musmar SeA, Kabir F, Batool I, Rasheed MA, Jamil F, et al. Biodiesel Production from *Melia azedarach* and *Ricinus communis* Oil by Transesterification Process. *Catalysts*. 2020;10(4):427. [<DOI>](#).
54. Khan IU, Chen H, Yan Z, Chen J. Extraction and Quality Evaluation of Biodiesel from Six Familiar Non-Edible Plants Seeds. *Processes*. 2021;9(5):840. [<DOI>](#).
55. Anastasi U, Sortino O, Cosentino S, Patanè C. Seed yield and oil quality of perennial castor bean in a Mediterranean environment. *International Journal of Plant Production*. 2015;9(1):99-116.
56. Ramanjaneyulu A, Anudradha G, Ramana MV, Reddy A, Gopal NM. Multifarious uses of castor (*Ricinus communis* L.). *International Journal of Economic Plants*. 2017;4(4):170-6. [<URL>](#).
57. Kondaiah A, Rao YS, Kamitkar ND, Ibrahim SJA, Chandradass J, Kannan T. Influence of blends of castor seed biodiesel and diesel on engine characteristics. *Materials Today: Proceedings*. 2021;45:7043-9. [<DOI>](#).
58. Salihu B, Gana AK, Apuyor B. Castor oil plant (*Ricinus communis* L.): botany, ecology and uses. *International Journal of Science and Research*. 2014;3(5):1333-41.
59. Shombe GB, Mubofu EB, Mlowe S, Revaprasadu N. Synthesis and characterization of castor oil and ricinoleic acid capped CdS nanoparticles using single source precursors. *Materials Science in Semiconductor Processing*. 2016;43:230-7. [<DOI>](#).
60. Aydin K, Sarıbiyık OY, Özcanlı M, Serin H, Serin S. Biodiesel Production from *Ricinus Communis* Oil and Its Blends with Soybean Biodiesel. *Strojniski Vestnik/Journal of Mechanical Engineering*. 2010;56(12). [<URL>](#).
61. Dias J, Araújo J, Costa J, Alvim-Ferraz M, Almeida M. Biodiesel production from raw castor oil. *Energy*. 2013;53:58-66. [<DOI>](#).

62. Ismail S, Abu S, Rezaur R, Sinin H. Biodiesel production from castor oil and its application in diesel engine. ASEAN Journal on Science and Technology for Development. 2014;31(2):90-100.
63. Jamil MF, Uemura Y, Kusakabe K, Ayodele OB, Osman N, Ab Majid NMN, et al. Transesterification of mixture of castor oil and sunflower oil in millichannel reactor: FAME yield and flow behaviour. Procedia engineering. 2016;148:378-84. [<DOI>](#).
64. Magriotis ZM, Carvalho MZ, Priscila F, Alves FC, Resende RF, Saczk AA. Castor bean (*Ricinus communis* L.) presscake from biodiesel production: An efficient low cost adsorbent for removal of textile dyes. Journal of Environmental Chemical Engineering. 2014;2(3):1731-40. [<DOI>](#).
65. Sattanathan R. Production of biodiesel from castor oil with its performance and emission test. Int J Sci Res. 2015;4(1):273-9.



Ethnobotany, Phytochemistry, Ethnopharmacology, and Toxicity of *Euclea divinorum* Hiern (Ebenaceae): A Review

Timothy Omara^{1,2*} , Bernard Otieno Sadia^{1,2} , Immaculate Mbabazi^{1,2} ,
Augastine Okwir³ 

¹Department of Chemistry and Biochemistry, School of Sciences and Aerospace Studies, Moi University, P.O. Box 3900-30100, Eldoret, Kenya.

²Africa Centre of Excellence II in Phytochemicals, Textile and Renewable Energy (ACE II PTRE), Moi University, P.O. Box 3900-30100, Eldoret, Kenya.

³Department of Chemistry, Faculty of Science, Kyambogo University, P. O. Box 1, Kampala, Uganda.

Abstract: *Euclea divinorum* Hiern (Ebenaceae) is a medicinal plant widely used in Yemen, Eastern and Southern Africa in traditional phytotherapy. This review was an attempt to compile a comprehensive report on its ethnomedicinal uses, phytochemicals, pharmacological activities, and toxicity, lending credence to the use of its various parts in herbal medicine. The literature encountered indicated that herbal formularies from different parts of *Euclea divinorum* (*E. divinorum*) are majorly used for traditional treatment of odontological, dermatological, respiratory, reproductive, and gastrointestinal ailments. At least 18 compounds have been isolated and characterized in extracts of *E. divinorum*, while 31 others have been identified in the crude extracts analyzed by GC-MS. Extracts, as well as isolated compounds from *E. divinorum* stem, stem barks, leaves, and roots, showed renoprotective, antiproliferative, antinociceptive, contractile, proteolytic, diuretic, antiprotozoal, anti-giardial, antioxidant, anti-inflammatory, antimicrobial, molluscicidal, and insecticidal activities. Further research is warranted to explore other pharmacological properties such as antsnake venom, aphrodisiac, antidiabetic, analgesic, and antimycobacterial activities and the responsible bioactive compounds in the different parts of *E. divinorum* claimed in herbal medicine. The composition and bioactivities of essential oils from this species also warrant further studies.

Keywords: *Euclea divinorum*, chewing sticks, naphthoquinone, triterpene, flavonoid.

Submitted: September 29, 2021. **Accepted:** February 24, 2022 .

Cite this: Omara T, Sadia B, Mbabazi I, Okwir A. Ethnobotany, Phytochemistry, Ethnopharmacology and Toxicity of *Euclea divinorum* Hiern (Ebenaceae): A Review. JOTCSA. 2022;9(2):355-72.

DOI: <https://doi.org/10.18596/jotcsa.1001676>.

***Corresponding author:** prof.timo2018@gmail.com, prof.timo2018@mu.ac.ke, Tel: +254-742777349.

INTRODUCTION

Natural products from plants, animals, fungi, bacteria, and other biomaterials are recognized globally as veritable sources of the most known and yet-to-be discovered therapeutically effective allopathic drugs (1,2). This is due to their structural diversity, which is crucial in tackling the current multi-drug resistance crisis vis-à-vis synthetic molecules, which are tedious to produce or possess side effects owing to their lack of specificity (3). Plants are by far the most used organisms for their

supposed medicinal potential since time immemorial. They are used by more than 80% of the global population for the management of various ailments and conditions (4). This is evident in developing countries where there are shrinking health services, poverty and the aphorism that herbal medicines are more effective, safe, accessible, affordable, and culturally acceptable (5-7). Thus, intensive ethnobotanical, phytochemical, and pharmacological investigations have been carried out on medicinal flora worldwide in the past decades.

The medicinal plant *Euclea divinorum* Hiern is a deciduous shrub from the persimmon or ebony (Ebenaceae) family which, consists of over 768 shrubs and trees placed in four major genera: *Diospyros* L., *Euclea* L., *Lissocarpa* L., and *Royena* L. (8,9). The family name Ebenaceae is derived from the genus *Ebenus*, first published by Otto Kuntze in 1891, implying that it is a later homonym of *Ebenus* L. genus in the Fabaceae family (10). The genus *Euclea* has a genesis of its name from the Greek word "eukleia", meaning "of good report" or "famous", which alludes to the fine ebony-like wood of some species in it (11). The species *E. divinorum* was first named by William Phillip Hiern for its popular use by diviners (*sangomas*) in some parts of Africa, hence the epithet "divinorum" (11-13). The shrub grows to about 6 m tall, with a much-branched grey-green crown, and is commonly found in Eastern and Southern Africa (14-17). It has simple leaves (Figure 1) which are coriaceous and lanceolate, with wavy margins, sub-opposite or alternate, usually 3.5-9 cm long and 1-2.5 cm wide (11). The flowers are cup-shaped, creamy and characteristically small. Usually, the male and female flowers occur on separate trees. The berries

(fruits) are round, single-seeded, and fleshy (12). The common synonyms of this species include *E. racemosa* Murr. subsp. *schimperi* (*E. schimperi* A. DC.) (18), *E. lanceolata* sensu Hiern (13), *E. huillensis* Gürke, *E. katangensis* De Wild., *E. keniensis* R.E.Fr., *E. kiwuensis* Gürke and *E. stuhlmannii* Gürke and *E. stuhlmannii* Gürke (19).

E. divinorum inhabits grasslands, thickets, open bushlands, and margins of evergreen forests at altitudes of up to 2700 m (19). In some areas, it is considered a fast establishing, unpalatable, and fire-resistant invasive species (20-22). The species is distributed from Sudan through Ethiopia, Zimbabwe, Namibia, Botswana, Swaziland, and South Africa (23-31). It has also been reported in the Soqotra Archipelago of Yemen (27, 32-35). *E. divinorum* has been considerably researched. However, information on this species remains largely scattered in electronic reports. This review was an attempt to provide a comprehensive overview of its ethnobotany, phytochemistry, ethnopharmacology, and toxicity. The present review sheds light on and lends credence to the use of *E. divinorum* plant organs in the traditional management of various ailments claimed in folklore.



(a)



(b)



(c)

Figure 1: Different parts of *E. divinorum* used in traditional medicine (a) leaves, (b) root bark, and (c) twigs. The photos were taken by Immaculate Mbabazi from Elgeythatakwet, Kenya.

METHODOLOGY

This study is a non-systematic review that analyzed scholarly reports and peer-reviewed articles published on *E. divinorum* in open literature dated up to September 2021. The reviewed literature was retrieved electronically from PubMed, Science Direct, Scopus, Google Scholar, Springer Link, Taylor and Francis Online, Wiley Online Library, and Web of Science Core Collection. A further general search was performed using Google search engine to find other documents, reports, botanical databases and theses from various university repositories. The search keywords used singly and in combination were *Euclea divinorum*, *Euclea divinorum*, *E. divinorum*, magic guarri, and diamond-leaved *Euclea*. The reports were screened for their relevance and inclusion in the review. Ethnobotany (traditional medicinal uses), non-medicinal or commercial uses, phytochemistry, ethnopharmacology, cytotoxicity, and genotoxicity profile data of *E. divinorum* were collected to highlight gaps for future studies.

RESULTS AND DISCUSSION

Non-Medicinal (Textile, Cosmeceutical, and Economic) Uses of *E. divinorum*

The roots, leaves, and other parts of *E. divinorum* showed high tannin contents (36,37), which constitutes an inherent defense mechanism against herbivory of species in the *Euclea* genus (10). They are therefore widely used in Tanzania, Zimbabwe, Kenya, Botswana, and Yemen as purple ink, black dye for mats, wool, for tanning leather, basket ware, and other textiles, especially when a mordant of iron-rich mud is used after dyeing (11,38-42).

The roots are usually chewed to impart a red color to the mouth and lips (23,34,35,39). In Ethiopia, Zimbabwe, South Africa, Tanzania, and Kenya, the whole fruits (black sweet berries) are eaten and used for making beverages (juice and beer), though it also provides firewood, shade, amenity and timber (18,19,39,43-48). The leaves are burnt to produce plant ash as an edible salt (49).

The leaves, fruits, dried or fresh parts (e.g. stems) are used for making corrals (kraal), house ceilings, building poles, spoons, grain stores, tool handles, walking sticks, and forage for cattle and camels in Ethiopia, Kenya, Tanzania, and Yemen (18,19,34,35,45,50). The branches are used in Kenya (51) and South Western Ethiopia (52) to purify drinking water in which they are added and left to soak in the water for several hours. They are also used to treat milk, to improve digestibility and palatability, or to preserve it (42,53). In some parts of Africa, the small branches of this species are hung at the doorsteps of houses as "a good luck charm" (11). Furthermore, its tolerance of soils containing high levels of heavy metals (particularly arsenic) has made it an indicator of gold reefs or deposits (11) and has since been utilized in the recovery of gold mine pit wastes.

Ethnomedicinal Uses of *E. divinorum*

The medicinal relevance of a plant is often reflected by its high frequency of use and citation in ethnobotanical surveys (54). *E. divinorum* is called magic guarri, diamond leaf, toothbrush tree, or diamond leaved *Euclea* in English (12). As shown in **Table 1**, *E. divinorum* has many local names by which it is known within local communities across Africa and Yemen.

Table 1: Local names of *E. divinorum* used across Africa and Yemen.

Folk name (vernacular name)	Country	Reference(s)
<i>Nhlangula</i> (Xitsonga), <i>mutangule</i> (Venda), <i>Motlhakola</i> (Tswana), <i>umhlangula</i> (Zulu), <i>towerghwarrie</i> (Afrikaans), <i>mohlakola</i> (Northern Sotho), <i>umhlangula</i> , <i>umdlelanyamatane</i> (Swati), <i>nhlangula</i> (Tsonga)	South Africa, Lesotho	(11,12,55)
<i>Umdlelanyamatane</i> (siSwati)	Swaziland	(31)
<i>Kapcheptuin</i> , <i>Olkinyie</i> , <i>Uswet</i> (Markweta), <i>mdaa</i> , <i>mdala</i> , <i>msirisha</i> (Swahili), <i>msanganetu</i> (Batemi) <i>olkinyei</i> (Maa), <i>akado</i> , <i>ochol</i> , <i>Ochondradoho</i> (Luo), <i>Ikimusi</i> (Kuria), <i>Mukinyai</i> , <i>Kikuthi/Mukinyei</i> (Kamba), <i>Kumuchanjasi</i> (Luhya)	Kenya	(23,48,56-64)
<i>Omudime</i> (Oshiwambo)	Namibia	(39,65)
<i>Umushikiri</i> (Kinyarwanda)	Rwanda	(66)
<i>Omusikizi</i> (Lunyankore), <i>Emuc</i> (Langi), <i>Kasalagala/Muda</i> (Lusoga), <i>nsikizi</i> (Luganda)	Uganda	(12,67-71)
<i>Mi'eessa</i> (Oromiffa), <i>Dedeho</i> (Amharic)	Ethiopia	(30,72-74)
<i>Mdaa</i> (Swahili), <i>Msekela</i>	Tanzania	(75)
<i>Mushangura</i> (Shona), <i>Umtshekesane</i> (Ndebele)	Zimbabwe	(12,13)
<i>Munyansyabweli</i>	Zambia	(76)

Several formulations containing different parts of *E. divinorum* singly or in combination with other plant parts are used for the treatment of both human and animal ailments. The range of treated diseases includes malignancies, central nervous system,

odontological, dermatological, respiratory, gastrointestinal, reproductive, venereal, and general ailments or infections (Table 2; Figure 2). The most used parts are the roots and the root bark, probably because of their ability to accumulate therapeutic

phytochemicals, which are responsible for the treatment of various ailments (77). Generative and/or reproductive structures such as flowers, fruits, and seeds, which are also reputed to accumulate phytochemicals, are less commonly used, probably because the plant blossoms once a year (from August to December) (11). As a result of the use of such structures, plant organs for medication would be limited throughout the year.

Other than the foregoing medicinal uses, *E. divinorum* is also used in various cultural practices. For example, the plant is given to candidates during initiation by the Sebei of Uganda or used in important "koresek" Sebei ceremonies (rituals of

purification). Among the Sabaot of Kenya, the leaves are used as sleeping mats for initiates during their period of seclusion (18). Its root powder is applied onto incisions to remove spells in Uganda (78). The leaves and roots of this species are also used for love affairs (75). In Ethiopia, *E. divinorum* along with other trees such as *Cordia africana* Lam., *Ehretia cymosa* (Thonn.) and *Maesa lanceolata* Forssk. are symbolically revered as *Haaganaa* trees (trees ordained by mystical powers) and are used in rituals of avoiding inauspicious omen, idiotism, homicide case resolution and mythical power expression (72). In South Africa, *E. divinorum* is used in magical practices (79).

Table 2: Ethnomedicinal uses of different parts of *E. divinorum* based on encountered literature.

Ailment(s) treated/uses	Part(s) used	Preparation or administration	Country	Reference (s)
1. General infections/conditions				
Malaria	Root bark, roots, leaves	Decoction. May also be used with roots of <i>Hagenia abyssinica</i> and <i>Grewia ferruginea</i>	Kenya, Zimbabwe, Ethiopia	(30,44,80-85)
Blood cleanser/purifier	Fruits, roots	Chewed and saliva swallowed	Kenya, Yemen	(35,63)
Arthritis	Roots	Powder applied to incisions	Uganda	(78)
Used as a cathartic to induce purgation	Roots, bark, fruits	Roots are chewed after gentle warming over an open flame. Usually followed by a cup of strong tea. Soup made from bark, fruits and roots may also be taken	Kenya, South Africa, Tanzania	(19,48,64,84,86,87)
Bleeding	Bark, seeds, roots, leaves	Applied topically on fresh bleeding wounds	Namibia, South Africa, Yemen	(65,88)
Stroke	Roots	Decoction/infusion taken	Kenya, Tanzania	(75,85,89)
Chest pains, headache, internal body swellings called "kati"	Roots	Decoction prepared with <i>Croton megalocarpus</i> roots taken	Kenya, South Africa	(19,84,86,87)
Various ailments and for good health (as a tonic or an invigorant)	Stem bark, roots, fruits	Bark or with roots are boiled with meat soup and taken. Fruits chewed. Added to children's milk	Kenya, Uganda, Tanzania	(15,52,62,63,86,90-92)
2. Odonatological diseases/dental hygiene				
Used as a mouth antiseptic/disinfectant, clean and whiten the teeth (toothbrushes/ <i>misawk</i>), treat gum bleeding, toothache, tooth cavity	Branches (twigs), root bark, roots	Chewed roots/ powdered root barks, mixed with little water and salt, and inserted into the tooth cavity/for toothache. Roots are used for brushing teeth for dental hygiene. Dried root/bark powder rubbed to clean teeth	Kenya, Yemen, Uganda, Zimbabwe, South Africa, Tanzania	(18,19,32,34,35,39,43,52,84,87,93)
3. Reproductive system diseases and conditions				
Venereal diseases/infections (syphilis, gonorrhoea,	Roots, leaves	Root extract with those of <i>Carissa edulis</i> (Forsk.) Vahl and <i>Carica papaya</i> L. taken. Decoction may be taken directly	Kenya, Zambia, Ethiopia	(30,61,76,94-97)

Ailment(s) treated/uses	Part(s) used	Preparation or administration	Country	Reference (s)
genital herpes, oral candidiasis, abscesses)				
Infertility	Roots	Decoction taken	Kenya	(61)
Miscarriage	Roots	Decoction drunk	Uganda	(78)
Managing delayed and protracted labour, post-partum haemorrhage, and removing things retained after birth	Leaves, roots	Chewed	Kenya	(56)
Cervical cancer, prophylaxis of cancer	Leaves, fruits	Infusion drunk, fruits chewed as a prophylaxis	Uganda	(63,67,98)
Salpingitis	Roots	Powder drunk as tea	Uganda	(78)
4. Dermatological conditions				
Skin infections (rash, abscesses, disorders, irritations, ringworms, pimples, chickenpox, inflammation, eczema)	Leaves, root bark, roots, fruits	Applied topically (add leaf/root powder to jelly and smear or bark powder to water and apply) or boiled to take a bath. Fruits chewed	South Africa, Yemen, Uganda, Ethiopia, Kenya	(32,34,35,55,63,69,70,79,97,99)
Leprosy, scabies	Leaves	Not reported	Ethiopia	(30)
Snakebites	Roots, bark	Crushed & applied on incision made on the bite area, used with dry roots of <i>Tragia brevipes</i> , <i>Gardenia volkensii</i> and <i>Plectranthus barbatus</i>	Kenya, Uganda	(78,100-102)
Jaundice	Roots	Decoction drunk	Uganda, Tanzania	(75,78)
Wound healing, antiseptic, disinfectant, cicatrizing against infection, used as a maturative	Roots	Not reported	South Africa	(103)
Rabies	Leaves	Not reported	Ethiopia	(30)
5. Respiratory ailments				
Tuberculosis, cough, respiratory disorders	Roots, fruits, leaves	Chewed	Uganda, Kenya	(63,68,85)
Pneumonia	Roots, bark	Decoction prepared with <i>Croton megalocarpus</i> roots taken	Kenya, South Africa	(19,84,86,87)
6. Gastrointestinal infections and metabolic disorders and ailments				
Ulcers	Roots	Decoction taken	Swaziland	(31)
Abdominal upsets	Fruits	Chewed	Kenya	(63)
Amebiasis, tapeworm	Leaves	Not reported	Ethiopia	(30)
Constipation, anthelmintic, abdominal pain	Roots, leaves	Not reported	Kenya, South Africa, Ethiopia	(58,85,87,97,104)

Ailment(s) treated/uses	Part(s) used	Preparation or administration	Country	Reference (s)
Stomach pain, stomachache, deworming Appetizer	Roots, bark, leaves	Decoction taken	South Africa, Kenya	(84,87)
	Roots, bark	Root decoction. Bark added to soup with <i>Rhamnus prinoides</i> and taken	Kenya	(18,48)
Diabetes	Root bark	Decoction taken	Kenya	(57)
Kidney infection/problems, hepatitis	Stem bark, root bark	Crushed and used	Ethiopia	(73,97)
7. Ethnoveterinary uses	Stem bark			(60)
Used as an analgesic General veterinary diseases	Fruits	Decoction given	Kenya	(105)

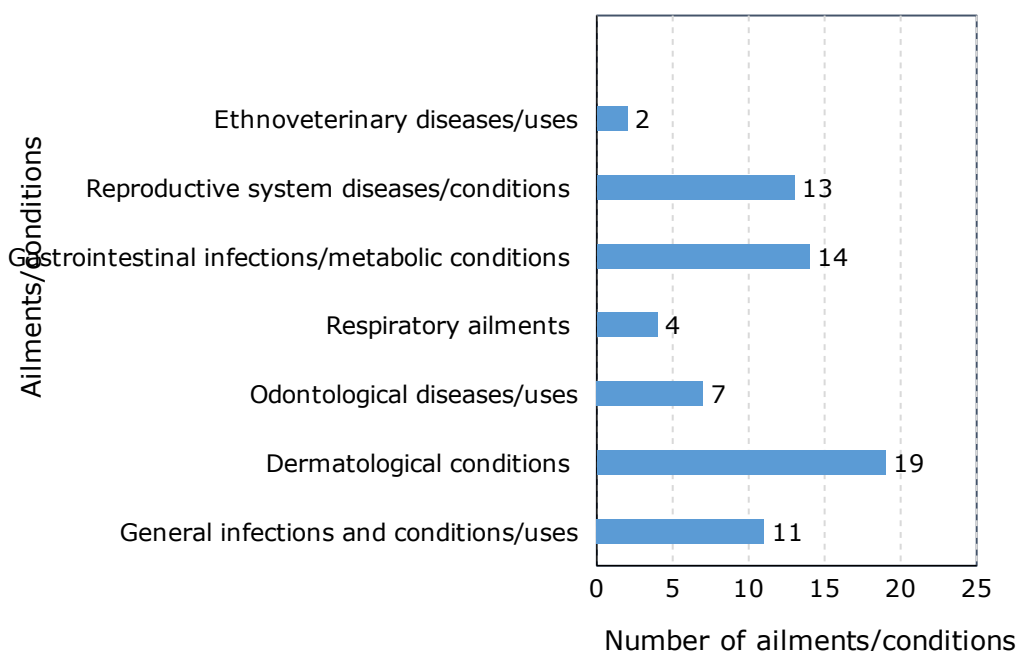


Figure 2: Major groups of ailments and conditions treated using preparations of *E. divinorum*.

Phytochemistry of *E. divinorum*

Phytochemical investigations on *E. divinorum* extracts have been conducted. Conventional phytochemical screening of organic and aqueous extracts of *E. divinorum* have been carried out. Tannins, saponins, flavonoids, terpenes, alkaloids, steroids, terpenoids, and reducing compounds were identified as the major secondary metabolites (Table 3).

For quantification of phytochemicals, an earlier study reported total phenolic and water-soluble phenolic contents of 122.7 mg/g and 77.1 mg/g, respectively and tannin by protein precipitation of 94 mg/g from the bark of *E. divinorum* (62).

Mbabazi et al. (2021) quantified the polyphenol content of n-hexane, ethanol and dichloromethane (DCM) extracts of *E. divinorum* leaves, stems and root barks (106). The total phenolic and total flavonoid contents were the highest in ethanol, followed by DCM and then n-hexane extracts. The order of abundance recorded was root barks > tender stems > leaves (Table 4). However, the total flavonoid content was the highest in ethanol extract followed by n-hexane and lastly DCM extract. The high polyphenols content is hypothesized to be the reason for the inhibition of growth of teeth-attacking bacteria by the parts of this species used in dental hygiene and controlling dental caries (106).

Table 3. Secondary metabolites reported in *E. divinorum* extracts.

Part(s) used	Solvent(s) used	Metabolites detected	Author(s)
Leaves, stem, root bark	n-hexane, DCM, ethanol	Alkaloids, flavonoids, cardiac glycosides, phenols, saponins, quinones, steroids, tannins, terpenes and volatile oils	(106)
Root bark	Ethyl acetate	Alkaloids, flavonoids, saponins, tannins, terpenoids	(25)
Stem, roots	DCM	Alkaloids, flavonoids, glycosides, phenolics, saponins, tannins, terpenes	(107)
Roots	Ethyl acetate	Alkaloids, flavonoids, steroids and terpenes	(27)
Roots	Methanol, distilled water	Flavonoids, saponins, tannins, terpenoids, steroids, cardiac glycosides	(108)
Roots, root bark	Methanol, ether, distilled water	Tannins, saponins, alkaloids, steroids, terpenoids, reducing compounds, flavonoids, steroids, terpenoids, flavonoid aglycones	(90)
Leaves, roots, stems	DCM : methanol	Anthraquinones, alkaloids, saponins, tannins, polyphenols, terpenoids	(109)
Roots	DCM	Triterpenoids, amino acids, resins, tannins	(110)
Roots	Methanol	Phenolic acids, tannins	(111)
Leaves, fruits	Methanol	Polyphenols, tannins, sterol/triterpenes, glycosides, carbohydrates	(30)

Table 4: Total polyphenolic content of the *E. divinorum* parts.

Polyphenol	Plant organ	n-hexane extract	*DCM extract	Ethanol extract
Total phenolic content	Leaves	299.0	1190.0	1516.0
	Tender stems	231.0	828.0	2800.0
	Root barks	472.0	1569.0	3105.0
Total flavonoid content	Leaves	84.3	23.4	63.10
	Tender stems	55.6	27.6	81.60
	Root bark	193.3	96.1	309.70

Pioneering elucidative studies of bioactive compounds in *E. Divinorum*, just like in other *Euclea* species, led to the identification of naphthoquinones, triterpenes and flavonoids. For example, 7-methyljuglone, mamegakinone, diospyrin, and isodiospyrin were reported in the root extract of *E. divinorum*, but stems and green fruits extracts had no naphthoquinones (See Figure 3; 112). Cruz-Costa et al. (113) reported the presence of 7-methyljuglone, diospyrin, 2-methylnaphthazarin, betulin, diosindigo A, and lupeol in petroleum ether extract of *E. divinorum* roots (Figure 3). Flavonoids: (2R:3R)-aromadendrin-3-O-β-L-arabinopyranoside, catechin, quercitrin, and myricitrin were later characterized in the ethanolic extracts of *E. divinorum* aerial parts (14).

Phytochemical characterization of chloroform extract of *E. divinorum* root bark led to the identification of

naphthoquinones, triterpenoids and flavonoids viz: 7-methyljuglone, isodiospyrin, betulin, lupeol, catechin, 3-β-(5-hydroxyferuloly)lup-20-(30)-ene, shinalene, and lupene (114). Further, the bioactive compounds in the leaves of *E. divinorum* were characterized and two new compounds: Euclenal A or 8-hydroxy-3-methoxy-1-naphthaldehyde and Euclenal B or 4-hydroxy-3,8-dimethoxy-1-naphthaldehyde were identified (52). A new naphthalene derivative: 8-hydroxy-6-methoxy-1-naphthaldehyde or euclenal was identified in ethyl acetate extract of *E. divinorum* leaves (115) (Figure 3). Recently, Kilonzo et al. identified γ-sitosterol, germanicol, and oxacycloheptadec-8-en-2-one, (8Z) in ethyl acetate extract of *E. divinorum* root bark by GC-MS (Table 5). In another report, Mbabazi et al. (2021) identified 28 compounds GC-MS in n-hexane and dichloromethane extracts of *E. divinorum* leaves, tender stems, and root barks (Table 5) (106).

Table 5: Compounds identified in extracts of *E. divinorum* by GC-MS.

Part	Extractant	Compounds identified
Root bark	Ethyl acetate	<p>γ-sitosterol Germanicol Oxacycloheptadec-8-en-2-one, (8Z) 1-Methyl-2-Pyrrolidinone Eicosane</p>
Leaves	n-hexane	<p>Tetratriacontane 2-Hydroxy-2-methyl-8,8-diphenyl-octa-5,7-dien-3-one Eicosane Tetratriacontane Palmitic acid Ethyl palmitate Ethyl-9,12-octadecadienoate Ethyl 9α-linolenate</p>
Tender stems	n-hexane	<p>4,8,12,16-Tetramethylheptadecan-4-olide Tetracosane 9-Tricosene Heptacosanol Hexatriacontane Heneicosane Eicosane Tetratriacontane Hexatriacontane</p>
Root bark	n-hexane	<p>1,4-Naphthoquinone 7-Ethoxycoumarin 4-Vinyl guaiacol Squalene Eicosane Tetratriacontane Ethyl palmitate Heptacosanol</p>
Leaves	DCM	<p>Squalene Octadecanal Cis, cis,cis-7,10,13-Hexadecatrienal Tetradecyl acrylate Octacosanal Eicosane</p>
Tender stems	DCM	<p>Tetratriacontane Hexatriacontane Tetratetracontane γ-Tocopherol 2-Ethylhexyl acrylate</p>
Root bark	DCM	<p>2,6,11-Trimethyldodecane 3,4-Methylenedioxybenzylacetone 9-Hexadecen-1-ol</p>

Pharmacological Profile of *E. divinorum*

Different extracts and isolated compounds from *E. divinorum* have been investigated and reported to have antiproliferative (antitumor), antinociceptive, anti-giardial, renoprotective, antiprotozoal, molluscicidal, insecticidal, contractile, proteolytic, diuretic, antioxidant, anti-inflammatory, and antimicrobial activities.

Antiproliferative and antitumor activity

Some isolated compounds from *E. divinorum* (**1**, **4**, **6**, **8**, **10**, **13-15**) were assessed for their antitumor potential against BC-1 (human breast cancer), Lu-1 (human lung cancer), HT (human fibrosarcoma), KB (human nasopharyngeal carcinoma), KB-V (vinblastine resistant KB evaluated in the presence and absence of vinblastine), Me-1 (human melanoma), P-388 (murine lymphocytic leukemia), A431 (human epidermoid carcinoma), Col-2 (human colon cancer), LNCaP (human prostate cancer), ZR-75-1 (human breast cancer) and U373 (human glioblastoma) cell lines (114). The authors reported that compounds **1** and **13** exhibited strong cytotoxicity, while the rest of the compounds were not cytotoxic. Interestingly, **1** was cytotoxic to all the cancer cells and the most intense responses were registered for KB, P-388, LNCaP, ZR-75-1 and U373 cells at concentrations of 4.8, 0.1, 0.8, 2.2 and 2.7 µg/mL, respectively. On the other hand, **13** was highly selective and showed cytotoxicity only against two cancer cells (P-388 and ZR-75-1) at 2.1 and 4.2 µg/mL, respectively. The antiproliferative activity of the crude extracts of this species has not been reported.

Renoprotective activity

The potential of crude methanolic extract, and methanolic and aqueous fractions of *E. divinorum* leaves to reduce gentamicin-induced nephrotoxicity in rats was investigated (74). The authors reported that the extract and fractions reversed gentamicin-mediated alterations by decreasing tubular necrosis, serum and oxidant markers, and increment in antioxidant molecules. The renoprotective effect decreased with an increase in crude extract dosage whereas maximum protection was afforded at 100 mg/kg of the methanolic fraction for *in vivo* and *in vitro* studies. The authors postulated that the renoprotective effect of the extract and fractions could be due to the antioxidant potentials of their moderately polar phytochemicals (74).

Antimicrobial activity

Kirui et al. (2015) indicated that the aqueous extract of the whole plant of *E. divinorum* retarded the growth of bacterial colonies in water (51). In another research, ethanolic extracts of *E. divinorum* leaves and barks were assessed for their inhibitory activity against some selected oral pathogens (116). The extracts did not inhibit the growth of *Candida albicans* (*C. albicans*) unlike *Streptococcus mutans* where the of the inhibition zone diameters (ZOI)

were 6.0 mm and 2.4 mm at 2 mg and 3 mg of extracts per disk, respectively. The reported minimum inhibitory concentration (MIC) ranged from 3.1 to 25.0 µg/mL against *Actinomyces naeslundii*, *Actinomyces israelii*, *Streptococcus mutans*, *Actinobacillus actinomycetemcomitans*, and *Porphyromonas gingivalis*.

The ethanolic extracts of leaves, stem barks, and roots of *E. divinorum* showed antibacterial activity against *Escherichia coli* (*E. coli*), *Staphylococcus aureus* (*S. aureus*), *Campylobacter jejuni*, *Streptococcus pyogenes*, and *Shigella sonnei* with ZOI varying from 10 mm to 14 mm (117). Aqueous extracts exerted bacteriostatic activity against *E. coli*, *S. aureus*, *Shigella sonnei* and *Campylobacter jejuni* with the same range of ZOI, but did not inhibit the growth of *Streptococcus pyogenes*, *Bacillus cereus*, *Pseudomonas aeruginosa*, and *Salmonella typhi*. The root extract only inhibited the growth of *Streptococcus pyogenes* with a ZOI of 13 mm (117). Later, Geyid et al. (2005) found that methanolic extract of *E. divinorum* leaves retarded the growth of *C. albicans* and *Cryptococcus neoformans* (*C. neoformans*) when tested at 4000 µg/mL (30). Mining (48) reported ZOI of 17.6, 10.6, 6.0, 12.6 and 6.6 mm for DCM extract of *E. divinorum* leaves against *E. coli*, *S. aureus*, *Pseudomonas aeruginosa*, *Bacillus subtilis*, and *C. albicans*.

In another investigation (111), the root methanolic extract of *E. divinorum* exhibited antimicrobial activity against multidrug-resistant *Staphylococcus* strains (*S. epidermidis* 847, *S. haemolyticus* 535, and *S. aureus* North German Epidemic strain with ZOI of 24 mm, 16 mm, and 26 mm, respectively), *S. aureus*, *Bacillus subtilis*, *Micrococuss flavus*, *E. coli*, *Pseudomonas aeruginosa* and *Candida maltosa* with a ZOI of 24 mm, 12 mm, 18 mm, 11 mm, 15 mm, and 10 mm. Another team (118) evaluated the antifungal activities of some Venda plant extracts against *C. albicans*, *Candida krusei*, and *C. neoformans* isolated from South African AIDS patients. The n-hexane extract of *E. divinorum* leaves was more active against *C. neoformans* with a ZOI of 8 mm at 10 µL. No bioactivity was observed against the other fungi.

The aqueous and DCM/methanol extracts of *E. divinorum* roots had no antimicrobial activity against *E. Coli*, while DCM extract had a ZOI of 10.30 mm (110). In the same study, DCM extract had ZOI of 10.75 mm and 10.00 mm against *Streptococcus aureus* and *Lactobacillus acidophilus*, respectively. The DCM/methanol extracts had ZOI of 9.13 mm, 10.80 mm and 6.70 mm while aqueous extracts had no inhibitory activity. In another study, crude root extracts of *E. divinorum* showed ZOI of 9.00 mm and 13.00 mm for *Streptococcus mutans* and *Streptococcus sanguinis*, with MICs of 1,250 µg/mL and 2,500 µg/mL, respectively (109).

Ethanollic extracts of *E. divinorum* stem bark exhibited anti-mycoplasmal activity against *Mycoplasma mycoides* subsp. *mycoides* (Afadé, B 237, Gladysdale, PG1 and V5), *Mycoplasma mycoides* subsp. *capri* (Y-Goat, 95010, G1313.94, M-18 and G1255/94) and *Mycoplasma capricolum* subsp. *capricolum* (Mcc) 6443-90 with MIC of 0.500 mg/mL, 0.417 mg/mL and 0.500 mg/mL against the strains, respectively (60). In another investigation, the antibacterial screening indicated that ethyl acetate extract of *E. divinorum* root was effective in inhibiting *E. coli* (ZOI = 17 mm) while *S. aureus* was resistant to the extract (ZOI = 9 mm; same as that of ethanol used as negative control) (27). Methanolic, methanol : DCM and aqueous extracts of *E. divinorum* were reported to have no inhibitory or bactericidal effects against Methicillin-Resistant *S.aureus*, *S.aureus*, *S.mutans* and *C.albicans* (119).

Another report indicated that DCM extract of *E. divinorum* roots exerted the highest antifungal activity (ZOI = 30 mm) against *Trichophyton mentagrophytes*. Its antifungal activity was comparable to that of the ethyl acetate (ZOI = 20 mm) and methanolic (ZOI = 25 mm) extracts against the six tested fungal strains: *Absidia corymbifera*, *Aspergillus fumigatus*, *Candida krusei*, *Microsporium gypseum*, *Mucor* species and *Trichophyton mentagrophytes* with ZOI ranging between 15 mm and 20 mm (34). Acetonic and aqueous extracts of *E. divinorum* roots were indicated to exert antifungal activity against *C. albicans*, *Microsporium canis* and *Trichophyton rubrum* with average MIC of 0.23 to 0.47 mg/mL (79). Kilonzo et al. (25) reported that petroleum ether, ethyl acetate and aqueous extracts of *E. divinorum* leaves, stem bark and root bark showed antimicrobial activity against *S. aureus* (MIC = 0.718 to >25 mg/mL), *Klebsiella pneumoniae* (MIC = 0.718 >25 mg/mL), *E. coli* (MIC = 0.718 >25 mg/mL), *Salmonella typhi* (MIC = 0.718 to >25 mg/mL), *C. albicans* (MIC = 0.718 to >25 mg/mL), and *C. neoformans* (MIC = 0.718 to >25 mg/mL).

Mbabazi et al. (2020) in a comparative study investigated the antimicrobial activity of *E. divinorum* leaves, tender stems and root bark and a formulated herbal toothpaste from its extracts against oral pathogens (120). The plant materials were extracted sequentially by maceration with dichloromethane, n-hexane and ethanol. The root barks ethanolic extract was the most active with a MIC of 25 µg/mL, 50 µg/mL, 25 µg/mL and 25 µg/mL against *Streptococcus pyogenes*, *S. aureus*, *E. coli* and *C. albicans*. Herbal toothpaste formulated with the ethanolic extract of *E. divinorum* root barks had the highest activity against the tested microorganisms (ZOI = from 7.67 mm to 22.67 mm) compared to Colgate herbal toothpaste formulated with fluoride as the active ingredient (ZOI = 5.00 mm to 16.33 mm).

Anti-giardial and antiprotozoal activities

To validate the gastrointestinal use of *E. divinorum* in traditional medicine, a pioneering investigation concluded that methanolic extracts of its roots and barks did not cause death of *Giardia lamblia* trophozoites at 500 ppm and 1000 ppm (121). The methanolic extract of *E. divinorum* roots showed antiprotozoal (antiplasmodial, antileishmanial and antitrypanosomal) activities with IC₅₀ of 37.5 ± 4.7 µg/mL, >64.0 ± 0.0 µg/mL, 22.5 ± 4.7 µg/mL and 33.1 ± 5.3 µg/mL against *Plasmodium falciparum* K1 strain, *Leishmania infantum*, *Trypanosoma cruzi* and *Trypanosoma brucei* Squib-427 strain (122). The antiplasmodial results were corroborated by another report from Kenya in which methanolic extract of *E. divinorum* root barks had antiplasmodial activity with IC₅₀ of 6.9 µg/mL and 12.4 µg/mL against D6 and W2 *P.falciparum* strains, respectively (123).

Antinociceptive, antioxidant and anti-inflammatory activities

Mwonjoria et al. (2018) reported that DCM extracts of *E. divinorum* stems and roots showed significant antinociceptive effects in the second phase of formalin-induced nociception when tested at doses of 50 mg and 100 mg on Wistar rats (107). Feyissa et al. (2013) reported that the maximum percentage inhibitions of 1,1-diphenyl-2-picrylhydrazyl (DPPH) at 2000 mg/mL by the methanolic fraction, aqueous fraction and crude methanolic extract of *E. divinorum* leaves were 82.5%, 74.5% and 62.5%, respectively (74). In another report, IC₅₀ between 8.30 and >1000 µg/mL were reported on *E. divinorum* leaf extracts in DPPH radical and nitric oxide antioxidant assays (124). In anti-inflammatory activity assay, the recorded Cyclooxygenase-2 (COX-2) inhibition at 10 µg/mL was 71.12%. In a recent report, the IC₅₀ values of DCM, ethyl acetate, and methanolic (direct and sequential) extracts of *E. divinorum* obtained in DPPH radical scavenging activity were 690.5 µg/mL, 680.8 µg/mL, 550.0 µg/mL, and 225.0 µg/mL, respectively (34).

Contractile, proteolytic and diuretic activities

The folkloric use of *E. divinorum* to induce or augment labour, manage protracted labour and post-partum haemorrhage was validated through investigation of the contractile activity of its aqueous and ethanolic root barks extracts (125). The extracts stimulated uterine tissue contractility and augmented its response to oxytocin. The increase in uterine contractions as a percentage relative to negative controls was particularly significant in pregnant rabbit tissues in the presence of oxytocin, where increments of up to 245% were observed.

Aqueous extract of *E. divinorum* twigs inhibited 50% of proteolytic activity against *Bacteroides gingivalis*, *Bacteroides intermedius*, and *Treponema denticola* at concentrations ranging from 10 µg/mL up to 200

µg/mL (126). Another report (127) indicated that aqueous extracts of *E. divinorum* and *Rhus natalensis* had high inhibitory effects on the proteolytic activities of *Porphyromonas gingivalis*, *Bacteriodes intermedius* and *Treponema denticola*, which indicates that the extracts could reduce the virulence of these periodontopathic bacteria as well as the rate of dental plaque formation.

Further, the assessment of the diuretic potential of methanolic and aqueous extracts of *E. divinorum* roots in Sprague Dawley rats revealed that methanolic extract produced significant diuresis at 200 mg/kg and 400 mg/kg while aqueous extract produced significant diuresis at all tested doses (108).

Molluscicidal and insecticidal activities

E. divinorum methanolic extract had molluscicidal activity against *B. glabrata* in 48 hours at concentrations under 500 µg/mL (128). Examining the insecticidal activity of *E. divinorum* to verify its use in the management of storage pests indicated that its n-hexane and DCM leaf extracts caused 35% and 60% mortality when tested against bean weevils (*Acanthoscelides obtectus*) at 1000 ppm (48). However, the essential oils have not been tested for its insecticidal potential.

Adverse side effects, toxicity and genotoxicity profiles of *E. divinorum* extracts

E. divinorum root extract is traditionally reported to have laxative effects which is counteracted by inclusion of half glass of *Achyranthes aspera* leaves and *Ficus natalensis* roots or barks (89). The petroleum ether/ethyl acetate (1:1) and methanolic extracts of *E. divinorum* roots were reported to be cytotoxic to human ECV-304 cells with IC₅₀ values of 11.6 µg/mL and 36.0 µg/mL, respectively (32). Another study reported the IC₅₀ value of 27.5 ± 3.6 µg/mL for methanolic extract of *E. divinorum* roots against human lung fibroblast MRC-5 SV2 cells (122). Acute toxicity studies of methanolic extract of *E. divinorum* leaves indicated that it was safe when administered orally at 2000 mg/kg (74). Even after a period of 72 hours, the animals tolerated the administered dose, with no appreciable changes in behaviour (motor activity, diarrhoea, breathing, alertness, restlessness, convulsions, coma and appearance). Since no mortality was recorded within 14 days, the lethal dose (LD₅₀) was indicated to be more than 2000 mg/kg (74).

The methanolic, methanol: DCM and aqueous extracts of *E. divinorum* were reported to be non-cytotoxic (119). Al-Fatimi (2019), reported the low cytotoxicity (IC₅₀ values of 240.0 to 900.5 µg/mL) of DCM, ethanolic and methanolic extracts of *E. divinorum* roots from Yemen against human amniotic epithelial cells line (FL-cells) (34). n-hexane and DCM extracts of leaves showed lethality against brine shrimp with LD₅₀ of 952.0 and 689.9

ppm (48). These reports indicate that some extracts of this species are potentially cytotoxic.

An investigation examining the genotoxic activity in human peripheral blood lymphocytes of some South African plants (129) reported that DCM extract of *E. divinorum* roots induced DNA damage, which were however lower than that of the positive control (1 mM potassium bichromate). Another report, carried out by the same team (130), indicated that DCM extract rather than the methanolic extract of *E. divinorum* roots was toxic in the Ames test.

CONCLUSION

Euclea divinorum possesses a long history of use in herbal medicine in Africa and Yemen. Significant strides have been made in the past decades in isolating, elucidating, and evaluating the bioactive compounds as well as pharmacological activities of this species. Some identified compounds have been reported to have remarkable *in vitro* and *in vivo* bioactivity. Thus, the folkloric claims of using this species in managing various ailments are credible, but further research is warranted to explore other pharmacological properties such as antsnake venom, aphrodisiac, antidiabetic, analgesic, and antimycobacterial activities, the responsible compounds in the different parts of *E. divinorum* and their mechanisms of action. More toxicity studies are needed to demonstrate sufficient proof for human safety when employing *E. divinorum* extracts and/or isolated components. Further research into the content and bioactivities of essential oils derived from this plant is warranted. Clinical trials using *E. divinorum* extracts and isolated substances are also necessary. Indigenous groups should be encouraged to prioritize its protection due to its broad ethnomedicinal, economic, and cultural value.

ABBREVIATIONS

C. albicans: *Candida albicans*; *C. neoformans*: *Cryptococcus neoformans*; DCM: Dichloromethane; *E. coli*: *Escherichia coli*; *E. divinorum*: *Euclea divinorum*; MIC: Minimum Inhibitory Concentration; *S. aureus*: *Staphylococcus aureus*; ZOI: Zone inhibition diameter.

CONFLICT OF INTEREST

The authors declare that there is no conflict of interest regarding the publication of this paper.

ACKNOWLEDGEMENTS

The authors are grateful to the World Bank and the Inter-University Council of East Africa (IUCEA) for the scholarship awarded to Immaculate Mbabazi through the Centre of Excellence II in Phytochemicals, Textile and Renewable Energy (ACE II PTRE) at Moi University, Kenya, that prompted this review.

REFERENCES

1. Amit Koparde A, Chandrashekar Doijad R, Shripal Magdum C. Natural Products in Drug Discovery. In: Perveen S, Al-Taweel A, editors. Pharmacognosy - Medicinal Plants [Internet]. IntechOpen; 2019 [cited 2022 Feb 26]. [<URL>](#).
2. Omara T, Kiprof AK, Ramkat RC, Cherutoi J, Kagoya S, Moraa Nyangena D, et al. Medicinal Plants Used in Traditional Management of Cancer in Uganda: A Review of Ethnobotanical Surveys, Phytochemistry, and Anticancer Studies. Evidence-Based Complementary and Alternative Medicine. 2020 Mar 16;2020:1–26.
3. the International Natural Product Sciences Taskforce, Atanasov AG, Zotchev SB, Dirsch VM, Supuran CT. Natural products in drug discovery: advances and opportunities. Nat Rev Drug Discov. 2021 Mar;20(3):200–16.
4. WHO. WHO Global Report on Traditional and Complementary Medicine [Internet]. World Health Organization; 2021 [cited 2022 Feb 26]. [<URL>](#).
5. Schultz F, Anywar G, Wack B, Quave CL, Garbe L-A. Ethnobotanical study of selected medicinal plants traditionally used in the rural Greater Mpigi region of Uganda. Journal of Ethnopharmacology. 2020 Jun;256:112742.
6. Tabuti JRS, Kukunda CB, Waako PJ. Medicinal plants used by traditional medicine practitioners in the treatment of tuberculosis and related ailments in Uganda. Journal of Ethnopharmacology. 2010 Jan;127(1):130–6.
7. Tugume P, Kakudidi EK, Buyinza M, Namaalwa J, Kamatenesi M, Mucunguzi P, et al. Ethnobotanical survey of medicinal plant species used by communities around Mabira Central Forest Reserve, Uganda. J Ethnobiology Ethnomedicine. 2016 Dec;12(1):5.
8. Anonymous. The Plant List. Ebenaceae [Internet]. The Plant List. 2021 [cited 2022 Feb 26]. [<URL>](#).
9. Duangjai S, Wallnofer B, Samuel R, Munzinger J, Chase MW. Generic delimitation and relationships in Ebenaceae sensu lato: evidence from six plastid DNA regions. American Journal of Botany. 2006 Dec 1;93(12):1808–27.
10. Anonymous. Ebenaceae [Internet]. Ebenaceae. 2021. [<URL>](#).
11. Mothogoane M. Euclea divinorum Hiern [Internet]. Euclea divinorum Hiern. 2014. [<URL>](#).
12. Orwa C, Mutua A, Kindt R, Jamnadass R, Anthony S. Euclea divinorum Hiern (Ebenaceae) [Internet]. Agroforestry Database: a tree reference and selection guide version 4.0; 2021. [<URL>](#).
13. Hyde M, Wursten B, Ballings P, Coates Palgrave M. Flora of Zimbabwe: Species information: Euclea divinorum [Internet]. Zimbabweflora; 2021. [<URL>](#).
14. Dagne E, Alemu M, Sterner O. Flavonoids from Euclea divinorum. Bull Chem Soc Eth. 1993;7(2):87–92.
15. Grinsven M, Parkipuny M, Johns T. Euclea divinorum (Ebenaceae) bark is a high-potential tanning material. Econome Botany. 1999;53:220.
16. Smith TM, Goodman PS. Successional Dynamics in an Acacia Nilotica-Euclea Divinorum Savannah in Southern Africa. The Journal of Ecology. 1987 Sep;75(3):603.
17. Ivens G. The effects of arboricides on East African trees and shrubs IV. Tarchonanthus camphoratus L. and Euclea divinorum Hiern. Tropical Agriculture, Trinidad and Tobago. 1960;37(2):143–52.
18. Maundu P. Traditional Food Plants of Kenya [Internet]. 1999. 288 p. [<URL>](#).
19. Lovett J, Ruffo C, Gereau R, Taplin J. Field Guide to the Moist Forest Trees of Tanzania [Internet]. The Society for Environmental Exploration, UK and the University of Dar es Salaam, Tanzania; 2005. [<URL>](#).
20. Wahungu GM, Gichohi NW, Onyango IA, Mureu LK, Kamaru D, Mutisya S, et al. Encroachment of open grasslands and Acacia drepanolobium Harms ex B.Y.Sjöstedt habitats by Euclea divinorum Hiern in Ol Pejeta Conservancy, Kenya. Afr J Ecol. 2013 Mar;51(1):130–8.
21. Mutunga Kavwele C. Time Series Monitoring of Bush Encroachment by “Euclea divinorum“ in Ol Pejeta Conservancy Laikipia, Kenya. IJNREM. 2017;2(5):85.
22. Parker JWPL, Parker AM. Herbicide Control of Euclea Divinorum— Preliminary Experiments. East African Agricultural and Forestry Journal. 1964 Oct;30(2):89–93.
23. Njuguna P. Euclea divinorum Hiern. Jansen P, Cardon D, editors. Wageningen, Netherlands: PROTA (Plant Resources of Tropical Africa / Ressources végétales de l’Afrique tropicale); 2005.
24. Anonymous. Euclea divinorum Hiern [Internet]. Board of Trustees of the Royal Botanic Gardens, Kew; 2021 [cited 2022 Feb 26]. [<URL>](#).
25. Kilonzo M, Rubanza C, Richard U, Sangiwa G. Antimicrobial activities and phytochemical analysis

- of extracts from *Ormocarpum trichocarpum* (Taub.) and *Euclea divinorum* (Hiern) used as traditional medicine in Tanzania. *Tanzania J Hlth Res.* 2020 Sep 10;21(2):1-12.
26. Hutchings A. Zulu medicinal plants: An inventory. [Internet]. University of Natal press; 1996. <URL>.
27. Shumba L. Phytochemical composition and bacterial activity of *Euclea divinorum* [Internet] [Master of Science Thesis]. [Zimbabwe]: Bindura University of Science Education; 2018. <URL>.
28. Mostert T, Bredenkamp G, Klopper H, Verwey C, Mostert R, Hahn N. Major vegetation types of the Soutpansberg Conservancy and the Blouberg Nature Reserve, South Africa: original research. *Koedoe.* 2008;50(1):32-48.
29. Scogings P. Large herbivores and season independently affect woody stem circumference increment in a semi-arid African savanna. *Plant Ecology.* 2014;215:1433-43.
30. Geyid A, Abebe D, Debella A, Makonnen Z, Aberra F, Teka F, et al. Screening of some medicinal plants of Ethiopia for their anti-microbial properties and chemical profiles. *Journal of Ethnopharmacology.* 2005 Mar;97(3):421-7.
31. Amusan OOG, Dlamini PS, Msonthi JD, Makhubu LP. Some herbal remedies from Manzini region of Swaziland. *Journal of Ethnopharmacology.* 2002 Feb;79(1):109-12.
32. Al-Fatimi M, Friedrich U, Jenett-Siems K. Cytotoxicity of plants used in traditional medicine in Yemen. *Fitoterapia.* 2005 Jun;76(3-4):355-8.
33. Sharam G, Sinclair ARE, Turkington R. Establishment of Broad-leaved Thickets in Serengeti, Tanzania: The Influence of Fire, Browsers, Grass Competition, and Elephants¹. *Biotropica.* 2006 Sep;38(5):599-605.
34. Al-Fatimi. Antifungal Activity of *Euclea divinorum* Root and Study of its Ethnobotany and Phytopharmacology. *Processes.* 2019 Oct 1;7(10):680.
35. Miller G, Morris M. *Ethnoflora of the Soqotra Archipelago.* Edinburgh, UK: The Royal Botanic Garden; 2004.
36. Scogings P, Siko S, Taylor R. Calibration of a hand-held instrument for measuring condensed tannin concentration based on UV- and red-excited fluorescence. *African Journal of Range & Forage Science.* 2014 Jan 2;31(1):55-8.
37. Hattas D, Julkunen-Tiitto R. The quantification of condensed tannins in African savanna tree species. *Phytochemistry Letters.* 2012 Jun;5(2):329-34.
38. Manyim S, Kiprop AK, Mwasiagi JI, Achisa CM, Odero MP. Dyeing of cotton fabric with *Euclea divinorum* extract using response surface optimization method. *RJTA [Internet].* 2021 May 5 [cited 2022 Feb 26]; <URL>.
39. Maroyi A. The Gathering and Consumption of Wild Edible Plants in Nhema Communal Area, Midlands Province, Zimbabwe. *Ecology of Food and Nutrition.* 2011 Nov;50(6):506-25.
40. China CR, Hilonga A, Nyandoro SS, Schroeffer M, Kanth SV, Meyer M, et al. Suitability of selected vegetable tannins traditionally used in leather making in Tanzania. *Journal of Cleaner Production.* 2020 Apr;251:119687.
41. Cunningham AB, Milton SJ. Effects of basket-weaving industry on mokola palm and dye plants in northwestern Botswana. *Econ Bot.* 1987 Jul;41(3):386-402.
42. Cardon D. *Dyes and Tannins.* PROTA Foundation; 2005.
43. Bussmann RW, Gilbreath GG, Solio J, Luturo M, Lutuluo R, Kunguru K, et al. Plant use of the Maasai of Sekenani Valley, Maasai Mara, Kenya. *J Ethnobiology Ethnomedicine.* 2006 Dec;2(1):22.
44. Maundu P, Berger D, Ole Saitabau C, Nasieku J, Kipelian M, Mathenge S, et al. *Ethnobotany of the Loita Maasai People and Plants Working Paper 8.* 2001;
45. Gemedo-Dalle T, Maass BL, Isselstein J. Plant Biodiversity and Ethnobotany of Borana Pastoralists in Southern Oromia, Ethiopia. *Economic Botany.* 2005 Jan;59(1):43-65.
46. Mashile SP, Tshisikhawe MP, Masevhe NA. Indigenous fruit plants species of the Mapulana of Ehlanzeni district in Mpumalanga province, South Africa. *South African Journal of Botany.* 2019 May;122:180-3.
47. Rampedi IT, Olivier J. Traditional Beverages Derived from Wild Food Plant Species in the Vhembe District, Limpopo Province in South Africa. *Ecology of Food and Nutrition.* 2013 May;52(3):203-22.
48. Mining J. Bioactive Metabolites Of Selected Kenyan Plants Used As Biopesticides Against *Acanthoscelides obtectus* in Bungoma District, Kenya [Internet] [Master of Science Thesis]. [Nairobi, Kenya]: Jomo Kenyatta University of Agriculture and Technology; 2008. <URL>.
49. *Euclea divinorum*-Hiern [Internet]. *Plants For A Future.* 2021. <URL>.

50. Habte M, Eshetu M, Andualem D, Maryo M, Legesse A. The inventory of camel feed resource and the evaluation of its chemical composition in south-east rangelands of Ethiopia. *Vet Med Sci*. 2021 Jul;7(4):1172–84.
51. Kirui JK, Kotut K, Okemo PO. Efficacy of aqueous plant extract in disinfecting water of different physicochemical properties. *Journal of Water and Health*. 2015 Sep 1;13(3):848–52.
52. Ng'ang'a MM, Hussain H, Chhabra S, Langat-Thoruwa C, Al-Harrasi A, Krohn K, et al. Eucleal A and B: Two new naphthalene derivatives from *Euclea divinorum*. *Chinese Chemical Letters*. 2012 May;23(5):576–8.
53. den Biggelaar C, Mureithi W. Using tree species to treat milk for palatability and preservation. *Intermediate Technology Food Chain*. 2000;26:6–7.
54. Omara T, Kiprop AK, Kosgei VJ. *Albizia coriaria* Welw ex Oliver: a review of its ethnobotany, phytochemistry and ethnopharmacology. *ADV TRADIT MED (ADTM) [Internet]*. 2021 Jul 21 [cited 2022 Feb 26]; <URL>.
55. Setshego MV, Aremu AO, Mooki O, Otang-Mbeng W. Natural resources used as folk cosmeceuticals among rural communities in Vhembe district municipality, Limpopo province, South Africa. *BMC Complement Med Ther*. 2020 Dec;20(1):81.
56. Kaingu CK, Oduma JA, Kanui TI. Practices of Traditional Birth Attendants in Machakos District, Kenya. *Journal of Ethnopharmacology*. 2011 Sep;137(1):495–502.
57. Keter LK, Mutiso PC. Ethnobotanical studies of medicinal plants used by Traditional Health Practitioners in the management of diabetes in Lower Eastern Province, Kenya. *Journal of Ethnopharmacology*. 2012 Jan;139(1):74–80.
58. Gakuya DW, Itonga SM, Mbaria JM, Muthee JK, Musau JK. Ethnobotanical survey of biopesticides and other medicinal plants traditionally used in Meru central district of Kenya. *Journal of Ethnopharmacology*. 2013 Jan;145(2):547–53.
59. Kokwaro JO, Johns T, Kokwaro JO. *Luo biological dictionary*. Nairobi: East African Educational Publishers; 1998. 264 p.
60. Kama-Kama F, Midiwo J, Nganga J, Maina N, Schiek E, Omosa LK, et al. Selected ethno-medicinal plants from Kenya with in vitro activity against major African livestock pathogens belonging to the "Mycoplasma mycoides cluster." *Journal of Ethnopharmacology*. 2016 Nov;192:524–34.
61. Kamanja I, Mbaria J, Gathumbi P, Mbaabu M, Lanyasunya A, Gakuya D, et al. Medicinal plants used in the management of sexually transmitted infections by the Samburu Community Kenya. 2015;
62. Johns T, Mahunnah RLA, Sanaya P, Chapman L, Tickin T. Saponins and phenolic content in plant dietary additives of a traditional subsistence community, the Batemi of Ngorongoro District, Tanzania. *Journal of Ethnopharmacology*. 1999 Jul;66(1):1–10.
63. Kigen G, Kipkore W, Wanjohi B, Haruki B, Kemboi J. Medicinal plants used by traditional healers in Sangurur, Elgeyo Marakwet County, Kenya. *Phcog Res*. 2017;9(4):333.
64. Kigen G, Maritim A, Some F, Kibosia J, Rono H, Chepkwony S, et al. Ethnopharmacological survey of the medicinal plants used in Tindiret, Nandi County, Kenya. *Afr J Trad Compl Alt Med*. 2016 Mar 16;13(3):156.
65. Maroyi A, Cheikhyoussef A. A comparative study of medicinal plants used in rural areas of Namibia and Zimbabwe. 2015; <URL>.
66. White F. *Flore d'Afrique Centrale (Zaire – Rwanda – Burundi): Ebenaceae*. 1987.
67. Gumisiriza H, Sesaaazi CD, Olet EA, Kembabazi O, Birungi G. Medicinal plants used to treat "African" diseases by the local communities of Bwambara sub-county in Rukungiri District, Western Uganda. *Journal of Ethnopharmacology*. 2021 Mar;268:113578.
68. Tabuti JRS, Kukunda CB, Waako PJ. Medicinal plants used by traditional medicine practitioners in the treatment of tuberculosis and related ailments in Uganda. *Journal of Ethnopharmacology*. 2010 Jan;127(1):130–6.
69. Anywar G, Kakudidi E, Byamukama R, Mukonzo J, Schubert A, Oryem-Origa H. Indigenous traditional knowledge of medicinal plants used by herbalists in treating opportunistic infections among people living with HIV/AIDS in Uganda. *Journal of Ethnopharmacology*. 2020 Jan;246:112205.
70. Namukobe J, Lutaaya A, Asimwe S, Byamukama R. An Ethnobotanical Study of Medicinal Plants used in the Management of Dermatological Disorders in Buyende and Kayunga Districts, Uganda. *EJMP*. 2021 Mar 16;15–40.
71. Obakiro SB, Kiprop A, Kowino I, Kigundu E, Odero MP, Omara T, et al. Ethnobotany, ethnopharmacology, and phytochemistry of traditional medicinal plants used in the management of symptoms of tuberculosis in East Africa: a systematic review. *Trop Med Health*. 2020 Dec;48(1):68.

72. Roba GO. Trees symbolism, conservation and threat in Guji Oromo, Southern Ethiopia. Lu Z, editor. *Cogent Social Sciences*. 2021 Jan 1;7(1):1880681.
73. Lulekal E, Kelbessa E, Bekele T, Yineger H. An ethnobotanical study of medicinal plants in Mana Angetu District, southeastern Ethiopia. *J Ethnobiology Ethnomedicine*. 2008 Dec;4(1):10.
74. Feyissa T, Asres K, Engidawork E. Renoprotective effects of the crude extract and solvent fractions of the leaves of *Euclea divinorum* Hierns against gentamicin-induced nephrotoxicity in rats. *Journal of Ethnopharmacology*. 2013 Feb;145(3):758-66.
75. Augustino S, Gillah PR. Medicinal Plants in Urban Districts of Tanzania: Plants, Gender Roles and Sustainable Use. *int forest rev*. 2005 Mar 1;7(1):44-58.
76. Chinsambu KC. Ethnobotanical Study of Plants Used in the Management of HIV/AIDS-Related Diseases in Livingstone, Southern Province, Zambia. Evidence-Based Complementary and Alternative Medicine. 2016;2016:1-14.
77. Saxena M, Saxena J, Nema R, Singh D, Gupta A. Phytochemistry of medicinal plants. *Journal of pharmacognosy and phytochemistry*. 2013;1(6).
78. Tabuti JRS, Lye KA, Dhillion SS. Traditional herbal drugs of Bulamogi, Uganda: plants, use and administration. *Journal of Ethnopharmacology*. 2003 Sep;88(1):19-44.
79. Shikwambana N, Mahlo SM. A Survey of Antifungal Activity of Selected South African Plant Species Used for the Treatment of Skin Infections. *Natural Product Communications*. 2020 May;15(5):1934578X2092318.
80. Pascaline J, Charles M, George O, Lukhoba C. An inventory of medicinal plants that the people of Nandi use to treat malaria. *J Anim Plant Sci*. 2011;9:1192-200.
81. Lukwa N, Mutambu S, Makaza N, Molgaard P, Furu P. PERCEPTIONS ABOUT MALARIA TRANSMISSION AND CONTROL USING ANTI-MALARIA PLANTS IN MOLA, KARIBA, ZIMBABWE. *Nigerian Journal of Natural Products and Medicine*. 2001 Jan 1;5(1):4-7.
82. Hunde D, Asfaw Z, Kelbessa E. Use of traditional medicinal plants by people of 'Boosat'sub district, Central Eastern Ethiopia. *Ethiopian Journal of Health Sciences [Internet]*. 2006;16(2). [<URL>](#).
83. Orwa JA, Mwitari PG, Matu EN, Rukunga GM. Traditional healers and the management of malaria in Kisumu District, Kenya. *E Af Med Jrnl*. 2008 Mar 26;84(2):51-5.
84. Ruth L, Manani Solomon D. Ethnobotanical survey and propagation of some endangered medicinal plants from south Nandi district of Kenya. *J Anim Plant Sci*. 2010;8(3):1016-43.
85. Odongo S. Medicinal plants of Chuka community in Tharaka Nithi County, Kenya and some of their selected essential elements [Internet] [Master of Science Thesis]. [Nairobi, Kenya]: Kenyatta University; 2013. [<URL>](#).
86. Kokwaro J. Medicinal plants of East Africa. East African Literature Bureau, Nairobi, Kenya; 1976.
87. van Wyk B-E, van Oudtshoorn B, Gericke N. Medicinal plants of South Africa. Pretoria, South Africa: Briza Publications; 1997. 304 p.
88. Smith CA, Phillips EP, Van Hoepen E. Common Names of South African Plants [Internet]. Government Printer, South Africa; 1966. (Botanical Research Institute botanical survey memoir). [<URL>](#).
89. Kamau LN, Mbaabu PM, Mbaria JM, Gathumbi PK, Kiama SG. Ethnobotanical survey and threats to medicinal plants traditionally used for the management of human diseases in Nyeri County, Kenya. *CellMed*. 2016;6(3):21-1.
90. Onyango C, Gakuya L, Mathooko FM, Maina J, Nyaberi M, Makobe M, et al. Phytochemical studies on herbal plants commonly used for processing and preserving meat and milk. *Journal of Applied Biosciences*. 2014;73:5942-8.
91. Kokwaro JO. Medicinal plants of East Africa. 3rd ed. Nairobi, Kenya: University of Nairobi Press; 2009. 478 p.
92. Johns T, Mhoro EB, Sanaya P, Kimanani EK. Herbal remedies of the Batemi of Ngorongoro District, Tanzania: a quantitative appraisal. *Econ Bot*. 1994 Jan;48(1):90-5.
93. Ngari F, Wanjau R, Njagi E, Gikonyo N. Herbal Materials Used in Management of Oral Conditions in Nairobi, Kenya. *Journal of Oral Health & Community Dentistry*. 2014;8(1).
94. Johns T, Kokwaro JO, Kimanani EK. Herbal remedies of the Luo of Siaya District, Kenya: Establishing quantitative criteria for consensus. *Econ Bot*. 1990 Sep;44(3):369-81.
95. Tadesse M, Demissew S. Plants Used in African Traditional Medicine as Practiced in Ethiopia and Uganda. *Botany* 2000. 1992;

96. Balemie K, Kelbessa E, Asfaw Z. Indigenous medicinal plant utilization, management and threats in Fentalle area, Eastern Shewa, Ethiopia. *Ethiopian Journal of Biological Sciences*. 2004;3(1):37–58.
97. Abate G, Demissew S. Etse Debdabe. In Addis Ababa, Ethiopia: Artistic Printing Press; 1989. p. 123.
98. Gumisiriza H, Birungi G, Olet EA, Sesaazi CD. Medicinal plant species used by local communities around Queen Elizabeth National Park, Maramagambo Central Forest Reserve and Ihimbo Central Forest Reserve, South western Uganda. *Journal of Ethnopharmacology*. 2019 Jul;239:111926.
99. Mabona U, Van Vuuren SF. Southern African medicinal plants used to treat skin diseases. *South African Journal of Botany*. 2013 Jul;87:175–93.
100. Kipkore W, Wanjohi B, Rono H, Kigen G. A study of the medicinal plants used by the Marakwet Community in Kenya. *J Ethnobiology Ethnomedicine*. 2014 Dec;10(1):24.
101. Okello SV, Nyunja RO, Netondo GW, Onyango JC. Ethnobotanical study of medicinal plants used by sababots of Mt. Elgon Kenya. *Afr J Trad Compl Alt Med [Internet]*. 2010 Jul 30 [cited 2022 Feb 26];7(1). [<URL>](#).
102. Fatuma Some GK. Ethnomedicinal Plants Traditionally Used by the Keiyo Community in Elgeyo Marakwet County, Kenya. *J Biodivers Biopros Dev [Internet]*. 2014 [cited 2022 Feb 26];01(03). Available from: [<URL>](#).
103. Verschaeve L, Van Staden J. Mutagenic and antimutagenic properties of extracts from South African traditional medicinal plants. *Journal of Ethnopharmacology*. 2008 Oct;119(3):575–87.
104. Muthee JK, Gakuya DW, Mbaria JM, Kareru PG, Mulei CM, Njonge FK. Ethnobotanical study of anthelmintic and other medicinal plants traditionally used in Loitokitok district of Kenya. *Journal of Ethnopharmacology*. 2011 Apr;135(1):15–21.
105. Njoroge GN, Bussmann RW. Herbal usage and informant consensus in ethnoveterinary management of cattle diseases among the Kikuyus (Central Kenya). *Journal of Ethnopharmacology*. 2006 Dec;108(3):332–9.
106. Mbabazi I, Wangila P, Krsquo;Owino IO. Comparison of the phytochemical composition of *Euclea divinorum* (Ebenaceae) leaves, tender stems and root bark. *Adv J Chem B [Internet]*. 2021 Aug [cited 2022 Feb 26];3(3). [<DOI>](#).
107. Mwonjoria J, Ngeranwa J, Githinji C, Wanyonyi A. Antinociceptive effects of dichloromethane extract of *Euclea divinorum* Lin. *Journal of Pharmacognosy and Phytochemistry*. 2018;7(6):1104–7.
108. Woldemedhin B, Nedi T, Shibeshi W, Sisay M. Evaluation of the diuretic activity of the aqueous and 80% methanol extracts of the root of *Euclea divinorum* Hiern (Ebenaceae) in Sprague Dawley rats. *Journal of Ethnopharmacology*. 2017 Apr;202:114–21.
109. Nyaitondi OD, Wanjau RN, Nyambaka H, Hassanali A. Anti-bacterial properties and GC-MS analysis of extracts and essential oils of selected plant product. *J Nat Prod Biochem*. 2018 Feb 1;16(1):44–58.
110. Ngari FW, Gikonyo NK, Wanjau RN, Njagi EM. Safety and antimicrobial properties of *Euclea divinorum* Hiern, chewing sticks used for management of oral health in Nairobi County, Kenya. *J Pharm Biomed Sci*. 2013;3(3):1–8.
111. Mothana RA, Lindequist U, Gruenert R, Bednarski PJ. Studies of the in vitro anticancer, antimicrobial and antioxidant potentials of selected Yemeni medicinal plants from the island Soqatra. *BMC Complement Altern Med*. 2009 Dec;9(1):7.
112. van der Vijver LM, Gerritsma K. Naphthoquinones of *Euclea* and *Diospyros* species. *Phytochemistry*. 1974;
113. Cruz-Costa M, Lopes MH, Paul MI, Ferreira MA, Correia-Alves A. Naphthoquinones and triterpenoids of *Euclea divinorum*. *Phytochemistry*. 1976;
114. Ng'ang'a MM, Hussain H, Chhabra S, Langat-Thoruwa C, Krohn K, Hussain J, et al. Eucleanal: A New Naphthalene Derivative from *Euclea divinorum*. *Natural Product Communications*. 2012 Feb;7(2):1934578X1200700.
115. More G, Tshikalange TE, Lall N, Botha F, Meyer JJM. Antimicrobial activity of medicinal plants against oral microorganisms. *Journal of Ethnopharmacology*. 2008;119(3):473–7.
116. Obi CL, Potgieter N, Bessong PO, Masebe T, Mathebula H, Molobela P, et al. In vitro antibacterial activity of Venda medicinal plants. *South African Journal of Botany*. 2003 Jul;69(2):199–203.
117. More G, Tshikalange TE, Lall N, Botha F, Meyer JJM. Antimicrobial activity of medicinal plants against oral microorganisms. *Journal of Ethnopharmacology*. 2008 Oct;119(3):473–7.
118. Samie A, Tambani T, Harshfield E, Green E, Ramalivhana J, Bessong P. Antifungal activities of selected Venda medicinal plants against *Candida albicans*, *Candida krusei* and *Cryptococcus neoformans* isolated from South African AIDS

- patients. African Journal of Biotechnology. 2010;9(20).
119. Mutuku A. Antimicrobial Activity Of Warburgia ugandensis, Euclea divinorum, Rhus vulgaris, Ocimum gratissimum and Clausena anisata Against Oral Pathogenic Microorganisms [Internet] [Master of Science Thesis]. [Eldoret, Kenya]: University of Eldoret; 2018. [<URL>](#).
120. Mbabazi I, Wangila P, K'Owino IO. Antimicrobial activity of Euclea divinorum hern (ebenaceae) leaves, tender stems, root bark and an herbal toothpaste formulated from its ethanolic root bark extract. 2020;3(3):8-16. [<URL>](#).
121. Johns T, Faubert GM, Kokwaro JO, Mahunnah RLA, Kimanani EK. Anti-giardial activity of gastrointestinal remedies of the Luo of East Africa. Journal of Ethnopharmacology. 1995 Apr;46(1):17-23. [<DOI>](#).
122. Mothana R, Al-Musayeib N, Matheeussen A, Cos P, Maes L. Assessment of the in Vitro Antiprotozoal and Cytotoxic Potential of 20 Selected Medicinal Plants from the Island of Soqotra. Molecules. 2012 Dec 3;17(12):14349-60. [<DOI>](#).
123. Muthaura CN, Keriko JM, Mutai C, Yenesew A, Gathirwa JW, Irungu BN, et al. Antiplasmodial potential of traditional phytotherapy of some remedies used in treatment of malaria in Meru-Tharaka Nithi County of Kenya. Journal of Ethnopharmacology. 2015 Dec;175:315-23. [<DOI>](#).
124. Twilley D, Langhansová L, Palaniswamy D, Lall N. Evaluation of traditionally used medicinal plants for anticancer, antioxidant, anti-inflammatory and anti-viral (HPV-1) activity. South African Journal of Botany. 2017 Sep;112:494-500. [<DOI>](#).
125. Kaluwa Kaingu C, Oduma JA, Kanui T. Preliminary investigation of contractile activity of Ricinus communis and Euclea divinorum extracts on isolated rabbit uterine strips. Journal of Ethnopharmacology. 2012 Jul;142(2):496-502. [<DOI>](#).
126. Homer KA, Manji F, Beighton D. Inhibition of protease activities of periodontopathic bacteria by extracts of plants used in Kenya as chewing sticks (mswaki). Archives of Oral Biology. 1990;35(6):421-4. [<DOI>](#).
127. Homer KA, Manji F, Beighton D. Inhibition of peptidase and glycosidase activities of Porphyromonas gingivalis, Bacteroides intermedius and Treponema denticola by plant extracts. J Clin Periodontol. 1992 May;19(5):305-10. [<DOI>](#).
128. Chapman L, Johns T, Mahunnah RLA. Saponin-like *in vitro* characteristics of extracts from selected non-nutrient wild plant food additives used by Maasai in meat and milk based soups. Ecology of Food and Nutrition. 1997 Feb;36(1):1-22. [<DOI>](#).
129. JLS, Elgorashi EE, Maes A, Van Gorp U, De Kimpe N, van Staden J, et al. Investigating the safety of plants used in South African traditional medicine: Testing for genotoxicity in the micronucleus and alkaline comet assays. Environ Mol Mutagen. 2003;42(3):144-54. [<DOI>](#).
130. Elgorashi E. Screening of medicinal plants used in South African traditional medicine for genotoxic effects. Toxicology Letters. 2003 Jul 20;143(2):195-207. [<DOI>](#).



Recent Studies on Antioxidant, Antimicrobial and Ethnobotanical Uses of *Hypericum perforatum* L. (*Hypericaceae*)

Emre YILMAZOĞLU^{1*} , İbrahim Metin HASDEMİR¹ , Belma HASDEMİR² 

¹Istanbul University-Cerrahpasa, Department of Chemical Engineering, Istanbul, 34320, Turkey

²Istanbul University-Cerrahpasa, Department of Chemistry, Istanbul, 34320, Turkey

Abstract: *Hypericum perforatum* L. (*Hypericaceae*) is one of the medicinal plants whose value has increased rapidly in recent years. It is especially popular for its use in the treatment of mild and moderate depression, as well as for the treatment of skin diseases, internal and external inflammatory wounds, neurological disorders, and the metabolism-disrupting effects of free radicals. Besides, it shows inhibitory effects against different kinds of microorganisms such as bacteria, fungus, and protozoa. Antimicrobial biofilms generated by the plant are its most potent output, unlike its essential oil which does not have much value in itself as much as its ingredients that can be converted into more valuable products. Its usage as a folk remedy has a wide application area in various cultures. It is thought that compiling studies on various aspects of this plant will benefit future studies. The present paper reports on studies on the antibacterial, antioxidant, and therapeutic properties of *Hypericum perforatum*, as well as on the composition of its essential oil.

Keywords: *Hypericum perforatum*, medicinal plants, antioxidants, antimicrobials, essential oil.

Submitted: November 17, 2021. **Accepted:** February 24, 2022.

Cite this: Yılmazoğlu E, Hasdemir İM, Hasdemir B. Recent Studies on Antioxidant, Antimicrobial and Ethnobotanical Uses of *Hypericum perforatum* L. (*Hypericaceae*). JOTCSA. 2022;9(2):373-94.

DOI: <https://doi.org/10.18596/jotcsa.1024791>.

***Corresponding author. E-mail:** emre.yilmazoglu@iuc.edu.tr.

INTRODUCTION

Hypericum is a genus belonging to the *Hypericaceae* family and comprising about 500 species that are growing widely and has been utilized in folk medicine for many centuries (1,2). *Hypericum perforatum* is a herbaceous perennial plant growing in the tropical and sub-tropical regions of Europe, Asia, North Africa, and North America. It is usually 30-60 cm tall but can grow up to 1.5 m on the Pacific coast of America. The leaves can be arranged

singly, oppositely, or spirally (Figure 1). There are five sepals and five petals in the flower's bud. Its leaves are oval in shape and its flowers are bright yellow. (3-5). It grows mostly on roadsides, with thorny plants and in arid lands. Because it blooms about June 24, the Memorial Day of Baptist John, the plant is commonly known as St. John's Wort in English, Johanniskraut in German, Herbe de la Saint-Jean in French, Erba di San Giovanni in Italian, and Hierba de San Juan in Spanish (6).



Figure 1: Flower and leaves of *H. perforatum*.

The name of the “*perforatum*” epithet belonging to the genus *Hypericum* was given because of the oil guts in its flowers and leaves. The red or black oil glands of the *H. perforatum* are made up of hypericin and its derivatives, whereas the transparent ones are made up of essential oils and other active ingredients that are not found in hypericins (7,8). The fact that *H. perforatum*, which has been used for various purposes in alternative medicine since ancient times, is widely pharmacologically effective has led to studies in many fields such as pharmacy, medicine, dentistry, agriculture, and cosmetics.

Hypericum species contain many secondary metabolites in at least 11 different classes, including naphthodianthrones, phloroglucinol derivatives, flavonoids, organic acids, essential oils, amino acids, xanthenes, tannins, procyanidins, and other water-soluble compounds. From the main active ingredients, those of naphthodianthrones’ class are effective in the treatment of depression up to moderate severity, while those of the phloroglucinol class are effective in the treatment of wounds, burns, and inflammation (9). Another issue that has come to the fore in recent years is the increase in the use of organic and alternative medicine products. Medicinal and aromatic plants and products derived from them are often used as medicines, both in strengthening immunity and for treating diseases. This necessitates a deeper understanding of the beneficial and harmful properties of plants to produce more useful products. In recent years, the consumption of products obtained from *Hypericum* species has increased, and nowadays, it is one of the most consumed medicinal plants in the world (10). Although its extracts are used generally, it is known that its essential oil has good neuroprotective, antimicrobial, and antioxidant effects (5).

According to a review of literature, there have been several studies, about 300 publications per year

regarding *H. perforatum*, in many fields, primarily chemistry, biology, and medicine.

In this paper, studies on the plant's activity against microorganisms, antioxidant content, medicinal use, essential oil qualities, extraction methods, drying procedures, and active components (hypericin and hyperforin) were reviewed.

ANTIMICROBIAL ACTIVITY

One of the most prominent features of the plant is its antibacterial and antimicrobial properties (11). These properties gain more value when taken together with its wound healing and anti-inflammatory effect. The effectiveness of the plant against harmful microorganisms has been evaluated in many studies. The degree of inhibitions in various culture media have been assessed, in vivo and in vitro (12,13).

The most effective parts of the plant were flowers against gram-positive bacteria (*S. aureus*), gram-negative bacteria (*K. pneumoniae*, *P. aeruginosa*, *S. enteritidis*, *E. coli*), and yeast (*C. albicans*). Leaves were effective against *Aspergillus niger*. The antibacterial effect of the plant was stronger against gram-positive microorganisms than against gram-negative ones (14). Furthermore, the properties of various biofilms with *H. perforatum* were also studied. The inhibition efficiency of the biofilm produced with ethanolic extract and polyurethane foam remained low against gram-negative, *E. coli* and against *C. albicans*. However, the gram-positive *S. aureus* inhibition rate reached 90.85% (15). Güneş and Tihminlioğlu (2017) achieved the same result (16). On the other hand, biofilms made from chitosan, gelatin and the plant were more inhibitory against gram negative *S. typhi* than against *E. coli* and gram positive *S. aureus* (17). Methanolic macerate and aqueous decoction extract showed the best results after vancomycin, while liquid commercial ethanolic extract, methanolic solution of a commercial tablet product, macerates in

sunflower, olive, and two unknown vegetable oils did not show any effect against the *S. aureus* (18). Also, among three different *Hypericum* species, *H. perforatum* showed the strongest anti-infectious effect against *Toxoplasma gondii*, an intracellular parasite, due to the hyperforin it contains (19).

pH, water permeability (17), mechanical testing, swelling behavior, surface hydrophobicity (16), water activity test, Low-Field Nuclear Magnetic Resonance (LF-NMR) analysis, texture analysis, and L*-a*-b* color tests (20), were investigated as the

physical properties of biofilms in different studies. Vapor permeability and stretching ratio are higher in films with oil additives, but decrease as the oil concentration increases. The degree of swelling is lower, the tensile stress decreases further as the oil additive increases. The contact angle is slightly increased. Cell renewal rate is highest with 0.5% oil (16).

Studies that evaluated the effectiveness of *H. perforatum* against microorganisms are summarized in Table 1.

Table 1: Antibacterial and antifungal activities of *H. perforatum*.

Reference	Microorganism	Classification
(12-18,21-29)	<i>Staphylococcus aureus</i>	gram-positive bacterium
(12,22)	<i>Staphylococcus epidermidis</i>	
(23,28)	<i>Sarcina lutea</i>	
(12,17,28,30)	<i>Bacillus subtilis</i>	
(28,30)	<i>Bacillus mycoides</i>	
(23,26,31)	<i>Bacillus cereus</i>	
(28)	<i>Mycobacterium phlei</i>	
(28)	<i>Corynebacterium michiganes</i>	
(27,32)	<i>Corynebacterium diphtheriae</i>	
(27)	<i>Streptococcus pyogenes</i>	
(27)	<i>Streptococcus agalactiae</i>	
(12,21,27,33)	<i>Enterococcus faecalis</i>	
(31,34)	<i>Listeria monocytogenes</i>	
(21-23)	<i>Micrococcus luteus</i>	
(13,14,30,33)	<i>Klebsiella pneumoniae</i>	
(13,14,22,23)	<i>Salmonella enteritidis</i>	
(17,22,33)	<i>Salmonella typhimurium</i>	
(31)	<i>Salmonella infantis</i>	
(13-17,21,26-28,31,33)	<i>Escherichia coli</i>	
(21,28)	<i>Proteus vulgaris</i>	
(21,23)	<i>Proteus mirabilis</i>	
(13,14,23,33)	<i>Pseudomonas aeruginosa</i>	
(20)	<i>Pseudomonas plecoglossicida</i>	
(20,30)	<i>Pseudomonas fluorescens</i>	
(20,26,27)	<i>Pseudomonas aeruginosa</i>	
(20)	<i>Pseudomonas sp. MChB</i>	
(30)	<i>Pseudomonas phaseolicola</i>	
(30)	<i>Pseudomonas glycinea</i>	
(22,23)	<i>Pseudomonas tolaasii</i>	
(30)	<i>Erwinia caratovora</i>	
(30)	<i>Entrobacter cloaceae</i>	
(23,30)	<i>Agrobacterium tumefacies</i>	
(30)	<i>Azotobacter chrococum</i>	
(35,36)	<i>Aeromonas hydrophila</i>	
(31)	<i>Helicobacter pylori</i>	
(31)	<i>Campylobacter coli</i>	
(26)	<i>Chronobacter sakazakii</i>	
(28)	<i>Penicillium chrysogenum</i>	fungi
(22)	<i>Penicillium funiculosum</i>	
(37)	<i>Penicillium canescens</i>	
(28)	<i>Fusarium avenaceum</i>	
(37)	<i>Fusarium oxysporum</i>	
(37)	<i>Alternaria alternata</i>	
(28)	<i>Mucor plumbeum</i>	

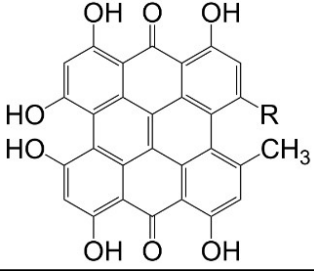
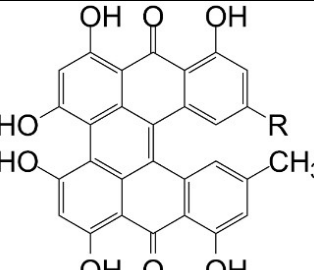
(22)	<i>Cladosporium cladosporioides</i>	
(22)	<i>Trichoderma viride</i>	
(13-15,22-24,27,28,33,38)	<i>Candida albicans</i>	
(38)	<i>Candida utilis</i>	
(38)	<i>Candida tropicalis</i>	
(38)	<i>Candida krusei</i>	
(38)	<i>Candida parapsilosis</i>	
(38)	<i>Candida glabrata</i>	
(13,14,22)	<i>Aspergillus niger</i>	
(24)	<i>Aspergillus fumigatus</i>	fungi
(37)	<i>Aspergillus glaucus</i>	
(37)	<i>Phialophora fastigiata</i>	
(21)	<i>Pythium ultimum</i>	
(21)	<i>Trichophyton mentagrophytes</i>	
(24)	<i>Trichophyton rubrum</i>	
(39)	<i>Plasmopara halstedii</i>	
(25)	<i>Rhizopus stolonifer</i>	
(24)	<i>Leishmania infantum</i>	
(24)	<i>Trypanosoma rhodesiense</i>	protozoa
(24)	<i>Plasmodium falciparum</i>	
(24)	<i>Trypanosoma cruzi</i>	

ANTIOXIDANT ACTIVITY

Hypericum perforatum contains many important bioactive substances, some of which, such as naphthodianthrone and phloroglucinols have direct medical effect (Figure 2). Others contribute to human health in various ways due to its antioxidant effects. Antioxidant substances defend the metabolism against free radicals, especially reactive oxygen species formed in the body. Thus, the development of diseases such as cancer is prevented, and overall immunity is enhanced.

Secondary metabolites occur as plants' response to biotic and abiotic stress factors like water, light, temperature, CO₂, abundance of nitrogen and other nutritious compounds, geographical environment, genetic features, harvest time, contaminants,

elicitors, harmful microorganisms, herbivores, etc (40,41). In their studies, Eray et al. (2020) and Karimi et al. (2022) investigated how the different growing conditions of *H. perforatum* affect the formation of secondary metabolites. In this way, it may be possible to prepare cultural planting conditions for specific purposes (8,42). Another cultural planting study has prepared for the aim of producing a powerful radical scavenger (43). Pan et al. (2004) isolated the protoplast from the calluses obtained from the hypocotyl parts of the plant and used it in the regeneration of the plant. With this work, an important step was taken towards the production of designed plants (44). In a study about genes expression according to the growing conditions, especially temperature, the mechanisms that are activated by various genes are mentioned (45).

	Hypericin	R = CH ₃
	Pseudohypericin	R = CH ₂ OH
	Protohypericin	R = CH ₃
	Protopseudohypericin	R = CH ₂ OH

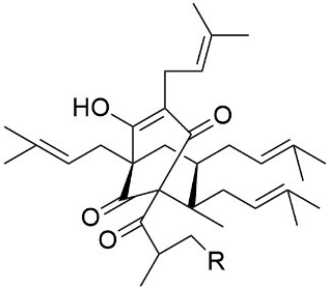
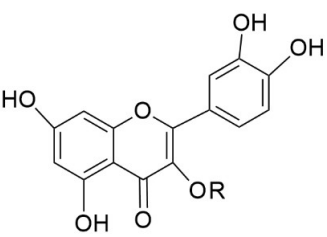
	Hyperforin	R = H
	Adhyperforin	R = CH ₃
	Rutin	R = Glucose-Rhamnose
	Hyperoside	R = Galactose
	Quercetin	R = H
	Quercitrin	R = Rhamnose
	Isoquercitrin	R = Glucose
	Pentose	R = Quercetin-3-O-pentoside

Figure 2: Major ingredients of *H. perforatum* extracts.

In a warmer and lighter environment, the proportion of all bioactive components was higher. While phenolic and flavonoid substances were more abundant in vegetative and flowering stages, hyperforin decreased continuously, unlike previous studies. While hypericin increased with high temperatures and light, it started to decrease with flowering in low temperatures and light (46). Rutin content was higher in the budding phase. Quercitrin, quercetin, and I3, II8-biapigenin were higher in the full-flowering phase. Hyperoside content did not change (47). Almost all bioactive ingredients were found to be reduced in a plant afflicted with ash yellows phytoplasma infection. The rate of essential oil also decreased significantly (40).

The main chemical components and biological activities of *H. perforatum* subspecies and other *Hypericum* taxa were compiled by Kladar et al. (48). *H. perforatum* subsp. *perforatum* is richer in flavonoids, tannins, and phenolic acids compared to the *angustifolium* subspecies and contains rutin unlike others (12). *Hypericum perforatum* ssp *veronense* includes a higher rate of hypericin, hyperforin and phenolic components than *Hypericum perforatum* ssp *perforatum* (49). Inhibition rates and antioxidant capacities of 9 *Hypericum* species against 7 microorganisms were investigated after a three-day maceration period. *H. perforatum* could not stand out in terms of antibacterial effect, but especially the flowers of the plant showed the highest antioxidative effect (73100 µmol α-tocopherol acetate/g extract). The

antioxidant capacity of the plant organs varied depending on flavonoid contents in flowers (11.7%), leaves, and stems (7.4%) (13). It has been understood that different parts of the plant contain different major components. Ciccarelli et al. (2001) examined the composition of oil glands in plant parts (7). Total phenolic and flavonoid contents as well as 2,2-diphenyl-1-picrylhydrazyl (DPPH) free radical scavenging power, β-carotene-linoleic acid total antioxidant activity, ferric reducing antioxidant power, Cupric reducing antioxidant capacity (CUPRAC) metal chelating power and antimicrobial effects of some *Hypericum* species were measured. *H. perforatum*, *H. salsugineum* and *H. aviculariifolium* epithets were compared to Butylated Hydroxy Anisole (BHA) and Butylated Hydroxy Toluene (BHT). While *H. perforatum* had the lowest antioxidant activity, total phenolic content, and Fe chelating power, *H. aviculariifolium* exhibited the highest Cu chelating power and total flavonoid content (14).

In terms of antioxidant activity, it is recommended to brew for 5-10 minutes at 80-100°C as the best method of use. Preparation of the tea, which became red in 3 minutes, was not enough to see naphthodianthrones. Apart from this, phenolic acids and chlorogenic acid also increased significantly after 3 minutes (50). While the rates of bioactive components increased with the decoction time up to 20 minutes, the rates decreased with infusion time. Decoction process was more efficiently than infusion. Likewise, it gives products whose

antioxidant activities are more than twice as high (51).

Quercetin is an important phenolic compound that has powerful antioxidant and antiradical activity even in minor amounts (52). It is higher in palm oil macerate and lower in olive oil macerate, compared with the sunflower oil macerate of *H. perforatum*. While it was claimed that quercetin has a protective effect on the stomach against cold restriction stress, the highest protection was obtained when working with the lowest quercetin (53). Firenzuoli et al. (2004) discussed the effects of flavonoid content in nutrition as risks and therapeutic opportunities (54).

After a period of exposing to sunlight in olive, sunflower, and palm oil for 40 days, 0.02% (v/v) BHA or α -tocopherol antioxidants were added in some extracts, separately. The appearance, odor, relative density, and acid number of the extracts were analyzed during a shelf life for 3, 6, and 12 months at room conditions. Although palm oil is a more stable vegetable oil to heat effect, it gives a lower quality extract. Characteristics of the extracts with antioxidants are satisfying after 12 months, but the samples without antioxidants degrade after 6 months. BHA and α -tocopherol affect the extracts similarly (55). According to Arsić (2016), a homemade *H. perforatum* olive-oil macerate made easily can have some unique properties such as longer shelf life and higher total flavonoid content (56).

Methanolic extracts contained more hypericin and hyperforin, but the aqueous solutions were rich in antioxidant compounds (57). In particular, the extracts with epicatechin, catechin, protocathechuic acid, gallic acid, quercetin, and kaempferol as components were effective against colon cancer cells (58–60).

In addition to antioxidant content (61–64), total chlorophylls, total carotenoids, phenolic substances (65,66), polysaccharides (67), and xanthonic contents (68) were also examined. Accordingly, the antioxidant activity was enhanced by all these compounds.

Different active oxygen sources were used to describe the antioxidant and antiradical effects of various medicinal plants. By voltamperometric electrical experiments, *H. perforatum* has been found to be more effective against hydrogen peroxide than hydroxyl radical and more useful in oxidizing molecular oxygen (69).

When studies were compared, it was discovered that as the water ratio increased in the ethanol-water mixture, the phenolic substance content increased as well, but the aqueous extract had a low content: 14.35-16.72, 53.84, 128.82, and 4.44 mg gallic acid equivalent per g dry matter of extracts

with ethanol/water (7:3) (70), ethanol/water (1:1) (66), ethanol/water (3:7) (71), and water (72), respectively. In terms of DPPH scavenging effectiveness, the first and third extracts had almost the same concentration for eliminating 50% of the DPPH radical (IC₅₀) (3.17 and 3.48-5.68 g/ml), but the extract of equivalent volumes was not so effective (242.323 g/ml). Likewise, in terms of phenolic material content, the activity in the form of acetone>ethanol>petroleum ether was as ethanol>acetone>petroleum ether in terms of DPPH scavenging potential (37).

The high bioactive properties of methanolic extracts have also attracted attention in many studies (14,26,61,63,73,74). When chloroform or acetone were added, the DPPH removal efficiency of the extracts increased (26,49), while water, ethyl acetate, and chloroform alone had a low effect (26,73).

Öztürk et al. (2009) showed that leaves contained more phenolic substances and flavonoids than flowers. After the step with the solvent of methanol:water (7:3), the yield of the plant, which was treated twice with ethyl acetate, increased. Similarly, the leaves were generally more effective than flowers in terms of DPPH scavenging effect (75).

MEDICINAL USES

The medicinal effects of the plants are quite diverse, they are mostly used for their antidepressant and wound healing properties. They are good for many ailments and provide benefits in different ways, especially in the treatment of neurological and oncological disorders. Although they are often classified as over-the-counter drugs from a medical point of view, in recent years there has been an increase in the usage of *H. perforatum* as an alternative treatment method and as a supportive practice for the main treatments.

Hypericum perforatum, which is one of the commonly used over-the-counter psychotropic herbal remedies, is especially used in the treatment of depression, anxiety, and insomnia. There are also studies on bipolar disorder (76). A study has been conducted to show that antioxidant and antidepressant effects work together against restraint stress, which is one of the important events that cause oxidative damage in the brain (77). The genes it affects were included in a study conducted to better understand its neuroprotective effect (78).

Strong anti-MAO-A, anti- α -glucosidase activity, antihyperglycemic agents, treatment of cognitive impairments such as Alzheimer's Disease are determined (79). It has been stated that its using before Alzheimer's Disease treatment has a positive effect due to some components like (+)-catechin

and (-)-epicatechin (80). One of the most effective plant's mechanisms to relieve the symptoms of Alzheimer is the inhibition of neuronal acetylcholinesterase activity (70). Hyperforin and hypericin are known to be highly effective components against Alzheimer's disease, particularly (81,82).

Preventive for myringosclerosis (83), therapeutic for renal ischemia reperfusion injury (84), acute injuries or contusions, myalgia, first-degree burns (85,86), protective of central nervous system (73,87,88), and immune booster (89) effects are given comprehensively. As neuroprotective products, methanolic extracts have good inhibition activities against enzymes of acetylcholinesterase and butyrylcholinesterase and free radicals such as DPPH, DMPD, and NO (73).

There have been many studies on the usage of hypericin in photodynamic therapy processes. During photodynamic therapy using the extract of the plant or hypericin directly, it is desirable to treat diseased cells, not healthy cells. It has been understood that the use of hypericin, which inhibits neutrophilic respiratory burst oxidase together with the enhancing effect of vitamin C, will give a much better result in this regard (90). On the other hand, the probable reason why the plant causes less photosensitivity than pure hypericin is that the antioxidants it contains, strengthen the cells against harmful effects (91). Interaction between occurring photodynamic effect of hypericin and some proteins was investigated in a few aspects (92). It is effective in protection from UV irradiation induced lipid peroxidation (93). When hypericin uptake sensitizes eye epithelial cells to sunlight, it was observed that 0.1-10 μM hypericin uptake developed necrosis and apoptosis in UV-A and visible light. Considering the information in the literature, it was understood that the possibility of cataractogenesis in the eye would increase in the case of sun exposure by taking the herb (94). Using yeast genes, *H. perforatum* has been found to affect 52 genes that work on intra and intercellular transports and signal transduction in humans (95).

Preventing the adverse consequences of lipid dysregulation in some physiological cases such as obesity, fatty liver, and type 2 diabetes by hypericin are other prominent features, in addition to the long-lasting protective effect of hyperforin on pancreatic β -cells (96,97). It shows not only therapeutic but also protective properties. For example, it provides antimutagenic protection against the harmful effects of the chemotherapeutic cyclophosphamide (98). The oxidizing low-density lipoprotein shows an atherogenic effect in the body and can cause cholesterol-related deaths. Thanks to lipophilic active ingredients of the plant such as hypericin, pseudohypericin and hyperforin, *H. perforatum* has been found to provide antiatherogenic benefit by inhibiting this protein

together with its antidepressant and antioxidant effects (99). It can be used as an alternative to mouthwashes after third molar surgery (100). To understand its antiaging effect, its usage against D-galactose has been studied (101). It has been found that the antidepressant mechanism of action includes a decrease of concentrations of corticosterone and pro-inflammatory cytokines in plasma (102). Antioxidant activity, causing apoptosis and modulating Ca^{2+} influx effects, can be used in the treatment of oxidative stress in neutrophil cells against Behcet's disease (103). It was reported that the wound healing effect of the plant was not related to its hypericin content but to components such as quinoids, xanthenes, and flavonoids (104). High contents of xanthenes were reported in the methanolic *H. perforatum* seeds' extract. These compounds are also associated with antioxidant and antimicrobial activities (74).

It was shown that the plant has no effect on intraperitoneal adhesion formation (105) and smoking cessation (106) but reduce alcohol addiction due to its antidepressant effect (107).

Information on the usage of the herb in the treatment of different illnesses, especially depression, and its drug interactions have been compiled in many studies, because many medicinal and aromatic herbs can have harmful effects on the metabolism as well as positive effects. Over-the-corner drugs like *H. perforatum* should not be used without consulting the pharmacists, and maximum attention should be paid to their interactions with prescription drugs (108-115). Although it has high interactions with many antidepressant drugs and synergistic effects with different plants, it can be used by adding it to various herbal teas (65).

On the one hand, the use of *H. perforatum* by local people has been reported in many reviews, where some gave suggestions for using it (1,116-126). On the other hand, the report prepared by the European Medicines Agency is a study that should be taken into consideration regarding the use of the plant for various medicinal purposes (127). While undiluted hypericin and hyperforin show prooxidant effects, they start to show a stronger antioxidant effect as they are diluted. When ingested, they will not be possible to remain undiluted, so the prooxidant effects are not encountered, but excessive intake may be harmful in this regard. The recommended dose is 300 mg consumed three times a day. In this case, it was diluted 1:10-1:20 so that sufficient antioxidant effect was provided (128).

Hypericum perforatum can be used alone or with other plants for feeding cattle. When used as a forage additive, it improves the ruminal nitrogen cycle and volatile fatty acid formation without damaging local beneficial microorganisms (129). When added to Atlantic salmon (*Salmo salar*) feed,

it strengthens the immune system and shows an antioxidative effect against crowding stress (130).

Studies on the harmful side of the plant are also continuing. It is known that long-term or high dose usage causes sensitivity to light, oedema, and alopecia on the skin. Along with antidepressant effects, side effects such as itching, dizziness, constipation, fatigue (131), anxiety, insomnia, restlessness, diarrhea (132), gastrointestinal upset, and dry mouth (133) might be detected depending on the person using it. It has been determined that its use as a nutritional supplement creates anomalies in liver and testicular cells by causing a decrease in nucleic acid and nonprotein sulfhydryl and an increase in malondialdehyde (134). A remarkable study on the use of the plant in cosmetics was published in 2014. Both the methods of use and the points to be considered are discussed in a very broad scope (135).

It can induce disorders when used with other antidepressants, monoamine oxidase (MAO) inhibitors, cytochrome P-450 mixed function oxidases (MFO), reserpine, narcotics, or substances that increase photosensitivity (85,136,137). It was found that various *Hypericum perforatum* extracts prepared with ethanol or DMSO significantly inhibited the CYP1A2, CYP2A6, CYP2C9, CYP2C19, and CYP3A4 cytochrome P-450 enzymes. These enzymes actually convert the drug into a form that your body can use more effectively and makes some drugs be excreted from the body without being effective, so more care should be taken with the consumption of this plant when using drugs. (110,133,138,139). Also, the enzyme group has a healing effect on 2,4,6-trinitrobenzenesulfonic acid (TNBS) colitis, inflammatory bowel disease, and

intestinal cerulein-induced pancreatitis (60,140,141).

In different studies, heavy metals were found in herbalists' products. The high levels of Al, Cd, K, Mg, Mn, Pb, Zn, Co, Cu, Cr, Ca, Ba, B, Li, Na, Fe, and Ni in the samples once again showed that uncontrolled producers play with public health (142–147)). When the fatty acid composition and other quality values of 23 Turkish homemade and commercial olive oil macerates were examined, it was found that some products were adulterated (148).

The production of antioxidant and anticancer effective nanoparticles obtained from the solution prepared with the aqueous extract of the plant and silver nitrate has emerged as a new trend that can be used in different fields. These nanoparticles, which can be used in medical device coatings, antibacterial products, cosmetics, food, and pharmacy, can also be employed both as medicine and as drug carrier thanks to their unique physical and chemical properties (86,149). Utilization of *H. perforatum* in nanoparticulate carrier systems was investigated in many studies (150–152).

ESSENTIAL OIL COMPOSITION

There are many papers on the essential oil analysis of *Hypericum perforatum*. According to those, it is understood that not only oil composition, but also major compounds are changed due to internal and external factors of the plant, such as genetic characteristics, plant organs, climate, soil, season, growth phase, collection time and procedures, drying method, analysis method, etc (153,154). A summary of the studies on the essential oil of the plant is given in Table 2.

Table 2: Main essential oil components of *H. perforatum*.

Reference	Main compounds (Concentration %)	Harvesting location
(33)	α -Pinene (30.92%) β -Pinene (18.32%) Caryophyllene (15.26%) Germacrene d (9.23%) β -cis-Ocimene (7.85%)	Arad county, Romania
(38)	Germacrene D (23%) β -Caryophyllene (14%) Bicyclogermacrene (5%),	Kirklareli, Turkey
(40)	Caryophyllene (30.0%) Germacrene D (19.64%) β -Copaene (7.09%) γ -Amorphene (6.28%)	Bologna, Italy (Ash yellows infected samples)
(146)	α -Pinene (8.1%) n-Nonane (7.0%) Globulol (5.5%)	Southern Estonia
	(E)- β -Caryophyllene (19.2%) γ -Muuorulene (8.7%) γ -Amorphene (6.5%)	Central Estonia
	α -Pinene (14.3%) Germacrene d (13.7%) 2-Methyloctane (11.3%) β -Pinene (6.8%)	Northern Estonia
(154)	β -Selinene Bicyclogermacrene 2-Tetradecene α -Amorphene	Gaziantep and Tunceli, Turkey
(155)	Caryophyllene oxide (15.3%) β -Caryophyllene (7.3%) 1-Tetradecanol (7.0%)	Provence-Alpes-Côte d'Azur, France (Vegetative stage)
	Caryophyllene oxide (17.0%) β -Caryophyllene (16.8%) Spathulenol (12.7%)	Provence-Alpes-Côte d'Azur, France (Floral budding stage)
	β -Caryophyllene (18.3%) Caryophyllene oxide (15.9%)	Provence-Alpes-Côte d'Azur, France (Flowering stage)
	Caryophyllene oxide (18.5%) β -Caryophyllene (9.1%)	Provence-Alpes-Côte d'Azur, France (Fruiting stage)
(156)	2-Methyl-octane (20.5%) α -Pinene (13.7%) Spathulenol (9.8%) n-Hexadecanoic acid (4.0%)	Different locations of Southeast Serbia
(157)	β -Caryophyllene (14.8%) (E)- β -Farnesene (7.1%) ar-Curcumene (13.0%) Germacrene D (17.8%)	Val-d'Arc, Provence-Alpes-Côte d'Azur, France
	β -Caryophyllene (28.4%) Germacrene D (37.3%)	Pertuis, Provence-Alpes-Côte d'Azur, France
	β -Caryophyllene (26.1%) Dodecanol (7.5%) α -Selinene (15.5%) Germacrene D (6.3%)	Saint-Cyr, Provence-Alpes-Côte d'Azur, France
	β -Caryophyllene (24.1%) β -Selinene (6%) Bicyclogermacrene (5.8%) Germacrene D (29.1%)	Mérindol, Provence-Alpes-Côte d'Azur, France
	Spathulenol (21.1%) γ -Muuorulene (7.7%) Nerolidol (6.5%) Branched Tetradecanol (9.1%)	Bandol, Provence-Alpes-Côte d'Azur, France

	β-Caryophyllene (13.3%) γ-Murolene (6.9%) (E,E)-α-Farnesene (8.4%) Spathulenol (21.5%) Caryophyllene oxide (18.4%)	Meailles, Provence-Alpes-Côte d'Azur, France
(158)	β-Caryophyllene (22.3%) 2-Methyl octane (17.3%) 2-Methyldodecane (6.0%)	Panëevo, Serbia
	α-Pinene (35.0%) β-Pinene (23.4%) 2-Methyl octane (13.5%)	Terimi, Greece
(159)	2,6-Dimethylheptane α-Pinene β-Caryophyllene 2-Methyl-3-buten-2-ol	Izmir, Turkey
(160)	n-Triacontane (16.3%) n-Heneicosane (14.4%) n-Tetracosane (13.8%) n-Nonacosane (13.3%)	Sobina, Serbia
	n-Tetratriacontane (25.96%) 1,2-Benzenedicarboxylic acid (13.4%) Phytol (7.1%)	Sobina, Serbia
(161)	α-Pinene (61.8%) 3-Carene (7.5%) β-Caryophyllene (5.5%)	Gaziantep, Turkey
(162)	α-Pinene (21.0%) 2-Methyl-octane (12.6%) γ-Murolene (6.9%) Spathulenol (6.4%)	Ioannina, Greece
(163)	β-Caryophyllene (14.2%) 2-Methyl-octane (13.1%) 2-Methyl-decane (7.9%)	Rujan mountain, Serbia
(164)	β-Caryophyllene (11.7%) Caryophellene oxide (6.3%) Spathulenol (6.0%) α-Pinene (5.0%)	Tashkent, Uzbekistan
(165)	Longifolen (18.7%) γ-Eudesmole (10.7%) Spathulenol (6.9%) Bicyclogermacrene (5.5%)	Mashhad, Iran (Before flowering)
	α-Cadinene (27.17%) Bicyclogermacrene (16.93%) Spathulenol (6.95%) γ-Eudesmole (6.52%)	Mashhad, Iran (Full flowering)
	Longifolen (22%) β-Bisabolene (9%) Spathulenol (8.45%) Glubulol (5.15%)	Mashhad, Iran (Fruit set)
(166)	δ-Cadinene (11.6%) 2,6-Dimethyl-heptane (10.9%) (E)-Caryophyllene (9.9%) α-Humulene (7.1%)	Galogah, Iran
	δ-Cadinene (22.6%) (E)-Caryophyllene (12.2%) α-Humulene (11.3%) α-Pinene (9.0%) 2,6-Dimethyl-heptane (7.4%)	Nor, Iran
	2,6-Dimethyl-heptane (15.0%) n-Nonane (11.1%) δ-Cadinene (11.0%) α-Pinene (8.7%) β-Funebrene (6.7%)	Javaherdeh, Iran

	α -Pinene (14.4%) δ -Cadinene (10.6%) 2,6-Dimethyl-heptane (9.8%) 3-Methyl-nonane (8.1%)	Darrod, Iran
	α -Pinene (21.9%) n-Nonane (9.8%) 2,6-Dimethyl-heptane (9.1%) n-Dodecanol (6.8%) γ -Himachalene (6.0%)	Tonekabon, Iran
	α -Pinene (23.6%) 2,6-Dimethyl-heptane (13.5%) γ -Cadinene (8.7%) 3-Methyl-nonane (5.7%)	Toskestan, Iran
	α -Pinene (26.0%) 2,6-Dimethyl-heptane (15.2%) β -Pinene (11.6%) δ -Cadinene (10.2%)	Kharw, Iran
	α -Pinene (25.7%) 2,6-Dimethyl-heptane (15.1%) β -Funebrene (12.4%) γ -Cadinene (9.6%)	Lahijan, Iran
	γ -Cadinene (16.9%) 2,6-Dimethyl-heptane (6.3%) n-Tetradecanol (6.3%) α -Pinene (6.2%)	Mashhad, Iran
	2,6-Dimethyl-heptane (36.1%) α -Pinene (23.6%) 3-Methyl-nonane (10.1%)	Azadshahr, Iran
(167)	Ledene oxide II (8.91%) Humulene epoxide II (7.90%) <i>cis</i> -Phytol (7.89%)	10 accessions from the field collection, Vilnius, Lithuania
	Docosane (10.80%) Spathulenol (9.10%) Caryophyllene oxide (7.76%)	
	Spathulenol (10.01%) Eicosane (9.01%) Caryophyllene oxide (6.92%)	
	Dodecanoic acid (9.63%) Caryophyllene oxide (9.27%) Hexadecanoic acid (7.61%)	
	Hexadecanoic acid (12.87%) Spathulenol (12.16%) Caryophyllene oxide (7.99%) Tetradecanol (6.94%)	
	Hexadecanoic acid (10.05%) Caryophyllene oxide (9.28%) Spathulenol (8.17%)	
	Ledol (9.31%) Caryophyllene oxide (8.41%) Spathulenol (6.71%)	
	Caryophyllene oxide (18.73%) Caryophyllene oxide (11.31%) Spathulenol (8.51%)	
	Salvial-4(14)-en-1-one (8.44%) Hexadecanoic acid (8.13%) Tetradecanol (7.88%)	
(168)	Germacrene D (29.5%) β -Eudesma-4(15),7-dien-1-ol (9.1%) α -Cadinol (6.2%) Caryophyllene oxide (6.1%)	

	Germacrene D (14.8%) β-Eudesma-4(15),7-dien-1-ol (11.7%) funebrol (6.7%) Germacrene D (23.2%) Funebrol (6.1%) Caryophyllene oxide (6.0%) α-Cadinol (5.8%)	Svencioniai district, Lithuania Ukmerge district, Lithuania
	Germacrene D (12.7%) Caryophyllene oxide (11.9%) β-Caryophyllene (9.6%)	Zarasai district, Lithuania
	Germacrene D (15.7%) β-Caryophyllene (8.8%) Caryophyllene oxide (7.0%)	Marijampole district, Lithuania
	Germacrene D (14.0%) β-Caryophyllene (7.8%) β-Eudesma-4(15),7-dien-1-ol (6.5%)	Vilnius district, Lithuania
	Germacrene D (12.0%) β-Caryophyllene (10.5%)	Marijampole district, Lithuania
	Germacrene D (16.1%) Caryophyllene oxide (13.1%) (Z)-β-Farnesene (8.2%)	Vilnius city, Lithuania
	Germacrene D (12.7%) (Z)-β-Farnesene (9.0%) β-Caryophyllene (8.2%) Dodecanol (6.1%)	Vilnius city, Lithuania
	Germacrene D (13.6%) Tetradecanal (9.4%) Tetradecanol (9.4%) Caryophyllene oxide (7.2%) β-Caryophyllene (6.8%)	Moletai city, Lithuania
(169)	Caryophyllene oxide (35.8%) β-Caryophyllene (11.1%) Spathulenol (8.0%) Dimethylheptane (6.6%)	Varėna district, Lithuania
	Caryophyllene oxide (17.5%) Germacrene D (9.8%) Spathulenol (7.5%) α-Cadinol (5.3%) β-Caryophyllene (5.2%)	Varėna district, Lithuania
	Caryophyllene oxide (14.2%) β-Caryophyllene (11.4%) Germacrene D (10.1%) β-Farnezene (8.0%) Spathulenol (7.1%)	Alytus district, Lithuania
	Caryophyllene oxide (13.4%) β-Caryophyllene (12.0%) Germacrene D (7.8%) α-Pinene (6.9%)	Vilnius district, Lithuania
	β-caryophyllene (18.3%) Caryophyllene oxide (15.7%) Germacrene D (10.1%) Spathulenol (7.1%)	Elektrėnai district, Lithuania
	β-Caryophyllene (19.1%) Caryophyllene oxide (12.5%) Spathulenol (8.5%) Germacrene D (6.8%)	Vilnius city, Lithuania
	β-Caryophyllene (13.2%) Caryophyllene oxide (11.8%) Germacrene D (5.9%) Spathulenol (5.6%)	Vilnius city, Lithuania
	β-Caryophyllene (10.5%) Caryophyllene oxide (7.0%)	Rokiškis district, Lithuania

	Spathulenol (6.9%) δ-Cadinene (6.7%) β-Farnezene (6.1%)	
	Germacrene D (16.1%) Caryophyllene oxide (13.1%) β-Farnezene (8.2%) Spathulenol (5.6%)	Vilnius city, Lithuania
	Germacrene D (31.5%) α-Muurolene-14-hydroxy (9.1%) α-Cadinol (6.2%) Caryophyllene oxide (6.1%)	Lazdijai district, Lithuania
(170)	Germacrene D (22.8%) 2-Methyloctane (10.8%) α-Pinene (10.1%) β-Caryophyllene (6.6%)	Vermion mountains, Greece (Wild samples)
	Germacrene D (18.9%) 2-Methyloctane (17.8%) β-Caryophyllene (10.3%) T-Muurolol (5.6%)	Vermion mountains, Greece (Cultivated samples)

The plant with the lowest essential oil yield in the growth phase reaches the highest yield when it starts to bud. Its main components remain the same, but the total number of components changes. Since it starts to grow, the proportion of aliphatic compounds has decreased. On the other hand, sesquiterpenoids reach the highest level during

budding and sesquiterpenes at flowering stage. The monoterpene rate has also increased gradually and approached 10% (155). Essential oil contents of flowers, leaves, and stems were investigated. The prominent class in leaves (74%) is sesquiterpenes, while about half of the oil in flowers (44%) and stem (50%) is non-terpenes (156).

Major compounds in the essential oils obtained in different research are given in Figure 3.

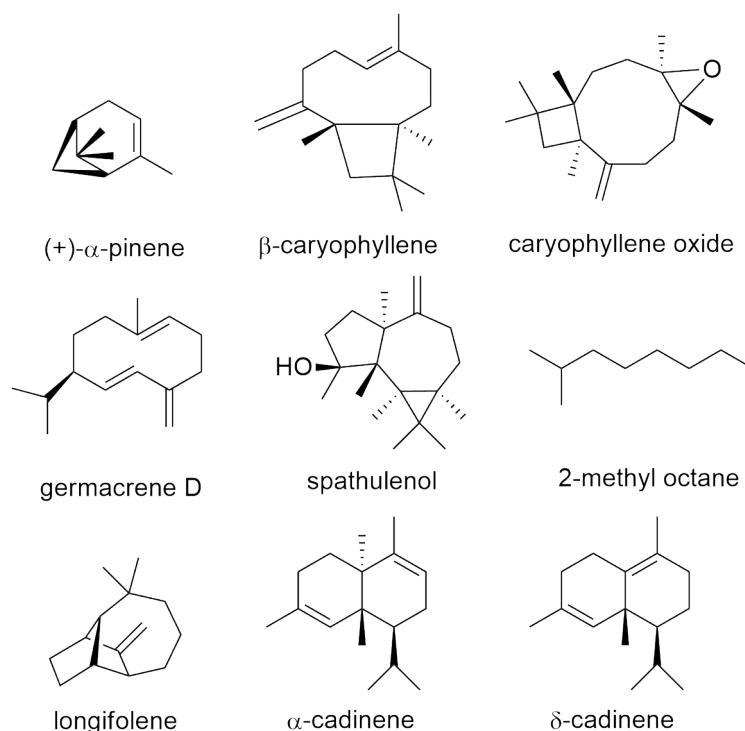


Figure 3: Major ingredients of different *H. perforatum* essential oils.

Essential oils of five different *H. perforatum* samples from France were examined. The major constituents were β-caryophyllene, caryophyllene oxide, ar-curcumene, germacrene D, and spathulenol (157). A study comparing the essential oil contents of

herbs collected from Greece and Serbia gave interesting results. β-caryophyllene, which represented 22% in Serbian oil, was found to be less than 1% in Greek oil, whereas there were higher rates of α and β-pinene. While a very

important part of Greek oil consisted of monoterpenes, sesquiterpenes and aliphatic hydrocarbons were prominent in other oils (158). Hışıl et al. (2005) reported that 2,6-dimethylheptane, α -pinene, β -caryophyllene, and 2-methyl-3-buten-2-ol were found as the main volatile components (159). The major essential compounds were: β -selinene (19.4%), bicyclogermacrene (15.3%), 2-tetradecene (8.2%), and α -amorphene (8.1%), in the air-dried aerial parts from Turkey (154). A review has been prepared on the essential oil of the plant and its ingredients (171).

Hatami et al. (2012) studied the SC-CO₂ extraction of *H. perforatum* and determined the required assumptions for modelling. It was assumed that temperature and pressure are homogeneously distributed in the reactor, all of the solid particles were of equal-sized and round-shaped, the concentration did not change radially, the local equilibrium was established at the fluid and solid interfaces and this equilibrium was linear, the amount of solid and therefore the reactor volume did not change during the process, the physical properties of the solvent remained constant and it flowed through the reactor in the plug flow model (172).

The difference created using CO₂ in the extraction of the herb collected from Albania was investigated. Soxhlet extraction with hexane and hydrodistillation were performed for comparison. A yield very close to hexane (2.73% vs 2.5%) was obtained at half the temperature (40°C) and half the time (1.5 h) with CO₂ (173). The efficiency was lower in the operation with liquid CO₂, but the rate of essential oil was higher (6.4%) than with supercritical CO₂. It was observed that the increase in pressure enhanced the efficiency but did not change the essential oil yield after a certain point. The main components in the liquid phase were n-triacontane (16.33%), n-heneicosane (14.41%), n-tetracosane (13.83%), n-nonacosane (13.26%) and in the supercritical phase were n-tetratriacontane (25.95%), 1,2-benzenedicarboxylic acid (13.44%), phytol (7.13%) (160). While either the temperature or pressure was lower, the other had to increase. On the other hand, since the solubility of CO₂ was directly dependent on its density, 313 K and 20 MPa were determined as the optimum extraction conditions (172).

Solvent-free microwave extraction (SFME) is one of the most interesting extraction methods in recent times. Moisture content, microwave power, and microwave time were investigated (72). All these three parameters increase the extraction efficiency. The parameters other than the duration were effective on the extracted content. Experimentally, the highest efficiency was found to be 0.365 g/100 g (d.m.) under conditions of high radiation power (468 W), high radiation duration (33 min) and low moisture content (43%). Efficiency was calculated

as 0.405 g/100 g (d.m.) with response surface method. Although SFME made the extraction effective, the antioxidant content of the product was lower than ascorbic acid. The prominent ingredients in the product are phenolic components. A product with higher sesquiterpene content was obtained with hydrodistillation, and a product with higher terpenoid content was obtained with SFME. The reason for their increased ratio is that terpenoids absorb radiation better because they are more polar (174).

CONCLUSION

In this study, a comprehensive and actual review of the studies on *Hypericum perforatum* is given. When looking at the studies, different aspects can be seen, such as botanic, medicine, organic chemistry, chemical engineering, etc. In summary, *H. perforatum* has a wide range of uses thanks to certain active ingredients in its composition. It is not the species that contains the most hypericin and hyperforin substances, but it is the most commonly used species of *Hypericum* because it can grow in many places, has been studied for a long time, and contains a wider range of components. It is used not only as over-the-corner medicine but also in prescription treatment processes. It can also be used as a food additive due to its antimicrobial and antioxidant effects. Although maceration is a common method of use when it is fresh, there are no studies on the drying process. Its extraction can be carried out with traditional methods (soxhlet extraction, stirred extraction) as well as modern methods (accelerated solvent extraction, supercritical fluid extraction). Its essential oil generally includes derivatives of caryophyllene, pinene, germacrene, selinene, and cadinene compounds, although its composition varies regionally.

CONFLICT OF INTEREST

The authors declare that they have no known competing financial interests or personal relationships that could have appeared to influence the work reported in this paper.

REFERENCES

1. Greeson JM, Sanford B, Monti DA. St. John's wort (*Hypericum perforatum*): A review of the current pharmacological, toxicological, and clinical literature. *Psychopharmacology (Berl)*. 2001;153(4):402–14. <DOI>.
2. Sun P, Kang T, Xing H, Zhang Z, Yang D, Zhang J, et al. Phytochemical changes in aerial parts of *Hypericum perforatum* at different harvest stages. *Rec Nat Prod*. 2019;13(1):1–9. <DOI>.
3. Robson NKB. Studies in the genus *Hypericum* L. (Guttiferae). 8. Sections 29. *Brathys* (part 2) and 30. *Trigynobrathys*. *Bull Nat Hist Museum [Internet]*. 1990;20:1–151. ISBN: 0-565-08026-1 . <URL>.

4. Hosni K, Msaâda K, Ben Taârit M, Ouchikh O, Kallel M, Marzouk B. Essential oil composition of *Hypericum perforatum* L. and *Hypericum tomentosum* L. growing wild in Tunisia. *Ind Crops Prod*. 2008;27(3):308–14. [<DOI>](#).
5. Ji YY, Yang JY, Zhang RF, Chen QY, Xu R, Wei XJ, et al. Chemical characterization, neuroprotective, antimicrobial and enzyme inhibitory activities of *Hypericum* volatile oils. *Ind Crops Prod* [Internet]. 2021;172(August):113991. [<DOI>](#).
6. Robson NKB. The Natural History Botany Series. *Bull Nat Hist Museum*. 2002;32(2).
7. Ciccarelli D, Andreucci AC, Pagni AM. Translucent glands and secretory canals in *Hypericum perforatum* L. (Hypericaceae): Morphological, anatomical and histochemical studies during the course of ontogenesis. *Ann Bot*. 2001;88(4):637–44. [<DOI>](#).
8. Karimi M, Ahmadi N, Ebrahimi M. Red LED light promotes biomass, flowering and secondary metabolites accumulation in hydroponically grown *Hypericum perforatum* L. (cv. Topas). *Ind Crops Prod* [Internet]. 2022;175(November 2021):114239. Available from: [<DOI>](#).
9. Barnes J, Anderson LA, Phillipson JD. St John's wort (*Hypericum perforatum* L.): a review of its chemistry, pharmacology and clinical properties. *J Pharm Pharmacol*. 2001;53(5):583–600. [<DOI>](#).
10. Ekor M. The growing use of herbal medicines: issues relating to adverse reactions and challenges in monitoring safety. *Front Neurol*. 2014;4:1–10. [<DOI>](#).
11. Saddiqa Z, Naeem I, Maimoona A. A review of the antibacterial activity of *Hypericum perforatum* L. *J Ethnopharmacol* [Internet]. 2010;131(3):511–21. Available from: [<DOI>](#).
12. Maleš Ž, Brantner AH, Sovič K, Pilepić KH, Plazibat M. Comparative phytochemical and antimicrobial investigations of *Hypericum perforatum* L. subsp. *perforatum* and *H. perforatum* subsp. *angustifolium* (DC.) Gaudin. *Acta Pharm*. 2006;56(3):359–67. [<URL>](#).
13. Radulović N, Stankov-Jovanović V, Stojanović G, Šmelcerović A, Spitteller M, Asakawa Y. Screening of in vitro antimicrobial and antioxidant activity of nine *Hypericum* species from the Balkan. *Food Chem*. 2007;103(1):15–21. [<DOI>](#).
14. Maltas Cagil E, Uysal A, Yildiztugay E, Aladağ M, Yildiz S, Kucukoduk M. Investigation of antioxidant and antibacterial activities of some *Hypericum* species. *Fresenius Environ Bull*. 2013;22(3a):862–9.
15. Nazlı O, Baygar T, Demirci Dönmez ÇE, Dere Ö, Uysal Aİ, Aksözek A, et al. Antimicrobial and antibiofilm activity of Polyurethane/*Hypericum perforatum* extract (PHPE) composite. *Bioorg Chem*. 2019;82:224–8. [<DOI>](#).
16. Güneş S, Tihminlioğlu F. *Hypericum perforatum* incorporated Chitosan films as potential bioactive wound dressing material. *Int J Biol Macromol*. 2017;102:933–43. [<DOI>](#).
17. Yıldırım N, Küçük İ. Preparing and characterization of St. John's wort (*Hypericum perforatum*) incorporated wound dressing films based on Chitosan and gelatin. *J Fac Eng Archit Gazi Univ*. 2020;35(1):127–35. [<DOI>](#).
18. Lyles JT, Kim A, Nelson K, Bullard-Roberts AL, Hajdari A, Mustafa B, et al. The chemical and antibacterial evaluation of St. John's wort oil macerates used in Kosovar traditional medicine. *Front Microbiol*. 2017;8(SEP):1–19. [<DOI>](#).
19. Shinjyo N, Nakayama H, Li L, Ishimaru K, Hikosaka K, Suzuki N, et al. *Hypericum perforatum* extract and Hyperforin inhibit the growth of neurotropic parasite *Toxoplasma gondii* and infection induced inflammatory responses of glial cells in vitro. *J Ethnopharmacol*. 2021;267:113525. [<DOI>](#).
20. Jarzębski M, Smulek W, Baranowska HM, Masewicz Ł, Kobus-Cisowska J, Ligaj M, et al. Characterization of St. John's wort (*Hypericum perforatum* L.) and the impact of filtration process on bioactive extracts incorporated into carbohydrate-based hydrogels. *Food Hydrocoll*. 2020 Jul 1;104:105748. [<DOI>](#).
21. Conforti F, Statti GA, Tundis R, Bianchi A, Agrimonti C, Sacchetti G, et al. Comparative chemical composition and variability of biological activity of methanolic extracts from *Hypericum perforatum* L. *Nat Prod Res*. 2005;19(3):295–303. [<DOI>](#).
22. Rančić A, Soković M, Vukojević J, Simić A, Marin P, Duletić-Laušević S, et al. Chemical composition and antimicrobial activities of essential oils of *Myrrhis odorata* (L.) Scop, *Hypericum perforatum* L and *Helichrysum arenarium* (L.) Moench. *J Essent Oil Res*. 2005;17(3):341–5. [<DOI>](#).
23. Saroglou V, Marin PD, Rancic A, Veljic M, Skaltsa H. Composition and antimicrobial activity of the essential oil of six *Hypericum* species from Serbia. *Biochem Syst Ecol*. 2007;35(3):146–52. [<DOI>](#).
24. Orhan IE, Kartal M, Gülpinar AR, Cos P, Matheussen A, Maes L, et al. Assessment of antimicrobial and antiprotozoal activity of the olive oil macerate samples of *Hypericum perforatum* and their LC-DAD-MS analyses. *Food Chem* [Internet]. 2013;138(2–3):870–5. [<DOI>](#).
25. Bazamova YG, Ivanchenko OB. Investigation of the composition of biologically active substances in extracts of wild plants. *Vopr Pitan* [Internet]. 2016;85(5):100–7. [<URL>](#).
26. Del Monte D, De Martino L, Marandino A, Fratianni F, Nazzaro F, De Feo V. Phenolic content, antimicrobial and antioxidant activities of *Hypericum perforatum* L. *Ind Crops Prod* [Internet]. 2015;74:342–7. [<DOI>](#).
27. Schempp CM, Pelz K, Wittmer A, Schöpf E, Simon JC. Antibacterial activity of Hyperforin from St. John's wort, against multiresistant *Staphylococcus aureus* and gram-positive bacteria. *Lancet*. 1999;353(9170):2129. [<DOI>](#).
28. Reichling J, Weseler A, Saller R. A current review of the antimicrobial activity of *Hypericum perforatum* L. *Pharmacopsychiatry*. 2001;34(SUPPL. 1):116–8. [<DOI>](#).

29. Schempp CM, Windeck T, Hezel S, Simon JC. Topical treatment of atopic dermatitis with St. John's wort cream - A randomized, placebo controlled, double blind half-side comparison. *Phytomedicine*. 2003;10(Supplement IV):31-7. [<DOI>](#).
30. Milosevic T, Solujic S, Sukdolak S. In vitro study of ethanolic extract of *Hypericum perforatum* L. on growth and sporulation of some bacteria and fungi. *Turkish J Biol*. 2007;31(4):237-41. [<URL>](#).
31. Mekinić IG, Skroza D, Ljubenković I, Katalinić V, Šimat V. Antioxidant and antimicrobial potential of phenolic metabolites from traditionally used Mediterranean herbs and spices. *Foods*. 2019;8(11):579-95. [<DOI>](#).
32. Isacchi B, Bergonzi MC, Carnevali F, van der Esch SA, Vincieri FF, Bilia AR. Analysis and stability of the constituents of St. John's wort oils prepared with different methods. *J Pharm Biomed Anal*. 2007 Dec 21;45(5):756-61. [<DOI>](#).
33. Moleriu L, Jianu C, Bujanca G, Doros G, Misca C, Ilie OC, et al. Essential oil of *Hypericum perforatum*: The chemical composition and antimicrobial activity. *Rev Chim*. 2017;68(4):687-92.
34. Rafieian-Kopaei M, Saki K, Bahmani M, Ghafourian S, Sadeghifard N, Taherikalani M. Listeriosis phytotherapy: A review study on the effectiveness of Iranian medicinal plants in treatment of Listeriosis. *J Evidence-Based Complement Altern Med*. 2017;22(2):278-83. [<DOI>](#).
35. Mohammadi G, Rafiee G, El Basuini MF, Van Doan H, Ahmed HA, Dawood MAO, et al. Oregano (*Origanum vulgare*), St John's wort (*Hypericum perforatum*), and lemon balm (*Melissa officinalis*) extracts improved the growth rate, antioxidative, and immunological responses in Nile Tilapia (*Oreochromis niloticus*) infected with *Aeromonas hydrophil*. *Aquac Reports*. 2020;18:100445. [<DOI>](#).
36. Boyanova L. Comparative evaluation of the activity of plant infusions against *Helicobacter pylori* strains by three methods. *World J Microbiol Biotechnol*. 2014;30(5):1633-7. [<DOI>](#).
37. Mašković PZ, Mladenović JD, Cvijović MS, Aćamović-Doković G, Solujčić SR, Radojković MM. Phenolic content, antioxidant and antifungal activities of acetonetic, ethanolic and petroleum ether extracts of *Hypericum perforatum* L. *Hem Ind*. 2011;65(2):159-64. [<DOI>](#).
38. Alan S, Demirci B, Iscan G, Kose YB, Baser KHC. Composition and anticandidal activity of the essential oil of *Hypericum perforatum* L. *Asian J Chem*. 2010;22(2):1315-20.
39. Er Y, Özer N, Katircioğlu YZ. Determination of anti-mildew activity of essential oils against downy mildew of sunflower caused by *Plasmopara halstedii*. *J Plant Dis Prot* [Internet]. 2020;127(5):709-13. Available from: [<DOI>](#).
40. Bruni R, Pellati F, Bellardi MG, Benvenuti S, Paltrinieri S, Bertaccini A, et al. Herbal drug quality and phytochemical composition of *Hypericum perforatum* L. affected by ash yellows phytoplasma infection. *J Agric Food Chem*. 2005;53(4):964-8. [<DOI>](#).
41. Carrubba A, Lazzara S, Giovino A, Ruberto G, Napoli E. Content variability of bioactive secondary metabolites in *Hypericum perforatum* L. *Phytochem Lett* [Internet]. 2021;46(September):71-8. Available from: [<DOI>](#).
42. Eray N, Dalar A, Turker M. The effects of abiotic stressors and signal molecules on phenolic composition and antioxidant activities of in vitro regenerated *Hypericum perforatum* (St. John's wort). *South African J Bot*. 2020;133:253-63. [<DOI>](#).
43. Mir MY, Kamili AN, Hassan QP, Rafi S, Parray JA, Jan S. In vitro regeneration and free radical scavenging assay of *Hypericum perforatum* L. *Natl Acad Sci Lett* [Internet]. 2019;42(2):161-7. Available from: [<DOI>](#).
44. Pan ZG, Liu CZ, Murch SJ, Saxena PK. 2004 SIVB Congress Symposium Proceedings 'Thinking outside the Cell': Optimized chemodiversity in protoplast-derived lines of St. John's wort (*Hypericum perforatum* L.). *Vitr Cell Dev Biol - Plant*. 2005;41(3):226-31. [<DOI>](#).
45. Velada I, Ragonezi C, Arnholdt-Schmitt B, Cardoso H. Reference genes selection and normalization of oxidative stress responsive genes upon different temperature stress conditions in *Hypericum perforatum* L. *PLoS One*. 2014;9(12):e115206. [<DOI>](#).
46. Radušienė J, Karpavičienė B, Stanius Ž. Effect of external and internal factors on secondary metabolites accumulation in St. John's wort. *Bot Lith*. 2013;18(2):101-8.
47. Bagdonaite E, Mártonfi P, Repčák M, Labokas J. Variation in concentrations of major bioactive compounds in *Hypericum perforatum* L. from Lithuania. *Ind Crops Prod*. 2012;35(1):302-8.
48. Kladar N, Srđenović B, Grujić N, Rat M, Gavarić N, Anačkov G, et al. St. John's wort (*Hypericum* Spp.) - relation between the biological source and medical properties. In: Davis HR, editor. *Hypericum: Botanical Sources, Medical Properties and Health Effects* [Internet]. Nova Science Publishers; 2015. p. 53-80. Available from: [<URL>](#).
49. Sagratini G, Ricciutelli M, Vittori S, Öztürk N, Öztürk Y, Maggi F. Phytochemical and antioxidant analysis of eight *Hypericum* taxa from Central Italy. *Fitoterapia*. 2008;79(3):210-3. [<DOI>](#).
50. Kelebek H, Sevindik O, Selli S. LC-DAD-ESI-MS/MS-Based phenolic profiling of St. John's wort teas and their antioxidant activity: Eliciting infusion induced changes. *J Liq Chromatogr Relat Technol* [Internet]. 2019;42(1-2):9-15. [<DOI>](#).
51. Sentkowska A, Biesaga M, Pyrzynska K. Effects of brewing process on phenolic compounds and antioxidant activity of herbs. *Food Sci Biotechnol*. 2016;25(4):965-70. [<DOI>](#).
52. Sierzant K, Katarzyna P-B, Janina G. Antioxidant properties of natural polyphenolic extracts from selected in model systems. *Żywność Nauk Technol Jakość*. 2012;6(85):41-53. [<URL>](#).
53. Arsic I, Žugic A, Antic DR, Zdunic G, Dekanski D, Markovic G, et al. *Hypericum perforatum* L.

- Hypericaceae/Guttiferae sunflower, olive and palm oil extracts attenuate cold restraint stress - Induced gastric lesions. *Molecules*. 2010;15(10):6688–98. [<DOI>](#).
54. Firenzuoli F, Gori L, Crupi A, Neri D. Flavonoids: Risks or therapeutic opportunities? *Recenti Prog Med*. 2004;95(7–8):345–51. PMID: 15303543. [<URL>](#).
55. Arsić I. Preparation and characterization of St. John's wort herb extracts using olive, sunflower and palm oils. *Acta Fac Medicae Naissensis*. 2016;33(2):119–26. [<DOI>](#).
56. Şahin S, Çiğeroğlu Z, Kurtulbaş E, Pekel AG, İbibik K. Kinetics and thermodynamics evaluation of oxidative stability in Oleum hyperici: A comparative study. *J Pharm Biomed Anal*. 2020;183:113148. [<DOI>](#).
57. Franchi GG, Nencini C, Collavoli E, Massarelli P. Composition and antioxidant activity in vitro of different St. John's wort (*Hypericum perforatum* L.) extracts. *J Med Plants Res*. 2011;5(17):4349–53. [<DOI>](#).
58. Silva BA, Malva JO, Dias ACP. St. John's wort (*Hypericum perforatum*) extracts and isolated phenolic compounds are effective antioxidants in several in vitro models of oxidative stress. *Food Chem*. 2008;110(3):611–9. [<DOI>](#).
59. Kaliora AC, Kogiannou DAA, Kefalas P, Papassideri IS, Kalogeropoulos N. Phenolic profiles and antioxidant and anticarcinogenic activities of Greek herbal infusions; balancing delight and chemoprevention? *Food Chem [Internet]*. 2014;142:233–41. [<DOI>](#).
60. Şehirli AO, Cetinel S, Ozkan N, Selman S, Tetik S, Yuksel M, et al. St. John's wort may ameliorate 2,4,6-Trinitrobenzenesulfonic acid colitis of rats through the induction of Pregnane X receptors and/or P-Glycoproteins. *J Physiol Pharmacol*. 2015;66(2):203–14.
61. Škerget M, Kotnik P, Hadolin M, Hraš AR, Simonič M, Knez Ž. Phenols, proanthocyanidins, flavones and flavonols in some plant materials and their antioxidant activities. *Food Chem*. 2005;89(2):191–8. [<DOI>](#).
62. Chen CL, Huang CH, Sung JM. Antioxidants in aerial parts of *Hypericum sampsonii*, *Hypericum japonicum* and *Hypericum perforatum*. *Int J Food Sci Technol*. 2009;44(11):2249–55. [<DOI>](#).
63. Labun P, Salamon I. Methanol extracts of St. John's wort (*Hypericum perforatum* L.), horsetail (*Equisetum arvense* L.) and their comparison of antioxidant efficacy. *Adv Environ Biol*. 2011;5(2):426–426. [<URL>](#).
64. Orčić DZ, Mimica-Dukić NM, Francišković MM, Petrović SS, Jovin ET. Antioxidant activity relationship of phenolic compounds in *Hypericum perforatum* L. *Chem Cent J*. 2011;5(1):1–8. [<DOI>](#).
65. Parzhanova AB, Petkova NT, Ivanov IG, Ivanova SD. Evaluation of biologically active substance and antioxidant potential of medicinal plants extracts for food and cosmetic purposes. *J Pharm Sci Res*. 2018;10(7):1804–9.
66. Chimshirova R, Karsheva M, Diankov S, Hinkov I. Extraction of valuable compounds from Bulgarian St. John's wort (*Hypericum perforatum* L.). Antioxidant capacity and total polyphenolic content. *J Chem Technol Metall*. 2019;54(5):952–61.
67. Zlobin AA, Martinson EA, Ovechkina IA, Durnev EA, Ovodova RG, Litvinets SG. Composition and properties of pectin polysaccharides of St. John's wort *Hypericum perforatum* L. *Russ J Bioorganic Chem*. 2012;38(7):697–701. [<DOI>](#).
68. Li W, Sun YN, Yan XT, Yang SY, Choi CW, Hyun JW, et al. Isolation of Xanthones from adventitious roots of St. John's wort (*Hypericum perforatum* L.) and their antioxidant and cytotoxic activities. *Food Sci Biotechnol*. 2013;22(4):945–9. [<DOI>](#).
69. Gromovaya VF, Shapoval GS, Mironyuk IE, Nestyuk N V. Antioxidant properties of medicinal plants. *Pharm Chem J*. 2008;42(1):25–8. [<DOI>](#).
70. Božin B, Kladar N, Grujić N, Anačkov G, Samojlik I, Gavarić N, et al. Impact of origin and biological source on chemical composition, anticholinesterase and antioxidant properties of some St. John's wort species (*Hypericum* Spp., *Hypericaceae*) from the central Balkans. *Molecules*. 2013;18(10):11733–50. [<DOI>](#).
71. Seyrekoğlu F, Temiz H. Effect of extraction conditions on the phenolic content and DPPH radical scavenging activity of *Hypericum perforatum* L. *Turkish J Agric - Food Sci Technol*. 2020;8(1):226. [<DOI>](#).
72. Abdelhadi M, Meullemiestre A, Gelicus A, Hassani A, Rezzoug SA. Intensification of *Hypericum perforatum* L. oil isolation by solvent-free microwave extraction. *Chem Eng Res Des [Internet]*. 2015;93(April):621–31. [<DOI>](#).
73. Altun ML, Yilmaz BS, Orhan IE, Citoglu GS. Assessment of Cholinesterase and Tyrosinase inhibitory and antioxidant effects of *Hypericum perforatum* L. (St. John's wort). *Ind Crops Prod [Internet]*. 2013;43(1):87–92. [<DOI>](#).
74. Heinrich M, Lorenz P, Daniels R, Stintzing FC, Kammerer DR. Lipid and phenolic constituents from seeds of *Hypericum perforatum* L. and *Hypericum tetrapterum* Fr. and their antioxidant activity. *Chem Biodivers [Internet]*. 2017;14(8):42–9. [<URL>](#).
75. Öztürk N, Tunçel M, Potoğlu-Erkara İ. Phenolic compounds and antioxidant activities of some *Hypericum* species: A comparative study with *H. perforatum*. *Pharm Biol*. 2009;47(2):120–7. [<URL>](#).
76. Sarris J, Panossian A, Schweitzer I, Stough C, Scholey A. Herbal medicine for depression, anxiety and insomnia: A review of psychopharmacology and clinical evidence. *Eur Neuropsychopharmacol [Internet]*. 2011;21(12):841–60. [<DOI>](#).
77. Kumar A, Garg R, Prakash AK. Effect of St. John's wort (*Hypericum perforatum*) treatment on restraint stress-induced behavioral and biochemical alteration in mice. *BMC Complement Altern Med [Internet]*. 2010 Dec 7;10(1):18. [<URL>](#).
78. Jungke P, Ostrow G, Li JL, Norton S, Nieber K, Kelber O, et al. Profiling of hypothalamic and Hippocampal gene expression in chronically stressed rats treated with St. John's wort extract (STW 3-VI) and Fluoxetine. *Psychopharmacology (Berl)*. 2011;213(4):757–72. [<DOI>](#).

79. Kladar N, Anačkov G, Srđenović B, Gavarić N, Hitl M, Salaj N, et al. St. John's wort herbal teas – Biological potential and chemometric approach to quality control. *Plant Foods Hum Nutr.* 2020;75(3):390–5. [<DOI>](#).
80. Kraus B, Wolff H, Heilmann J, Elstner EF. Influence of *Hypericum perforatum* extract and its single compounds on Amyloid- β mediated toxicity in microglial cells. *Life Sci.* 2007;81(11):884–94. [<DOI>](#).
81. Griffith T, Varela-Nallar L, Dinamarca M, Inestrosa N. Neurobiological effects of Hyperforin and its potential in Alzheimer's disease therapy. *Curr Med Chem.* 2010;17(5):391–406. [<DOI>](#).
82. Doukani K, Selles ASM, Bouhenni H. Hypericin and pseudohypericin. In: *Naturally Occurring Chemicals Against Alzheimer's Disease* [Internet]. Elsevier Inc.; 2021. p. 155–65. [<DOI>](#).
83. Eçilmez OK, Kökten N, Ekici AİD, Kalcioğlu MT, Yesilada E, Tekin M. The effect of *Hypericum perforatum* L. (St. John's wort) on prevention of myringosclerosis after myringotomy in a rat model. *Int J Pediatr Otorhinolaryngol.* 2015;79(7):1128–34. [<DOI>](#).
84. Abolfathi AA, Doustar Y, Mortazavi P, Rezai A. Effect of *Hypericum perforatum* extract on renal ischemic reperfusion injury in rats. *Journal of Animal and Veterinary Advances.* 2011; 10(24): 3244–8.
85. Poppenga RH. Herbal medicine: potential for intoxication and interactions with conventional drugs. *Clin Tech Small Anim Pract.* 2002;17(1):6–18. [<DOI>](#).
86. Guleken Z, Depciuch J, Ege H, İlbay G, Kalkandelen C, Ozbeyli D, et al. Spectrochemical and biochemical assay comparison study of the healing effect of the Aloe vera and *Hypericum perforatum* loaded nanofiber dressings on diabetic wound. *Spectrochim Acta - Part A Mol Biomol Spectrosc.* 2021;254. [<DOI>](#).
87. Paulke A, Schubert-Zsilavec M, Wurglics M. Determination of St. John's wort flavonoid-metabolites in rat brain through high performance liquid chromatography coupled with fluorescence detection. *J Chromatogr B.* 2006;832(1):109–13. [<DOI>](#).
88. Oliveira AI, Pinho C, Sarmiento B, Dias ACP. Neuroprotective activity of *Hypericum perforatum* and its major components. *Front Plant Sci.* 2016;7(JULY2016):1–15. [<DOI>](#).
89. Sultan MT, Buttxs MS, Qayyum MMN, Suleria HAR. Immunity: Plants as effective mediators. *Crit Rev Food Sci Nutr.* 2014;54(10):1298–308. [<DOI>](#).
90. Laggner H, Schmid S, Goldenberg H. Hypericin and photodynamic treatment do not interfere with transport of vitamin C during respiratory burst. *Free Radic Res.* 2004;38(10):1073–81. [<DOI>](#).
91. Schmitt LA, Liu Y, Murphy PA, Petrich JW, Dixon PM, Birt DF. Reduction in Hypericin-induced phototoxicity by *Hypericum perforatum* extracts and pure compounds. *J Photochem Photobiol B Biol.* 2006;85(2):118–30. [<DOI>](#).
92. Lu WD, Atkins WM. A novel antioxidant role for ligandin behavior of Glutathione S-Transferases: Attenuation of the photodynamic effects of Hypericin. *Biochemistry.* 2004;43(40):12761–9. [<DOI>](#).
93. Trommer H, Neubert RHH. Screening for new antioxidative compounds for topical administration using skin lipid model systems. *J Pharm Pharm Sci.* 2005;8(3):494–506. [<DOI>](#).
94. He Y-Y, Chignell CF, Miller DS, Andley UP, Roberts JE. Phototoxicity in human lens epithelial cells promoted by St. John's wort. *Photochem Photobiol.* 2004;80(3):583. [<DOI>](#).
95. McCue PP, Phang JM. Identification of human intracellular targets of the medicinal herb St. John's wort by chemical-genetic profiling in yeast. *J Agric Food Chem.* 2008;56(22):11011–7. [<DOI>](#).
96. Mayurnikova LA, Zinchuk SF, Davydenko NI, Gilmulina SA. Development of a functional basis of phyto-beverages with an increased antioxidant activity for the correction of nutrition of patients with Diabetes mellitus. *Foods Raw Mater.* 2017;5(2):178–88.
97. Novelli M, Masiello P, Befly P, Menegazzi M. Protective role of St. John's wort and its components Hyperforin and Hypericin against diabetes through inhibition of inflammatory signaling: Evidence from in vitro and in vivo studies. *Int J Mol Sci.* 2020;21(21):1–35. [<DOI>](#).
98. Peron AP, Mariucci RG, de Almeida I V., Düsman E, Mantovani MS, Vicentini VEP. Evaluation of the cytotoxicity, mutagenicity and antimutagenicity of a natural antidepressant, *Hypericum perforatum* L. (St. John's wort), on vegetal and animal test systems. *BMC Complement Altern Med.* 2013;13(April 2007):1–9. [<DOI>](#).
99. Laggner H, Schreier S, Hermann M, Exner M, Mühl A, Gmeiner BMK, et al. The main components of St. John's wort inhibit low-density lipoprotein atherogenic modification: A beneficial 'side effect' of an OTC antidepressant drug? *Free Radic Res.* 2007;41(2):234–41. [<DOI>](#).
100. Kaplan V, Hasanoglu Erbasar GN, Cigerim L, Altay Turgut HA, Cerit A. Effect of St. John's wort oil and olive oil on the postoperative complications after third molar surgery: Randomized, double-blind clinical trial. *Clin Oral Investig.* 2021;25:2429–38. [<DOI>](#).
101. Mohammadirad A, Aghamohammadali-Sarraf F, Badii S, Faraji Z, Hajiaghaee R, Baeeri M, et al. Anti-aging effects of some selected Iranian folk medicinal herbs-biochemical evidences. *Iran J Basic Med Sci.* 2013;16(11):1170–80. [<URL>](#).
102. Grundmann O, Lv Y, Kelber O, Butterweck V. Mechanism of St. John's wort extract (STW3-VI) during chronic restraint stress is mediated by the interrelationship of the immune, oxidative defense, and neuroendocrine system. *Neuropharmacology* [Internet]. 2010;58(4–5):767–73. Available from: [<DOI>](#).
103. Nazirog˘lu M, Çig˘ B, Özgül C. Modulation of oxidative stress and Ca²⁺ mobilization through TRPM2 channels in rat dorsal root ganglion neuron by *Hypericum perforatum*. *Neuroscience.* 2014;263:27–35. [<DOI>](#).

104. Öztürk N, Korkmaz S, Öztürk Y. Wound-healing activity of St. John's wort (*Hypericum perforatum* L.) on chicken embryonic fibroblast. *J Ethnopharmacol*. 2007;111(1):33-9. [<DOI>](#).
105. Hizli D, Hizli F, Köşüş A, Yılmaz S, Köşüş N, Haltaş H, et al. Effect of *Hypericum perforatum* on intraperitoneal adhesion formation in rats. *Arch Med Sci*. 2014;10(2):396-400. [<DOI>](#).
106. Kitikannakorn N, Chaiyakunapruk N, Nimpitakpong P, Dilokthornsakul P, Meepoo E, Kerdpeng W. An overview of the evidences of herbals for smoking cessation. *Complement Ther Med* [Internet]. 2013;21(5):557-64. Available from: [<DOI>](#).
107. Tomczyk M, Zovko-Končić M, Chrostek L. Phytotherapy of alcoholism. *Nat Prod Commun*. 2012;7(2):273-80. [<DOI>](#).
108. Saller R, Melzer J, Reichling J. Johanniskraut (*Hypericum perforatum*): Ein plurivalenter rohstoff für traditionelle und moderne therapien. *Forschende Komplementarmedizin und Klass Naturheilkd*. 2003;10(SUPPL. 1):33-40. [<DOI>](#).
109. Tesch BJ. Herbs commonly used by women: An evidence-based review. *Am J Obstet Gynecol*. 2003;188(5):44-55. [<DOI>](#).
110. Lawvere S, Mahoney MC. St. John's wort. *Am Fam Physician*. 2005;72(11):2249-54.
111. Lam YWF, Huang S-M, Hall SD. Herbal supplements-drug interactions: Scientific and regulatory perspectives. 1st ed. New York: CRC Press; 2006.
112. Elmer GW, Lafferty WE, Tyree PT, Lind BK. Potential interactions between complementary/alternative products and conventional medicines in a medicare population. *Ann Pharmacother*. 2007;41(10):1617-24. [<DOI>](#).
113. Dunne FJ. The 'natural health service': Natural does not mean safe. *Adv Psychiatr Treat*. 2009;15(1):49-56. [<DOI>](#).
114. Shi S, Klotz U. Drug interactions with herbal medicines. *Clin Pharmacokinet*. 2012;51(2):77-104. [<DOI>](#).
115. Doğan Ö, Avcı A. Bitkilerle tedavi ve ilaç etkileşimleri. *Türkiye Klin*. 2018;4(1):49-54.
116. Ip N, Pang T, Ip F. Recent development in the search for effective antidepressants using traditional Chinese medicine. *Cent Nerv Syst Agents Med Chem*. 2008;8(1):64-71. [<DOI>](#).
117. Paksoy MY, Selvi S, Savran A. Ethnopharmacological survey of medicinal plants in Ulukışla (Nig de-Turkey). *J Herb Med* [Internet]. 2016;6(1):42-8. [<DOI>](#).
118. Sargin SA, Selvi S, López V. Ethnomedicinal plants of Sarigöl district (Manisa), Turkey. *J Ethnopharmacol* [Internet]. 2015;171:64-84. [<DOI>](#).
119. Cakilcioglu U, Khatun S, Turkoglu I, Hayta S. Ethnopharmacological survey of medicinal plants in Maden (Elazig-Turkey). *J Ethnopharmacol* [Internet]. 2011;137(1):469-86. Available from: [<DOI>](#).
120. Krasteva A, Baeva M, Gogova T, Dessev T, Yovchev A. Proceedings Of The 6th CIGR Section VI International Symposium "Towards A Sustainable Food Chain" Food Process, Bioprocessing And Food Quality Management. In: Functional components in Bulgarian herbs and possibilities for usage in bread making. Nantes-France; 2011.
121. Spiridon I, Bodirlau R, Teaca CA. Total phenolic content and antioxidant activity of plants used in traditional Romanian herbal medicine. *Cent Eur J Biol*. 2011;6(3):388-96. [<DOI>](#).
122. Polat R, Cakilcioglu U, Satil F. Traditional uses of medicinal plants in Solhan (Bingöl - Turkey). *J Ethnopharmacol*. 2013;148(3):951-63. [<DOI>](#).
123. Zhang R, Ji Y, Zhang X, Kennelly EJ, Long C. Ethnopharmacology of *Hypericum* species in China: A comprehensive review on ethnobotany, phytochemistry and pharmacology. *J Ethnopharmacol* [Internet]. 2020;254:112686. [<DOI>](#).
124. Solati K, Karimi M, Rafieian-Kopaei M, Abbasi N, Abbaszadeh S, Bahmani M. Phytotherapy for wound healing: The most important herbal plants in wound healing based on Iranian ethnobotanical documents. *Mini Rev Med Chem* [Internet]. 2021;21(4):500-19. [<DOI>](#).
125. Sargin SA, Akçicek E, Selvi S. An ethnobotanical study of medicinal plants used by the local people of Alaşehir (Manisa) in Turkey. *J Ethnopharmacol*. 2013;150(3):860-74. [<DOI>](#).
126. Korkmaz M, Karakuş S, Özçelik H, Selvi S. An ethnobotanical study on medicinal plants in Erzincan, Turkey. *Indian J Tradit Knowl*. 2016;15(2):192-202. [<URL>](#).
127. Committee on Herbal Medicinal Products. Assessment report on *Hypericum perforatum* L., herba. European medicines agency Evaluation of Medicines for Human Use. London; 2018.
128. Hunt EJ, Lester CE, Lester EA, Tackett RL. Effect of St. John's wort on free radical production. *Life Sci*. 2001;69(2001):181-90. [<DOI>](#).
129. Soliva CR, Widmer S, Kreuzer M. Ruminal fermentation of mixed diets supplemented with St. John's wort (*Hypericum perforatum*) flowers and pine (*Pinus mugo*) oil or mixtures containing these preparations. *J Anim Feed Sci*. 2008;17(3):352-62.
130. Reyes-Cerpa S, Vallejos-Vidal E, Gonzalez-Bown MJ, Morales-Reyes J, Pérez-Stuardo D, Vargas D, et al. Effect of yeast (*Xanthophyllomyces dendrorhous*) and plant (Saint John's wort, lemon balm, and rosemary) extract based functional diets on antioxidant and immune status of Atlantic salmon (*Salmo salar*) subjected to crowding stress. *Fish Shellfish Immunol* [Internet]. 2018;74:250-9. [<URL>](#).
131. Fiume MZ. Final report on the safety assessment of *Hypericum perforatum* extract and *Hypericum perforatum* oil. *Int J Toxicol*. 2001;20(Suppl. 2):31-9.

132. Alzoubi KH, Abdel-Hafiz L, Khabour OF, El-Elimat T, Alzubi MA, Alali FQ. Evaluation of the effect of *Hypericum triquetrifolium* Turra on memory impairment induced by chronic psychosocial stress in rats: Role of BDNF. *Drug Des Devel Ther.* 2020;14:5299–314. <DOI>.
133. Feucht C, Patel DR. Herbal medicines in pediatric neuropsychiatry. *Pediatr Clin North Am.* 2011;58(1):33–54. <DOI>.
134. Aleisa AM. Cytological and biochemical effects of St. John's wort supplement (a complex mixture of St. John's wort, rosemary and spirulina) on somatic and germ cells of Swiss albino mice. *Int J Environ Res Public Health.* 2008;5(5):408–17. <DOI>.
135. Becker LC, Bergfeld WF, Belsito D V., Hill RA, Klaassen CD, Liebler DC, et al. Amended safety assessment of *Hypericum perforatum*-derived ingredients as used in cosmetics. *Int J Toxicol.* 2014;33(6):5S-23S. <DOI>.
136. Meredith MJ. Herbal nutraceuticals: A primer for dentists and dental hygienists. *J Contemp Dent Pract.* 2001;2(2):1–15. <DOI>.
137. Natural medicines comprehensive database: St. John's wort [Internet]. Therapeutic Research Center (TRC) Healthcare. 2020 [cited 2021 Mar 29]. <URL>.
138. Strandell J, Neil A, Carlin G. An approach to the in vitro evaluation of potential for Cytochrome P450 enzyme inhibition from herbals. *Phytomedicine.* 2004;11:98–104. <DOI>.
139. Zabłocka-Słowińska K, Jawna K, Grajeta H, Biernat J. Interactions between preparations containing female sex hormones and dietary supplements. *Adv Clin Exp Med.* 2014;23(4):657–63. <URL>.
140. Genovese T, Mazzon E, Di Paola R, Muià C, Crisafulli C, Menegazzi M, et al. *Hypericum perforatum* attenuates the development of Cerulein-induced acute pancreatitis in mice. *Shock.* 2006;25(2):161–7. <DOI>.
141. Dost T, Ozkayran H, Gokalp F, Yenisey C, Birincioglu M. The effect of *Hypericum perforatum* (St. John's wort) on experimental colitis in rat. *Dig Dis Sci* [Internet]. 2009 Jun 27;54(6):1214–21. <DOI>.
142. Gomez MR, Cerutti S, Olsina RA, Silva MF, Martínez LD. Metal content monitoring in *Hypericum perforatum* pharmaceutical derivatives by atomic absorption and emission spectrometry. *J Pharm Biomed Anal.* 2004;34(3):569–76. <DOI>.
143. Ražić S, Onjia A, Dogo S, Slavković L, Popović A. Determination of metal content in some herbal drugs - Empirical and chemometric approach. *Talanta.* 2005;67(1):233–9. <DOI>.
144. Gomez MR, Cerutti S, Sombra LL, Silva MF, Martínez LD. Determination of heavy metals for the quality control in Argentinian herbal medicines by ETAAS and ICP-OES. *Food Chem Toxicol.* 2007;45(6):1060–4. <DOI>.
145. Djukić-Čosić D, Stanojević A, Djekić-Ivanković M, Čurčić M, Plamenac-Bulat Z, Antonijević B, et al. Cadmium content in *Hypericum perforatum* L. and *Thymus serpyllum* L. from localities of the mountains Rtanj and Ozren. *Vojnosanit Pregl.* 2011;68(11):930–4.
146. Helmja K, Vaher M, Püssa T, Orav A, Viitak A, Levandi T, et al. Variation in the composition of the essential oils, phenolic compounds and mineral elements of *Hypericum perforatum* L. growing in Estonia. *Nat Prod Res.* 2011;25(5):496–510. <DOI>.
147. Tavli ÖF, Hazman Ö, Büyükben A, Yilmaz FN, Özbek Çelik B, Eroglu ÖZkan E. Pharmacognostic research on *Hypericum perforatum* samples sold by herbalists in Istanbul. *Ankara Univ Eczac Fak Derg.* 2020;44(2):265–80. <DOI>.
148. Orhan IE, Kartal M, Gülpinar AR, Yetkin G, Orlikova B, Diederich M, et al. Inhibitory effect of St. John's Wort oil macerates on TNF α -induced NF- κ B activation and their fatty acid composition. *J Ethnopharmacol* [Internet]. 2014;155(2):1086–92. Available from: <DOI>.
149. Alahmad A, Feldhoff A, Bigall NC, Rusch P, Scheper T, Walter J-G. *Hypericum perforatum* L.-mediated green synthesis of silver nanoparticles exhibiting antioxidant and anticancer activities. *Nanomaterials.* 2021;11(2):487. <DOI>.
150. Manea AM, Ungureanu C, Meghea A. Effect of vegetable oils on obtaining lipid nanocarriers for sea buckthorn extract encapsulation. *Comptes Rendus Chim* [Internet]. 2014;17(9):934–43. <DOI>.
151. Manea AM, Vasile BS, Meghea A. Antioxidant and antimicrobial activities of green tea extract loaded into nanostructured lipid carriers. *Comptes Rendus Chim* [Internet]. 2014;17(4):331–41. <DOI>.
152. Kalliantas D, Kallianta M, Kordatos K, Karagianni CS. Micro-nano particulate compositions of *Hypericum perforatum* L in ultra high diluted succussed solution medicinal products. *Heliyon* [Internet]. 2021;7(4):e06604. Available from: <DOI>.
153. Kazlauskas S, Bagdonaite E. Quantitative analysis of active substances in St. John's wort (*Hypericum perforatum* L.) by the high performance liquid chromatography method. *Med* [Internet]. 2004;40(10):975–81. Available from: <DOI>.
154. Yüce E. Analysis of the essential oils of two *Hypericum* species (*H. lanuginosum* var. *lanuginosum* Lam. and *H. perforatum* L.) from Turkey. *Hacettepe J Biol Chem.* 2016;44(1):29–29. <URL>.
155. Schwob I, Bessiere JM, Masotti V, Viano J. Changes in essential oil composition in Saint John's wort (*Hypericum perforatum* L.) aerial parts during its phenological cycle. *Biochem Syst Ecol.* 2004;32(8):735–45. <DOI>.
156. Smelcerovic A, Spittler M, Ligon AP, Smelcerovic Z, Raabe N. Essential oil composition of *Hypericum* L. species from Southeastern Serbia and their chemotaxonomy. *Biochem Syst Ecol.* 2007;35(2):99–113. <DOI>.
157. Schwob I, Bessière JM, Viano J. Composition of the essential oils of *Hypericum perforatum* L. from Southeastern France. *Comptes Rendus - Biol.* 2002;325(7):781–5. <DOI>.

158. Chatzopoulou PS, Markovic T, Radanovic D, Koutsos T V., Katsiotis ST. Essential oil composition of Serbian *Hypericum perforatum* local population cultivated in different ecological conditions. *J Essent Oil-Bearing Plants*. 2009;12(6):666–73. <DOI>.
159. Hışıl Y, Şahin F, Omay SB. Kantaronun (*Hypericum perforatum* L.) bileşimi ve tıbbi önemi. *Int J Hematol Oncol* [Internet]. 2005;15(4):212–8. Available from: <DOI>.
160. Smelcerovic A, Lepojevic Z, Djordjevic S. Sub- and supercritical CO₂-extraction of *Hypericum perforatum* L. *Chem Eng Technol*. 2004;27(12):1327–9. <DOI>.
161. Çakir A, Duru ME, Harmandar M, Ciriminna R, Passannanti S, Piozzi F. Comparison of the volatile oils of *Hypericum scabrum* L. and *Hypericum perforatum* L. from Turkey. *Flavour Fragr J*. 1997;12(4):285–7. <DOI>.
162. Pavlović M, Tzakou O, Petrakis P V., Couladis M. The essential oil of *Hypericum perforatum* L., *Hypericum tetrapterum* fries and *Hypericum olympicum* L. growing in Greece. *Flavour Fragr J*. 2006;21(1):84–7. <DOI>.
163. Gudžić B, Dordević S, Palić R, Stojanović G. Essential oils of *Hypericum olympicum* L. and *Hypericum perforatum* L. *Flavour Fragr J*. 2001;16(3):201–3.
164. Başer KHC, Ozek T, Nuriddinov HR, Demirci AB. Essential oils of two *Hypericum* species from Uzbekistan. *Chem Nat Compd*. 2002;38(1):54–7.
165. Azizi M. Change in content and chemical composition of *Hypericum perforatum* L. oil at three harvest time. *J Herbs, Spices Med Plants*. 2008;13(2):79–85.
166. Morshedloo MR, Ebadi A, Maggi F, Fattahi R, Yazdani D, Jafari M. Chemical characterization of the essential oil compositions from Iranian populations of *Hypericum perforatum* L. *Ind Crops Prod* [Internet]. 2015;76:565–73. Available from: <http://dx.doi.org/10.1016/j.indcrop.2015.07.033>
167. Venskutonis PR, Bagdonaite E. Comparative study on essential oil composition of different accessions of St. John's wort (*Hypericum perforatum* L.). *J Essent Oil Bear Plants*. 2011;14(4):442–52. <DOI>.
168. Mockute D, Bernotiene G, Judzentiene A. The essential oils with dominant Germacrene D of *Hypericum perforatum* L. growing wild in Lithuania. *J Essent Oil Res*. 2008;20(2):128–31. <DOI>.
169. Mockute D, Bernotiene G, Judzentiene A. Volatile compounds of the aerial parts of wild St. John's wort (*Hypericum perforatum* L.) plants. *Chemija*. 2003;14(2):108–11. <URL>.
170. Chatzopoulou PS, Koutsos T V., Katsiotis ST. Chemical composition of the essential oils from cultivated and wild grown St. John's wort (*Hypericum perforatum*). *J Essent Oil Res*. 2006;18(6):643–6. <DOI>.
171. Crockett SL. Essential oil and volatile components of the genus *Hypericum* (Hypericaceae). *Nat Prod Commun*. 2010;5(9):1493–506. <DOI>.
172. Hatami T, Glisic SB, Orlovic AM. Modelling and optimization of supercritical CO₂ extraction of St. John's wort (*Hypericum perforatum* L.) using genetic algorithm. *J Supercrit Fluids* [Internet]. 2012;62:102–8. <DOI>.
173. Taraj K, Ciko L, Malollari I, Andoni A, Ylli F, Ylli A, et al. Eco-extraction of essential oil from Albanian *Hypericum perforatum* L. and characterisation by spectroscopy techniques. *J Environ Prot Ecol*. 2019;20(1):188–95. <URL>.
174. Orio L, Cravotto G, Binello A, Pignata G, Nicola S, Chemat F. Hydrodistillation and in situ microwave-generated hydrodistillation of fresh and dried mint leaves: A comparison study. *J Sci Food Agric*. 2012;92(15):3085–90. <DOI>.



Chemical Constituents of the Stem Bark of *Prunus africana* and Evaluation of their Antibacterial Activity

Desalegn Abebe Deresa^{1,*} , Zelalem Abdissa¹ , Getahun Tadesse Gurmessa¹ ,
and Negera Abdissa^{2,*} 

¹Department of Chemistry, College of Natural and Computational Sciences, Wollega University, Nekemte, Ethiopia

²Department of Chemistry, College of Natural Sciences, Jimma University, Jimma, Ethiopia

Abstract: Chromatographic separation of the methanolic extract of *Prunus africana* stem bark led to the isolation of five compounds (β - sitosterol (**1**), benzoic acid (**2**), two oleanolic derivatives (**3** and **4**), and *p*-hydroxybenzoic acid (**5**). The structures of compounds were elucidated based on 1D and 2D NMR spectral data and compared with reported literature values. This is the first report of benzoic acid and its derivatives from the genus *Prunus*. The crude extract and isolated compounds were evaluated for their antibacterial activity against five bacterial strains (*E. coli*, *S. aureus*, *S. flexineri*, *S.typhimurium*, and *P. aeruginosa*) using disc diffusion assay and showed good antibacterial activity against the tested strains. The crude extract showed potent activity (21.03 ± 0.05 mm) against *P. aeruginosa*, which is even greater than the reference drug gentamycin (14.06 ± 0.09 mm). The antibacterial activity of *P.africana* extract and isolated compounds supports its traditional use, suggesting that it could be considered as a source of bioactive compounds in antimicrobial drug development.

Keywords: *Prunus africana*, oleanolic acid derivatives, benzoic acid, *p*-hydroxybenzoic acid, β -sitosterol, antibacterial activity.

Submitted: September 29, 2021 . Accepted: February 24, 2022.

Cite this: Deresa D, Abdissa Z, Gurmessa G, Abdissa N. Chemical Constituents of the Stem Bark of *Prunus africana* and Evaluation of their Antibacterial Activity. JOTCSA. 2022;9(2):395-414.

DOI: <https://doi.org/10.18596/jotcsa.1001676>.

***Corresponding Author. Email:** negeraabdisa@gmail.com ; Tel. +251913354086.

INTRODUCTION

Prunus africana, belonging to the Rosaceae family, is the only species of the genus *Prunus*, which comprises more than 400 species found in Africa. It is widely used in traditional medicine in southern, eastern, and central African countries (1) to treat prostatic cancer and related conditions across various communities for many years (2-4). The stem bark is used by herbalists in the treatment of various ailments including prostate problems, stomach aches, urinary and bladder infections, chest pain, malaria, microbial infections, and renal disease (5-9). In Ethiopia, the traditional healers use infusions of leaves, decoctions of stem and root barks of *P. africana* to treat urinary disorders, diarrhea, stomach ache, wounds, and bacterial

diseases (10). The pharmacological efficacy of the plant is believed to be due to its various phytochemical constituents (11). However, the phytochemical and bioactivity information pertaining to the stem bark of this plant are limited. Therefore, and as part of the ongoing search for new bioactive compounds from Ethiopian medicinal plants, the study was aimed at investigating the phytochemical constitution of the stem bark extract of *P. africana* and evaluating its antibacterial activity.

MATERIALS AND METHODS

General Method

Solvents and reagents used for extraction and purification of compounds are of analytical and HPLC grade. Analytical TLC pre-coated sheets

ALUGRAM®Xtra SIL G/UV₂₅₄ (layer: 0.20 mm silica gel 60 with fluorescent indicator UV_{F254/365}) was used for purity analysis. For column chromatography, silica gel 100-200 mesh was used. Chromatograms were visualized on TLC by spraying with 10% H₂SO₄ and heating on hot plate. NMR spectra data were recorded on an Avance 600 MHz spectrometer (Bruker, Billerica, MA, USA, at 600 MHz (¹H) and 150 MHz (¹³C)). Chemical shifts were expressed in parts per million (ppm) downfield of trimethylsilane (TMS) as internal reference for ¹H resonances, and referenced to the central peak of the appropriate deuterated solvent's resonances (residual CDCl₃ and DMSO at δ_H 7.26 for protons and δ_C 77.0 for carbons). Whatman filter paper No.3, DMSO, Petri dishes, and gentamycin were used in antibacterial analysis.

Plant Material

The stem barks of *P. africana* were collected from Horro Buluk, Horro Guduru Wollega zone, Oromia regional state, Ethiopia in September, 2019. The plant material was identified by an expert in botany (Dr. Fekadu Gurmessa) and the voucher specimen (DAD003Pa) has been deposited in the Wollega University Herbarium, then washed thoroughly with tap water, cut into small pieces, and dried under shade.

Extraction and Isolation

The powdered stem barks of *P. africana* (1 kg) were extracted with methanol (3x3 L) at room temperature for 48 h with occasional shaking. The crude extract was filtered from marc using Whatman filter paper. The solvent was evaporated under reduced pressure using rotary evaporator at 40 °C. A dark brown residue was obtained (40 g, 4%). Thirty-eight grams of the sample were subjected to liquid-liquid partition successively with n-hexane, dichloromethane, and ethyl acetate. The resulting phases were concentrated and afforded, respectively, 5 g, 8 g, and 12 g of residues. The TLC analysis of dichloromethane and ethyl acetate extracts showed six similar spots with the same R_f value of 0.72, 0.60, 0.59, 0.45, 0.33, 0.30 in n-hexane/ethyl acetate (7:3) solvent system. The two extracts were then combined together and subjected to column chromatography on silica gel for isolation of the compounds. About 18 g of extract were adsorbed on 26 g of silica gel and subjected to column chromatography, packed with silica gel (320 g). The mobile phase consisted of hexane with an increasing gradient of ethyl acetate, starting with 10:0 hexane:ethyl acetate, then 9:1, to 8:2 until 4:6, 200 mL each. The elution rate was 10 drops per minute to afford 50 major fractions. The resulting fractions of similar TLC profiles were combined together. Fractions 5-10 (2% EtOAc in n-hexane) were combined afforded 15 mg and purified by Sephadex LH-20 (eluting with CH₂Cl₂/MeOH; 1:1) to give β -sitosterol (**1**, 12 mg) while fractions 15-20 (3% EtOAc in hexane) showed similar TLC profiles

and were combined to give 30 mg and purified by Sephadex LH-20 (eluting with CH₂Cl₂/MeOH; 1:1) to give benzoic acid (**2**, 20 mg). Fractions 26-30 (5% EtOAc in hexane) showed similar spots combined together (afforded 35 mg) and purified by Sephadex LH-20 (eluting with CH₂Cl₂/MeOH; 1:1) to give a mixture of two oleanolic derivatives, **3** and **4** (30 mg). Fractions 35-40 (10% EtOAc in hexane) were similarly showed similar TLC profiles combined together (afforded 20 mg) and further purified by Sephadex LH-20 (eluting with CH₂Cl₂/MeOH; 1:1) to give *p*-hydroxy-benzoic acid (**5**, 15 mg).

Pathogenic Bacterial Strains

Five pathogenic bacterial strains were purchased from the Department of Biology of Wollega University and used for the evaluation of antibacterial activities. One gram-positive, *Staphylococcus aureus* (ATCC25923), and four gram-negative: *Escherichia coli* (ATCC25922); *Pseudomonas aeruginosa* (ATCC27853); *Salmonella typhimurium* (ATCC13311); *Shigella flexneri* (ATCC29903).

Antibacterial Activity Assay

The antibacterial activities of methanol extract and isolated compounds were tested against five bacterial strains using the disc diffusion method as described by Wayne (2012) with a slight modification (12). The test solutions were prepared with known weight of crude extract (1.5 mg) and isolated compounds were dissolved in 1 mL of DMSO. A 0.6 mm diameter, sterile Whatman test disk was placed on the surface of the inoculated Mueller Hinton Agar in a 90 mm petri dish and soaked with 0.0015 g/mL of the crude extract and the isolated compounds. The antibacterial activity was determined by measuring the zone of growth inhibition surrounding the disks. Gentamycin (10 μ g) and DMSO were used as positive and negative controls, respectively. The tested samples were allowed to diffuse for 30 minutes, and the plates were then kept in an incubator at 37 °C for 48 h (13). The experiments were carried out in triplicate and the mean of inhibition zones' diameters were calculated.

RESULTS AND DISCUSSION

The stem barks of *P. africana* were extracted with methanol then sequentially partitioned in n-hexane, dichloromethane and ethyl acetate. The dichloromethane and ethyl acetate extracts were combined and subjected to column chromatography for further purification and afforded five compounds **1-5** (Figure 1).

Compound **1** was isolated as white crystalline substance with a melting point of 134-135 °C. ¹H NMR spectrum (Table 1) showed an olefinic proton at δ_H 3.54 (1H, tdd, 11.2, 6.5, 4.6 Hz) corresponds H-6 and oxymethine proton at δ_H 3.54 (1H, tdd,

11.2, 6.5, 4.6 Hz) for H-3. It also showed proton signals at δ_H 0.69 (3H, s), 1.02 (3H, s), 0.94 (3H, d, 6.5 Hz), 0.84 (3H, d, 6.8 Hz), 0.81 (3H, d, 6.8 Hz), 0.85 (3H, t, 7.2 Hz) for six methyl groups and were assigned to H-18, H-19, H-21, H-26, H-27 and H-29, respectively.

The ^{13}C NMR (Table 1) spectrum showed signals for 29 carbon atoms including signals for six methyl carbons (δ_C 19.8, 19.4, 19.1, 18.8, 11.9 and 11.8),

eleven methylene carbons (δ_C 42.2, 39.8, 37.3, 33.9, 31.9, 31.6, 28.3, 26.1, 24.3, 23.1 and 21.1), nine methine carbons (δ_C 121.7, 71.8, 56.8, 56.1, 50.1, 45.8, 36.2, 31.9 and 29.2) and three quaternary carbon atoms (δ_C 140.7, 42.3 and 36.5). This was in agreement with existing literature spectra of typical β -sitosterol (14). Therefore, based on these spectral data and comparison with literature values, the compound was identified as β -sitosterol.

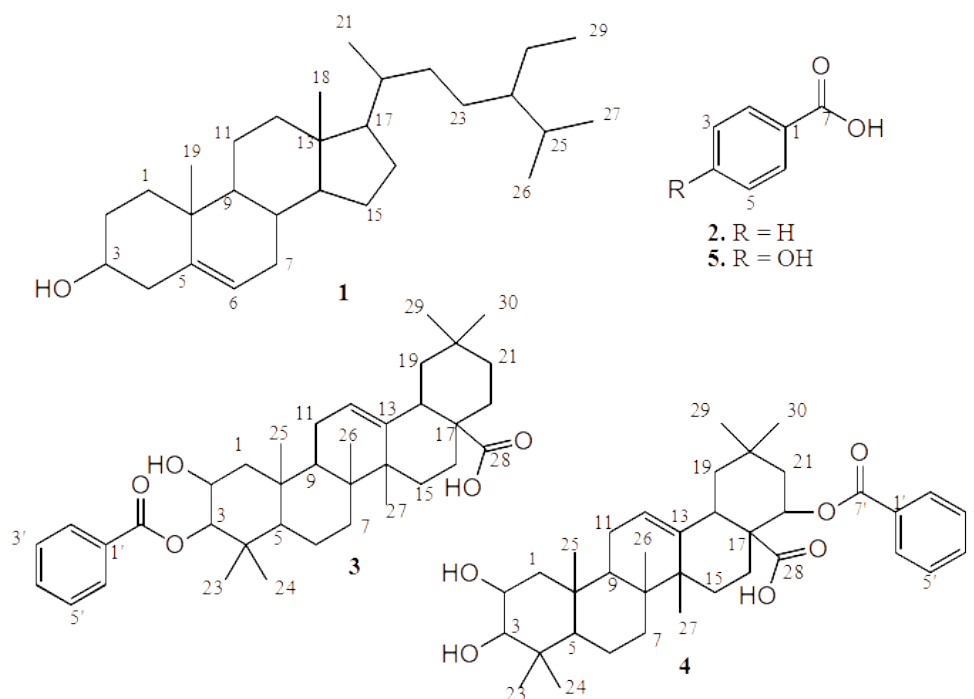


Figure 1: Structures of the isolated compounds from of *P. Africana* stem barks.

Compounds **2** and **5** were isolated as white crystalline solids. Their structures were readily identified as benzoic acid and p-hydroxy-benzoic acid, respectively, on the basis of their ^1H and ^{13}C -NMR spectra data (Table 2). Five mutually coupled aromatic protons including the ortho and meta identical protons in the ^1H NMR spectrum along with seven carbon signals corresponding to five aromatic methines and two quaternary carbon atoms (one for carboxylic acid) in the ^{13}C NMR were observed for compound **2** in agreement with (15). However, the presence of only four aromatic protons in the ^1H NMR spectrum and four methine carbons and three quaternary carbon atoms including one oxygenated aromatic carbon in the ^{13}C -NMR for compound **5** revealed the structure of compound **5** as p-hydroxy-benzoic acid. It is worth mentioning that this is the first report of benzoic acid and its derivative from the genus *Prunus*. The co-occurrence of benzoic acid in this plant is then possible that the coupling could have occurred between oleanolic acid and benzoic acid to form compounds **3** and **4** through esterification.

Compounds **3** and **4** were co-isolated as a mixture (deduced from the difference in carbon signal intensities, proton integration, carbon NMR spectral patterns, and 2D correlations) and obtained as a white amorphous solid. Their ^1H and ^{13}C NMR spectral data (Table 3) were virtually identical, with a few differences in the number of methine carbons and methylene carbons. Based on the carbon signal intensities and exhaustive analyses of 2D NMR correlations (^1H - ^1H)-COSY, (^1H - ^{13}C)-HMBC, (^1H - ^{13}C)-HSQC and NOES, the two compounds were characterized as follows:

The ^1H NMR spectrum (Table 3) of compound **3** consists of signals at δ_H 0.91, 0.96, 0.95, 0.98, 0.94, 1.04 and 1.15 integrated for three protons each indicating the presence of seven methyl groups. It also showed an olefinic proton signal at δ_H 5.30 (1H, t, 3.7 Hz) and two oxy-methine protons at δ_H 4.02(1H, m,) and 3.45 (1H, m) and were assigned to H-12, H-2 and H-3, respectively. These arguments were corroborated by the presence of two olefinic (δ_C 122.6 and 143.7) and two oxygenated methine carbons (δ_C 66.6 and 78.9) carbon signals in the ^{13}C -NMR spectrum (Table 3).

The ^{13}C NMR and DEPT spectra exhibited 30 carbon resonances in the aliphatic and olefinic regions with the resonance at δ_{C} 183.8 attributed to carboxylic acid carbon. These NMR data and further analyses of HSQC, COSY and HMBC were in a good agreement with oleanolic-12-ene type pentacyclic triterpenoid derivative (16, 17).

The ^1H NMR spectrum showed proton signals in the aromatic region at 8.11 (2H, d, 7.5 Hz, H-2' and H-6'), 7.62 (1H, t, 7.6 Hz, H-4') 7.49 (2H, t, 7.8 Hz, H-3' and H-5') which corresponded to protons for mono-substituted benzene moiety. The ^{13}C -NMR and DEPT spectra also displayed the presence of seven carbon signals, accountable to five aromatic methine carbons (δ_{C} 130.2, 128.5, 133.8, 128.5, 130.2), aromatic quaternary (δ_{C} 132.5) and carboxylic (δ_{C} 171.2) carbon atoms, supporting the presence of benzoic ester moiety. The position of the benzoic ester group was established at C-3 (δ_{C} 78.9) of the oleanolic acid on the basis of HMBC correlation, indicating long-range cross coupling between H-3 (δ_{H} 3.45) and the carbonyl carbon (δ_{C} 171.2) of the benzoic ester group. Thus, based on the above spectroscopic evidence and compared with literature reports (16, 17), compound **3** was identified as oleanolic acid-3-benzoate.

The ^1H and ^{13}C NMR spectral data (Table 3) of compound **4** were also similar to those of compound **3** with the presence of seven methyl groups (at δ_{H} 0.94 (3H, H-26), 0.87 (3H, H-24), 1.20 (3H, H-29), 0.76 (3H, H-25), 0.92 (3H, H-30), 1.08 (3H, H-23), 1.10 (3H, H-27)), the carboxylic acid (δ_{C} 183.5) and olefinic (δ_{H} 5.27, H-12) groups of the oleanolic acid moiety. The presence of benzoic ester moiety was also evident that signals at δ_{H} 7.72 (2H, dd, 5.7, 3.3 Hz, H-3' and H-5'), 7.62 (1H, t, 7.6 Hz, H-4'), 7.55 (2H, dd, 5.3, 3.3 Hz, H-2' and H-6') correspond to aromatic protons and signal at δ_{C} 167.8 for carbonyl carbon of the benzoic ester group as in compound **3**. The only notable difference is the chemical shift value for the methylene, 22- CH_2 (δ_{H} 1.85; δ_{C} 32.8), as would be in compound **3**, has been replaced by a set of signal corresponding to oxy-methine (δ_{H} 4.23; δ_{C} 68.2). In this case, the position of the benzoic ester group was established at C-22 following the long-range HMBC coupling of H-22 (δ_{H} 4.23) with

ester carbonyl carbon, C-7' (δ_{C} 167.8) (Figure 2). Therefore, based on the above spectroscopic evidence, compound **4** was identified as oleanolic acid-22-benzoate.

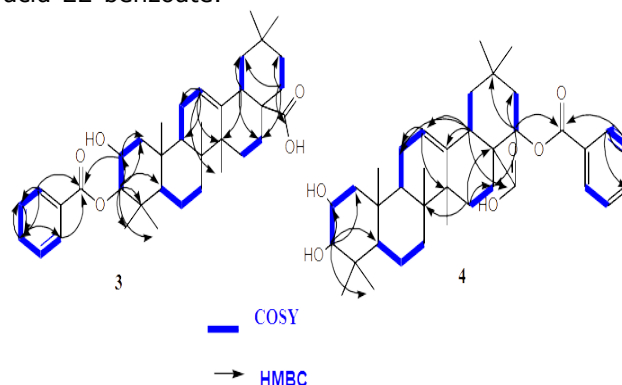


Figure 2: COSY and HMBC correlations of compound **3** and **4**.

The disk diffusion assay was employed to determine the antibacterial activities of the extract and isolated compounds against five bacterial species: *Staphylococcus aureus* (ATCC25923), *Escherichia coli* (ATCC25922), *Pseudomonas aeruginosa* (ATCC27853), *Salmonella typhimurium* (ATCC13311) and *Shigella flexneri* (ATCC29903). The antibacterial activity test (Table 4) showed varying degrees of inhibition of bacterial growth. The crude extract showed considerable activity on both Gram-positive and Gram-negative bacterial strains with inhibition zones ranging from 9.67 ± 0.47 to 21.03 ± 0.05 mm. The highest activity (21.03 ± 0.05 mm) was observed against *P. aeruginosa*, which is even greater than that of the reference drug (gentamycin, 14.06 ± 0.09 mm) against the same strain (18). Whereas the isolated compounds showed moderate activities against all test strains. This variation in bacterial growth inhibition, by the extract and the isolated compounds, could be related to the synergistic effect of various compounds or to minor compounds present in the crude extract that were not isolated. In general, the remarkable activities of *P. africana* crude extract support its traditional use and suggest that it could be used as a potential candidate in the development of novel antibacterial agents.

Table 1: ¹H NMR (600 MHz) and ¹³C NMR spectral data for compound **1** (in CDCl₃)

No.	Compound 1		β-sitosterol (14)		Appearance
	δ _c	δ _H (m, J in Hz)	δ _c	δ _H (m, J in Hz)	
1	37.3		37.3		CH ₂
2	31.9		31.7		CH ₂
3	71.8	3.54(1H, tdd, 11.2, 6.5,4.6 Hz)	71.8	3.53(1H, tdd, 4.5, 4.2, 3.8 Hz)	CH
4	42.2		42.3		CH ₂
5	140.7		140.7		C
6	121.7	5.35(1H dd,5.0 ,2.3 Hz)	121.7	5.36 (1H, t, 6.4 Hz)	CH
7	31.6		31.7		CH ₂
8	31.9		31.9		CH
9	50.1		50.2		CH
10	36.5		36.5		C
11	21.1		21.1		CH ₂
12	39.8		39.8		CH ₂
13	42.3		42.3		C
14	56.1		56.8		CH
15	24.3		24.6		CH ₂
16	28.3		28.3		CH ₂
17	56.8		56.1		CH
18	11.9	0.69(3H, s)	11.9	0.63(3H, s)	CH ₃
19	19.4	1.02(3H, s)	19.4	1.01(3H, s)	CH ₃
20	36.2		32.5		CH
21	18.8	0.94(3H,d, 6.5 Hz)	18.8	0.93 (3H, d, 6.5 Hz)	CH ₃
22	33.9		33.9		CH ₂
23	26.1		26.1		CH ₂
24	45.8		45.9		CH
25	29.2		28.9		CH
26	19.8	0.84(3H, d, 6.8 Hz)	19.8	0.83 (3H, d, 6.4 Hz)	CH ₃
27	19.1	0.81(3H, d, 6.8, Hz)	18.8	0.81 (3H, d, 6.4 Hz)	CH ₃
28	23.1		23.1		CH ₂
29	11.8	0.85(3H, t, 7.2 Hz Hz)	11.9	0.84 (3H, t, 7.2 Hz)	CH ₃

Table 2: ¹H and ¹³C NMR (600 MHz) spectral data for compound **2** (in CDCl₃) and **5** (DMSO).

No.	Compound 2			Compound 5		
	δ _c	δ _H (m, J in Hz)	Appearance	δ _c	δ _H (m, J in Hz)	Appearance
1	129.2	-	C	121.8	-	C
2 & 6	130.1	8.16(2H,d,7.2 Hz)	CH	131.9	7.79(2H,d, 8.7Hz)	CH
3 & 5	128.3	7.49(2H,t,7.8Hz)	CH	115.6	6.82(2H,d,8.7Hz)	CH
4	133.7	7.64(1H,t,7.4Hz)	CH	162.1	-	C
7	172.6	12.50(1H,br.s)		167.6	12.43(1H,br.s)	

Table 3: ¹H and ¹³C NMR (600 MHz) spectral data for compound **3** and **4** (in CDCl₃)

No.	Compound 3			Compound 4		
	δ_c	δ_H (m, J in Hz)	Appearance	δ_c	δ_H (m, J in Hz)	Appearance
1	41.7		CH ₂	40.9		CH ₂
2	66.6	4.02(1H,ddd,4.8, 9.6,11.4Hz)	CH	66.6	4.02(1H,ddd,4.8, 9.6,11.4Hz)	CH
3	78.9	3.45(1H,d,2.5Hz)	CH	78.8	3.45(1H,d,2.5 Hz)	CH
4	39.0		C	38.8		C
5	52.4	2.22(1H,dd,13.3,1.8Hz)	CH	48.1	1.23(1H,dd,13.3,1.8 Hz)	CH
6	18.0		CH ₂	17.9		CH ₂
7	32.4		CH ₂	32.7		CH ₂
8	39.5		C	39.7		C
9	47.3	1.62 (1H, d, 7.6 Hz)	CH	47.3	1.62 (1H, d, 7.6 Hz)	CH
10	38.4		C	38.3		C
11	23.4		CH ₂	23.3		CH ₂
12	122.6	5.30(1H,t,3.7Hz)	CH	125.6	5.27(1H,t,3.7 Hz)	CH
13	143.7		C	138.0		C
14	41.9		C	42.0		C
15	29.7		CH ₂	27.9		CH ₂
16	22.9		CH ₂	23.8		CH ₂
17	47.9		C	48.1		C
18	41.6	2.85 (1H, dd, 13.7,4.7 Hz)	CH	40.9	2.84 (1H, dd,13.7, 4.7 Hz)	CH
19	45.9		CH ₂	46.5		CH ₂
20	30.6		C	30.7		C
21	33.8		CH ₂	38.7		CH ₂
22	32.8		CH ₂	68.2	4.23(1H,dd,11.4,5.9 Hz)	CH
23	28.9	1.04(3H,s)	CH ₃	28.5	1.08(3H,s)	CH ₃
24	21.2	0.96(3H,s)	CH ₃	17.0	0.87(3H,s)	CH ₃
25	16.3	0.98(3H, s)	CH ₃	16.5	0.76(3H, s)	CH ₃
26	10.9	0.91(3H, s)	CH ₃	14.1	0.94(3H, s)	CH ₃
27	26.1	1.15(3H,s)	CH ₃	24.1	1.10(3H,s)	CH ₃
28	183.8		C=O	183.5		C=O
29	33.1	0.95(3H, s)	CH ₃	32.4	1.20(3H, s)	CH ₃
30	23.6	0.94(3H, s)	CH ₃	23.7	0.92(3H, s)	CH ₃
1'	132.5		C	132.5		C
2'	130.2	8.11(1H, d, 7.5Hz)	CH	130.9	7.55(1H,dd, 5.7,3.3Hz)	CH
3'	128.5	7.49(1H,t, 7.8Hz)	CH	128.8	7.73(1H, dd,5.7,3.3Hz)	CH
4'	133.8	7.62(1H,t, 7.6Hz)	CH	133.7	7.62(1H,t, 7.6Hz)	CH
5'	128.5	7.49(1H,t, 7.8Hz)	CH	128.8	7.75(1H, dd,5.7,3.4Hz)	CH
6'	130.2	8.11(1H, d, 7.5Hz)	CH	130,9	7.53(1H,dd, 5.7,3.3Hz)	CH
7'	171.2		C=O	167.8		C=O

Table 4: Antibacterial activities of crude extract and isolated compounds from *P.africana*.

Sample	Bacteria inhibition zone (mm)				
	<i>E.coli</i>	<i>S. aureus</i>	<i>S. flexineri</i>	<i>S.typhimurium</i>	<i>P. aeruginosa</i>
Extract	9.67±0.47	11.10±0.08	14.23±0.21	10.03±0.05	21.03±0.05
1	7.13±0.12	8.25±0.20	7.08±0.06	8.13±0.10	7.66±0.24
2	7.50±0.08	8.08±0.12	13.00±0.08	12.58±0.31	10.08±0.12
Mixture (3&4)	8.07±0.05	7.66±0.24	8.04±0.06	13.41±0.12	7.05±0.07
5	9.02±0.02	8.48±0.02	11.07±0.05	14.41±0.12	9.33±0.47
Gentamycin	22.13±0.05	19.05±0.04	20.03±0.05	20.10±0.03	14.06±0.09
DMSO	-	-	-	-	-

CONCLUSIONS

Phytochemical investigation of methanol extract of stem barks of *P.africana* led to the isolation of five compounds; β -sitosterol (**1**), benzoic acid (**2**), two oleanolic derivatives (**3** and **4**) and p-hydroxybenzoic acid (**5**). Compound **2** and **5** are reported for the first time in the genus *Prunus*. The crude extract showed strong activity against *P. aeruginosa*, whereas the isolated compounds showed moderate activity against the tested strains. The antibacterial activity displayed by the extract support the traditional use of this plant against various ailments caused by bacteria. Further comprehensive evaluations, including *in vivo* activity and cytotoxicity tests could be done for conclusive decision on the potential candidacy of *P. africana* for formulation and medicinal uses.

CONFLICT OF INTERESTS

The authors declare that they have no conflicts of interest.

Availability of Data and Material

NMR data of compounds are available and attached as supporting information.

ACKNOWLEDGEMENTS

Mr. Desalegn.A is thankful to Wollega University, Ethiopia for material and financial support for his PhD study. This work was supported by the International Foundation for Sciences, Stockholm, Sweden, through a grant to Negera Abdissa (IFS, Grant No: F/5778-2).

REFERENCES

1. Stewart KM. The African cherry (*Prunus africana*): Can lessons be learned from an over-exploited medicinal tree?. *Journal of ethnopharmacology*. 2003; 89(1):3-13. <DOI>.
2. Bodeker G, van 't Klooster C, Weisbord E. *Prunus africana* (Hook. f.) Kalkman: the overexploitation of a medicinal plant species and its legal context. *The Journal of Alternative and Complementary Medicine*. 2014; 20(11):810-22. <DOI>.
3. Jimu L. Threats and conservation strategies for the African cherry (*Prunus africana*) in its natural range-A review. *Journal of Ecology and the Natural Environment*. 2011; 3(4):118-30. <DOI>.
4. Komakech R, Kang Y, Lee JH, Omuja F. A review of the potential of phytochemicals from *Prunus africana* (Hook f.) Kalkman stem bark for chemoprevention and chemotherapy of prostate cancer. *Evidence-Based Complementary and Alternative Medicine*. 2017; 13. <DOI>.
5. Betti JL, Belinga SJ, Samba D. Stock of *Prunus africana* stems on the mount Cameroon forest. *African Journal of Plant Science*. 2011; 5(13):781-9. <DOI>.
6. Bii C, Korir KR, Rugutt J, Mutai C. The potential use of *Prunus africana* for the control, treatment and management of common fungal and bacterial infections. *Journal of medicinal plants research*. 2010;4(11):995-8. <DOI>.
7. Pascaline J, Charles M, George O, Lukhoba C. An inventory of medicinal plants that the people of Nandi use to treat malaria. *Journal of Animal and Plant Science*. 2011; 9:1192-200. <URL>.
8. Otieno NE, Analo C. Local indigenous knowledge about some medicinal plants in and around Kakamega forest in western Kenya. *F1000Research*. 2012;1. <DOI>.
9. Mwitari PG, Ayeka PA, Ondicho J, Matu EN, Bii CC. Antimicrobial activity and probable mechanisms of action of medicinal plants of Kenya: *Withania somnifera*, *Warbugia ugandensis*, *Prunus africana* and *Plectranthus barbatus*. *PloS one*. 2013;8(6):e65619. <DOI>.
10. Mesfin F, Demissew S, Teklehaymanot T. An ethnobotanical study of medicinal plants in Wonago Woreda, SNNPR, Ethiopia. *Journal of Ethnobiology and Ethnomedicine*. 2009; 5(1):1-8. <DOI>.
11. Kadu CA, Parich A, Schueler S, Konrad H, Muluvi GM, Eyog-Matig O, Muchugi A, Williams VL, Ramamonjisoa L, Kapinga C, Foahom B. Bioactive constituents in *Prunus africana*: geographical

variation throughout Africa and associations with environmental and genetic parameters. *Phytochemistry*. 2012 Nov 1;83:70-8. <DOI>.

12. Wayne P. A. Performance Standards for Antimicrobial Disc Susceptibility Test, Approved Standard: M02-A11, National Committee for Clinical Laboratory Standards (NCCLS), New York, USA, 11th edition. 2012;32(1), 1-76. <URL>.

13. Nascimento G., Locatelli J., Freitas P., Silva G. Antibacterial activities of plant extracts and phytochemicals on antibiotic resistant. *Bacteria*. *Braz. J. Microbiol.* 2000;31, 247-256. <DOI>.

14. Chaturvedula VS, Prakash I. Isolation of Stigmasterol and Sitosterol from the dichloromethane extract of *Rubus suavissimus*. *International current pharmaceutical journal*. 2012;1(9):239-42. <DOI>.

15. Tadesse G, Reneela P, Dekebo A. Isolation and characterization of natural products from *Helinus mystachnus* (Rhamnaceae). *J. Chem. Pharm. Res.* 2012;4(3):1756. <URL>.

16. Ngo QM, Cao TQ, Woo MH, Min BS, Weon KY. Cytotoxic Triterpenoids from the Fruits of *Ligustrum japonicum*. *Natural Product Sciences*. 2018; 24(2):93-8. <DOI>.

17. Gwandu UZ, Dangoggo SM, Faruk UZ, Halilu EM, Yusuf AJ, Mailafiya MM. Isolation and Characterization of Oleanolic Acid Benzoate from the Ethylacetate Leaves Extracts of *Vernonia ambigua* (Kotschy Ex. Peyr). *Journal of Chemical Society of Nigeria*. 2020 Aug 30;45(5). <DOI>.

18. Dey N, Chatterjee D, Choudhury MK, Das S. Antibacterial activity of *Prunus africana* stem bark extract against *Shigella* spp. *World J Pharm Pharm Sci.* 2017 Jun 25;6(9):1155-60. <URL>.

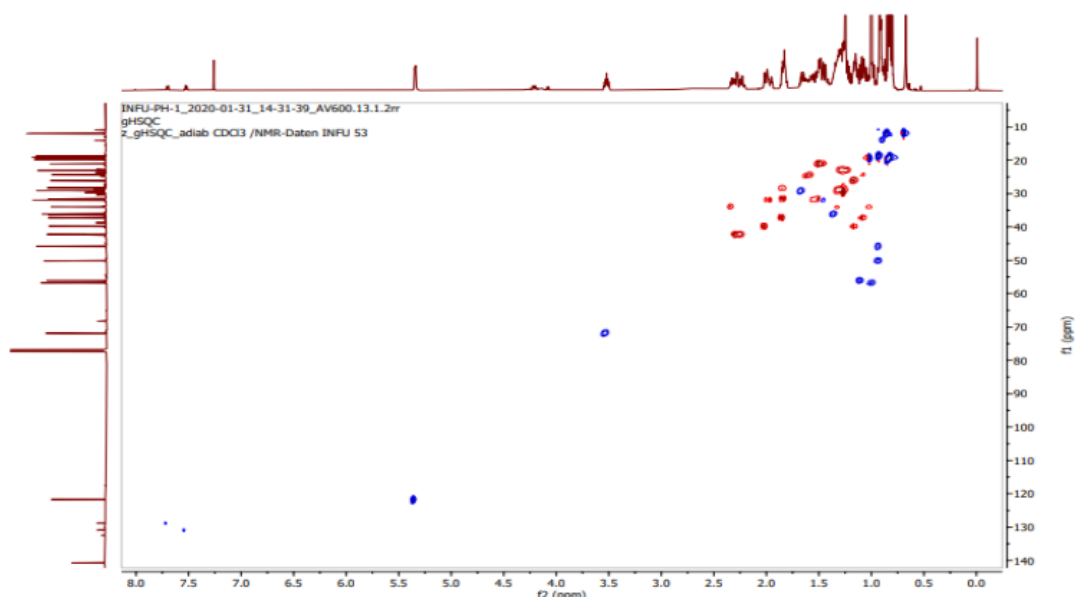


Figure S3: The HSQC spectrum of PH-1(1) observed at 500 MHz for CDCl₃ solution at 25 °C.

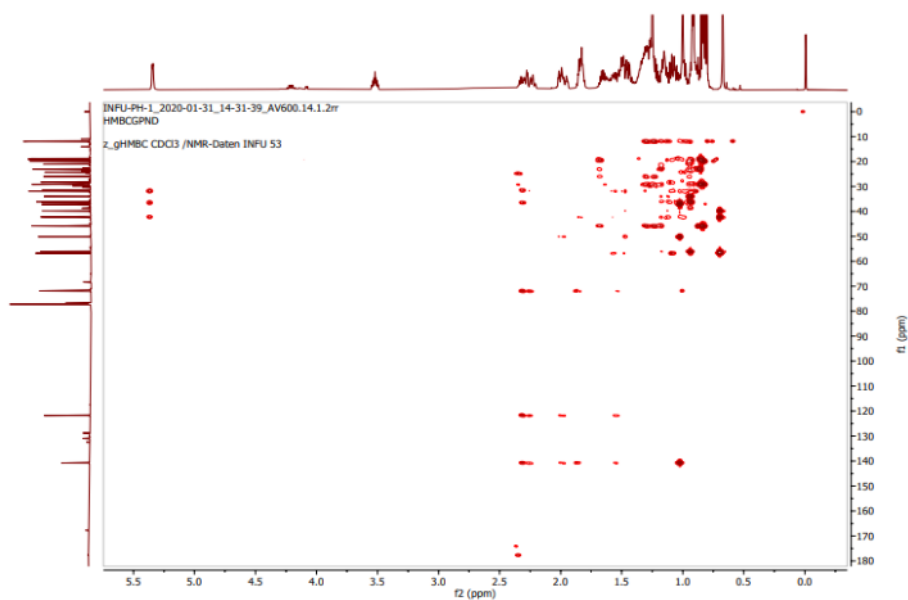


Figure S4: The HMBC spectrum of PH-1(1) observed at 500 MHz for CDCl₃ solution at 25 °C.

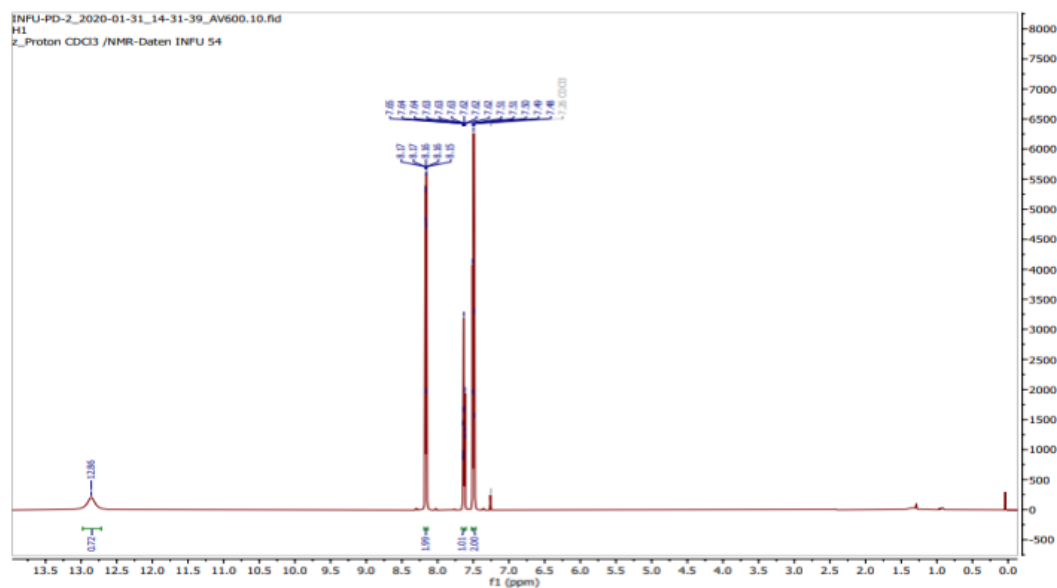
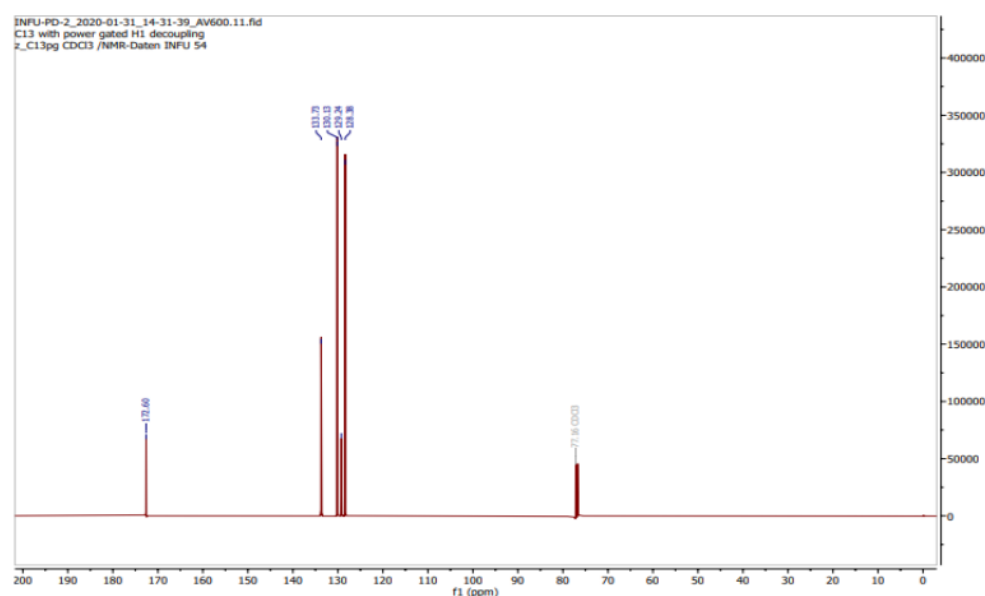


Figure S5: The ^1H NMR spectrum of PD-2(2) observed at 500 MHz in CDCl_3 at 25 °C. Assignments are given in Table 2.



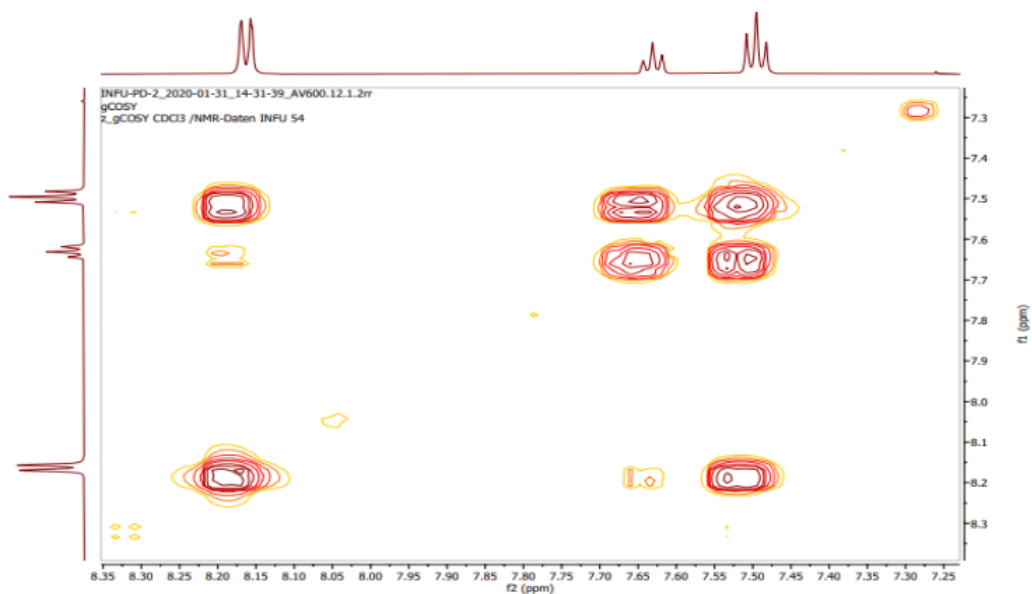


Figure S7: The COSY spectrum of PD-2(2) observed at 500 MHz for CDCl₃ solution at 25 °C.

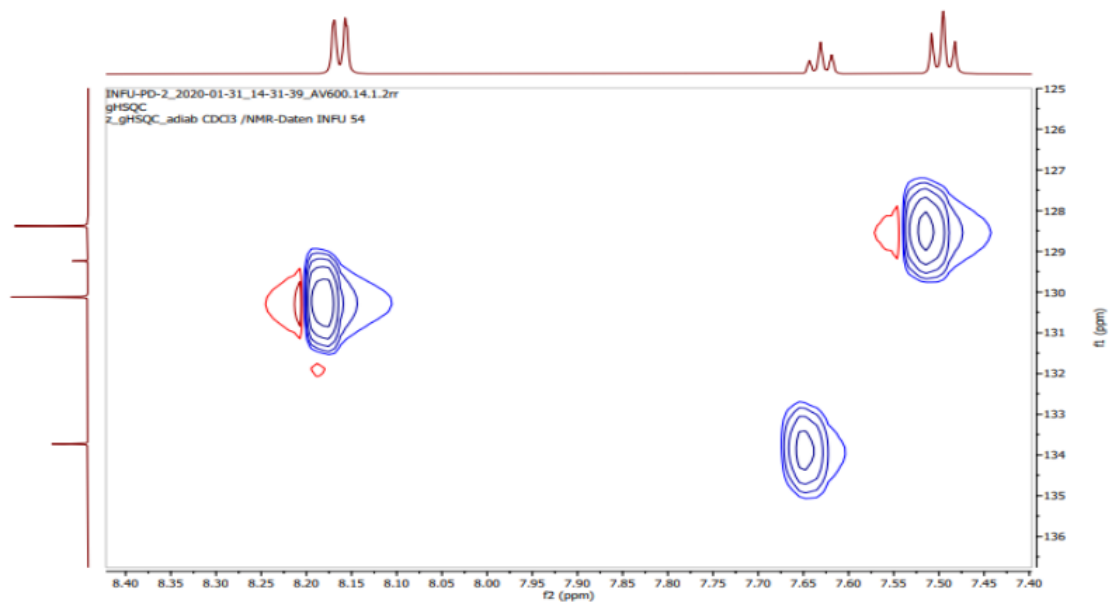


Figure S8: The HSQC spectrum of PD-2(2) observed at 500 MHz for CDCl₃ solution at 25 °C.

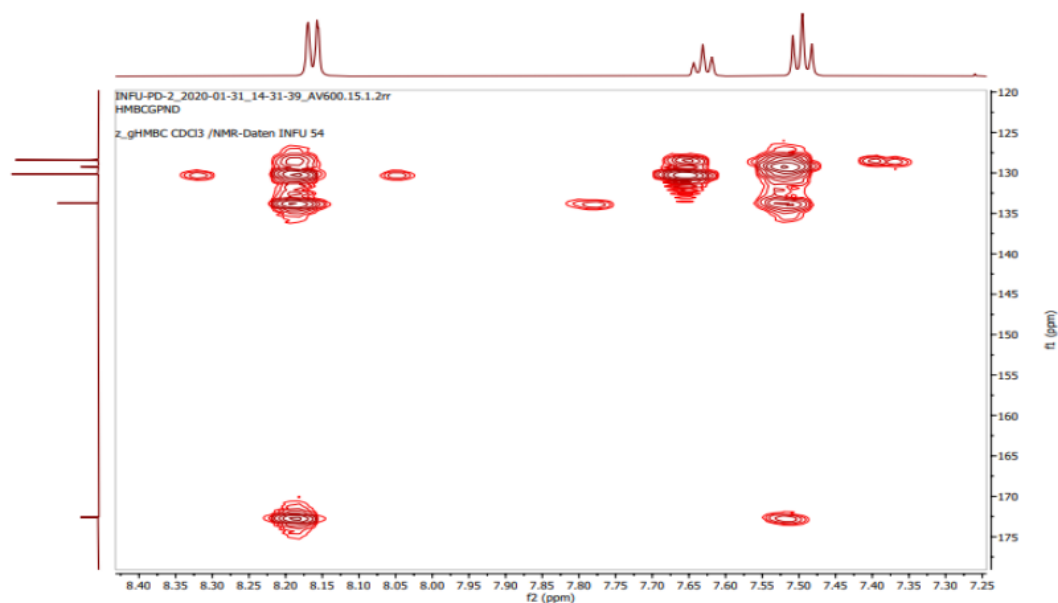


Figure S9: The HMBC spectrum of PD-2(2) observed at 500 MHz for CDCl_3 solution at 25 °C.

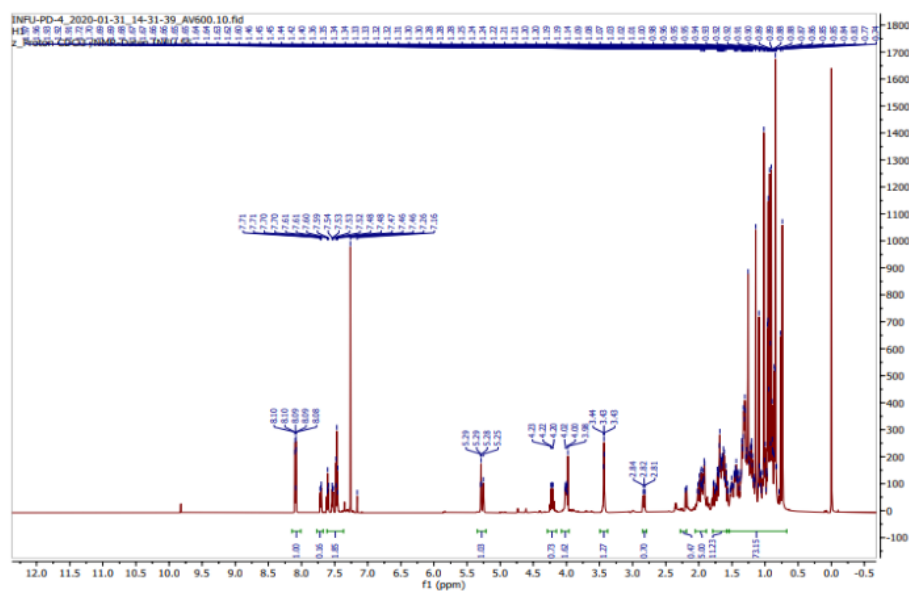


Figure S10: The ^1H NMR spectrum of PD-4(3 and 4) observed at 500 MHz in CDCl_3 at 25 °C. Assignments are given in Table 3.

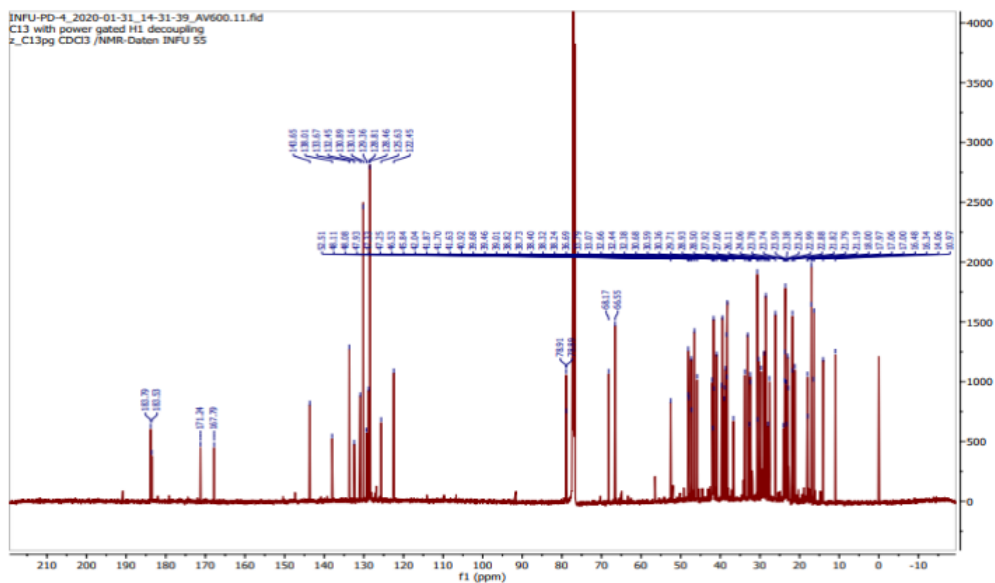


Figure S11: The ^{13}C NMR spectrum of PD-4(3 and 4) observed at 125 MHz in CDCl_3 at 25 °C. Assignments are given in Table 3.

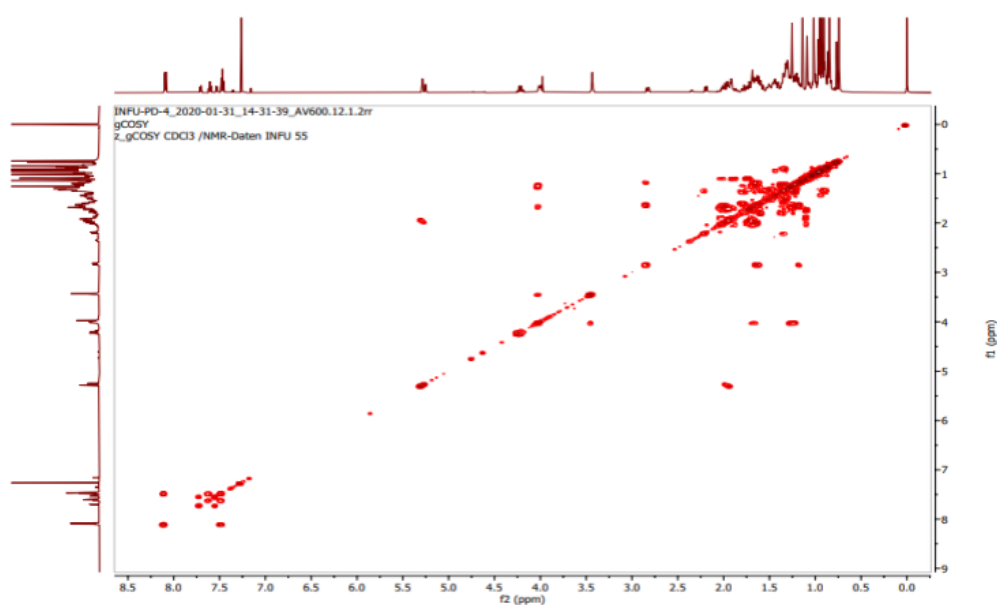


Figure S12: The COSY spectrum of PD-4(3 and 4) observed at 500 MHz for CDCl_3 solution at 25 °C.

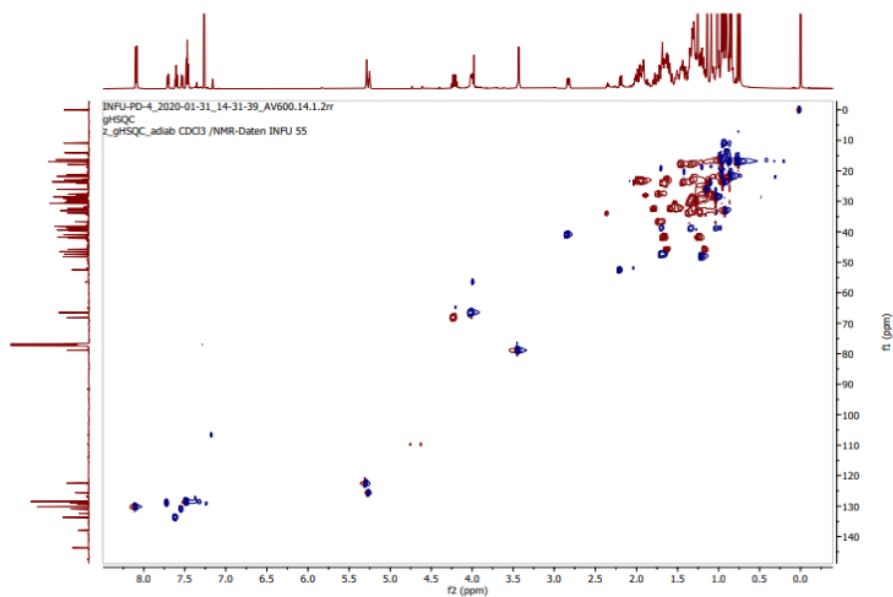


Figure S13: The HSQC spectrum of PD-4(3 and 4) observed at 500 MHz for CDCl₃ solution at 25 °C.

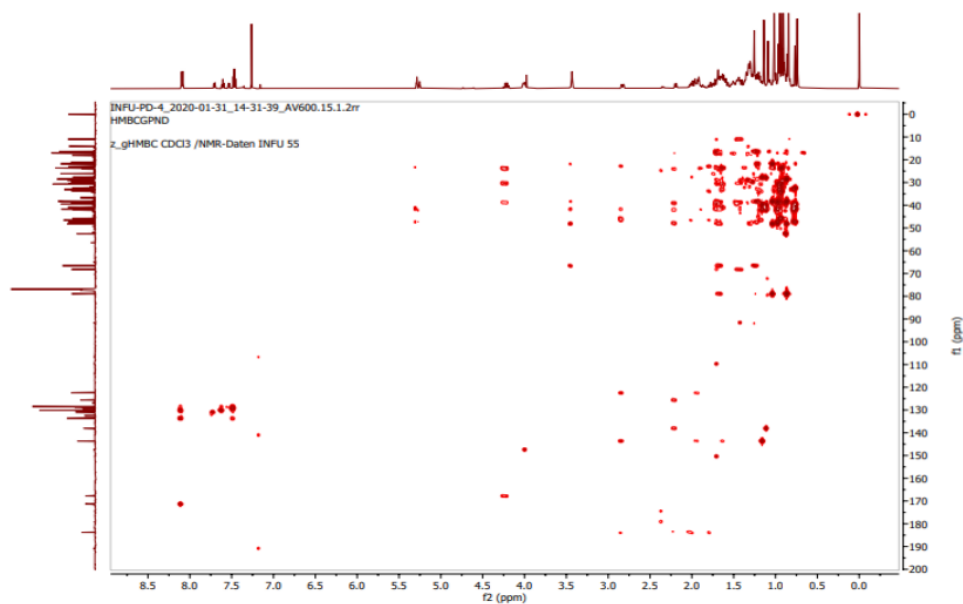


Figure S14: The HMBC spectrum of PD-4(3 and 4) observed at 500 MHz for CDCl₃ solution at 25 °C.

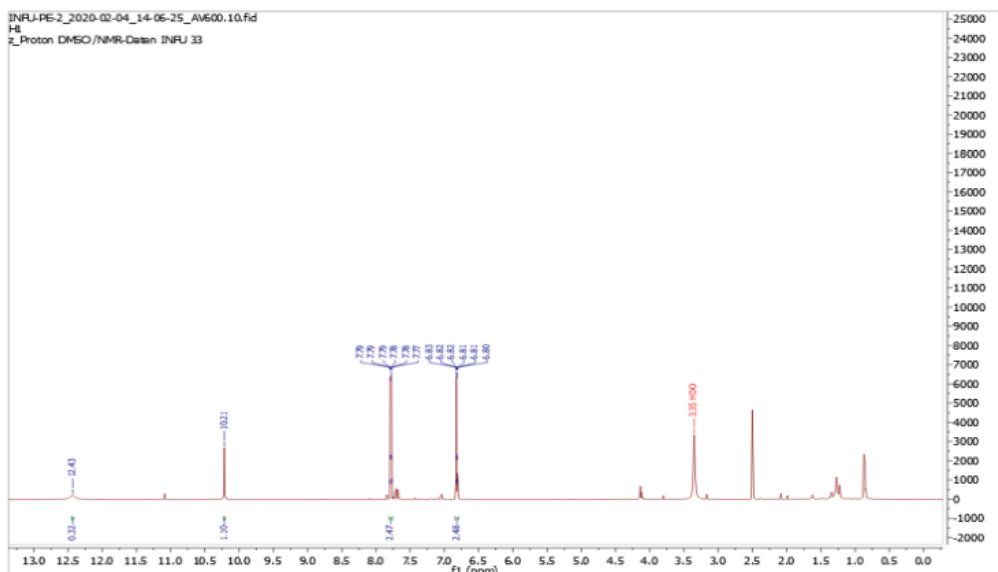


Figure S15: The ¹H NMR spectrum of PE-2(5) observed at 500 MHz in DMSO at 25 °C. Assignments are given in Table 2.

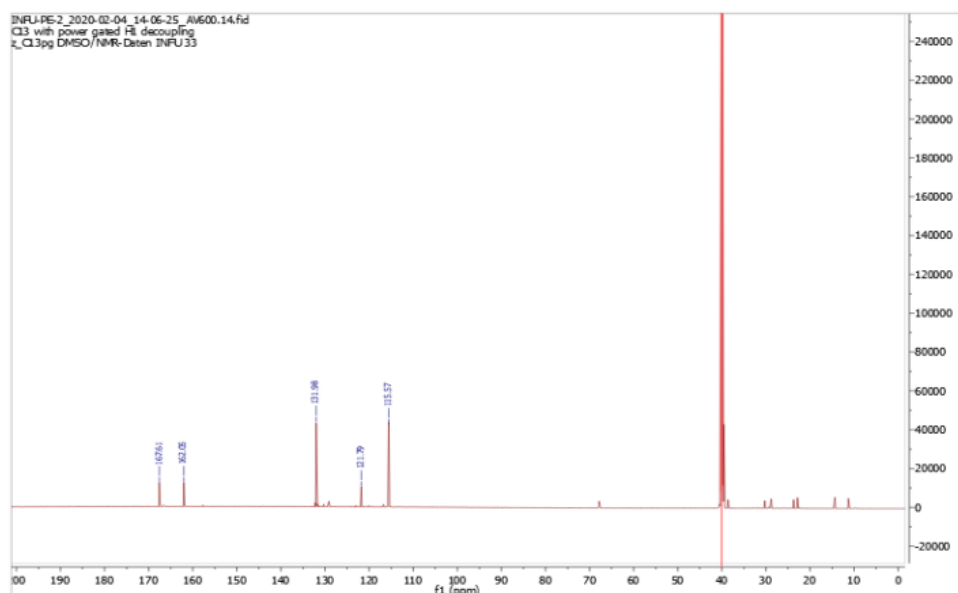


Figure S16: The ¹³C NMR spectrum of PE-2(5) observed at 125 MHz in DMSO at 25 °C. Assignments are given in Table 2.

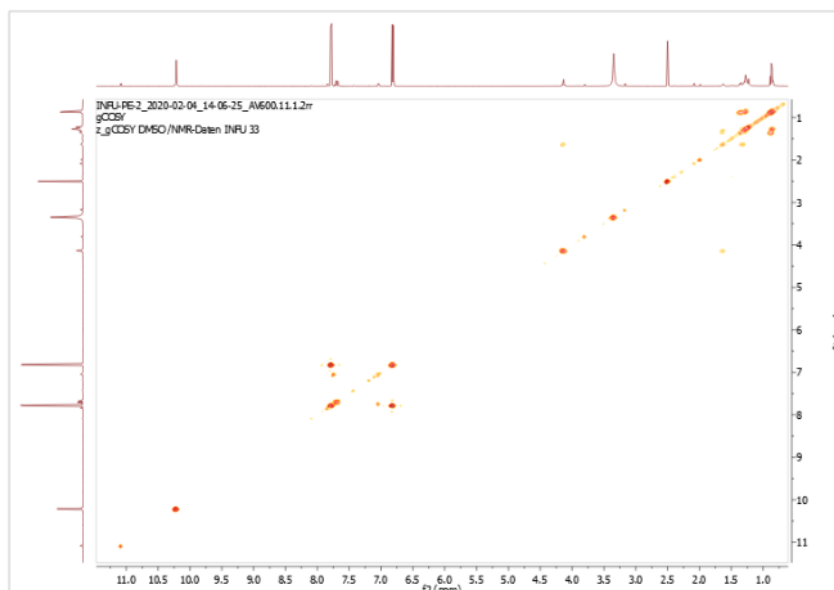


Figure S17: The COSY spectrum of PE-2(5) observed at 500MHz for DMSO solution at 25 °C

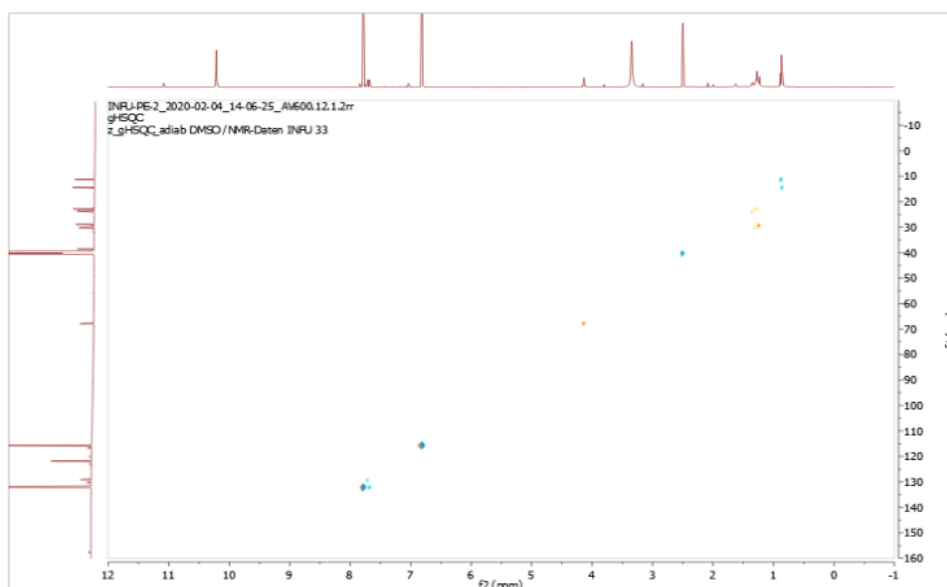


Figure S18: The HSQC spectrum of PE-2(5) observed at 500 MHz for DMSO solution at 25 °C.

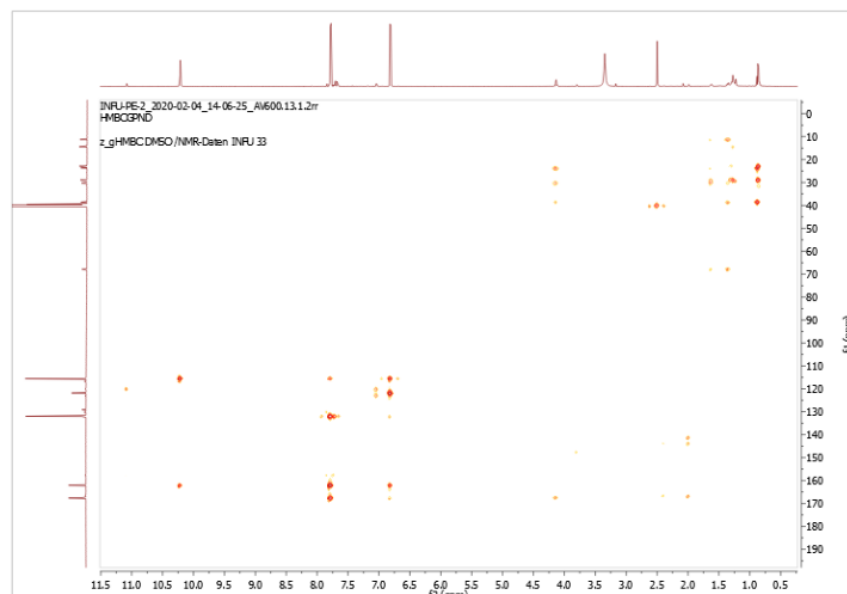


Figure S19: The HMBC spectrum of PE-2(5) observed at 500 MHz for DMSO solution at 25 °C

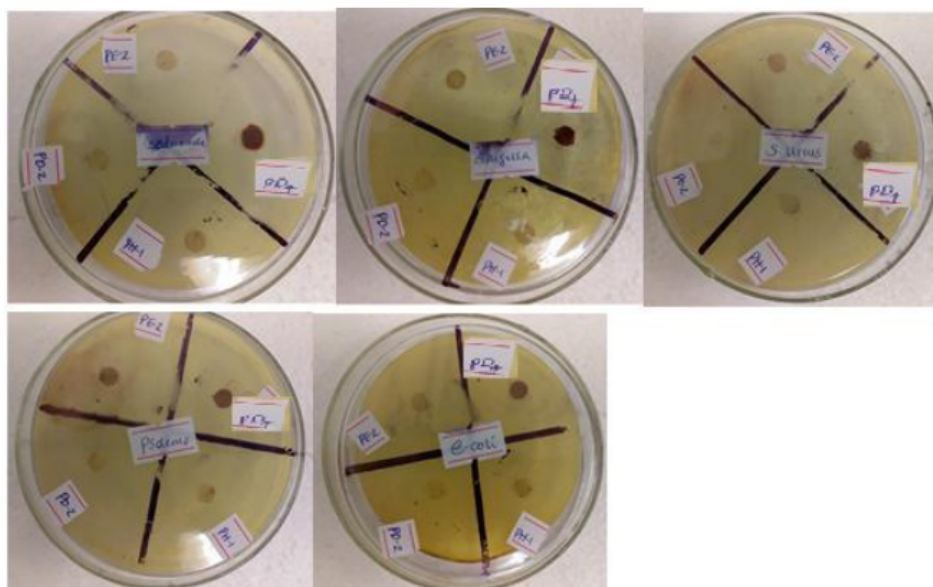


Figure S20: Antibacterial analysis of Crude Extracts, isolated compounds and gentamycin at 10 µg/mL concentration. Key 1: -: PH-1(1) PD-2(2), PD-4(3 and 4), PE-2(5)

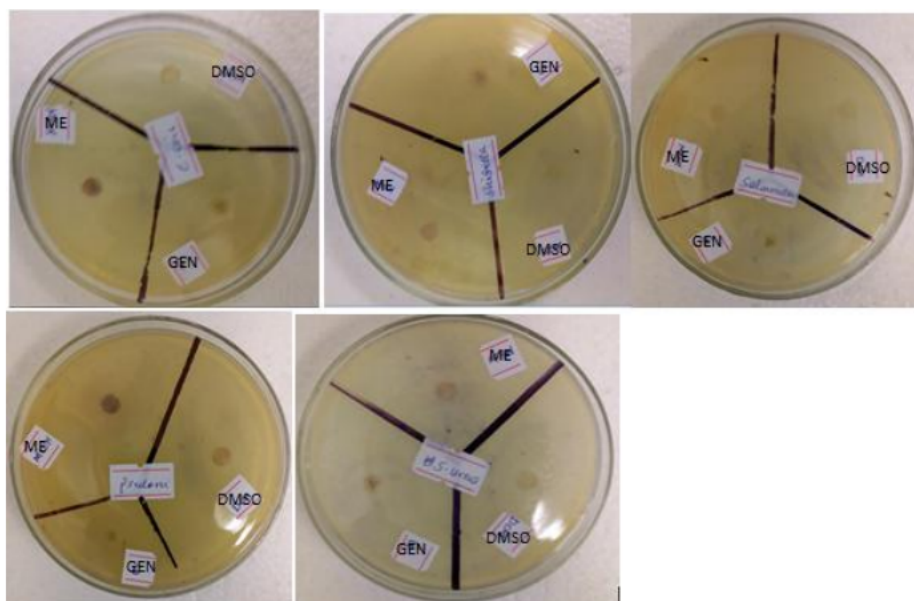


Figure S21: Antibacterial analysis of Crude Extracts, isolated compounds and gentamycin at 10 µg/mL concentration. Key 2: -: GEN-Gentamycin, DMSO-Dimethylsulfoxide, ME-Methanol extract.



Algerian *Bunium incrassatum* Seeds: Effects of Extraction Solvent Polarity on Phenolic Profile and Antioxidant Activity

Fethi Toul^{1*} , Amina Djendar² , Meryem Seladji³ , Farid Berroukeche^{4,5} 

¹Laboratory of Valorization of Plant Resources and Food Security in Semi-Arid Areas, Mohammed Tahri University, Department of Biology, Bechar, Algeria.

²Abu Bakr Belkaïd University, Department of Biology, Tlemcen, Algeria.

³Ahmed Ben Bella University-Oran 1, Department of biology, Oran, Algeria.

⁴Laboratory of Physiology, Pathophysiology and Biochemistry of Nutrition, Abu Bakr Belkaïd University, Department of Biology, Tlemcen, Algeria.

⁵Mohammed Tahri University, Faculty of Medicine, Bechar, Algeria.

Abstract: *Bunium incrassatum*, commonly called 'Talghouda', is one of the most important plant species in the traditional Algerian pharmacopoeia, used for medicinal and culinary purposes. Despite its benefits, it still remains a scientifically neglected species, particularly in terms of its phenolic profile. The current study sought to evaluate the influence of the variation in solvents' polarities on the phenolic profile of *B.incrassatum* seeds by conventional spectrophotometric techniques and also by high-performance liquid chromatography, as well as their effects on the antioxidant activity of extracts using DPPH and β -carotene bleaching assays. Methanol extract showed the highest DPPH scavenging ability and also the highest inhibitory potential against the bleaching of β -carotene ($IC_{50}=0.15\pm 0.02$ and 0.41 ± 0.03 mg/mL, respectively). Thirteen phenolic compounds were identified, a flavanol (catechin), two flavonols (kaempferol, quercetin), two flavanones (hesperetin, naringenin) and eight phenolic acids: caffeic acid, chlorogenic acid, ellagic acid, ferulic acid, gallic acid, p-coumaric acid, sinapic acid, and syringic acid. These results support the few previous studies showing that *Bunium incrassatum*, as an endemic species, is a valuable source of bioactive compounds that requires further investigations.

Keywords: *Bunium incrassatum*, seeds, phenolic compounds, antioxidant potential, RP-HPLC.

Submitted: January 15, 2022. **Accepted:** March 03, 2022 .

Cite this: Toul F, Djendar A, Seladji M, Berroukeche F. Algerian *Bunium incrassatum* Seeds: Effects of Extraction Solvent Polarity on Phenolic Profile and Antioxidant Activity. JOTCSA. 2022;9(2):415-22.

DOI: <https://doi.org/10.18596/jotcsa.1058060>.

*Corresponding author. E-mail: toul.fethi@univ-bechar.dz

INTRODUCTION

The food industry, like many other industries, relies on synthetic additives, which are now one of the most widespread means of food preservation due to their availability and price (1). Recently, there has been an increasing interest in plants' natural products from the public and food manufacturers, especially phenolic compounds, for their physiological properties affecting human health, including antioxidant activity (2).

Algerian flora appears to be extremely rich in medicinal and aromatic plants, providing an intriguing field for supplementary ethno-medicinal and phytochemical research (3). *Bunium incrassatum* (Boiss.) Batt. & Trab., vernacularly called 'Talghouda', is an endemic species of northern Algeria belonging to the Apiaceae family (4), frequently mentioned in the Algerian traditional pharmacopoeia. The tubers are used for the treatment of thyroid problems, either taken alone or in mixtures of two or more ingredients, such as honey, olive oil, and goat milk (5). Sharif

Al-Idrissi (1100-1175 AD) mentioned that Berbers took 10 g of its powdered tubers in a mixture with the water of cooked *Tribulus terrestris* on an empty stomach to disintegrate kidney stones and also as anthelmintic (6). In addition, dried and powdered tubers are regarded as astringent, anti-diarrheic, anti-hemorrhoidal, for bronchitis, and cough treatment (7). In the collective memory of Algerian society, it is considered as the symbol of misery, which recalls the famine of the years of poverty, especially during the Second World War and the period of national revolution between 1954-1962, when it was consumed as bread after being powdered and mixed with wheat flour (8). Despite the importance of *B. incrassatum* in folk medicine and its historical position within Algerian society, only a few studies have been conducted, only on tubers, to investigate its biological activities: the effect of tubers' extracts on biochemical, hematological, ovarian, and uterine parameters (3, 9); antimicrobial activity (7); antioxidant activity (10, 11); chemical composition of extracts (7, 11) and essential oil (10, 12). The current study attempted to evaluate, for the first time to our knowledge, the effects of solvents' polarities on the chemical composition, especially the phenolic profile, of extracts derived from the seeds of *Bunium incrassatum*, as well as their impacts on the antioxidant activity.

EXPERIMENTAL SECTION

Plant material

The seeds of *Bunium incrassatum* were collected in June 2016, in Djebala, Tlemcen, Algeria. Species identification was carried out at the laboratory of botany, Department of Biology, Faculty of Nature and Life Sciences, Earth and Universe Sciences, Abu Bakr Belkaid University of Tlemcen, Algeria.

Preparation of extracts

Twenty grams of shade air-dried seeds, freshly ground, were sequentially extracted under reflux for 1 h with increasing polarity solvents (Petroleum ether, Chloroform, Ethyl acetate, Methanol, and Water). The extracts were then concentrated to dryness.

Total Phenolic Content

The amounts of total phenolic compounds in methanolic extracts were determined by Folin-Ciocalteu reagent assay (13). Gallic acid was used as standard for the calibration curve. The total phenolic content (TPC) was expressed as milligrams of gallic acid equivalents per gram of extract (mg GAE/g E).

Total Flavonoid Content

As described by Zhishen et al. (1999)(14), the total flavonoid contents (TFC) of extracts were

expressed as milligrams of catechin equivalents per gram of extract (mg CE/g E).

Condensed Tannin Content

Using vanillin assay method (15), the concentrations of tannins were expressed as milligrams of tannic acid equivalents per gram of extract (mg CE/g E) from a calibration curve.

DPPH radical scavenging assay

Fifty microliters of various concentrations of extracts were mixed with 1950 μ L of a 0.025 g/L methanolic DPPH solution. The mixture was shaken vigorously and allowed to stand at room temperature in the dark for 30 min. The absorbance was measured at 515 nm (16). The radical scavenging activity (RSA) was calculated as a percentage of DPPH discoloration using the following equation:

Where A_{blank} is the absorbance negative control and A_{sample} is the absorbance of the tested compound. The concentration providing 50% of inhibition (IC50) was calculated from the graph plotted of inhibition percentages against extract concentrations. BHA was used as the reference compound.

β -carotene bleaching assay

The antioxidant activity of extracts was evaluated using β -carotene-linoleate model system, as described by Moure et al. (2000) (17). β -carotene (0.2 mg) was dissolved in 1 mL of chloroform then mixed with 20 μ L of purified linoleic acid and 200 mg of Tween 40 emulsifier. Chloroform was then evaporated under vacuum evaporator and the resulting mixture was immediately diluted in 100 mL of distilled water. 4 mL of this reaction mixture were mixed with 0.2 mL of various extracts concentrations or positive control (BHA). After being homogenized, the absorbance at 470 nm was immediately recorded at $t=0$ min, against a blank consisting of the emulsion without β -carotene. The capped tubes were placed in a water bath at 50 °C for 120 min. A negative control consisted of 0.2 ml distilled water or solvent instead of extract. The antioxidant activity (AA) was calculated to the following equation:

Where $A_{A(120)}$ is the absorbance of the antioxidant at 120 min; $A_{C(120)}$ is the absorbance of the negative control at 120 min; $A_{C(0)}$ is the absorbance of the negative control at 0 min.

Hydrolysis for HPLC

For HPLC analysis, the selected extracts were hydrolyzed under reflux in a 1.2 M HCl water bath for 1 h. Hydrolyzed samples were then filtered through a 0.45 μ m syringe-driven filter before injection (18).

Chromatographic identification of phenolic compounds by RP-HPLC

A 20 μ L of an aliquot of sample solution was separated using high performance liquid chromatography system (YL 9100 HPLC system, Korea). Reversed-phase chromatography was performed on a C18 column (250 \times 4.6mm; 5 μ m). Data were monitored and analyzed using Clarity data-processing system. The mobile phase consisted of solvent A (water/formic acid 0.4%) and solvent B (acetonitrile). Solvents' gradient was used as followed: 0–2 min, 1% B; 2–15 min, 7% B; 15–25 min, 20% B; 25–35 min, 40% B; 35–46 min, 100% B; 46–47 min, 100% B; 47–48 min, 1% B; 48–55 min, 1% B. The flow rate was 1.2 ml/min. UV-detection was performed at 280 nm. Phenolic compounds were identified according to their retention times as well as to their spectral matching with 18 reference standards.

Statistical analysis

Except yields, all data were expressed as mean \pm standard derivation (SD) of three replicates and were statistically analyzed using one-way ANOVA followed by Tukey test ($p < 0.05$) on a SigmaPlot 12.2 software.

RESULTS

Total phenolic, flavonoid, and tannin contents

The highest content of TPC, as shown in Table 1, was recorded in methanol extract (185.04 \pm 4.00 mg GAE/g E) followed by petroleum ether and aqueous extracts (141.65 \pm 1.92 and 101.20 \pm 3.64 mg GAE/g E, respectively). Ethyl acetate extract showed the highest amount of TFC (89.26 \pm 3.13 mg CE/g E) followed by methanol and chloroform extracts (72.07 \pm 3.80 and 56.65 \pm 1.72 mg CE/g E). Methanol extract and among all extracts exhibited the highest content in CTC (33.42 \pm 3.56 mg TAE/g E).

Antioxidant activity

The antioxidant potential of extracts was assessed following two different assays in two different media. In the DPPH assay, all extracts exhibited significant radical scavenging abilities in comparison to the reference compound (BHA, 0.09 \pm 0.00 mg/mL), where methanol extract showed, as the most potent, an IC₅₀ equal to 0.15 \pm 0.02 mg/mL, followed by petroleum ether extract with 0.21 \pm 0.03 mg/mL. The remaining extracts were between aqueous and chloroform extracts (0.29 \pm 0.02 and 0.48 \pm 0.03 mg/mL, respectively).

The methanolic extract also exhibited the highest inhibitory effect against the bleaching of β -carotene (0.41 \pm 0.03 mg/mL) which was 80% more potent than ethyl acetate extract as the weakest one (1.60 \pm 0.09 mg/mL). Even stronger, methanol extract remains 70% less potent as compared to the reference compound (BHA, 0.24 \pm 0.00 mg/mL).

Chromatographic identification of phenolic compounds by RP-HPLC

Based on three parameters (extraction yields, phenolic content, and antioxidant potential), two extracts have been selected for the qualitative profiling of phenolic compounds by RP-HPLC (methanol and petroleum ether extracts). These two extracts have been hydrolyzed in an acidic medium before being injected to free the bound phenolic compounds. The obtained chromatograms, represented in Figures 1-2, compared to those of 18 reference standards, showed several main peaks with intense absorption at the selected wavelength (280 nm). Analyzing these chromatograms, thirteen phenolic compounds were identified: six in methanol extract (five phenolic acids and a flavanone) and seven in petroleum ether (three phenolic acids, two flavonols, a flavanol and a flavanone).

Table 1: Phenolic contents and antioxidant activities of *Bunium incrassatum* seeds' extracts.

Extracts	Yields (%)	TPC ^B (mg GAE/g E)	TFC ^B (mg CE/g E)	CTC ^B (mg TAE/g E)	IC50 ^{B,C} DPPH (mg/mL)	IC50 ^{B,C} β -Carotene (mg/mL)
Aqueous extract	3.0	101.20±3.64 ^a	46.61±0.91 ^a	30.24±1.83 ^a	0.29±0.02 ^a	0.87±0.01 ^a
Methanol extract	7.1	185.04±4.00 ^b	72.07±3.80 ^b	33.42±3.56 ^b	0.15±0.02 ^b	0.41±0.03 ^b
Chloroform extract	2.9	71.25±2.01 ^c	56.65±1.72 ^b	16.34±0.66 ^c	0.48±0.03 ^c	1.13±0.22 ^c
Ethyl acetate extract	2.2	95.51±4.34 ^d	89.26±3.13 ^c	5.28±0.09 ^d	0.34±0.01 ^d	1.60±0.09 ^d
Petroleum ether extract	8.5	141.65±1.92 ^e	55.33±2.28 ^d	8.16±0.37 ^e	0.21±0.03 ^e	0.54±0.01 ^d
BHA ^A	/	/	/	/	0.09±0.00	0.24±0.02

^AReference compound; ^Bmean±SD (n=3) by one-way ANOVA (Tukey test, p<0.05); ^CConcentration that showed 50% activity. TPC, total phenolic content; TFC, total flavonoid content; CTC, condensed tannin content; BHA, butylated hydroxyanisole.

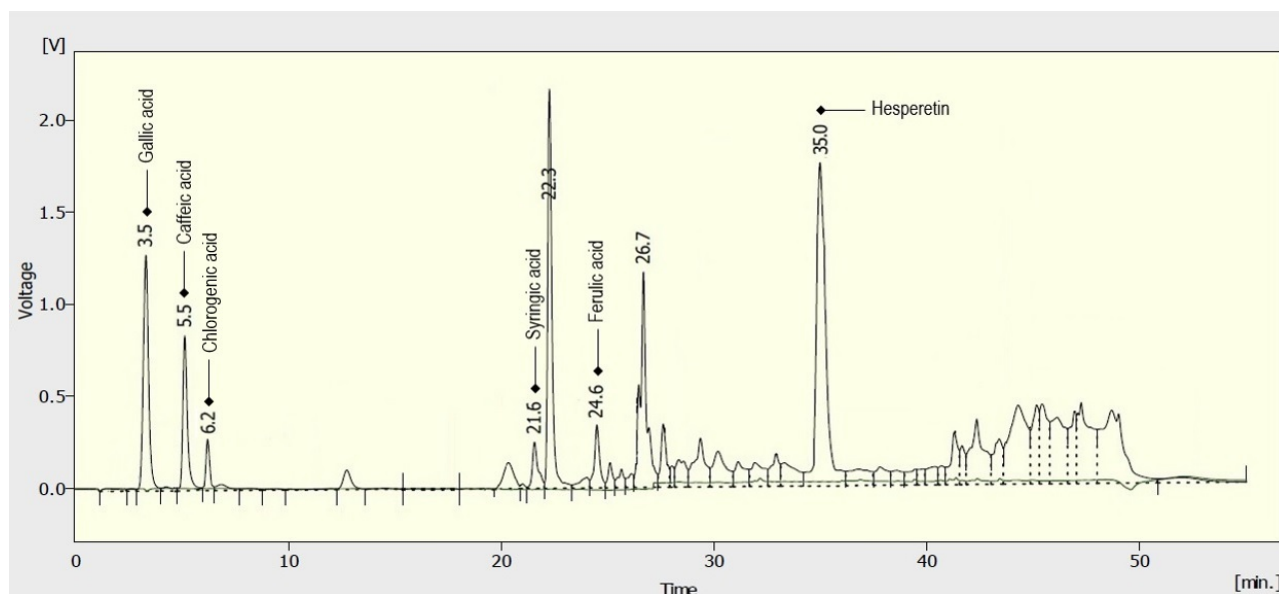


Figure 1: HPLC chromatogram of methanol extract of *Bunium incrassatum* seeds'.

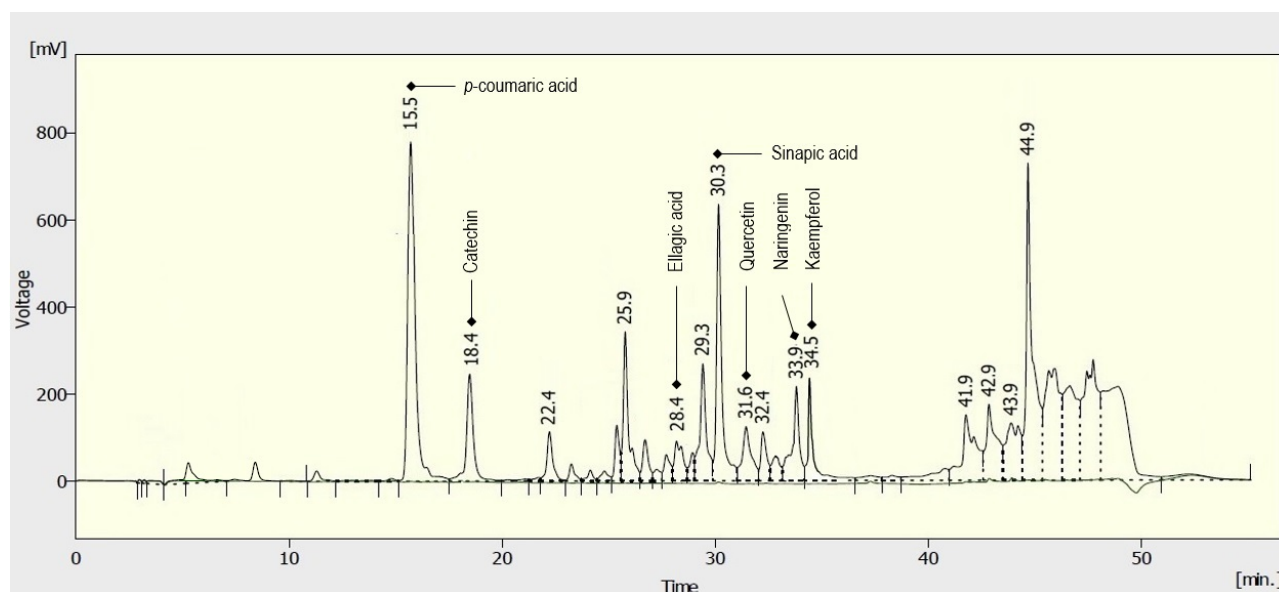


Figure 2: HPLC chromatogram of petroleum ether extract of *Bunium incrassatum* seeds'.

DISCUSSION

Phenolics are undoubtedly the most abundant secondary metabolites of plants. Even abundant, their extraction turns out to be difficult, due to their large chemical variability. There is no universal extraction procedure suitable for the extraction of all plant phenolics (19). It is generally known that the solubility of polyphenols depends on the chemical nature of the plant sample, as well as on the polarity of used solvents (20, 21) and mostly on the extraction protocol conditions' (extraction time, temperature, and pH)(22). All

previous studies have reported only on the tubers' chemical composition and the antioxidant activity of their extracts. As far as we know, the present study is the first to investigate the phenolic profile and antioxidant activity of different solvent extracts of *Bunium incrassatum* seeds.

The results of yields and phenolic contents showed a large variability between extracts. Firstly, petroleum ether extract, followed by methanol, had the highest extraction yields, respectively. Secondly, methanol showed the highest TPC content, followed by petroleum ether. Thirdly,

ethyl acetate was the best solvent, recording the highest TFC content, and finally, methanol showed the highest CTC content, followed by the aqueous extract. These results strongly disagree with those reported by Adelifar et al. (2021) (23) where methanol extracts of different organs, including seeds prepared from four different *Bunium* species (*B.cylindricum*, *B.paucifolium*, *B.persicum*, and *B.wolffii*) showed much lower contents of TPC, TFC, and TTC (total tannin content). Dehimi et al. (2020) (11) reported even lower phenolic contents in different solvent extracts of *B.incrassatum* tubers. These noted differences may be due to the variability in phenolic compounds between species of the same genus or organs of the same species, and even due to environmental conditions in which the plants have grown (24).

Regarding antioxidant activity, it is well known that the measurement of antioxidant potentials of plants' extracts must be conducted using tests based on different mechanisms since each assay can reflect only the chemical reactivity under the specific conditions applied to it. In both selected assays, DPPH scavenging potential and β -carotene bleaching assay, all tested extracts, compared to the reference compound, showed good to moderate potentials, which increased with the increasing concentrations of phenolics in a dose-dependent manner and were much higher than those reported by Dehimi et al. (2020) (11) and even higher than those reported by Zengin et al. (2019) (25) and Adelifar et al. (2021) (23), in which four different species of *Bunium* from Turkey showed less potent effects. The highest antioxidant activity shown by methanol and petroleum ether extracts may be due to a synergistic effect of the compounds they contain. It has also been proven that the antioxidant activity of plant extracts is related to their phenolic content, suggesting a correlation between TPC and antioxidant activity (26).

With regards to the individual phytochemicals, 13 phenolic compounds were identified in both extracts. On the one hand, gallic acid, caffeic acid, chlorogenic acid, syringic acid, ferulic acid, and hesperetin were present in methanol extract. All these compounds were previously found to possess antioxidant properties. Hajimehdipoor et al. (2014) highlighted the synergistic antioxidant effect of several phenolic acids' combinations, where the binary combination of gallic acid and caffeic acid enhanced their antioxidant potential (137%), followed by gallic acid and chlorogenic acid (28%); while the ternary combination of gallic acid, caffeic acid, and chlorogenic acid showed a lower synergistic effect (25.7%)(27). Another study reported that antioxidant activity showed an extremely significant positive correlation with TPC, TFC, ferulic acid, caffeic acid, and chlorogenic acid

(28). In addition to the intense absorption of the main peaks as recorded for Hesperetin, which is known as a strongly antioxidant flavonoid (29), synergy may explain why methanol extract was the most potent one. On the other hand, the chemical analysis of petroleum ether extract, as the second potent extract, showed the presence of ellagic acid, *p*-coumaric acid, sinapic acid, catechin, quercetin, kaempferol, and naringenin. The presence of these phenolic compounds in such nonpolar solvent can be explained by the fact that they are sparingly soluble in high polarity solvents such as water and highly soluble in medium and low polarity solvents (30). In addition, it was reported that these compounds possess various biological and pharmacological properties, such as anticarcinogenic effects, superoxide scavenging, metal chelating, and antioxidant activities, and could be used for several applications in pharmacy (31, 32). *P*-coumaric acid is a hydroxycinnamic acid found in fruits. Its presence correlated significantly with antioxidant activity, unlike sinapic acid, which showed a negative correlation (28). Ackland et al. (2005) and Campbell et al. (2006) reported, respectively, that the binary combination of quercetin and kaempferol as well as the ternary combination of quercetin, kaempferol, and naringenin inhibited cancer cell proliferation in a dose dependent manner without cytotoxicity (33, 34). Another study reported that the combination of ellagic acid and quercetin synergistically induces cell apoptosis and suppresses proliferation in leukemia cells better than each separately (35). This may explain the high antioxidant efficiency of bioactive compounds that petroleum ether extract contains as compared to the reference compound (BHA), which is a strong synthetic antioxidant. But as usual for synthetic additives, BHA has been accepted as possibly carcinogenic to humans by the International Agency for Research on Cancer (IARC) due to the toxicological data on its mechanism of action (36). It should also be noted that all identified compounds have been reported previously in several studies performed on different species of *Bunium* (25, 37, 38), but none of them was about the seeds of *B.incrassatum*.

CONCLUSION

The present study provides novel information about the phytochemical composition of *B.incrassatum* seeds as well as the interesting antioxidant activity of their extracts, which has never been investigated before. The obtained results suggest that the antioxidant activity of the studied extracts can be associated with the presence and synergistic effects of combinations of phenolic compounds, especially phenolic acids and flavonoids. Thus, this plant could be considered as an excellent source of bioactive compounds, especially polyphenols with considerable

antioxidant activity, which could represent an important option for food, cosmetics, and pharmaceutical industries to be supplied with natural antioxidants as an alternative to synthetic additives.

CONFLICT OF INTEREST

Authors state no conflict of interest.

REFERENCES

- Carocho M, Morales P, Ferreira ICFR. Natural food additives: Quo vadis? Trends in Food Science & Technology. 2015 Oct;45(2):284–95. <DOI>.
- Khatua S, Mitra P, Chandra S, Acharya K. *In Vitro* Protective Ability of *Ramaria aurea* Against Free Radical and Identification of Main Phenolic Acids by HPLC. Journal of Herbs, Spices & Medicinal Plants. 2015 Oct 2;21(4):380–91. <DOI>.
- Ramchoun M, Sellam K, Harnafi H, Alem C, Benlyas M, Khallouki F, et al. Investigation of antioxidant and antihemolytic properties of *Thymus satureioides* collected from Tafilalet Region, south-east of Morocco. Asian Pacific Journal of Tropical Biomedicine. 2015 Feb;5(2):93–100. <DOI>.
- Hammoudi N, Hafid H, Moumen Y, Chentouh S, Djebaili H, Boulahbel S. Effect of organic materials extract from *Bunium incrassatum* (Talghouda) roots on hematological and histological parameters of the adrenal glands in the pregnant rabbits, *Oryctolagus cuniculus*. Journal of New Technology and Materials. 2020;10(1):38–43.
- Taïbi K, Ait Abderrahim L, Helal F, Hadji K. Ethnopharmacological study of herbal remedies used for the management of thyroid disorders in Algeria. Saudi Pharmaceutical Journal. 2021 Jan;29(1):43–52. <DOI>.
- Halimi A. Les plantes médicinales en Algérie. Ed Berti, Algérie. 2004;42.
- Bousetla A, Zellagui A, Derouiche K, Rhouati S. Chemical constituents of the roots of Algerian *Bunium incrassatum* and evaluation of its antimicrobial activity. Arabian Journal of Chemistry. 2015 May;8(3):313–6. <DOI>.
- Robin M. Enquête sur le niveau de vie des populations rurales constantinoises de la conquête jusqu'en 1919. Essai d'histoire économique et sociale. 1962;
- Attoui N, Berroukeche F, Toul F. Effect of the roots of Algerian *Bunium incrassatum* on biological, biochemical and histological parameters of mature female rats. Plant Archives. 2021 Apr;21:201–9.
- Hayet EK, Hocine L, Meriem EK. Chemical composition and biological activities of the essential oils and the methanolic extracts of *Bunium incrassatum* and *Bunium alpinum* from Algeria. J Chil Chem Soc. 2017 Mar;62(1):3335–41. <DOI>.
- Khadidja D, Zouina D, Saliha D, Anis B, Abd Raouf M, Seddik K. A Contribution to the Valorization of Two Medicinal Plants: *Atriplex Halimus* Sub. Sp. *Schweinfurthii* and *Bunium Incrassatum*, Growing in the Region of M'sila (North-East Algeria). Indian Journal of Novel Drug Delivery. 2021;12(4):208–16.
- Bousetla A, Kurkcuoglu M, Konuklugil B, Baser KHC, Rhouati S. Composition of Essential Oil from *Bunium incrassatum* from Algeria. Chem Nat Compd. 2014 Oct;50(4):753–5. <DOI>.
- Singleton V. Colorimetry of total phenolics with phosphomolybdic-phosphotungstic acid reagents. Meth Enzymol. 1999;299:152–78. <URL>.
- Zhishen J, Mengcheng T, Jianming W. The determination of flavonoid contents in mulberry and their scavenging effects on superoxide radicals. Food Chemistry. 1999 Mar;64(4):555–9. <DOI>.
- Julkunen-Tiitto R. Phenolic constituents in the leaves of northern willows: methods for the analysis of certain phenolics. J Agric Food Chem. 1985 Mar;33(2):213–7. <DOI>.
- Sánchez-Moreno C, Larrauri JA, Saura-Calixto F. A procedure to measure the antiradical efficiency of polyphenols. Journal of the Science of Food and Agriculture. 1998;76(2):270–6. <DOI>.
- Moure A, Franco D, Sineiro J, Domínguez H, Núñez MJ, Lema JM. Evaluation of Extracts from *Gevuina avellana* Hulls as Antioxidants. J Agric Food Chem. 2000 Sep 1;48(9):3890–7. <DOI>.
- Hertog MGL, Hollman PCH, Venema DP. Optimization of a quantitative HPLC determination of potentially anticarcinogenic flavonoids in vegetables and fruits. J Agric Food Chem. 1992 Sep;40(9):1591–8. <DOI>.
- Dai J, Mumper RJ. Plant Phenolics: Extraction, Analysis and Their Antioxidant and Anticancer Properties. Molecules. 2010 Oct 21;15(10):7313–52. <DOI>.
- Pedrosa MC, Ueda JM, Heleno S, Melgar B, Ivanov M, Soković M, et al. Antimicrobial Activity of Aqueous Plant Extracts as Potential Natural Additives. Proceedings. 2020 Nov 9;70(1):79. <DOI>.
- Toul F, Moussouni S, Ghembaza N, Zitouni A, Djendar A, Atik-Bekkara F, et al. Identification of phenolic compounds in the buds of Algerian *Pistacia atlantica* desf. Subsp. *atlantica* by antioxidant activity guided fractionation. Journal of Complementary and Integrative Medicine [Internet]. 2021 Sep 6 [cited 2022 Mar 5];0(0). <DOI>.
- Roselló-Soto E, Martí-Quijal F, Cilla A, Munekata P, Lorenzo J, Remize F, et al. Influence of Temperature, Solvent and pH on the Selective Extraction of Phenolic Compounds from Tiger Nuts by-Products: Triple-TOF-LC-MS-MS Characterization. Molecules. 2019 Feb 22;24(4):797. <DOI>.

23. Adelifar N, Rezanejad F. A comparative study of essential oil constituents, total phenolics and antioxidant capacity of the different organs of four species of the genus *bunium*. *Flavour Fragr J*. 2021 May;36(3):384–94. <DOI>.
24. Küçükbay FZ, Tekin Z. Evaluation of phytochemical contents and antioxidant activity of pomegranate flower. *Journal of the Turkish Chemical Society Section A: Chemistry*. 2020 Feb 15;7(1):37–42. <DOI>.
25. Zengin G, Paksoy MY, Aumeeruddy MZ, Glamocilja J, Sokovic M, Diuzheva A, et al. New insights into the chemical profiling, cytotoxicity and bioactivity of four *Bunium* species. *Food Research International*. 2019 Sep;123:414–24. <DOI>.
26. Benamar H, Marouf A, Bennaceur M. Phytochemical composition, antioxidant and acetylcholinesterase inhibitory activities of aqueous extract and fractions of *Pistacia atlantica* subsp. *atlantica* from Algeria. *Journal of Herbs, Spices & Medicinal Plants*. 2018 Jul 3;24(3):229–44. <DOI>.
27. Hajimehdipoor H, Shahrestani R, Shekarchi M. Investigating the synergistic antioxidant effects of some flavonoid and phenolic compounds. *Research Journal of Pharmacognosy*. 2014;1(3):35–40.
28. Hou J, Liang L, Su M, Yang T, Mao X, Wang Y. Variations in phenolic acids and antioxidant activity of navel orange at different growth stages. *Food Chemistry*. 2021 Oct;360:129980. <DOI>.
29. Kim JY, Jung KJ, Choi JS, Chung HY. Hesperetin: A Potent Antioxidant Against Peroxynitrite. *Free Radical Research*. 2004 Jul;38(7):761–9. <DOI>.
30. Cayman Chemical 2021 [Internet]. Cayman Chemical. 2021. Available from: <https://www.caymanchem.com/Home>
31. Heleno SA, Martins A, Queiroz MJRP, Ferreira ICFR. Bioactivity of phenolic acids: Metabolites versus parent compounds: A review. *Food Chemistry*. 2015 Apr;173:501–13. <DOI>.
32. Toul F, Belyagoubi-Benhammou N, Zitouni A, Atik-Bekkara F. Antioxidant activity and phenolic profile of different organs of *Pistacia atlantica* Desf. subsp. *atlantica* from Algeria. *Natural Product Research*. 2017 Mar 19;31(6):718–23. <DOI>.
33. Ackland ML, Van De Waarsenburg S, Jones R. Synergistic antiproliferative action of the flavonols quercetin and kaempferol in cultured human cancer cell lines. *In vivo*. 2005;19(1):69–76.
34. Campbell JK, King JL, Harmston M, Lila MA, Erdman JW. Synergistic Effects of Flavonoids on Cell Proliferation in Hepa-1c1c7 and LNCaP Cancer Cell Lines. *J Food Science*. 2006 May;71(4):S358–63. <DOI>.
35. Mertens-Talcott SU, Talcott ST, Percival SS. Low Concentrations of Quercetin and Ellagic Acid Synergistically Influence Proliferation, Cytotoxicity and Apoptosis in MOLT-4 Human Leukemia Cells-. *The Journal of Nutrition*. 2003 Aug 1;133(8):2669–74. <DOI>.
36. Baran A, Yildirim S, Ghosigharehaghaji A, Bolat İ, Sulukan E, Ceyhun S. An approach to evaluating the potential teratogenic and neurotoxic mechanism of BHA based on apoptosis induced by oxidative stress in zebrafish embryo (*Danio rerio*). *Hum Exp Toxicol*. 2021 Mar;40(3):425–38. <DOI>.
37. Shariffar F, Yassa N, Mozaffarian V. Bioactivity of major components from the seeds of *Bunium persicum* (Boiss.) Fedtch. *Pakistan journal of pharmaceutical sciences*. 2010;23(3).
38. Souilah N, Bendif H, Ullah Z, Hamel T. LC-MS/MS simultaneous determination of 37 bioactive compounds in *Bunium crassifolium* Batt. and its biological activities. *Jrp*. 2021;25(4)(25(4)):450–63. <DOI>.



A Simple Spectrophotometric Determination of Amoxicillin in Drug Samples

Adem ASAN^{1*} , Nada SEDDIQ¹ 

¹Ondokuz Mayıs University, Faculty of Art and Science, Department of Chemistry, Samsun, Turkey

Abstract: In this study, a fast and simple spectrophotometric method was developed for the determination of amoxicillin in drugs without any extraction steps. The developed method is based on the formation of a colored ion pair complex between bromocresol green and amoxicillin in dimethyl sulfoxide-acetonitrile (50 % v/v) medium. The absorbance of the bluish green complex is measured at a wavelength of 630 nm. The factors that affect the ion pair complex formation, such as time, reagent concentration, etc., have been optimized. Under the optimum conditions, the developed method had an average recovery of 98.16% with a relative standard deviation of 3.62 % and showed a very good linear behavior obeying Lambert-Beer's law in the range 1-18 $\mu\text{g mL}^{-1}$ of amoxicillin concentration. The developed method has been successfully applied to both tablet and powder forms of pharmaceutical preparations. The standard addition method and statistical parameters were applied to test the accuracy of the proposed method, and the obtained results from the two methods showed good agreement with each other.

Keywords: Amoxicillin, bromine cresol, drug sample, spectrophotometric method.

Submitted: August 04, 2021. **Accepted:** March 03, 2022.

Cite this: Asan A, Seddiq N. A Simple Spectrophotometric Determination of Amoxicillin in Drug Samples. JOTCSA. 2022;9(2):423-32.

DOI: <https://doi.org/10.18596/jotcsa.978686>.

***Corresponding author. E-mail:** aasan@omu.edu.tr.

INTRODUCTION

Amoxicillin is a semi-synthetic antibiotic that belongs to the penicillin family. It is a broad-spectrum antibiotic that is taken with oral route. Amoxicillin is effective against gram-positive and gram-negative microorganisms where it is attached to the cell wall of the bacteria and causes their death. It is found as amoxicillin trihydrate in drugs (1). The structure of amoxicillin is shown in Figure 1.

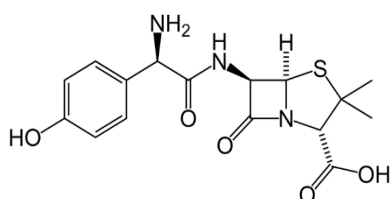


Figure 1: The chemical structure of amoxicillin.

In the last decade, amoxicillin has been mainly used to treat infections of the middle ear (otitis media), tonsils (tonsillitis and tonsillopharyngitis), throat (laryngitis), pharynx (pharyngitis), lungs (bronchitis, pneumonia), and urinary tract (2,3).

In the literature, HPLC⁴⁻⁷ has been reported as the main used chromatographic technique for the determination of amoxicillin. Potentiometry (8), spectrofluorometry (9), flow injection analysis methods (10,11), thin layer chromatography (12), voltammetry (13), LC-MS (14), capillary electrophoresis (15,16), atomic absorption spectroscopy (17) were among the various methods that have been developed for amoxicillin determination.

Among the mentioned methods, spectrophotometric technique is the most widely used method because it is simple to apply and does not require expensive equipment. Spectrophotometric detection is based

on the formation of a colored (charge-transfer or ion-pair) complex between the drug and a reagent. Color intensity can be then estimated by measuring the absorption intensity by a visible spectrophotometer. The charge-transfer complex is also known as the electron-donor-acceptor (EDA) complex, in which fraction of electronic charge is transferred between the molecular entities. Previous spectrophotometric methods for amoxicillin determination have included the formation of complexes with hematoxylin (18), molybdenum and thiocyanate (19), Folin-Ciocalteu's phenol reagent (20), methylene blue (21), bromocresol green (22), 2,4-dinitrophenylhydrazine (23), diazotized p-aminobenzoic acid and diazotized procaine (24), and 4-bromobenzaldehyde (25). In addition to that, some non-derivative and derivative UV spectrophotometric methods were developed (26-30).

In this work, a UV-Visible spectrophotometric method for the determination of amoxicillin was developed by modifying the method by Keskar and Jugade (22). In the mentioned work, dimethyl sulfoxide (DMSO) was used as a solvent. In this study, by using dimethyl sulfoxide-acetonitrile (DMSO-AcN) mixture (50 % v/v) the absorbance was increased, thus the detection limit was reduced and the linear working range was extended. The developed method was based on the formation of an ion-pair complex between amoxicillin and bromocresol green in dimethyl sulfoxide-acetonitrile (50% v/v). The absorbance was measured at the wavelength 630 nm. The most important advantages of this method are that it did not require pretreatment steps such as extraction and it was performed at room temperature. After the method was optimized with standard solutions, it was successfully applied for the determination of amoxicillin in drug samples.

MATERIAL AND METHODS

Chemicals and Apparatus

All chemicals required for the experiments were obtained from Sigma-Aldrich and Merck companies and were used as purchased without any further purification. Thermo SCIENTIFIC EVOLUTION 220 UV-Visible Spectrophotometer (USA) was used for all the spectrophotometric measurements.

Amoxicillin Solution Preparation

Amoxicillin standard solutions were prepared from amoxicillin trihydrate stored at -20°C. A stock solution of amoxicillin (0.01 M) was prepared by dissolving 0.209 g of amoxicillin trihydrate in the appropriate volume of dimethyl sulfoxide-acetonitrile mixture (50% v/v).

Bromocresol Green Solution Preparation

A stock solution of bromocresol green (0.001 M) was prepared by dissolving 0.0349 g of bromocresol green in the appropriate volume of dimethyl sulfoxide-acetonitrile mixture (50% v/v).

Sample Preparation

LARGOPEN dry powder and LARGOPEN tablets (BILIM PHARMACEUTICALS Beyoğlu ISTANBUL) containing amoxicillin were purchased from the local pharmacy. For the tablets, 5 tablets were accurately weighed to determine the weight of an average tablet where it was found to be 1.3687 g. Then, these five tablets were powdered in a mortar and 0.05 g of this powder was dissolved in 10 mL volumetric flask with dimethyl sulfoxide-acetonitrile mixture (50% v/v) to obtain a homogeneous solution (1 tablet was equivalent to 1176.47 mg amoxicillin trihydrate). For the dry powder, 147.06 mg of the dry powder was directly dissolved in 10 mL volumetric flasks with dimethyl sulfoxide-acetonitrile mixture (50 % v/v) to obtain a homogeneous solution.

Methods

In this work, UV-Visible spectrophotometric method was developed for the determination of amoxicillin. The method involves the formation of an ion-pair complex between amoxicillin and bromocresol green in dimethyl sulfoxide-acetonitrile (50 % v/v) medium. The ion-pair complex shows maximum absorbance at 630 nm and all measurements were taken at this wavelength throughout the study. The optimum conditions for the complex formation were established using standard solutions, then the method was successfully applied for the determination of amoxicillin in drug samples.

RESULTS AND DISCUSSION

The spectrum of Amoxicillin Solution

The spectrum of amoxicillin solution (0.01 M) that was prepared in dimethyl sulfoxide-acetonitrile (50 % v/v) was scanned between 200-750 nm as shown in Figure 2.

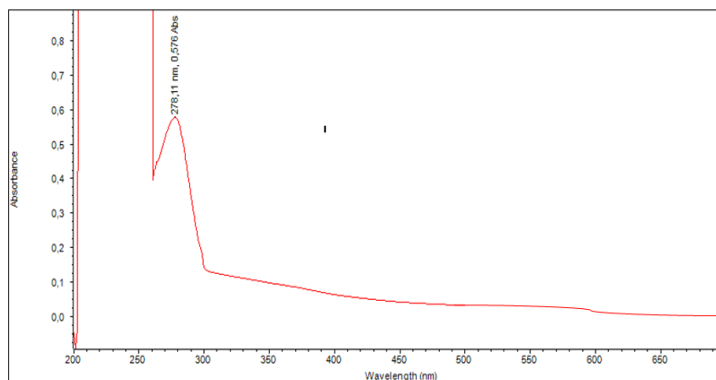


Figure 2: The spectrum of amoxicillin solution (1×10^{-2} M) in the spectral range 200-750 nm.

It can be seen in Figure 2 that the amoxicillin solution has a maximum absorbance at 270 nm.

The Spectrum of Bromocresol Green Solution

The spectrum of the bromocresol green solution (0.001 M) that was prepared in dimethyl sulfoxide-acetonitrile (50 % v/v) was scanned between 200-750 nm as in Figure 3.

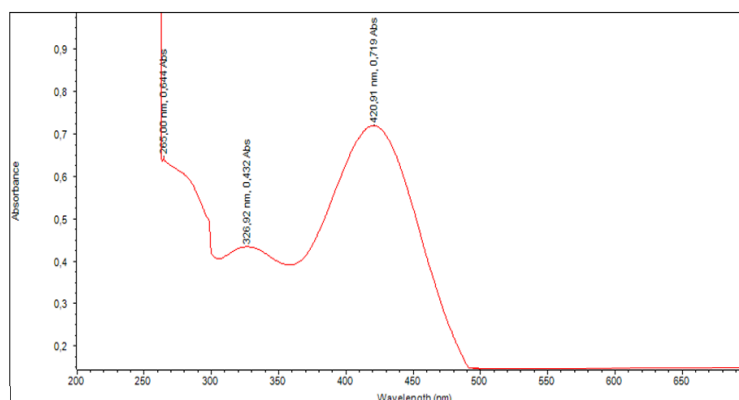


Figure 3: The spectrum of bromocresol green solution (1×10^{-3} M) in the spectral range of 200-750 nm.

As can be seen in Figure 3, bromocresol green shows maximum absorbance at 420 nm.

The Spectrum of the Resulting Ion-Pair Complex

When amoxicillin solution (5×10^{-3} M) and bromocresol green solution (5×10^{-3} M) are mixed at room temperature a turquoise ion-pair complex is instantly formed. The spectrum of the formed complex is shown in Figure 4.

As can be seen in Figure 4, the ion-pair complex that formed between amoxicillin and bromocresol

green shows maximum absorbance at 630 nm. Neither amoxicillin nor bromocresol green show any absorption at this wavelength. Therefore, the absorbance that is measured at the wavelength 630 nm is only due to the formation of the ion-pair complex.

Optimization of the Experimental Conditions

The effects of various parameters on the absorption intensity of the ion-pair complex that formed from the reaction between amoxicillin and bromocresol green were optimized.

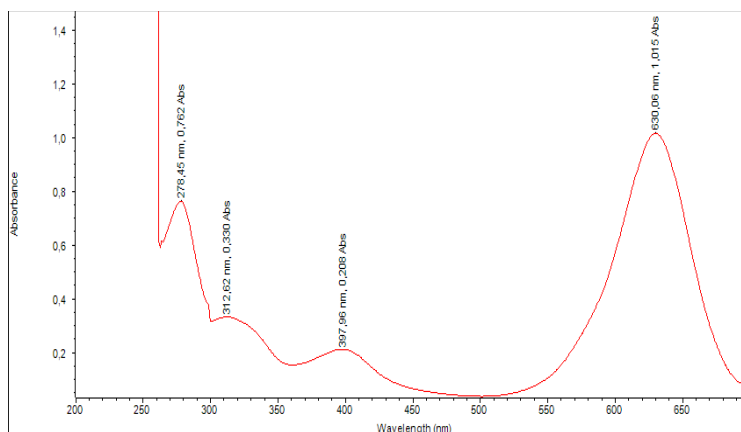


Figure 4: The spectrum of the ion-pair complex that was formed from amoxicillin (5×10^{-3} M) with bromocresol green (5×10^{-3} M).

Effect of Solvents

To investigate the effects of solvents on various variables related to the reaction between amoxicillin and bromocresol green such as solubility, complex formation, and maximum absorbance, absorption

intensity was measured using different solvents (dimethyl sulfoxide-acetonitrile mixture, methyl alcohol, ethyl alcohol, acetone, acetonitrile, chloroform, dichloromethane). The obtained data are shown in Figure 5.

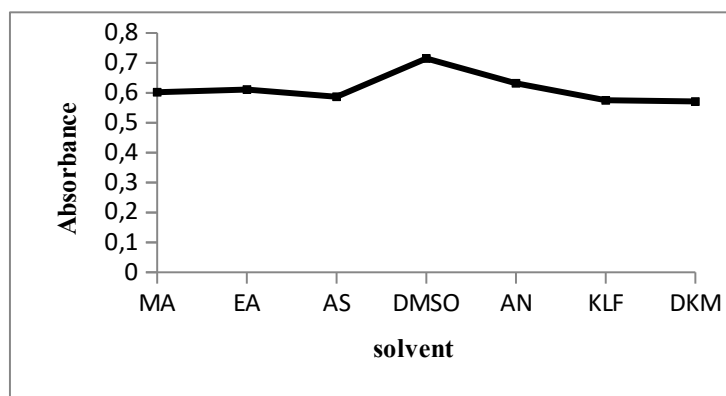


Figure 5: The effect of different solvents on ion-pair complex formation and absorption, (DMSO: dimethyl sulfoxide-acetonitrile, MA: methyl alcohol, EA: ethyl alcohol, AS: acetone, AN: acetonitrile, KLF: chloroform, DKM: dichloromethane)

As can be seen in the figure, among the tested solvents, the highest absorbance value was achieved with dimethyl sulfoxide-acetonitrile mixture, so it was selected for the subsequent steps.

Stoichiometric Ratio

The combining ratio was evaluated by the Continuous Variation Method (Job's method). Amoxicillin and bromocresol green solutions with identical analytical concentrations were mixed in a way that keeps the total volume and the total moles of the two reactants constant but the mole ratio of them varies systematically. The absorbance of each

mixture was measured, and then the absorbance was plotted against the mole fraction of one reactant. For this purpose, solutions with the concentrations of 1×10^{-4} , 2×10^{-4} and 3×10^{-4} M were prepared by the appropriate dilution of the amoxicillin and bromocresol green stock solutions that were previously prepared. 10 mixtures with different mole fractions were prepared from these solutions with a total volume of 10 mL, and constant total moles of the two reactants. The absorbance values of these solutions were measured at 630 nm and plotted against the mole fraction of amoxicillin. The resulting graph is shown in Figure 6.

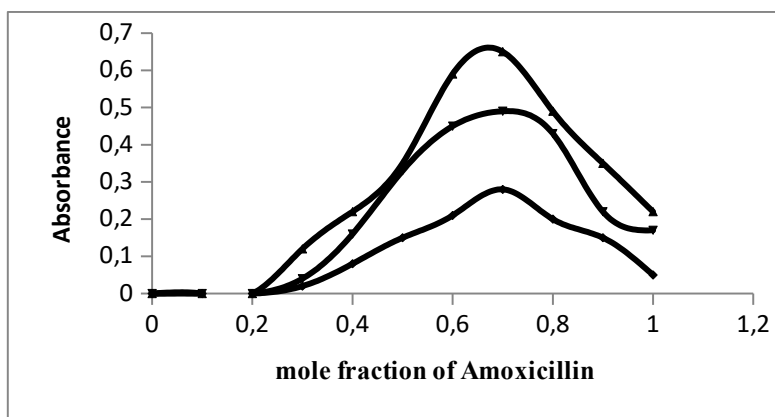


Figure 6: The combining ratio between amoxicillin and bromocresol green according to the continuous variation method (series 1 (diamond): 1×10^{-4} M; series 2 (square): 2×10^{-4} M; series 3 (triangle): 3×10^{-4} M)

As can be seen in Figure 6, the stoichiometric ratio between amoxicillin and bromocresol green is 2:1.

Effect of Reaction Time

When the two solutions of amoxicillin and bromocresol green were mixed a turquoise color

immediately developed. The absorbance values of the resulting complex were measured for one hour at an interval of 10 minutes and the results were presented in Figure 7.

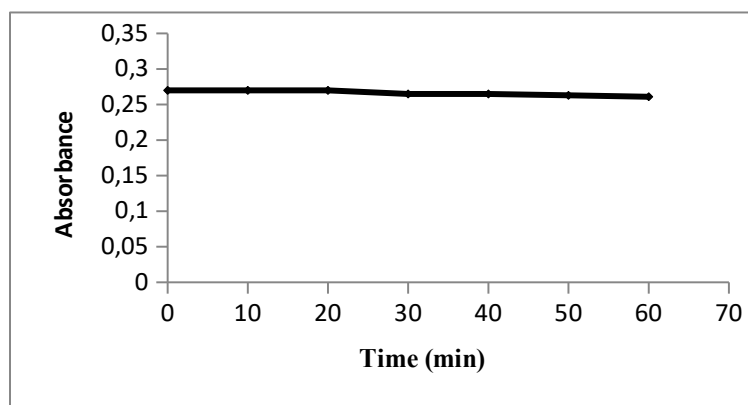


Figure 7: The change in absorbance over time. The complex formed between 2×10^{-5} M amoxicillin and 1×10^{-6} M bromocresol green in DMSO solvent and measured at 630 nm.

As seen in Figure 7, there is no significant change in the absorption of the formed complex at room temperature, and the complex remains stable for at least one hour.

Effect of Bromocresol Concentration

In order to determine the optimum bromocresol green concentration, varying volumes of

bromocresol were added to amoxicillin and the absorbance was measured at 630 nm. It was observed that the color intensity increased with the increasing of bromocresol green concentration up to 9×10^{-6} M and decreased after this value. Figure 8 shows the effect of bromocresol green concentration on the absorption intensity of the ion-pair complex.

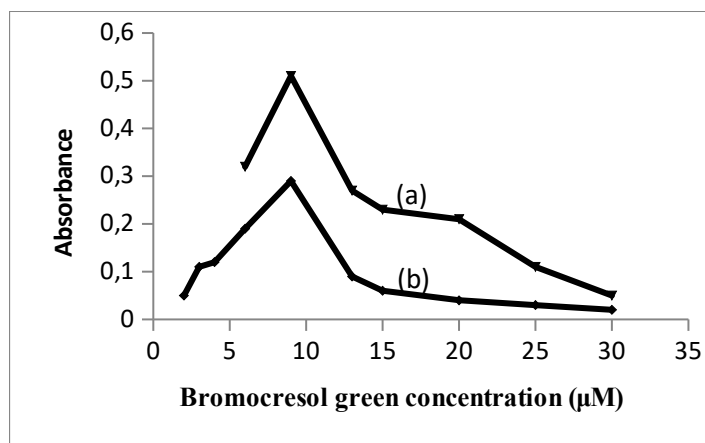


Figure 8: Effect of bromocresol green concentration on the formed complex, (a) 14 µg/mL amoxicillin, (b) 6 µg/mL amoxicillin.

Analytical Characteristics of the Proposed Spectrophotometric Method

After optimizing the experimental conditions of the reaction between amoxicillin and bromocresol green, analytical studies were carried out to determine the range of linear changes between the absorption intensity and amoxicillin concentration.

For this purpose, a series of standard solutions were prepared with different amoxicillin concentrations while the bromocresol green concentration was kept constant. The absorbance of the formed ion-pair complex was measured at 630 nm and a calibration graph was constructed from the obtained data (Figure 9).

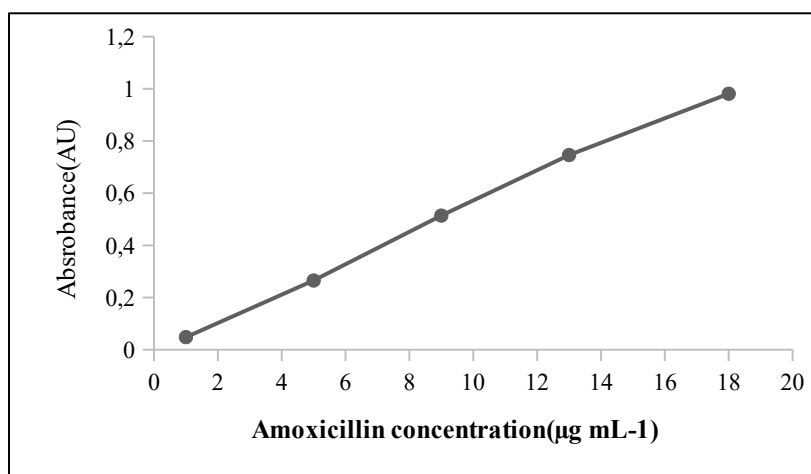


Figure 9: Calibration graph of amoxicillin.

The analytical parameters obtained from the calibration graph are listed in Table 1. The calibration graph of the absorption intensity was plotted against amoxicillin concentration, and the analytical parameters were obtained by the least squares method. Beer's law was obeyed over the concentration range of 1-18 µg mL⁻¹ as shown in Figure 9, and the analytical parameters obtained

accordingly were given in Table 1. The regression coefficient of the calibration curve was 0.9976. Limit of detection (LOD) and limit of quantification (LOQ) values were calculated from the equation as $LOD=3.3s/m$ and $LOQ=10s/m$; where s is the standard deviation of the absorbance values that obtained at the same concentration, and m stands for the slope of the calibration curve (31).

Table 1: Analytical parameters obtained from the calibration graph of amoxicillin determined by the proposed spectrophotometric method.

Parameters	Values
λ_{\max} (nm)	630
Linear range ($\mu\text{g mL}^{-1}$)	1-18
Regression equation*	$A = 0.00556C$
correlation coefficient (r^2)	0.9976
slope	0.0551
Intercept	0.0062
LOD ($\mu\text{g mL}^{-1}$)	0.05
LOQ ($\mu\text{g mL}^{-1}$)	0.15
molar absorptivity ($\text{L}\cdot\text{mol}^{-1}\cdot\text{cm}^{-1}$)	1.538×10^3

*(A: absorbance, C: concentration in $\mu\text{g mL}^{-1}$)

Interference Studies

The proposed method was applied on Largopen drugs containing amoxicillin in tablets and powder forms. Drug prospectus stated that there are no excipients in the Largopen tablet, while the powder form contains sucrose as an excipient. Since there is no interaction between sucrose and bromocresol green, interference effects have not been investigated.

Pharmaceutical Application of the Developed Spectrophotometric Method

After the parameters of the developed spectrophotometric method for amoxicillin determination were optimized, it was applied for the analysis of two pharmaceutical preparations (amoxicillin-containing tablet and powder drugs) in order to determine amoxicillin content. Amoxicillin is a broad-spectrum antibiotic that is effective against both gram-positive and gram-negative

microorganisms and belongs to the penicillin family. It is used in pharmaceuticals as amoxicillin trihydrate. Some of its trade names are Amoxil manufactured by Glaxosmithkline, Alfoxil manufactured by Actavis, Amoxina manufactured by Mustafa Nevzat and Largopen manufactured by Bilim Pharmaceuticals. In the study, the proposed method was applied successfully on both tablet and powder drugs produced by Bilim Pharmaceuticals. Sample solutions were prepared as mentioned before by dissolving the sample in dimethyl sulfoxide-acetonitrile mixture. Then, bromocresol green solution was added to the prepared solutions and the absorbance of the formed complex was measured at 630 nm. Taking required dilutions into account, amoxicillin concentration in pharmaceuticals was estimated from the calibration curve. Spectra obtained from real sample solutions are shown in Figures 10 and 11.

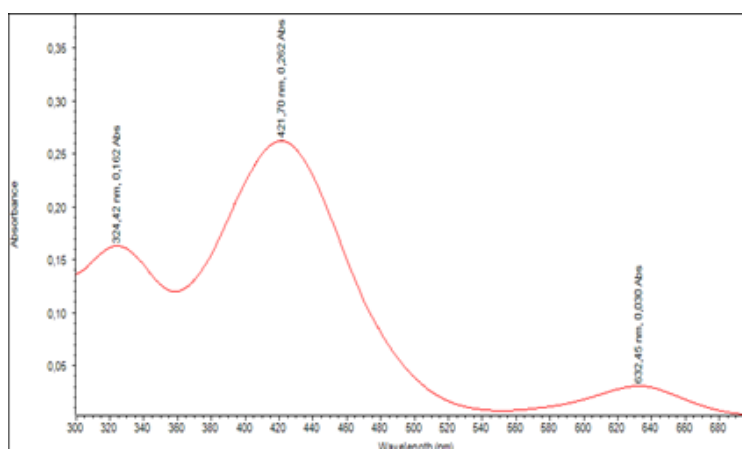


Figure 10: Spectrum obtained from Largopen (tablet) sample solution.

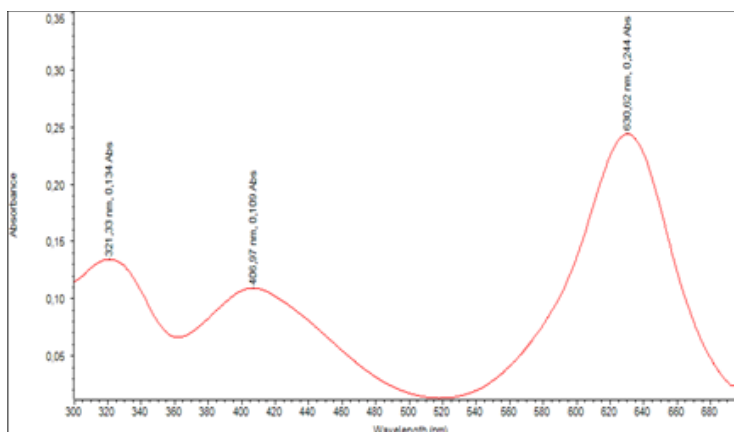


Figure 11: Spectrum obtained from Largopen (powder) sample solution.

On the other hand, the method of standard addition was applied for amoxicillin determination in both drug samples. Increasing concentrations of amoxicillin standard solutions were added to five separate parts of each drug sample, then bromocresol green was added to each of them and the volume was completed to 10 mL with dimethyl

sulfoxide-acetonitrile (50% v/v). The absorbance was measured at the wavelength 630 nm. The concentration of amoxicillin in each drug sample was calculated by referring to the calibration curve and the results were compared with each other as shown in Table 2.

Table 2: Amoxicillin concentrations in drug samples and the statistical parameters by spectrophotometric method and standard addition method.

Sample	declared content	Amoxicillin ($\mu\text{g/mL}$)*			
		Spectrophotometric method	Standard addition method	F test	t test
Largopen (tablet)	10	8.23 \pm 1.12	7.49 \pm 0.89	4.82	1.94
Largopen (powder)	10	7.98 \pm 0.75	7.16 \pm 0.02	3.97	1.67

*Mean and standard deviation of three replicates ($GS = \bar{x} \pm \frac{ts}{\sqrt{N}}$, 95% confidence interval)

(95% confidence level $F = 6.39$ and $t = 2.21$)

The content of amoxicillin in each one of the two drug samples was determined by both the developed spectrophotometric method and the standard addition method. Both t -test and F -test were performed for the developed method. t values were found to be 1.94 and 1.67. The results showed that the calculated values of t were lower than the critical value ($t = 2.31$, 95% confidence level), so there is no significant difference between the results obtained from the two methods at 95% confidence level. On the other hand, the F -test was applied to find out whether there is a significant difference between the precisions of the two methods applied. In all cases, the calculated values of F (4.82 and 3.92) were lower than the critical value ($F = 6.39$, 95% confidence level). These results showed that there is no significant difference between the

developed spectrophotometric method and the standard addition method and that the developed method can be successfully applied to real samples.

Recovery Studies (Precision and Accuracy)

Recovery studies were carried out to investigate the effects of additives found in the studied drug samples on the developed spectrophotometric method for amoxicillin determination. For this purpose, a known amount of standard amoxicillin was added to the prepared drug samples that also contain a known amount of amoxicillin. Then the ion-pair complex was formed by adding bromocresol green and the absorbance values were measured at 630 nm. Amoxicillin concentrations were calculated using the calibration graph and the results were listed in Table 3.

Table 3: Recovery% and other parameters of drug samples containing (10 mg)* of amoxicillin.

	Amount Added (labelled) (mg)	Amount Found (mg)	Recovery %
Amoxicillin	10	9.72	97.21
	10	9.81	98.10
	10	9.92	99.20
			\bar{x} : 98.16
			SD: 0.34
			RSD%: 3.62
		RE%: -6.30	

*Average of three replicate (SD: standard deviation; RSD: relative standard deviation; RE: relative error).

As can be seen in the table, the proposed method was successfully applied for the determination of amoxicillin in drug samples where the recovery values found in the range of 97.21-99.20% (average 98.16%) and relative standard deviation was 3.62%.

CONCLUSION AND RECOMMENDATIONS

In this study, a simple, fast, and selective spectrophotometric method that does not require extraction processes was developed for the determination of amoxicillin. The method is based on measuring the absorption intensity of the ion-pair complex formed between amoxicillin and bromocresol green at 630 nm. The developed method was optimized and successfully applied to

analyze two different drug samples containing amoxicillin. The results were obtained from both the calibration graph and the standard addition method, and they were given comparatively. The results obtained from the proposed method were also compared using the statistical tests and found to be in good agreement with the other method.

The comparison of the proposed method with the previously some reported methods is presented in Table 4. The proposed method enabled the LOD 0.05 $\mu\text{g mL}^{-1}$ for amoxicillin without complex pre-treatment. The developed method was found to be versatile and have many advantages over the previously reported methods. The method is utilized a single step reaction with no extraction process and no simpler compared to reported methods.

Table 4: Comparison of other methods in the literature.

Method	Sample	LOD ($\mu\text{g mL}^{-1}$)	Reference
FIA	Pharmaceutical formulations	0.571	(11)
Voltammetry	Drug and urine	0.50	(13)
HPLC	Bulk drug	0.347	(7)
Capillary electrophoresis	Animal plasma samples	0.280	(16)
Spectroscopy	Pharmaceutical preparations	0.05	This work

With the developed method, significantly lower limit of detection, wider dynamic range, and higher selectivity were obtained for amoxicillin determination. The method does not require the use of complex equipment and it has the potential to be applied in the routine analysis of amoxicillin in different pharmaceutical formulations.

REFERENCES

- Zheng F, Wang S, Wen S, Shen M, Zhu M, Shi X. Characterization and antibacterial activity of amoxicillin-loaded electrospun nano-hydroxyapatite/poly(lactic-co-glycolic acid) composite nanofibers. *Biomaterials*. 2013 Jan;34(4):1402-12. <DOI>.
- Lim WS, Gander S, Finch RG, McFarlane JT. A novel method for collecting and detecting amoxicillin in urine: a tool for testing antibiotic compliance in the community. *Journal of Antimicrobial Chemotherapy*. 2000 Nov 1;46(5):835-7. <DOI>.
- Kaur SP, Rao R, Nanda S. Amoxicillin: a broad spectrum antibiotic. *Int J Pharm Pharm Sci*. 2011;3(3):30-7.
- Lee TL, D'Arconte L, Brooks MA. High-Pressure Liquid Chromatographic Determination of Amoxicillin in Urine. *Journal of Pharmaceutical Sciences*. 1979 Apr;68(4):454-8. <DOI>.
- De Abreu LP, Ortiz RAM, de Castro SC, Pedrazzoli J. HPLC determination of amoxicillin comparative bioavailability in healthy volunteers after a single dose administration. *J Pharm Sci*. 2003;6(2):223-30.

6. Douša M, Hosmanová R. Rapid determination of amoxicillin in premixes by HPLC. *Journal of Pharmaceutical and Biomedical Analysis*. 2005 Feb;37(2):373-7. <DOI>.
7. Basavaiah K, Tharpa K, Prasad NR, Hiriyantha S, Vinay K. Determination of amoxicillin in pharmaceutical forms by visible spectrophotometry and HPLC. 2009; Available from: <URL>.
8. Shoukry MM. Potentiometric studies of binary and ternary complexes of amoxicillin. *Talanta*. 1992 Dec;39(12):1625-8. <DOI>.
9. El Walily AFM, Abdel-Kader Gazy A, Belal SF, Khamis EF. Selective spectrofluorimetric determination of phenolic β -lactam antibiotics through the formation of their coumarin derivatives. *Journal of Pharmaceutical and Biomedical Analysis*. 1999 Aug;20(4):643-53. <DOI>.
10. Li Y, Tang Y, Yao H, Fu J. Determination of ampicillin and amoxicillin by flow injection chemiluminescence method based on their enhancing effects on the luminol-periodate reaction. *Luminescence*. 2003 Nov;18(6):313-7. <DOI>.
11. Xiaofeng X, Zhenghua S. Ultrasensitive determination of amoxicillin using chemiluminescence with flow injection analysis. *Journal of Spectroscopy*. 2006; 20(1): 37-43. <URL>.
12. Indrayanto G, Sa TK, Widjaja S. Simultaneous Determination of Amoxicillin Trihydrate and Clavulanate Potassium in Pharmaceutical Preparations by Thin-Layer Chromatography/Densitometry. *Journal of AOAC INTERNATIONAL*. 2000 Nov 1;83(6):1493-6. <DOI>.
13. Fouladgar M, Hadjmohammadi MR, Khalilzadeh MA, Biparva P, Teymoori N, Beitollah H. Voltammetric determination of amoxicillin at the electrochemical sensor ferrocenedicarboxylic acid multi wall carbon nanotubes paste electrode. *Int J Electrochem Sci*. 2011;6:1355-66. <URL>.
14. Kotte SCB, Tulam VK, Chinta RR, Raghavan S, Dubey P, Murali P. Qualitative analysis of amoxicillin, ampicillin, cephalexin by quadrupole-time of flight (LCMS) using electrospray ionization. *International Journal of ChemTech Research*. 2012;4:855-61.
15. Pajchel G, Pawłowski K, Tyski S. CE versus LC for simultaneous determination of amoxicillin/clavulanic acid and ampicillin/sulbactam in pharmaceutical formulations for injections. *Journal of Pharmaceutical and Biomedical Analysis*. 2002 Jun;29(1-2):75-81. <DOI>.
16. Hernández M, Borrull F, Calull M. Determination of amoxicillin in plasma samples by capillary electrophoresis. *Journal of Chromatography B: Biomedical Sciences and Applications*. 1999 Aug;731(2):309-15. <DOI>.
17. Issa M, Nejem M, Al-Kholy M, El-Abadla S, Helles S, Saleh A. An indirect atomic absorption spectrometric determination of ciprofloxacin, amoxicillin and diclofenac sodium in pharmaceutical formulations. *J Serb Chem Soc*. 2008;73(5):569-76. <DOI>.
18. Raghavendra G, Suryanarayana R. Spectrophotometric method for the determination of ampicillin and amoxicillin. *J Pharm Res*. 2010;3:869-72.
19. Mohamed GG. Spectrophotometric determination of ampicillin, dicloxacillin, flucloxacillin and amoxicillin antibiotic drugs: ion-pair formation with molybdenum and thiocyanate. *Journal of Pharmaceutical and Biomedical Analysis*. 2001 Feb;24(4):561-7. <DOI>.
20. Shafique Ahmad A, Rahman N, Islam F. Spectrophotometric Determination of Ampicillin, Amoxicillin, and Carbenicillin Using Folin-Ciocalteu Phenol Reagent. *Journal of Analytical Chemistry*. 2004 Feb;59(2):119-23. <DOI>.
21. Prasad B, Gupta S. Extraction spectrophotometric method for the determination of certain β -lactam antibiotics with methylene blue. 2000;62(4):261-6.
22. Keskar MR, Jugade RM. A new spectrophotometric method for determination of amoxicillin using bromocresol green. *World Journal of Pharmacy and Pharmaceutical Sciences*. 2014;3(2):1340-8.
23. Nagaraja P, Shrestha AK. Spectrophotometric Method for the Determination of Drugs Containing Phenol Group by Using 2, 4- Dinitrophenylhydrazine. *E-Journal of Chemistry*. 2010;7(2):395-402. <DOI>.
24. Al-Uzri WA. Spectrophotometric determination of amoxicillin in pharmaceutical preparations through diazotization and coupling reaction. *IJ S*. 2012;53(4):713-23.
25. Abdul-Sattar JA, Atia A-JK, Kadhom SA, Mohammed-Ali LF. Spectrophotometric Determination of Amoxicillin-Application to Capsules. *Al-Mustansiriyah J Sci*. 2009;20(4):35-42.
26. Gujral RS, Haque SM. Simultaneous Determination of Potassium Clavulanate and Amoxicillin Trihydrate in Bulk, Pharmaceutical Formulations and in Human Urine Samples by UV Spectrophotometry. *Int J Biomed Sci*. 2010 Dec;6(4):335-43. PMID: 23675211.
27. Ünal K, Palabiyik İM, Karacan E, Onur F. Spectrophotometric determination of amoxicillin in pharmaceutical formulations. *Turk J Pharm Sci*. 2008;5(1):1-16.
28. Tavallali H, Rasti S. Simultaneous determination of amoxicillin and clavulanate potassium by derivative spectrophotometric method. *Int J Pharm Tech Res*. 2013;5(3):2475-80.
29. Radhi ER, Ali KJ. Spectrophotometric Study for Comparison of Amoxicillin Trihydrate and Levofloxacin Hemihydrate Determination Using Bromocresol Green. *International Journal of Pharmaceutical Research*. 2019;11(1):1107-13.
30. Hamed AH, Ibrahim SK, DHAHIR S, Mhemeed AH. Indirect Spectrophotometric Determination of Amoxicillin by oxidative with Cerium ammonium nitrate using Arsenazo III as a reagent. *Chemical Science*. 2019;8(2):289-94.
31. Ermer J, Miller JHM. Method Validation in Pharmaceutical Analysis A Guide to Best Practice [Internet]. 2006 [cited 2022 Mar 3]. ISBN: 978-3-527-31255-9. <URL>.



Microwave-Assisted Extraction of *Prunus cerasus* L. Peels: Citric Acid-Based Deep Eutectic Solvents

Ebru Kurtulbaş* 

Istanbul University - Cerrahpaşa, Chemical Engineering Department, 34320, Avclar, Istanbul, Turkey

Abstract: In the present study, waste by-products of one of the most popular fruit juices in the World has been valorized for its high-added value ingredients. Peels of sour cherry (*Prunus cerasus* L.) have been extracted by deep eutectic solvent (DES)-based microwave-assisted extraction method (MAE). DES system contained citric acid as hydrogen bond acceptor (HBA) and ethylene glycol as hydrogen bond donor (HBD) (1/4, molar ratio). In order to optimize the MAE system Central Composite Design (CCD) of Response Surface Method (RSM) has been used. The measured variables were the yields of total phenolic content (TPC), total anthocyanins (TA), and cyanidin-3-glucoside. Optimum conditions were determined as 0.1 g of peel and a 50 % (v/v) water contribution to the DES for the maximum recovery of TPC (16.85 mg-GAE/g-FP), TA (3.39 mg-cyn-3-glu/g-FP) and cyanidin-3-glucoside (mg/g-FP) in the MAE of sour cherry peels. The relationship between the responses was also established.

Keywords: Green chemistry; deep eutectic solvents; waste by-products; optimization; anthocyanins.

Submitted: December 07, 2021. **Accepted:** February 24, 2022.

Cite this: Kurtulbaş E. Microwave-Assisted Extraction of *Prunus cerasus* L. Peels: Citric Acid-Based Deep Eutectic Solvents. JOTCSA. 2022;9(2):433-442.

DOI: <https://doi.org/10.18596/jotcsa.1033685>.

***Corresponding author. E-mail:** ebru.kurtulbas@iuc.edu.tr.

INTRODUCTION

The valorization of waste by-products from agri-food products has been a popular issue recently. The most consumed fruits, such as citrus peels (1-3), banana peels (4), apple peels (5), mango peels (6), apricot and peach peels (7), pomegranate peels (8), and sour cherry peels (9), were investigated in terms of extraction and their bioactive properties. Since Turkey is one of the primary countries in the world producing sour cherries (10), its peel has been selected to observe its polyphenol ingredients in the current study. Its medicinally therapeutic properties, such as antimicrobial (11), antioxidant, anti-tumor (12), anti-cancer, and anti-inflammatory

(13) effects, have also been proven by various studies. Therefore, recovery of the related fine chemicals from biomass has been a very valuable issue nowadays. In order to propose a green process for obtaining the bioactive ingredients from sour cherry peels, microwave-assisted extraction (MAE) method has been adopted in the present study. The advantages of the MAE over conventional methods are demonstrated in Figure 1 (14). On the other hand, a deep eutectic solvent (DES) including citric acid (hydrogen bond acceptor) and ethylene glycol (hydrogen bond donor) was integrated into the MAE to be able to propose a more environmentally friendly procedure.

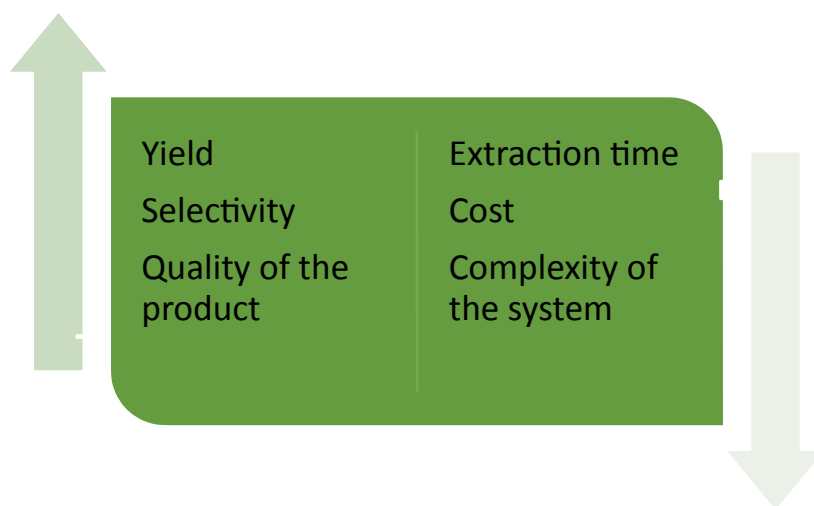


Figure 1: Advantages of MAE.

In order to optimize the process conditions to achieve the maximum yields of extraction, central composite design (CCD) of response surface method (RSM) has been exploited. The yields of the system have been evaluated according to the total phenolic content (TPC), total anthocyanin (TA), and cyanidin-3-glucoside level. Cyanidin-3-glucoside was particularly chosen due to the fact that it is one of the primary phenolic compounds in the sour cherry peel extract (9,15). The independent parameters were selected as water amount in the DES and mass of raw material, where extraction time and microwave power were determined depending on the preliminary experiments. The relationship between the dependent variables was also presented in terms of correlation coefficient.

MATERIAL AND METHODS

Materials

Citric acid ($\geq 99.5\%$), ethylene glycol ($\geq 99.5\%$), methanol ($\geq 99.9\%$), ethanol ($\geq 99.9\%$), and hydrochloric acid were purchased from Merck (Darmstadt, Germany). Folin-Ciocalteu reagent, sodium carbonate ($\geq 99.0\%$), gallic acid ($\geq 98.0\%$), formic acid ($\geq 98.0\%$), acetonitrile ($\geq 99.9\%$), and

cyanidin-3-glucoside were purchased from Sigma-Aldrich (St. Louis, MO, USA).

Regarding plant material (sour cherry), the samples were obtained from DIMES Food located in Turkey. The peels were kept at $-20\text{ }^{\circ}\text{C}$ after being separated from the fruits. Fresh samples were used in the study.

DES Preparation

A heating and mixing method was adopted to prepare the selected system ($1/4$ molar ratio, citric acid/ethylene glycol) depending on the previous study (16). Citric acid was used as hydrogen bond acceptor (HBA), whilst ethylene glycol was the hydrogen bond donor (HBD) in DES mixture.

MAE Procedure

MAE of sour cherry peels was performed by a laboratory scale microwave system (NEOS-GR, Milestone Srl, Italy). Table 1 shows the selected parameters and their levels used in this study. The effects of water addition to the DES and the amount of raw material were investigated. The power of the microwave was kept stable at 500 W for 3 min of extraction time with 50 mL of solvent, depending on the preliminary experiments.

Table 1: Process parameters of MAE for the extraction of bioactive substances from sour cherry peels.

Parameter	Symbol	Code with level		
		-1	0	1
Mass (g)	A	0.1	0.3	0.5
Water ratio (% v/v)	B	20	35	50

Chromatographic and Spectrophotometric Analysis

The cyanidin-3-glucoside content of extracts was determined by Agilent 1260 chromatographic equipment (Agilent, Waldbronn, Germany), while TPC and TA of the sour cherry extracts were analyzed spectrophotometrically using a UV spectrophotometer (PG Instruments,

T60/Leicestershire, England). The detailed information on high-performance liquid chromatography (HPLC) method for the quantification of cyanidin-3-glucoside was reported in the earlier paper (15).

Spectrophotometric measurements of TPC were performed at 765 nm. Extracted samples were

diluted with water first. Then, Folin-Ciocalteu reagent and sodium carbonate solutions were added and left for incubation for 30 min (17). The output was given in gallic acid equivalents per gram of fresh plant sample (mg-GAE/g-FP). On the other hand, spectrophotometric measurements of TA were carried out at 520 and 700 nm (9). The output was given in cyanidin-3-glucoside equivalents per gram of fresh plant sample (mg-cyn-3-glu/ g-FP).

RSM

The extraction process was modeled using the response surface approach. By applying a mathematical and statistical technique, RSM was provided with an association between the variables. Table 1 gives the selected independent parameters with their levels. In this research, RSM was exploited to optimize the amount of TPC, TA, and

cyanidin-3-glucoside by using Design expert program (12th edition). Central composite design was selected as subtype of RSM. ANOVA (Analysis of Variance) test was employed to analyze the means of three replicates on Prism 9 software (GraphPad, San Diego, CA). Tukey's test was used to measure the significance between means through.

RESULTS AND DISCUSSION

Table 2 presents the experimental design and the findings depending on the conditions for the extraction of biomolecules from sour cherry peels by MAE process. Central composite design (CCD) was selected as subtype of RSM. 13 experimental runs were designed by the CCD for the MAE system with 3 factors and 2 levels.

Table 2: Experimental results formed by CCD*.

	A: Mass (g)	B: Water ratio (% <i>v/v</i>)	TPC (mg-GAE/g-FP)	TA (mg-cyn-3-glu/g-FP)	Cyanidin-3-glucoside (mg/g-FP)
1	0.5	35	9.68±0.001 ^a	2.08±0.000 ^a	2.10±0.002 ^a
2	0.3	35	9.28±0.002 ^b	2.12±0.001 ^b	1.00±0.002 ^b
3	0.1	50	16.62±0.000 ^c	3.31±0.001 ^c	5.49±0.001 ^c
4	0.3	35	9.28±0.003 ^d	2.20±0.002 ^d	1.04±0.003 ^d
5	0.3	35	9.56±0.001 ^e	2.24±0.003 ^e	1.36±0.001 ^e
6	0.3	50	9.67±0.002 ^f	2.47±0.004 ^f	1.67±0.000 ^f
7	0.1	35	17.70±0.001 ^g	3.22±0.002 ^g	4.35±0.001 ^g
8	0.5	50	8.45±0.000 ^h	2.21±0.003 ^h	2.58±0.002 ^h
9	0.1	20	18.14±0.004 ⁱ	2.69±0.002 ⁱ	3.91±0.001 ⁱ
10	0.3	35	7.96±0.001 ^j	2.10±0.003 ^j	1.15±0.003 ^j
11	0.5	20	7.14±0.000 ^k	1.85±0.001 ^k	2.65±0.001 ^k
12	0.3	20	7.15±0.001 ^l	1.57±0.000 ^l	0.72±0.000 ^l
13	0.3	35	9.89±0.001 ^m	2.35±0.001 ^m	1.03±0.001 ^m

* Data are given as the mean (3 replicates) ± standard deviation

**The values with different superscript letters in a column are significantly different ($p < 0.05$).

Modeling Study

Quadratic models derived for MAE system for the extraction of phytochemicals from sour cherry peels are given below (Eqs. 1-3):

$$Y_{\text{TPC}} = 9.24 - 4.53A + 0.3841B + 0.7075AB + 4.34A^2 - 0.9359B^2 \quad (\text{Eq. 1})$$

$$Y_{\text{TA}} = 2.20 - 0.5126A + 0.3144B - 0.0649AB + 0.4717A^2 - 0.1603B^2 \quad (\text{Eq. 2})$$

$$Y_{\text{Cyanidin-3-glucoside}} = 1.07 - 1.07A + 0.4120B - 0.4120AB + 2.28A^2 + 0.2488B^2 \quad (\text{Eq. 3})$$

ANOVA (analysis of variance) test results for 3 responses (TPC, TA, and cyanidin-3-glucoside) are given in Table 3. All of the quadratic models generated for TPC, TA, and cyanidin-3-glucoside are statistically significant ($P < 0.0001$) at 95% of confidence interval. The coefficients of

determination of second-order equations are extremely strong ($R^2 > 0.97$), which means that 97.12%, 96.28%, and 99.28% of the variabilities in the Y (response) values can be described by the quadratic models. Moreover, R^2 s are in reasonable agreement with the adjusted R^2 s, supporting the

significance of the derived models. Moreover, a non-significant lack of fit also backs the models up ($P > 0.05$). Furthermore, the coefficient of variation ($<10\%$) demonstrates the reliability of the experimental output.

Optimization Study

The ANOVA table (Table 3) also provides us with an identification of the effects of process parameters on the responses. P-values of less than 0.05 demonstrate the importance of the terms. Generally, the amount of the raw material has been found to be the most effective at $P < 0.0001$ for the three responses. On the other hand, the second order was much more effective for the third response (cyanidin-3-glucoside) considering its highest F-value.

Design-Expert software also has the opportunity to provide us with 3D (three dimensional) images in order to comprehend these process effects visually. Figures 2a, 2b, and 2c show the effects of process parameters (amount of peels and water content in the DES) on the MAE system for TPC, TA, and cyanidin-3-glucoside yields, respectively. In general, increasing the mass resulted in lower yields. This might be expectable due to the mass transfer phenomenon, where the amount of solvent in contact with the solid material decreases. Regarding water addition into the DES, water's amount in the solvent enhanced the extraction in terms of all dependent variables. Water has an important role in deep eutectic mixtures in several respects, such as improving the viscosity problems and increasing the polarity (18).

Table 3: Analysis of variance test results.

	Source	Sum of Squares	df	Mean Square	F Value	p-value Prob > F	
TPC (mg-GAE/g-FP)	Model	179.74	5	35.95	47.16	< 0.0001	significant
	A-	123.14	1	123.14	161.56	< 0.0001	
	B-	0.8851	1	0.8851	1.16	0.3169	
	AB	2.00	1	2.00	2.63	0.1491	
	A ²	52.04	1	52.04	68.28	< 0.0001	
	B ²	2.42	1	2.42	3.17	0.1180	
	Residual	5.34	7	0.7622			
	Lack of Fit	3.18	3	1.06	1.96	0.2616	not significant
	Pure Error	2.16	4	0.5395			
	Cor Total	185.08	12				
<i>C.V. = 8.08 %</i>		<i>R²=0.9712</i>		<i>Adjusted R²=0.9506</i>		<i>Predicted R²=0.8094</i>	
TA (mg-cyn-3-glu/ g-FP)	Model	2.80	5	0.5605	36.27	< 0.0001	significant
	A-	1.58	1	1.58	102.02	< 0.0001	
	B-	0.5931	1	0.5931	38.38	0.0004	
	AB	0.0169	1	0.0169	1.09	0.3310	
	A ²	0.6145	1	0.6145	39.76	0.0004	
	B ²	0.0709	1	0.0709	4.59	0.0694	
	Residual	0.1082	7	0.0155			
	Lack of Fit	0.0677	3	0.0226	2.23	0.2271	not significant
	Pure Error	0.0405	4	0.0101			
	Cor Total	2.91	12				
<i>C.V. = 5.31 %</i>		<i>R²=0.9628</i>		<i>Adjusted R²=0.9363</i>		<i>Predicted R²=0.7447</i>	
Cyanidin-3-glucoside (mg/g-FP)	Model	26.94	5	5.39	192.56	< 0.0001	significant
	A-	6.86	1	6.86	245.01	< 0.0001	
	B-	1.02	1	1.02	36.40	0.0005	
	AB	0.6791	1	0.6791	24.27	0.0017	
	A ²	14.35	1	14.35	512.96	< 0.0001	
	B ²	0.1710	1	0.1710	6.11	0.0427	
	Residual	0.1959	7	0.0280			
	Lack of Fit	0.1098	3	0.0366	1.70	0.3033	not significant
	Pure Error	0.0860	4	0.0215			
	Cor Total	27.13	12				
<i>C.V. = 7.48 %</i>		<i>R²=0.9928</i>		<i>Adjusted R²=0.9876</i>		<i>Predicted R²=0.9650</i>	

As we already mentioned, RSM approach also provided us with optimization of a system in order to maximize the yields (19). Table 4 summarizes the optimum conditions and the maximum findings. In order to verify the results, a validation study was also performed. The difference between the actual

and predicted values depending on the derived second-order models also confirms the reliability of the outcome. Figures 3a, 3b, and 3c also demonstrate the agreement of experimental and estimated results with each other for every response.

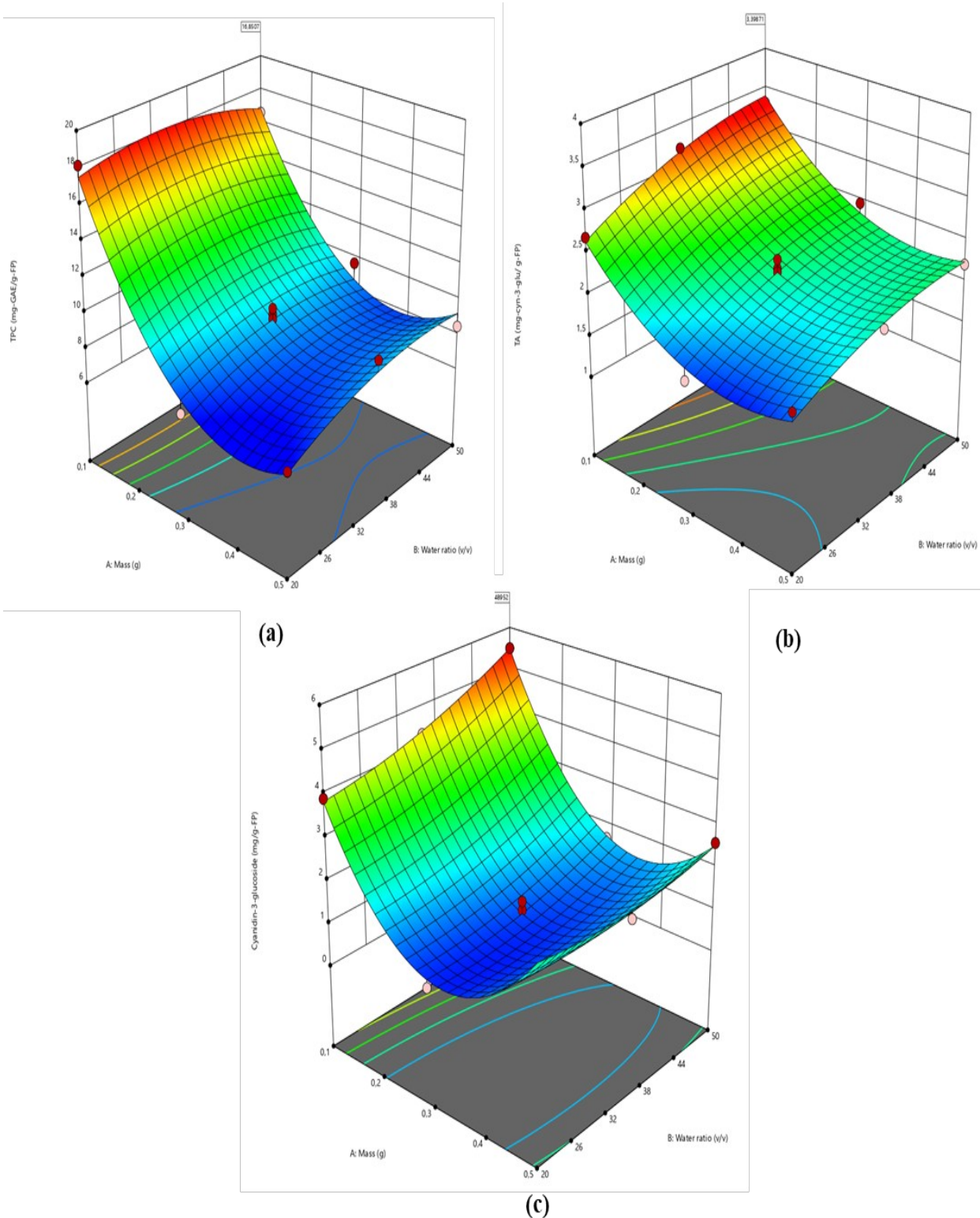


Figure 2: Response surface plot for the TPC (a), TA (b), and cyanidin-3-glucoside (c) as a function of mass to water ratio.

Table 4: Verification results of the optimum conditions for the MAE.

Optimum Extraction Conditions		Response	Predicted	Experimental	Error
A (g)	B (% v/v)				
0.1	50	TPC	16.85	17.10	1.46%
		TA	3.39	3.45	1.74%
		Cyanidin-3-glucoside	5.49	5.52	0.54%

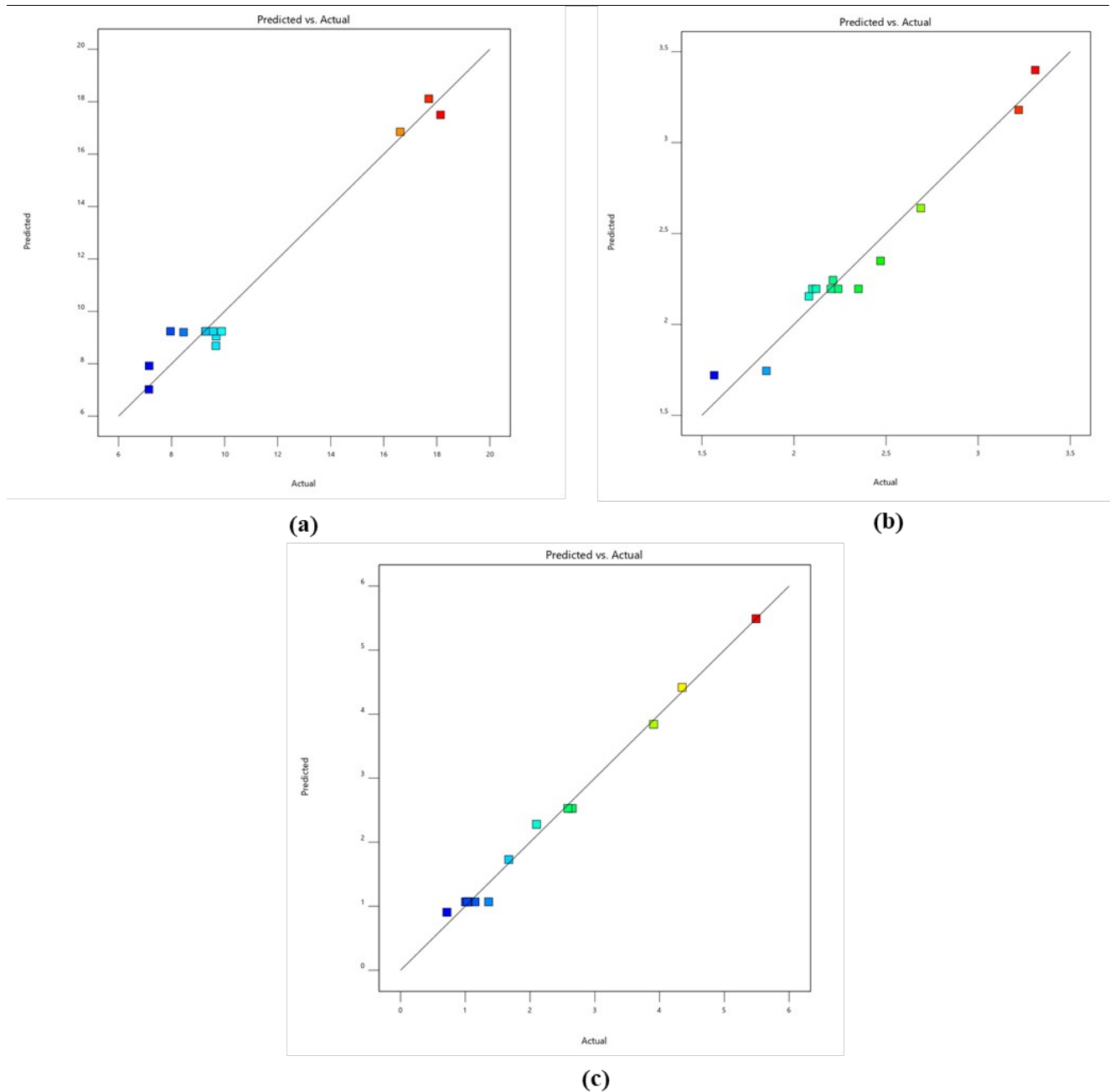
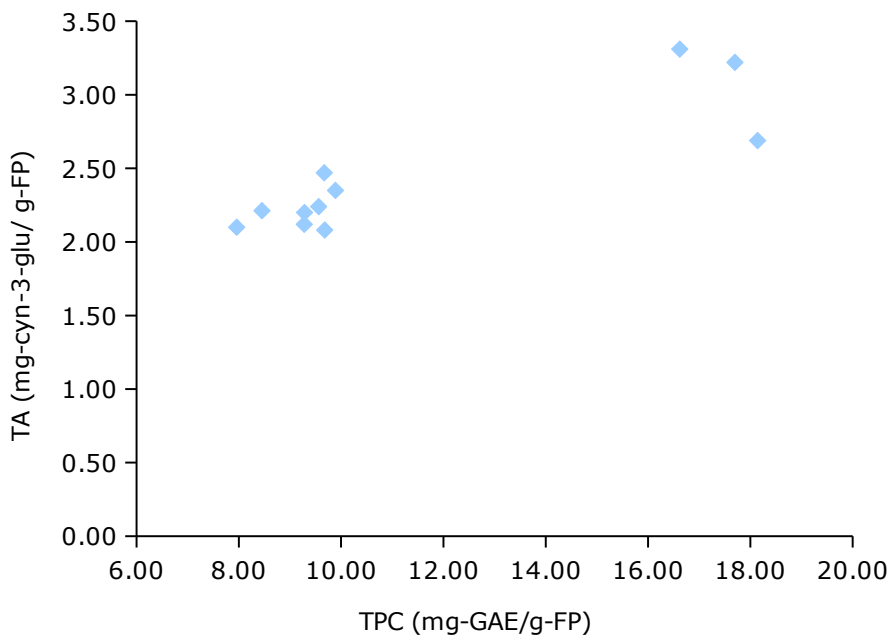


Figure 3: Actual findings versus predicted findings for TPC (a), TA (b), and cyanidin-3-glucoside (c).

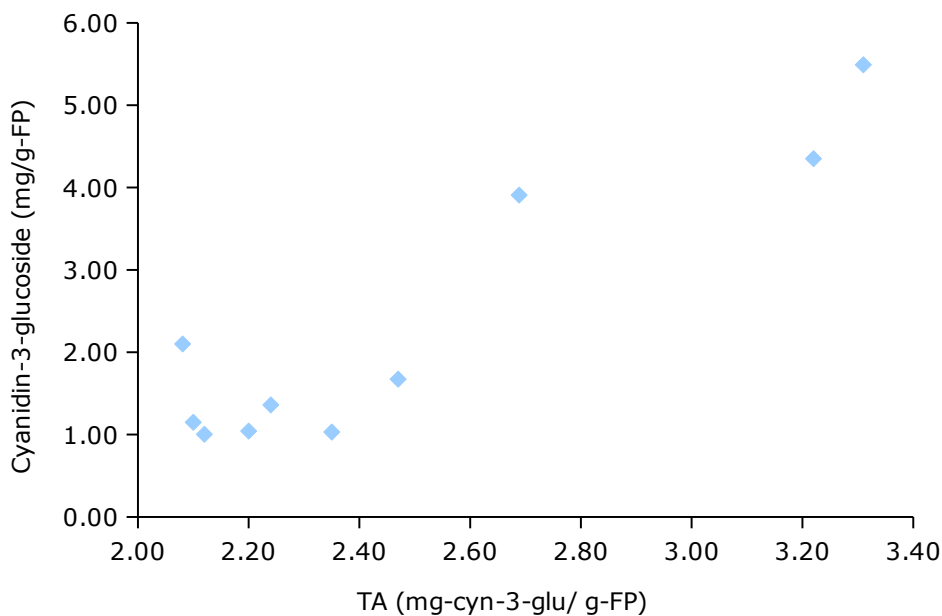
Evaluation of Bioactivity Test Results

The relationship between the measured values has also been established by means of correlations (r), as seen in Figure 4. When the correlation between TPC and TA is examined (Figure 4a), it can be concluded that TA makes a significant contribution

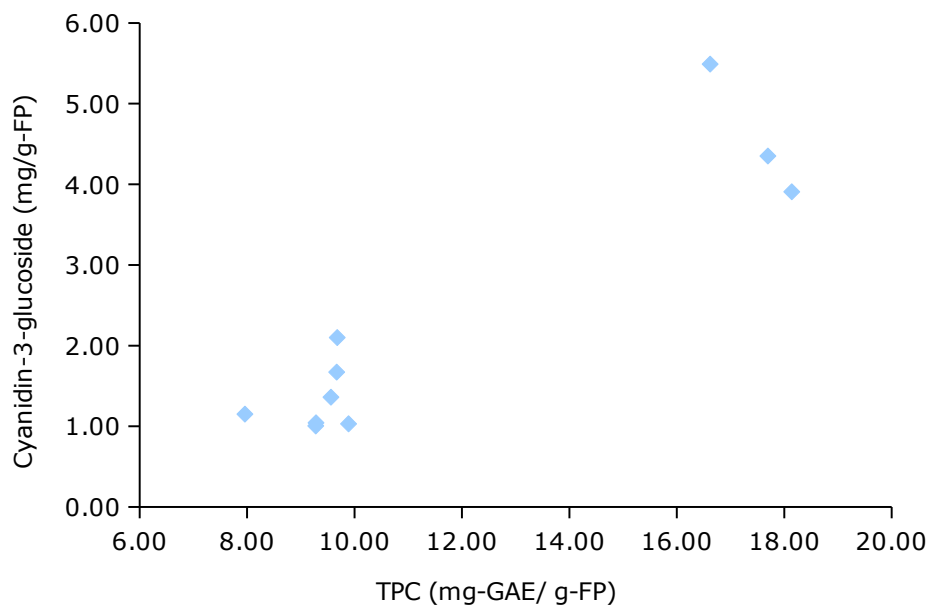
to the total amount of phenolic substances ($r > 0.80$). Similarly, there is a strong agreement between cyanidin-3-glucoside and TPC/TA ($r > 0.80$). As a result, cyanidin-3-glucoside seems to be one of the principal phenolic components in sour cherry peels.



(a)



(b)



(c)

Figure 4: Correlation between TPC and TA (a), TA and cyanidin-3-glucoside (b), and TPC and cyanidin-3-glucoside (c).

CONCLUSIONS

Microwave-assisted extraction was applied to recover fine chemicals from waste by-products of sour cherry peels. The yields were evaluated in terms of total phenolic, anthocyanin, and cyanidin-3-glucoside content. Central Composite Design with the Desing Expert software has been successfully employed for the current extraction system. The suggested second-order equations are very adequate to describe the experimental data based on several statistical indicators (F-values, P-values, non-significant lack of fit, R^2 , adjusted R^2 , predicted R^2 , and low coefficient of variation). Moreover, the relationship between anthocyanin and cyanidin-3-glucoside contents and the total phenolics of the extracts also points out that anthocyanins make a notable contribution to the total phenolics.

CONFLICT OF INTEREST

The author declares that she has no conflict of interest.

REFERENCES

- Kim DS, Lim S Bin. Semi-Continuous Subcritical Water Extraction of Flavonoids from Citrus unshiu Peel: Their Antioxidant and Enzyme Inhibitory Activities. *Antioxidants* 2020, Vol 9, Page 360. 2020 Apr;9(5):360. [<DOI>](#).
- Liew SS, Ho WY, Yeap SK, Bin Sharifudin SA. Phytochemical composition and in vitro antioxidant activities of Citrus sinensis peel extracts. *PeerJ*. 2018 Aug;2018(8):e5331. [<DOI>](#).
- Long X, Zeng X, Yan H, Xu M, Zeng Q, Xu C, et al. Flavonoids composition and antioxidant potential assessment of extracts from Gannanzao Navel Orange (*Citrus sinensis* Osbeck Cv. Gannanzao) peel. *Nat Prod Res*. 2021;35(4):702–6. [<DOI>](#).
- González-Montelongo R, Gloria Lobo M, González M. Antioxidant activity in banana peel extracts: Testing extraction conditions and related bioactive compounds. *Food Chem*. 2010 Apr;119(3):1030–9. [<DOI>](#).
- Suárez B, Álvarez ÁL, García YD, Barrio G del, Lobo AP, Parra F. Phenolic profiles, antioxidant activity and in vitro antiviral properties of apple pomace. *Food Chem*. 2010 May 1;120(1):339–42. [<DOI>](#).
- Suleria HAR, Barrow CJ, Dunshea FR. Screening and Characterization of Phenolic Compounds and Their Antioxidant Capacity in Different Fruit Peels. *Foods* 2020, Vol 9, Page 1206 [Internet]. 2020 Sep 1 [cited 2021 Nov 26];9(9):1206. [<DOI>](#).
- Zhao X, Zhang W, Yin X, Su M, Sun C, Li X, et al. Phenolic Composition and Antioxidant Properties of Different Peach [*Prunus persica* (L.) Batsch] Cultivars in China. *Int J Mol Sci* 2015, Vol 16, Pages 5762-5778 [Internet]. 2015 Mar 12 [cited 2021 Nov 26];16(3):5762–78. [<DOI>](#).
- Fazio A, Iacopetta D, Torre C La, Ceramella J, Muià N, Catalano A, et al. Finding solutions for

- agricultural wastes: antioxidant and antitumor properties of pomegranate Akko peel extracts and β -glucan recovery. *Food Funct* [Internet]. 2018 Dec 13 [cited 2021 Nov 26];9(12):6618–31. <DOI>.
9. Kurtulbaş Şahin E, Bilgin M, Şahin S. Automatic solvent extraction of sour cherry peels and storage stability of the products. *Biomass Convers Biorefinery* [Internet]. 2020 Aug 21 [cited 2020 Sep 21];1–11. <DOI>.
10. Toydemir G, Capanoglu E, Gomez Roldan MV, De Vos RCH, Boyacioglu D, Hall RD, et al. Industrial processing effects on phenolic compounds in sour cherry (*Prunus cerasus* L.) fruit. *Food Res Int*. 2013 Aug 1;53(1):218–25. <DOI>.
11. Kołodziejczyk K, Sójka M, Abadias M, Viñas I, Guyot S, Baron A. Polyphenol composition, antioxidant capacity, and antimicrobial activity of the extracts obtained from industrial sour cherry pomace. *Ind Crops Prod*. 2013;51:279–88. <DOI>.
12. Okur İ, Baltacıoğlu C, Ağçam E, Baltacıoğlu H, Alpas H. Evaluation of the Effect of Different Extraction Techniques on Sour Cherry Pomace Phenolic Content and Antioxidant Activity and Determination of Phenolic Compounds by FTIR and HPLC. *Waste and Biomass Valorization* [Internet]. 2019 Dec 1 [cited 2021 Nov 26];10(12):3545–55. <DOI>.
13. Demirdöven A, Karabiyikli Ş, Tokatli K, Öncül N. Inhibitory effects of red cabbage and sour cherry pomace anthocyanin extracts on food borne pathogens and their antioxidant properties. *LWT - Food Sci Technol*. 2015 Sep 1;63(1):8–13. <DOI>.
14. Zhang HF, Yang XH, Wang Y. Microwave assisted extraction of secondary metabolites from plants: Current status and future directions. *Trends Food Sci Technol*. 2011 Dec 1;22(12):672–88. <DOI>.
15. Şahin EK, Bilgin M, Şahin S. Recovery of anthocyanins from sour cherry (*Prunus cerasus* L.) peels via microwave assisted extraction: monitoring the storage stability. *Preparative Biochemistry & Biotechnology*. 2020; 51(7): 686-96. <DOI>.
16. Kurtulbaş E, Pekel AG, Bilgin M, Makris DP, Şahin S. Citric acid-based deep eutectic solvent for the anthocyanin recovery from *Hibiscus sabdariffa* through microwave-assisted extraction. *Biomass Convers Biorefinery*. 2020; 12: 351-60. <DOI>.
17. Albarri R, Toprakçı İ, Kurtulbaş E, Şahin S. Estimation of diffusion and mass transfer coefficients for the microwave-assisted extraction of bioactive substances from *Moringa oleifera* leaves. *Biomass Convers Biorefinery*. 2021; <DOI>.
18. Yücel M, Şahin S. An eco-friendly and sustainable system for monitoring the oleuropein-rich extract from olive tree (*Olea europaea*) leaves. *Biomass Convers Biorefinery*. 2021 May;1–14. <DOI>.
19. Bezerra MA, Santelli RE, Oliveira EP, Villar LS, Escalera LA. Response surface methodology (RSM) as a tool for optimization in analytical chemistry. *Talanta*. 2008;76(5):965–77. <DOI>.



Waste Polyurethane Reinforced Polyester Composite, Production and Characterization

Maruf Hurşit DEMİREL¹ , Ercan AYDOĞMUŞ*² 

¹Firat University, Faculty of Science, Department of Chemistry, Elazığ, Turkey.

²Firat University, Faculty of Engineering, Department of Chemical Engineering, Elazığ.

Abstract: In this research, new composite materials were improved by reinforcing the environment-polluting waste polyurethane (WPU) to unsaturated polyester (UP). Polyester composites were produced with WPU, UP, methyl ethyl ketone peroxide (MEKP), and cobalt octoate (Co. Oc.). The effect of WPU on the changes in density, Shore D hardness, thermal conductivity coefficient, thermal stability, and porosity of the obtained composites were investigated. According to the findings, as WPU ratio increased in the composite, both the thermal conductivity coefficient and the density of the composite decreased. Shore D hardness was been found to decrease as the rate of WPU in polyester composites raised. The use of optimum WPU ratios (7 wt.%) in composite production improved some thermo-physical properties of polyester composite. The high use of WPU negatively affected both the surface morphology and thermal stability of the polyester composite. In addition, the parameters affecting the production of polyester composites were optimized according to response surface methodology (RSM).

Keywords: Polyester composite, density, Shore D hardness, thermal conductivity.

Submitted: May 14, 2021. **Accepted:** March 01, 2022.

Cite this: Demirel M, Aydoğmuş E. Waste Polyurethane Reinforced Polyester Composite, Production and Characterization. JOTCSA. 2022;9(2):443-52.

DOI: <https://doi.org/10.18596/jotcsa.937332>.

***Corresponding Author. E-mail:** ercanaydogmus@firat.edu.tr.

INTRODUCTION

Studies on the hybrid use of polymers are increasingly widespread in the literature. The bond structure, hardness, brittleness, density, porosity, mechanical and thermal properties of polymers enable them to be used for different purposes according to the sectors. In this research using unsaturated polyester and polyurethane hybrid composites, it has been observed that the mechanical properties give optimum results at 5 wt.% polyurethane content (1).

Utilizing rubber waste as additives and fillers eliminates the environmental problem and ensures economic polymer composites. It has been determined that the thermal stability of the polyurethane composites obtained with 5 wt.%, 10 wt.%, and 20 wt.% waste rubber reinforcement

has improved. Also, rubber reinforcement increased the density of the polyurethane and strengthened its mechanical properties. Rubber increased the surface roughness and high compressibility of the polyurethane composite while reducing its porosity (2-5).

Polyurethane's physical and chemical properties, epoxy and polyester resins are improved with polymers such as waste rubber. It has been demonstrated that the thermal stability and thermoset properties of the composite matrix obtained can be improved. It is a resin that is used with epoxy, coatings, adhesives, fibrous structures, or particle filters. Epoxy resins have been used to produce composite materials as a thermosetting polymer with high chemical, thermal, and electrical resistance. It is preferred in many applications due to its improved thermal and mechanical properties

according to the purpose of use. Studies have also been conducted to improve the unsaturated polyester resin's mechanical performance and thermal stability with the isocyanate component (6,7).

Physical and chemical characterization processes have been carried out on an article that is made of sugar palm stems reinforced with epoxy, polyester, and polyurethane resin. The performance of palm stem filler varies between 2 wt.% and 10 wt.% and 90 wt.%, and 98 wt.% resin mixtures have been mixed under high pressure, and temperature, and their performances are compared. As the amount of filler by mass has been increased, the density of all three resins has decreased, and their porosity has gone up. Although the mechanical strength of composites increased, by 6 wt.% for polyurethane and up to 8 wt.% for polyester and epoxy, a negative effect on high usage rates has been observed (8).

In another study, acoustic damping flexible polyurethane foams have been synthesized using saturated aliphatic polyesters, methylene diphenyl diisocyanate, and other reagents. It has been observed that many physical properties, such as average cell size, distribution, surface roughness, and open-cell structure, are affected by microphase separation. Although the cell size decreased from 360 nm to 180 nm, it was determined that the compressive strength, open-cell structure, roughness, and cell size distribution also increased. Besides, it has been observed that polyurethanes with higher microphase separation have higher sound absorption efficiencies (9).

This study aims to use non-recyclable waste polyurethane in the polyester composite. While the density, thermal conductivity coefficient, and hardness of unsaturated polyesters decreased, their porosity and processability also increased. Thus, both environmentally problematic wastes have been used, and economical polyester composites have been obtained.

MATERIALS AND METHODS

Commercial waste polyurethane was supplied by the insulation company (İçmeli Erdem, Elazığ). The polyester components (methyl ethyl ketone peroxide (MEKP), cobalt octoate (Co. Oc.), and unsaturated polyester (UP)) were purchased from Turkuaz Polyester. For the experimental study, the factory wastes were ground into a -50/100 mesh particle size and dried at 105 °C, then added to pure unsaturated polyester and homogenized for 15 minutes at 1000 rpm at room temperature. Then, the chemical reaction was started with the help of certain amounts of MEKP and Co. Oc. catalysts. At room temperature, the mixture was mixed at 1500 rpm for 2 minutes, then poured into standard molds and allowed to cure for 1 day (20-22).

The experimental study plan and chemical composition ratios are given in Table 1. Waste polyurethane and unsaturated polyester ratios were changed by keeping Co. Oc. and MEKP ratios constant (27).

Thermogravimetric analysis (TGA) of polyester composites was performed with a Q600 STD-TA device. Besides, the surface morphologies of the composites were examined with the Carl Zeiss Ultra Plus Gemini Fesem device (SEM).

RESULTS AND DISCUSSIONS

The physical and chemical properties of the polyester composite have been characterized depending on the use of waste polyurethane in different proportions by mass. In this research, properties of polyester composites such as density, Shore D hardness, thermal conductivity coefficient, and thermal stability have been determined. As seen in Figure 1, the density of the composite decreases as the waste rate goes up.

As shown in Figure 2, the Shore D hardness of polyester composite decreased as the waste polyurethane ratio increased.

Figure 3 shows how waste polyurethane improved the insulation property of the polyester composite. In other words, it reduced the thermal conductivity coefficient.

Table 1: Experimental working plan and chemical compositions.

Experiment No	WPU (wt.%)	UP (wt.%)	Co. Oc. (wt.%)	MEKP (wt.%)
1	0	98	0.5	1.5
2	2	96	0.5	1.5
3	4	94	0.5	1.5
4	7	91	0.5	1.5
5	10	88	0.5	1.5
6	15	83	0.5	1.5

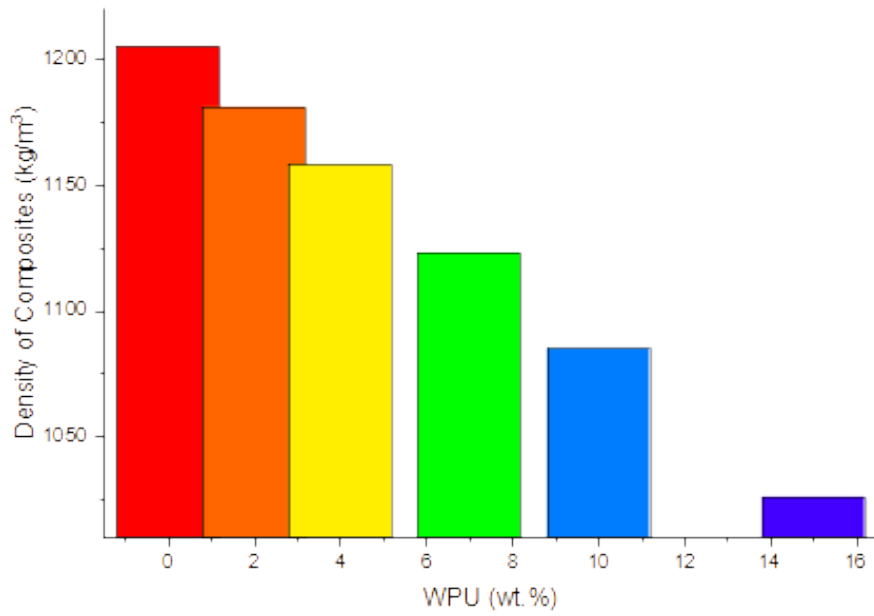


Figure 1: The change of density of the polyester composite with WPU (wt.%)

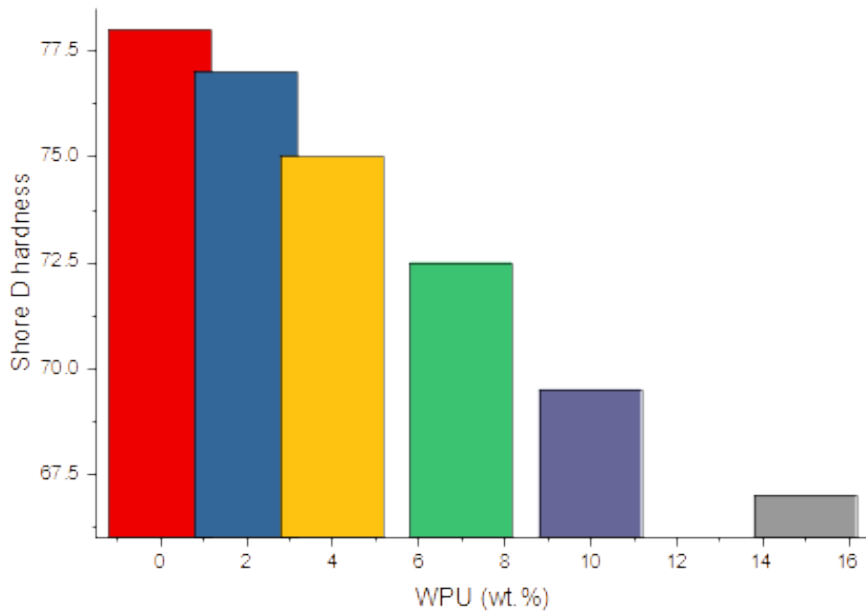


Figure 2: The variation of Shore D hardness of the polyester composite with WPU rate.

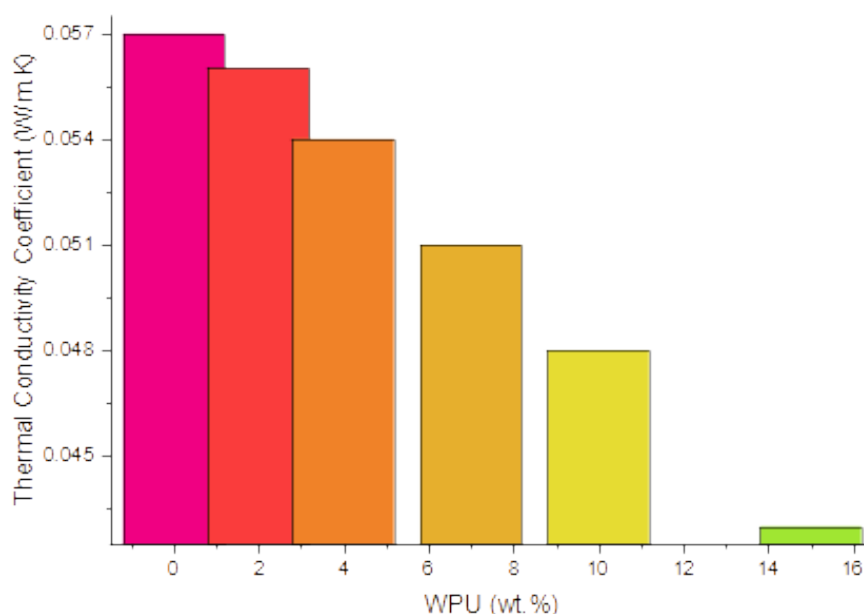


Figure 3: The change of thermal conductivity of the polyester composite with WPU (wt.%).

RSM Results for the Polyester Composites

Response surface methodology (RSM) can express the relationship between response functions and experimental data by entering the program. Optimum parameters can be determined by choosing models suitable for the data obtained in the designed experiments. It can be expressed using high-order polynomials for modeling complex systems and the most appropriate statistical approaches (10-14).

According to RSM results (Table 2), density with the natural logarithmic model, Shore D hardness with power model, and thermal conductivity coefficient with the inverse model have been preferred. The best models have been determined by statistical analysis of experimental and theoretical data (23,24).

Table 2: Evaluation of RSM results with statistical analysis.

Transform	Source	SST	F-value	P-value	R ²	Std. Dev.	Mean	C.V.%
Natural log	Quadratic	0.0465	14.64	0.0032	0.9993	0.0013	7.04	0.0108
Power	Quadratic	0.3178	177.16	0.0001	0.9994	0.0299	73.86	0.0405
Inverse	Quadratic	0.9362	5.88	0.0317	0.9833	0.2820	19.82	1.420

Figure 4 shows the effect of the waste polyurethane and unsaturated polyester rates on the composite density. The density of the composite was found to decrease as the amount of PU in the polyester mixture increased.

As it can be seen in Figure 5, Shore D hardness of the composite obtained decreased as the WPU ratio by mass increased. According to the RSM

model results, polyester composite materials with the desired hardness can be produced by using WPU and UP at certain rates (15-19).

In Figure 6, the thermal conductivity coefficient went up in direct proportion to the UP rate, while it went down inversely with WPU rate. In other words, the increase in WPU ratio by mass has improved the composite's insulation feature.

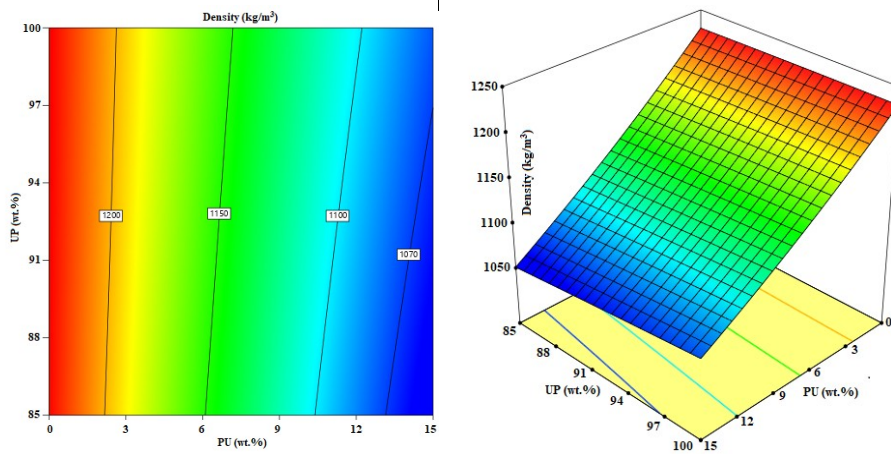


Figure 4: Variation of the density with WPU (wt.%) and UP (wt.%).

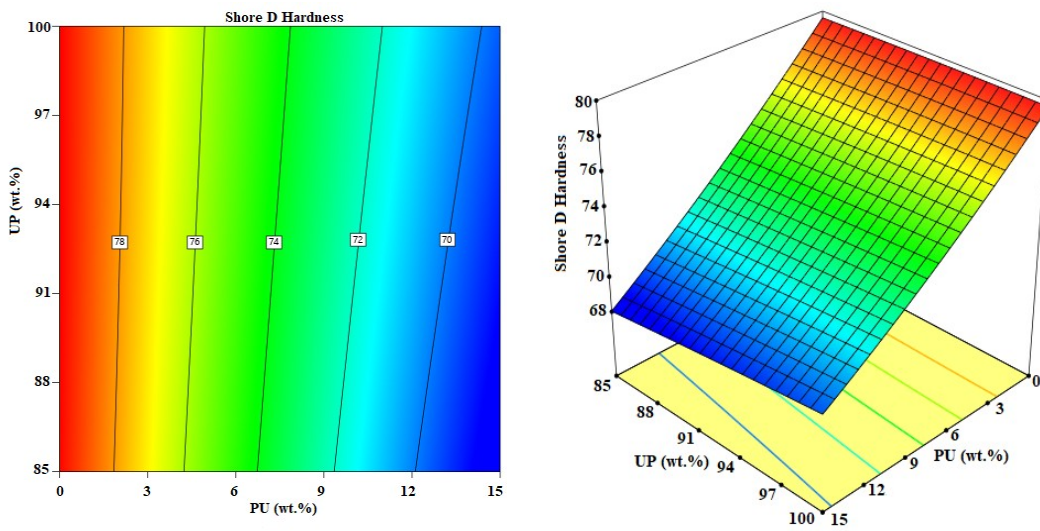


Figure 5: Change of Shore D hardness with WPU (wt.%) and UP (wt.%).

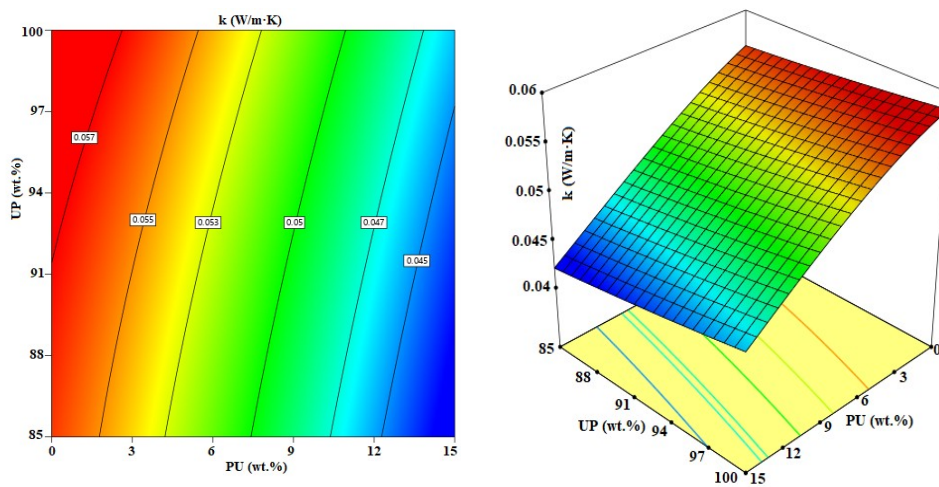


Figure 6: Variation of the thermal conductivity with WPU (wt.%) and UP (wt.%).

The equations of density, Shore D hardness, and the thermal conductivity coefficient are expressed according to the RSM results in Eq. 1, Eq. 2, and Eq. 3, respectively.

$$\ln(\rho) = +7.05331 - 0.019229 \cdot WPU + 0.001252 \cdot UP + 0.000094 \cdot WPU \cdot UP + 0.000054 \cdot WPU^2 - 6.29244 \cdot 10^{-6} \cdot UP^2 \quad (\text{Eq. 1})$$

$$\text{ShoreD} = +73.56643 - 1.47215 \cdot WPU + 0.128089 \cdot UP + 0.006933 \cdot WPU \cdot UP + 0.007418 \cdot WPU^2 - 0.000671 \cdot UP^2 \quad (\text{Eq. 2})$$

$$1/k = +15.25232 + 0.673490 \cdot WPU + 0.091456 \cdot UP - 0.005520 \cdot WPU \cdot UP + 0.012817 \cdot WPU^2 - 0.000726 \cdot UP^2 \quad (\text{Eq. 3})$$

The study has been modeled by using experimental and theoretical data. A large number of variables that affect the response of the system were examined, so the response of the process to changes in process parameters could be defined by RSM (25,26). The fact that it can be applied successfully in many different processes and enables the determination of the optimum point by considering too many responses makes the

response surface method stand out from other optimization methods (15-19).

Figure 7 shows the SEM image of the pure polyester composite, and Figure 8 shows that of the WPU (10 wt.%) reinforced composite. WPU reinforcement enhanced the porosity of the polyester composite, according to surface morphologies.

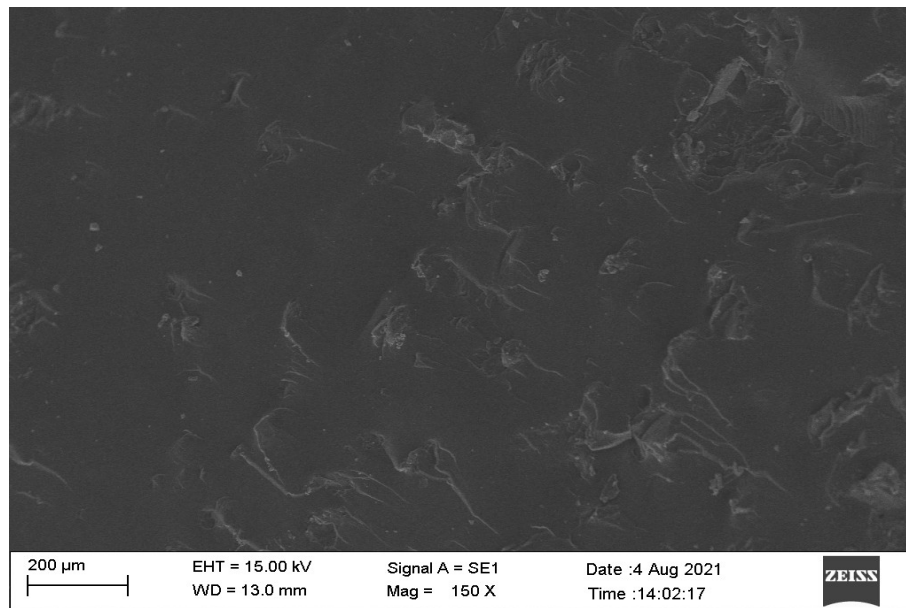


Figure 7: SEM image of the pure polyester composite (Experiment 1).

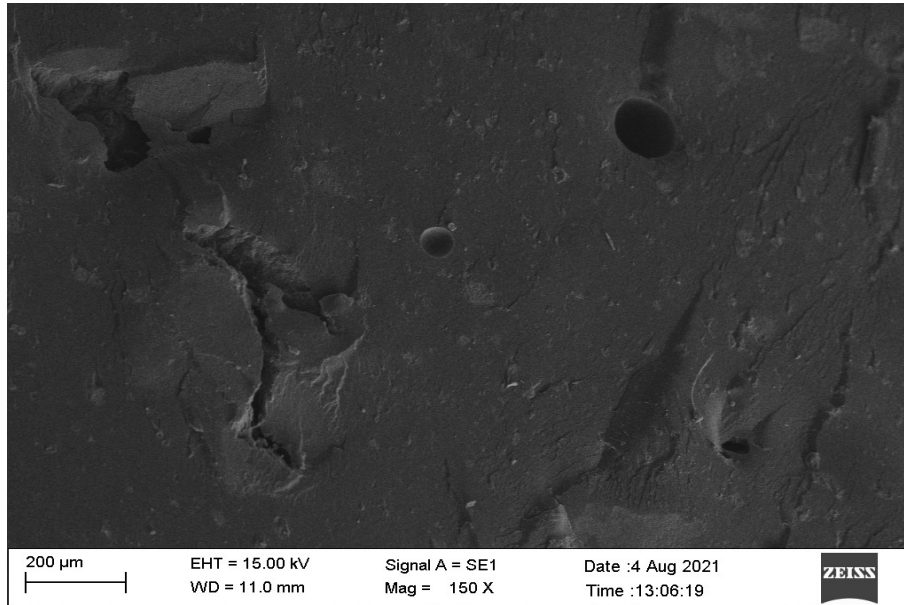


Figure 8: SEM image of the pure polyester composite (Experiment 5).

When the TGA curves (Figure 9) were studied, it was discovered that the pure polyester composite (Experiment 1) had a more stable thermal

deterioration behavior than the WPU reinforced composite (Experiment 5).

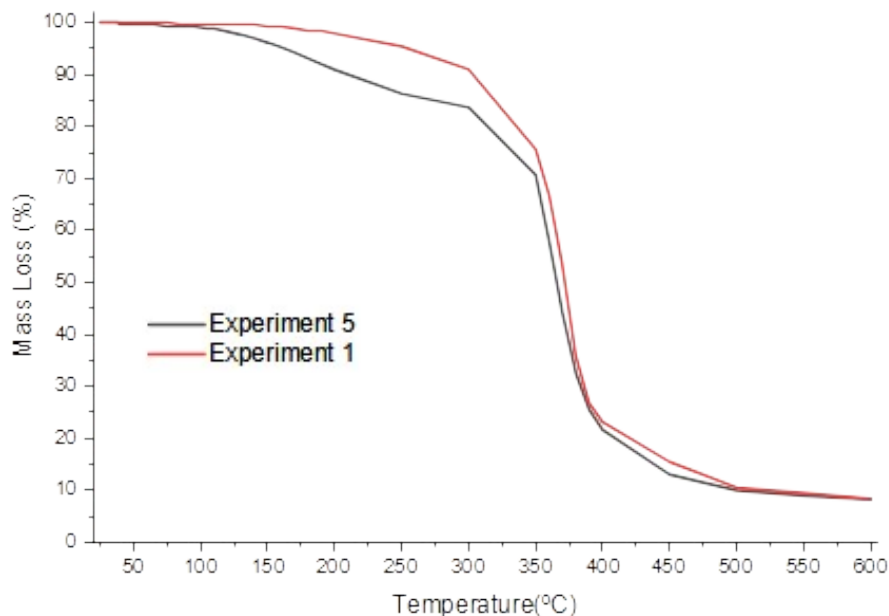


Figure 9: TGA curves of the pure polyester and 10 wt.% WPU reinforced composites.

CONCLUSIONS

This research was carried out to prevent environmental pollution from waste sponges, which are only partially recyclable, and to produce economic polyester composites. A low-density, easy to process, more flexible, and insulating composite has been produced. According to the

experimental and theoretical results, both the density and thermal conductivity coefficient of polyester composites decreased as the WPU ratio by mass increased. When the SEM images were examined, the high WPU ratio by mass caused irregular porosity in the surface of the polyester composite. As seen in TGA curves, the use of high WPU by mass has reduced the thermal stability of

the polyester composite. Also, the Shore D hardness of polyester composite decreased as the WPU ratio raised.

REFERENCES

1. Abdollahi Baghban S, Khorasani M, Sadeghi GMM. Soundproofing flexible polyurethane foams: The impact of polyester chemical structure on the microphase separation and acoustic damping. *J Appl Polym Sci*. 2018 Dec 10;135(46):46744. [<DOI>](#).
2. Silva NGS, Cortat LICO, Orlando D, Mulinari DR. Evaluation of rubber powder waste as reinforcement of the polyurethane derived from castor oil. *Waste Management*. 2020 Oct;116:131–9. [<DOI>](#).
3. Hu D, Jia Z, Zhong B, Lin J, Liu M, Luo Y, et al. Method for improving the mechanical performance and thermal stability of unsaturated polyester resin/waste-printed circuit board nonmetals composites via isocyanate chemistry. *J Appl Polym Sci*. 2017 Aug 15;134(31):45129. [<DOI>](#).
4. Hejna A, Korol J, Przybysz-Romatowska M, Zedler Ł, Chmielnicki B, Formela K. Waste tire rubber as low-cost and environmentally-friendly modifier in thermoset polymers – A review. *Waste Management*. 2020 May;108:106–18. [<DOI>](#).
5. Hejna A, Olszewski A, Zedler Ł, Kosmela P, Formela K. The Impact of Ground Tire Rubber Oxidation with H₂O₂ and KMnO₄ on the Structure and Performance of Flexible Polyurethane/Ground Tire Rubber Composite Foams. *Materials*. 2021 Jan 21;14(3):499. [<DOI>](#).
6. Włoch M, Ostaszewska U, Datta J. The Effect of Polyurethane Glycolysate on the Structure and Properties of Natural Rubber/Carbon Black Composites. *J Polym Environ*. 2019 Jun;27(6):1367–78. [<DOI>](#).
7. Semlali Aouragh Hassani F-Z, Ouarhim W, El Achaby M, Tamraoui Y, Bensalah M-O, Rodrigue D, et al. Recycled tires shreds based polyurethane binder: Production and characterization. *Mechanics of Materials*. 2020 May;144:103351. [<DOI>](#).
8. Silva NGS, Cortat LICO, Orlando D, Mulinari DR. Evaluation of rubber powder waste as reinforcement of the polyurethane derived from castor oil. *Waste Management*. 2020 Oct;116:131–9. [<DOI>](#).
9. Singh R, Singh B, Tarannum H. Mechanical properties of jute fiber-reinforced UP/PU hybrid network composites. *Polymers and Polymer Composites*. 2019 Nov;27(9):546–56. [<DOI>](#).
10. Ravikumar P, Suresh AR, Rajeshkumar G. An Investigation into the Tribological Properties of Bidirectional Jute/Carbon Fiber Reinforced Polyester Hybrid Composites. *Journal of Natural Fibers*. 2020 May 18;1–11. [<DOI>](#).
11. Thakre AA. Prediction of Erosion of Polyetherimide and Its Composites Using Response Surface Methodology. *Journal of Tribology*. 2015 Jan 1;137(1):011603. [<DOI>](#).
12. Sathiyamurthy S, Syed Abu Thaheer A, Jayabal S. Modelling and optimization of mechanical behaviors of Al₂O₃-coir-polyester composites using response surface methodology. *Indian Journal of Engineering and Materials Sciences*. 2013;20(1):59–67. [<URL>](#).
13. Li T-T, Wang R, Lou CW, Lin J-H. Evaluation of high-modulus, puncture-resistance composite nonwoven fabrics by response surface methodology. *Journal of Industrial Textiles*. 2013 Oct;43(2):247–63. [<DOI>](#).
14. Hassan MZ, Sapuan SM, Roslan SA, Aziz SA, Sarip S. Optimization of tensile behavior of banana pseudo-stem (*Musa acuminata*) fiber reinforced epoxy composites using response surface methodology. *Journal of Materials Research and Technology*. 2019 Jul;8(4):3517–28. [<DOI>](#).
15. Rajamurugan TV, Shanmugam K, Palanikumar K. Analysis of delamination in drilling glass fiber reinforced polyester composites. *Materials & Design*. 2013 Mar;45:80–7. [<DOI>](#).
16. Rajamurugan TV, Shanmugam K, Rajakumar S, Palanikumar K. Modelling and Analysis of Thrust Force in Drilling of GFRP Composites Using Response Surface Methodology (RSM). *Procedia Engineering*. 2012;38:3757–68. [<DOI>](#).
17. Jagadish, Bhowmik S, Ray A. Prediction and optimization of process parameters of green composites in AWJM process using response surface methodology. *Int J Adv Manuf Technol*. 2016 Nov;87(5–8):1359–70. [<DOI>](#).
18. Shieh C-J, Akoh CC, Koehler PE. Formulation and optimization of sucrose polyester physical properties by mixture response surface methodology. *J Amer Oil Chem Soc*. 1996 Apr;73(4):455–60. [<DOI>](#).
19. Koç B, Kaymak-Ertekin F. Yanıt Yüzey Yöntemi ve Gıda İşleme Uygulamaları. *Gıda*. 2010 Feb 1;35(1):1–8. [<URL>](#).
20. Orhan R, Aydoğmuş E, Topuz S, Arslanoğlu H. Investigation of thermo-mechanical characteristics of borax reinforced polyester composites. *Journal of Building Engineering*. 2021 Oct;42:103051. [<DOI>](#).
21. Aydoğmuş E, Arslanoğlu H, Dağ M. Production of waste polyethylene terephthalate reinforced biocomposite with RSM design and evaluation of thermophysical properties by ANN. *Journal of Building Engineering*. 2021 Dec;44:103337. [<DOI>](#).
22. Aydoğmuş E, Arslanoğlu H. Kinetics of thermal decomposition of the polyester nanocomposites. *Petroleum Science and Technology*. 2021 Jul 18;39(13–14):484–500. [<DOI>](#).
23. Aydoğmuş E, Demirpolat AB, Arslanoğlu H. Isothermal and non-isothermal drying behavior for grape (*Vitis vinifera*) by new improved system: exergy analysis, RSM, and modeling. *Biomass Conv Bioref*. 2022 Feb;12(2):527–36. [<DOI>](#).
24. Demirpolat AB, Aydoğmuş E, Arslanoğlu H. Drying behavior for *Ocimum basilicum* Lamiaceae with the new

system: exergy analysis and RSM modeling. Biomass Conv Bioref. 2022 Feb;12(2):515-26. [<DOI>](#).

25. Aydođmuş E, Dađ M, Yalçın ZG, Arslanođlu H. Synthesis and characterization of EPS reinforced modified castor oil-based epoxy biocomposite. Journal of Building Engineering. 2022 Apr;47:103897. [<DOI>](#).


26. Şahal H, Aydođmuş E. PRODUCTION AND

CHARACTERIZATION OF PALM OIL BASED EPOXY BIOCOMPOSITE BY RSM DESIGN. Hittite Journal of Science and Engineering [Internet]. 2021 Nov 30 [cited 2022 Mar 10]; [<DOI>](#).

27. Yanen C, Aydođmuş E. Characterization of Thermo-Physical Properties of Nanoparticle Reinforced the Polyester Nanocomposite. Dicle Üniversitesi Fen Bilimleri Enstitüsü Dergisi. 2021 Dec 30;10(2):121-32. [<URL>](#).



Development of Functional Guar Gum-Based Highly Water Absorbent and Investigation of Reaction Parameters

Sapna^a, Jay Singh^b and Arpit Sand*^a 

^aDepartment of Chemistry, Manav Rachna University, Faridabad 121001, India

^bDepartment of Chemistry, Institute of Science, Banaras Hindu University, Varanasi 221005 India

Abstract: The present article describes guar-gum (GG) polysaccharide-based eco-friendly highly water absorbable polymer network with itaconic acid (IA) and acrylamide (AAM) as monomers, prepared due to characteristic features such as natural abundance, biocompatibilities, and biodegradability as well as biological and physicochemical properties. The solution polymerization technique was used successfully to synthesize the GG-g-PIA-co-AAm co-polymer. In this method, IA and AAm monomer polymerize onto polysaccharides GG in an aqueous medium at 70 °C with potassium persulfate (KPS) acting as a chemical initiator and N, N'-methylene-bisacrylamide (N-MBA) acting as a cross-linker. The maximum allowed time to complete the reaction was 1 hour and 20 minutes. The consequence of the neutralization degree of itaconic acid, GG, AAm, N-MBA, and KPS was optimized. Surface morphology and binding behavior of prepared GG-g-PIA-co-AAm were characterized by FTIR and SEM microscopy. The grafting (between GG and IA and AAm and crosslinking reactions were produced by a solid chemical empathy between the NH₂ groups in the guar gum and the carboxylic groups in the poly itaconic acid, leading to the formation of amide bonds. Various parameters like free-absorbency capacity (FAC) as high as possible and (AUL) were also studied for efficient absorbent polymers. A hypothetical mechanism for polymeric reaction during polymerization has been proposed.

Keywords: Solution Polymerization, highly absorbent polymer, free-absorbency capacity (FAC), Absorbency under load, FTIR

Submitted: October 18, 2021. **Accepted:** February 27, 2022.

Cite this: Sapna, Singh J, Sand A. Development of Functional Guar Gum-Based Highly Water Absorbent and Investigation of Reaction Parameters. JOTCSA. 2022;9(2):453-64.

DOI: <https://doi.org/10.18596/jotcsa.1011386>.

***Corresponding author. Email:** arpit@mru.edu.in

INTRODUCTION

Highly absorbent polymers are cross-linked polymers (hydrophilic) that can engage and recall enormous capacities of water and solute particles in a swollen state, because of the presence of -COOH, -NH₂, -OH, and other hydrophilic groups attached to the polymeric backbone (1-2). The highly absorbent polymer is usually composed of ionic monomers and is branded by a short cross-linking density, which results in large watery curiosity sizes (up to 1000 times their weight) (3-4). Remarkably, these competent absorbent nets can grip and recall aqueous solutions up to several hundred times their weight, even while under pressure. Highly absorbent

polymers are used in a wide range of applications, including sanitation goods such as adult incontinence products, baby diapers (5) and feminine napkins (6), forestry, agriculture, horticulture, drug distribution, food storage, waste water management (11), tissue work, and biosensor (12). Because of their biocompatibility and biodegradability (15-16), natural polymers (13-14) and their derivatives (from wood or plant-based biomass) act as highly absorbents to store water and have an excellent ability to absorb water multiple times their weight.

Furthermore, GG is a naturally occurring polysaccharide derived from the guar plant that is

water-soluble, and normally nonionic. The GG is unsolvable in carbon-based solvents such as esters, alcohols, ketones, and hydrocarbons with only the exclusion of formamide. For GG, water is the most suitable solvent, and its forms at high viscosity appear uniform at very low GG concentration and at high viscosity from colloidal solution. With the existence of several OH groups across the chain, GG forms H₂ bonding in an aqueous solution, which can be explained by the big deal of its performance. The main problem of GG hurts from some interruptions like biodegradability, which restricts its application but it possesses applications like stabilizing, thickening, gelling, emulsifying, binding, etc., which can be improved through the addition of vinyl monomers (=CH₂) (IA/AAm) hydrophilic nature and extremely sensitive for polymerization.

The GG has been added by various monomers (17-20) to modify the properties of GG and greatly expands into a highly absorbent, which involved water absorbency and swelling amount. Many initiators, such as KMnO₄ (21-22), Cu²⁺(23), potassium bromate (KBrO₃) (24), KPS (25), ammonium peroxydisulfate (NH₄)₂S₂O₈ (26-27), ceric ions (Ce IV), adopted in the different type of polymerization (28-29). In case of polysaccharides, more research was done in the case of chitosan based superabsorbent polymers (30-34)

Feasible alternatives to acrylic acid and methacrylic acid-based polymers are IA and their derivatives. The main feature of IA today is that its manufacture does not depend on sources such as petrochemicals. IA deliberate its polymerization in an aqueous phase and water as a solvent for polymerization (redox pair/ initiators) received more attention by detailed investigations of methacrylic acid, (35) acrylic acid, (36) and acrylamide (37). In natural polysaccharides, AAm is widely used as grafting material and is the most significant vinyl monomer for large polymer-add-on due to its hydrophilic nature. Antimicrobial properties are also developed by grafting of water-loving polymers such as PAAm.

In this paper, polysaccharides are a novel GG-based highly absorbent polymer offering enhanced performance. Polymers were synthesized by N-MBA working as a crosslinker, and KPS played the role of the initiator in polymerization for IA:AAm with water sponginess near 450 times its weight was investigated. The effect of the NaOH, N-MBA, and KPS, as well as the reaction on the resultant absorbent things, have conversed. Also, we studied the AUL of highly absorbent polymers.

EXPERIMENTAL

Materials

IA (Sigma-Aldrich), acrylamide (Merck), GG (viscosity average molecular weight: k300 Da) was purchased from Hindustan Gums Ltd. KPS, N-MBA,

potassium bromate (KBrO₃), ammonium peroxydisulfate (NH₄)₂S₂O₈, ceric ammonium nitrate ((NH₄)₂Ce(NO₃)₆), and potassium mono sulfate(PMS) acquired from Sigma-Aldrich were used exactly as received. NaOH and NaCl were bought from E-Merck. The remaining materials were AR grade and solution prepared with DI water.

Initiator Induced Polymerization of Comonomers (IA/AAm) onto GG

GG powder 0.4 g dm⁻³ and 75 mL DI water were added into the 3-necked reactor with stirring at 400 RPM until the uniform solution was formed. The predefined quantity of itaconic acid monomer was partly defused by the drop-wise addition of 8N NaOH solution below cooling in an ice bath to remove exothermic neutralization reaction temperature. Prepared mol ratios of itaconic acid monomerto 8N NaOH solution were 1:0.65, 1:0.70, 1:0.75, 1:0.80, and 1:0.85. The neutralization ratio prop is well-defined as follows:

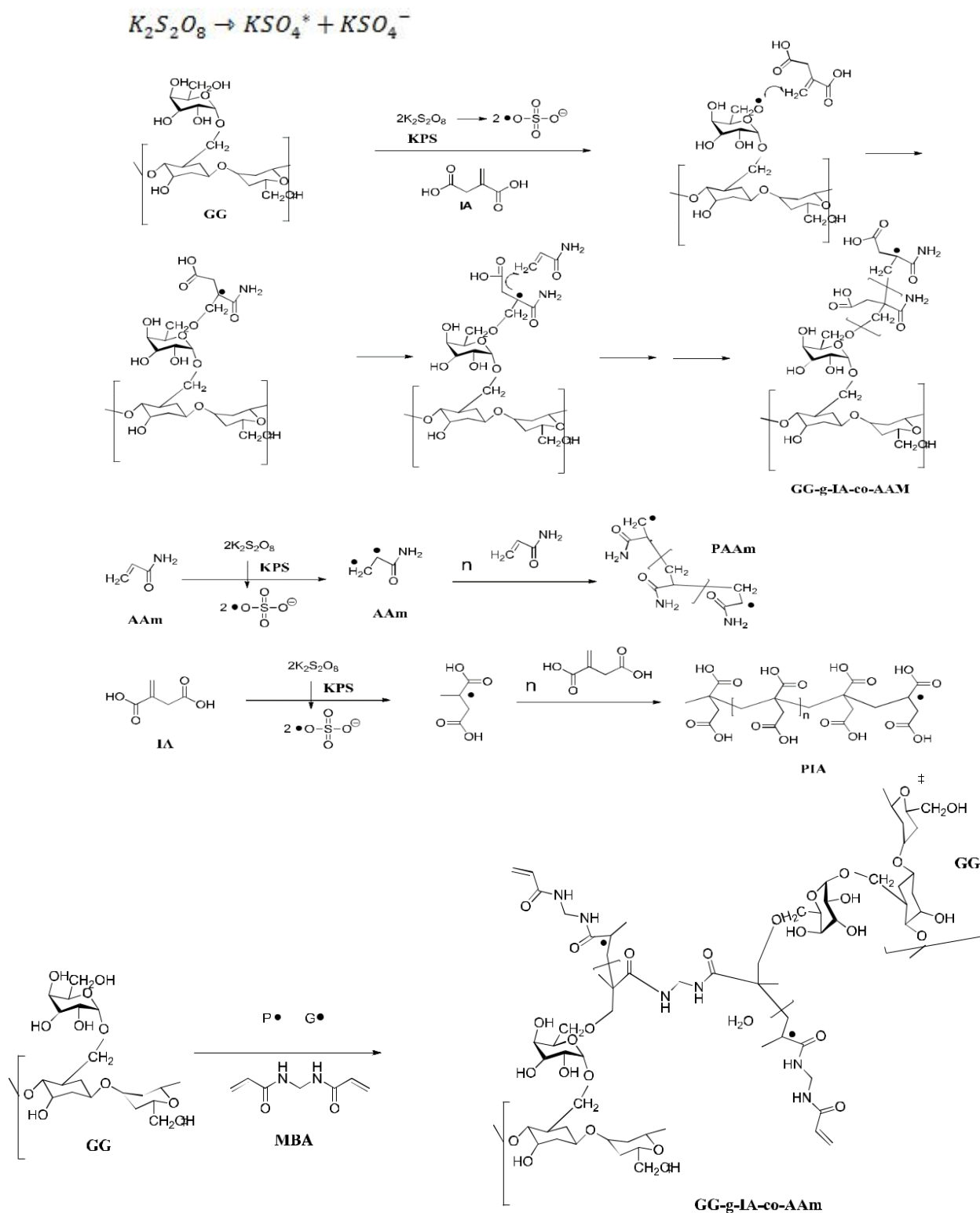
$$\text{prop} = \frac{n_a}{n_b} \quad (\text{Eq. 1})$$

Where n_a and n_b are the mol figures of itaconic acid monomer and NaOH, respectively. Then a 3-necked reactor was positioned in an oil immersion predetermined at the preferred temperature (70°C) filled with Nitrogen. The neutralized IA was drop-wise added to the 3 neck reactor with the help of dropping funnel containing GG, pre-determined amounts (1 g) of AAm, and (0.5–0.2 g) N-MBA, with stirring and degassed by blowing nitrogen for 30 minutes. After a desirable interval, 0.05 mol/L KPS (radical initiator) added. The induced polymerization of co-monomers was allowed to proceed at 70°C in nitrogen, (inert medium) 2h with magnificent at 600 RPM. The blend was permissible to cool at ambient temperature. GG-g-PIA-co-AAm was washed away by ethanol and dehydrated in a 60°C oven for 48h to persistent weight. After grinding, the powdered highly absorbent polymer (GG-g-PIA-co-AAm) was stored away from light heat and moisture. The yield of the polymerization was planned as the weight ratio of addition after the graft co-polymerization to IA/AAm monomer by the following equation-2:

$$\text{Yield} = \frac{W_{\text{GG-PIA-co-AAm}} - W_{\text{GG}}}{W_{\text{IA+AAm}}} \quad (\text{Eq. 2})$$

Where WGG-g-PIA-co-AAm is the weight of the graft copolymer (GG-g-PIA-co-AAm), WGG is the weight of the unique GG, and $W_{\text{IA+AAm}}$ is the weight of the comonomer.

The mechanism of polymerization and crosslinking reaction: (Scheme 1) planned as first the KPS as described in the previous study and then various reactions given as follows:



Scheme 1: Mechanism of polymerization and reaction involved.

CHARACTERIZATION

Infrared spectra (IR) were taken on a Bruker FT-IR spectrometer (Vector 33 Germany). SEM, (Hitachi

S-5200 Japan) was used to detect the morphology of the highly absorbent polymer.

Free water absorbency measurement

Free water absorbency for prepared polymers was determined by the well-known tea bag method (38). In this method, acrylic gauze with fine meshes usually known as a teabag, in which precisely weighted highly absorbent polymer (+0.3-0.03 g) per unit size (average) between 255-395 micrometers, was absorbed totally in 300 mL of NaCl solution for 1h to spread equilibrium swelling. At that time the extra solution is decanted by dangling the tea bag until no water fell off. The allowed water absorbency calculated in relation to equilibrated swelling (Q_{eq}) was specified by the equation:

$$Q_{eq} = \frac{W_{TB,f} - W_{TB,i}}{W_{i-g-PIA-co-AAm}} \quad (\text{Eq. 3})$$

Where W_{g-g-PIA-co-AAm} is the weight of the dehydrated GG-g-PIA-co-AAmtriturate, W_{TB,f}, and W_{TB,i} are the weight of the teabag afterward and beforehand water uptake, correspondingly.

Absorbency Under Load (AUL) measurement

AUL technique was adopted for measurement in which a cylindrical piston permitting pressure solicitation on the highly absorbent polymer placed in the medium, i.e., enlargement of particles. Water absorbance of polymeric material underneath deed for changing pressure was detected. The experiment established an easily varying cylindrical piston preserved exclusively on a glass tube fitted by pricked bottommost diskette. The calculated amount of highly absorbent polymer was retained in the cylindrical piston, and weight was put on the cylindrical piston to alter the pressure. All the assembly was secure and kept in a trench

surrounding 0.8 wt. percent NaCl. In this method that solution height outside the width of a highly absorbent polymer. The swelling amount underfed was measured over a period of period for an assumed weight at ambient temperature.

AUL calculated with the use of Equation 4.

$$AUL \left(\frac{g}{g} \right) = \frac{W_1 - W_0}{W_0} \quad (\text{Eq. 4})$$

Where W₁ swollen gel weight (under the given pressure) and W₀ is polymer weight (dry).

RESULT AND DISCUSSION

Proof of Grafting

The Fourier transfer spectra of polysaccharide guar gum explained in Figure-1 and peak at 3346 and 2909 cm⁻¹ due to -OH vibration (widening) and -C-H vibration (stretching) respectively. Peak 1420 and 1300 cm⁻¹ assigned due to scissoring (-CH₂) and vibration bending (-OH) respectively. CH-O-CH₂ stretching (39) is assigned by the peak at 1080 cm⁻¹. Figure 2 explains the Fourier transfer spectra of highly absorbent polymer GG-g-PIA-co-AAm obtained by the copolymerization process. The shifting of peak 3344 cm⁻¹ to 3610 cm⁻¹ when related with spectra of guar gum due to -OH vibration (splayed) guar gum which shows dipping asset elaborate in polymeric reactions. The peak at 2955 cm⁻¹ assigned for stretching vibration (C-H) and angular distortion (widening) C=C stretching at 1610 cm⁻¹ further confirmed the polymerization reaction. -CN bond peak allocated at 1411 cm⁻¹ and 719~668 cm⁻¹ accredited to NH flapping vibration.

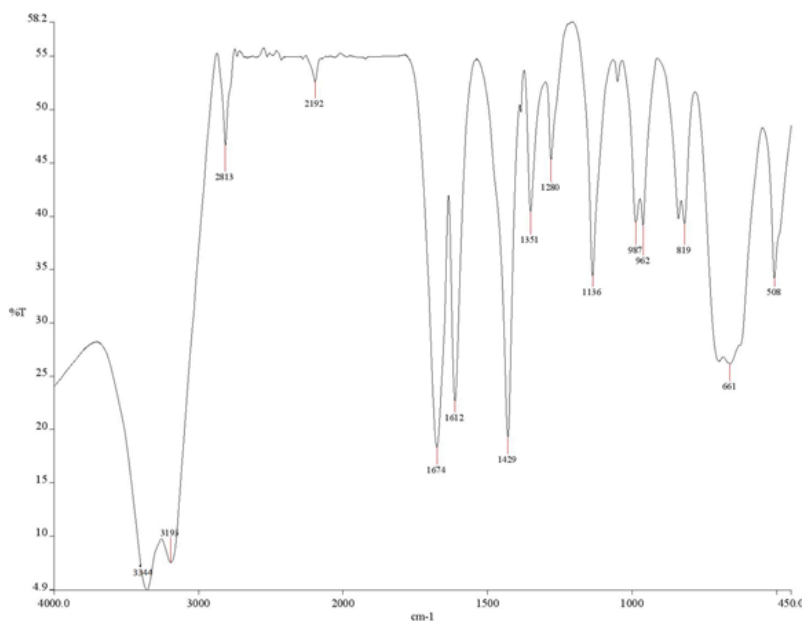


Figure 1: FT-IR spectrum of GG.

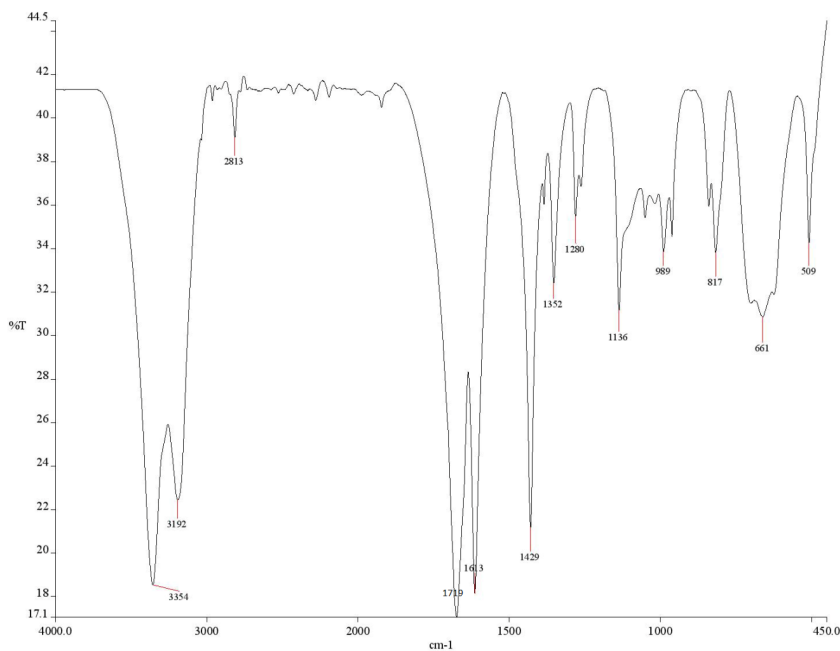


Figure 2: FT-IR spectrum of GG-g-PIA-co-Aam.

Scanning Electron Microscopy (SEM)–Guar gum and GG-g-PIA-co-AAm morphology was studied by SEM analysis characterized native guar gum (Figure 3a) precast with rotund structures but highly absorbent

polymer showed that (GG-g-PIA-co-AAm), uneven shaped (junkyard) gatherings were invented due to IA/AAm combined and represented in Figure 3(b).

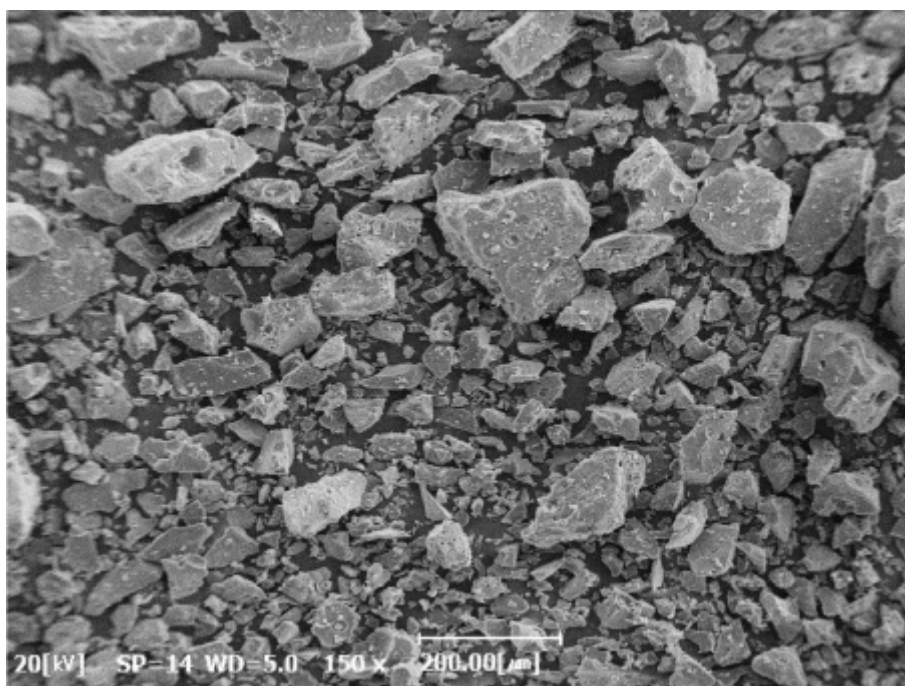


Figure 3(a) SEM micrograph of GG.

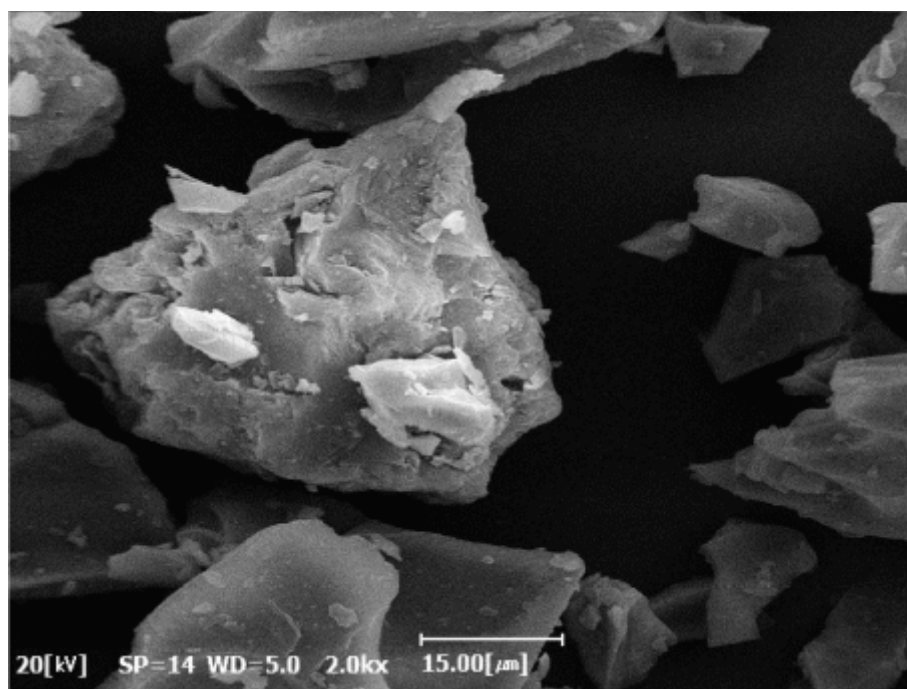


Figure 3(b): SEM micrograph of GG-*g*-PIA-*co*-Aam.

Optimization of Solution Polymerization

Choice of Initiators

There are several initiation systems available for the polymerization, but for the selection of the best initiation system for the vinyl monomers' polymerization onto natural polysaccharides, we tested five altered arrangements which includes potassium bromate (KBrO_3), KPS, ammonium peroxydisulfate ($(\text{NH}_4)_2\text{S}_2\text{O}_8$), ceric ammonium nitrate ($\text{H}_8\text{N}_8\text{CeO}_{18}$), and potassium mono sulfate (Table-1). KPS gave the best result, which included the highest yield and conversion after 3-hour polymerization. But in the case of KBrO_3 ,

($\text{H}_8\text{N}_8\text{CeO}_{18}$), PMS, and $(\text{NH}_4)_2\text{S}_2\text{O}_8$ gave 85, 75, 64, and 60 of conversion, respectively. Absorbency of the highly absorbent polymer was the peak value (21.7 g/g) for the KPS scheme in saline solution (0.9 wt% NaCl). Firstly, potassium persulfate ions ($\text{O}_8\text{S}_2^{2-}$) are readily disconnected to sulfate-anion-radicals (thermally), which abstract H_2 from the -OH groups on C_2 atom in the GG chain to form consistent alkoxy radicals (40). These radicals started the grafting of IA/AAM onto GG polysaccharides, which lead to cross-linked polymers in the company of N-MBA cross-linker.

Table 1: Effect of Various Initiators on Free Radical Polymerization of GG-*g*-PIA-*co*-AAM ^a.

Initiator	Yield (%)	Absorbency (g/g)
Potassium persulfate (KPS)	92	28
Potassium Bromate (KBrO_3)	87	24
Ceric Ammonium Nitrate (CAN)	77	20
Potassium Monosulfate (PMS)	66	17
Ammonium Peroxydisulfate ($(\text{NH}_4)_2\text{S}_2\text{O}_8$)	62	15

Influence of initiator concentration

The influence of the initiator (KPS) concentration on the reaction (polymeric) and H₂O absorbency for highly absorbent polymer was also investigated. The KPS concentration changed from 0.1 to 1.1 weight percent to monomers. The water absorbency of the highly absorbent polymer was improved primarily by

growing the KPS concentration up to 0.5 wt. percent, but it reduced later, as shown in Figure-4. When KPS was used as in free radical polymerization it was clear that the molecular weight will fall with the increase of the KPS amount. A further reason for falls in the MW is that the comparative quantity of polymeric arrangement

surfaces increases at levels of KPS concentration. A bimolecular collisions, which in turn raises the cross-linker density (19).
 rise in the status of the dismissingstep reaction by

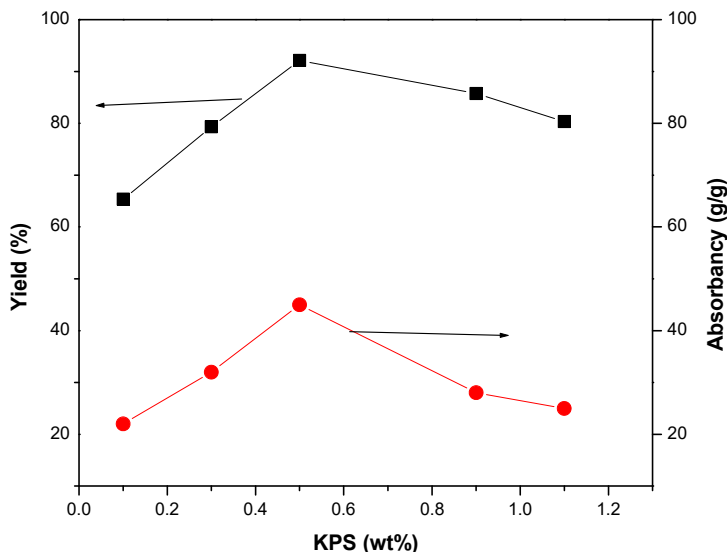
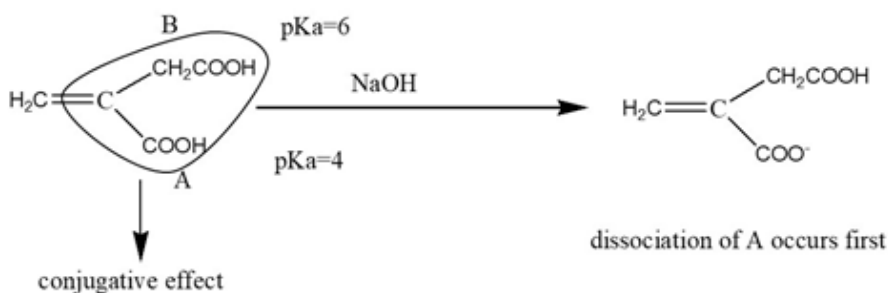


Figure 4: Effect of KPS concentration on (a) yield of graft polymerization and (b) absorbency of the resulting GG-g-PIA-co-AAm.

Influence of degree of neutralization (Dn)

The effect neutralization degree ranges from 50 to 90 percent of IA on the water absorbency (Figure-5). As the neutralization degree of IA rised, water absorbency rised from 50 to 70%. The gripping effect of in-between carboxylate and carboxylic acid groups was explained by the fall in water absorbency and higher in each group, which could be explained the polymerization process naturalization mechanism (Scheme 2). In previously

reported work, two carboxyl groups have dissimilar PKa (4 and 6) -COOH groups assigned by A and B in the scheme-3. When IA neutralize group A (represented by -COOH next to =bond in conjugative effect generated with A while B carboxyl group in which CH2 worked as an electron-donor. In this particular case, carboxyl group assigned by A dissociate first and easily explain the influence of the degree of neutralization during the polymerization process.



Scheme 2: Mechanism of partial neutralization of Ia monomer.

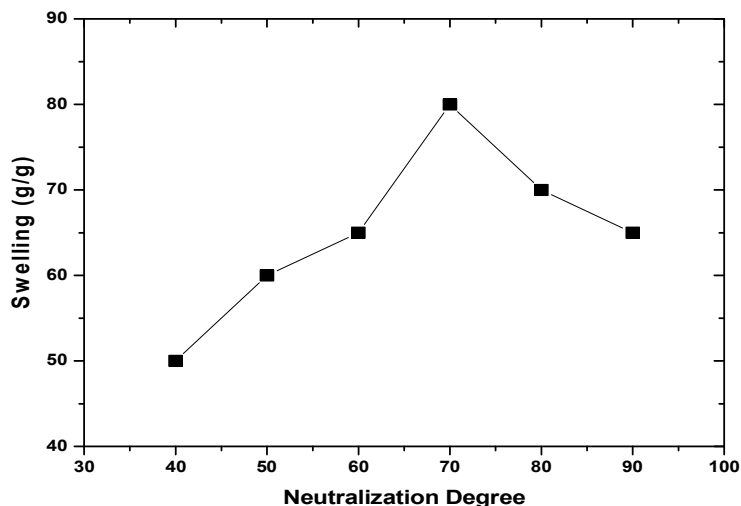


Figure 5: Effect of Neutralizing Agent on the swelling ratio.

The process of neutralization of 50 to 70% can be explained by the above discussion based on decarboxylation (41) and shifting of radicals to -CH₂- group and associates extra radical -COOH group as represented in Scheme 2.

Estimation of AUL

The water absorbency of our synthesized highly absorbent polymer varied as a result of external factors such as swelling medium, applied pressure, and so on. Because absorbency under load AUL is proportional to mechanical strength to the gel, AUL can be calculated using the gelling power of adult diapers and superabsorbent polymers (42). 180

minutes was the appropriate time to reach supreme absorbency for several highly absorbent polymers. The AUL values are natural above this period. Based on the standard test technique approved for calculating AUL, the performance of the highly absorbent polymer swollen in 0.8 weight percent Na Clunder with a weight of 7200 Pa was unrushed. In highly absorbent polymers, the AUL values are 12-21g/g and are firm at many applied pressures also, to create the swelling pressure coefficient (SWC). The swelling pressure coefficient (SWC) was intended from the slope of the graph, plotted using applied load and swelling fraction, which was observed to be 0.7% Pa as opitomized in Figure-6.

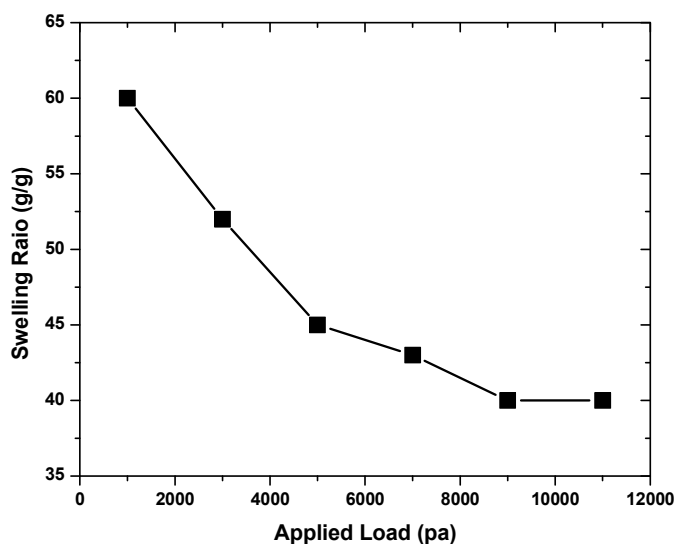


Figure 6: Influence of applied pressure on swelling ratio of GG-g-PIA-co-Aam.

Effect of N,N'-methylenebisacrylamide concentration

Figure-6 represents the effect of N-MBA with a varying amount of 0.3 to 1.3 wt. percent monomer. In this case, detection yield was high at 0.3 to 0.7 wt. percent for monomer maximum swelling and

high polymerization yield, with detection yield exceeding 85%. In the previous study (43) it was very low but in our case, it showed good permanence using squat N-MBA amount with high swelling water. The concentration of higher cross-linkers reduced space between polymer chains and,

then, the highly cross-linked inflexible construction cannot be extended to hold a large quantity of water on the growing quantity of N-MBA. The smaller the

space between the (polymer) units, the more the highly cross-linked rigid preparation cannot expand to capture a large amount of water (44).

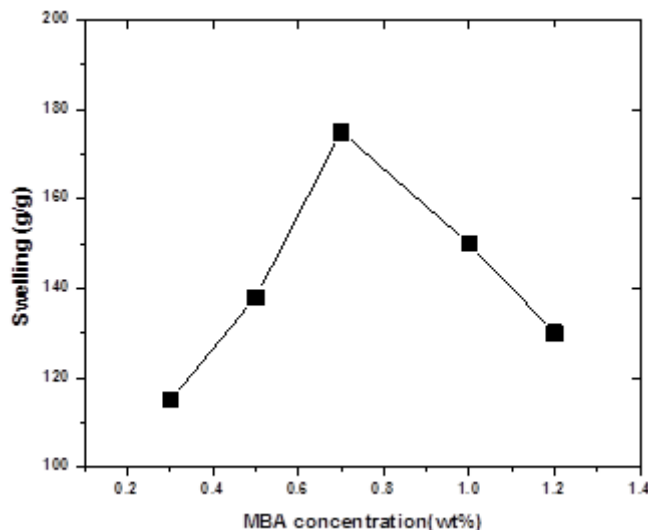


Figure 7: Effect of N-MBA concentration on the Swelling ratio.

Effect of GG concentration on Water Absorbency

Figure 8 represents the variation of guar gum between 0.7 to 1.7 g.dm⁻³ on water absorbency

between 0.7 and 1.7 g.dm³ and falls with rise as the quantity of guar gum due to change in viscosity medium limits the monomer convenience and rise the polymer unit which falls in water absorbency.

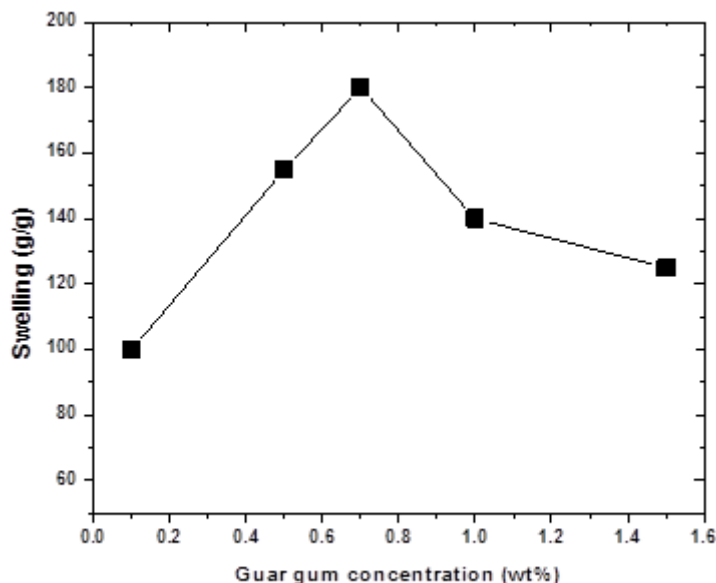


Figure 8 Effect of GG concentration on swelling.

CONCLUSION

In this investigation, the synthesis of highly absorbent polymer (GG-g-PIA-co-AAm) performed by polymerization (free radical) using KPS and N-MBA as initiator and cross-linker respectively, at 70°C in an inert atmosphere, and their influence on polymerization, were studied. At 70% degree of neutralization, we obtained a high water absorption

level, and Fourier transfer and SEM analysis confirmed the synthesis of the proposed highly absorbent polymer. In the presence of acrylamide, highly absorbent polymer materials expand the gel strength (swollen one) and minimize the price of the product. It was observed that highly absorbent polymers (GG-g-PIA-co-AAm) have comparatively decent potential to hold water and NaCl (saline solutions) both as values of the free absorbency

(free swelling) and as values of AUL. The highly absorbent water-absorbing and water-holding polymer can be mainly applied to pads and diapers and unsanitary uses.

REFERENCES

- Ahmed EM, Aggor FS, Awad AM, El-Aref AT. An innovative method for preparation of nanometal hydroxide superabsorbent hydrogel. *Carbohydrate Polymers*. 2013 Jan;91(2):693-8. <DOI>.
- Anirudhan TS, Tharun AR, Rejeena SR. Investigation on Poly(methacrylic acid)-Grafted Cellulose/Bentonite Superabsorbent Composite: Synthesis, Characterization, and Adsorption Characteristics of Bovine Serum Albumin. *Ind Eng Chem Res*. 2011 Feb 16;50(4):1866-74. <DOI>.
- Bakass M, Mokhlisse A, Lallemand M. Absorption and desorption of liquid water by a superabsorbent polymer: Effect of polymer in the drying of the soil and the quality of certain plants. *J Appl Polym Sci*. 2002 Jan 10;83(2):234-43. <DOI>.
- Li A, Zhang J, Wang A. Utilization of starch and clay for the preparation of superabsorbent composite. *Bioresource Technology*. 2007 Jan;98(2):327-32. <DOI>.
- Khairkar SR, Raut AR. Synthesis of Chitosan-graft-Polyaniline-Based Composites. *AJMSE*. 2014 Oct 14;2(4):62-7. <DOI>.
- Chen Z, Liu M, Qi X. Synthesis and Properties of a Superabsorbent Polymer Prepared by Copolymerization of Sodium Acrylate with Sodium 1-(Acryloyloxy)propan-2-yl Phosphate. *Macromol React Eng*. 2007 Feb 7;1(2):275-83. <DOI>.
- Dadhaniya PV, Patel MP, Patel RG. Swelling and dye adsorption study of novel superswelling [Acrylamide/N-vinylpyrrolidone/3(2-hydroxyethyl carbamoyl) acrylic acid] hydrogels. *Polym Bull*. 2006 May;57(1):21-31. <DOI>.
- Dhodapkar R, Borde P, Nandy T. Super absorbent polymers in environmental remediation. *Global NEST Journal*. 2009;11(2):223-34. <URL>.
- Kim J, Lee K-W, Hefferan TE, Currier BL, Yaszemski MJ, Lu L. Synthesis and Evaluation of Novel Biodegradable Hydrogels Based on Poly(ethylene glycol) and Sebacic Acid as Tissue Engineering Scaffolds. *Biomacromolecules*. 2008 Jan 1;9(1):149-57. <DOI>.
- Kosemund K, Schlatter H, Ochsenhirt JL, Krause EL, Marsman DS, Erasala GN. Safety evaluation of superabsorbent baby diapers. *Regulatory Toxicology and Pharmacology*. 2009 Mar;53(2):81-9. <DOI>.
- Lokhande HT, Varadarajan PV. A new Guargum-based superabsorbent polymer synthesised using gamma radiation as a soil additive. *Bioresource Technology*. 1992 Jan;42(2):119-22. <DOI>.
- Xie L, Liu M, Ni B, Zhang X, Wang Y. Slow-release nitrogen and boron fertilizer from a functional superabsorbent formulation based on wheat straw and attapulgite. *Chemical Engineering Journal*. 2011 Feb;167(1):342-8. <DOI>.
- Sung Y, Kim T-H, Lee B. Syntheses of carboxymethylcellulose/graphene nanocomposite superabsorbent hydrogels with improved gel properties using electron beam radiation. *Macromol Res*. 2016 Feb;24(2):143-51. <DOI>.
- Silveira JLM, Bresolin TMB. Pharmaceutical use of galactomannans. *Quím Nova*. 2011;34(2):292-9. <DOI>.
- Dodi G, Hritcu D, Popa M. Carboxymethylation of guar gum: synthesis and characterization. *Cellulose chemistry and Technology*. 2011;45(3):171. <URL>.
- Srivastava A, Mishra V, Singh SK, Kumar R. Vanadium(V)/mandelic acid initiated graft copolymerization of acrylamide onto guar gum in an aqueous medium. *J Appl Polym Sci*. 2010 Feb 15;115(4):2375-85. <DOI>.
- Zhang S-F, He Y-F, Wang R-M, Wu Z-M, Song P-F. Preparation of emulsifier-free acrylate cross-linkable copolymer emulsion and application in coatings for controlling indoor humidity. *Iran Polym J*. 2013 Jun;22(6):447-56. <DOI>.
- Guilherme MR, Aouada FA, Fajardo AR, Martins AF, Paulino AT, Davi MFT, et al. Superabsorbent hydrogels based on polysaccharides for application in agriculture as soil conditioner and nutrient carrier: A review. *European Polymer Journal*. 2015 Nov;72:365-85. <DOI>.
- Sand A, Vyas A. Superabsorbent polymer based on guar gum-graft-acrylamide: synthesis and characterization. *J Polym Res*. 2020 Feb;27(2):43. <DOI>.
- Ko SY, Sand A, Shin NJ, Kwark Y-J. Synthesis and Characterization of Superabsorbent Polymer Based on Carboxymethyl Cellulose-graft-Itaconic Acid. *Fibers Polym*. 2018 Feb;19(2):255-62. <DOI>.
- Sand A, Shin N-J, Nam H-G, Kwark Y-J. Effects of Reaction Parameters on Water Absorption of Poly(itaconic acid) Superabsorbent Particles Synthesized by Inverse Suspension Polymerization. *Fibers Polym*. 2021 Apr;22(4):898-903. <DOI>.
- Sand A, Yadav M, Behari K. Synthesis and characterization of alginate-g-vinyl sulfonic acid with a potassium peroxydiphosphate/thiourea system. *J Appl Polym Sci*. 2010 Dec 15;118(6):3685-94. <DOI>.
- Saber-Samandari S, Saber-Samandari S, Heydaripour S, Abdouss M. Novel carboxymethyl cellulose based nanocomposite membrane: Synthesis, characterization and application in water treatment. *Journal of Environmental Management*. 2016 Jan;166:457-65. <DOI>.
- Lin Q, Gao M, Chang J, Ma H. Adsorption properties of crosslinking carboxymethyl cellulose grafting dimethyldiallylammonium chloride for cationic and anionic dyes. *Carbohydrate Polymers*. 2016 Oct;151:283-94. <DOI>.
- Wang Z, Ning A, Xie P, Gao G, Xie L, Li X, et al. Synthesis and swelling behaviors of carboxymethyl cellulose-based superabsorbent resin hybridized with graphene oxide. *Carbohydrate Polymers*. 2017 Feb;157:48-56. <DOI>.

26. Tran TH, Okabe H, Hidaka Y, Hara K. Removal of metal ions from aqueous solutions using carboxymethyl cellulose/sodium styrene sulfonate gels prepared by radiation grafting. *Carbohydrate Polymers*. 2017 Feb;157:335–43. [<DOI>](#).
27. Sand A, Kwark Y-J. Modification of guar gum through grafting of acrylamide with potassium bromate/thiourea redox initiating system. *Fibers Polym*. 2017 Apr;18(4):675–81. [<DOI>](#).
28. Sand A, Vyas A, Gupta AK. Graft copolymer based on (sodium alginate-g-acrylamide): Characterization and study of Water swelling capacity, metal ion sorption, flocculation and resistance to biodegradability. *International Journal of Biological Macromolecules*. 2016 Sep;90:37–43. [<DOI>](#).
29. Bajpai UDN, Bajpai AK. A new technique for the study of the kinetics of adsorption of polymers onto surfaces. *Polym Int*. 1993;32(1):43–51. [<DOI>](#).
30. Kumar S, Krishnakumar B, Sobral AJFN, Koh J. Bio-based (chitosan/PVA/ZnO) nanocomposites film: Thermally stable and photoluminescence material for removal of organic dye. *Carbohydrate Polymers*. 2019 Feb;205:559–64. [<DOI>](#).
31. Hsan N, Dutta PK, Kumar S, Bera R, Das N. Chitosan grafted graphene oxide aerogel: Synthesis, characterization and carbon dioxide capture study. *International Journal of Biological Macromolecules*. 2019 Mar;125:300–6. [<DOI>](#).
32. Kumar S, de A. e Silva J, Wani MY, Dias CMF, Sobral AJFN. Studies of Carbon Dioxide Capture on Porous Chitosan Derivative. *Journal of Dispersion Science and Technology*. 2016 Feb;37(2):155–8. [<DOI>](#).
33. Kumar S, Koh J. Physicochemical and optical properties of chitosan based graphene oxide bionanocomposite. *International Journal of Biological Macromolecules*. 2014 Sep;70:559–64. [<DOI>](#).
34. Kumar S, Dutta J, Dutta PK. Preparation and characterization of N-heterocyclic chitosan derivative based gels for biomedical applications. *International Journal of Biological Macromolecules*. 2009 Nov;45(4):330–7. [<DOI>](#).
35. Kuchta F-D, van Herk AM, German AL. Propagation Kinetics of Acrylic and Methacrylic Acid in Water and Organic Solvents Studied by Pulsed-Laser Polymerization. *Macromolecules*. 2000 May 1;33(10):3641–9. [<DOI>](#).
36. Lacić I, Beuermann S, Buback M. PLP–SEC Study into Free-Radical Propagation Rate of Nonionized Acrylic Acid in Aqueous Solution. *Macromolecules*. 2003 Dec 1;36(25):9355–63. [<DOI>](#).
37. Vestberg R, Nilsson C, Lopes C, Lind P, Eliasson B, Malmström E. Thiophene-cored 2,2-bis(methylol)propionic acid dendrimers for optical-power-limiting applications: Optical-Power-Limiting Applications. *J Polym Sci A Polym Chem*. 2005 Mar 15;43(6):1177–87. [<DOI>](#).
38. Pascal P, Winnik MA, Napper DH, Gilbert RG. Pulsed laser study of the propagation kinetics of acrylamide and its derivatives in water. *Macromolecules*. 1993 Aug;26(17):4572–6. [<DOI>](#).
39. Veličković SJ, Džunuzović ES, Griffiths PC, Lacić I, Filipović J, Popović IG. Polymerization of itaconic acid initiated by a potassium persulfate/ N,N - dimethylethanolamine system. *J Appl Polym Sci*. 2008 Dec 5;110(5):3275–82. [<DOI>](#).
40. Sharma P, Dagar A, Sapna, Vyas A, Sand A. Superabsorbent composites (SACs) based on xanthan gum-g-poly (itaconic acid)/kaolinite. *Polym Bull*. 2021 Nov;78(11):6441–54. [<DOI>](#).
41. Pourjavadi A, Harzandi AM, Hosseinzadeh H. Modified carrageenan 3. Synthesis of a novel polysaccharide-based superabsorbent hydrogel via graft copolymerization of acrylic acid onto kappa-carrageenan in air. *European Polymer Journal*. 2004 Jul;40(7):1363–70. [<DOI>](#).
42. Pourjavadi A, Hosseinzadeh H. Synthesis and Properties of Partially Hydrolyzed Acrylonitrile-co-Acrylamide Superabsorbent Hydrogel. *Bulletin of the Korean Chemical Society*. 2010 Nov 20;31(11):3163–72. [<DOI>](#).
43. Yadav M, Sand A, Kumar Mishra D, Behari K. A study toward the physicochemical properties of graft copolymer (partially carboxymethylated guar gum- g - N , N ' - dimethylacrylamide): Synthesis and characterization. *J Appl Polym Sci*. 2010 Jul 15;117(2):974–81. [<DOI>](#).
44. Sadeghi M. Synthesis of a biocopolymer carrageenan-g-poly(AAm-co-IA)/ montmorillonite superabsorbent hydrogel composite. *Braz J Chem Eng*. 2012 Jun;29(2):295–305. [<DOI>](#).



Exploration of Role of Concentration on Sensing Activities Using Novel Unsymmetrical Schiff Bases

Saranya Dhasarathan , Selvaraj Shunmugaperumal , Kamatchi Selvaraj P* 

PG & Research Department of Chemistry, Government Arts College for Men (Autonomous), Nandanam, Chennai-600 035, (Affiliated to University of Madras), Tamil Nadu, India.

Abstract: Simultaneous condensation reaction of thiocarbohydrazide with simple aromatic aldehyde and highly reactive ferrocenecarboxaldehyde resulted in unusual unsymmetrical Schiff bases associated with multi-metal ion sensing property. Spectral characterization methods indicate the formation of the new materials. The guest-host relationship established between various metal ions and receptors changes the electronic spectra drastically, and for the addition of Cu^{2+} ions, the formation of an MLCT charge transfer band around 465 nm, responsible for the coordination of metal ions with receptors, has been noticed. Enhanced ΔE_p (132- 219 mV) values derived from the anodic and cathodic potential data suggested a quasi-reversible process. The various ΔI_{pa} (%) deduced from the I_{pa} amount detected from the recorded responses of applied potential on the different metals added, and metal-free receptor solution, revealed the concentration of metal ions required for the effective sensing process.

Keywords: Azomethine; cation sensors; ferrocene; binding attitude

Submitted: October 13, 2021. **Accepted:** February 28, 2022.

Cite this: Dhasarathan S, Shunmugaperumal S, Kamatchi Selvaraj P. Exploration of Role of Concentration on Sensing Activities Using Novel Unsymmetrical Schiff Bases. Journal of the Turkish Chemical Society Section A: Chemistry. 2022;9(2):465-78.

DOI: <https://doi.org/10.18596/jotcsa.1008926>.

*Corresponding author. E-mail: porbal96@gmail.com.

INTRODUCTION

Heavy metal ion detection always attracts scientists due to its role in environmental maintenance, catalytic and biological reactions. Steps involved in industrial and agricultural activities keep introducing cations and anions into the environment (1). Instrumental methods of detection of the above ions include high cost, enormous time, and less accuracy (2, 3). Chemosensors decrease the problems faced in instrumental methods by giving selective binding to the ions with detectable changes in response to applied potential, electronic spectral disparity, and emission spectra (4). The ability of Schiff bases to coordinate with metal ions is exploited extensively in sensor development (5-7).

Acquisition of Hg^{2+} ions affects the central nervous system in humans and generates dizziness,

disorderliness in sleeping, deformity in limbs and loss of life from over consumption (8-10). Copper is essential for life as it is present in enzymes and proteins responsible for energy production (11). Elevated levels of copper result in Alzheimer's disease, autism, and Tourette's syndrome (12-14). Exposure to nickel initially causes irritation, nausea and vomiting. After some time, victim experiences chest stiffness, palpitation, weakness, and sweating. This may lead to cardiac arrest or respiratory distress syndrome (15-17).

Manganese-containing enzymes control many biological reactions (18). Excessive intake roots to the generation of reactive oxygen species and results in Parkinson's disorder (19-22). Lead, as a poisonous metal adds learning deficits, lowered IQ, and abnormal behavior in children and adult's acquaintance anaemia, increase in blood pressure,

fertility reduction, failure of renal & cerebral function and also loss of life (23-25). Carcinogenesis occurs in kidney, liver, lung, brain, bone, testis, and blood stream by the acquisition of cadmium ions into the biological system (26-28).

The present paper discusses the preparation, characterization, and exploration of the sensing ability of new unsymmetrical Schiff bases. *N'*-((*E*)-4-nitrobenzylidene)-2-((*E*)-2-(ferrocenylidene)hydrazine-1-carbothiohydrazide) and *N'*((*E*)-4-*N,N*-dimethylaminobenzylidene)-2-((*E*)-2-(ferrocenylidene)hydrazine-1-carbothiohydrazide).

EXPERIMENTAL

Materials

Ferrocenecarboxaldehyde, 4-nitrobenzaldehyde, *p*-dimethylaminobenzaldehyde, carbon disulfide, hydrazine hydrate, and silica gel employed were of analytical grade, from Merck chemical industries. Metal salts (AR grade) like HgCl₂, CuCl₂, MnCl₂, NiCl₂, Cd(OAc)₂, and Pb(OAc)₂ were purchased from Sigma-Aldrich. HPLC grade acetonitrile was acquired from E-Merck and absolute ethanol was obtained from Commercial Alcohols, Canada. Supporting electrolyte tetrabutylammonium perchlorate [99+ %] was bought from Chemical Center, Mumbai.

Instruments

Heraeus C-H-N rapid analyzer was used to analyze the C, H, and N contents of the sample. KBr pellets of the sample were loaded into the Perkin-Elmer 337 spectrometer to record the FTIR spectra in the range of 400-4000 cm⁻¹. Shimadzu model UV-1800 240V spectrophotometer was employed to record the UV-visible spectra between 200 and 800 nm wavelength. Proton NMR spectra were recorded on 500 MHz, BRUKER AVANCE spectrometer using C₂D₅OD as the solvent. Bruker Daltonics Esquire 3000 spectrometer was employed to obtain the mass spectra. Responses to the applied potential were observed on CHI electrochemical analyzer 1200B model equipped with platinum wire counter electrode, Ag/AgCl reference electrode, and glassy carbon working electrode.

Synthesis of *N'*-((*E*)-4-nitrobenzylidene)-2-((*E*)-2-(ferrocenylidene)hydrazine-1-carbothiohydrazide) [R1]

Refluxing the mixture of 3 moles of hydrazine hydrate and 1 mole of carbon disulfide at 80 °C in the presence of the catalyst 2-chloroethanol (0.15 mole) for 10 hours yielded thiocarbohydrazide (29). Mixture containing 0.01 mole of 4-nitrobenzaldehyde and 0.01 mole of ferrocenecarboxaldehyde. 180 mL of ethanol were added with stirring (half an hour) to 0.01 mole of purified thiocarbohydrazide in 25 mL of ethanol and then refluxed for 6-7 hours. The reaction mixture was filtered after cooling, then concentrated to get the crude product. Purification of *N'*-((*E*)-4-nitrobenzylidene)-2-((*E*)-2-(ferrocenylidene)hydrazine-1-carbothiohydrazide) was carried out in a silica gel column using ethanol as eluent. Color: reddish orange. Yield: 0.5939 g (82%), m.p. 180 °C.

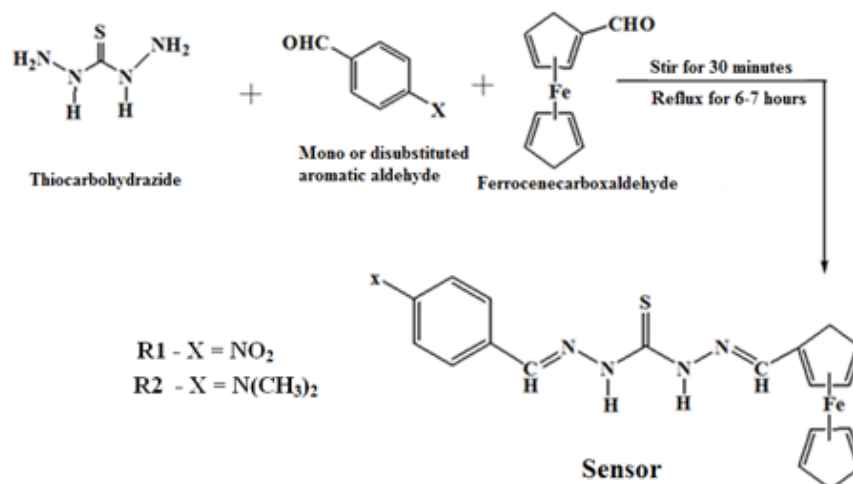
Synthesis of *N'*((*E*)-4-*N,N*-dimethylaminobenzylidene)-2-((*E*)-2-(ferrocenylidene)hydrazine-1-carbothiohydrazide) [R2]

To a solution of 0.01 mole of thiocarbohydrazide in 25 mL of ethanol, another solution containing 0.01 mole of *p*-dimethylaminobenzaldehyde and 0.01 mole of ferrocene carboxaldehyde in 180 mL of ethanol was added slowly with stirring for half an hour, then refluxed for 6-7 hours. Greenish yellow colored reaction mixture was cooled, filtered, and concentrated to get the crude product. Purification of the crude sample in a silica gel column using ethanol as eluent yielded reddish yellow-colored *N'*((*E*)-4-*N,N*-dimethylamino benzylidene)-2-((*E*)-2-(ferrocenylidene)hydrazine-1-carbothiohydrazide) [R2]. Yield: 0.5404 g, (91%), Color: Reddish yellow, m.p. 60 °C.

RESULTS AND DISCUSSION

Elemental and Mass Spectral Analysis

Elemental analysis data of the synthesized receptor were in agreement with the theoretically calculated ones, R1- C₁₉H₁₇N₅O₂SFe (%): C, 50.61; H, 3.73; N, 15.51; Fe, 12.18. R2 - C₂₁H₂₃N₅O₂SFe (%): H, 5.32; C, 58.30; N, 16.23; Fe, 12.70. Mass spectra of the compounds R1 and R2 contained molecular peaks at (ESI) m/z 434 and 434, respectively, which ascertain the formation of anticipated material.



Scheme 1: Synthesis of the sensor molecule.

Vibrational Assignment

The ferrocene cyclopentadienyl ring's tilt stretching vibration and C-H out of plane bend vibrations of R1 appeared as peaks of about 479 cm^{-1} and 816 cm^{-1} , respectively (30). The δ -C-C-H bending vibration in the pentacyclic ring emerged near 933 cm^{-1} . The 1104 cm^{-1} peak was fixed for ring breathing vibration (31). The C=S group stretching vibration, C-C stretching vibration of pentacyclic ring and NO_2 group vibration arises at 1336 cm^{-1} , 1514 cm^{-1} and 1566 cm^{-1} respectively. The Schiff base development is authorized by the appearance of -C=N stretching vibration peak at 1650 cm^{-1} (30). The aromatic stretching vibration transpired at 2064 cm^{-1} . Stretching vibration due to secondary amine and hydration water became apparent around $3360 - 3400\text{ cm}^{-1}$. Stretching vibrational modes of CH_3 groups present in R2 became obvious near 2916 cm^{-1} (32) along with all other peaks appeared for R1 .

NMR Spectral Analysis

Receptor R1 proton NMR spectrum (Figure 2) in $\text{C}_2\text{D}_5\text{OD}$ possess pertinent peaks and are earmarked as given here - **R1**: 8.2 (s, 2H, NCH) , $7.9\text{ (m, 4H aromatic)}$, $4.9\text{ (m, 2H, cp subst.)}$ 4.4 (m, 2H, cp

subst.) $4.3\text{ (s, 5H, cp unsubst.)}$, 1.2 (s, 2H, 2NH) **R2**: 8.1 (s, 2H, NCH) , $7.4\text{ (m, 2H, aromatic)}$, $6.7\text{ (d, 2H, aromatic)}$, $4.7\text{ (m, 2H, cp subst)}$, $4.5\text{ (m, 2H, cp subst)}$, $4.2\text{ (s, 5H, cp unsubst)}$, $3.0\text{ (s, 6H, N(CH}_3)_2)}$, 1.1 (s, 2H, 2NH) .

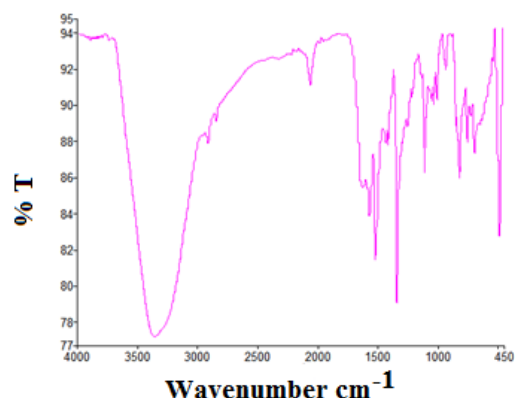


Figure 1: FTIR spectrum of R1.

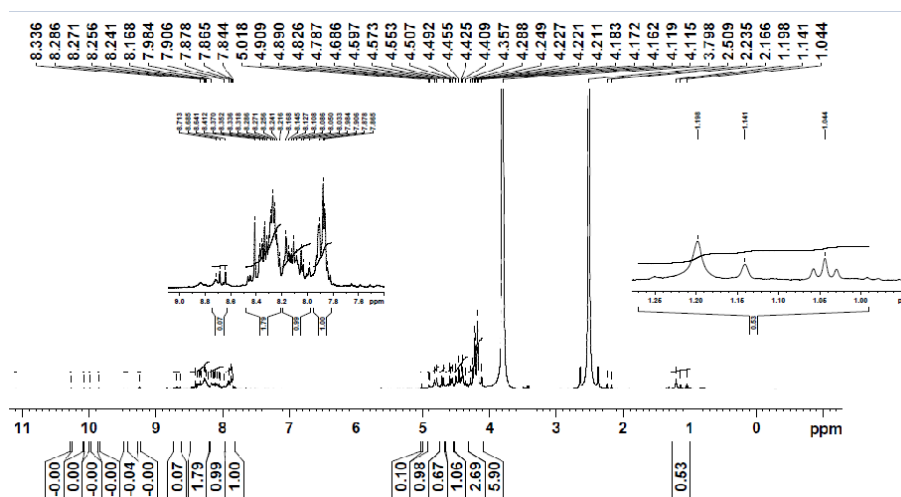


Figure 2: Proton NMR spectrum of R1.

Binding Aptitude Analysis Using UV-Titration Method

To 2.5 mL of 1×10^{-5} M R1 solution taken in the quartz cell, incremental additions of 20 μ L of various metal salt solutions (1×10^{-2} M) were added using micro pipette (during the titration) and the spectral changes were recorded for analysis. Alcoholic solutions of Pb, Cd & Mn salts and acetonitrile solutions of Hg, Ni & Cu salts were used in titration

studies. UV-visible spectrum of R1 in acetonitrile had a peak at 258 nm and two shoulders near 300 nm and 358 nm. In ethanol medium two peaks are visible at 241 nm, 313 nm and a shoulder at 354 nm (Figure 3a&3b). Aromatic ring transitions ($n-n^*$) were assigned (33) for UV region shoulders and peaks and an intramolecular charge transfer transition (34) was allocated for visible region shoulder.

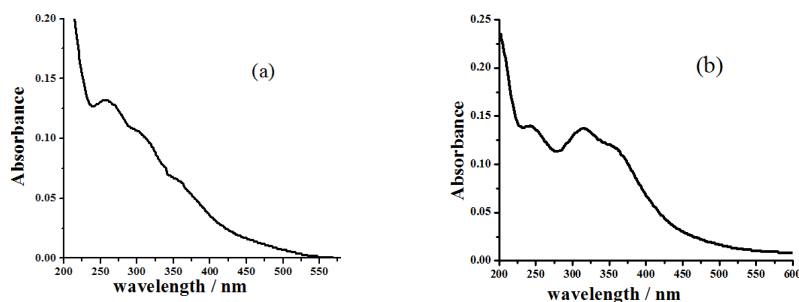


Figure 3: Electronic spectrum of R1 in (a) acetonitrile (b) ethanol.

Successive addition of Cu^{2+} ions drastically changed the spectrum of R1 (Figure 4a) with the generation of MLCT band (Figure 4b) at 465 nm (35) accountable for the association of metal ion with

receptor and disappearance of 258 nm peak with the transformation of 300 nm shoulder to a peak (Figure 4c) at 296 nm (blue-shift).

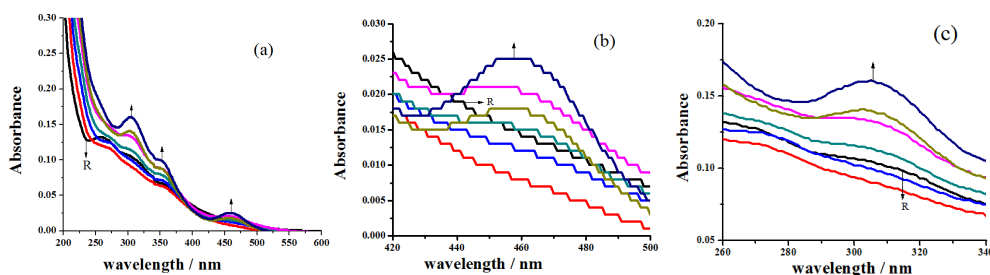


Figure 4: Spectral changes recorded for the addition of Cu^{2+} ions to R1 (a) Overall changes (b) MLCT band formation (c) conversion of shoulder into peak.

Incremental addition of Hg^{2+} ions lead to the development of new peak around 237 nm (Figure 5a). Blue shift of 242 nm peak to 234 nm and 315 nm peak to 311 nm resulted from the addition of Pb^{2+} ions (Figure 5b). Red shift of 258 nm shoulder to 272 nm originated from the raise of Ni^{2+} ions

(Figure 5c). Appreciable variations were recorded for the increase of Cd^{2+} & Mn^{2+} ions. Transformation of $n\text{-}\pi^*$ transition peaks of R1 upon the addition of various metal ion supposes that R1 is capable of sensing Cu^{2+} , Hg^{2+} , Ni^{2+} , Pb^{2+} , Cd^{2+} and Mn^{2+} ions.

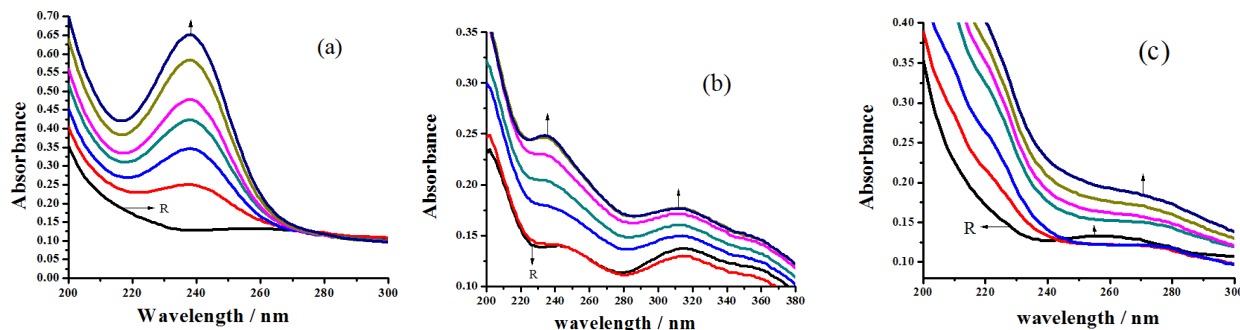


Figure 5: Spectral changes noticed in spectrum of R1 for the addition of (a) Hg^{2+} ions, (b) Pb^{2+} ions, (c) Ni^{2+} ions.

The presence of electron donating methyl group in the aromatic part substituted imine group, might cause the $n\text{-}\pi^*$ transition to happen meritoriously. This might be the reason for the appearance of prominent peak at 335 nm (Figure 6a) in

acetonitrile medium and at 350 nm (Figure 6b) in ethanol. A shoulder at 310 nm was also recorded in alcoholic medium, in addition to the above mentioned peak.

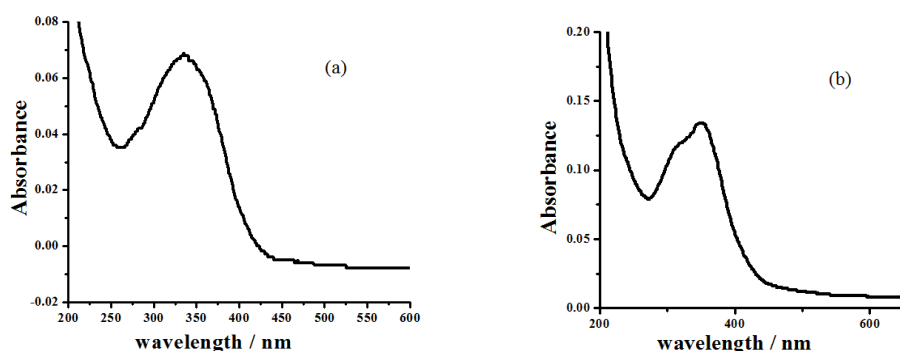


Figure 6: Electronic spectra of R1 in (a) acetonitrile, (b) ethanol.

Recognition ability of R2 towards Cu^{2+} ions was revealed by the formation of an MLCT band at 461 nm along with blue shift of 337 nm to peak 310 nm (Figure 7a). Locking attitude of R2 towards Hg^{2+} was revealed by the formation of new peak at 237 nm (Fig 7b). Disappearances of 337 nm peaks with simultaneous appearance of shoulder at 278 nm

(Figure 7c) for the addition of Ni^{2+} ions also revealed the sensing ability of R2. Conversion of 357 nm peak to shoulder on increasing the concentration of Pb^{2+} ions and acceptable upsurge in the absorbance value of R2 for the cumulative addition of Mn^{2+} & Cd^{2+} also unveiled the binding aptitude of R2.

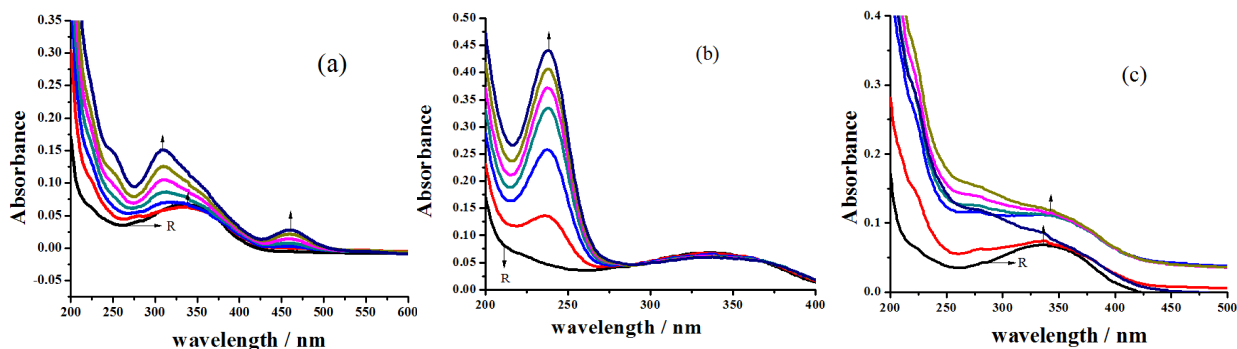


Figure 7: Spectral changes noticed in the spectrum of R2 for the addition of (a) Cu²⁺ ions, (b) Hg²⁺ ions, (c) Ni²⁺ ions.

Assessment of Concentration Required for Effective Sensing

The required concentration for the recognition of metal ions by the newly synthesized sensor was calculated from the anodic current value observed for the oxidation peak realized for the applied potential under anaerobic conditions. In Figure 8,

cyclic voltammograms of R1 (1X10⁻³ M) recorded for different scan rates (20, 50 & 100 mV/s) were presented. The calculated values of I_{pa}, I_{pc}, and ΔE_p are presented in Table 1. The ΔE_p (132- 219 mV) values derived from the anodic and cathodic potential data were greater than the expected 59 mV of a reversible process (36).

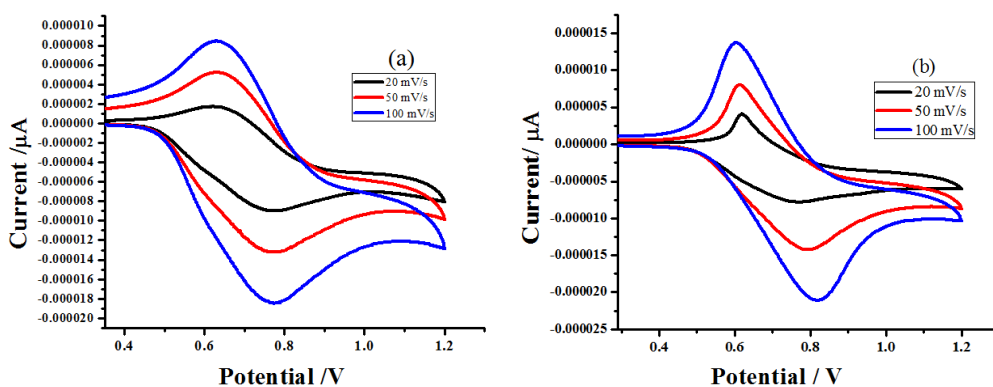


Figure 8: CV of R1 with different scan rate in (a) acetonitrile and (b) ethanol.

Table 1: Electrochemical parameters of R1 (1X10⁻³M).

Scan Rate- mV/ sec	E _{pa} (V)	E _{pc} (V)	ΔE _p (V)	E _{1/2} (V)	I _{pa} x10 ⁻⁶ (μA)	I _{pc} x10 ⁻⁶ (μA)
Solvent –Acetonitrile						
20	0.765	0.631	0.134	0.698	-0.914	1.709
50	0.765	0.629	0.136	0.697	-1.322	5.303
100	0.774	0.627	0.147	0.71	-1.841	8.503
Solvent – Ethanol						
20	0.766	0.619	0.147	0.692	-0.788	4.002
50	0.793	0.613	0.18	0.703	-1.414	8.027
100	0.820	0.601	0.219	0.710	-2.124	13.760

CV titration studies were carried out by adding 20 μL of either 1×10^{-3} M or 1×10^{-1} M metal salts' solution to 10 mL of 1×10^{-3} molar R1 solution taken in the three-compartment cell. The registered cyclic voltammograms had a varied amount of positive potential shift for oxidation peak and a negative

potential shift for reduction peak, which unveiled the different metal ion sensing nature of newly synthesized receptors (37, 38). Voltammograms recorded for the addition of Cd^{2+} ions are presented in Figure 9.

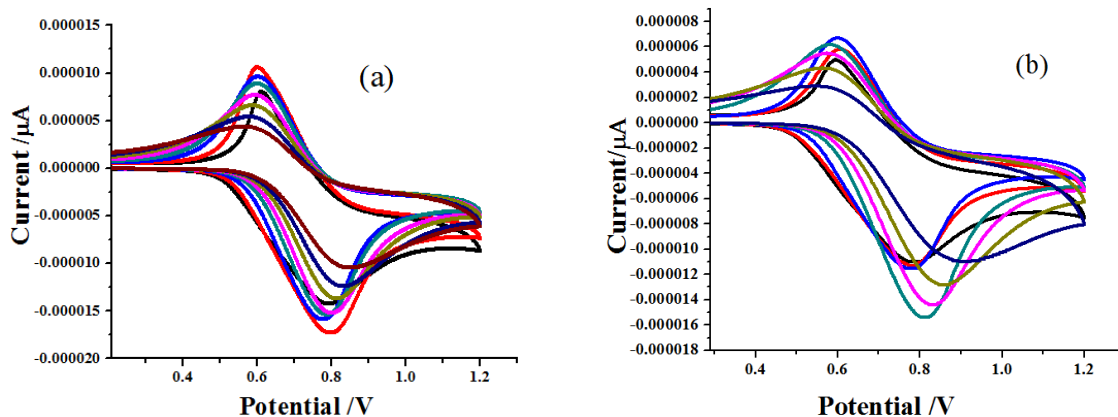


Figure 9: Deviations in the voltammogram of R1 for the addition of Cd^{2+} ions, **(a)** 1×10^{-3} M, **(b)** 1×10^{-1} M.

Electronic configuration of the metal ion may affect its binding nature to the receptor. The difference in the I_{pa} and ΔE_p values (Table 2) observed for the varied metal ions with 1×10^{-3} M concentration (Figure 10) matched with the above expectation. The repulsive force operating between metal cation and oxidized ferrocene unit was also a reason for

the noticed variations in the I_{pa} & ΔE_p (39). The order of binding of R1 estimated from the ΔI_{pa} (%), deliberated from the I_{pa} amount detected for the oxidation wave of sensor's solution and different metal ions added to it, was Cd, 86.5% > Ni, 33.2% > Hg, 24.6% > Pb, 13.6% > Mn, 8.4% > Cu, 3.9%.

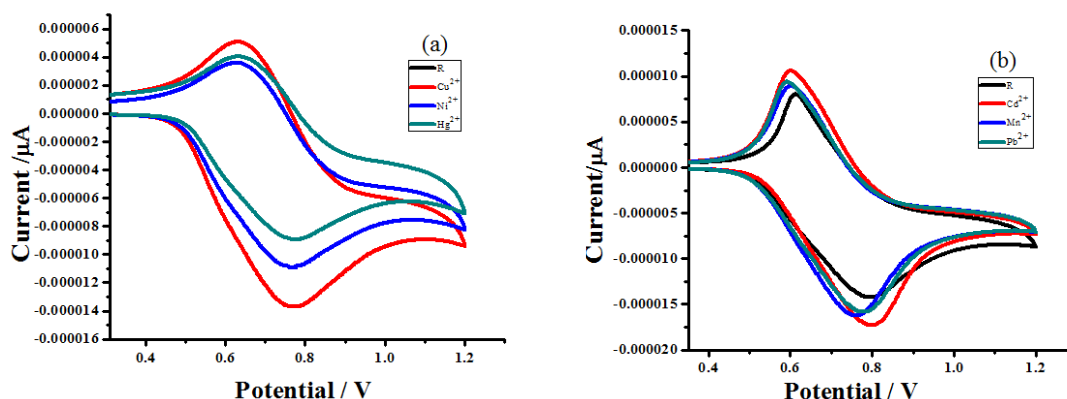


Figure 10: CV of R1 (1×10^{-3} M) with dissimilar metal ions (1×10^{-3} M) in **(a)** acetonitrile and **(b)** ethanol [at 50 mV/s scan rate].

Table 2: CV data for the addition of dissimilar metal ions under equimolar conditions [at 50 mV/s scan rate].

Addition	E_{pa} (V)	E_{pc} (V)	ΔE_p (V)	$E_{1/2}$ (V)	$I_{pa} \times 10^{-5}$ (μA)	$I_{pc} \times 10^{-6}$ (μA)
Solvent - Acetonitrile						
Receptor	0.765	0.629	0.136	0.697	-1.322	5.303
Cu^{2+}	0.767	0.635	0.132	0.701	-1.380	5.091
Ni^{2+}	0.765	0.633	0.132	0.699	-1.087	3.539
Hg^{2+}	0.775	0.637	0.138	0.706	-8.917	3.998
Solvent - Ethanol						
Receptor	0.793	0.613	0.18	0.703	-1.414	8.027
Cd^{2+}	0.794	0.598	0.196	0.696	-1.743	1.078
Mn^{2+}	0.757	0.602	0.155	0.679	-1.638	8.769
Pb^{2+}	0.778	0.596	0.182	0.687	-1.586	9.293

The order of sensing power of R1 under multimolar conditions (1×10^{-3} M, R1/ 1×10^{-1} M, Mn^{2+}), derived from the ΔI_{pa} (%), which in turn were calculated from the I_{pa} values (Table 3), was Mn, 59.3%>Pb, 44.3%>Cd, 27.1%>Cu, 15.9%>Ni, 2.9%>Hg,

1.8%. Appraisal of binding order of R1 under dissimilar concentrations of metal ion revealed that R1 was more potent than Cd, Ni, and Hg ions at lower concentrations, and dominant over Mn, Pb, and Cd at higher concentrations (Figure 11).

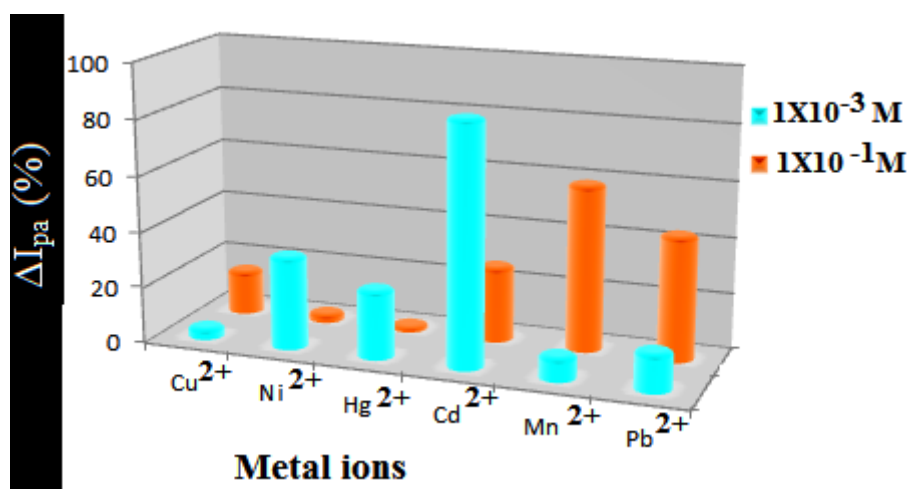
**Figure 11:** Chart showing the concentration required and sensing ability of R1.

Table 3: CV data for the addition of dissimilar metal ions under multimolar conditions [at 50 mV/s scan rate].

Addition	E_{pa} (V)	E_{pc} (V)	ΔE_p (V)	E_{1/2} (V)	I_{pa} × 10⁻⁵ (μA)	I_{pc} × 10⁻⁶ (μA)
Solvent – Acetonitrile						
Receptor	0.765	0.629	0.136	0.697	-1.322	5.303
Cu²⁺	0.798	0.666	0.132	0.732	-1.282	4.457
Ni²⁺	0.788	0.646	0.142	0.717	-1.328	5.145
Hg²⁺	0.767	0.639	0.128	0.703	-1.202	5.205
Solvent - Ethanol						
Receptor	0.793	0.613	0.18	0.703	-1.414	8.027
Cd²⁺	0.777	0.609	0.168	0.693	-1.134	5.845
Mn²⁺	0.774	0.609	0.165	0.691	-8.161	3.264
Pb²⁺	0.777	0.602	0.175	0.689	-1.096	4.470

Table 4: Electrochemical data of R2 (1X10⁻³M) with different scan rates.

Scan Rate- mV/s	E_{pa} (V)	E_{pc} (V)	ΔE_p (V)	E_{1/2} (V)	I_{pa} × 10⁻⁵ (μA)	I_{pc} × 10⁻⁶ (μA)
Solvent –Acetonitrile						
20	0.818	0.706	0.112	0.762	-6.934	1.240
50	0.827	0.704	0.123	0.765	-1.061	2.926
100	0.827	0.696	0.131	0.761	-1.473	5.551
Solvent – Ethanol						
20	0.657	0.601	0.056	0.629	-3.296	4.903
50	0.706	0.612	0.094	0.659	-6.096	1.754
100	0.736	0.605	0.131	0.670	-8.845	3.677

The change in trend of I_{pa}, I_{pc} & ΔE_p values assessed for R2 (Table 4) with different scan rate are similar to the behavior of R1.

Concentration assessment experiment of R2 was also carried out using the same method adopted for R1. The order of binding ability of R2 estimated from ΔI_{pa} (%) values under homo-molar

concentrations was Ni, 48.7%>Hg, 37.8%>Pb, 34.2%>Mn, 24.5%>Cd, 8.6%>Cu, 6.8% (Table 5), and at hetero-molar conditions was (Ni, 46.1%>Cd, 37.3%>Cu, 34.1%>Pb, 29.3%>Hg, 26.8%>Mn, 0.0%) (Table 6). The pictorial presentation of the role of metal ion concentration required for effective sensing of R2 is given in Figure 12.

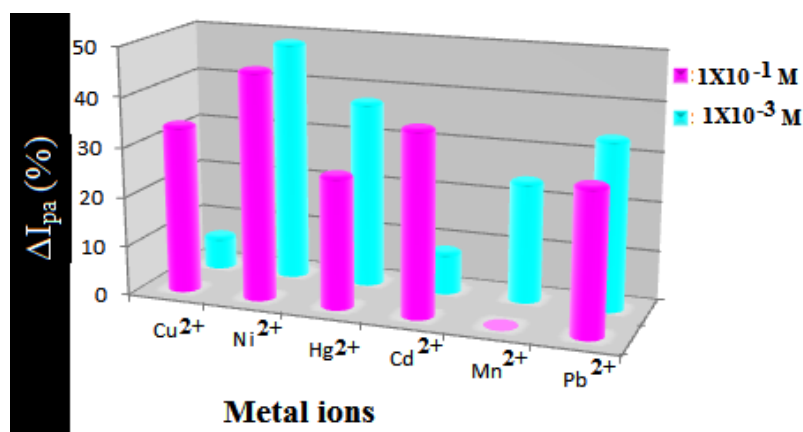


Figure 12: Chart showing the concentration required and sensing ability of R2.

Table 5: CV data for the addition of dissimilar metal ions under homo-molar conditions [at 50 mV/s scan rate].

Addition	E _{pa} (V)	E _{pc} (V)	ΔE _p (V)	E _{1/2} (V)	I _{pa} × 10 ⁻⁵ (μA)	I _{pc} × 10 ⁻⁶ (μA)
Solvent – Acetonitrile						
Receptor	0.827	0.704	0.123	0.765	-1.061	2.926
Cu²⁺	0.814	0.706	0.108	0.76	-1.075	2.727
Ni²⁺	0.758	0.625	0.133	0.691	-5.056	5.741
Hg²⁺	0.814	0.702	0.112	0.758	-1.530	4.705
Solvent - Ethanol						
Receptor	0.706	0.612	0.094	0.659	-6.096	1.754
Cd²⁺	0.728	0.616	0.112	0.672	-5.855	1.920
Mn²⁺	0.775	0.580	0.195	0.677	-1.151	2.326
Pb²⁺	0.741	0.597	0.144	0.669	-6.525	1.154

Table 6: CV data for the addition of dissimilar metal ions under heteromolar conditions [at 50 mV/s scan rate].

Addition	E _{pa} (V)	E _{pc} (V)	ΔE _p (V)	E _{1/2} (V)	I _{pa} × 10 ⁻⁵ (μA)	I _{pc} × 10 ⁻⁶ (μA)
Solvent – Acetonitrile						
Receptor	0.827	0.704	0.123	0.765	-1.061	2.926
Cu²⁺	0.811	0.666	0.145	0.738	-7.4381	1.926
Ni²⁺	0.784	0.666	0.118	0.738	-6.633	1.577
Hg²⁺	0.791	0.676	0.115	0.733	-6.284	2.140
Solvent - Ethanol						
Receptor	0.706	0.612	0.094	0.659	-6.096	1.754
Cd²⁺	0.762	0.587	0.175	0.674	-1.123	2.801
Mn²⁺	-	-	-	-	-	-
Pb²⁺	0.747	0.582	0.165	0.664	-8.372	1.239

CONCLUSION

The formation of unsymmetrical Schiff bases, when ferrocenecarboxaldehyde is present as one of the reactants, is barred due to the high reactivity of ferrocene component. Efforts made by our team resulted to the preparation, characterization, and exploration of the sensing ability of *N'*-((*E*)-4-nitrobenzylidene)-2-((*E*)-2-(ferrocenylidene)hydrazine-1-carbothiohydrazide and *N'*((*E*)-4-*N,N*-dimethylaminobenzylidene)-2-((*E*)-2-(ferrocenylidene) hydrazine-1-carbothiohydrazide. FTIR, ¹HNMR, and Mass spectral analyses materialize the characterization of the above compounds. Competency in identifying the ions of metals like Cu, Ni, Hg, Cd, Mn & Pb by the newly synthesized compound was realized in UV-Visible titration studies. The role of concentration on the sensing activity of the sensors R1 and R2 resulted from the anodic current values obtained in CV studies.

CONFLICTS OF INTEREST

The authors declare that there are no conflicts.

ACKNOWLEDGEMENT

The support extended by Dr. K. Pandian, Professor of Inorganic Chemistry, at the University of Madras is gratefully acknowledged. The research scholar, D.Saranya wishes to record her thanks to the State Government of Tamil Nadu, India for the annual research assistant grant.

REFERENCES

- 1a.** Malik LA, Bashir A, Qureashi A, Pandith AH. Detection and removal of heavy metal ions: a review. *Environ Chem Lett.* 2019 Dec;17(4):1495–521. [<DOI>](#). **1b.** Nagajyoti PC, Lee KD, Sreekanth TVM. Heavy metals, occurrence and toxicity for plants: a review. *Environ Chem Lett.* 2010 Sep;8(3):199–216. [<DOI>](#).
- 2a.** Bansod B, Kumar T, Thakur R, Rana S, Singh I. A review on various electrochemical techniques for heavy metal ions detection with different sensing platforms. *Biosensors and Bioelectronics.* 2017 Aug;94:443–55. [<DOI>](#). **2b.** Gong T, Liu J, Liu X, Liu J, Xiang J, Wu Y. A sensitive and selective sensing platform based on CdTe QDs in the presence of l -cysteine for detection of silver, mercury and copper ions in water and various drinks. *Food Chemistry.* 2016 Dec;213:306–12. [<DOI>](#).
- 3.** Tian M, Fang L, Yan X, Xiao W, Row KH. Determination of Heavy Metal Ions and Organic Pollutants in Water Samples Using Ionic Liquids and Ionic Liquid-Modified Sorbents. *Journal of Analytical Methods in Chemistry.* 2019 Oct 31;2019:1–19. [<DOI>](#).
- 4a.** Zhang M, Shi J, Liao C, Tian Q, Wang C, Chen S, et al. Perylene Imide-Based Optical Chemosensors for Vapor Detection. *Chemosensors.* 2020 Dec 22;9(1):1. [<DOI>](#). **4b.** Elke K, Jermann E, Begerow J, Dunemann L. Determination of benzene, toluene, ethylbenzene and xylenes in indoor air at environmental levels using diffusive samplers in combination with headspace solid-phase microextraction and high-resolution gas chromatography–flame ionization detection. *Journal of Chromatography A.* 1998 Nov;826(2):191–200. [<DOI>](#).
- 5.** Berhanu AL, Gaurav, Mohiuddin I, Malik AK, Aulakh JS, Kumar V, et al. A review of the applications of Schiff bases as optical chemical sensors. *TrAC Trends in Analytical Chemistry.* 2019 Jul;116:74–91. [<DOI>](#).
- 6.** Borah N, De S, Gogoi A, Das G. A series of benzothiazole-based Schiff bases for the colorimetric sensing of fluoride and acetate ions: acetate-induced turn-on fluorescence for selectivity. *New J Chem.* 2020;44(43):18703–13. [<DOI>](#).
- 7.** Abu-Dief AM, Mohamed IMA. A review on versatile applications of transition metal complexes incorporating Schiff bases. *Beni-Suef University Journal of Basic and Applied Sciences.* 2015 Jun;4(2):119–33. [<DOI>](#).
- 8.** Garza-Lombó C, Posadas Y, Quintanar L, Gonsebatt ME, Franco R. Neurotoxicity Linked to Dysfunctional Metal Ion Homeostasis and Xenobiotic Metal Exposure: Redox Signaling and Oxidative Stress. *Antioxidants & Redox Signaling.* 2018 Jun 20;28(18):1669–703. [<DOI>](#).
- 9.** Jain R, Singh SK, Advani U, Kohli S, Sharma N. Mercury toxicity and its management. *Int Res J Pharm.* 2013 Sep 9;4(8):38–41. [<DOI>](#).
- 10.** Farina M, Avila DS, da Rocha JBT, Aschner M. Metals, oxidative stress and neurodegeneration: A focus on iron, manganese and mercury. *Neurochemistry International.* 2013 Apr;62(5):575–94. [<DOI>](#).
- 11.** Qi X, Jun EJ, Xu L, Kim S-J, Joong Hong JS, Yoon YJ, et al. New BODIPY Derivatives as OFF–ON Fluorescent Chemosensor and Fluorescent Chemodosimeter for Cu²⁺: Cooperative Selectivity Enhancement toward Cu²⁺. *J Org Chem.* 2006 Mar 31;71(7):2881–4. [<DOI>](#).
- 12.** Taylor AA, Tsuji JS, Garry MR, McArdle ME, Goodfellow WL, Adams WJ, et al. Critical Review of Exposure and Effects: Implications for Setting Regulatory Health Criteria for Ingested Copper. *Environmental Management.* 2020 Jan;65(1):131–59. [<DOI>](#).
- 13.** Bao J, Xing Y, Feng C, Kou S, Jiang H, Li X. Acute and sub-chronic effects of copper on survival, respiratory metabolism, and metal accumulation in *Cambaroides dauricus*. *Sci Rep.* 2020 Dec;10(1):16700. [<DOI>](#).
- 14.** Brewer GJ. Copper toxicity in the general population. *Clinical Neurophysiology.* 2010 Apr;121(4):459–60. [<DOI>](#).
- 15.** Chakraborty S, Rayalu S. Detection of nickel by chemo and fluoro sensing technologies. *Spectrochimica Acta Part A: Molecular and Biomolecular Spectroscopy.* 2021 Jan;245:118915. [<DOI>](#).
- 16.** Song X, Fiati Kenston SS, Kong L, Zhao J. Molecular mechanisms of nickel induced neurotoxicity and chemoprevention. *Toxicology.* 2017 Dec;392:47–54. [<DOI>](#).
- 17.** Das KK, Reddy RC, Bagoji IB, Das S, Bagali S, Mullur L, et al. Primary concept of nickel toxicity – an overview.

Journal of Basic and Clinical Physiology and Pharmacology. 2019 Mar 26;30(2):141–52. <DOI>.

18a. Erikson KM, Syversen T, Aschner JL, Aschner M. Interactions between excessive manganese exposures and dietary iron-deficiency in neurodegeneration. *Environmental Toxicology and Pharmacology*. 2005 May;19(3):415–21. <DOI>. **18b.** Peres TV, Aschner M. Nutritional, Genetic, and Molecular Aspects of Manganese Intoxication. In: *Molecular, Genetic, and Nutritional Aspects of Major and Trace Minerals* [Internet]. Elsevier; 2017 [cited 2022 Mar 11]. p. 367–76. <DOI>. **19.** Harischandra DS, Ghaisas S, Zenitsky G, Jin H, Kanthasamy A, Anantharam V, et al. Manganese-Induced Neurotoxicity: New Insights Into the Triad of Protein Misfolding, Mitochondrial Impairment, and Neuroinflammation. *Front Neurosci*. 2019 Jun 26;13:654. <DOI>.

20. Peres TV, Schettinger MRC, Chen P, Carvalho F, Avila DS, Bowman AB, et al. "Manganese-induced neurotoxicity: a review of its behavioral consequences and neuroprotective strategies." *BMC Pharmacol Toxicol*. 2016 Dec;17(1):57. <DOI>.

21. Peres TV, Aschner M. Nutritional, Genetic, and Molecular Aspects of Manganese Intoxication. In: *Molecular, Genetic, and Nutritional Aspects of Major and Trace Minerals* [Internet]. Elsevier; 2017 [cited 2022 Mar 11]. p. 367–76. <DOI>.

22. Guilarte TR. Manganese and Parkinson's Disease: A Critical Review and New Findings. *Environ Health Perspect*. 2010 Aug;118(8):1071–80. <DOI>.

23. Ashraf U, Kanu AS, Deng Q, Mo Z, Pan S, Tian H, et al. Lead (Pb) Toxicity; Physio-Biochemical Mechanisms, Grain Yield, Quality, and Pb Distribution Proportions in Scented Rice. *Front Plant Sci* [Internet]. 2017 Feb 28 [cited 2022 Mar 11];8. <DOI>.

24. Boskabady M, Marefati N, Farkhondeh T, Shakeri F, Farshbaf A, Boskabady MH. The effect of environmental lead exposure on human health and the contribution of inflammatory mechanisms, a review. *Environment International*. 2018 Nov;120:404–20. <DOI>.

25a. Wani AL, Ara A, Usmani JA. Lead toxicity: a review. *Interdisciplinary Toxicology*. 2015 Jun 1;8(2):55–64. <DOI>. **25b.** Mani MS, Nayak DG, Dsouza HS. Challenges in diagnosing lead poisoning: A review of occupationally and nonoccupationally exposed cases reported in India. *Toxicol Ind Health*. 2020 May;36(5):346–55.

26. Genchi G, Sinicropi MS, Lauria G, Carocci A, Catalano A. The Effects of Cadmium Toxicity. *IJERPH*. 2020 May 26;17(11):3782. <DOI>.

27. Rafati-Rahimzadeh M, Rafati-Rahimzadeh M, Kazemi S, Moghadamnia A. Cadmium toxicity and treatment: An update. *Caspian J Intern Med* [Internet]. 2017 Jun [cited 2022 Mar 11];8(3): 135-45. <DOI>.

28. Rani A, Kumar A, Lal A, Pant M. Cellular mechanisms of cadmium-induced toxicity: a review. *International Journal of Environmental Health Research*. 2014 Jul 4;24(4):378–99. <DOI>.

29a. A. Metwally M, E. Khalifa M, Koketsu M. Thiocarbonylhydrazides: Synthesis and Reactions. *Chemistry*.

2012 Aug 31;2(2):38–51. <DOI>. **29b.** Andleeb H, Hussain M, Abida Ejaz S, Sevigny J, Farman M, Yasinzai M, et al. Synthesis and computational studies of highly selective inhibitors of human recombinant tissue non-specific alkaline phosphatase (h-TNAP): A therapeutic target against vascular calcification. *Bioorganic Chemistry*. 2020 Aug;101:103999. <DOI>.

30a. Constantinescu C, Matei A, Ion V, Mitu B, Ionita I, Dinescu M, et al. Ferrocene carboxaldehyde thin films grown by matrix-assisted pulsed laser evaporation for non linear optical applications. *Applied Surface Science*. 2014 May;302:83–6. <DOI>. **30b.** Bodenheimer JS, Low W. A vibrational study of ferrocene and ruthenocene. *Spectrochimica Acta Part A: Molecular Spectroscopy*. 1973 Sep;29(9):1733–43. <DOI>.

31. Gryaznova TP, Katsyuba SA, Milyukov VA, Sinyashin OG. DFT study of substitution effect on the geometry, IR spectra, spin state and energetic stability of the ferrocenes and their pentaphosphoryl analogues. *Journal of Organometallic Chemistry*. 2010 Nov;695(24):2586–95. <DOI>.

32a. Çatıkkaş B. Raman and FT-IR Spectra, DFT and SQMFF calculations for N,N-Dimethylaniline. *PEN* [Internet]. 2017 Jun 24 [cited 2022 Mar 11];5(2):237-44. <DOI>. **32b.** Lu R, Gan W, Wu B, Zhang Z, Guo Y, Wang H. C–H Stretching Vibrations of Methyl, Methylene and Methine Groups at the Vapor/Alcohol ($n = 1-8$) Interfaces. *J Phys Chem B*. 2005 Jul 1;109(29):14118–29. <DOI>.

33. Barwiolek M, Kaczmarek-Kędziera A, Muziol TM, Jankowska D, Jezierska J, Bieńko A. Dinuclear Copper(II) Complexes with Schiff Bases Derived from 2-Hydroxy-5-Methylisophthalaldehyde and Histamine or 2-(2-Aminoethyl)pyridine and Their Application as Magnetic and Fluorescent Materials in Thin Film Deposition. *IJMS*. 2020 Jun 28;21(13):4587. <DOI>.

34. Benramdane R, Benghanem F, Ourari A, Keraghel S, Bouet G. Synthesis and characterization of a new Schiff base derived from 2,3-diaminopyridine and 5-methoxysalicylaldehyde and its Ni(II), Cu(II) and Zn(II) complexes. *Electrochemical and electrocatalytic studies. Journal of Coordination Chemistry*. 2015 Feb 1;68(3):560–72. <DOI>.

35a. Northcote-Smith J, Kaur P, Suntharalingam K. A Cancer Stem Cell Potent Copper(II) Complex with a S, N, S-Schiff base Ligand and Bathophenanthroline. *Eur J Inorg Chem*. 2021 May 14;2021(18):1770–5. **35b.** Ciesiński KL, Haas KL, Franz KJ. Development of next-generation photolabile copper cages with improved copper binding properties. *Dalton Trans*. 2010;39(40):9538. <DOI>.

36a. Kamatchi P, Selvaraj S, Kandaswamy M. Synthesis, magnetic and electrochemical studies of binuclear copper(II) complexes derived from unsymmetrical polydentate ligands. *Polyhedron*. 2005 Jun;24(8):900–8. <DOI>. **36b.** Samin AJ. A one-dimensional stochastic approach to the study of cyclic voltammetry with adsorption effects. *AIP Advances*. 2016 May;6(5):055101. <DOI>.

- 37a.** Li M, Wang R. Synthesis and multi-response research of a highly selective fluorescent chemosensor for Zn²⁺. IOP Conf Ser: Earth Environ Sci. 2017 Apr;61:012043. [<URL>](#). **37b.** Miller SR, Gustowski DA, Chen Z, Gokel GW, Echegoyen L, Kaifer AE. Rationalization of the unusual electrochemical behavior observed in lariat ethers and other reducible macrocyclic systems. Anal Chem. 1988 Oct 1;60(19):2021-4. [<DOI>](#).
- 38a.** Alfonso M, Tárraga A, Molina P. Ferrocene-based multichannel molecular chemosensors with high selectivity and sensitivity for Pb(ii) and Hg(ii) metal cations. Dalton Trans. 2010;39(37):8637. [<DOI>](#). **38b.** Medina JC, Goodnow TT, Rojas MT, Atwood JL, Lynn BC, Kaifer AE, et al. Ferrocenyl iron as a donor group for complexed silver in ferrocenyldimethyl[2.2]cryptand: a redox-switched receptor effective in water. J Am Chem Soc. 1992 Dec;114(26):10583-95. [<DOI>](#).
- 39a.** Kamal A, Kumar S, Kumar V, Mahajan RK. Selective sensing ability of ferrocene appended quinoline-triazole derivative toward Fe (III) ions. Sensors and Actuators B: Chemical. 2015 Dec;221:370-8. [<DOI>](#). **39b.** Sanan R, Kang TS, Mahajan RK. Complexation, dimerisation and solubilisation of methylene blue in the presence of biamphiphilic ionic liquids: a detailed spectroscopic and electrochemical study. Phys Chem Chem Phys. 2014;16(12):5667. [<DOI>](#).



Enhancement of the O₂ Sensitivity: ZnO, CuO, and ZnO/CuO Hybrid Additives' Effect on Meso-Tetraphenylporphyrin Dye

Merve Zeyrek Ongun^{1*}

¹Dokuz Eylul University, Chemistry Technology Program, Izmir, 35360, Turkey

Abstract: Semiconductor metal oxide materials have attracted great interest in gas sensors due to their high sensitivity to many target gases. In this study, an oxygen-sensitive optical chemical sensor was prepared in thin-film form by immobilizing meso-tetraphenylporphyrin (H₂TPP) in silicon matrix in the presence of ZnO, CuO and ZnO/CuO hybrid nanoparticles as additives. Characterization of synthesized metal oxide powders was performed using XPS, XRD, SEM, and PL spectroscopy. Emission and decay time measurements of H₂TPP-based materials were investigated between the concentration range of 0% and 100% [O₂] in thin-film forms. The intensity-based signal drops of the additive-free form of porphyrin dye toward oxygen were calculated as 70%. Whereas, the oxygen sensitivities of H₂TPP-based sensor slides were measured as 80%, 75%, and 88% in the presence of ZnO, CuO, and ZnO/CuO hybrid particles, respectively. The usage of porphyrin dye with ZnO/CuO hybrid additive provided higher oxygen sensitivity, larger linear response range, higher Stern-Volmer constant (KSV) value and faster response time compared to the undoped form, ZnO and CuO additive-doped forms of H₂TPP. The response and the recovery times of the porphyrin-based sensing slide along with ZnO/CuO hybrid particles have been measured as 10 and 20 s. These results make the H₂TPP along with the metal oxide additives promising candidates as oxygen probes.

Keywords: Photoluminescence, oxygen sensor, H₂TPP, ZnO, CuO, ZnO/CuO hybrid.

Submitted: December 02, 2021. **Accepted:** March 10, 2022.

Cite this: Zeyrek Ongun M. Enhancement of the O₂ Sensitivity: ZnO, CuO, and ZnO/CuO Hybrid Additives' Effect on Meso-Tetraphenylporphyrin Dye. JOTCSA. 2022;9(2):479-94.

DOI: <https://doi.org/10.18596/jotcsa.1031613>.

***Corresponding author. E-mail:** merve.zeyrek@deu.edu.tr. Telephone number: 05309372673.

INTRODUCTION

Oxygen is used as a reactant or product (1) in industrial processes, clinical (2), biomedical (3), environmental (4), and chemical analysis (5), and therefore, continuous and accurate determination of dissolved and gaseous O₂ levels is of great importance. In recent decades, optical chemical sensors based on spectroscopic changes are currently preferred for oxygen detection due to many advantages such as easy fabrication, high sensitivity, low detection limit, and low cost. Most optical sensors are fabricated by doping different types of oxygen-sensitive organic dyes into gas permeable sol-gel or polymeric matrices. There are

different types of organic dyes such as transition metal complexes of ruthenium (2), iridium (6), palladium (7), platinum (8), osmium (9), pyrene (10), and porphyrin and derivatives (11) used as oxygen-induced optical sensors based on the working principle of luminescence-quenching. One of the most important phosphorescence dyes used in oxygen gas sensors is metal-free and metal-carrier forms of tetraphenylporphyrins (TPPs), because of their long fluorescence lifetimes (microsecond to millisecond range), high oxygen sensitivity, large Stokes' shifts, high quantum yields, fast response times, and long stabilities. Table 1 summarizes previous studies with different porphyrin derivatives (12-20).

Table 1: Comparison of the oxygen sensing properties of porphyrin derivatives.

Sensitive dye	Matrix material	Sensitivity	Dynamic working range	Detection limit	Response time (N2-O2 / O2-N2)	Stability	Ref.
PdTPA PtTPA PdTPP PtTPP	poly(TMSP)	Ksv (% ⁻¹) 3.05 2.48 0.47 0.63	0-100% pO ₂	0.00098 0.012 0.0062 0.0047	6; 5; 13; 6 / 117; 46 s	After 8 months 20% lost	(12)
PdTFPP PdTCPP	Sol-gel	I ₀ /I ₁₀₀ 21.7 7.4	0-40 mg/L	NR	NR / NR	NR	(13)
PdTFPP	Silica-gel	KSV 67 kPa ⁻¹	0.02-100 Pa	NR	150ms / NR	NR	(14)
PdTPP	PMMA	KSV 0.071 Torr ⁻¹	0-200 Torr ⁻¹	NR	NR / NR	After 9 months 75% lost	(15)
PdTPTBP	Silicone rubber	KSV 0.921 hPa ⁻¹	213 hPa to 0 hPa O ₂	NR	<1s / NR	NR	(16)
PtTFPP	PS	KSV (% ⁻¹) 0.018	0-100% pO ₂	NR	NR / NR	NR	(17)
H ₂ TPP H ₂ TPA H ₂ OHe	poly(TMSP)	I ₀ /I ₁₀₀ 1.46 2.85 2.16	0-100% pO ₂	NR	NR / NR	After 3 months 6% lost	(18)
ZnTPP H ₂ TPP	poly(TMSP)	KSV (% ⁻¹) 0.0052 0.0384	0-20% pO ₂	NR	2 / 3 s	After 5 months 2% lost	(19)
H ₂ TPP	plastic-clad silica optic fiber	KSV = 7.5 × 10 ⁻⁴ Torr ⁻¹ I ₀ / I ₁₀₀ ≈ 1.55	55-760 Torr ⁻¹	NR	1s / NR	NR	(20)
H ₂ TPP H ₂ TPP-ZnO H ₂ TPP-CuO H ₂ TPP-ZnO/CuO Hybrid	poly(TMSP)	I ₀ /I ₁₀₀ 3.39 6.02 4.88 7.35	0-100% pO ₂	1.25 × 10 ⁻² 2.21 × 10 ⁻² 1.89 × 10 ⁻² 2.84 × 10 ⁻²	16; 12; 14; 10 s / 34; 24; 28; 20 s	After 6 months 3% lost	This work

NR= Not Reported

The sensing properties of fluorescent dyes depend on the interactions between the kind of solid matrix and the type of micro-environment of dyes. The appropriate polymer matrix can play a role as an enhancer agent in the oxygen sensitivity properties and provide mechanical stability due to being a rigid support material. However, the polymer-immobilized organic dyes still need some further modifications to improve their oxygen sensing performances. To increase the oxygen sensitivity of organic dyes, different ligand groups are attached to the structure of the dye, which can interact with oxygen groups during dye synthesis, or different semiconducting metal oxides known to have oxygen

adsorption abilities are added to the dye as a dopant during the preparation of the chemical sensor.

Semiconducting metal oxides (SMO) are promising candidate materials for gas sensing applications due to their easy production methods, high sensitivity to many target gases, low cost and being highly compatible with other processes (21). According to the literature, many gas sensor studies containing metal oxide nanoparticles due to porous structure and change of conductivity properties are based on electrical measurement. Recently, the use of many metal oxide nanoparticles such as ZnO, CuO, NiO₂,

TiO₂, etc. has become a new and popular application to improve electronic tape structure and enhance gas detection performance. Wang et al. reported that the CO gas detection capability of CuO/ZnO composite nanostructure was measured by the relative resistance techniques (22). Jiang et al. found that the fabricated ure and Pr-modified ZnO nanofibers synthesized using electrospinning-calcination techniques showed intensity-based O₂ sensing responses as 52% and 71%, at 115 °C, respectively (23). Inspired by these studies, today researchers include metal oxides with gas adsorption properties in optical chemical sensor studies. The advantage of fluorescence-based measurement is to be seen as an alternative in the absence of electrical contact between the resulting impurities and nanostructures. Last decades, many approaches were used such as adding some dopants like metals (Au (24), Ag (25), etc.) and/or metal oxides (SnO₂ (26), ZnO (27), TiO₂ (28), CuO (29) and Fe₂O₃ (30), etc.) because of their gas adsorption properties. Mariammal and colleagues reported that ZnO and ZnO:CuO nanoparticle-based sensing composites were used to detect ethanol vapor using the fiber optic sensor method (31). The emission and excitation spectra of transparent nanocolumnar porous ZnO thin films prepared by plasma-enhanced chemical vapor deposition were measured in the presence and absence of dissolved oxygen by Sanchez-Valencia et al. (32). Nowadays, researchers work on the enhancement of the gas sensitivity properties of organic dyes by supplementing additives such as metal and/or metal oxides. Jiang and co-workers fabricated a ratiometric optical sensor for dissolved oxygen in a form of nanofiber and thin-film using together Ag NPs and (Ru(dpp)₃Cl₂) composite via immobilized in polymethylmethacrylate matrix (33). Ozturk et al. investigated the effect of Ag NPs and ionic liquids (1-butyl-3-methylimidazolium tetrafluoroborate) on oxygen sensitivity of the ruthenium (II) dye in a form of fiber materials and nanoporous film structures (34). Ongun developed a high sensitive oxygen-induced sensor including the meso-tetraphenylporphyrin (H₂TPP) dye encapsulated in a silicon matrix in the presence of additives as Ag NPs and ionic liquids (ILs) (35). Oguzlar reported that the Fe₃O₄ and Fe₃O₄@Ag NPs as additives were used for improving oxygen sensing properties of the [Ru(bpy)₃]²⁺ dye both in EC thin-film and nanofiber form (36).

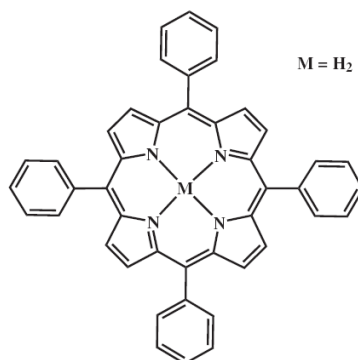
In this study, we aimed to improve the oxygen-induced sensitivity of commercially available meso-tetraphenylporphyrin (H₂TPP) dye in the presence of

different metal oxide additives. While both ZnO and CuO particles were produced by the sol-gel method, ZnO/CuO hybrid nanoparticles were synthesized using the complex directed hybridization method. The synthesized particles were characterized using photoluminescence spectroscopy (PL), X-ray photoelectron spectroscopy (XPS), X-ray diffraction spectroscopy (XRD), and scanning electron microscopy (SEM). The oxygen sensing responses of the H₂TPP-based composites along with metal oxide additives embedded in the poly(1-trimethylsilyl-1-propyne) matrix were tested by measuring the fluorescence-based emission spectra and decay time measurements. The relative signal intensity (I_0/I_{100}) values of H₂TPP along with the ZnO, CuO, and ZnO/CuO hybrid additives were found as 6.02, 4.88, and 7.35 between the concentration range of 0 and 100% [O₂], respectively. The enhancement of the emission-based optical properties and the decay kinetics can be based on the adherence of the oxygen molecules to the surface or inside of the metal oxide crystalline structures via adsorption. The usage of the ZnO, CuO and ZnO/CuO hybrid particles along with the H₂TPP resulted in higher oxygen sensitivity, faster response, more linear calibration plots, and better sensor dynamics compared to the non-additive free-form of dye.

EXPERIMENTAL SECTION

Reagents

Precursors were used without further purification in the synthesis of metal oxide nanoparticles. Zinc acetate dihydrate (Zn(CH₃COO)₂×2H₂O, ≥99%), zinc nitrate heptahydrate (Zn(NO₃)₂×7H₂O, ≥99%), and copper(II) acetate dihydrate (Cu(CH₃COO)₂×2H₂O, ≥99%) were purchased from Sigma Aldrich. Oxygen sensitive fluorescent dye, free-form of meso-tetraphenylporphyrin (H₂TPP), was supplied from Sigma-Aldrich. The structural formula of the employed metal-free porphyrin dye was shown in Scheme 1. Poly(1-trimethylsilyl-1-propyne) (poly(TMSP)) as polymeric support material was provided by ABCR Company. 1-Butyl-3-methylimidazolium tetrafluoroborate [BMIM][BF₄], used as an ionic liquid (IL), was obtained from Fluka. Sodium hydroxide (NaOH, ≥99%) was from Alfa-Aesar Sigma-Aldrich. The solvents of ethanolamine (≥98%) and toluene (≥99%) were purchased from Sigma-Aldrich. Mylar, polyester support for thin-film preparation, was supplied from DuPont polymers. Cylinders of nitrogen and oxygen gases (99.99%) were provided from Tinsa Gas, Izmir, Turkey.



Scheme 1: Structural formula of the metal-free tetraphenylporphyrin (H_2TPP).

Instrumentation

The phase structure of the synthesized powders was investigated by an X-ray diffractometer (XRD, Thermo Scientific ARL X-ray diffractometer, Cu-K α , 1.5405 Å, 45kV, 44mA). Thermo Scientific K-Alpha X-ray Photoelectron Spectrometer (XPS) equipped monochromatic Al-K α source was used to determine the elemental compositions of metal oxide particles. For morphological characterization, microstructure images were studied at different magnifications by COXEM EM-30 Plus scanning electron microscopy (SEM). The excitation-emission spectra were measured via Edinburgh FLSP920 spectrometer (PL). Decay time measurements under the excitation of a microsecond flash lamp were determined by the photoluminescence spectrometer operating on the time-dependent single-photon count (TCSPC) principle. Oxygen and nitrogen gases were mixed between 0% and 100% [O_2] concentration range using a gas blending system (Sonimix 7000A) and the gas mixture was introduced to the sensing thin film membrane in septum-sealed cuvette at room temperature via a diffuser needle.

Syntheses of ZnO, CuO and ZnO/CuO Hybrid Particles

The ZnO and CuO particles were synthesized by the sol-gel method. For the production of ZnO NPs, 0.5 M Zn(NO $_3$) $_2$ ·7H $_2$ O solution was added dropwise into the 1 M NaOH solution and heated at 70 °C for 2 h. The obtained white precipitates were dried at 200 °C for 1 h and then calcinated at 500 °C for 2 h (25). Similarly, in the preparation of CuO NPs, Cu(CH $_3$ COO) $_2$ ·2H $_2$ O powder (0.5 M) was dissolved in isopropanol, stirred and heated for 1 h at 50 °C. The pH value of the copper solution was adjusted using ethanolamine. The black precipitates were dried at 100 °C for 5 h and calcinated at 600 °C for 2 h, respectively (37). To prepare the ZnO/CuO hybrid NPs were used the complex directed hybridization method; 0.5 M Zn(CH $_3$ COO) $_2$ ·2H $_2$ O and 0.5 M Cu(CH $_3$ COO) $_2$ ·2H $_2$ O solutions were dissolved separately in distilled water and then mixed. While 10 M NaOH solution was added dropwise, the solution was stirred with a magnetic

stirrer. The final solution was heated for 12 h at 100 °C, then the calcination process was applied for 3 h at 500 °C (38).

Preparation of H $_2$ TPP-based oxygen sensing slides

Nowadays, researchers work on the enhancement of O $_2$ -sensing characteristics of porphyrin dyes along with different kinds of additives embedded in several polymeric matrices. The fluorescent-based sensing abilities of gas sensors are severely connected to the type of solid matrix and possible additive. In our previous works, we found that poly(TMSP) is an ideal polymeric matrix according to the optical transparency, high diffusibility toward oxygen, and stability. Therefore, poly(TMSP) was selected as a polymeric support material due to the high polymer permeability (oxygen permeability coefficient ($L = 7700 \text{ cm}^3 \text{ (STP) cm/cm}^2 \cdot \text{s} \cdot \text{cm Hg}$) and rapidly in contact with molecular oxygen (11,18). Also, we found in our previous work that the best ionic liquid additive is the [BMIM][BF $_4$] in terms of compatibility and oxygen gas solubility in a polymeric matrix and providing long-term stability to the indicator dye doped-sensing slides (39). Considering this information, thin films were prepared by placing meso-tetraphenylporphyrin (H_2TPP) dye embedded in poly(TMSP) matrix along with both different metal oxide additives and ionic liquid in close proximity.

The homogenous sensing slides were prepared by mixing 75 mg of poly(TMSP), 0.25 mg porphyrin dye, and 25 mg of [BMIM][BF $_4$] in 2.5 mL toluene under magnetic stirring. To improve the oxygen sensitivity of the H_2TPP dye, 0.25 mg of metal oxide (ZnO, CuO and ZnO/CuO hybrid) particles were individually added to the cocktail solution. Table 2 presents the compositions of the utilized cocktails. Afterwards, the prepared viscous solutions were coated onto a Mylar support using the knife spread method. Tencor Alpha Step 500 Profilometer was used to measure the thickness of the coated thin films ($7.63 \pm 0.18 \mu\text{m}$ ($n = 8$)). The measurements were recorded after each thin film was cut to appropriate sizes and placed in the septum cuvette.

Table 2: Cocktail compositions used as oxygen-sensing agents.

Dye	Cocktail Name	poly(TMSP) (mg)	toluene (mL)	ILs (mg)	Additive/ ZnO (mg)	Additive/ CuO (mg)	Additive/ ZnO/CuO Hybrid (mg)
	C1	75	2.5	25	-	-	-
H ₂ TPP (0.5 mg)	C2	75	2.5	25	0.5	-	-
	C3	75	2.5	25	-	0.5	-
	C4	75	2.5	25	-	-	0.5

RESULTS AND DISCUSSION

Characterization of metal oxide particles

The structural changes of the produced particles were examined by XRD (Figure 1 (a)). XRD peaks of the ZnO [JCPDS No. 36-1451] at $2\theta = 31.8^\circ, 34.5^\circ, 47.5^\circ, 56.5^\circ, 62.9^\circ, 66.4^\circ, 67.9^\circ, 69.2^\circ, 72.6^\circ$ and 77.0° were observed, consist with (100), (002), (101), (102), (110), (103), (112), (004) and (202) crystallographic planes of the ZnO hexagonal wurtzite phase, respectively (40). The diffraction peaks of the CuO [JCPDS No. 48-1548] at $2\theta =$

$32.6^\circ, 35.7^\circ, 38.9^\circ, 49.0^\circ, 53.6^\circ, 61.7^\circ, 66.2^\circ, 68.4^\circ, 66.2^\circ, 68.4^\circ$ corresponding to (110), (002), (111), (202), (020), (202), (113), (022), (220), (312), and (203) crystallographic planes of the CuO, which indicates that the CuO is monoclinic (41). Additionally, the diffraction peaks of the ZnO/CuO hybrid (1:1 molar ratio) nanocomposite were well matched with the above JCPDS cards, and the XRD patterns can be easily indexed to a mixed crystal phase containing a hexagonal wurtzite ZnO phase and a monoclinic (38).

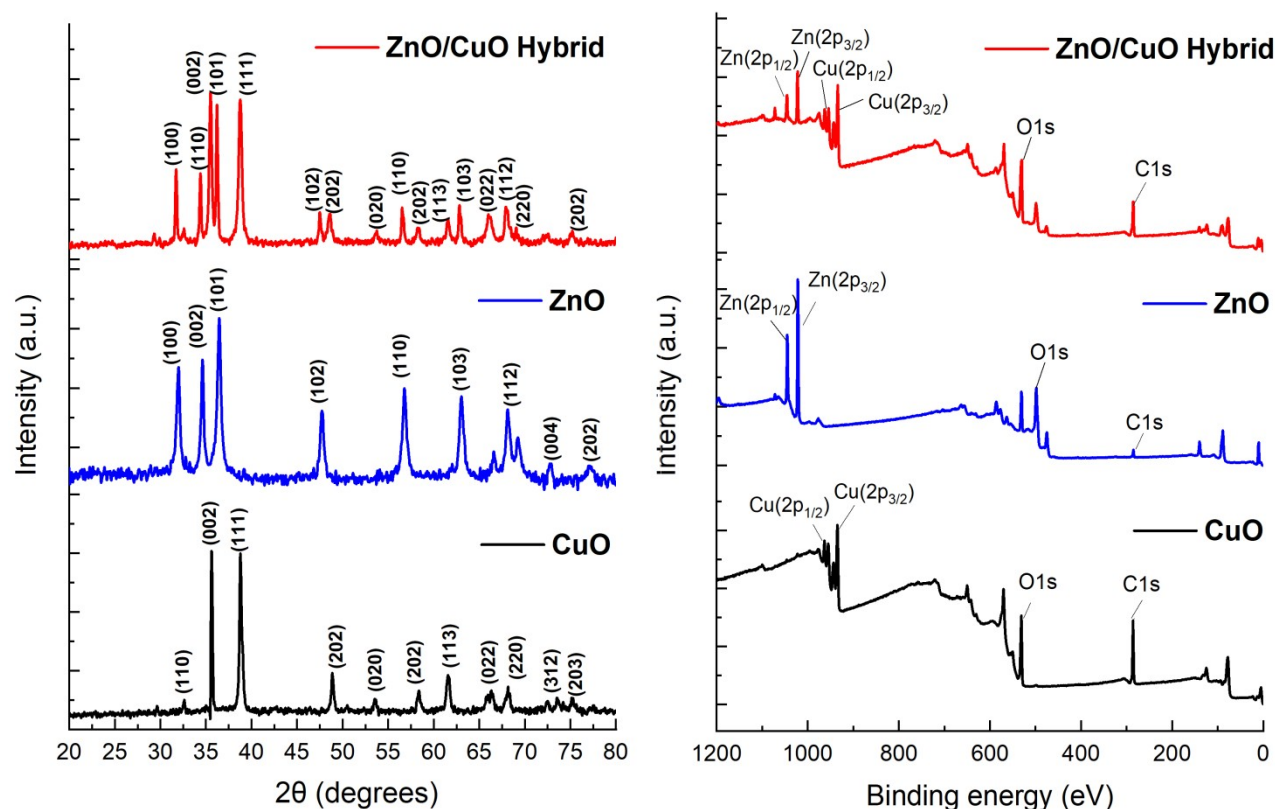


Figure 1: (a) XRD patterns, and (b) XPS spectra of ZnO, CuO and ZnO/CuO hybrid particles.

XPS analysis was studied to clarify the chemical structure of all prepared particles in terms of weight (%) values and binding energies of elements (Table 3). Figure 1 (b) shows that the XPS spectrum of

ZnO/CuO hybrid, ZnO and CuO structures and the binding energies related to Zn2p, Cu2p, O1s, and C1s peaks. When the binding energies of the ZnO/CuO hybrid structure are compared with the

pure form of ZnO structures, it is seen that the binding energy for Zn2p (1022 eV) shifts to higher binding energy (~ 0.3 eV) than for the pure form of ZnO. Furthermore, the binding energy of Cu2p (933 eV) shifted to lower energy (~ 0.7 eV) than pure CuO upon the ZnO/CuO hybrid structure formation. These shifts in binding energies can be attributed to differences in the electronegativity of metal ions. The electronegativity of Cu^{2+} is 2.0 while Zn^{2+} is 1.7 and for this reason, Cu^{2+} can easily remove electrons from Zn^{2+} . The electron shielding effect of Cu^{2+} increases and the main peak of Cu2p moves

toward lower binding energy, while Zn2p moves to the higher binding energy. For the ZnO/CuO hybrid, ZnO and CuO structures, the peaks of O1s coincide with the binding energies of 531.15, 531.04, and 531.26 eV (Table 3). According to previous studies, the peaks observed around ~ 530 eV were attributed to the lattice oxygen and the presence of O_2^- and O^- on the surface of the metal oxide structure. It has been also reported that the sensor detection performance is due to its ability to adsorb oxygen on the metal oxide surface (42).

Table 3: Binding energy (BE) and atomic weight (%) values of all metal oxide particles.

Name	ZnO/CuO Hybrid		ZnO		CuO	
	Peak BE	Weight (%)	Peak BE	Weight (%)	Peak BE	Weight (%)
Zn2p	1022.06	28.18	1021.78	74.82	-	-
Cu2p	933.85	31.05	-	-	934.59	49.57
O1s	531.15	25.20	531.04	18.62	531.26	28.91
C1s	285.16	15.57	285.29	6.56	286.04	21.52

Figure 2 (a), (b) and (c) show SEM micrographs that characterize the morphologies and microstructures of ZnO, CuO, and ZnO/CuO hybrid particles at $\times 10.0$ k magnification, respectively. According to the results, the aggregation of nanoparticles may be based on the high surface areas and energies of

ZnO and CuO particles. The formation of p-n heterojunctions along with pores and voids between p-type CuO and n-type ZnO in ZnO/CuO particles also contributes to gas sensitivity (31). As can be seen, there are much finer pores and cavities in the structure of the ZnO/CuO hybrid material.

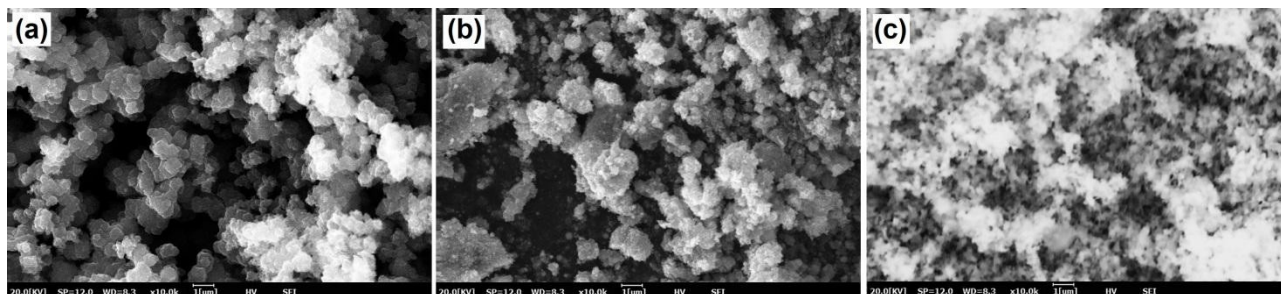


Figure 2: SEM images of (a) ZnO, (b) CuO, (c) ZnO/CuO hybrid particles at $\times 10.0$ k magnification.

Spectral behavior of H_2TPP along with metal oxide particles

Herein, we investigated the oxygen-induced spectral response of the H_2TPP along with nanoscale ZnO, CuO and ZnO/CuO hybrid particles in the poly(TMSP)-based thin films. When the H_2TPP -based sensing slides were excited at 420 nm, yielded with two emission bands at 652 and 717 nm. In all of the forms under study, the oxygen-induced emission intensities decreased which can be used as the analytical signal with the increasing quencher

amounts between the concentration ranges of 0-100% $[\text{O}_2]$. The relative signal change resulting from dynamic quenching depends on triple oxygen quenching the excited-state fluorescence of H_2TPP -based sensing composites through collisions. The following Stern-Volmer equation was used, which reveals the relationship between quencher concentration and fluorescence intensities, as it is most suitable for linearizing experimental data in the concentration interval of 0-100% $[\text{O}_2]$ (Eq. 1);

$$\frac{I_0}{I} = 1 + K_{SV}[\text{O}_2] \quad (\text{Eq. 1})$$

where I_0 and I are the fluorescence intensities in the absence and presence of quencher, respectively, KSV is the Stern–Volmer constant and $[O_2]$ is the oxygen concentration. When all other variables are kept constant, the higher the KSV, the lower concentration of quencher required to quench the luminescence (19).

The oxygen-induced fluorescence spectra of C1, C2, C3, and C4 composites were shown between Figure 3 and 6, respectively. When the porphyrin dye was used along with the metal oxide nanoparticles in the poly(TMSP) matrix in close proximity, it became extremely sensitive toward oxygen. The C1

exhibited a 70% signal drop for the 0-100% $[O_2]$ range, the C2, C3 and C4 composites yielded 80%, 75%, and 88% signal changes when exposed to the same concentration range of the oxygen, respectively. The comparative calibration plots of the utilized composites for the concentration range of 0–100% $[O_2]$ and the related equations of the calibration curves were reported in Figure 7 and Table 3, respectively. All of the H_2TPP -based sensing slides in the presence of metal oxide additives revealed linearly emission-based response in direction of decrease and exhibited good linearity and high regression coefficient (R^2) values in oxygenated conditions.

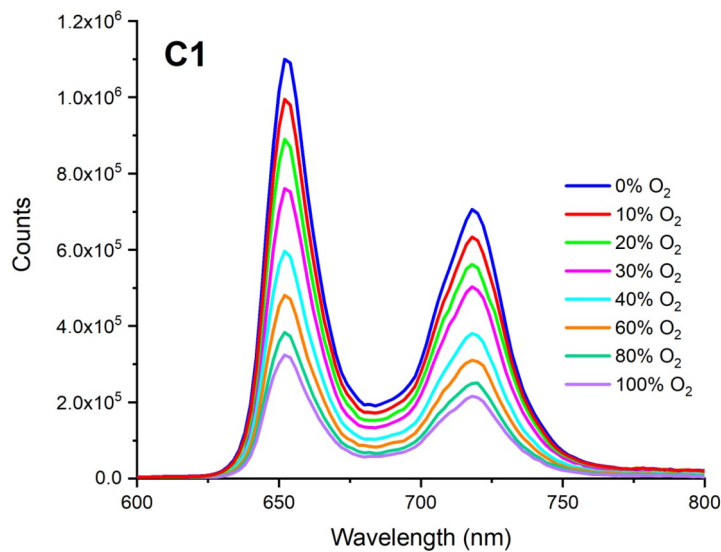


Figure 3: The oxygen induced-emission spectra of C1 in poly(TMSP) thin film for the concentration range of 0–100%.

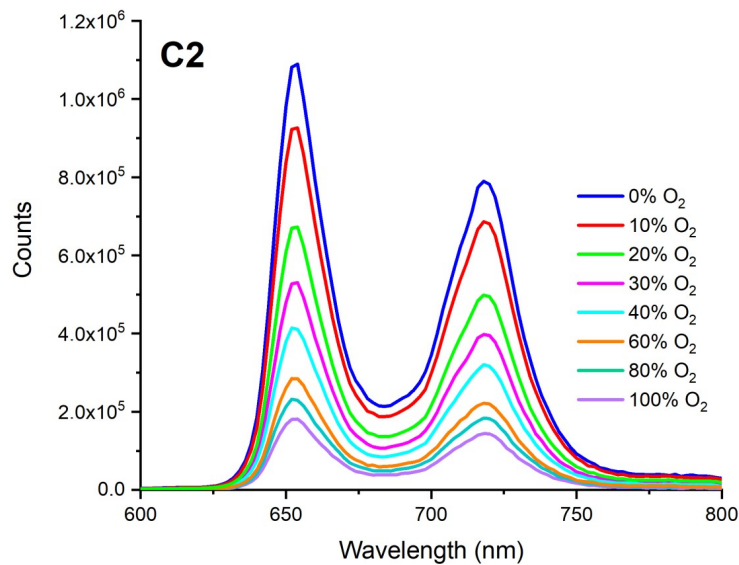


Figure 4: The oxygen induced-emission spectra of C2 in poly(TMSP) thin film for the concentration range of 0–100%.

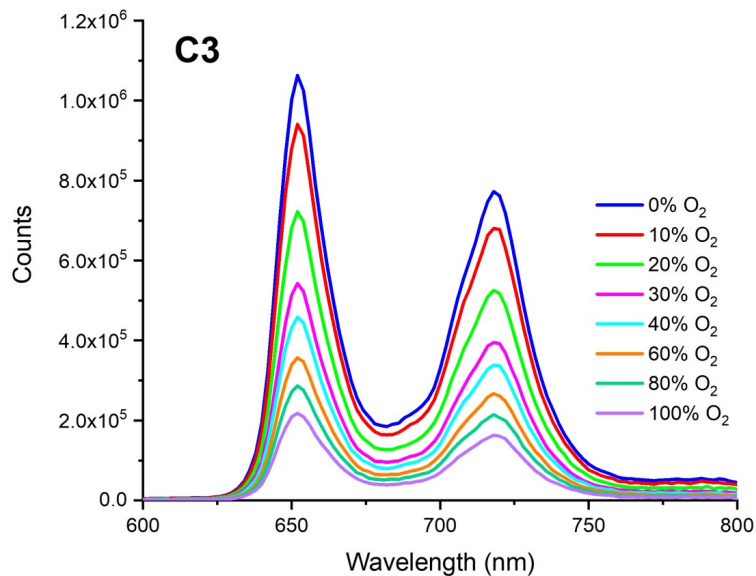


Figure 5: The oxygen induced-emission spectra of C3 in poly(TMSP) thin film for the concentration range of 0–100%.

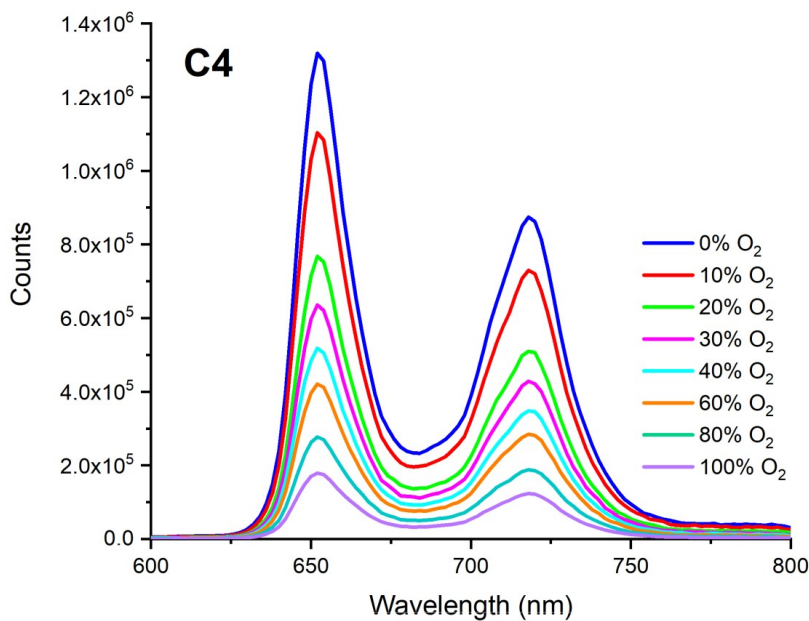


Figure 6: The oxygen induced-emission spectra of C4 in poly(TMSP) thin film for the concentration range of 0–100%.

When the emission-based signal drops of the utilized composites between 0% and 100% [O₂] were compared, C4 exhibited a superior linear response and a fairly high slope on the calibration plot relative to C1, C2, and C3; this case can be considered an indicator of the hypersensitivity of the

ZnO/CuO hybrid particle doped composite for the analyte. However, a linearized calibration plot of the C4 composite can be defined as; $y=0.0604x+1$ and the R² value of 0.9817 for the concentration range of 0-100% [O₂].

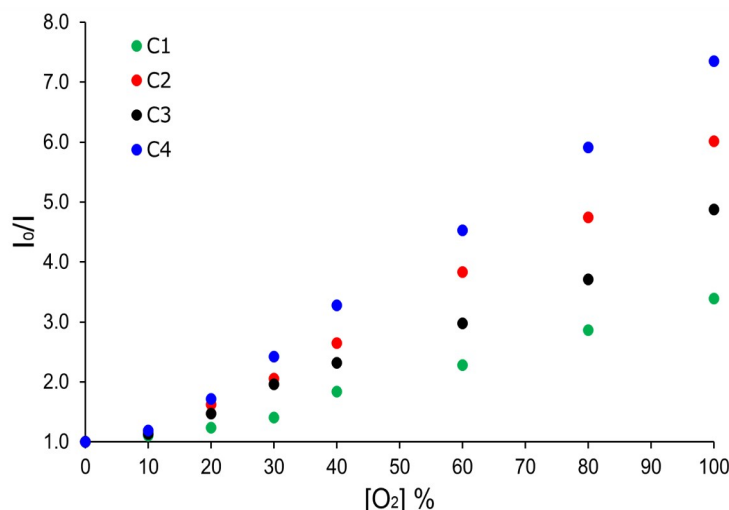


Figure 7: The comparative calibration plots of the C1, C2, C3, and C4 composites for the concentration range of 0-100% [O₂].

Table 4 reveals the equations of the calibration curves, the regression coefficients, the Stern-Volmer constants (K_{sv}), the relative signal changes (I_0/I_{100}) and the limit of detection (LOD) values of the utilized composites. The I_0/I_{100} ratio has been accepted as a display of indicator sensitivity where I_0 and I_{100} are the signal intensities of the indicator dye in the lack of and the maximum concentration levels of quencher, respectively. Nevertheless, the researches to improve the I_0/I_{100} parameter of the H₂TPP are still in progress. Herein, the utilization of the ZnO, CuO and ZnO/CuO hybrid powders along with the H₂TPP in the silicon matrix resulted in enhanced sensitivity with respect to the former literature (18,19). The I_0/I_{100} values were found to be 3.39, 6.02, 4.88, and 7.35 for the C1, C2, C3, and C4, respectively. The Stern-Volmer (K_{sv}) values, which quantifies the quenching efficiency of the sensor, were found in the range of 2.25×10^{-2} –

6.04×10^{-2} for all of the thin film-based composites. As a result, it can be concluded that C4 exhibits better oxygen gas sensitivity as it shows higher relative signal change and KSV values compared to other cocktails. This result makes the C4 composite an encouraging sensor slide for developing a luminescence-based oxygen detecting device. Also, the limit of detection (LOD) value is calculated using both the slope of the extinction plot in the calibration graph and the resolution of the spectroscopic instrument and calculated by dividing the $0.003/\text{slope}$ at a signal-to-noise ratio of 3.0. Considering the fully-nitrogen gas moiety as the blank, the LOD values for the C1, C2, C3, and C4 were found to be 1.25×10^{-2} p[O₂]% (1.66×10^{-1} mg/L), 2.21×10^{-2} p[O₂]% (2.94×10^{-1} mg/L), 1.89×10^{-2} p[O₂]% (2.51×10^{-1} mg/L), and 2.84×10^{-2} p[O₂]% (3.78×10^{-1} mg/L), respectively (Table 4).

Table 4: Optical properties and O₂ sensitivity of H₂TPP dye included sensing agents.

Cocktail name	Equation (Conc.range of 0–100% [O ₂])	Stern-Volmer constant K_{sv}	Regression coefficient R^2	I_0/I_{100}	LOD (p[O ₂]%)	LOD (mg/L)
C1	$y=0.0225x + 1$	2.25×10^{-2}	0.9702	3.39	1.25×10^{-2}	1.66×10^{-1}
C2	$y=0.0471x + 1$	4.71×10^{-2}	0.9798	6.02	2.21×10^{-2}	2.94×10^{-1}
C3	$y=0.0355x + 1$	3.55×10^{-2}	0.9785	4.88	1.89×10^{-2}	2.51×10^{-1}
C4	$y=0.0604x + 1$	6.04×10^{-2}	0.9817	7.35	2.84×10^{-2}	3.78×10^{-1}

In this study, we independently measured the absorption and the emission bands of the heterostructures of H₂TPP and all utilized additives to clarify the reasons behind the increase of oxygen-induced sensitivity. The normalized intensity-based spectra of ZnO, CuO and ZnO/CuO hybrid particles were individually shown in Figure 8 (a), (b) and (c), superimposed with the intensity-based spectrum of

the H₂TPP dye. All the utilized powders embedded in the poly(TMSP) thin-film were excited at their own excitation wavelength. Both ZnO, CuO and ZnO/CuO hybrid additives excited in a wide range wavelength, which covers the excitation band of H₂TPP, between 300 and 450 nm and emitted in broadband of approximately 400 to 720 nm.

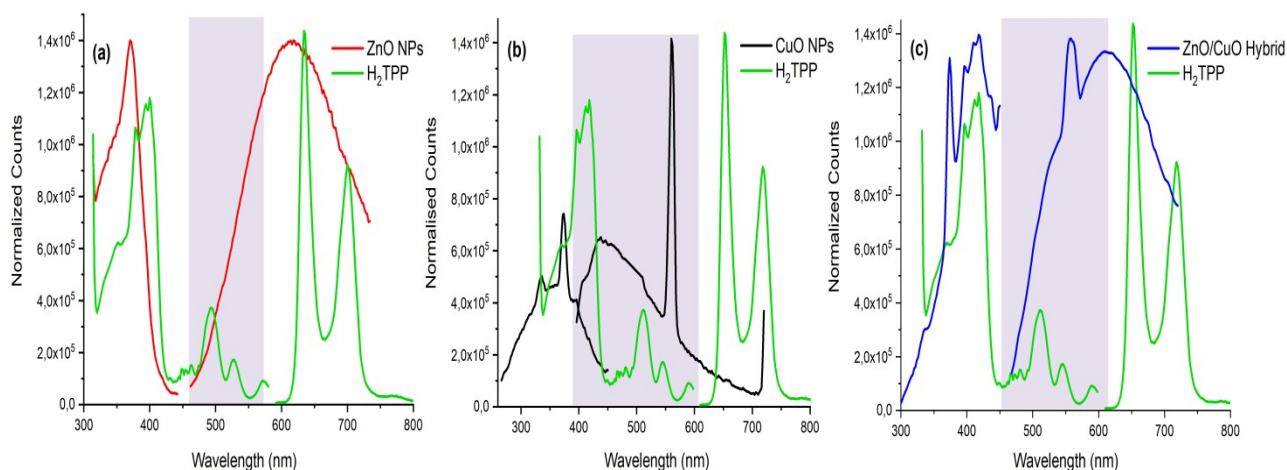


Figure 8: The excitation and emission spectra of the poly(TMSP) embedded H₂TPP, (a) ZnO, (b) CuO and (c) ZnO/CuO hybrid, individually.

The gas sensing performances of ZnO and CuO semiconductor materials are related to the oxygen adsorption and electron transfer process. The presence of active pores, void spaces and oxygen vacancies, which act as active centers for the adsorption of oxygen molecules, enable the semiconductor oxides to exhibit high gas sensing capacity. Also, the free electrons on the surface of ZnO and CuO semiconductors result in the enhancement of gas sensitivity by adsorbing a large number of oxygen species from the air. When CuO and ZnO materials have interacted, electrons can migrate from n-type ZnO to p-type CuO as a result of a strong effect between both semiconductor materials and hence more free electrons are available in this system. The more enhanced oxygen response of ZnO/CuO hybrid heterostructures is due to larger p-n junction depletion regions, larger surface area, and more oxygen adsorption at the surface, resulting from the formation of p-n heterojunctions between p-type CuO and n-type ZnO (31).

The enhancement in the oxygen sensitivity of H₂TPP in the presence of the metal oxide particles may be attributed to the strong excitation-emission abilities of the metal oxides, which act as a light-harvesting agent, and the energy transfer between the metal oxide particles and the dye. According to Figure 8 (a), (b) and (c), the emission bands of all utilized metal oxide additives partially overlaps with the absorption band of the H₂TPP, which makes interaction and an energy transfer from the metal oxide particles (donor) to the porphyrin dye (acceptor), possible. The strong absorption and the broadband emission of ZnO and CuO semiconductor materials are associated with a charge transfer from the 2p levels of the O₂ at the valence band (VB) to the 3d orbitals of the metal ions lying in the conduction band (CB). However, the coexistence of the CuO and ZnO nanocrystals in the hybrid

structure resulted in an unexpected enhancement in the oxygen sensitivity of the H₂TPP. The broad emission band (from 450 to 720 nm) of the ZnO/CuO hybrid crystals may be attributed to the direct electron transitions between the CB and the VB or the transition of the electrons from the defect orbitals to the CB or VB. However, the emission performance corresponds to the green-yellow region of the spectrum of ZnO/CuO hybrid particles originating from metal ions and cavities of oxygen, interstitial metal ions, electronic transitions between interstitial metal ions, and oxygen antisite increases the oxygen detection abilities of H₂TPP (25,42,43).

Decay Time Measurements

In this work, the luminescence decay time kinetics of all the used sensing slides were measured under oxygenated and deoxygenated atmosphere (Figure 9). When excited at 418 nm, the H₂TPP-based composites exhibited tri-exponential and bi-exponential decays in oxygen-free and fully-oxygenated conditions, respectively. Short and long decay time components and their distribution statistics for all sensing slides were shown in Table 5. The observed multi-exponential features in decay kinetics may be ascribed to as the structural features of the fluorophore composites and the hassle of the accessibility of the quencher. In deoxygenated moieties, the decay-time values of the undoped- and the additive doped-H₂TPP composites varied between 2.40 and 2.47 μ s for the short lifetime components and between 100.86 and 109.32 μ s for the long one. When exposed to oxygen, the shorter decay time components between 2.98 and 1.06 μ s and the longer lifetime components between 11.54 and 9.88 μ s were observed for all of the sensing slides. When exposed to oxygen, the longer lifetime component got lost (around \sim 100.00 μ s) and the average decay times showed a decrease of 20, 30, 25, and 40% for C1, C2, C3, and C4, respectively.

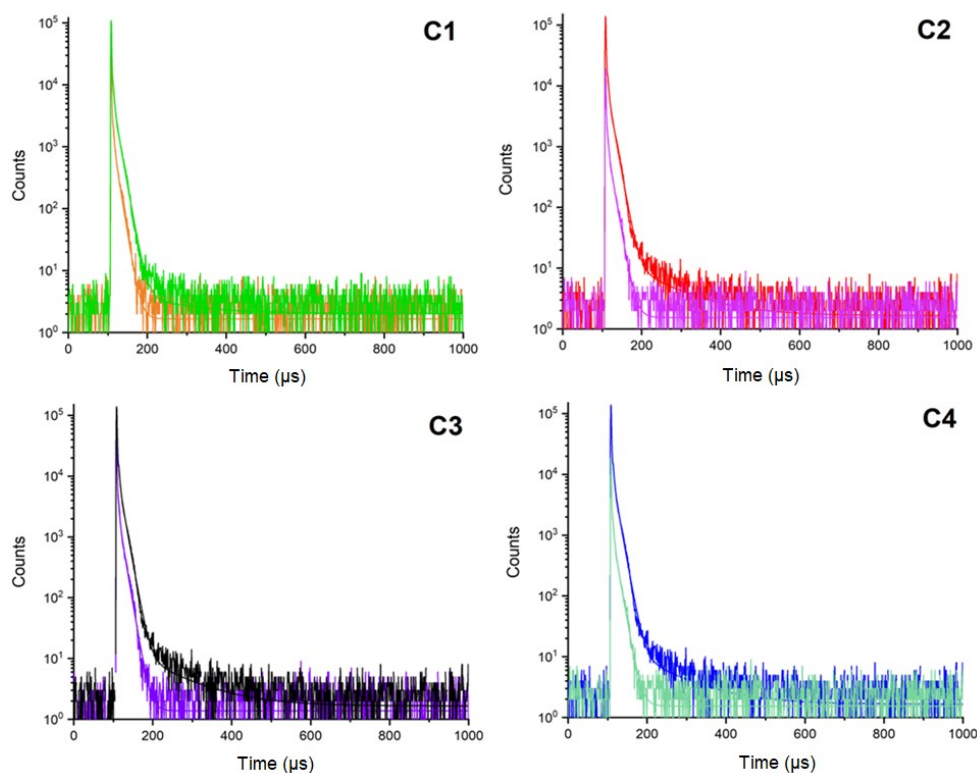


Figure 9: The decay kinetics of C1, C2, C3, and C4 under exposure to under fully-nitrogen and fully-oxygen atmosphere.

In fully oxygenated moieties, the increased signal decrease rates observed in both the emission-based intensity and the decay kinetics can be explained by the existence of metal oxides providing better adsorption properties of oxygen. In such metal oxide particles, the adsorbed oxygen gas diffuses to the inside or subsurface layer of the oxygen-induced luminescent dye. Also, the adsorbed or diffused gas in metal oxide semiconductors creates potential barriers between the oxide grains, which reduction in electrical conductivity. This charge mobility in metal oxides, which affects luminescence and conductivity decreases in decay time values (44).

Reversibility and Stability of the H₂TPP-based Composites

Response-regeneration time and stability are significant properties of optical sensor performance. The intensity-based kinetic response of the H₂TPP-based composites along with the ZnO, CuO and ZnO/CuO hybrid additives were individually investigated and evaluated to time under fully-

nitrogen and fully-oxygen atmosphere. The reversible signal cycles for kinetic measurements were measured along 1000 s. After exposure to fully-oxygenated atmosphere, the response times of C1, C2, C3, and C4 were measured as 16, 12, 14, and 10 s, and the regeneration times for the reverse direction were determined as 34, 24, 28, and 20 s, respectively (Figure 10). Considering these results, when compared to the other H₂TPP based-sensing slides, the C4 showed better response-regeneration time and repeatability results over multiple detection cycles under conditions of constantly changing gas concentrations between 0% and 100% O₂. Also, no significant decrease was monitored in the oxygen-induced intensities and decay kinetics of the sensing agents when stored at the ambient air of the laboratory conditions ($20 \pm 1^\circ\text{C}$) in the dark for 6 months. The utilized sensing slides had lost their original intensity-based signal values less than 3%, but they still had the potential for O₂ gas measurements.

Table 5: Decay kinetics of C1, C2, C3, and C4 embedded in the poly(TMSP)-based thin films.

Sample	τ_0 (0% O ₂)	Decay Time (μ s)	Std. Dev. (μ s)	Rel. (%)	τ_0 (100% O ₂)	Decay Time (μ s)	Std. Dev. (μ s)	Rel. (%)
C1	τ_2	2.47	0.07	21.48	τ_2	2.98	0.16	33.46
	τ_3	11.73	0.08	77.27	τ_3	11.54	0.20	66.54
	τ_4	107.98	1.08	1.25	τ_4	-	-	-
	T_{avr}		10.95 μ s		T_{avr}		8.67 μ s	
C2	τ_2	2.45	0.06	22.43	τ_2	2.19	0.14	35.38
	τ_3	11.96	0.07	76.60	τ_3	10.44	0.19	64.62
	τ_4	109.32	1.22	0.97	τ_4	-	-	-
	T_{avr}		10.77 μ s		T_{avr}		7.52 μ s	
C3	τ_1	2.46	0.07	21.41	τ_1	2.82	0.09	33.98
	τ_2	11.72	0.08	77.34	τ_2	11.19	0.12	66.02
	τ_3	107.12	1.06	1.26	τ_3	-	-	-
	T_{avr}		10.94 μ s		T_{avr}		8.34 μ s	
C4	τ_1	2.40	0.06	19.91	τ_1	1.06	0.01	38.77
	τ_2	11.69	0.06	79.10	τ_2	9.88	0.06	61.23
	τ_3	100.86	0.09	0.99	τ_3	-	-	-
	T_{avr}		10.72 μ s		T_{avr}		6.46 μ s	

CONCLUSION

In this work, we reported the effect of the gas adsorption properties of metal oxide additives on the oxygen sensitivity of the H₂TPP via the enhancement in the emission spectra. The XRD, XPS, SEM, and PL spectroscopic techniques were used for the characterization of the synthesized ZnO, CuO and ZnO/CuO hybrid particles. The oxygen-sensitivities of the H₂TPP-based composites and the interactions between the porphyrin dye and the metal oxide additives were tested with fluorescence-based measurements and decay time kinetics. The relative signal changes (I_0/I_{100}) of 3.39,

6.02, 4.88, and 7.35 were reported for the poly(TMSP) embedded C1, C2, C3, and C4, respectively. The most sensitive detection slide, C4, showed a linear response for the concentration range of 0-100% [O₂] with an R² value of 0.9817 and a high slope on the calibration graph. The enhancement in the oxygen-induced sensitivity of H₂TPP should be attributed not only to the excitation-emission abilities of the ZnO/CuO hybrid additives but also to the free electrons formed during the generation of heterojunction between ZnO and CuO in the synthesis of the ZnO/CuO structure, which facilitates the adsorption of O₂ molecules on the surface.

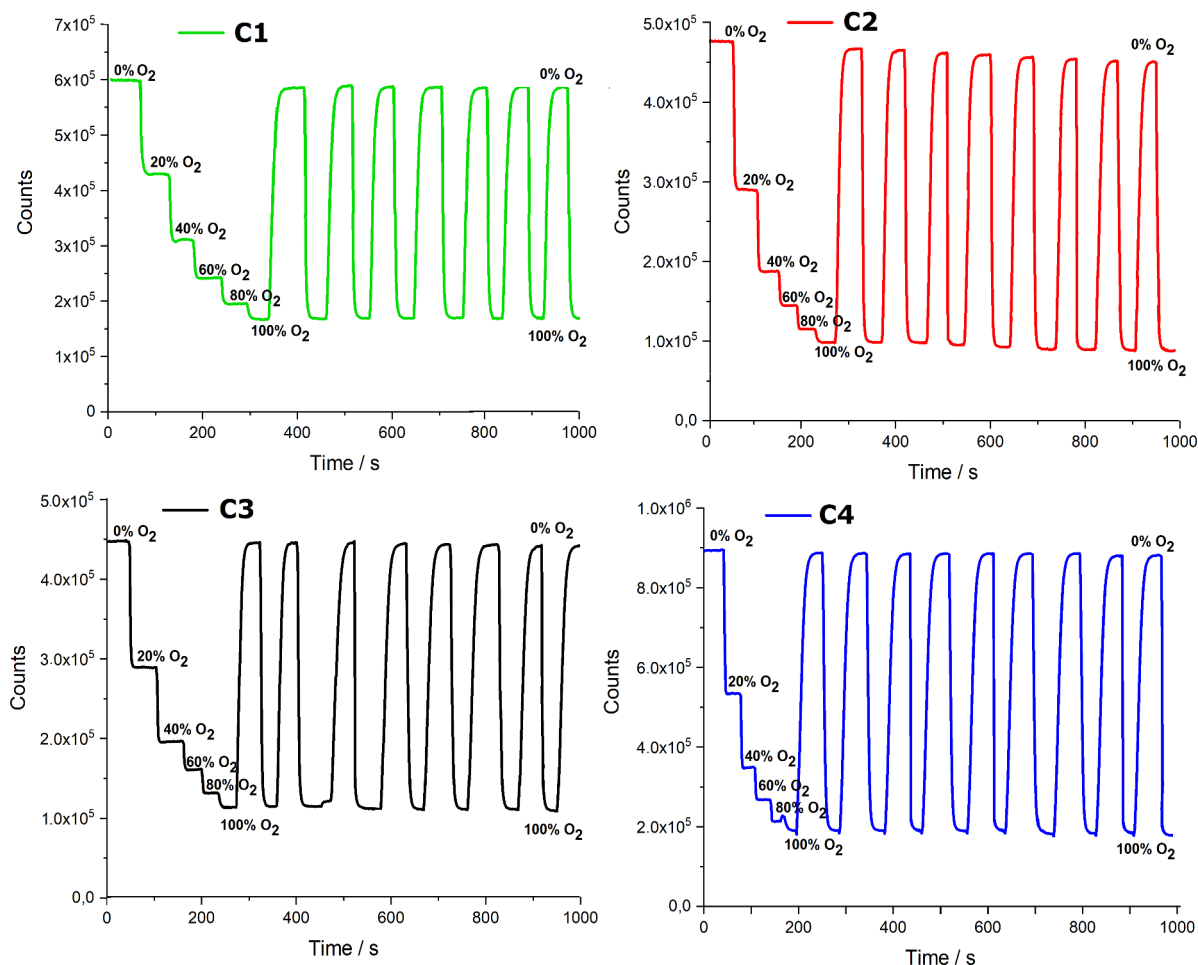


Figure 10: Intensity-based kinetic response of C1, C2, C3, and C4 composites between the oxygen concentrations of 0% and 100%.

ACKNOWLEDGMENT

Financing for steady-state and decay time measurements of meso-tetraphenylporphyrin dye was obtained from Dokuz Eylul University Scientific Research Funds (Project no: 2018.KB.FEN.039). Also, XRD, XPS, and PL measurements were performed in the Center for Fabrication and Applications of Electronic Materials (EMUM). I would like to thank them all.

CONFLICT OF INTEREST

The author declares that there are no conflicts of interest.

REFERENCES

1. Passard G, Dogutan DK, Qiu M, Costentin C, Nocera DG. Oxygen reduction reaction promoted by manganese porphyrins. *ACS Catal.* 2018;8(9):8671–9. [<DOI>](#).
2. Xu Y, Yang D, Huo S, Ren J, Gao N, Chen Z, et al. Carbon dots and ruthenium doped oxygen sensitive nanofibrous membranes for monitoring the respiration of

agricultural products. *Polym Test.* 2021;93:106957. [<DOI>](#).

3. Canaparo R, Foglietta F, Limongi T, Serpe L. Biomedical applications of reactive oxygen species generation by metal nanoparticles. *Materials (Basel).* 2021;14(1):53. [<DOI>](#).
4. Wang G, Chen H. Oxygen consumption for the combustion of sewage sludge: a potential environmental parameter determined by an electrochemical YSZ oxygen sensor. *Int J Environ Anal Chem.* 2020;1–10. [<DOI>](#).
5. Kuang C, Wang S, Luo M, Cai J, Zhao J. Investigation of CuO-based oxygen carriers modified by three different ores in chemical looping combustion with solid fuels. *Renew Energy.* 2020;154:937–48. [<DOI>](#).
6. Ongun MZ, Sahin M, Akbal T, Avsar N, Karakas H, Ertekin K, et al. Synthesis, characterization and oxygen sensitivity of cyclophosphazene equipped-iridium (III) complexes. *Spectrochim Acta Part A Mol Biomol Spectrosc.* 2020;239:118490. [<DOI>](#).
7. Monash A, Marciano D, Fass R, Dvash Y, Rosen O. Phosphorescent palladium-tetrabenzoporphyrin indicators for immunosensing of small molecules with a novel optical device. *Talanta.* 2021;224:121927. [<DOI>](#).

8. Xing Y, Wang L, Liu C, Jin X. Effects of fluorine and phenyl substituents on oxygen sensitivity and photostability of cyclometalated platinum (II) complexes. *Sensors Actuators B Chem.* 2020;304:127378. [<DOI>](#).
9. Ge C, Zhu J, Ouyang A, Lu N, Wang Y, Zhang Q, et al. Near-infrared phosphorescent terpyridine osmium (II) photosensitizer complexes for photodynamic and photooxidation therapy. *Inorg Chem Front.* 2020;7(20):4020-7. [<DOI>](#).
10. Bolognesi M, Moschetto S, Trapani M, Prescimone F, Ferroni C, Manca G, et al. Noncovalent functionalization of 2D black phosphorus with fluorescent boronic derivatives of pyrene for probing and modulating the interaction with molecular oxygen. *ACS Appl Mater Interfaces.* 2019;11(25):22637-47. [<DOI>](#).
11. Ongun MZ, Topal SZ, Yel Z, Ertekin K, Önal E, Hirel C. Improvement of the O₂ detection: Substituent's effect on Pd (II) meso-tetraphenylporphyrin probes. *Sensors Actuators B Chem.* 2019;288:316-24. [<DOI>](#).
12. Önal E, Ay Z, Yel Z, Ertekin K, Gürek AG, Topal SZ, et al. Design of oxygen sensing nanomaterial: synthesis, encapsulation of phenylacetylide substituted Pd (II) and Pt (II) meso-tetraphenylporphyrins into poly (1-trimethylsilyl-1-propyne) nanofibers and influence of silver nanoparticles. *RSC Adv.* 2016;6(12):9967-77. DOI: [<DOI>](#).
13. Chu C-S, Chuang C-Y. Ratiometric optical fiber dissolved oxygen sensor based on metalloporphyrin and CdSe quantum dots embedded in sol-gel matrix. *J Lumin.* 2015;167:114-9. [<DOI>](#).
14. Borisov SM, Lehner P, Klimant I. Novel optical trace oxygen sensors based on platinum (II) and palladium (II) complexes with 5, 10, 15, 20-meso-tetrakis-(2, 3, 4, 5, 6-pentafluorophenyl)-porphyrin covalently immobilized on silica-gel particles. *Anal Chim Acta.* 2011;690(1):108-15. [<DOI>](#).
15. Oige K, Avarmaa T, Suisalu A, Jaaniso R. Effect of long-term aging on oxygen sensitivity of luminescent Pd-tetraphenylporphyrin/PMMA films. *Sensors Actuators B Chem.* 2005;106(1):424-30. [<DOI>](#).
16. Mueller BJ, Burger T, Borisov SM, Klimant I. High performance optical trace oxygen sensors based on NIR-emitting benzoporphyrins covalently coupled to silicone matrixes. *Sensors Actuators B Chem.* 2015;216:527-34. [<DOI>](#).
17. Amao Y, Asai K, Okura I. Oxygen sensing based on lifetime of photoexcited triplet state of platinum porphyrin-polystyrene film using time-resolved spectroscopy. *J Porphyr Phthalocyanines.* 2000;4(3):292-9. [<DOI>](#).
18. Topal SZ, Ongun MZ, Önal E, Ertekin K, Hirel C. Hyperporphyrin effect on oxygen sensitivity of free meso-tetraphenylporphyrins. *Dye Pigment.* 2017;144:102-9. [<DOI>](#).
19. Topal SZ, Önal E, Ertekin K, Oter O, Gürek AG, Hirel C. Significant sensitivity and stability enhancement of tetraphenylporphyrin-based optical oxygen sensing material in presence of perfluorochemicals. *J Porphyr Phthalocyanines.* 2013;17(06n07):431-9. [<DOI>](#).
20. Potyrailo RA, Hieftje GM. Oxygen detection by fluorescence quenching of tetraphenylporphyrin immobilized in the original cladding of an optical fiber. *Anal Chim Acta.* 1998;370(1):1-8. [<DOI>](#).
21. Arafat MM, Dinan B, Akbar SA, Haseeb A. Gas sensors based on one dimensional nanostructured metal-oxides: a review. *Sensors.* 2012;12(6):7207-58. [<DOI>](#).
22. Wang JX, Sun XW, Yang Y, Kyaw KKA, Huang XY, Yin JZ, et al. Free-standing ZnO-CuO composite nanowire array films and their gas sensing properties. *Nanotechnology.* 2011;22(32):325704. [<DOI>](#).
23. Jiang T, Du B, Zhang H, Yu D, Sun L, Zhao G, et al. High-performance photoluminescence-based oxygen sensing with Pr-modified ZnO nanofibers. *Appl Surf Sci.* 2019;483:922-8. [<DOI>](#).
24. Qu X, Yang R, Tong F, Zhao Y, Wang M-H. Hierarchical ZnO microstructures decorated with Au nanoparticles for enhanced gas sensing and photocatalytic properties. *Powder Technol.* 2018;330:259-65. [<DOI>](#).
25. Ongun MZ. Tuning CO₂ sensitivity of HPTS by ZnO and ZnO@ Ag nanoparticles. *J Photochem Photobiol A Chem.* 2020;400:112664. [<DOI>](#).
26. Yin X-T, Dastan D, Wu F-Y, Li J. Facile synthesis of SnO₂/LaFeO₃- XNX composite: photocatalytic activity and gas sensing performance. *Nanomaterials.* 2019;9(8):1163. [<DOI>](#).
27. Paliwal A, Sharma A, Tomar M, Gupta V. Carbon monoxide (CO) optical gas sensor based on ZnO thin films. *Sensors Actuators B Chem.* 2017;250:679-85. [<DOI>](#).
28. Castellero P, Roales J, Lopes-Costa T, Sánchez-Valencia JR, Barranco A, González-Elipe AR, et al. Optical gas sensing of ammonia and amines based on protonated porphyrin/TiO₂ composite thin films. *Sensors.* 2017;17(1):24. [<DOI>](#).
29. Chethana DM, Thanuja TC, Mahesh HM, Kiruba MS, Jose AS, Barshilia HC, et al. Synthesis, structural, magnetic and NO₂ gas sensing property of CuO nanoparticles. *Ceram Int.* 2021;47(7):10381-7. [<DOI>](#).
30. Priya AK, Sunny A, Karthikeyan B, Sastikumar D. Optical, spectroscopic and fiber optic gas sensing of potassium doped α -Fe₂O₃ nanostructures. *Opt Fiber Technol.* 2020;58:102304. [<DOI>](#).
31. Mariammal RN, Ramachandran K. Study on gas sensing mechanism in p-CuO/n-ZnO heterojunction sensor. *Mater Res Bull.* 2018;100:420-8. [<DOI>](#).
32. Sanchez-Valencia JR, Alcaire M, Romero-Gómez P, Macias-Montero M, Aparicio FJ, Borrás A, et al. Oxygen optical sensing in gas and liquids with nanostructured ZnO thin films based on exciton emission detection. *J Phys Chem C.* 2014;118(18):9852-9. [<DOI>](#).
33. Jiang Z, Yu X, Zhai S, Hao Y. Ratiometric dissolved oxygen sensors based on ruthenium complex doped with silver nanoparticles. *Sensors.* 2017;17(3):548. [<DOI>](#).
34. Ozturk O, Oter O, Yildirim S, Subasi E, Ertekin K, Celik E, et al. Tuning oxygen sensitivity of ruthenium

- complex exploiting silver nanoparticles. *J Lumin.* 2014;155:191–7. [<DOI>](#).
35. Ongun MZ. Development of Highly Sensitive Metal-Free Tetraphenylporphyrin-Based Optical Oxygen Sensing Materials along with ILs and AgNPs. *Celal Bayar Univ J Sci.* 2019;15(1):131–8. DOI: [<DOI>](#).
36. Oguzlar S. Development of highly sensitive [Ru (bpy) 3] 2+-Based optical oxygen sensing thin films in the presence with Fe3O4 and Fe3O4@ Ag NPs. *Opt Mater (Amst).* 2020;101:109772. [<DOI>](#).
37. Yildirim B, Keskin OY, Oguzlar S, Birlik I, Azem FA, Ertekin K. Manipulation of brightness and decay kinetics of LuAG: Ce3+ and YAG: Ce3+ by simple metal oxides in polymeric matrices. *Opt Laser Technol.* 2021;142:107226. [<DOI>](#).
38. Yang C, Cao X, Wang S, Zhang L, Xiao F, Su X, et al. Complex-directed hybridization of CuO/ZnO nanostructures and their gas sensing and photocatalytic properties. *Ceram Int.* 2015;41(1):1749–56. [<DOI>](#).
39. Ongun MZ, Oter O, Sabancı G, Ertekin K, Celik E. Enhanced stability of ruthenium complex in ionic liquid doped electrospun fibers. *Sensors Actuators B Chem.* 2013;183:11–9. [<DOI>](#).
40. Acedo-Mendoza AG, Infantes-Molina A, Vargas-Hernández D, Chávez-Sánchez CA, Rodríguez-Castellón E, Tánori-Córdova JC. Photodegradation of methylene blue and methyl orange with CuO supported on ZnO photocatalysts: The effect of copper loading and reaction temperature. *Mater Sci Semicond Process.* 2020;119:105257. [<DOI>](#).
41. Zhu D, Wang L, Yu W, Xie H. Intriguingly high thermal conductivity increment for CuO nanowires contained nanofluids with low viscosity. *Sci Rep.* 2018;8(1):1–12. DOI: [<DOI>](#).
42. Wang X, Li S, Xie L, Li X, Lin D, Zhu Z. Low-temperature and highly sensitivity H2S gas sensor based on ZnO/CuO composite derived from bimetal metal-organic frameworks. *Ceram Int.* 2020;46(10):15858–66. [<DOI>](#).
43. Oguzlar S, Ongun MZ, Ertekin K. Investigation of light induced interactions between ZnO nano-particles and red emitting phosphor blends of Eu2+/Dy3+ doped strontium aluminate and Eu2+ doped Ca- α -Sialon. *J Lumin.* 2021;118236. [<DOI>](#).
44. Aydin I, Ertekin K, Demirci S, Gultekin S, Celik E. Sol-gel synthesized Sr4Al14O25: Eu2+/Dy3+ blue-green phosphorous as oxygen sensing materials. *Opt Mater (Amst).* 2016;62:285–96. [<DOI>](#).



Determination of Heavy Metals in Tobacco Leaves and Their Growing Soils in Assosa District, Benshangul Gumuz Regional State, Ethiopia

Tsegaye MELKAMU , Abera GURE , Tsegaye Girma ASERE* 

Jimma University, Department, Department of Chemistry, Jimma, Ethiopia

Abstract: Tobacco is a commercial plant that can accumulate heavy metals in its leaves. In this study, we investigated the levels of selected heavy metals (Mn, Cu, Zn, Cd, and Pb) in tobacco leaves and their growing soils from Assosa District, Benshangul Gumuz Regional State, Ethiopia. Both samples were collected from five tobacco farmlands. The samples were digested before quantitative determinations of the metals via inductively coupled plasma optical emission spectroscopy (ICP-OES). Repeatability and recovery studies were used to evaluate the efficiency of the method. Repeatability was evaluated by analyzing replicate samples and expressed as relative standard deviations (RSD) were below 10.0. Recovery or percent recovery (%R) studies, which were performed by spiking known concentrations of metals into the samples, ranged from 85.67 - 111.33% and 84.25 - 114.00% for tobacco leaves and soil samples, respectively, indicating that the employed method is valid for the analysis of the metals. The concentrations of metals in tobacco leaf samples were: 0.75 -1.18 mg/kg, Mn; 0.11-0.21 mg/kg, Cu; 0.58-1.16 mg/kg, Zn; and not quantified (NQ) - 0.01 mg/kg, Cd. In soil samples, their concentrations were: 1.59-8.04 mg/kg, Mn; 0.32 - 0.38 mg/kg, Cu; and 0.29 - 1.26 mg/kg, Zn; and 0.17 - 0.31 mg/kg, Pb. Except in one tobacco leaf sample, Pb was below the limit of quantification (LOQ). Similarly, in all soil samples, the concentration of Cd was below LOQ. The findings indicate that the concentrations of the studied heavy metals in both tobacco leaves and soil samples are below their WHO permissible limits in soil and plants. However, the levels of Zn in Amba and Basha tobacco leaves were higher than the WHO permissible limit in plants.

Keywords: Tobacco leaves, Soils, Heavy metals, Digestion

Submitted: November 14, 2021. **Accepted:** March 02, 2022.

Cite this: Melkamu T, Gure A, Asere TG. Determination of Heavy Metals in Tobacco Leaves and Their Growing Soils in Assosa District, Benshangul Gumuz Regional State, Ethiopia. JOTCSA. 2022;9(2):495-504.

DOI: <https://doi.org/10.18596/jotcsa.1023438>.

***Corresponding author. E-mail:** tsegaye96@gmail.com.

INTRODUCTION

Metals are involved in many biological processes of living systems. Plants can absorb and accumulate a wide range of essential, micro-essential, and toxic metals from their growing soils (1). In particular, toxic heavy metals accumulated in plants may affect their metabolic activities by interacting with DNA and proteins and causing oxidative deterioration of biological macromolecules (2). Metals such as Zn, Cu, Mn, Mo, Co, and Ni are essential because they are necessary in different biological processes and developmental

pathways (3). However, essential metals can be harmful to plants when their uptakes are higher than the required levels (4,5). For instance, an excess of Zn causes metabolic disorders and possibly results in the plant's death (6).

On the other hand, metals like Pb, Cd, As, Hg, Cr, and Se are highly toxic to plants and humans, even in small amounts (7-9). Pb and As are classified as carcinogenic to humans (10), while Cd is associated with bone and kidney diseases (11). Previous studies indicated that cigarette smokers had higher concentrations of Cd (6), Pb (12), and

As (13) in their biological samples than nonsmokers. Nonsmokers can also take in some amounts of toxic metals when cigarette smokers smoke in their vicinity (12). Therefore, monitoring the levels of heavy metals in tobacco is essential for protecting the environment and the health of human beings.

Tobacco (*Nicotiana tabacum L.*) is a commercial plant since its leaves are commonly used for making cigarettes (14). Traditionally, people use it also for snuffing, chewing, and pipe smoking (15). The plant may absorb and accumulate heavy metals from the soil through its roots (16–18). For example, the tobacco plant absorbs Cd from the soil and may accumulate the metal in its different parts: leaves, roots, and stems (9). The accumulated heavy metals in the leaves may transfer from the cured and processed tobacco to the cigarette smokers (9,19). Plants take up varied amounts of metals based on metal types and the content in which they occur in the soil and the plant species (1). The transfer of these metals from the soil to the plants is influenced by a number of factors, including the type of the soil, pH, chemical speciation of the metal, and the quality of water used for watering (20,21). The use of fertilizers and pesticides may result in greater metal concentrations in soils and plants (22).

In Ethiopia, tobacco is grown by individual farmers and state-owned farms for commercial purposes. For example, Virginia (74%), Oriental (22%), and Burley (4%) are the three most commonly cultivated tobacco varieties on state farms, which are used for cigarette production (15). Most of these farms are located in Shewa Robit (North Showa), Billate, Hawasa, Wolaita (Sidamo), and Nura-Era (Hararghe), where 500 to 900 MT-cured tobacco leaves are produced every year on 2000 hectares of land (14). People in Ethiopia have become accustomed to Khat (48.2%), tobacco (29.9%), and alcohol (18.9%), indicating the high prevalence of tobacco addiction next to Khat (23).

In Assosa District, Benshangul Gumuz Regional State, western Ethiopia, tobacco is widely grown, by individual farmers. People of this region use tobacco leaves for chewing and making traditional cigarettes. During tobacco production, farmers use agrochemicals, which may lead to the enrichment of the soils with heavy metals such as Cu, Zn, Cd, and others (24). Therefore, in this study, the levels of selected heavy metals: Zn, Cd, Pb, Mn, and Cu in tobacco leaves and their growing soils from Assosa District were determined using ICP-OES. To the best of our knowledge, there is no previous report on the levels of heavy metals in tobacco leaves and their growing soil from the study area.

MATERIAL AND METHODS

Chemicals and Reagents

All chemicals and reagents used were of analytical grade. HNO₃ (69%) and HCl (37%) supplied by Loba chemie pvt. Ltd (Jehangir villa, Mumbai, India), and H₂O₂ (30%) from RDH Labor chemi kalien GmbH & Co KG (Seelze, Germany) were used for digestion of tobacco leaf and soil samples. Stock standard solutions of the metals (Mn, Cu, Zn, Pb, and Cd), 1000 mg/L prepared as nitrate for each metals in 0.5 mol/L HNO₃ were purchased from Luba Chemical Pvt. Ltd (Mumbai, India).

Instrument and Apparatus

A ceramic mortar and pestle were used for the grinding of tobacco leaves and soil samples. An analytical balance KERN ABS-N · ABJ-NM, Model ABS 120-4N (Balingen, Germany) was used for weighing samples. A heating oven, M 3040 P, with a working temperature ranging from 50 to 250 °C (Elektro-mag, Turkey) was used for the drying of samples. Glass beakers (100-400 mL) and an aluminium hot plate magnetic stirrer (CB/SB series, SB 302) from The Carl roth GmbH + Co.KG (Karlsruhe, Germany) were employed for wet digestion of tobacco and soil samples. Inductively coupled plasma optical emission spectroscopy (ICP-OES), Optima 8000, supplied by PerkinElmer, Inc. (Waltham, USA) was used for the quantitative determination of targeted heavy metals.

Study Area and Period

The study area was conducted in Assosa District, Benshangul Gumuz Regional State, Ethiopia, which is at 10°04'N longitude, 34°31'E latitude, and 1572 m elevation above sea level. Assosa City, the capital city of the regional state, is located 659 km away from Addis Ababa, Ethiopia, which has an estimated area of 49,289.46 km². It has a tropical climate and gets about 1236 mm of annual rainfall and an average temperature of 28.2 °C. Tobacco is widely grown in the regional state, including Assosa District, for local consumption as cigarettes and chewing its leaves. The study was conducted from May to October 2017.

Sample Collection

Representative tobacco leaf samples were systematically collected from five different tobacco farmlands in Assosa District, namely, Tsentseha, Belmili, Ateto, Amba, and Basha. From each farmland, five samples were collected from different sites. At each sampling site, four leaves per plant, from the bottom to the tip of the stalk position, were collected from five tobacco plants. The collected samples from the same farmland were combined to form a single composite sample (14). Similarly, soil samples were collected at 0.0 - 30 cm depth from the same sites where tobacco

leaf samples were collected. The collected soil samples from the same farmland were combined and homogenized to form a single composite sample. Both tobacco leaves and soil samples were collected in polyethylene bags and transported to Jimma University Analytical Chemistry laboratory for further pretreatments.

Sample Preparation and Analysis

Before drying at 105 °C in an oven, tobacco leaf samples were washed with distilled water. The samples were digested following the method reported by Imran et al. (2013) (25) with some modifications. The dried samples were then ground using mortar and pestle. Subsequently, 0.5 g was taken into a 125 mL Erlenmeyer flask. Then, a mixture of 5 mL HNO₃ and 4 mL H₂O₂ was added. After that, the flask was covered with a watch glass and gently heated on a hot plate for 30 minutes. After cooling, 5 mL HNO₃ were added and gently heated for a few minutes. Then, 5 mL of HCl:HNO₃ (1:1) were added and heated for 15 minutes. Finally, the resulting digest was cooled and filtered using Whatman No 42 filter paper into a 50 mL volumetric flask. The remaining volume was filled to the mark with double-distilled water and made ready for the subsequent analysis of the target metals.

Similarly, soil samples were dried in the open air, ground, and sieved through a 2 mm sieve. Then, 0.5 g was taken into a 125 mL Erlenmeyer flask. Subsequently, after adding 12 mL of aqua regia HCl:HNO₃ (3:1, v/v) and 2 mL of H₂O₂ the flask was covered with a watch glass and heated on a hot plate at 110 °C for 45 min. Eventually, the resulting digest was cooled and filtered using Whatman No 42 filter paper into a 50 mL volumetric flask. Then, the remaining volume was adjusted with double-distilled water and made ready for the subsequent analysis of the target metals.

During the construction of calibration curves, a series of standard solutions were prepared from the stock standard solution of each target metal by dilution. Laboratory blank samples were prepared by a mixture of reagents, following the procedures used for digestion of tobacco leaves and soil samples. Replicate samples are prepared and measured.

Data Analysis

One-way ANOVA at a confidence level of 95% was employed to compare the levels of the studied heavy metals among tobacco leaves and soil samples. Pearson correlation coefficient was used to evaluate the correlation between the target metals content in tobacco leaves and their farmland soils. The obtained concentrations of the heavy metals were reported as mean ± RSD.

Quality Control

All laboratory glassware was soaked in 10% HNO₃ overnight and rinsed with double distilled water before use. Double distilled water was used to dilute, clean, and prepare all solutions throughout the laboratory work.

Precision and Accuracy

The precision of the results was evaluated by the relative standard deviation of the results obtained from triplicate samples (n=3). The accuracy of the results was evaluated by recovery studies. For a recovery study, a standard solution containing a mixture of 2 mg/L Mn, Zn, and Cu and 0.2 mg/L of Pb and Cd was spiked onto tobacco and soil samples collected from Tsentseha farmland. The spiked samples were then digested in the same earlier procedure used for tobacco leaves and soil samples. The resulting digests were diluted with double-distilled water to the required volume for subsequent analysis. All samples were prepared and measured in replicates.

Limits of Detection and Quantification

The limits of detection (LOD) and quantification (LOQ) of each element were determined based on the blank reagent method (26). Accordingly, five reagent blanks were digested and diluted following the procedure used for tobacco leaves and soil samples. Each digest was then analyzed in triplicates. Finally, the LOD and LOQ of each element were determined by using the standard deviation of the blank (SD) and slope of the calibration curve (S) as indicated by Eq.1 and Eq.2, respectively (26). Table 1 shows the instrumental detection limit (IDL), LOD, and LOQ of the studied metals in tobacco leaf and soil samples.

$$\text{LOD} = 3\text{SD}/S \quad (\text{Eq. 1})$$

$$\text{LOQ} = 10\text{SD}/S \quad (\text{Eq. 2})$$

Where: SD and S are the standard deviation of the blank and slope of the calibration curve, respectively.

RESULTS AND DISCUSSION

Validation of the Procedure

The accuracy of the digestion procedure was evaluated by determining the percent of recovery (%R) of the spiked tobacco leaves and soil samples due to the lack of certified reference materials in our laboratory (27). Table 1 shows the %R for tobacco leaf and soil samples. The obtained recoveries for the spiked tobacco samples ranged from 85.67 ± 5.52 to 111.33 ± 5.19%. Similarly, the obtained recoveries for soil samples ranged from 84.25 ± 3.27 - 114.00 ± 6.14%. These values are within the accepted range for the analysis of heavy metals in plant and soil samples,

indicating that the employed digestion procedure has the required accuracy for analysis of the target heavy metals. The precision studies, expressed as

RSD for both tobacco leaves and soil samples, were < 10%, which is also acceptable for the analysis of the target metals.

Table 1. Recovery results of tobacco leaves and soil samples.

Analyte	IDL	LOD	LOQ	%R ± RSD	
				Tobacco	Soil
Mn	0.0014	0.07	0.08	105.67 ± 5.21	84.25 ± 3.27
Cu	0.0097	0.068	0.0701	111.33 ± 5.19	96.00 ± 8.53
Zn	0.0059	0.125	0.132	85.67 ± 5.52	107.25 ± 5.87
Cd	0.0027	0.005	0.008	108.50 ± 9.78	114.00 ± 6.14
Pb	0.042	0.05	0.06	95.00 ± 9.12	106.67 ± 7.16

The concentration of Metals in the Tobacco Leaves

In the present study, the levels of three micronutrients: Mn, Cu, and Zn as well as two non-

essential (toxic) metals: Cd and Pb were determined in tobacco leaves grown in Assosa District, Ethiopia. Table 2 presents the obtained concentrations of the studied metals in tobacco leaf samples.

Table 2. Average of metal concentrations in tobacco leaf samples (mean ± RSD, n = 3).

Sample site	Concentration of metals (mg/kg)				
	Mn	Cu	Zn	Cd	Pb
Tsentsehalo	1.09 ± 1.19	0.11 ± 0.74	0.58 ± 1.14	0.01 ± 1.23	ND
Belmili	0.96 ± 0.52	0.15 ± 0.03	0.58 ± 0.28	NQ	NQ
Ateto	1.09 ± 0.72	0.20 ± 0.10	0.74 ± 0.74	NQ	NQ
Amba	0.75 ± 1.26	0.21 ± 1.26	1.16 ± 1.56	0.01 ± 0.61	0.07 ± 0.95
Basha	1.18 ± 0.39	0.17 ± 0.03	1.05 ± 1.32	0.01 ± 9.52	NQ
WHO limits in plants (28)	-	10	0.6	0.02	2

NQ: not quantified; ND: not detected

As can be seen from Table 2, the concentrations of Mn in tobacco leaf samples ranged from 0.75 mg/kg - 1.18 mg/kg. The highest concentration of Mn (1.18 mg/kg) was found in the tobacco leaves of Basha farmland, and the lowest (0.75 mg/kg) was detected in the tobacco leaves of Amba farmland. The concentrations of Cu in the tobacco leaves ranged from 0.11 to 0.21 mg/kg. The highest concentration of Cu (0.21 mg/kg) was determined in tobacco leaf samples collected from Amba farmland. The lowest concentration of Cu was detected in tobacco leaves of Tsentsehalo farmland. The obtained concentrations of Zn ranged from 0.58 to 1.16 mg/kg. The lowest concentration of Zn was detected in tobacco leaf samples collected from Tsentsehalo and Belmili, whereas the highest concentration was obtained in tobacco leaves from the Amba farmland.

The findings revealed that the studied tobacco leaf samples have lower concentrations of Cu and Zn than tobacco leaf samples from state farms of Billate and Shewa Robit, Ethiopia (14). This variation could be due to the soil type, pH, use of agrochemicals (fertilizers and pesticides), climatic conditions, and tobacco variety (24). The findings

show that the levels of studied heavy metals in the tobacco leaves were below their WHO permissible limits, except for the levels of Zn in tobacco leaves from Amba and Basha farmlands (Table 2).

In the current study, except for tobacco leaf samples collected from Amba farmland, which contained 0.07 mg/kg of Pb, other tobacco leaf samples had Pb concentrations either below LOD or LOQ. Likewise, the concentration of Cd in tobacco leaf samples collected from Belmili and Ateto farmlands was also below LOQ value. However, tobacco leaf samples collected from Tsentsehalo, Amba, and Basha farmlands exhibited similar Cd content, i.e., 0.01 mg/kg, which is much lower than the earlier report from Billate and Shewa Robit, Ethiopia (14).

In general, the trend of concentrations of the studied metals in tobacco leaf samples collected from Tsentsehalo, Belmili, Ateto, and Basha farmlands showed the following order: Mn > Zn > Cu > Cd. However, tobacco leaf samples collected from Amba farmland exhibited a different order: Zn > Mn > Cu > Cd > Pb.

The levels of the studied heavy metals in the present tobacco leaf samples were lower than those reported in the literature (14,29). For instance, the level of Mn obtained in the current raw tobacco leaves are much lower than the Mn level reported from tobacco cigarettes of different countries, such as Spain (112.03 mg/kg) (30), Nigeria (44.67-297.69 mg/kg) (31), Pakistan (45.03 mg/kg) (32), and Mexico (108-244.26) (33). These variations are may be due to the difference in the level of heavy metals in the soil where the plant has been cultivated. Similar to other plants, tobacco absorbs heavy metals from the soil and accumulates them in its leaves, stems, and roots (9). The processes of accumulation of metals in soils and their absorption by plants with subsequent translocation and bioaccumulation in leaves are well known (24,34). The other possible reason for the high concentration of Mn in the cigarettes could be the contamination of some heavy metals in the manufacturing process (31).

The concentration of Heavy Metals in the Soil Samples

The concentrations of the target heavy metals were also determined in the soil samples collected from tobacco farmlands. Table 3 shows the concentrations of the studied heavy metals in the soil samples.

In the studied soil samples, the observed concentrations of Mn ranged from 1.59 to 8.04 mg/kg. Its lowest and highest concentrations were recorded in soil samples collected from Belmili and Tsentsehalo farmlands, respectively. The content of Cu in the studied soil samples varied from 0.32 to 0.38 mg/kg. The levels of Zn ranged from 0.29 to 1.26 mg/kg. The lowest and highest concentrations of Zn were recorded in soil samples collected from Ateto and Basha farmlands, respectively. The findings demonstrated that the content of Mn, Cu, and Zn, in the studied soils, were lower than the WHO permissible limits in soil (28).

Table 3. Average of metal concentrations in soil samples (mean \pm RSD, n=3).

Sample site	Concentration of metals (mg/kg)				
	Mn	Cu	Zn	Cd	Pb
Tsentseha	8.04 \pm 0.28	0.35 \pm 0.45	0.69 \pm 1.14	ND	0.17 \pm 0.87
Belmili	1.59 \pm 0.20	0.38 \pm 1.76	0.45 \pm 0.29	ND	0.18 \pm 0.38
Ateto	7.28 \pm 0.55	0.37 \pm 0.41	0.29 \pm 2.44	NQ	0.24 \pm 1.03
Amba	6.38 \pm 0.72	0.35 \pm 0.30	0.43 \pm 2.33	NQ	0.22 \pm 1.72
Basha	5.98 \pm 0.54	0.32 \pm 1.05	1.26 \pm 1.19	ND	0.31 \pm 0.59
WHO limits in soil(28)	-	36	50	0.8	85

The Pb content of the soil samples ranged from 0.17 to 0.31 mg/kg. The highest concentration of Pb was obtained from the Basha farmland soil sample, whereas the lowest was observed from the Tsentsehalo farmland soil sample. The concentration of Cd in all the studied soil samples was either below LOQ or LOD and thus reported as NQ or ND, respectively. In general, soil samples from the Tsentsehalo, Belmili, Amba, and Basha farmlands showed the following order of metal content: Mn > Zn > Cu > Pb. However, for Ateto farmland, the observed order was different: Mn > Cu > Zn > Pb. The slight variations in the heavy metal content may be due to the difference between the growing soils or anthropogenic sources such as fertilizers and pesticides used during the cultivation of the plant or other proximate crops (21).

Statistical Analysis

One-way ANOVA was used to compare the variations of the concentrations in the heavy

metals in the studied samples. Pearson correlation coefficient was also employed to evaluate where the heavy metal content of tobacco leaves is either related to their growing soil metal content or not (35). The ANOVA results showed the presence of a statistically significant difference at 95% ($P < 0.05$) confidence level in the concentrations of Mn, Cu, and Zn in tobacco leaf samples and Mn, Zn, and Pb in soil samples. The observed variations may be due to the difference of mineral content in the farmland soils.

Table 4 indicates the Pearson correlation coefficient. The content of Mn in tobacco leaves has shown a weak positive correlation with Mn in the soil, which indicates the low dependence of Mn in the tobacco leaves on its amount in the farmland soil. Similarly, Cu in soil and Cu in tobacco leaves have a negligible correlation. However, the content of Zn in tobacco leaves exhibited a moderately positive correlation with the level of Zn in the soil. This shows that the

concentration of Zn in tobacco leaves is moderately dependent on the level of Zn in the farmland soil.

Table 4. The Pearson correlation coefficient of metal content in tobacco leaves and soil samples.

		Soil sample			
		Mn	Cu	Zn	Pb
Tobacco leaves	Mn	0.23	-0.33	0.57	0.40
	Cu	0.04	0.01	-0.30	0.49
	Zn	0.22	-0.64	0.32	0.67

Comparison of the Level of Metals with Literature Values

Many researchers have reported the concentration of metals in the raw tobacco leaves and the processed product, the tobacco cigarettes. Table 5 shows the reported concentrations of the studied heavy metals in tobacco cigarettes and raw tobacco leaves. As it can be seen in Table 5, very high concentrations of Cd (5.90-7.94 mg/kg) and Pb (17.21-74.78 mg/kg) were reported in tobacco cigarettes from Nigeria (31). Cd and Pb are non-essential and highly toxic metals, even at low concentrations, for plants and humans (16). Compared to the reported values, the raw tobacco leaves considered in this study showed lower concentrations of the studied metals. The observed concentrations of the target heavy metals in Assosa district tobacco leaves were also lower than

those reported in tobacco leaves collected from other regions of Ethiopia: Shewa Robite and Billate farmlands (14). The observed variations are may be due to the soil nature, repeated use of fertilizers and other agrochemicals on these farmlands rather than the farmlands considered in the present study. Generally, the observed concentrations of heavy metals in the tobacco leaves of Assosa District could be due to the availability of lower amounts of heavy metals in the farmland soils, which were lower than the WHO permissible limits in soil and plants (28). As a result, heavy metals' absorption and accumulation by tobacco plants in the study area were lower than those reported in raw tobacco leaves and tobacco cigarettes.

Table 5. Comparison of heavy metal levels (mg/kg dry mass) of the studies tobacco leaves with literature values.

Type	Metal concentrations (mg/kg)					Country	Reference
	Cd	Cu	Mn	Zn	Pb		
Tobacco Cigarettes	5.90-7.94	18.26-34.94	44.67-297.69	47.02-167.31	17.21-74.78	Nigeria	(31)
	0.18	NR	112.03	NR	0.60	Spain	(30)
	0.50	7.89	45.03	8.57	14.39	Pakistan	(32)
	0.18-3.07	NR	108-244.26	32.30-72.0	NR	Mexico	(33)
	1.73-2.02	Nd	Nd	Nd	0.38-1.16	Ireland	(36)
	0.45	14	NR	27	1.94	India	(9)
	0.65	Nd	Nd	Nd	0.27	Brazil	(37)
	0.18	4.13	NR	NR	0.64	China	(38)
	1.55	8.95	NR	79.3	ND	Ethiopa (Nyala)	(14)
Raw Tobacco Leaves	0.21	11.5	NR	NR	0.57	China	(38)
	1.20-1.30	4.38-7.30	NR	33.2-53.7	ND	Ethiopia (Billate & Shewa Robit)	(14)
	0.01	0.11-0.21	0.75-1.18	0.58-1.16	ND	Ethiopia (Assosa)	This study

NR Not reported; ND Not detected

CONCLUSION

In this study, the concentrations of toxic heavy metals (Cd and Pb), as well as micro-essential heavy metals (Cu, Mn, and Zn), were determined in tobacco leaves and their growing soil samples collected from five different tobacco farmlands in Assosa District, Benishangul-Gumuz Regional State, Ethiopia. Relatively, the highest concentrations of Mn were observed in both tobacco leaves and soil samples. However, the obtained concentrations of Cd and Pb were low in the studied samples. The study results demonstrated that the concentrations of the micronutrients (Mn, Cu, and Zn) in tobacco leaves and soil samples were below the WHO permissible limits in soils and plants. However, tobacco leaves collected from Amba and Basha farmlands contained slightly higher concentrations of Zn than the WHO permissible limit in plants. The heavy metal content of the studied tobacco leaves was much lower than the values reported in the literature.

ACKNOWLEDGMENTS

The first author would like to thank the Department of Chemistry, College of Natural Sciences, Jimma University, for funding and facilitating this research work.

REFERENCES

- Memon AR, Aktoprakligil D, Özdemir A, Vertii A. Heavy metal accumulation and detoxification mechanisms in plants. *Turk J Botany*. 2001;25(3):111-21.
- Jomova K, Valko M. Advances in metal-induced oxidative stress and human disease. *Toxicology [Internet]*. 2011;283(2-3):65-87. <DOI>.
- Tiwari S, Lata C. Heavy metal stress, signaling, and tolerance due to plant-associated microbes: An overview. *Front Plant Sci*. 2018;9(April):1-12.
- Khlifi R, Hamza-Chaffai A. Head and neck cancer due to heavy metal exposure via tobacco smoking and professional exposure: A review. *Toxicol Appl Pharmacol*. 2010;248(2):71-88.
- Nagajyoti PC, Lee KD, Sreekanth TVM. Heavy metals, occurrence and toxicity for plants: A review. Vol. 8, *Environmental Chemistry Letters*. 2010. p. 199-216.
- Zhang C, Miura J, Nagaosa Y. Determination of cadmium, zinc, nickel and cobalt in tobacco by reversed-phase high-performance liquid chromatography with 2-(8-quinolylazo)-4, 5-diphenylimidazole as a chelating reagent. *Anal Sci*. 2005;21(9):1105-10.
- Masindi V, Muedi KL. Environmental Contamination by Heavy Metals. *Heavy Met*. 2018;
- Salla V, Hardaway CJ, Sneddon J. Preliminary investigation of *Spartina alterniflora* for phytoextraction of selected heavy metals in soils from Southwest Louisiana. *Microchem J [Internet]*. 2011;97(2):207-12. Available from: <DOI>.
- Verma S, Yadav S, Singh I. Trace metal concentration in different Indian tobacco products and related health implications. *Food Chem Toxicol [Internet]*. 2010;48(8-9):2291-7. Available from: <DOI>.
- Järup L. Hazards of heavy metal contamination. *Br Med Bull*. 2003;68:167-82.
- Nnorom IC, Osibanjo O, Oji-Nnorom CG. Cadmium determination in cigarettes available in Nigeria. *African J Biotechnol*. 2005;4(10):1128-32.
- Afridi HI, Kazi TG, Kazi NG, Jamali MK, Arain MB, Sirajuddin, et al. Evaluation of cadmium, lead, nickel and zinc status in biological samples of smokers and nonsmokers hypertensive patients. *J Hum Hypertens [Internet]*. 2010;24(1):34-43. Available from: <DOI>.
- Lindberg AL, Goessler W, Gurzau E, Koppova K, Rudnai P, Kumar R, et al. Arsenic exposure in Hungary, Romania and Slovakia. *J Environ Monit*. 2006;8(1):203-8.
- Regassa G, Chandravanshi BS. Levels of heavy metals in the raw and processed Ethiopian tobacco leaves. *Springerplus*. 2016;5(1):1-9.
- Tassew Z, Chandravanshi BS. Levels of nicotine in Ethiopian tobacco leaves. *Springerplus*. 2015;4(1).
- Azeez SO, Saheed IO, Ashiyanbola IO. Assessment of Cr, Cd and Pb levels in tobacco leaves and selected cigarette samples from Ilorin Metropolis Kwara State, Nigeria. *J Appl Sci Environ Manag*. 2019;22(12):1937.
- Ajab H, Yaqub A, Malik SA, Junaid M, Yasmeen S, Abdullah MA. Characterization of toxic metals in tobacco, tobacco smoke, and cigarette ash from selected imported and local brands in Pakistan. *Sci World J*. 2014;2014.
- Lugon-Moulin N, Zhang M, Gadani F, Rossi L, Koller D, Krauss M, et al. Critical Review of the Science and Options for Reducing Cadmium in Tobacco (*Nicotiana Tabacum L.*) and Other Plants. *Adv Agron*. 2004;83(04):111-80.
- Angelova V, Ivanov K, Ivanova R. Effect of chemical forms of lead, cadmium, and zinc in polluted soils on their uptake by tobacco. *J Plant Nutr*. 2004;27(5):757-73.
- Bozhinova R. Heavy metal concentrations in soil and tobacco plants following long-term phosphorus fertilization. *Bulg J Agric Sci*. 2016;22(1):16-20.
- Golia EE, Dimirkou A, Mitsios IK. Levels of heavy metals pollution in different types of soil of Central Greece. *Bull Environ Contam Toxicol*. 2008;80(3):206-10.

22. Lecours N, Almeida GEG, Abdallah JM, Novotny TE. Environmental health impacts of tobacco farming: A review of the literature. *Tob Control*. 2012;21(2):191–6.
23. Selassie SG, Gebre A. Rapid assessment of drug abuse in Ethiopia. *Bull Narc [Internet]*. 1996;48(1–2):53–63. Available from: [<URL>](#).
24. Kelepertzis E. Accumulation of heavy metals in agricultural soils of Mediterranean: Insights from Argolida basin, Peloponnese, Greece. *Geoderma [Internet]*. 2014;221–222:82–90. Available from: [<DOI>](#).
25. Imran H, Gul T, Naz F, Brabazon D, Naher S. *Clinica Chimica Acta* Estimation of toxic elements in the samples of different cigarettes and their impact on human health of Irish hypertensive consumers. *Clin Chim Acta [Internet]*. 2013;426:51–7. Available from: [<DOI>](#).
26. ICH Q 2 (R1). European Medicines Agency: An unacceptable choice. *Prescrire Int*. 2011;20(121):278.
27. Miller JN, Miller JC. *Statistics and Chemometrics for Analytical Chemistry [Internet]*. Sixth. London: Pearson Education Limited, Edinburgh Gate, Harlow, Essex CM20 2JE, England; 2010. 297 p. Available from: [<URL>](#).
28. Alengebawy A, Abdelkhalik ST, Qureshi SR, Wang MQ. Heavy metals and pesticides toxicity in agricultural soil and plants: Ecological risks and human health implications. *Toxics*. 2021;9(3):1–34.
29. Golia EE, Dimirkou A, Mitsios IK. Heavy-metal concentration in tobacco leaves in relation to their available Soil fractions. *Commun Soil Sci Plant Anal*. 2009;40(1–6):106–20.
30. Rubio Armendáriz C, Garcia T, Soler A, Gutiérrez Fernández AJ, Glez-Weller D, Luis González G, et al. Heavy metals in cigarettes for sale in Spain. *Environ Res [Internet]*. 2015;143:162–9. Available from: [<DOI>](#).
31. Benson NU, Anake WU, Adedapo AE, Fred-Ahmadu OH, Ayejuyo OO. Toxic metals in cigarettes and human health risk assessment associated with inhalation exposure. *Environ Monit Assess*. 2017;189(12).
32. Ajab H, Yasmeen S, Yaqub A, Ajab Z, Junaid M, Siddique M, et al. Evaluation of trace metals in tobacco of local and imported cigarette brands used in Pakistan by spectrophotometer through microwave digestion. *J Toxicol Sci*. 2008;33(4):415–20.
33. Martínez T, Aguilar F, Lartigue J, Navarrete M, Cuapio LA, López C, et al. Analysis of Mexican cigarettes by INAA. *J Radioanal Nucl Chem*. 2008;278(2):365–70.
34. Rodríguez-Ortiz JC, Valdez-Cepeda RD, Lara-Mireles JL, Rodríguez-Fuentes H, Vázquez-Alvarado RE, Magallanes-Quintanar R, et al. Soil nitrogen fertilization effects on phytoextraction of cadmium and lead by tobacco (*Nicotiana tabacum* L.). *Bioremediat J*. 2006;10(3):105–14.
35. Abera G, Bhagwan SC, Taddese WG. Metals in green coffee beans from major coffee-growing regions of Ethiopia. *Chem Int [Internet]*. 2017;3 (4)(October):359–69. Available from: [<DOI>](#).
36. Afridi HI, Kazi TG, Talpur FN, Brabazon D, Naher S. Estimation of toxic elements in the samples of different cigarettes and their impact on human health of Irish hypertensive consumers. *Clin Chim Acta [Internet]*. 2013;426:51–7. Available from: [<DOI>](#).
37. De Sousa Viana GF, Garcia KS, Menezes-Filho JA. Assessment of carcinogenic heavy metal levels in Brazilian cigarettes. *Environ Monit Assess*. 2011;181(1–4):255–65.
38. Yang G, Li Z, Shi H, Wang J. Study on the determination of heavy-metal ions in tobacco and tobacco additives by microwave digestion and HPLC with PAD detection. *J Anal Chem*. 2005;60(5):480–5.



Stability Indicating RP-HPLC Method Development and Validation for Bosentan in Pharmaceutical Formulations

Didar TURKAN¹ , Mehmet Emrah YAMAN² , Alptug ATILA^{2*} , Yucel KADIOGLU² 

¹Ministry of Health, Turkish Medicines and Medical Devices Agency, Ankara, 06520, Turkey

²Ataturk University, Faculty of Pharmacy, Department of Analytical Chemistry, Erzurum, 25240, Turkey

Abstract: The development and validation of a novel, simple, and quick HPLC technique for measuring bosentan in pharmaceutical formulations was performed. The technique parameters were tuned to be 1 mL/min flow rate, variable column temperature, and a mobile phase combination of methanol-acetonitrile-water (20:50:30 v/v/v) to carry out this study. All measurements were carried out with a UV detector at a wavelength of 272 nm. Specificity, the limit of quantitation (LOQ), limit of detection (LOD), linearity, accuracy, precision, stability, recovery, and ruggedness were all tested. The technique was linear between 0.25 and 20 µg/mL, with precision (RSD%) and accuracy (RE%) of less than 3.0 and 2.7%, respectively. The LOQ and LOD values of method were 0.25 and 0.1 µg/mL, respectively. The 10 µg/mL of standard bosentan solution was found to be moderately stable in acidic and basic settings (0.1 M HCl and 0.1 M NaOH) but unstable in an oxidative environment (H₂O₂ solution; 3%). No interference from tablet excipients was observed in the HPLC method. The approach was successfully applied to pharmaceutical formulations obtained from a local pharmacy store.

Keywords: Bosentan, HPLC analysis, Drug Degradation, Bioanalytical Method Validation

Submitted: October 25, 2021. **Accepted:** March 11, 2022.

Cite this: Turkan D, Yaman M, Atila A, Kadioglu Y. Stability Indicating RP-HPLC Method Development and Validation for Bosentan in Pharmaceutical Formulations. JOTCSA. 2022;9(2):505-12.

DOI: <https://doi.org/10.18596/jotcsa.956110>.

***Corresponding author. E-mail:** alptug@atauni.edu.tr.

INTRODUCTION

Bosentan, also known as (4-tert-butyl-N-[6-(2-hydroxyethoxy)-5-(2-methoxyphenoxy)-2-(pyrimidine-2-yl)pyrimidin-4-yl]), is a non-selective oral dual endothelin A and B receptors antagonist (Figure 1). Bosentan is an oral medication used to treat pulmonary arterial hypertension (1,2). It has a high protein binding rate (98%) and is quickly absorbed after oral administration, especially to albumin. It has a 45-50 percent bioavailability. Within 3-5 hours, the plasma concentration reaches its maximum (3,4). Hepatic metabolism mostly removes Bosentan, with renal clearance accounting for just 0.9 percent of the total dosage (5).

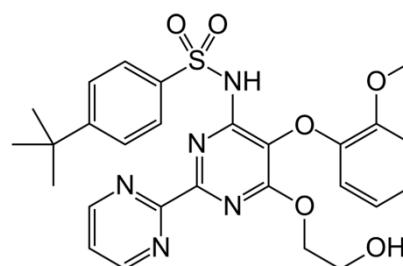


Figure 1: Chemical structure of bosentan.

Various analytical methods have been previously reported for the quantification of bosentan in pharmaceutical preparations including high-performance liquid chromatographic (HPLC) (6-10) and spectrophotometric (11-16) techniques. Besides, four different voltammetric methods for bosentan in pharmaceutical have been reported by

our group (17). The chromatographic separation methods, especially HPLC's, have become prior application in drug stability studies than the other techniques due to requirement of separation of degradation components during the stability tests (18). So far, there is two stability-indicating HPLC method for bosentan is available in the literature (19,20). However, these methods basically focused on the detection of degradation substances, therefore, the total analysis time of the methods are quite long for stability testing of single pharmaceutical substance. Therefore, a rapid stability-indicating HPLC techniques for bosentan are required.

As a result, this study outlines a novel HPLC technique for determining bosentan. This approach aimed to produce an easy and quick assay of bosentan with simple sample preparation and an acceptable analysis time and excellent accuracy. There is no need to remove the medication from the formulation excipient matrix in the suggested technique, which reduces quantization error. After dissolving and filtering, formulation samples can be utilized immediately. The proposed methodologies were utilized to determine the total drug content in bosentan pharmaceutical formulations that are commercially accessible. In addition, the current research covers the invention and validation of a stability-indicating HPLC technique for determining bosentan's stability and quantitative determination in the presence of its degradation products.

EXPERIMENTAL

Reagents and Chemicals

Bosentan was obtained from Actelion Pharmaceuticals (Allschwil, Switzerland). HPLC grade methanol and acetonitrile were obtained from Merck Germany. The mobile phase and solution were made with deionized water that was made fresh every day, filtered (0.45 m), and degassed in the laboratory using a sonicator. In the Turkish pharmaceutical market, bosentan tablet forms were purchased through pharmacies.

Instrumentation and Conditions for Chromatography

The chromatographic apparatus is an Agilent Technologies 1200 series HPLC system with a solvent degassing module (G1322A), quaternary gradient pump (G1312A), autosampler (G1313A), and thermostated column compartment (Agilent, USA) (G1316A).

For chromatographic separation, a reversed-phase ACE C18 column (250 x 4.6 mm, 5µm) was used. The mobile phase was a 20:50:30 (v/v/v) combination of methanol, acetonitrile, and water, and the column was kept at a variable temperature. Isocratic separation was conducted at a flow rate of

1 mL/min and an injection volume of 10 µL. It took 5 minutes to complete the analysis.

Preparation of Quality Control and Standard Solutions

Bosentan was produced as a stock solution in methanol at a concentration of 100 µg/mL. The stock solution was used to provide standard working solutions and quality control solutions (QC). The standard working solutions were prepared in 0.25, 0.75, 2, 5, 10, 15, and 20 µg/mL concentrations. The quality control solutions were made by diluting aliquots of bosentan stock solution to final concentrations of 0.3, 9, and 19 µg/mL.

Pharmaceutical Formulations Procedure

A total of ten bosentan tablets (Tracleer 125 mg and Diamond 125 mg) were precisely weighed and pulverized. A portion of this powder equal to one tablet's bosentan content was weighed and accurately placed into a 100 mL calibrated flask, where it was dissolved in methanol. The flask was then sonicated at room temperature for 10 minutes. In all cases, the resultant solutions were filtered using Whatman 42 filter paper and diluted to achieve a final concentration within the linearity limitations of the proposed technique.

Stress Testing Procedure

Stress testing was performed to assess the molecule's stability and confirm the analytical techniques' stability-indicating power according to ICH standards (ICH Q1A (R2)) (21). Thermal changes with acidic, basic, and oxidizing conditions were taken as the basis to create the experiment.

RESULTS AND DISCUSSION

Chromatographic Optimization

Several mobile phases were tried to determine the HPLC system appropriateness throughout the development and optimization of the technique for determining bosentan in tablets. The use of methanol with various amounts of acetonitrile and water was one of them. A mobile phase of methanol, acetonitrile, and water (20:50:30, v/v/v) was found to provide excellent separation and peak form. Because of the high acetonitrile concentration in the mobile phase combination, the retention period of bosentan decreased, resulting in a quick analysis time. Furthermore, it was discovered that altering the mobile phase's pH value had no significant influence on the intensity analysis time.

The Method's Validation

Specificity, linearity, accuracy, precision, the limit of detection (LOD), the limit of quantification (LOQ), recovery, and ruggedness were all tested in accordance with ICH Q2B guidelines (22).

Specificity

In the assay for bosentan, the effects of common excipients and additives were investigated for probable interference. The most widely utilized excipient in the pharmaceutical business was employed in this formulation. Corn starch, povidon, colloidal silicon dioxide, glycerol dibehenate, magnesium stearate, TiO_2 , Fe_2O_3 , and talc were shown to have no effect on the analytical results.

Linearity

For bosentan, standard solutions in the range of 0.25-20 $\mu\text{g/mL}$ (0.25, 0.75, 2, 5, 10, 15, and 20

$\mu\text{g/mL}$) were produced. The calibration curve was created by mapping each sample's peak area against its individual drug concentration (Figure 2). The results were displayed graphically by creating a calibration graph and matching the correlation coefficients on it. All of the calibration curves' correlation coefficients (R) were consistently greater than 0.9997. The least-squares technique was used to compute the linear regression equations using the Microsoft Excel® spreadsheet software, presented in Table 1.

Table 1: Linearity of bosentan.

Range ($\mu\text{g/mL}$)	LR	R ^a	LOD ($\mu\text{g/mL}$)	LOQ ($\mu\text{g/mL}$)
0.25 - 20	0	0	0	0

^a Based on three calibration curves, LR: Linear regression, R: Coefficient of correlation, y: Peak current, x: Bosentan concentration, LOD: Limit of detection, LOQ: Limit of quantification

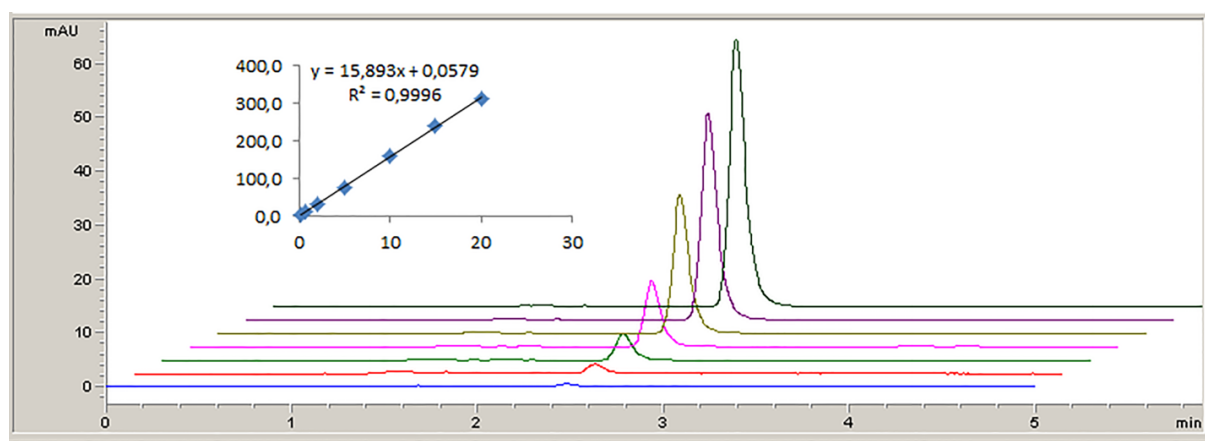


Figure 2: Calibration curve and overlaid chromatograms of bosentan at 272 nm wavelength.

Precision and accuracy

Accuracy was tested and evaluated as relative error (RE%) $[(\text{found concentration} - \text{spiked concentration}) / \text{spiked concentration}] \times 100\%$, and the precision of the HPLC method was determined by repeatability (intra-day) and intermediate precision (inter-day). It was expressed as relative standard deviation (RSD%) $[(\text{standard deviation} / \text{mean concentration}) \times 100\%]$ of a series of

measurements. Six separate tests of quality control solutions at low, medium, and high concentration levels (0.3, 9, and 19 $\mu\text{g/mL}$) of linearity range were used to evaluate each degree of accuracy and precision (Figure 3). Intra- and inter-day relative standard deviation values were ≤ 2.60 percent for all concentrations tested, and relative errors were ≤ 2.67 percent for all bosentan concentrations. Table 2 summarizes the findings.

Table 2: Accuracy and precision results of the proposed method.

Added ($\mu\text{g/mL}$)	Intra-day			Inter-day		
	Found \pm SD	Accuracy (RE%)	Precision (RSD%)	Found \pm SD	Accuracy (RE%)	Precision (RSD%)
3	3.11 \pm 0.06	-1.00	2.02	3.08 \pm 0.08	2.67	2.60
13	13.56 \pm 0.32	1.23	2.43	13.27 \pm 0.18	2.08	1.36
19	18.62 \pm 0.46	-2.00	2.47	19.23 \pm 0.12	1.21	0.62
3	3.02 \pm 0.07	0.67	1.66	3.07 \pm 0.07	2.33	2.28
13	13.25 \pm 0.28	1.92	0.38	13.32 \pm 0.28	2.46	2.10
19	19.11 \pm 0.56	0.58	0.94	19.15 \pm 0.56	0.79	2.92

SD: Standard deviation of six replicate determinations, RE%:Relative error, RSD%: Relative standard deviation,

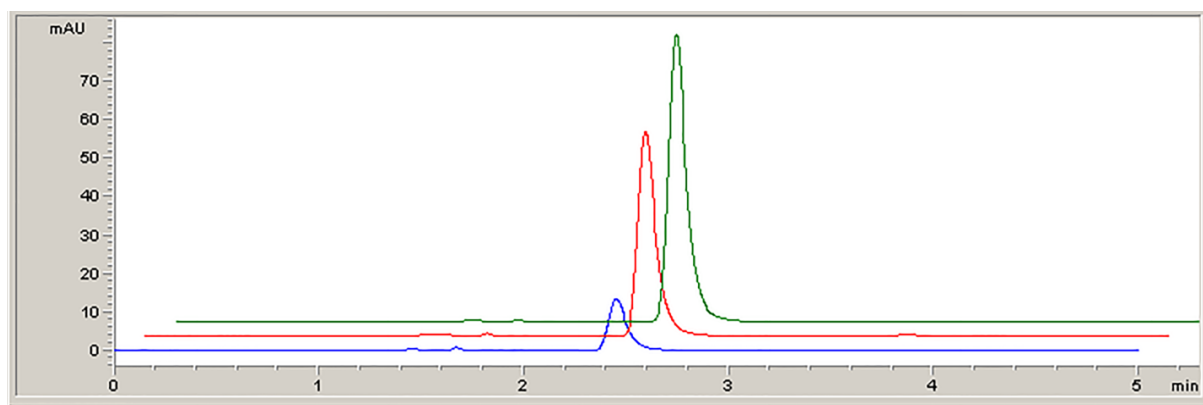


Figure 3: The overlapped chromatograms of quality control solutions of bosentan.

Limits of detection (LOD) and quantification (LOQ)

The LOD and LOQ were established by analyzing the standard solution at successively lower concentrations under the same chromatographic circumstances. The LOD and LOQ were calculated by reducing the signal-to-noise ratios to 3:1 and 10:1, respectively. Table 1 summarizes the LOD and LOQ values of the techniques.

Recovery

Recovery studies were validated using the standard addition method, which involved adding a known quantity (2 µg/mL) of pure pharmaceuticals to pre-

analyzed samples that had been spiked with a known amount of standard drug equivalent to 1, 11, and 17 µg/mL. The percent recovery was determined using the formula percent recovery = (T-A)/S100, where T represents the total quantity of drug estimated, a represents the drug provided by tablet powder, and S represents the amount of pure drug added.

The percent recoveries for various spiked levels varied from 99 to 102 percent, with an RSD percent of less than 4%, which is well within the allowed range, confirming the method's accuracy (Table 3).

Table 3: Recovery of bosentan in two tablet formulations.

Drug	Tablet Solution	Added (µg/mL)	Found±SD (µg/mL)	Recovery (%)	RSD %
Tracleer (125 mg)	2 mg/mL	1	3.02 ± 0.12	100.7	3.97
		11	12.68 ± 0.82	99.1	3.26
		17	18.82 ± 0.35	99.1	1.85
Diamond (125 mg)	2 mg/mL	1	3.06 ± 0.06	102.0	1.96
		11	13.21 ± 0.18	101.6	1.36
		17	18.95 ± 0.52	99.7	2.74

Ruggedness

Two separate analysts carried out five sets of experiments for these medicines, and the results in

this investigation showed no significant differences. Table 4 shows the results.

Table 4: The results of analyses of bosentan by a different analyst.

Method	Added (µg/mL)	Found (µg/mL) Mean±SD	Recovery %	RSD %
HPLC-UV	3	3.56±0.12	101.7	3.37
	9	9.21±0.14	102.3	1.52
	19	13.32±0.23	102.5	1.73

(n=6) Mean measurements of six replicate determinations.

The Method's Application in Stability Tests

The samples were stable when stored at ambient temperature, +4 °C, and -20 °C refrigeration temperatures for 24 hours (short-term), and refrigerated at +4 and -20 °C for 72 hours, according to stability analyses (long-term). Over the course of 72 hours, there was no substantial change in the analysis. The mean RSD% between peak areas for samples stored under refrigeration (4±1 °C), at room temperature (25±1 °C), and under refrigeration (-20±1 °C) was 1.37%, 1.85%, and 2.05%, respectively, indicating that the drug solution can be stored without degradation over the time interval studied.

Stress testing is also required by the ICH guideline on stability testing of drug substances and products to elucidate the inherent stability characteristics of the active substance and to provide rapid identification of differences that may arise from changes in manufacturing processes or source samples (21). The necessary tests are susceptibilities to acid, alkali, and oxidation hydrolysis stability.

Hydrolysis of acids and alkalis

0.2 mL aliquot of bosentan solution (50 µg/mL) was placed in a tiny rounded flask. 0.8 mL 0.1 M hydrochloric acid or 0.1 M sodium hydroxide was added to the solution. In a boiling water bath, the produced solutions were refluxed for 2 hours. The samples were chilled to room temperature (25±5°C) before being neutralized with an acid or base equal to the amount previously applied. 10 µL of the neutral solution was inserted into the HPLC apparatus (Figure 4).

Oxidation

Into a round-bottomed flask was transferred 0.2 mL of bosentan solution (50 µg/mL). The contents were then combined with 0.8 mL of a 30% hydrogen peroxide solution and allowed to react for 2 hours at room temperature (25±5 °C) with intermittent shaking. In the HPLC system, a volume of 10 µL was injected (Figure 4).

Comparison of the Method

In the literature, there are numerous investigations on the determination of bosentan in pharmaceuticals. From our group, the electrochemical detection methods have been reported for quantification of bosentan in pharmaceutical formulations (17). We were introduced simple, fast and reliable four different voltammetric assay method including cyclic voltammetry (CV), linear sweep voltammetry (LSV), square wave voltammetry (SWV) and differential pulse voltammetry (DPV) for bosentan. The calibration curves were constructed at the range of 5-40 µg/mL for LSV and 5-35 µg/mL for SWV and DPV methods, respectively. Das et al. (13) conducted spectrophotometric research using three

distinct techniques for determining bosentan in pharmaceuticals, with a linear range of 0.5-100 µg/mL for all methods. In 0.1 M NaOH, working solutions were produced. Narendra et al. (12) presented a novel spectrophotometric technique for measuring bosentan with a linearity range of 0.1-100 µg/mL and a correlation value of 0.999. Working solutions were produced in the presence of a buffer solution, and pH values were set to 3.5 for measurements. On the other hand, the suggested technique does not necessitate the use of acidic or basic media for the creation of working solutions, nor does it necessitate pH control throughout the analysis. Furthermore, within the prescribed concentration range, measurements were carried out with a higher correlation coefficient. Three distinct spectrophotometric techniques were established to measure bosentan in pharmaceuticals, according to another spectrophotometric approach described by Annapurna et al. (10). For techniques A, B, and C, the linearity ranges were determined to be 1-120, 5-120, and 2-120 µg/mL, respectively. Bosentan was found to be in the range of 10-90 µg/mL by Kumar et al. (11). The linear range was determined to be 0.25-20 µg/mL in our investigation, and it allowed for considerably more exact detection of bosentan. Suganthi et al. (16) presented a technique that combined UV spectrophotometric and HPTLC methodologies. It was said that with the HPTLC technique, very exact findings in a precise linear range could be produced. However, when considering the lengthy preparation procedure of the HPTLC approach, it is possible to conclude that the suggested method is more feasible. Muralidharan et al. (7) proposed a different chromatographic technique and used an LC-UV system, and they were able to do linear readings for bosentan in the concentration range of 5-70 ng/mL. Because of the mistakes that might occur during dilution, this concentration range is excessively sensitive to measuring medication solutions. Furthermore, the method's mobile phase contains an ammonium acetate buffer, and the pH value must be kept constant at 4.5 to correct the measurement of bosentan. In this study, we proposed mobile phase does not contain a buffer solution. With the HPLC-DAD technique, Jadhav et al. (19) conducted stability-indicating research to detect five possible process contaminants in bosentan monohydrate samples and degradation products. Our suggested approach allows for far more exact measuring.

CONCLUSION

For the quantitative measurement of bosentan in pharmaceutical formulations, an HPLC technique was devised and thoroughly validated. The suggested technique allows for the determination of bosentan in pharmaceutical formulations in a quick, easy, accurate, and repeatable manner, with no

interference from excipients. As a result, the devised approach may be utilized for quality control and analysis of bosentan stability samples.

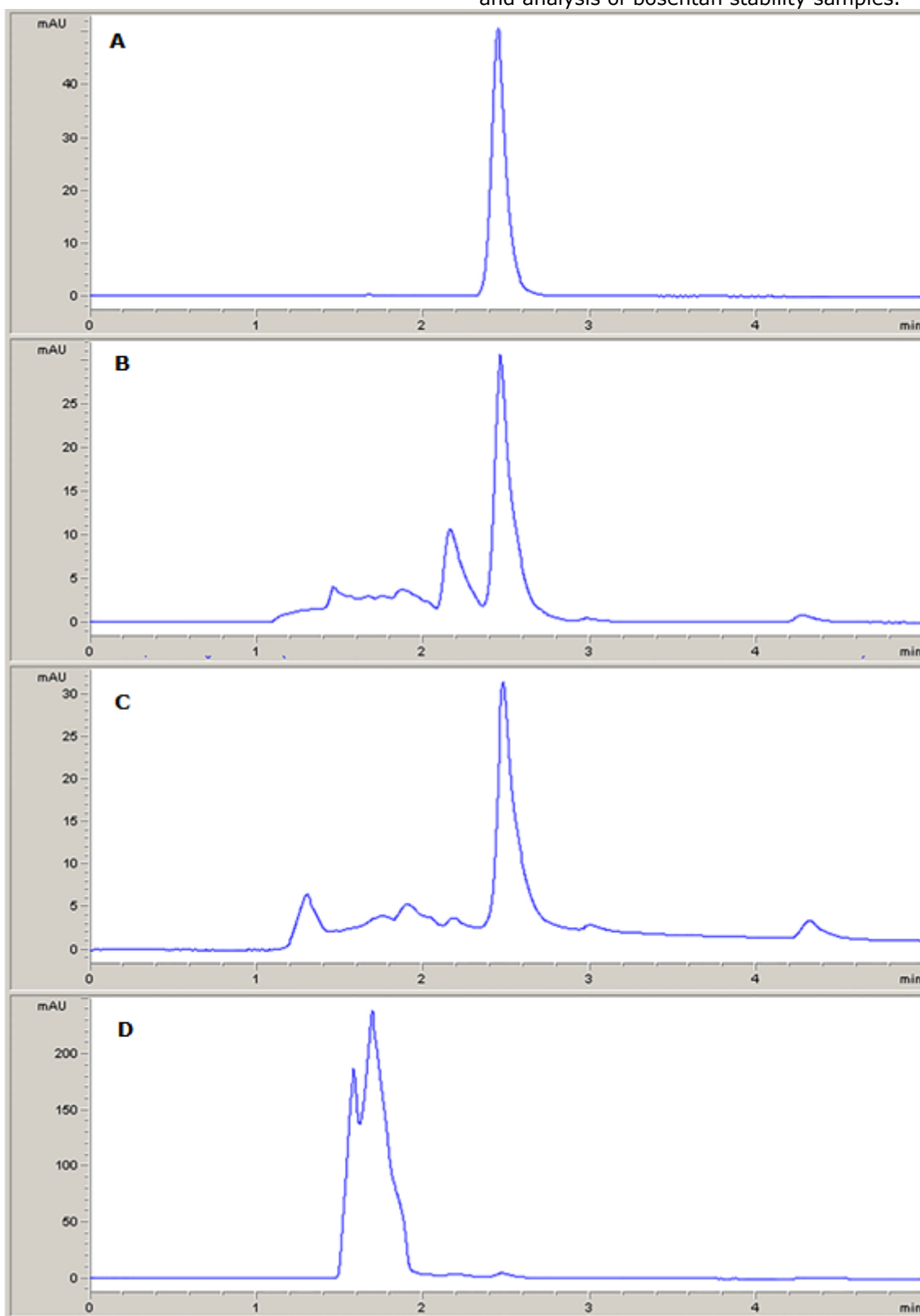


Figure 4: HPLC chromatograms representing degradation behavior of 15 µg/mL bosentan **A)** in no degradation media **B)** in acid **C)** in base **D)** in oxidation.

CONFLICT OF INTEREST

There are no conflicts of interest declared by the authors.

REFERENCES

- Motte S, McEntee K, Naeije R. Endothelin receptor antagonists. *Pharmacology & Therapeutics*. 2006 Jun;110(3):386–414. [<DOI>](#).
- Clozel M, Breu V, Gray GA, Kalina B, Löffler B, Burri K, et al. Pharmacological characterization of bosentan, a new potent orally active nonpeptide endothelin receptor antagonist. *Journal of Pharmacology and Experimental Therapeutics*. 1994;270(1):228–35.
- Rubin LJ, Badesch DB, Barst RJ, Galiè N, Black CM, Keogh A, et al. Bosentan Therapy for Pulmonary Arterial Hypertension. *N Engl J Med*. 2002 Mar 21;346(12):896–903. [<DOI>](#).
- Azim MS, Husain A, Mitra M, Bhasin PS. Pharmacological and pharmaceutical profile of Bosentan: A review. *Am J Pharm Tech Res*. 2012;4:135–47.
- Weber C, Gasser R, Hopfgartner G. Absorption, excretion, and metabolism of the endothelin receptor antagonist bosentan in healthy male subjects. *Drug metabolism and disposition*. 1999;27(7):810–5.
- Lavudu P, Rani AP, Chander AP, Sekaran CB. Determination of bosentan in pharmaceutical dosage forms by high performance liquid chromatography. *International Journal of Drug Delivery*. 2013;5(2):146.
- Muralidharan S, Kumar JR. Simple estimation of bosentan in tablet formulation by RP-HPLC. *American Journal of Analytical Chemistry*. 2012;3:715.
- Shahul HM, Jat RK, Indulatha VN. Method development and its validation for quantitative determination of bosentan in tablet dosage form by RP-HPLC. *J Drug Delivery Ther*. 2017 Mar 15;7(2):85–95. [<DOI>](#).
- Saidulu P, Masthanamma SK, Kumari VA. New validated RP-HPLC method for the determination of bosentan in bulk and dosage form. *Research Journal of Pharmacy and Technology*. 2015 May;8(5):549–53.
- Annapurna M, Pavani S, Anusha S, Harika M. Validated stability indicating RP-HPLC method for The determination of bosentan in presence of degradation products. *Indo American Journal of Pharmaceutical Research*. 2013;3(6):4528–40.
- Kumar AA, Kumar A, Sankar DG. Development, estimation and validation of prasugrel in bulk and in its pharmaceutical formulation by UV-Vis spectroscopic method. *Pharmanest*. 2011;2(1):37–9.
- Narendra A, Deepika D, Annapurna MM. New Spectrophotometric Method for the Determination of Bosentan - An Anti-Hypertensive Agent in Pharmaceutical Dosage Forms. *E-Journal of Chemistry*. 2012;9(2):700–4. [<DOI>](#).
- Das S, Narendra A, Kumar VR, Annapurna MM. Validated new spectrophotometric methods for the estimation of bosentan in bulk and pharmaceutical dosage forms. *Journal of Pharmaceutical Education & Research*. 2010;1(2):73–6.
- Lavudu P, Rani AP, Sekaran CB, Ramesh A, Kumar A. Application of spectrophotometry and high performance liquid chromatography for the analysis of Bosentan in pharmaceutical dosage form. *Chem Sci Transaction*. 2014;3(4):1242–53.
- Pavani B, Harshavardhan B, Sindhu P, Saharanya K. Method development and validation of bosentan by UV-Spectrophotometric Method. *Journal of Drug Development and Delivery*. 2018;1:34–8.
- Suganthi A, Lakshmi S, Vinod S, Ravi T. Development and validation of UV spectroscopic and HPTLC methods for the determination of Bosentan from tablet dosage form. *Sch Acad J Pharm*. 2014;3(2):123–7.
- Atila A, Yilmaz B. Determination of bosentan in pharmaceutical preparations by linear sweep, square wave and differential pulse voltammetry methods. *Iran J Pharm Res*. 2015;14(2):443–51. PMID: 25901151.
- Bakshi M, Singh S. Development of validated stability-indicating assay methods—critical review. *Journal of Pharmaceutical and Biomedical Analysis*. 2002 Jun;28(6):1011–40. [<DOI>](#).
- Jadhav SA, Landge SB, Jadhav SL, Niphade NC, Bembalkar SR, Mathad VT. Stability-indicating gradient RP-LC method for the determination of process and degradation impurities in bosentan monohydrate: An endothelin receptor antagonist. *Chromatography Research International*. 2011;2011:1–9. [<DOI>](#).
- Khan MA, Sinha S, Todkar M, Parashar V, Swamy K. Development and validation of a stability indicating analytical method for the related substances of Bosentan drug substance by HPLC. *Ame J Scien Ind Res*. 2012;3(2):69–80.
- Anonymous. ICH Topic Q 1 A (R2) Stability Testing of New Drug Substances and Products, European Medicines Agency, CPMP/ICH/2736/99. ICH; 2003.
- Anonymous. ICH Q2B Guideline Validation of Analytical Procedures: Methodology, (International Conference on Harmonization of Technical Requirements for the Registration of Drugs For Human Use. ICH; 1997.



Extraction, Optimization, and Characterization of Neem Seed Oil via Box-Behnken Design Approach

Ketema Beyecha Hundie^{1*} , Desalegn Abdissa Akuma² , Abreham Bekele Bayu³ 

¹ School of Chemical engineering, Process Engineering, Jimma institute of Technology, Jimma University, Jimma, Oromia, Ethiopia

^{2,3} School of Chemical Engineering, Environmental Engineering, Jimma institute of Technology, Jimma University, Jimma, Oromia, Ethiopia

Abstract: This study was aimed at extracting, optimizing, and characterizing the neem seed oil through Box-Behnken design. The effects of extraction parameters such as temperature (50-80°C), particle size (0.15–0.3 mm), and time (60-180 min) were considered. The extraction of oil was studied using the soxhlet extraction process, applying n-hexane as a solvent. The quadratic model was suggested to demonstrate optimal extraction parameters of 132.677 min, 64.416°C of temperature, and 0.212 mm of particle size using numerical optimization. The experimental yield of oil at optimum conditions 44.141%, which was close to the model-anticipated value. The physicochemical properties suggested that neem oil had an ash content of 2.1%, moisture content 4.61%, density 0.875 g/cm³, viscosity 33.5 mm²/s, specific gravity 0.88, saponification value 206.7 mg KOH/, iodine value 122.5 g I₂/100 g, acid value 1.81 mg KOH/g, and cetane number of 75. The extraction parameters had a significant effect on the yield of neem seed oil. However, the temperature and particle size had a higher effect compared to the extraction time. The most important unsaturated fatty acid is oleic acid (60.924 %). The properties of the oil revealed that the neem seed oil can be used as a potential source of material for industrial applications. It can be concluded that neem seeds have the potential to be used as industrial feedstocks in the future.

Keywords: Extraction, Neem Seed Oil, Property, Optimization

Submitted: December 22, 2021. **Accepted:** March 02, 2022.

Cite this: Beyecha Hundie K, Abdissa D, Bekele Bayu A. Extraction, Optimization, and Characterization of Neem Seed Oil via Box-Behnken Design Approach. JOTCSA. 2022;9(2):513–26.

DOI: <https://doi.org/10.18596/jotcsa.1039997>.

***Corresponding author. E-mail:** ketema.hundie@ju.edu.et.

INTRODUCTION

Since ancient times, humans have been searching in nature for resources that permit them to improve living conditions (1) and, consequently, sustain life span (2). Plant products or natural products show an important role in energy production(3), disease prevention and treatment through the enhancement of antioxidant activity (4), inhibition of bacterial growth, and modulation of genetic pathways (5).

One of these plants is *Azadirachta indica*, commonly known as the neem tree, which has been used since ancient times due to its potential applications and is

currently emerging as a possible therapeutic agent for various diseases (6) and for industrial applications (7). The neem plant is mainly cultivated in several parts of the world such as Asia, Africa (8), America, and Europe (9), where it has been utilized through centuries, in medical folklore. It should be noted that different parts of the neem tree, including the bark, seeds, flowers, leaves, and oil, are related to the aforementioned medical folklore in the discussion of certain medical considerations such as hypertension, cancer, diabetes and heart diseases (10).

Approximations of alternative medicine utilized today as main care are in the order of about 80% for developing countries (11). In Ethiopia, most people use the neem trees without knowing its applications (12). In some regions, the rural people use neem leaves for village medicine, especially to cure malaria and diabetes (13). The use of neem seed oils as antimicrobial and food preservative agents is of concern because of several reported side effects of synthetic oils (14). Various investigators have presented that neem is a potential source of materials for drug delivery (10), cosmetic industry, pharmaceutical industry, and production of renewable energy that does not compete with the food-based feedstock (15).

Given the several uses of neem oil and its cooperativeness of transformation for different usages as stated earlier, it is crucial to explore the mechanism of extraction of the neem oil, which significantly minimizes extraction parameters, while maximizing the quantity and quality of the oil (16). The choice of mechanism and solvent will depend on the nature of the chemical compound to be extracted (17,18). The solvent extraction process is generally preferred for the extraction of the neem

seed oil due to its low operating cost, higher oil yield, and lower turbidity compared to other methods (19). The solvent mostly employed for the extraction of oil is n-hexane due to its higher boiling point, stability, low corrosiveness, non-polarity, and high oil yield (20). Therefore, the goal of this work was the extraction, optimization, and characterization of neem seed oil utilizing the Box-Behnken experimental design.

EXPERIMENTAL DESIGN

Materials and chemicals

The neem seeds were collected from Jimma, Gibe, and Gambella, Ethiopia. The collected seeds were repeatedly washed and subsequently dried in an oven at 50°C for 24 hours to attain constant moisture content, and size reduction was conducted using laboratory mill.

All analytical grade chemicals were purchased from the chemical product suppliers (Piasa, Addis Ababa, Ethiopia).

The general Neem seed oil extraction process flow chart is indicated in Figure 1.

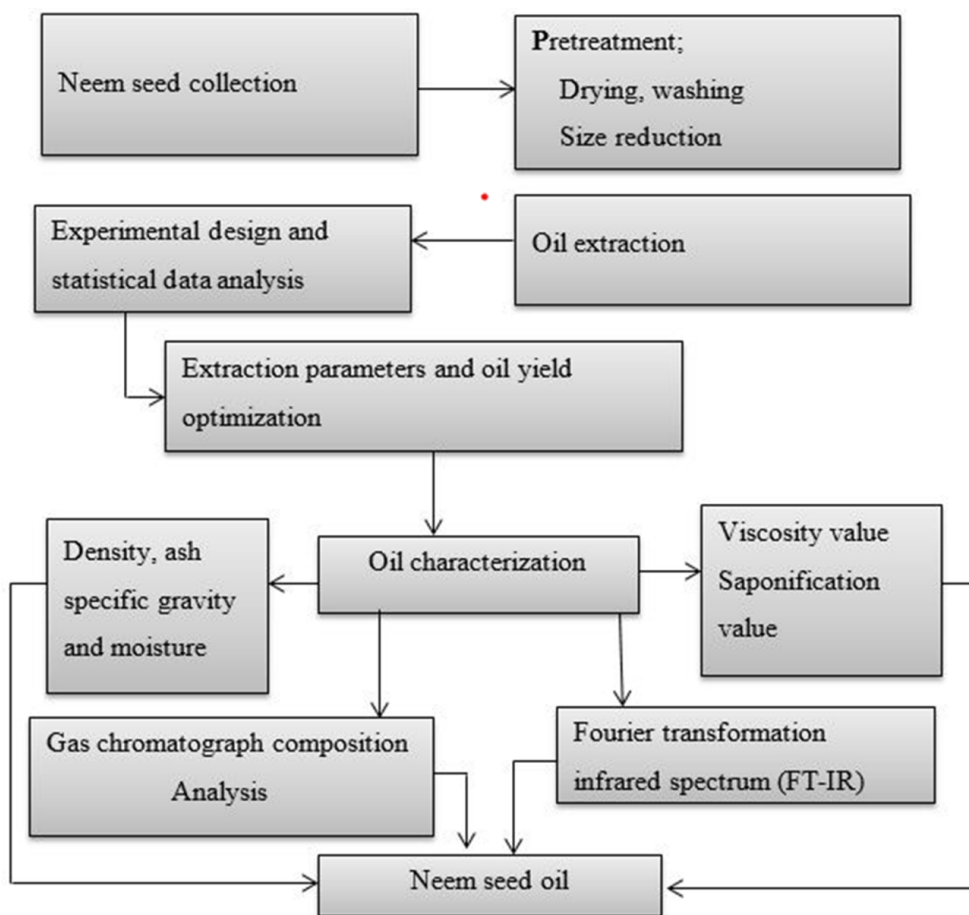


Figure 1: Neem seed oil extraction process flow chart.

Methodology

Oil Extraction

The extraction of neem seed oil was conducted as shown in Figure 1. A 500 ml soxhlet apparatus was utilized with the organic solvent n-hexane. The measured powder of the sample was added to a thimble and placed in a condenser. A flask containing a measured volume of the solvent was placed at the end of the soxhlet apparatus, and a condenser was fixed at the bottom. The parameters were adjusted to a temperature of 50-80°C, a particle size of 0.15-2 mm and a time of 60-180 min. At the time interval, the oil was collected in the volumetric flask, then centrifuged to separate the solid part from the solution, and evaporated, using a rotary evaporator to get solvent-free oil. The procedure was done in accordance with the standard previously reported (21), for the evaluation of the oils. The yield of oil was determined using Eq. (1).

$$\text{Oil Yield}(\%) = \frac{W_1 - W_2}{W_1} * 100 \quad (\text{Eq. 1})$$

Where: W_1 =Sample weight initially placed in the thimble and W_2 = sample weight after dried in the oven.

Experimental design and statistical data analysis

The experimental design to analyze the process parameters was carried out utilizing the Box-Behnken design method with the aim of parameter optimization for oil extraction. The Box-Behnken design consisted of three variables: time (60-180 min), temperature (50-80°C) and particle size (0.15-0.3 mm) as shown in Table 1. A total of 15 experimental runs (Table 2) were done with replication.

Table 1: Box-Behnken design parameters for neem seed oil extraction.

Factors	Codes	Minimum	Medium	Maximum
Reaction time (min)	A	60 (-1)	120(0)	180 (+1)
Particle size (mm)	B	0.15 (-1)	0.225(0)	0.3 (+)
Reaction temperature (°C)	C	50 (-1)	65(0)	80 (+1)

Statistical Data Analysis

The results obtained from the experiment data were evaluated employing the Box-Behnken design model. The model equation was examined using multiple regression analysis to measure the response through the linear interaction and quadratic effects of the process parameters suggested by the model.

$$Y = b_0 + \sum_{i=1}^n b_i X_i + \sum_{i=1}^n b_{ij} X_i^2 + \sum_{i=1}^n b_{ii} X_{ii}, X_{ij} \quad (\text{Eq. 2})$$

Where: Y is predicted yield %, i and j indicate linear and quadratic coefficients respectively, b_0 is the intercept, b_i is the linear model coefficient, n is the number of variables and X_{ii} , and X_{ij} are self-interaction and interaction between variables respectively.

Property of the Neem Seed Oil

Physicochemical property

The properties of neem seed oil such as specific gravity, density, iodine value, saponification value, and acid value, were analyzed according to the Association of Official Analytical Chemists (AOAC (1990) (22) and American Society of Testing Material (ASTM) (23,24).

Gas Chromatography of the Fatty Acid Composition Analysis

Gas chromatography-mass spectrometry was employed to analyze the fatty acid composition. It was carried out by electron ionization fashion on a GC-MS (GC = Agilent 8856B and MS =Agilent 6742

manufactured at German) system with a blended capillary column of 4.5% phenols-methyl Silphium (20 m × 0.30 mm × 0.30 mm; PN =18211-S-342HP-6 M-S) coupled to the mass detector for the sample analysis.

Fourier Transform Infrared Spectroscopy (FT-IR) Functional Group Analysis

The infrared spectra of the oil were recorded with a NaBr (alkalic halogenide)-pellet method utilizing a Tensor 30 FTIR spectrometer (Brukerash Optik, Gmch, USA) at a frequency ranging between 4000–400 cm^{-1} and a wavenumber precision of 0.1 cm^{-1} . All spectra were post-processed using an OBUS software (Brukerash Optik).

RESULTS AND DISCUSSION

Experimental Design and Statistical Data Analysis

The results of the Box-Behnken experimental design, shown in Table 2, indicated that oil yields were between 16.4 and 43.9% corresponding to extraction parameters of temperature (65°C), particle size (0.225 mm), and extraction time (120 min).

The experimental values were in agreement with the predicted ones obtained from Eq. (2) and generated in Eq. (3), as shown in Figure 2. An acceptable correspondence between the actual and predicted values of the yield was observed. The good correspondence between the predicted value, R-squared value (99.85%), R-predicted squared value (97.69%), and R-adjusted squared value (99.58%)

indicated a linear correspondence between the predicted and experimental values (Table 4). The results affirmed that both R-adjusted squared and

R-squared values were close to unity, which suggested that the model gave a good approximation of response in the considered range.

Table 2: Experimental design parameters Vs oil yields (actual and predicted values).

Run order	Factors			Responses (yield %)		Residual error
	A: Temperature	B: Particle size	C: Time	Actual	Predicted	
unit	°C	mm	min	%	%	
1	65	0.15	180	38.1	38.11	-0.0075
2	65	0.15	60	42.02	42.64	-0.6225
3	80	0.225	180	20.82	21.13	-0.3100
4	65	0.225	120	43.9	43.73	0.1667
5	50	0.225	60	36	35.69	0.3100
6	65	0.3	60	32.1	32.09	0.0075
7	65	0.3	180	29.49	28.87	0.6225
8	65	0.225	120	43.5	43.73	-0.2333
9	80	0.225	60	25.12	24.82	0.3050
10	50	0.3	120	26.01	26.33	-0.3175
11	65	0.225	120	43.8	43.73	0.0667
12	50	0.225	180	31.31	31.62	-0.3050
13	80	0.3	120	16.4	16.71	-0.3125
14	80	0.15	120	25.86	25.54	0.3175
15	50	0.15	120	37.6	37.29	0.3125

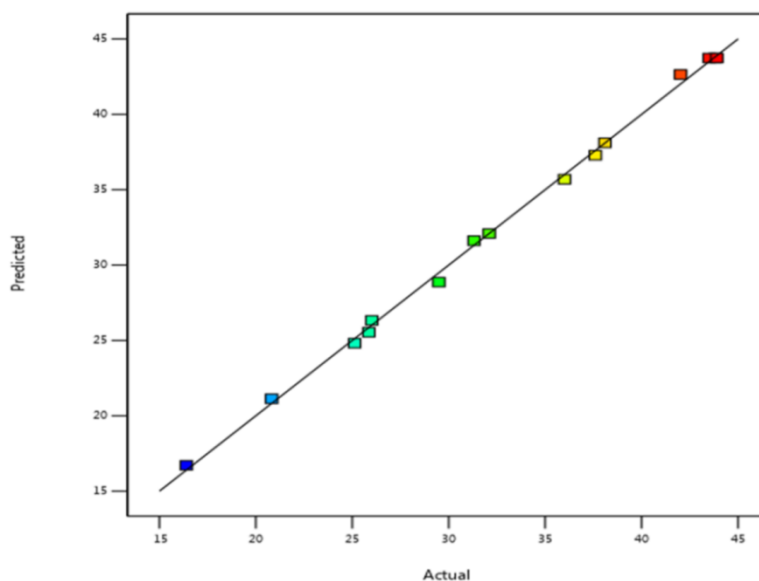


Figure 2: Experimental yield Vs predicted yield of the oil in percentage.

The accuracy of the formulated model has been verified by analyzing the residuals plot. The difference between the actual and calculated response is known as the residuals. Hence, for each experimental data set, there is a residual (25). The normal statistical distribution of the residuals is a prove of observational errors randomization. Studentized residuals are determined by separating the normalized residuals with their standard difference prediction, where they are fitted with a normal statistical distribution function (26). The residual-standard plots in Figure 3 were all in ± 6.25 intervals, suggesting that the model was consistent

with the experimental value with no error registered (25).

The experimental run versus the residuals was plotted as shown in Figure 3 (b), which outlines the residual result for each run. The plot indicates the degree of deviation between the test and anticipated values. The fitted regression analysis was very close to the plot, as the studentized residuals were placed within the ± 6.25 range. The precision of the quadratic demonstration was affirmed by the random distribution of residuals, as indicated in Figure 3(b). Therefore, it can be

concluded that a satisfactory description of the oil extraction process was accomplished by the

regression model and it does not spoil the constant variance assumption (27).

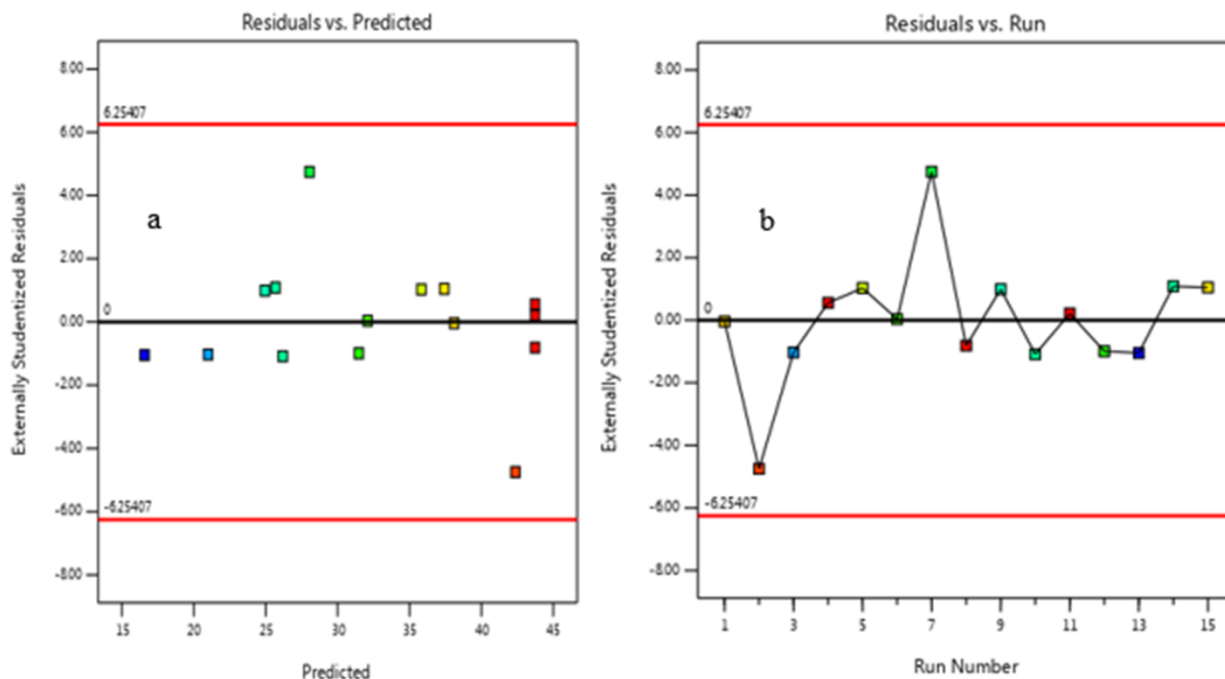


Figure 3: Residual Vs prediction (a) and Residual Vs Number of the runs (b).

The analysis of ANOVA is shown in Table 3. The model F-value of 367.49 and P-values of less than 0.0500 indicated that model terms were significant. In this case, all linear terms (temperature: A, particle size: B and time: C) and quadratic terms (A^2 , B^2 , and C^2) were significant models. However,

A -squared (A^2) term had the highest coefficient, which showed that curvature along this dimension was very significant. The ANOVA indicated in Table 3, and Eq(3) showed the largest degree of significance for this term and the model as a whole.

Table 3: ANOVA analysis for Quadratic model.

Source	Sum of Squares	df	Mean Square	F-value	p-value	
Model	1082.84	9	120.32	367.49	< 0.0001	Significant
A-Temperature	228.12	1	228.12	696.79	< 0.0001	
B-Particle size	195.82	1	195.82	598.12	< 0.0001	
C-Time	30.11	1	30.11	91.97	0.0002	
AB	1.13	1	1.13	3.46	0.1218	
AC	0.0380	1	0.0380	0.1161	0.7471	
BC	0.4290	1	0.4290	1.31	0.3041	
A^2	548.70	1	548.70	1675.97	< 0.0001	
B^2	95.11	1	95.11	290.52	< 0.0001	
C^2	38.53	1	38.53	117.69	0.0001	
Residual	1.64	5	0.3274			
Lack of Fit	1.55	3	0.5168	11.93	0.0784	Not significant
Pure Error	0.0867	2	0.0433			
Cor Total	1084.48	14				

The lack of fit test is also shown for the regression model analysis. It indicated the model's power to depict the relationship between the input and output parameters sufficiently. The model could indicate a lack of fit due to the comportment of unusually greater residuals existing from fitting the model or omitting from the model various necessary terms

(28). The lack of fit value for the extraction of the oil model indicates an F-value of 11.93 and a P-value of 0.0784 in this study. This outcome has shown that the quadratic model was well fitted to the experimental data. When the F-ratio gets so high, that the p-value falls below 0.05, then with

95% confidence, one or more of the factors was affecting the measured response (29).

The coefficient of prediction represents the expected change in response per unit change in factor value when all remaining factors are held constant (Table 4). The intercept in an orthogonal design is the

overall average response of all the runs. The coefficients are adjustments around that average based on the factor settings. When the factors are orthogonal, the VIFs are 1; VIFs greater than 1 indicate multi-collinearity. the higher the VIF, the more severe the correlation of factors. As a rough rule, VIFs of less than 10 are tolerable (30).

Table 4: Coefficients in terms of coded factors and coefficient of determination.

Coefficients in Terms of Coded Factors						
Factor	Coefficient Estimate	df	Standard Error	95%CI Low	95%CI High	VIF
Intercept	43.73	1	0.3303	42.88	44.58	
A-Temperature	-5.34	1	0.2023	-5.86	-4.82	1.00
B-Particle size	-4.95	1	0.2023	-5.47	-4.43	1.00
C-Time	-1.94	1	0.2023	-2.46	-1.42	1.00
AB	0.5325	1	0.2861	-0.2029	1.27	1.00
AC	0.0975	1	0.2861	-0.6379	0.8329	1.00
BC	0.3275	1	0.2861	-0.4079	1.06	1.00
A ²	-12.19	1	0.2978	-12.96	-11.42	1.01
B ²	-5.08	1	0.2978	-5.84	-4.31	1.01
C ²	-3.23	1	0.2978	-4.00	-2.46	1.01
Fit Statistics						
Coefficients		Value				
R-squared R ²		0.9985				
Adjusted R ²		0.9958				
Predicted R ²		0.9769				
Adeq Precision		57.8375				
Std. Dev.		0.5722				
Mean		32.80				
C.V. %		1.74				

C.V = coefficient of variation, Std.Dev. = standard deviation, VIF=Variance inflation factor

The quadratic models of regression analysis, suggested by the model, were expressed as follows in terms of coded factors:

$$\text{Yield (\%)} = 43.73 - 5.34A - 4.95B - 1.94C + 0.5325AB + 0.0975AC + 0.3275BC - 12.19A^2 - 5.08B^2 - 3.23C^2 \tag{Eq. 3}$$

The equation in terms of coded parameters can be used to form predictions about the response to given levels of each parameter. By default, the high levels of the parameters are coded as low levels (-1) and high levels (+1). The coded equations help to describe the relative influence of the variables by comparing the coefficients of the variables (31).

Effect of Extraction Parameters on the Yield of Oil

Effect of extraction temperature

The extraction process can occur at various temperatures based on the used solvent. Temperature is a critical parameter as it determines the reaction rate and yield of the produced oil (32). To find out the significance of extraction temperature on the conversion of oil, experiments were carried out at 50-80 °C (Figure 4(a)). The

effect of temperature on a reaction can be described through the theory of reaction kinetics. Enhancing the temperature will result in an enhancement fraction of particles that have greater speed and therefore have a higher kinetic rate, which results from the maximum yield of extraction (32). The highest yield of the oil was 43.9 % at an extraction temperature of 65°C. The yield of the oil was decreased beyond 65°C of extraction temperature; higher temperature accelerates the formation of saponification reaction which results in soap formation, as well as further increment of temperature is described to have an adverse effect on the conversion of the yield (31). In addition, maximum temperature resulted in a decrement of the yield, as hexane is lost because it starts to evaporate as the temperature approaches its boiling point (33).

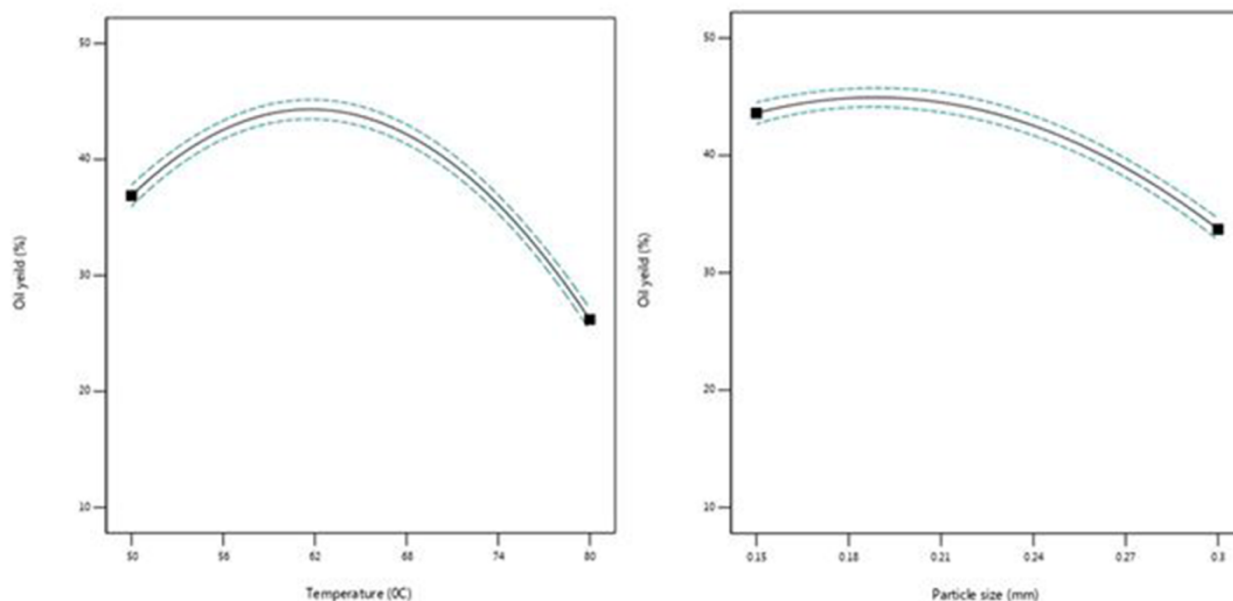


Figure 4: Effect of temperature (a) and particle size (b) on the extraction yield of oil.

Effects of particle size

It was indicated that the effectiveness of the biomass process is expected to be dependent on particle size (34). At optimum particle size, it is expected to bring up the speed of reaction between components; since the rate of reaction is influenced by the raw material accessibility and medium size of the molecule for better yield, while the bigger size of the molecule indicates a small amount of oil yield (35,36). Figure 4(b) shows the effects of particle size on oil yield while all other parameters are kept constant at zero levels; increasing the particle size to the maximum while keeping the other parameters constant results in a low oil yield. Increasing the particle size from 0.15-0.225 mm, results in the maximum yield of oil. The particle size of 0.225 mm was found to be the optimum point at which the maximum yield of oil was achieved. A particle size of above 0.3 mm has been observed to give an optimum yield of oil in the extraction of solid coconut oil (37–39).

Effect of extraction time

Another important process parameter that affects the yield of oil extraction is time. The extraction

time was studied between 60-80 min. The effect of extraction time on the yield of neem seed oil was shown in Figure 5. It could be determined that the yield of oil increased as extraction time moved up from 60 to 120 min and peaked at 120 min. This observation proposes that at the initial time of extraction, more oil was expelled from the neem seed (40,41). However, the rate was diminished with the increasing duration of time. At a longer extraction time, the negative impact of this factor on the yield was also considered (42,43).

Perturbation plot

The perturbation plot indicates the comparability between all parameters at a preferred point in the studied design space. The perturbation diagram for the yield of the extracted neem seed oil is demonstrated in Figure 6. The yield of extraction was described by changing only one variable over its range while the other variables were held constant. The plot shows the effect of all parameters at a central point in the design space (such as extraction time, particle size, and extraction temperature).

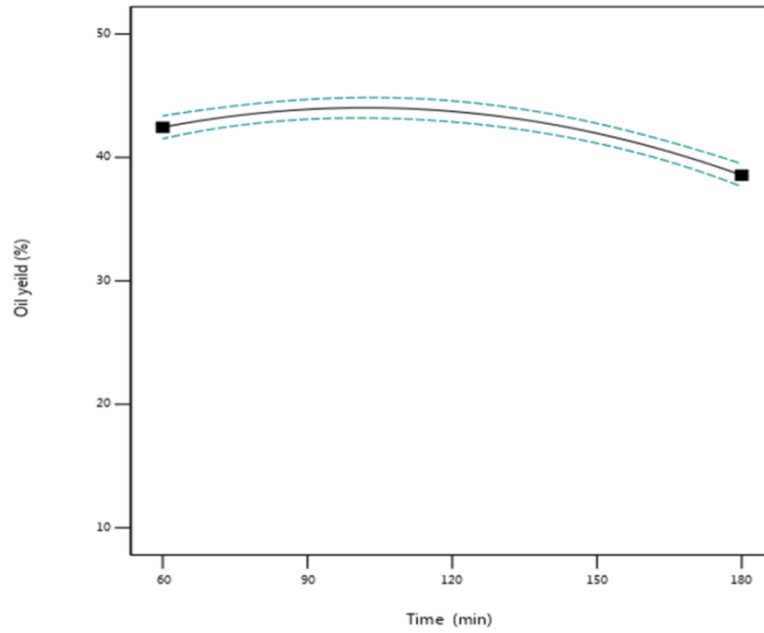


Figure 5: Effect of extraction time on the extraction yield of sandalwood oil.

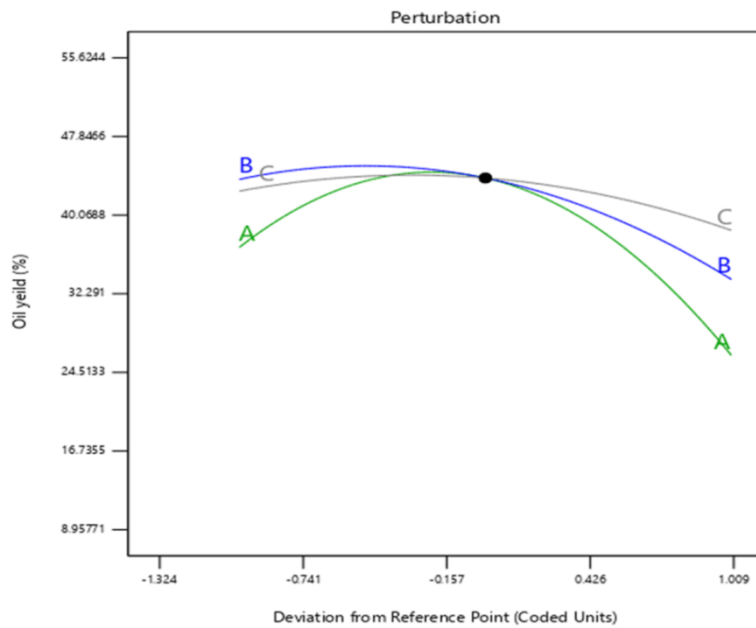


Figure 6: Perturbation plot for the extraction yield of neem oil response (A: Temperature, B: Particle size and C: Time).

All variables pointed to a negative result on the yield of extraction. The comparatively flat line of extraction time (C) shows a lower effect of this variable on the extraction yield of neem seed oil in the design space. It can be shown from Eq. (3) and Table 3 that extraction temperature and particle size had significant curvature effects on the yield. Through this comparability of coefficients in Eqn. (3), the majority of the significant variables were identified. In this way, the order of positive effects of the interaction terms on the yield of extraction was A-B, A-C and B-C; while the remaining

individual and quadratic terms had a negative influence on the yield of oil.

Optimization of oil extraction parameters

The goal of the study was to identify the optimal parameters for oil extraction. The optimized parameters were derived from the quadratic regression analysis proposed by the Box-Behnken design. Using Box-Behnken design, the optimal values for the developed regression model (Eqn. 2) and according to the described optimization criteria for selected variables, the optimization was conducted using the numerical method. The model

was applied by setting independent variables in the range with the goal of oil yield maximization. The model anticipated an optimal yield of oil, 44.081% at 64.416°C extraction temperature, 0.212 mm particle size, and 132.677 min of extraction time with the maximum desirability of 1 among 100 solutions proposed. This means it is possible to

select a series of combinations of the optimum parameters, which will enable maximum yield of oil. In addition, Figure 7 indicates the optimized process parameters for the extraction yield of neem seed oil. The experimental yield of oil (44.141%) at optimal parameters is close to the model-anticipated value of 44.081% within 0.136% of error value.

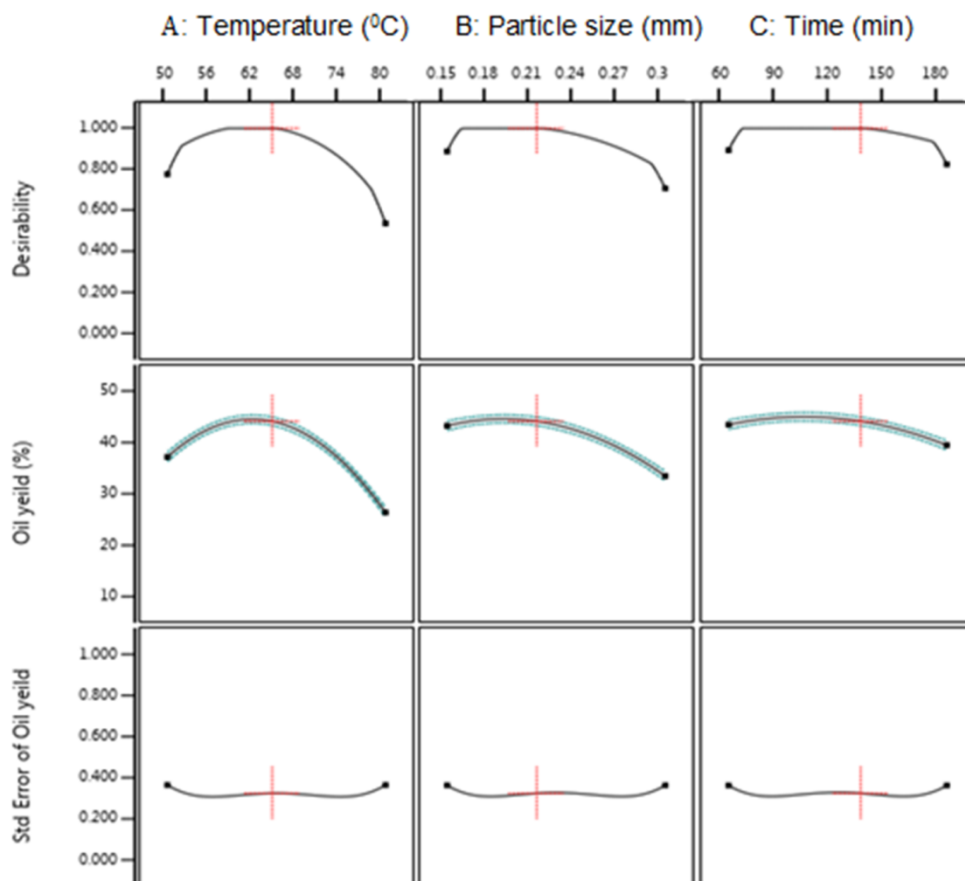


Figure 7: Shows the output (independent and dependent variables) of numerical optimization of the developed mathematical models.

Analysis of Properties of Neem Seed Oil

Physicochemical property

Different properties of the oil were analyzed according to AOAC (1990) and ASTM standards with modification as shown in Table 5.

The specific gravity of all the oils ranged from 0.84 to 0.91, which corresponds to the standard limit of 0.87-0.90 for non-edible oils (26). Density and gravity are important parameters for oil used in diesel fuel injection systems. The values must be maintained within tolerable limits to allow optimal air to fuel ratios for complete combustion. High-density biodiesel or its blend can lead to incomplete combustion and particulate matter emissions (37–39). In this study, 0.875 g/cm³ of density and 0.86 of specific gravity were obtained. Therefore, if this oil is used for biodiesel production, it will be safe since it fulfils the required criteria.

The ash content in oils is an important variable, at considerable quantity, to indicate the quality of the oil. An ash content of 2.1% has been recorded. Small ash content indicated that the extracted neem oil can be ignitable with a low amount of ash and can be used for biofuel production (44).

Iodine value is an indication of the unsaturation of fats and oils. The greater iodine value shows the higher unsaturation of oils and fats (26). Oils with iodine values greater than 120 are grouped as drying oils; those with iodine values of 60–120 are grouped as semi-drying oils; and those with iodine values below 60 are regarded as non-drying oils. In this study, the iodine value of the neem oil was 122.5 mgI₂/g, which is close to the standard specified by ASTM D763 (120 mg I₂/g) for dry oil, and this oil can be used in the cosmetic industry. People choose dry oils since they absorb into the skin within seconds of application, meaning that dry

oils indicate the same moisturizing advantages as wet oils, without missing a sticky residue on the hair or skin (45).

Acid values identify the appearance of oxidation products and corrosive free fatty acids as well as the degree of the lubricant's abasement. This is a necessary factor used to determine the quality of oil, since the lower the free fatty acid, the better the quality of the oil. More acidic value can contribute to severe corrosion in the internal combustion engine and fuel supply system (46). In this study 1.81(mg KOH/g) of acid value was recorded.

The saponification value is utilized in checking out debasement. The higher saponification value shows the existence of a higher percentage of fatty acids in the oil (44) and hence involves the possible trend to make soap; those difficulties in separation of products if used for producing biodiesel. This would also suggest that utilizing the oils for the production of biodiesel would result in a very low yield of the methyl ester. In this study, 206.7mg KOH/g of saponification value of oil was obtained, which is within the limit of ASTM standard.

Table 5: Physiochemical properties of neem seed oil.

Components	Value	ASTM 763 standard
Density (g/cm ³)	0.875	0.8-0.9
Moisture contents (%)	4.61	0.3-6.0
Ash contents (%)	2.31	1.5-4.5
viscosity (mm ² /s)	33.5	25-35.5
Iodine value (mg I ₂ /100g)	122.5	120
Saponification Value (mg KOH/g)	206.7	200-220
Acid value (mg KOH/g)	1.81	1.5-2.4

Fatty acid composition analysis with gas chromatography

The fatty acid constitution of the extracted neem seed oil was studied via the gas chromatography-mass spectrometry method. Five types of fatty acids were detected. As shown in Table 5, the predominant fatty acid was oleic acid adopted by

palmitic acid, caprylic acid, stearic and myristic acid, respectively. The chromatographic-mass spectrometry study revealed a considerable amount of unsaturated fatty acids in the oil of neem seeds. The fatty acid constitution of oil and its structures are presented in Table 6.

Table 6: Fat acid composition of neem seed oil.

Fatty acid type	Formula	Composition (%)
saturated fat acid		
Caprylic acid	C ₈ H ₁₆ O ₂	16.621
Myristic acid	C ₁₄ H ₂₈ O ₂	0.0058
Palmitic acid	C ₁₆ H ₃₂ O ₂	22.443
Stearic acid	C ₁₈ H ₃₆ O ₂	0.0062
Total		39.076
Unsaturated fatty acid		
Oleic acid	C ₁₈ H ₃₄ O ₂	60.924
Total		60.924

Fourier Transform Infrared Spectroscopy (FT-IR) Functional Group Analysis

The results of the FT-IR analysis of the neem seed oil is shown in Figure 8. The assimilation peak at different wavelengths was also indicated. The peak at 3006.26 cm⁻¹ is due to C-H asymmetrical stretch and the absorption peak at 2923.78 cm⁻¹ and 2855.25 are due to the C-H symmetric and antisymmetric stretch of the methyl group from the lipids (44). Peaks present at 1460.55 cm⁻¹ and

1376.06 cm⁻¹ are attributed to the C-H antisymmetric and symmetric deformation vibrations, respectively (46). The band at peaks of 1095.86 cm⁻¹, 1236.83 cm⁻¹, 1160.38 and 1236.83 cm⁻¹ corresponds to the C-O stretching vibration (46). The absorption at 1743.66 cm⁻¹ is also due to the C-O stretch and the peak at 720.79 cm⁻¹ is due to the C-H bond from the long branch of alkane (40,41).

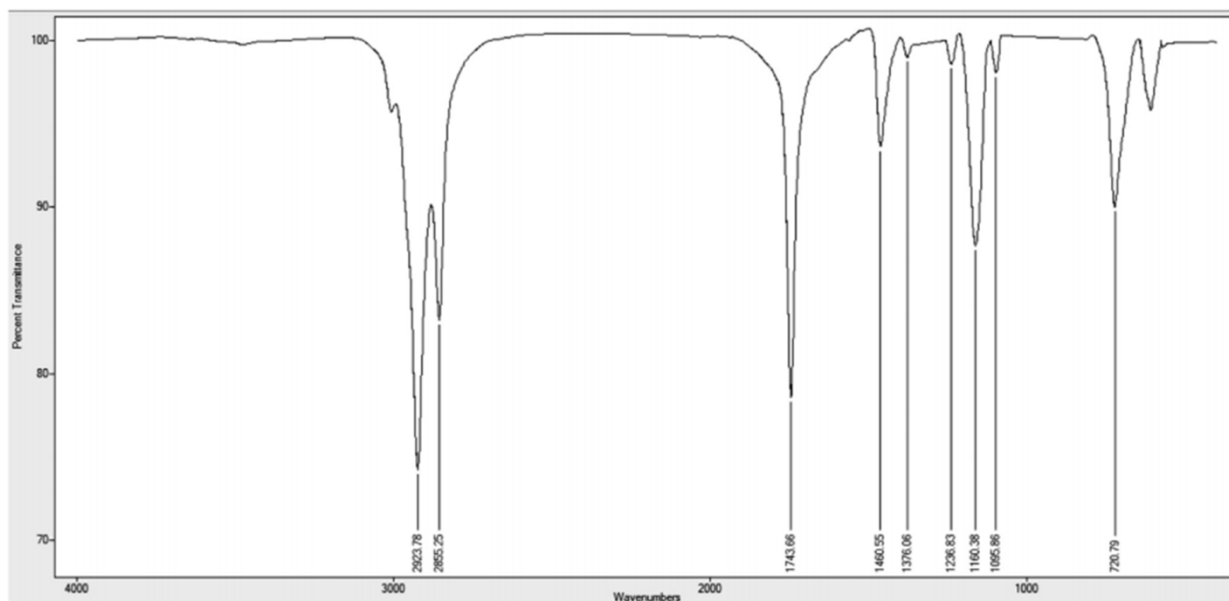


Figure 8: FTIR spectral analysis of neem seed oil at a frequency of 4000–400 cm^{-1} .

CONCLUSION

Neem seed oil was extracted using the Soxhlet extraction method. The effect of different extraction variables, such as extraction temperature, particle size, and extraction time, on oil yield was investigated by using Box-Behnken experimental design. The quadratic model was suggested to demonstrate optimum extraction parameters. Applying the numerical optimization of the desirability maximization technique, 132.677 min of extraction time, 64.416°C of extraction temperature, 0.212 mm of particle size, and 44.081% of oil yield were obtained at selected desirability. The experimental yield of oil (44.141%) at optimal parameters is close to the model-anticipated value of 44.081% within 0.135% of the error value. The study shows that the effects of temperature and particle size are found to be more significant compared to extraction time. The physicochemical characteristics of the extracted oil were also determined by using standard methods. The physicochemical properties of the oil reveal that the neem seed oil can be considered as a potential source of material for different products. The most common fatty acids in the neem seeds were oleic acid (60.924%), palmitic acid (22.443%), and caprylic acid (16.621%). The obtained results indicate the prospect of using neem seeds as a potential raw material in the industrial field in the future.

CONFLICT OF INTEREST

The author wishes to confirm that there is no conflict of interest associated with this paper for any material as well as financial.

ETHICAL APPROVAL

This article does not contain any studies with human participants or animals performed by any of the authors.

ACKNOWLEDGMENTS

Thanks to the School of Chemical Engineering as well as Addis Ababa University Institute of Technology and Colleagues of natural science for their support for this work.

FUNDING

The authors are grateful to Jimma University Institute of Technology for financial support for MEGA GRANT, RPD/JiT/0164/12/Code JiT_2019_36 research.

REFERENCES

1. Anand S, Sen A. Human Development and Economic Sustainability. World Development. 2000 Dec;28(12):2029–49. <DOI>.
2. Tomizawa A, Zhao L, Bassellier G, Ahlstrom D. Economic growth, innovation, institutions, and the Great Enrichment. Asia Pac J Manag. 2020 Mar;37(1):7–31. <DOI>.
3. Ram S, Mitra M, Shah F, Tirkey SR, Mishra S. Bacteria as an alternate biofactory for carotenoid production: A review of its applications, opportunities and challenges. Journal of Functional Foods. 2020 Apr;67:103867. <DOI>.
4. Ashaolu TJ. Immune boosting functional foods and their mechanisms: A critical evaluation of probiotics and prebiotics. Biomedicine & Pharmacotherapy. 2020 Oct;130:110625. <DOI>.

5. Rodrigo R, Miranda A, Vergara L. Modulation of endogenous antioxidant system by wine polyphenols in human disease. *Clinica Chimica Acta*. 2011 Feb;412(5-6):410-24. [<DOI>](#).
6. Fernandes SR, Barreiros L, Oliveira RF, Cruz A, Prudêncio C, Oliveira AI, et al. Chemistry, bioactivities, extraction and analysis of azadirachtin: State-of-the-art. *Fitoterapia*. 2019 Apr;134:141-50. [<DOI>](#).
7. Patel SM, Nagulapalli Venkata KC, Bhattacharyya P, Sethi G, Bishayee A. Potential of neem (*Azadirachta indica* L.) for prevention and treatment of oncologic diseases. *Seminars in Cancer Biology*. 2016 Oct;40-41:100-15. [<DOI>](#).
8. Patra JK, Das G, Lee S, Kang S-S, Shin H-S. Selected commercial plants: A review of extraction and isolation of bioactive compounds and their pharmacological market value. *Trends in Food Science & Technology*. 2018 Dec;82:89-109. [<DOI>](#).
9. Tschoeke PH, Oliveira EE, Dalcin MS, Silveira-Tschoeke MCAC, Sarmiento RA, Santos GR. Botanical and synthetic pesticides alter the flower visitation rates of pollinator bees in Neotropical melon fields. *Environmental Pollution*. 2019 Aug;251:591-9. [<DOI>](#).
10. Islas JF, Acosta E, G-Buentello Z, Delgado-Gallegos JL, Moreno-Treviño MG, Escalante B, et al. An overview of Neem (*Azadirachta indica*) and its potential impact on health. *Journal of Functional Foods*. 2020 Nov;74:104171. [<DOI>](#).
11. Büyüközkan G, Mukul E, Kongar E. Health tourism strategy selection via SWOT analysis and integrated hesitant fuzzy linguistic AHP-MABAC approach. *Socio-Economic Planning Sciences*. 2021 Apr;74:100929. [<DOI>](#).
12. Megersa M, Jima TT, Goro KK. The Use of Medicinal Plants for the Treatment of Toothache in Ethiopia. Evidence-Based Complementary and Alternative Medicine. 2019 Aug 20;2019:1-16. [<DOI>](#).
13. Chowdhury MSH, Koike M. Therapeutic use of plants by local communities in and around Rema-Kalenga Wildlife Sanctuary: implications for protected area management in Bangladesh. *Agroforest Syst*. 2010 Oct;80(2):241-57. [<DOI>](#).
14. Sharma S, Barkauskaite S, Jaiswal AK, Jaiswal S. Essential oils as additives in active food packaging. *Food Chemistry*. 2021 May;343:128403. [<DOI>](#).
15. Mitra S, Ghose A, Gujre N, Senthilkumar S, Borah P, Paul A, et al. A review on environmental and socioeconomic perspectives of three promising biofuel plants *Jatropha curcas*, *Pongamia pinnata* and *Mesua ferrea*. *Biomass and Bioenergy*. 2021 Aug;151:106173. [<DOI>](#).
16. Seljak T, Buffi M, Valera-Medina A, Chong CT, Chiamonti D, Katrašnik T. Bioliquids and their use in power generation – A technology review. *Renewable and Sustainable Energy Reviews*. 2020 Sep;129:109930. [<DOI>](#).
17. Sprakel LMJ, Schuur B. Solvent developments for liquid-liquid extraction of carboxylic acids in perspective. *Separation and Purification Technology*. 2019 Mar;211:935-57. [<DOI>](#).
18. Belwal T, Ezzat SM, Rastrelli L, Bhatt ID, Daglia M, Baldi A, et al. A critical analysis of extraction techniques used for botanicals: Trends, priorities, industrial uses and optimization strategies. *TrAC Trends in Analytical Chemistry*. 2018 Mar;100:82-102. [<DOI>](#).
19. Ghazanfari N, Mortazavi SA, Yazdi FT, Mohammadi M. Microwave-assisted hydrodistillation extraction of essential oil from coriander seeds and evaluation of their composition, antioxidant and antimicrobial activity. *Heliyon*. 2020 Sep;6(9):e04893. [<DOI>](#).
20. Tomić M, Ljubojević M, Mičić R, Simikić M, Dulić J, Narandžić T, et al. Oil from *Koelerutera paniculata* Lxm. 1772 as possible feedstock for biodiesel production. *Fuel*. 2020 Oct;277:118162. [<DOI>](#).
21. Hasni K, Ilham Z, Dharma S, Varman M. Optimization of biodiesel production from *Brucea javanica* seeds oil as novel non-edible feedstock using response surface methodology. *Energy Conversion and Management*. 2017 Oct;149:392-400. [<DOI>](#).
22. Falowo OA, Oloko-Oba MI, Betiku E. Biodiesel production intensification via microwave irradiation-assisted transesterification of oil blend using nanoparticles from elephant-ear tree pod husk as a base heterogeneous catalyst. *Chemical Engineering and Processing - Process Intensification*. 2019 Jun;140:157-70. [<DOI>](#).
23. Menkiti MC, Agu CM, Udeigwe TK. Extraction of oil from *Terminalia catappa* L.: Process parameter impacts, kinetics, and thermodynamics. *Industrial Crops and Products*. 2015 Dec;77:713-23. [<DOI>](#).
24. Esonye C, Onukwuli OD, Ofoefule AU. Optimization of methyl ester production from *Prunus Amygdalus* seed oil using response surface methodology and Artificial Neural Networks. *Renewable Energy*. 2019 Jan;130:61-72. [<DOI>](#).
25. Elkelawy M, Bastawissi HA-E, Esmail KK, Radwan AM, Panchal H, Sadasivuni KK, et al. Maximization of biodiesel production from sunflower and soybean oils and prediction of diesel engine performance and emission characteristics through response surface methodology. *Fuel*. 2020 Apr;266:117072. [<DOI>](#).
26. Mäkelä M. Experimental design and response surface methodology in energy applications: A tutorial review. *Energy Conversion and Management*. 2017 Nov;151:630-40. [<DOI>](#).
27. Abirami T, Loganaganandan M, Murali G, Fediuk R, Vickram Sreekrishna R, Vignesh T, et al. Experimental research on impact response of novel steel fibrous concretes under falling mass impact. *Construction and Building Materials*. 2019 Oct;222:447-57. [<DOI>](#).
28. Asfaram A, Ghaedi M, Ghezelbash GR, Pepe F. Application of experimental design and derivative spectrophotometry methods in optimization and analysis of biosorption of binary mixtures of basic dyes from aqueous solutions. *Ecotoxicology and Environmental Safety*. 2017 May;139:219-27. [<DOI>](#).

29. Azari A, Noorisepehr M, Dehghanifard E, Karimyan K, Hashemi SY, Kalhori EM, et al. Experimental design, modeling and mechanism of cationic dyes biosorption on to magnetic chitosan-lutaraldehyde composite. *International Journal of Biological Macromolecules*. 2019 Jun;131:633–45. [<DOI>](#).
30. Umanath K, Palanikumar K, Sankaradass V, Uma K. Optimization of wear properties on AA7075/Sic/Mos2 hybrid metal matrix composite by response surface methodology. *Materials Today: Proceedings*. 2021;46:4019–24. [<DOI>](#).
31. Twisk J, Bosman L, Hoekstra T, Rijnhart J, Welten M, Heymans M. Different ways to estimate treatment effects in randomised controlled trials. *Contemporary Clinical Trials Communications*. 2018 Jun;10:80–5. [<DOI>](#).
32. Sitepu EK, Heimann K, Raston CL, Zhang W. Critical evaluation of process parameters for direct biodiesel production from diverse feedstock. *Renewable and Sustainable Energy Reviews*. 2020 May;123:109762. [<DOI>](#).
33. Al-Muhtaseb AH, Osman AI, Murphin Kumar PS, Jamil F, Al-Haj L, Al Nabhani A, et al. Circular economy approach of enhanced bifunctional catalytic system of CaO/CeO₂ for biodiesel production from waste loquat seed oil with life cycle assessment study. *Energy Conversion and Management*. 2021 May;236:114040. [<DOI>](#).
34. Klinger JL, Westover TL, Emerson RM, Williams CL, Hernandez S, Monson GD, et al. Effect of biomass type, heating rate, and sample size on microwave-enhanced fast pyrolysis product yields and qualities. *Applied Energy*. 2018 Oct;228:535–45. [<DOI>](#).
35. Xiao R, Yang W, Cong X, Dong K, Xu J, Wang D, et al. Thermogravimetric analysis and reaction kinetics of lignocellulosic biomass pyrolysis. *Energy*. 2020 Jun;201:117537. [<DOI>](#).
36. Lu H, Ip E, Scott J, Foster P, Vickers M, Baxter LL. Effects of particle shape and size on devolatilization of biomass particle. *Fuel*. 2010 May;89(5):1156–68. [<DOI>](#).
37. Ambat I, Srivastava V, Sillanpää M. Recent advancement in biodiesel production methodologies using various feedstock: A review. *Renewable and Sustainable Energy Reviews*. 2018 Jul;90:356–69. [<DOI>](#).
38. Hoseinzadeh Hesas R, Arami-Niya A, Wan Daud WMA, Sahu JN. Preparation of granular activated carbon from oil palm shell by microwave-induced chemical activation: Optimisation using surface response methodology. *Chemical Engineering Research and Design*. 2013 Dec;91(12):2447–56. [<DOI>](#).
39. Peng WL, Mohd-Nasir H, Setapar SHM, Ahmad A, Lokhat D. Optimization of process variables using response surface methodology for tocopherol extraction from Roselle seed oil by supercritical carbon dioxide. *Industrial Crops and Products*. 2020 Jan;143:111886. [<DOI>](#).
40. Yadav KK, Gupta N, Kumar V, Khan SA, Kumar A. A review of emerging adsorbents and current demand for defluoridation of water: Bright future in water sustainability. *Environment International*. 2018 Feb;111:80–108. [<DOI>](#).
41. Bibi R, Ahmad M, Gulzar A, Tariq M. Effect of profenofos and citrus oil on *Cryptolaemus montrouzieri* Mulsant and *Chrysoperla carnea* Stephens, key predators of citrus mealybug, *Planococcus citri* (Risso), under laboratory conditions. *Int J Trop Insect Sci*. 2022 Feb;42(1):379–87. [<DOI>](#).
42. Redondo D, Venturini ME, Luengo E, Raso J, Arias E. Pulsed electric fields as a green technology for the extraction of bioactive compounds from thinned peach by-products. *Innovative Food Science & Emerging Technologies*. 2018 Feb;45:335–43. [<DOI>](#).
43. Chen Q, Dong W, Wei C, Hu R, Long Y. Combining integrated ultrasonic-microwave technique with ethanol to maximise extraction of green coffee oil from Arabica coffee beans. *Industrial Crops and Products*. 2020 Sep;151:112405. [<DOI>](#).
44. Rehan M, Gardy J, Demirbas A, Rashid U, Budzianowski WM, Pant D, et al. Waste to biodiesel: A preliminary assessment for Saudi Arabia. *Bioresource Technology*. 2018 Feb;250:17–25. [<DOI>](#).
45. Lacouture ME, Elizabeth Davis M, Elzinga G, Butowski N, Tran D, Villano JL, et al. Characterization and Management of Dermatologic Adverse Events With the NovoTTF-100A System, a Novel Anti-mitotic Electric Field Device for the Treatment of Recurrent Glioblastoma. *Seminars in Oncology*. 2014 Jun;41:S1–14. [<DOI>](#).
46. Chhabra M, Dwivedi G, Baredar P, Kumar Shukla A, Garg A, Jain S. Production & optimization of biodiesel from rubber oil using BBD technique. *Materials Today: Proceedings*. 2021;38:69–73. [<DOI>](#).



Accuracy Limits of Pair Distribution Function Analysis in Structural Characterization of Nanocrystalline Powders by X-ray Diffraction

Abolfazl Baloochiyan¹ , Merdan Batyrow¹ , Hande Öztürk^{1*} 

¹Özyeğin University, Department of Mechanical Engineering, İstanbul, 34794, Turkey

Abstract: We report the minimum errors of structural parameters, namely lattice parameter, crystallite size, and atomic displacement parameters, expected from Pair Distribution Function (PDF) analysis of nanocrystalline gold powders for the first time by a self-consistent computational methodology. Although PDF analysis has been increasingly used to characterize nanocrystalline powders by X-rays, the current literature includes no established error bounds to be expected from the resulting structural parameters. For accurate interpretation of X-ray diffraction data, these error bounds must be determined, and the obtained structural parameters must be cleared from them. Our novel methodology includes: **1)** simulation of ideal powder diffraction experiments with the use of the Debye scattering equation, **2)** pair distribution function analysis of the diffraction data with the Diffpy-CMI analysis software, and **3)** determination of the errors from PDF analysis of the simulated diffraction data by comparing them with real-space analysis of spherical gold nanocrystals that are 30 nm size and smaller. Our results show that except for the lattice parameters and even with an ideal crystalline powder sample and ideal diffraction data, the extracted structural parameters from PDF analysis diverge from their true values for the studied nanopowder. These deviations are dependent on the average size of the nanocrystals and the energy of the X-rays selected for the diffraction experiments, where lower X-ray energies and small-sized nanocrystalline powders lead to greater errors.

Keywords: Pair distribution function analysis, powder diffraction, X-rays, nanocrystalline powders, Debye scattering equation.

Submitted: October 13, 2021. **Accepted:** March 13, 2022.

Cite this: Baloochiyan A, Batyrow M, Öztürk H. Accuracy Limits of Pair Distribution Function Analysis in Structural Characterization of Nanocrystalline Powders by X-ray Diffraction. JOTCSA. 2022;9(2):527-44.

DOI: <https://doi.org/10.18596/jotcsa.1008896>.

***Corresponding author:** hande.ozturk@ozyegin.edu.tr.

INTRODUCTION

Nanomaterials are becoming an integral part of all manufacturing processes in industries ranging from food, cosmetics, and weaponry, since they promise tunable physical, electrical, mechanical, etc. properties (1,2) that can potentially bring revolutionary solutions to many problems in engineering designs. The number one step for controlled manufacturing and/or integration of nanomaterials in mass production is fast, reliable, and robust characterization, which must be performed with the highest amount of detail and resolution to optimize nanomaterials for best

performance. X-ray diffraction (XRD) is currently the gold standard characterization technique that promises these requirements while accessing atomic-scale information in a non-destructive manner (3). Although XRD was initially developed to investigate the atomic periodicity in crystalline materials, the technique has progressed enormously and has been extended to the analysis of amorphous materials as well. Among the most frequent practices of X-ray diffraction is powder diffraction. In this technique, one has no obligation to prepare high quality single crystalline samples, which is an obstacle for many materials (4), but can also investigate polycrystalline and powder forms of

materials as well. This has caught the attention of researchers working in the field of nanopowders, a class of nanomaterials consisting of nanocrystalline particles, and has resulted in further development of the XRD technique on nanoparticulate forms of matter.

In XRD analysis of nanopowders, there are mainly two methodologies one can follow: **1)** perform whole pattern modelling and refinement analysis assuming there is a unit cell model that represents the atomic ordering in the coherent domain of the material and work towards solving for that cell model from the diffraction data; or **2)** abandon the unit cell construct and perform modelling and refinement analysis of bond distance histograms of the coherent domains of the material by Fourier transforming the powder diffraction data (5). The first method is known as the structure solution methodology, and Rietveld refinement (6) is the most widely used algorithm in this context. The second method, known as the pair distribution function analysis, has been around for a while, but it has become popular with the development of open source computer programs (7) and the availability of synchrotron X-ray sources, enabling enormous progress in the capabilities of the technique.

For bulk crystalline materials where the atomic periodicity extends beyond hundreds of nanometers (8), crystallographic solutions are generally available from their diffraction data, and the resulting unit cell typically represents the average structural properties of the material. There is no guarantee that this solution is unique (9); however, one may complement X-ray analysis with independent, direct or indirect methods for confirmation, such as Transmission Electron Microscopy (TEM) or electrical conductivity, respectively. For nanocrystalline materials, crystallographic analysis is not as trivial as in bulk crystalline materials; in this case, atomic periodicity extends up to 100 nm or so, and thus typical diffraction data from such materials show structural features intermediate between those of crystalline and amorphous materials. There are certain regions in nanomaterials where the atomic stacking can be described as periodic, as in a regular crystal, and some other regions where this stacking cannot be considered periodic at all (10). For such materials, the assumption of a single unit cell representing the average atomic configuration within the material is unjustified (11). Therefore data analysis methods relying on the assumption of a unit cell model fail. In that case, pair distribution function analysis, assuming no particular atomic stacking within the scattering material and no single repeating unit cell, may be the right solution for structural analysis of nanocrystalline powders and is quickly becoming popular.

In an earlier work, we demonstrated that widespread crystallographic analysis routines, such as line profile analysis and Rietveld refinement, failed to retrieve the true lattice parameters of nanocrystalline powders (11) and identified the reason for failure as the incompatible single unit cell model used to represent the atomic configuration of atoms in nanocrystals. In the current work, we implement our self-consistent methodology to quantify the minimum errors within the structural parameters, i.e., lattice parameters, average crystallite sizes, and atomic displacement parameters, retrieved from pair distribution function analysis and evaluate how errors vary with respect to the energy of the X-rays and the average size of the nanocrystals studied. Our findings will potentially guide researchers working on the characterization of nanomaterials to use pair distribution function analysis properly with realistic expectations for accuracy, interpret their results correctly, and design their experimental setups better for improved accuracy in structural identification of nanocrystalline powders.

THEORY

A typical PDF experiment consists of: **1)** measuring the coherent X-ray scattering intensity $I_{coh}(q)$ from an ensemble of atoms in the kinematic scattering regime; **2)** manipulating this measurement to extract what is called the normalized total scattering function $S(q)$; **3)** a Fourier transformation to convert the total scattering function to another function of real space, r , that is an indirect representation of distances between pairs of atoms making up the crystal (5). This resulting transform is called the reduced pair distribution function $G(r)$, and it is then refined to extract structural parameters of the irradiated sample. These steps can be mathematically formulated as below:

$$I_{coh}(q) = \sum_{i=1}^N \sum_{j=1}^N f_i f_j \exp(iq \cdot [r_i - r_j]) \quad (\text{Eq. 1})$$

where N is the number of atoms that are irradiated by X-rays, $f = f(q)$ is the atomic scattering factor of the type of material which depends on the scattering angle 2θ and the irradiation wavelength, λ , r_i is the coordinate vector of the atom i from an arbitrary origin and i is the imaginary number, $\sqrt{-1}$.

A normalization is applied on I_{coh} to access the reduced total scattering function $S(q)$:

$$S(q) - 1 = \frac{I_{coh}(q)}{N \langle f \rangle^2 - \frac{f^2}{\langle f \rangle^2}} \quad (\text{Eq. 2})$$

Where q is the magnitude of the momentum transfer vector of the X-rays, with

$$q = |q| = \frac{4\pi \sin \theta}{\lambda} \text{ and } \langle f \rangle^2 \text{ is the squared average}$$

atomic scattering factor. In Eq. 2, we highlight the term 'coherent intensity' to emphasize that the reduced total scattering function is related only to the coherent portion of measured X-ray intensities, hence -if applicable- the measured diffraction data must be cleared from unwanted signal such as that resulting from multiple scattering, sample absorption, background scattering, etc. Once $S(q)$ is evaluated, the pair distribution function $G(r)$ can be obtained by the following Fourier-Sine transform:

$$G(r) = \frac{2}{\pi} \int_0^{\infty} q [S(q) - 1] \sin(qr) dq \quad (\text{Eq. 3})$$

As can be seen, the reduced pair distribution function $G(r)$ is theoretically accessible exactly from the measured coherent diffraction intensities by a standard normalization followed by a Fourier transform. But during real measurements, the upper limit of the integral in Eq. 3 is never infinite and is limited by the maximum scattering angle at which the diffraction intensities are recorded and the wavelength of X-rays. Accordingly, a truncated approximation of the Fourier-Sine transform is employed to obtain the reduced pair distribution function:

$$G(r) = \frac{2}{\pi} \int_{q_{min}}^{q_{max}} q [S(q) - 1] \sin(qr) dq \quad (\text{Eq. 4})$$

where $q_{max} = \frac{4\pi \sin(\theta_{max})}{\lambda}$. This truncation is

known to decrease the resolution of the real space function obtained from the Fourier transform (12). Similarly, the small angle scattering portion of the diffraction data is usually cropped, since diffraction intensities close to forward-scattering angles scale with the square of the total number of irradiated atoms and have the potential to burn the center of X-ray detectors due to extremely high photon counts, unless properly blocked. Secondly, including the small angle scattering portion in diffraction data results in an incompatibility with the expected input of the subsequent refinement process (13). Therefore, the small angle scattering portion is excluded from the integration, i.e.,

$$q_{min} = \frac{4\pi \sin \theta_{min}}{\lambda} \text{ and } \theta_{min} > 0.$$

$G(r)$ can also be evaluated using sample's real-space parameters. This can be accomplished by realizing that $G(r)$ is actually the local deviation of the number density of atom pairs from the average number density of irradiated atoms separated by a particular interatomic distance r . Using this definition, $G(r)$ can also be written as:

$$G(r) = \frac{1}{r} \sum_i^N \sum_j^N \left[\frac{f_i f_j}{\langle f \rangle^2} \delta(r - r_{ij}) \right] - 4\pi \rho_0 \quad (\text{Eq. 5})$$

where $\delta(r)$ is the Dirac delta function, $r_{ij} = |r_i - r_j|$ and ρ_0 is the average number density of the atomic ensemble. For an ensemble of atoms that are stacked perfectly periodic in 3 dimensions, like an ideal crystalline particle, Eq. 5 results in sharp and discrete Dirac delta functions, located at interatomic distances corresponding to characteristic interplanar distances of the crystallite. However, for all realistic crystalline and amorphous material samples measured at finite temperatures, the resulting thermal movement of atoms causes these Dirac delta functions to broaden, proportional to the amount of atomic displacement. Assuming random displacements of atoms around their average positions, each pair distribution peak can be numerically approximated by a Gaussian function. Hence, the width of these Gaussian functions can be used as a measure of the average displacements of atoms around their average positions, which can then be related to the Debye-Waller factor in X-ray diffraction experiments (5).

In conclusion, the main logic behind Pair Distribution Function refinement is to calculate a model $G(r)$ based on the initial atomic coordinates assumed for the diffracting sample (using Eq. 5) and refine this model against the $G(r)$ obtained from the diffraction signature of that sample (using Eqs. 2 and 4) until a predefined tolerance level is achieved between the two $G(r)$ functions. Unlike standard Rietveld refinement analysis commonly used in crystallographic studies of polycrystalline, single crystalline, and nanocrystalline materials, the PDF refinement is based on a least square error minimization process performed on *real-space data*, rather than reciprocal (or angular, 2θ) space.

METHODOLOGY

Here we describe the four main steps followed to study the accuracy limits of the structural parameters obtained from gold nanocrystalline powders using their X-ray diffraction data. These are: **1)** creating the atomic coordinates of a nanocrystalline particle and generating an ideal, monodispersed particle ensemble from it; **2)** calculating the expected powder diffraction data from this nanocrystalline particle ensemble; **3)** steps followed during preprocessing of the diffraction data; and **4)** pair distribution function analysis.

Creating Perfectly-Crystalline and Energy-Minimized Versions of Ideally Random, Monodispersed Nanocrystalline Powders

This step includes creating atomic coordinates of spherical gold nanocrystals with two versions: ideal nanocrystalline and energy minimized atomic configurations. For ideal crystalline nanoparticles, we assumed a lattice parameter of 4.0626 Å and created atomic coordinates in 3 dimensions by following the packing rules of face centered cubic

crystals. Spherical nanocrystals with variable diameters were generated. For energy-minimized nanocrystals, we used these ideal-crystalline atomic configurations as input and performed equilibrium molecular dynamics (EMD) simulations assuming a 0 Kelvin final temperature. EMD simulations were performed with the open-source LAMMPS code (14) combining the initial (ideal-crystalline) atomic coordinates with interatomic forces modeled by the

optimized embedded atom method (EAM) for gold atoms as suggested in the literature (15). These new coordinates were validated against similar work from past literature (11). Figure 1 shows the energy minimization process and the resulting atomic coordinates of ideal-crystalline and energy-minimized versions of a spherical gold nanoparticle with a 5 nm nominal diameter.

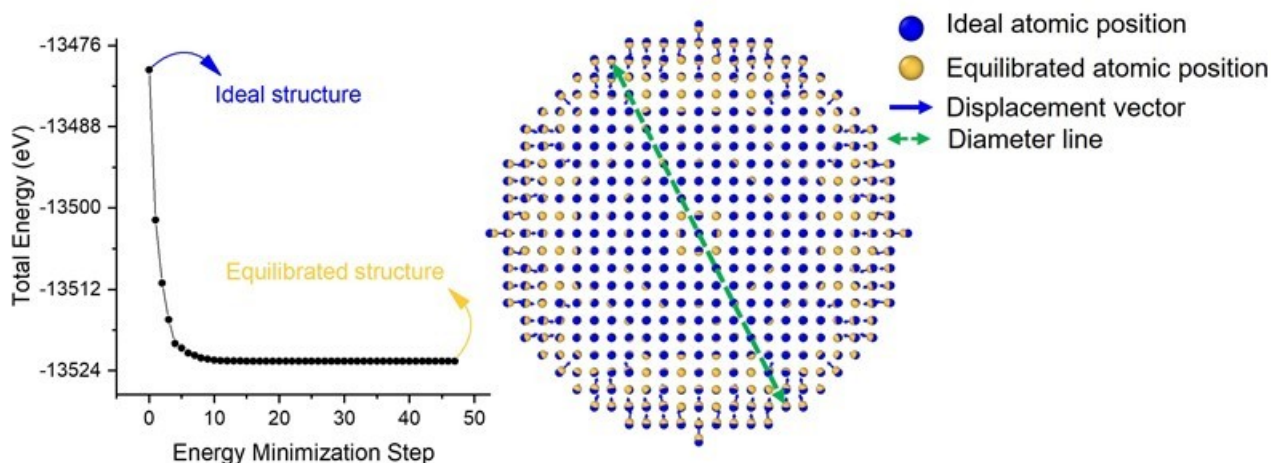


Figure 1: Left side: Change in the total energy of the spherical gold nanoparticle system during EMD simulations performed on ideal crystalline atomic configuration. The resulting energy-minimized atomic configuration has less total energy and is thermodynamically stable. The number of steps taken during the simulation was determined by the tolerance value of 10^{-8} . Right side: The atomic configurations of ideal-crystalline (blue markers) and energy-minimized versions (yellow markers) of the gold nanoparticle with a 5 nm nominal diameter. The blue arrows associated with blue markers show the relative displacement of atomic sites resulting from energy minimization. The green arrow drawn by dashed lines is one of the diameter lines we used to calculate the average size of the nanoparticle.

Once the atomic coordinates of a single gold nanoparticle are generated, we can create a monodispersed, ideal powder ensemble by considering a finite number of such particles and randomizing their orientation with respect to each other. The final set of atomic coordinates would constitute an ideal particle ensemble (powder) with a finite number of identical nanoparticles having random distribution of particle orientations. The diffracted intensities from such a finite particle ensemble would fluctuate around a mean value where the uncertainty in the intensities is inversely proportional to the number of particles considered (16). However, if we take the limit of the number of particles to infinity, then the orientationally-averaged diffracted X-ray intensities from these particles correspond to their ultimate limit with no statistical uncertainty. In this study, we focused on the accuracy limits of an X-ray analysis algorithm; hence, we chose to work with infinite-particle ensembles, eliminating statistical fluctuations in the diffraction data resulting from particle selection statistics.

Generation of Ideal Diffraction Profiles

The expected diffraction intensity distribution from infinitely large powders of gold nanocrystals was

computed by the Debye scattering equation (17). This equation has the following form:

$$\langle I(2\theta) \rangle = f_m(2\theta) f_n(2\theta) \sum_{m=1}^N \sum_{n=1}^N \frac{\sin(|q||r_{mn}|)}{|q||r_{mn}|} \quad (\text{Eq. 6})$$

Here $\langle I(2\theta) \rangle$ is the orientationally-averaged diffracted intensity distribution that is a function of the scattering angle 2θ , $|q|$ is the magnitude of the momentum transfer vector, $|r_{mn}| = |r_m - r_n|$ is the magnitude of the separation vector between atoms m and n , and $f_m(2\theta)$ is the atomic scattering factor of atom m , which is again angle dependent as q and is determined by the type of scattering material. For a monatomic crystal such as a gold nanoparticle, $f_m = f_n$; hence, $f_m(2\theta)f_n(2\theta) = f^2(2\theta)$. Finally, the upper limit of the summation N is the total number of atoms within a single nanoparticle. As seen from Eq. 6, one needs only the atomic coordinates of a single nanoparticle to generate the orientational average of the diffracted intensity distribution from a monodispersed ensemble of nanocrystals irradiated by monochromatic X-rays. This means that the Debye equation implicitly assumes that the

orientation distribution of nanocrystals making up the particle ensemble is ideally random, which also necessitates that the ensemble consists of an infinite number of identical crystals. Interested readers can follow classical texts (18) to confirm these assumptions behind the Debye equation.

To sum up, the Debye equation provides us with a powerful tool to test error bounds and applicability of X-ray analysis algorithms on diffraction data from nanocrystals, since we can work with noise-free, ideal diffraction data and have full control over the inputs to these algorithms.

In this study, the diffracted intensity data were obtained by the Debyer software¹, since coding Eq. 6 and directly running simulations with nanocrystals with large number of atoms N causes the computation time to explode quickly. This software optimizes the computation time neatly by generating histograms of available interatomic distance vectors, r_{mn} for each atom in the particle and considering only those terms that contribute appreciably to the diffracted intensities. Hence, it diverges slightly from the exact computation of the Debye equation. However, we confirmed that these deviations are minor, and do not affect our results, similar to past work (11). Next, we set the angular range as $2\theta \in (5^\circ, 180^\circ)$, angular spacing as $d\theta = 0.01^\circ$ and selected 5 different X-ray wavelengths from 0.21 to 1.54 Å, which are widely used in experimental studies². Five different particle diameters were considered when modelling the nanocrystalline powders, which ranged from 5 to 30 nm. This process resulted in 50 different X-ray diffraction data since we considered both ideal crystalline and energy-minimized versions of these 5 nanocrystalline particle ensembles. Examples of computed diffraction data are seen on the left side of Figure 2. Finally, we emphasize that these intensities do not contain any unwanted scattering signals or background other than the coherent, elastic scattering from gold atoms. Hence, they were used directly in the subsequent analysis steps. When working with experimental diffraction data, one needs to carefully clean up their data from inelastic scattering, refraction effects, counting and particle selection statistics, and systematic/human errors, if present, before further analysis (12).

Preprocessing of Diffraction Data

Before performing the pair distribution function analysis, one should process the powder diffraction data. Typically, this process entails obtaining the normalized total scattering function $S(q)$ from the intensity data and then performing the Fourier-Sine

transform of the data. In this work, we performed these steps using the pdfgetx3 code (19), which is part of the Diffpy-CMI package (7) due to the software's being widely used by the X-ray community in PDF analysis.

An important step while performing the Fourier-Sine transform of the intensity data is the proper removal of the small angle scattering component. This was done by visualizing our simulated diffraction data one by one and setting an angular threshold below which there would be considered a small angle scattering component of the diffracted signal. This region was determined separately for each wavelength considered and reported in the last column of Table 1 as $q_{min} = \frac{4\pi \sin \theta_{min}}{\lambda}$. Finally,

the default setting of $r_{poly}=0.9$ was used, since the minimum interatomic distance in our gold nanocrystals is around 2.872 Å, which is imposed by the stacking rules of the FCC unit cell, and $r_{poly}=0.9$ is not expected to affect our interatomic distances as explained by past literature (19). On the right side of Figure 2, examples of reduced pair distribution functions $G(r)$ resulting from preprocessing of diffraction profiles of 5, 10, and 15 nm spherical gold nanoparticles are shown.

Pair Distribution Function Analysis and Refinement

After the intensity data are transformed, the final step is the PDF refinement. We used the freely-available module Diffpy-cmi (7) to perform our refinements. At the beginning of a refinement, one needs to provide the transformed intensity files as well as a cif file (crystallographic information file) of the powder material as input. This cif file, which in our case is the one for gold, is used to initialize the structural parameters such as lattice parameter, thermal parameters, etc., to be refined. Then, the real space range over which the refinement will be performed is selected, and the parameters are refined one-by-one. Typical refinement parameters are: **1)** an arbitrary scaling factor used to match the nominal values of the calculated and modeled pair distribution functions; **2)** average lattice parameter; **3)** coherent particle size, which is a measure of the average extent of atomic periodicity for diffracting particles; **4)** a damping factor Q_{damp} used to quantify and implement the limited instrument resolution effects, such as X-ray wavelength and limited angular range of the X-ray detector, on the corresponding pair distribution function model; and **5)** thermal parameters such as Anisotropic Displacement Parameters (ADP) used to quantify static or dynamic, direction-dependent or independent, mean-squared atomic displacements from ideal lattice positions (20). During the refinement, the software tries to modify and match the modeled pair distribution function against that obtained from the Fourier Sine transform by a least-square optimization routine.

1 <https://debyer.readthedocs.io/en/latest/>

2 For simulations with $\lambda=0.21\text{Å}$, $d\theta = 0.001^\circ$ and $2\theta \in (0.1^\circ, 55^\circ)$ since $d\theta > 0.001^\circ$ was not narrow enough to resolve neighboring Bragg peaks clearly.

In this work, we started off by initializing the lattice parameter as 4.078 Å, crystal space group as Fm3m, B_{iso} as 0.001, a negligible but finite value to avoid crashing of the software since $B_{iso}=0$ corresponds to a case with Dirac delta functions as reduced pair distribution peaks, and instrument-related damping factor q_{damp} as 0.001, which is the default value assumed in Diffpy-cmi software, since our simulated data cannot be corrected against the refinement of a calibration material, unlike what is suggested in the literature (21). Next, we divided the whole refinement process into multiple steps; we refined the lattice parameter and the arbitrary

scaling factor first, the coherent particle size, assuming spherical particle shapes second, B_{iso} , i.e. the atomic displacement parameter, assuming isotropic displacement of atoms, third, and then all parameters were refined altogether last. The quality of the refinement was confirmed by two measures: R_w , which is a goodness-of-fit parameter reported by the software, and by visual inspection of the calculated and measured pair distribution functions. We observed that relying solely on R_w was misleading since there is no universally accepted reference value for R_w for a particular fit quality.

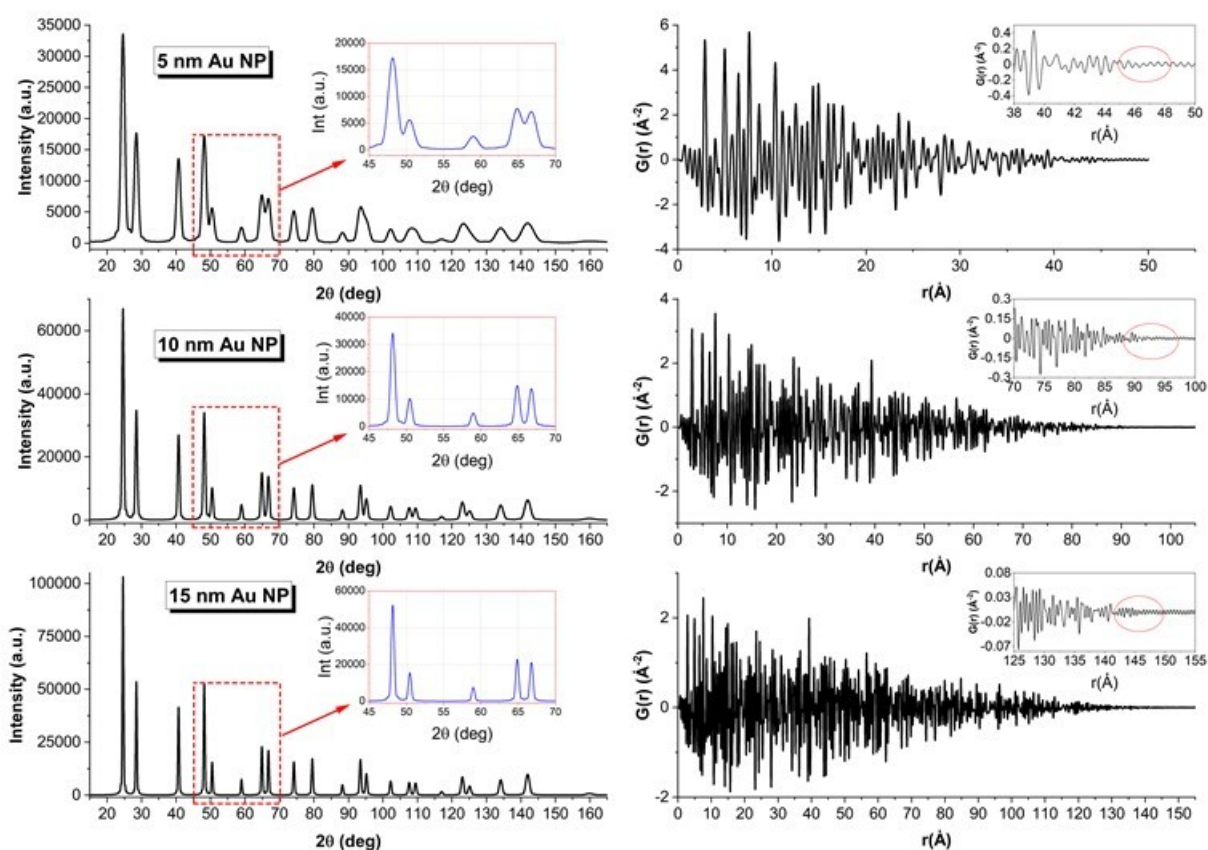


Figure 2: Left side: The simulated powder diffraction profiles of 5 nm (top), 10 nm (middle), 15 nm (bottom) diameter spherical gold nanoparticles assuming 1 Å wavelength X-rays. The insets show a close up view of the intensity distributions between 45° and 70°. Right side: The corresponding reduced pair distribution functions $G(r)$ of the diffraction profiles on the left. The insets are a close up view of the tails where $G(r)$ approaches background level.

RESULTS AND DISCUSSION

In this section, we report the outcomes of the pair distribution function analysis of diffraction data simulated from ideal, random, and monodispersed gold nanocrystals of various sizes and both in ideal crystalline and energy-minimized forms.

PDF Refinement of Diffraction Data from Ideal Crystalline Gold Nanopowders

An example of a successful PDF refinement is presented in Figure 3. Here, the diffraction data was

simulated based on an ideal ensemble of 5 nm diameter, ideal-crystalline spherical gold nanoparticles, and 1 Å wavelength of X-rays. The left and right sides of the figure show, respectively, the full (0-60 Å) and short range (1.5-20 Å) portions of the reduced pair distribution function, obtained from the diffraction data itself (G_{obs} shown by black squares) and the best fitting model (G_{fit} shown by red curves) obtained by the refinement process. Blue curves at the bottom of the graphs are residuals, $G_{obs}-G_{fit}$, that quantify the difference between observed data and the fitted model. The

full-range refinement plot demonstrates that, overall, the positions and relative intensities of the reduced pair distribution function were captured correctly. The correct positioning of the fit centers can be confirmed from the short-range refinement plot as well: here the $G_{\text{fit}}(r)$ peaks with major intensities belong to the relative number of interatomic distances with lengths equal to peak center positions. For an ideal FCC gold crystallite with lattice parameter of 4.0626 Å, we can confirm that the first few interatomic distances available are 2.873, 4.063, 5.745 Å etc., which are the first, second, and third nearest interatomic distances in the cell. These are also the positions of the first three $G(r)$ peaks, with the exception of the second peak, which shifted slightly off from its ideal

position, i.e., 4.063 Å. The reason behind the shift here is an overlapping neighboring peak centered around 4.30 Å, which is not an actual $G(r)$ peak but a Fourier truncation peak resulting from the limited q_{max} range of the intensity data (12). Finally, the full-range fit shows that the $G(r)$ functions decay decrease to a noise level between 40 and 50 Å. This is an indication that no atom pair exists with a separation distance larger than these limits. The exact value of this distance is determined by a shape form factor that is implemented in the Diffpy-cmi algorithm (22) and is interpreted as the size of the coherent particle domain. For an ideal crystalline particle, the coherent domain size equals the average diameter of the particle.

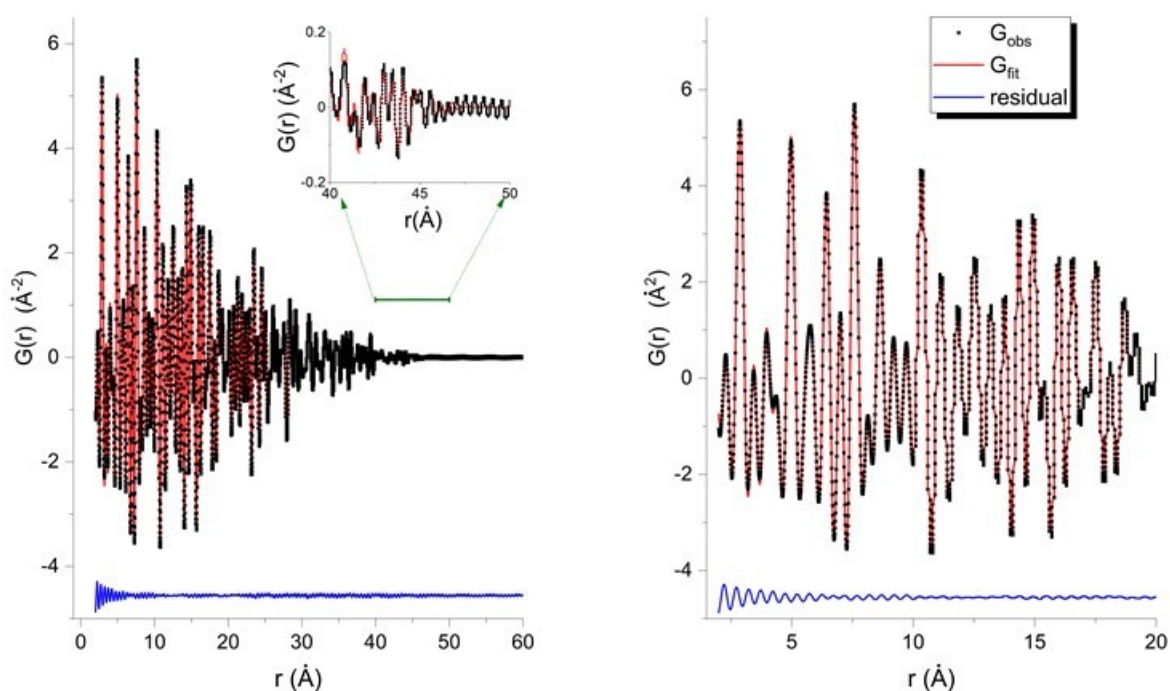


Figure 3: Left: Long range results of successful refinement of the diffraction data from 5 nm diameter ideal gold nanoparticles. The data was generated assuming 1 Å X-ray wavelength. The inset shows the tail of the fit for the real space interval of 40-50 Å. **Right:** Short range portion of the PDF analysis for the real space interval of 1.5-20 Å. The blue curve reports the residual between the observed $G(r)$ function and the fitted model.

Table 1 presents the systematic PDF refinement results performed on the diffraction data of ideal crystalline nanoparticle ensembles with variable particle sizes irradiated at 5 different wavelengths. Here, nominal size is the intended diameter of the nanocrystals making up the ideal powders, λ is the assumed wavelength of the X-rays while computing the diffraction data, a is the refined lattice parameter, D is the refined particle diameter

assuming spherical crystallites, q_{damp} and B_{iso} are the refined damping and isotropic atomic displacement factors of the modeled pair distribution function, respectively, $\Delta r = \frac{2\pi}{q_{\text{max}}}$ is the achievable real-space resolution of the processed diffraction data and finally, q_{min} and q_{max} are the minimum and maximum magnitudes of the momentum transfer vector allowed in the Fourier-Sine transform.

Table 1: PDF refinement results of diffraction data computed from ideal crystalline, spherical gold nanoparticle ensembles evaluated at 5 different wavelengths.

Nominal Size (Å)	λ (Å)	a (Å)	D (Å)	B_{iso} (Å ²)	R_w	Δr (Å)	q_{min} (1/Å)	q_{max} (1/Å)
48.75	0.21	4.06263	48.74	0.002	0.043	0.10	1.56	27.6
97.50	0.21	4.06261	97.64	0.001	0.028	0.10	1.56	27.6
150	0.21	4.06260	150.55	0.001	0.025	0.10	1.56	27.6
195	0.21	4.06260	195.45	0.001	0.019	0.10	1.56	27.6
293	0.21	4.06260	293.97	0.002	0.016	0.10	1.56	27.6
48.75	0.56	4.06260	48.81	0.006	0.053	0.28	1.56	22.4
97.50	0.56	4.06260	97.46	0.002	0.018	0.28	1.56	22.4
150	0.56	4.06260	150.54	0.002	0.017	0.28	1.56	22.4
195	0.56	4.06260	195.30	0.002	0.013	0.28	1.56	22.4
293	0.56	4.06260	293.51	0.002	0.011	0.28	1.56	22.4
48.75	0.71	4.06255	49.07	0.011	0.055	0.35	1.54	17.7
97.50	0.71	4.06258	97.78	0.006	0.044	0.35	1.54	17.7
150	0.71	4.06260	150.88	0.003	0.032	0.35	1.54	17.7
195	0.71	4.06260	195.68	0.002	0.028	0.35	1.54	17.7
293	0.71	4.06260	294.01	0.002	0.023	0.35	1.54	17.7
48.75	1.00	4.06249	48.82	0.013	0.035	0.50	1.64	12.6
97.50	1.00	4.06259	97.76	0.009	0.027	0.50	1.64	12.6
150	1.00	4.06260	150.78	0.002	0.024	0.50	1.64	12.6
195	1.00	4.06260	195.62	0.005	0.019	0.50	1.64	12.6
293	1.00	4.06264	294.07	0.004	0.015	0.50	1.64	12.6
48.75	1.54	4.06264	48.98	0.001	0.050	0.77	1.70	8.2
97.50	1.54	4.06262	97.83	0.001	0.033	0.77	1.70	8.2
150	1.54	4.06261	150.79	0.001	0.027	0.77	1.70	8.2
195	1.54	4.06261	195.67	0.002	0.023	0.77	1.70	8.2
293	1.54	4.06260	294.17	0.002	0.020	0.77	1.70	8.2

As can be seen, the refined lattice parameters agree well with the assumed lattice parameter ($a=4.0626$ Å) during generation of the atomic coordinates of the ideal crystalline spherical gold nanoparticles for all particle sizes considered and at all X-ray wavelengths. They fluctuate only at the fifth decimal, which is in fact outside the accuracy limits of the lattice parameter that can be obtained from our diffraction data due to our angular spacing being set as $d\theta=0.01^\circ$ and also the resolution of the pair distribution function analysis $\Delta r \gg 10^{-5}$ Å. Therefore, we can interpret these small fluctuations as resulting from numerical errors during the refinement process. When we look at the extracted diameters, we again see that they agree with the nominal particle diameters within 1% accuracy. There are two sources of error resulting in these small inaccuracies: the first one is the limited range of the q_{max} that approximates the Fourier Sine integral in Eq. 3 with a finite integration range, and the second one is the nominal particle shapes being far from ideal spheres. As explained in previous sections, ideal crystalline particles were obtained by carving out spheroidal shapes from an ideal 3D face-centered cubic lattice without considering the integrity of individual unit cells within the outer layers of the particle. Hence, these discrete spherical particles are actually spheroids with faceted surfaces (see Figure 1). The diameters of these shapes, therefore, are best expressed as a

distribution of diameters around a mean value rather than an ideal Dirac delta function, and the width of this distribution adds to the inaccuracies in the extracted diameters from the PDF analysis. Nevertheless, the lattice parameters and the average crystallite diameters are obtained quite nicely, and even with limited resolution of reduced pair distribution functions with q_{max} as low as 8.2 \AA^{-1} (12). Such high performances from PDF analysis are impossible to achieve with experimentally-obtained diffraction data from real nanocrystalline samples. Therefore these accuracy limits must be interpreted as the best-case-scenario or equivalently, the minimum errors to be expected from the capabilities of PDF analysis.

When we look at how the PDF-extracted structural parameters compare with their true values at different wavelengths of X-rays, we notice that the most sensitive parameter to the X-ray energy and particle size is the isotropic atomic displacement factor, B_{iso} . This is a correction factor used when analyzing powder diffraction data and quantifies how much of an intensity decay should be expected in the diffraction data of an irradiated powder due to the amplitude of thermal vibrations of its constituent atoms. Because these vibration amplitudes cause lattice points to become finite volumes rather than being dimensionless points in 3D space, an increase in the temperature of an irradiated sample must cause a decreased probability of constructive

interference between atomic planes since their ideal periodicity is eventually lost. This effect has been studied in past literature, and it was concluded that these thermal vibrations of atoms do not cause any broadening in the corresponding Bragg peaks of the diffraction data, but only suppress their intensities, with an uneven and larger influence on higher order reflections (23). Their effect on the reduced pair distribution peaks is a broadening, which is typically modeled by a convolution operation of the $G(r)$ peaks with a Gaussian function if the atomic vibrations are isotropic in all directions (12). Looking at Table 1, it can be seen that extracted B_{iso} values of all nanocrystal sizes vary between 0.001 and 0.013 Å². Although these non-zero atomic displacement parameters indicate the presence of atomic vibrations when there are none, they may result from numerical errors and the finite angular range of the diffraction data causing truncation errors in the Fourier transform since they are obtained from the PDF analysis of diffraction data computed from ideal nanocrystals where all constituent atoms are fixed at their lattice points ($B_{iso} = 0$). Finally, these erroneous B_{iso} values are generally higher for smaller particles than larger ones.

PDF refinement of diffraction data from energy-minimized Gold nanopowders

Table 2 presents our PDF refinement results of diffraction data simulated with energy-minimized versions of gold nanopowders considered previously. The difference here is that the atoms now experience finite displacements from their ideal lattice positions, since at 0 Kelvin temperature, the minimum-energy configurations of nanocrystalline particles do not necessarily correspond with those of an ideal FCC lattice, especially for surface-layer atoms as demonstrated in previous literature (11, 24). The static (time-independent) component of these displacements from the ideal lattice points are treated as microstrains in X-ray literature, and past work (25) showed that these microstrains were of compressive type at the nanoparticle surface, gradually decaying to a displacement-free core region of the nanoparticles, as seen in Figure 1. During PDF refinement, microstrain information was not extracted because there was no long-range atomic order assumed while refining for the modeled $G(r)$ functions. Instead, all atomic displacements are treated as contributions to B_{iso} , irrespective of whether they result from static or dynamic displacements caused by temperature-dependent atomic vibrations³ (20).

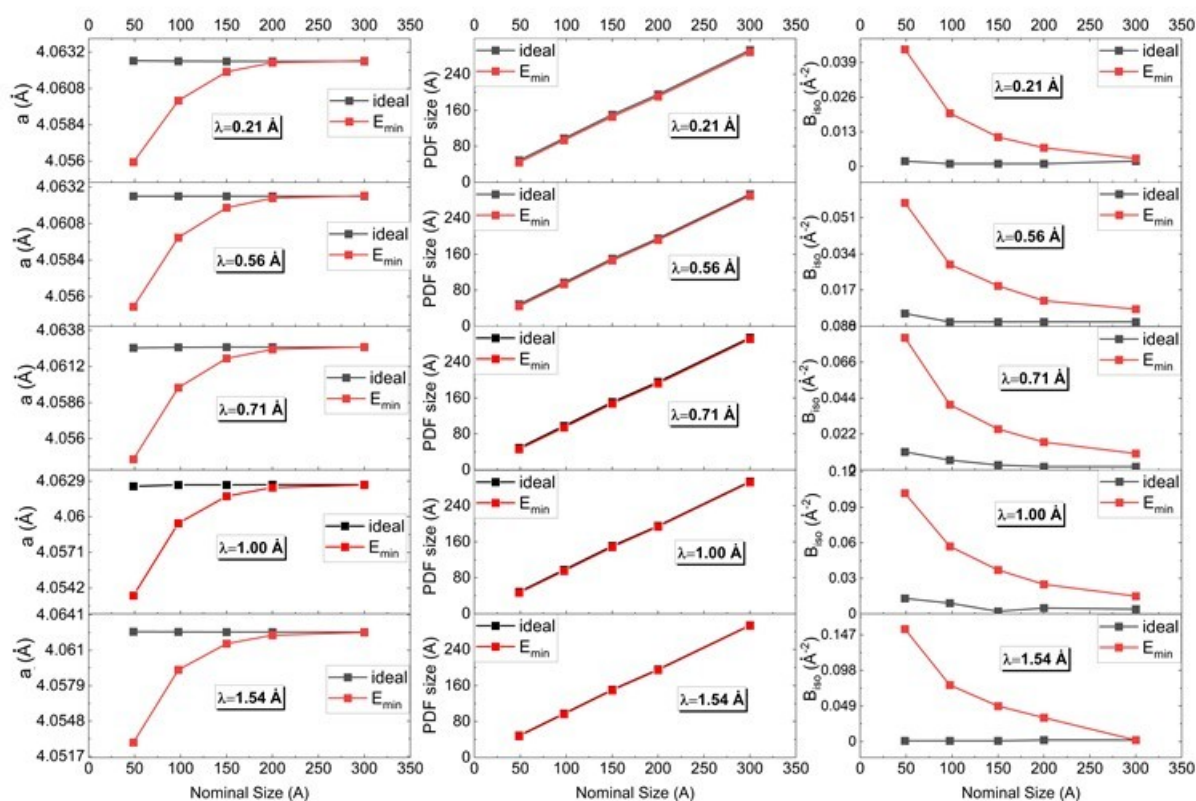
The findings in Table 2 confirm the inward movement of surface atoms as a result of the energy-minimization operation. As seen, for all wavelengths considered, the refined lattice parameters decrease with decreasing particle size. This can be explained by smaller nanocrystals experiencing much higher numbers of atomic displacements since they have a much higher proportion of their atoms on their surface layers compared to larger nanocrystals. These surface atoms are not fully coordinated with neighbor atoms as opposed to core atoms, so they can move more freely than core atoms. Hence, large amounts of inward displacement experienced by surface atoms cause a decrease in the average unit cell dimensions. With decreasing surface atom proportions in larger particles, the effect was less significant. Eventually, the lattice parameters of larger nanocrystals, such as those of 20 and 30 nm nominal diameters, are almost comparable to the initial lattice parameter of the particles, i.e. 4.0626 Å. This effect was confirmed in an earlier study as well (11) and is also visualized on the left side of Figure 3.

When looking at the extracted particle sizes, the indirect effect of the compressive strains on the nanoparticle surfaces can be noted. For all considered wavelengths, the refined diameters of energy-minimized nanoparticles are smaller than their ideal-crystalline counterparts. These differences are maximized for PDF refinement studies performed on the diffraction data computed with the smallest X-ray wavelengths ($\lambda = 0.21$ Å) than larger ones, as shown in the middle portion of Figure 4. The reason behind this wavelength-dependence is that the smallest wavelength enables the largest q_{max} range in the diffraction data and, correspondingly, the highest real-space resolution Δr and the minimum number of Fourier truncation errors. Therefore, the higher sensitivity in real-space enables the visibility of these small size differences. In addition, the reduction in the extracted diameters is bounded by the smallest nanocrystals ($\approx 10\%$) on the upper limit, and the largest nanocrystals on the lower limit ($\approx 2\%$), for all wavelengths studied. This is consistent with the different surface atom proportions of small and large nanocrystals and their resulting effects on the energy-minimization process.

³ As it can be noted, this treatment is inconsistent with the methodology followed in refinement methods based on structural solutions, such as Rietveld refinement, since the latter allows one to distinguish between microstrain and isotropic/anisotropic atomic displacements and extract both.

Table 2: PDF refinement results of diffraction data computed from energy-minimized Crystalline and spherical gold nanoparticle ensembles evaluated at 5 different wavelengths.

Nominal Size (Å)	λ (Å)	a (Å)	D (Å)	B_{iso} (Å ²)	Rw	Δr (Å)	Q_{min} (1/Å)	Q_{max} (1/Å)
48.75	0.21	4.05594	44.20	0.044	0.097	0.10	1.56	27.6
97.50	0.21	4.06000	93.48	0.020	0.047	0.10	1.56	27.6
150	0.21	4.06190	145.91	0.011	0.036	0.10	1.56	27.6
195	0.21	4.06251	191.01	0.011	0.036	0.10	1.56	27.6
293	0.21	4.06264	289.61	0.003	0.017	0.10	1.56	27.6
48.75	0.56	4.05534	44.85	0.058	0.071	0.28	1.56	22.4
97.50	0.56	4.05988	93.72	0.029	0.036	0.28	1.56	22.4
150	0.56	4.06185	146.38	0.019	0.030	0.28	1.56	22.4
195	0.56	4.06248	191.56	0.012	0.020	0.28	1.56	22.4
293	0.56	4.06263	289.86	0.008	0.012	0.28	1.56	22.4
48.75	0.71	4.05452	45.97	0.081	0.067	0.35	1.54	17.7
97.50	0.71	4.05968	94.51	0.040	0.044	0.35	1.54	17.7
150	0.71	4.06179	147.47	0.025	0.038	0.35	1.54	17.7
195	0.71	4.06244	192.69	0.017	0.030	0.35	1.54	17.7
293	0.71	4.06261	291.16	0.010	0.023	0.35	1.54	17.7
48.75	1.00	4.05359	46.82	0.102	0.055	0.50	1.64	12.6
97.50	1.00	4.05947	95.33	0.057	0.034	0.50	1.64	12.6
150	1.00	4.06167	148.44	0.037	0.028	0.50	1.64	12.6
195	1.00	4.06238	193.58	0.025	0.021	0.50	1.64	12.6
293	1.00	4.06259	292.15	0.015	0.016	0.50	1.64	12.6
48.75	1.54	4.05291	47.72	0.155	0.053	0.77	1.70	8.2
97.50	1.54	4.05929	96.39	0.078	0.038	0.77	1.70	8.2
150	1.54	4.06158	149.48	0.049	0.030	0.77	1.70	8.2
195	1.54	4.06232	194.53	0.033	0.024	0.77	1.70	8.2
293	1.54	4.06257	293.08	0.002	0.020	0.77	1.70	8.2

**Figure 4:** **Left:** Lattice parameters extracted from PDF refinement performed on simulated diffraction data of gold nanoparticle ensembles irradiated by five different wavelengths of X-rays. **Middle:** Refined average crystallite diameters from ideal-crystalline and energy-minimized nanoparticles. **Right:** Refined isotropic atomic displacement parameters B_{iso} from ideal-crystalline and energy-minimized nanoparticles.

Finally, when it comes to the extracted B_{iso} values, we notice that there is a significant increase in the refined values for energy-minimized nanoparticles compared with those of ideal nanocrystals. As explained in the beginning of this section, these increases could be the result of both static and dynamic atomic displacements if the refined diffraction data were experimentally obtained (12). In our case, however, we simulated the diffraction data based on the minimum-energy configurations of our nanocrystalline particles, where the energy-minimization algorithm ignored the zero-point vibrational movement of atoms (15, 23). As a result, the isotropic atomic displacement values extracted could only come from static displacements of atoms. Considering that the largest B_{iso} values obtained from the ideal-crystalline particle ensembles are around 0.013 \AA^2 , the B_{iso} values of energy-minimized nanoparticles that are in excess of 0.013 \AA^2 could be interpreted as contributed from static displacements of atoms. These static displacements of atoms are maximized for the smallest nanoparticles and minimized for the largest ones (see the right column of Figure 4), in accordance with changes in the remaining structural parameters.

Evaluation of Refined Structural Parameters Against Real-Space Structural Parameters

In order to evaluate the accuracy of our refinement results, we also computed the average structural parameters of our nanoparticle ensembles based on individual atomic coordinates. These atomistic calculations were performed by classifying all atoms according to their coordination numbers. This was done by counting the first nearest neighbors of all atoms within spheres of 3.2 \AA , radii centered at the positions of atoms. Those with a coordination number of 12 were considered core atoms, and the remaining ones were considered as surface layer atoms. Given the discrete atomic coordinates of a nanoparticle, the diameter distribution was calculated by surface atom coordinates. One diameter was calculated for each pair of surface atoms, provided that the line connecting these atoms crossed the center of the particle. This resulted in 525, 2205, 5359, 9105, and 20673 total numbers of diameters for 5, 10, 15, 20, and 30 nm particles, respectively. The minimum (D_{min}), maximum (D_{max}), average (D_{ave}), and standard deviation of these diameters for each particle are presented in Table 3. The last row reports the B_{iso} value for bulk gold, which was obtained by MD simulations using periodic boundary conditions in 3 dimensions and ignoring small size and surface effects formerly present in nanocrystalline gold particles.

Table 3: Structural parameters (average values and standard deviations) obtained from calculations based on atomic coordinates of energy-minimized gold nanoparticles. N_{surf}/N reports the ratio of the surface atoms' number to the total number of atoms in a single nanoparticle.

Nominal Size (Å)	$\frac{N_{surf}}{N}$	No. unit cell	a_{ave} (Å)	a_{std} (Å)	D_{min} (Å)	D_{max} (Å)	D_{ave} (Å)	D_{std} (Å)	B_{iso} (Å ²)
48.75	0.29	2539	4.0542	0.0256	43.43	48.23	45.89	1.4	0.026
97.50	0.15	24487	4.0588	0.0185	91.96	96.93	94.70	1.3	0.025
150	0.10	95396	4.0608	0.0145	144.82	149.87	147.59	1.4	0.022
195	0.078	213267	4.0618	0.0119	189.42	194.53	192.24	1.4	0.023
293	0.053	739799	4.0624	0.0087	286.95	292.05	289.73	1.4	N/A
Bulk	$\approx \infty$	$\approx \infty$	4.0626	≈ 0	N/A	N/A	N/A	N/A	0.019

The average lattice parameters of unit cells making up the energy-minimized nanoparticles were calculated by finite-strain theory. Here, all nanoparticles were decomposed into repeating unit cells, where a unit cell was constructed of one basis atom plus its 12 first-nearest neighbors. Under-coordinated surface atoms with a coordination number of less than 12 were eliminated from the calculation. To relate the average lattice parameters of the energy-minimized nanoparticles a_{ave} to that of the ideal crystalline nanoparticles a_0 , we used $\epsilon_{ave} = \frac{a_{ave} - a_0}{a_0}$, where $a_0 = 4.0626 \text{ \AA}$ and ϵ_{ave} is the average lattice strain (25). Next, ϵ_{ave} was calculated. After that, F was obtained and E was computed, and the three eigenvectors of the symmetric tensor E specified the relative variation $\Delta a/a_0$ of the lattice

by the following procedure: first, for each unit cell, a 3-by-3 deformation gradient F was computed by finding coordinate vectors connecting the basis atom to its first-nearest neighbor atoms in the reference structure, x_i , which were the ideal crystal coordinates in our case and in the deformed or energy-minimized structure, x_i' , with $i=1,2,\dots,12$. Then F was determined by a least-squares fit following the method from the literature (26, 27):

$$F X_i \approx x_i' \quad \forall i=1 \dots 12 \quad (\text{Eq.7})$$

$$E = \frac{1}{2} (F^T F - I) \quad (\text{Eq.8})$$

parameter in the principal directions of deformation. The mean strain ϵ_{ave} of all unit cells in the particle was then multiplied by a_0 to evaluate the average

lattice parameter a_{ave} of the energy-minimized nanoparticle. Table 3 presents the total number of unit cells considered for a given nanoparticle (column 3) along with the corresponding average lattice parameters and their standard deviations (4th and 5th columns, respectively). Finally, mean square displacements (MSD) of particles were calculated with LAMMPS without applying periodic boundary conditions to take into account the free surfaces of nanoparticles. Before each calculation, all particles were subjected to: **1)** heating up to 600 K within 50 ps; **2)** equilibration at 600 K for 50 ps; **3)** cooling back to 10K within 50 ps; and **4)** equilibration at 10 K for 100 ps in an NVT ensemble. MSD calculations were simulated at 10 K because molecular dynamics algorithms do not allow simulations at 0K. In the case of bulk gold, NPT ensemble was used instead of NVT to eliminate surface effects. After the equilibration step, a 1000 ps production run for MSD calculation was performed. We note that equilibration time significantly affects MSD. If the system is not equilibrated well, MSD is overestimated and contains high, time-dependent fluctuations. Thus, we increased the equilibration time at 10 K from 100 to 1000 and 2000 ps for 15 and 20 nm particles, respectively. However, we were not able to complete a full calculation for 30 nm particles in a reasonable time, so the corresponding B_{iso} for 30 nm particles was excluded from Table 3. Lastly, the isotropic atomic displacement parameter B_{iso} was calculated by $B_{iso} = 8\pi^2 MSD$. These are presented in the last column of Table 3.

As shown, an increase in the nominal size of the nanoparticles results in a dramatic decrease in the $\frac{N_{surf}}{N}$ ratio, which directly influences the average

lattice parameters obtained for the particles since the relative mobility of surface atoms compared to bulk atoms in a nanoparticle is significantly higher. Higher mobility of surface atoms, then, results in larger decreases in the average lattice parameters from 4.0626 Å. One may notice that the changes in a_{ave} are not as dramatic as those of $\frac{N_{surf}}{N}$ ratios;

the reason for that lies in our computation method of a_{ave} . As described, we only considered atoms that had full coordination, i.e. had exactly 12 nearest-neighbors, to construct a unit cell. Therefore, the most mobile surface atoms are not considered in our average unit cell calculations, which disregard the largest inward movements of the outermost-surface atoms. Secondly, the average diameters obtained from the particles correlate well with the nominal sizes. Compared with the D_{ave} values of ideal crystalline nanoparticles, which are 46.10, 94.90, 147.70, 192.30, and 289.80 \pm 1.5 Å, respectively, the D_{ave} of energy-minimized particles are smaller, but the difference is within the standard deviation of the diameter distributions (D_{std}). Hence, real space calculations do not indicate appreciable

size changes due to energy-minimization, at least not with the calculation method described here. Finally, looking at B_{iso} values, we immediately see their inverse relationship with the nominal sizes of the nanoparticles. This is expected and can be explained with similar arguments as the lattice parameter changes. Higher surface atom ratios enable much larger atomic movements, and these immediately increase the MSD values. At the ultimate limit of a bulk structure, B_{iso} converges to 0.019 Å², which is the minimum of all others.

Next, we compared the values in Table 3 with the PDF refinement results of energy-minimized particles in Table 2. However, this is not trivial since we have 5 sets of refined parameters for each X-ray wavelength and large changes in parameter values are observed at different wavelengths. Consistent with past literature (12), we select the refinement results for 0.21 Å, as reference value of PDF refinement since it yields the highest real-space resolution and minimum Fourier truncation errors. Comparing Table 3 with Table 2, we observe that the lattice parameters computed atomistically are slightly lower than those from PDF refinement, although the differences are at the third decimal and are within the standard deviations reported in Table 3. Considering that the atomistic simulations do neglect under-coordinated atoms, the observed agreement is surprisingly good. When we switch to refined diameters, we realize that they correlate well with the average diameters calculated within their standard deviations. Among the three structural parameters, refined B_{iso} values are the most divergent from their atomistically-computed counterparts. Although their magnitude orders are similar, the dramatic size dependence of the refined B_{iso} values is not confirmed by atomistic calculations. One reason for explaining the disagreement is the Gaussian model of atomic displacements assumed by the PDF refinement algorithm. As confirmed indirectly by the changes in the lattice parameters and average diameters, the atoms within energy-minimized nanoparticles do not experience random displacements as implied by Gaussian models. Atomic displacements are uneven at different atomic layers of the particles, and their directions are mostly inward. Hence, the incompatibility between assumed models of atomic movements contributes to the divergences in the extracted B_{iso} values. Secondly, our Fourier truncation errors are expected to cause large errors in the refined atomic displacement values from PDF, as shown in previously (12), since even with the smallest X-ray wavelength, our q_{max} value is still less than the suggested 30 Å⁻¹ limit. Thirdly, the B_{iso} values from the refinement of energy-minimized nanoparticles must be cleared from the minimum error limits for a fair comparison, even though Table 1 shows that their contribution is within 0.002 Å² for all sizes at $\lambda=0.21$ Å. Lastly, the refined B_{iso} values from PDF analysis are actually from the static

displacements of atoms, whereas our LAMMPS calculations consider hundreds of nanoparticle ensembles where only the dynamic atomic displacements are reported in the MSD calculations. This shows that even with error-free diffraction data, extracting atomic displacement parameters based on PDF analysis of X-ray diffraction data is a challenging task that requires carefully-planned data generation/collection strategies as well as compatible parameter definitions. Overall, the agreement between atomistic calculations and PDF-refined structural parameters of spherical gold nanoparticles is satisfactory.

CONCLUSIONS

In this study, we used atomistic calculations to generate and analyze ideal diffraction data from powders of spherical gold nanoparticles to evaluate the accuracy limits of Pair Distribution Function analysis in extracting the lattice parameter, average particle size, and atomic displacement values. Our results show that the minimum uncertainties in the extracted structural parameters from the diffraction data of ideal-crystalline nanoparticles are within $\pm 5 \times 10^{-5} \text{ \AA}$ the average lattice parameter, which is the most stable structural parameter irrespective of the X-ray wavelength selected. The diameters obtained from PDF analysis are closer to the maximum values of the diameter distributions of ideal crystalline particles since PDF analysis relies on analytical models to obtain average crystal sizes from the approximate position of where the $G(r)$ curve decays down to noise level. Still, the extracted sizes are within 1% of the nominal sizes. A high q_{max} value is desired for the highest resolution of crystallite size. Finally, B_{iso} values are bound within 0.013 \AA^2 for the systems we studied, with higher uncertainties present for the smallest nanocrystals and lower ones for the largest nanocrystals. The size dependencies on B_{iso} uncertainties are consistent with the experimental observations of surface atom mobility and its effects on nanoparticles with small crystallite sizes.

PDF analyses of energy-minimized nanoparticles revealed consistent trends with similar analyses performed with crystallographic solution algorithms (11). Decreasing lattice parameters with decreasing nominal particle size is confirmed with all selected X-ray wavelengths, although the amount of decrease depends on the q_{max} range of the diffraction data. However, the inward movement of surface atoms resulting from the energy-minimization process was not captured by the PDF method when q_{max} was less than 15 \AA^{-1} . This again confirms that PDF-based crystallite sizes are very sensitive to the wavelength selected. A significant increase in B_{iso} was observed as a result of the energy minimization for all particle sizes and for all X-ray wavelengths. The amount of enhancement was the most prominent for the smallest

nanoparticles since they have the largest ratio of surface atoms.

Atomistic calculations of structural parameters from energy-minimized nanoparticles agree fairly well with those obtained by PDF analysis. The lattice parameters and average particle sizes agree within their standard deviations. However, we were not able to directly correlate the refined B_{iso} values with those from real-space calculations. Possible reasons were identified as incompatible definitions of mean square displacements of atoms in the two methods compared, and large Fourier truncation errors resulting from limited q_{max} range. These could be significant when q_{max} is less than 30 \AA^{-1} , as reported previously (12).

To conclude, our results show that PDF analysis can be a strong tool for researchers who want to study the structural properties of nanocrystalline powders. The uncertainties in the refined parameters are quite low, even with less-than-ideal diffraction data and modest q_{max} values. Moreover, one can follow our proposed methodology to estimate the analysis errors for specific cases since our method is generalizable and uses open-source programs and optimized computation routines. However, we highlight that the estimated errors obtained from the proposed methodology would only yield the minimum expected uncertainties of structural parameters; when working with measured XRD data that contains undesirable scattering components such as photon counting and sampling statistics, size and/or lattice parameter distributions in the sample, background scattering, etc. the uncertainty to be expected must increase. Therefore, the accurate interpretation of X-ray diffraction data from nanocrystalline powders requires great care and meticulous analysis of different sources of error and their bounds.

CONFLICT OF INTEREST

The authors declare no conflicts of interest.

ACKNOWLEDGMENTS

We would like to thank Dr. İlknur Eruçar and Dr. Shangmin Xiong for helpful discussions and guidance on running molecular dynamics simulations of metallic nanocrystalline particles. This research used the resources of Özyeğin University High Performance Computing Center and was funded by the Scientific and Technological Research Council of Turkey (TÜBİTAK) under the BİDEB 2232 International Fellowship of Outstanding Researchers Program (Project no:118C268).

REFERENCES

1. Prasad N, Karthikeyan B. Tunable bandgap and blue emission of ZnS nanoparticles induced by controlled S

- vacancies. *Journal of Applied Physics*. 2019 Feb 28;125(8):085702. [<DOI>](#).
2. Tran N, Zhao W, Carlson F, Davidson JH, Stein A. Metal Nanoparticle–Carbon Matrix Composites with Tunable Melting Temperature as Phase-Change Materials for Thermal Energy Storage. *ACS Appl Nano Mater*. 2018 Apr 27;1(4):1894–903. [<DOI>](#).
3. Ingham B. X-ray scattering characterisation of nanoparticles. *Crystallography Reviews*. 2015 Oct 2;21(4):229–303. [<DOI>](#).
4. Kang S-JL, Park J-H, Ko S-Y, Lee H-Y. Solid-State Conversion of Single Crystals: The Principle and the State-of-the-Art. Green DJ, editor. *J Am Ceram Soc*. 2015 Feb;98(2):347–60. [<DOI>](#).
5. Neder RB, Proffen T. Exact and fast calculation of the X-ray pair distribution function. *J Appl Crystallogr*. 2020 Jun 1;53(3):710–21. [<DOI>](#).
6. Rietveld HM. A profile refinement method for nuclear and magnetic structures. *J Appl Crystallogr*. 1969 Jun 2;2(2):65–71. [<DOI>](#).
7. Juhás P, Farrow CL, Yang X, Knox KR, Billinge SJL. Complex modeling: a strategy and software program for combining multiple information sources to solve ill posed structure and nanostructure inverse problems. *Acta Crystallogr A Found Adv*. 2015 Nov 1;71(6):562–8. [<DOI>](#).
8. Petkov V, Bedford N, Knecht MR, Weir MG, Crooks RM, Tang W, et al. Periodicity and Atomic Ordering in Nanosized Particles of Crystals. *J Phys Chem C*. 2008 Jun 1;112(24):8907–11. [<DOI>](#).
9. Popa NC, Balzar D. Size-broadening anisotropy in whole powder pattern fitting. Application to zinc oxide and interpretation of the apparent crystallites in terms of physical models. *J Appl Crystallogr*. 2008 Jun 1;41(3):615–27. [<DOI>](#).
10. Bugaev AL, Guda AA, Lomachenko KA, Shapovalov VV, Lazzarini A, Vitillo JG, et al. Core–Shell Structure of Palladium Hydride Nanoparticles Revealed by Combined X-ray Absorption Spectroscopy and X-ray Diffraction. *J Phys Chem C*. 2017 Aug 24;121(33):18202–13. [<DOI>](#).
11. Xiong S, Öztürk H, Lee S-Y, Mooney PM, Noyan IC. The nanodiffraction problem. *J Appl Crystallogr*. 2018 Aug 1;51(4):1102–15. [<DOI>](#).
12. Toby BH, Egami T. Accuracy of pair distribution function analysis applied to crystalline and non-crystalline materials. *Acta Crystallogr A Found Crystallogr*. 1992 May 1;48(3):336–46. [<DOI>](#).
13. Farrow CL, Billinge SJL. Relationship between the atomic pair distribution function and small-angle scattering: implications for modeling of nanoparticles. *Acta Crystallogr A Found Crystallogr*. 2009 May 1;65(3):232–9. [<DOI>](#).
14. Plimpton S. Fast Parallel Algorithms for Short-Range Molecular Dynamics. *Journal of Computational Physics*. 1995 Mar;117(1):1–19. [<DOI>](#).
15. Sheng HW, Kramer MJ, Cadien A, Fujita T, Chen MW. Highly optimized embedded-atom-method potentials for fourteen fcc metals. *Phys Rev B*. 2011 Apr 20;83(13):134118. [<DOI>](#).
16. Öztürk H, Yan H, Hill JP, Noyan IC. Sampling statistics of diffraction from nanoparticle powder aggregates. *J Appl Crystallogr*. 2014 Jun 1;47(3):1016–25. [<DOI>](#).
17. Debye P. *Zerstreuung von Röntgenstrahlen*. *Ann Phys*. 1915;351(6):809–23. [<DOI>](#).
18. Warren BE. *X-ray diffraction*. Dover ed. New York: Dover Publications; 1990. 381 p. ISBN: 978-0-486-66317-3.
19. Juhás P, Davis T, Farrow CL, Billinge SJL. *PDFgetX3*: a rapid and highly automatable program for processing powder diffraction data into total scattering pair distribution functions. *J Appl Crystallogr*. 2013 Apr 1;46(2):560–6. [<DOI>](#).
20. Trueblood KN, Bürgi HB, Burzlaff H, Dunitz JD, Gramaccioli CM, Schulz HH, et al. Atomic Displacement Parameter Nomenclature. Report of a Subcommittee on Atomic Displacement Parameter Nomenclature. *Acta Crystallogr A Found Crystallogr*. 1996 Sep 1;52(5):770–81. [<DOI>](#).
21. Dippel A-C, Roelsgaard M, Boettger U, Schneller T, Gutowski O, Ruett U. Local atomic structure of thin and ultrathin films *via* rapid high-energy X-ray total scattering at grazing incidence. *IUCrJ*. 2019 Mar 1;6(2):290–8. [<DOI>](#).
22. Gilbert B. Finite size effects on the real-space pair distribution function of nanoparticles. *J Appl Crystallogr*. 2008 Jun 1;41(3):554–62. [<DOI>](#).
23. Guinier A. *X-Ray Diffraction: In Crystals, Imperfect Crystals, and Amorphous Bodies*. Dover Publications, Mineola, NY, USA; 2013. ISBN: 978-0-486-68011-8.
24. Huang WJ, Sun R, Tao J, Menard LD, Nuzzo RG, Zuo JM. Coordination-dependent surface atomic contraction in nanocrystals revealed by coherent diffraction. *Nature Mater*. 2008 Apr;7(4):308–13. [<DOI>](#).
25. Xiong S, Lee S-Y, Noyan IC. Average and local strain fields in nanocrystals. *J Appl Crystallogr*. 2019 Apr 1;52(2):262–73. [<DOI>](#).
26. Li group. Least-Square Atomic Strain [Internet]. 2005. [<URL>](#).
27. Stukowski A, Markmann J, Weissmüller J, Albe K. Atomistic origin of microstrain broadening in diffraction data of nanocrystalline solids. *Acta Materialia*. 2009 Mar;57(5):1648–54. ISBN: 978-0-486-68011-8.

Accuracy Limits of Pair Distribution Function Analysis in Structural Characterization of Nanocrystalline Powders by X-ray Diffraction

Abolfazl Baloochiyan¹, Merdan Batyrow¹, Hande Öztürk^{1*}

¹Özyeğin University, Department of Mechanical Engineering, İstanbul, 34794, Turkey

SUPPORTING INFORMATION

Additional details of our Molecular Dynamics (MD) simulations are provided in this section.

Force-field selection:

For MD simulations, interatomic forces were modeled with optimized embedded atom method (EAM) developed by Sheng et al. (2011) [15] and available online to be used with LAMMPS [14]. The force-field was highly optimized to match the experimental database and has been shown to have validity in the modeling of gold nanoparticles by Xiong et al. (2018) [11].

MD steps and results:

Before starting the MD simulations with LAMMPS, five separate spherical gold nanocrystal models with diameters of 5, 10, 15, 20, and 30 nm were generated from an FCC lattice with 4.0626 Å lattice parameter. This corresponded to the bulk lattice parameter of gold at 0 K calculated with the selected force-field. Generated nanocrystals were each placed in the center of a simulation box. The volume of the simulation box and the number of atoms in each nanocrystal are given in **Table S1**. An example of a 10 nm nanocrystal inside a simulation box is shown in **Figure S1**. Afterwards, MD simulations were performed with non-periodic boundary conditions applied in all directions since we were studying colloidal, free-standing gold nanocrystals. We followed six steps in the simulations, as shown in **Table S2**. They are as follows:

1) The energy minimization was performed with the force and energy change ratio criteria of 10^{-6} eV Å⁻¹ and 10^{-6} , respectively, for convergence within a maximum of 80 ps. Final atomic configuration obtained from this step was assumed to be energy-minimized at 0 K and was used in subsequent Pair Distribution Function analyses. The steps below were used for MSD (Mean Square Displacement) calculations.

2-4) Following energy minimization, an annealing simulation cycle was performed between 10-600 K in NVT ensemble by raising the temperature of the system and cooling it back. This step is important since it allows atoms to overcome their energy barriers and avoid local minimum energy configurations [25]. Total simulation length of this step was 150 ps.

5) Then, the system was equilibrated at 10 K temperature before MSD calculation. This step makes sure that system is energetically equilibrated at given conditions and results in reliable data out of MD. With respect to time, the temperature and energy change of the system, during annealing and equilibration, are shown in **Figures S2A** and **S2B**. Total simulation length of this step was 100 ps.

6) Finally, a production run was performed to calculate the MSD of the systems during the 1000 ps simulation as shown in **Figure S2C**.

Table S1 : The number of atoms and the volume of the simulation boxes used in MD runs of each nanocrystal

Size (nm)	Number of atoms	MD box volume (nm ³)
5	3589	324.81
10	28897	1622.23
15	106114	4947.76
20	231477	9938.38
30	781145	30371.33

Table S2 : MD steps with simulation parameters.

Step	Ensemble	Temperature (K)	Simulation time (ps)	Timestep (ps)	Note
1	-	0	80*	0.001	Energy minimization
2	NVT**	2 - 600	50		Annealing simulation
3		600	50		
4		600 - 10	50		
5		10	100		
6		10	1000		
					Production run - MSD calculation

* Specified time is the maximum allowed simulation time in case the given energy and force convergence criteria are not satisfied .

** In case of bulk system NPT ensemble is used.

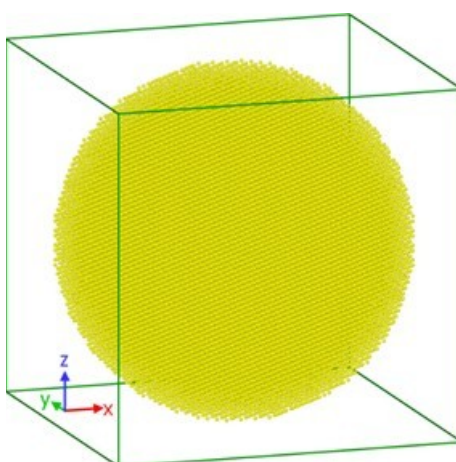


Figure S1: 10 nm diameter spherical gold nanocrystal model is shown inside its simulation box.

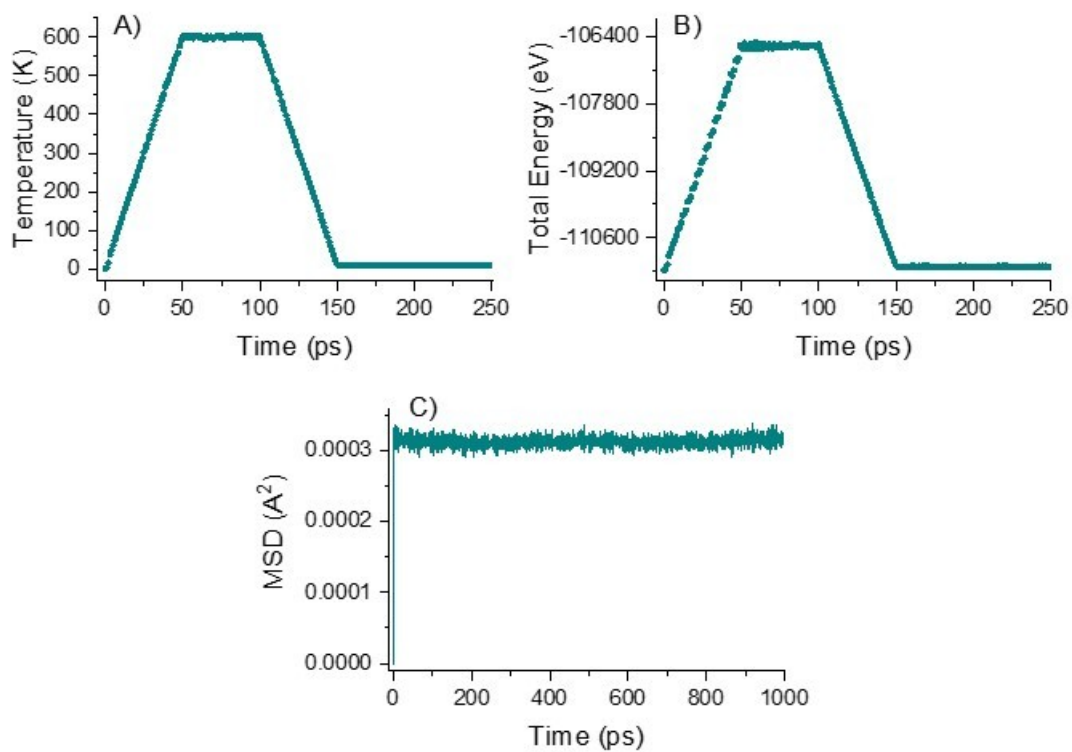


Figure S2: **A)** Temperature vs. time, **B)** Total energy vs. time, and **C)** MSD vs. time for 10 nm gold nanocrystal model.



Novel Functional Axially Substituted Silicon(IV) Phthalocyanine Derivative and its Photochemical Properties

Hülya YANIK* , Gülçin EKİNEKER 

University of Kocaeli, Department of Center for Stem Cell and Gene Therapies Research and Practice, 41001, Kocaeli, Turkey.

Abstract: Photodynamic therapy is a highly specific and clinically approved method in which the patient is administered a non-toxic photosensitizer to treat cancer. Phthalocyanines with their long-wavelength absorption and fluorescence from 650 to 800 nm can be used as photosensitizers for photodynamic therapy, and are used in clinical studies. Our work aims to synthesize functionally new di-axially *N*-Boc-ethanolamine substituted silicon(IV) phthalocyanine (**PS-2**). Structural characterization of this novel **PS-2** via FT-IR, mass, ¹H NMR, and UV-Vis spectroscopy was performed. Photochemical properties (photodegradation quantum yields (Φ_d) and singlet oxygen quantum yield (Φ_Δ) of **PS-2**, which are the first steps in cancer treatment, were investigated.

Keywords: Photodynamic therapy, Singlet Oxygen Quantum Yield, Silicon(IV) Phthalocyanine.

Submitted: September 15, 2021. **Accepted:** March 18, 2022.

Cite this: Yanık H, Ekineker G. Novel Functional Axially Substituted Silicon(IV) Phthalocyanine Derivative and its Photochemical Properties. JOTCSA. 2022;9(2):545-52.

DOI: <https://doi.org/10.18596/jotcsa.995902>.

***Corresponding author.** E-mail: h.yanik.82@gmail.com

INTRODUCTION

Cancer is defined as a complex disease that is influenced by genetic and environmental conditions caused by the uncontrolled growth and division of cells. Today, it is a very common disease and causes most deaths worldwide. According to the reports of the World Health Organization (WHO), approximately 10 million deaths occurred in 2020 was due to this disease (1).

Common cancer treatment methods include chemotherapy, radiation therapy, and surgery. It is known that these methods used have serious side effects such as diarrhea, dermatological, swallowing difficulties, alopecia, gastrointestinal problems, vomiting, and destruction of the immune system (2). Therefore, there is a need for alternative treatment approaches with fewer side effects and new molecules that can be used in these approaches. Photodynamic Therapy (PDT) is an alternative approach to this traditional method of treatment. PDT occurs as a result of the

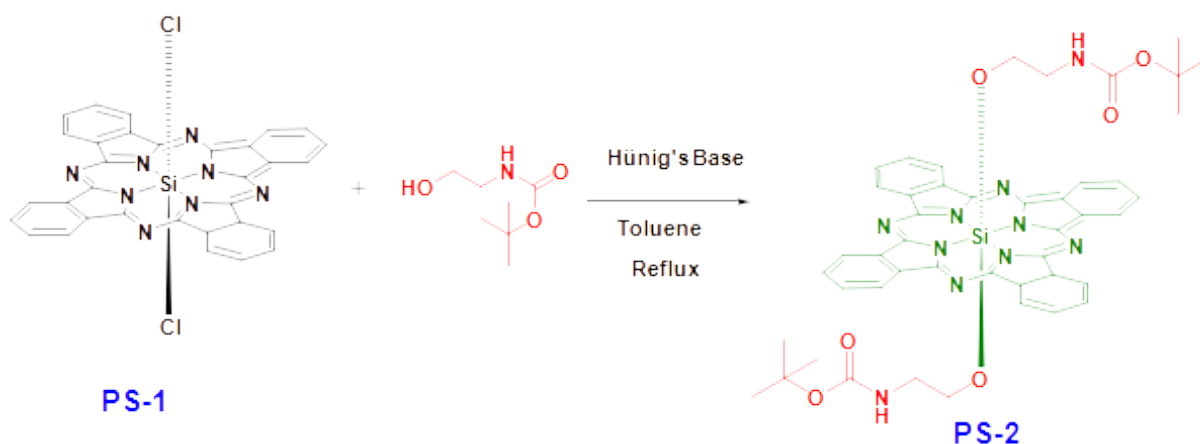
photochemical interaction of light and PDT agents. Photodynamic therapy works with light, oxygen and a light-sensitive substance called a photosensitizer (PS). When the photosensitizer molecule is stimulated with the light of the appropriate wavelength, the molecular oxygen in the environment turns into an active oxygen type called singlet oxygen and it kills the cell in which the photosensitizer is located (3). Photosensitizer (PS) can be applied intravenously or after surgery (4, 5) in photodynamic therapy treatment.

Photosensitizers used in PDT should be able to produce high singlet oxygen, have fluorescence ability, and have strong absorption at a high wavelength. Due to the ability of synthetic modifications, phthalocyanines can have a high absorption wavelength (670-700 nm) and a high molar absorption coefficient. Since phthalocyanine structure is very similar to hemoglobin and chlorine, they have the feature of being used in biological applications (6, 7). When the previous studies were

examined, it was seen that phthalocyanines had very effective photosensitizing properties (8).

The largest disadvantage of phthalocyanines is the low solubility in organic solvents, and aggregation due to their planar ring association. To overcome this disadvantage, phthalocyanines must be axially, peripherally, or non-peripherally substituted with various ligands which can affect their photophysical and photochemical properties (9-14).

In this study, we focused on silicon(IV) phthalocyanine because of its gain to non-aggregation ability *via* axial substitution. For this purpose, *N*-Boc ethanolamine was used as an axial ligand on silicon(IV) phthalocyanine, thereby obtaining a novel functional silicon(IV) phthalocyanine photosensitizer. Novel di-axially *N*-Boc ethanolamine substituted silicon(IV) phthalocyanine (**PS-2**) was synthesized and characterized. Photochemical properties were examined to investigate its applicability in photodynamic therapy.



Scheme 1: Synthetic route of **PS-2**.

Synthesis of Silicon(IV) Phthalocyanine (**PS-2**)

Hünig's base (1 mL), dry toluene (4 mL), and an excess of *N*-Boc ethanolamine (0.2 g, 0.04 mol) were added with dichlorosilicon(IV)phthalocyanine (**PS-1**). The reaction temperature was heated to 115 °C for 18 hours and then brought to room temperature (Scheme 1). The reaction mixture was poured into water, then filtered. The precipitate was washed with water and ethanol and then the solid material was dried in vacuo. The blue solid was purified by thin-layer chromatography (TLC) using silica gel and a dichloromethane/ethanol (25: 1) solvent system as the eluent. Yield: 22% (28 mg). C₄₆H₄₆N₁₀O₆Si, MW: 863.02. m.p. >250 °C. FT-IR ν_{max} /cm⁻¹: 3326, 2957, 2921, 2853, 1739, 1458, 1378, 1179, 1090, 1048, 882, 832, 722, 702. MALDI-TOFF-MS *m/z*: Calc. for C₄₆H₄₆N₁₀O₆Si 863.02, found: 1111.94 [M+DIT+Na]⁺. ¹H NMR (CDCl₃) δ (ppm): 9.64 (s, 8H, Ar-H), 8.36 (s, 8H, Ar-H), 6.88 (t, 2H, NH), 4.16 (t, 4H, O-CH₂), 3.69

N-Boc-ethanolamine 98% and *N,N*-diisopropylethylamine (Hünig's base), solvents, and chemicals were purchased from Aldrich and used as received. 1,3-Diiminoisoindoline and dichlorosilicon(IV) phthalocyanine were synthesized as described in the literature (15). All solvents were purified as described by Perrin and Armarego (16). The FT-IR spectrum was taken from between 4000 and 650 cm⁻¹ with a Perkin-Elmer Spectrum 100 FT-IR spectrometer. The mass spectrum was recorded with MALDI (matrix-assisted laser desorption ionization) using BRUKER Micro-ex LT using 1,8,9-anthracenetriol, dithranol (DIT) as a matrix. The ¹H-NMR spectrum was recorded in CDCl₃ solutions on a Varian 400 MHz spectrometer. The electronic absorption spectra were taken with a Thermo Scientific 2001 UV spectrophotometer in the UV-Vis range at room temperature.

(t, 4H, -NH-CH₂), 1.45 (s, 18H, -CH₃). UV-Vis (DMSO): λ_{max} , nm (log ϵ): 676 (5.47), 607 (4.73), 355 (5.01).

Investigation of Photochemical Properties

Photochemical quantum yield properties (photodegradation and singlet oxygen) of **PS-2** were examined with a photochemical measuring system. A 300 W quartz lamp, a water filter, and a 600 nm filter for ultraviolet and infrared radiation were used for photo-chemical property measurements. Filters that have the appropriate wavelength (670 nm) for the wavelength of photosensitizer were also used for the same purpose. The light intensities were calculated with a POWER MAX5100 power meter (Mole electron detector built-in).

The singlet oxygen quantum yield (Φ_{Δ}) was calculated as described in the literature (17). 1,3-

Diphenylisobenzofuran (DPBF) was used as a singlet oxygen specific trap (converts endoperoxide derivatives with singlet oxygen) and the solution concentration was lowered by 3×10^{-5} M to avoid chain reactions induced by DPBF in the presence of singlet oxygen (18). The ratio of photosensitizer and DPBF solution was prepared 2:1 in the dark. The UV-Vis spectra were taken to analyze the change in absorbance of the DPBF compound at 417 nm. Singlet oxygen quantum yield (Φ_{Δ}) was calculated using Eq. 1 .

$$\Phi_{\Delta} = \Phi_{\Delta}^{std} \frac{R \cdot I_{abs}^{std}}{R^{std} \cdot I_{abs}} \quad (\text{Eq. 1})$$

The photodegradation quantum yield (Φ_d) was determined as described in the literature (17). To determine the photodegradation quantum yield, the same photochemical measurement setup was used that was used for the singlet oxygen quantum yield. To that end, photosensitizer compound (**PS-2**) was dissolved in DMSO. Then **PS-2** was exposed to appropriate light at specific intervals, and then these UV-Vis spectra were recorded to determine the change in the Q band of **PS-2** to determine. The quantum yield of photodegradation (Φ_d) was calculated using Eq. 2.

$$\Phi_d = \frac{(C - C_0) V \cdot N_A}{I_{abs} St} \quad (2)$$

RESULTS AND DISCUSSION

Synthesis

The synthesis step for axially *N*-Boc ethanolamine substituted silicon(IV) phthalocyanine (**PS-2**) was shown in Scheme 1. The reaction conditions were studied for the axial substitution and used Hünig's base (N, N-diisopropylethylamine) in this study. For the synthesis of di-axially *N*-Boc ethanolamine substituted silicon(IV) phthalocyanine (**PS-2**), dichlorosilicon(IV) phthalocyanine, toluene as solvent, Hünig's base, and an excess of *N*-Boc-ethanolamine were used. **PS-2** was characterized by various spectroscopic techniques such as ^1H NMR, MALDI-TOF(+) mass, UV-Vis, FT-IR.

In the FT-IR spectrum of **PS-2**, an -NH stretching was monitored at 3326 cm^{-1} , C-O stretching was monitored at 1048 cm^{-1} and aliphatic C-H stretches were monitored at 2921 cm^{-1} and 2853 cm^{-1} , respectively (Figure 1). The molecular ion peak was monitored at $1111.94 \text{ [M+Na+DIT]}^+$ in the mass spectrum of **PS-2** (Figure 2).

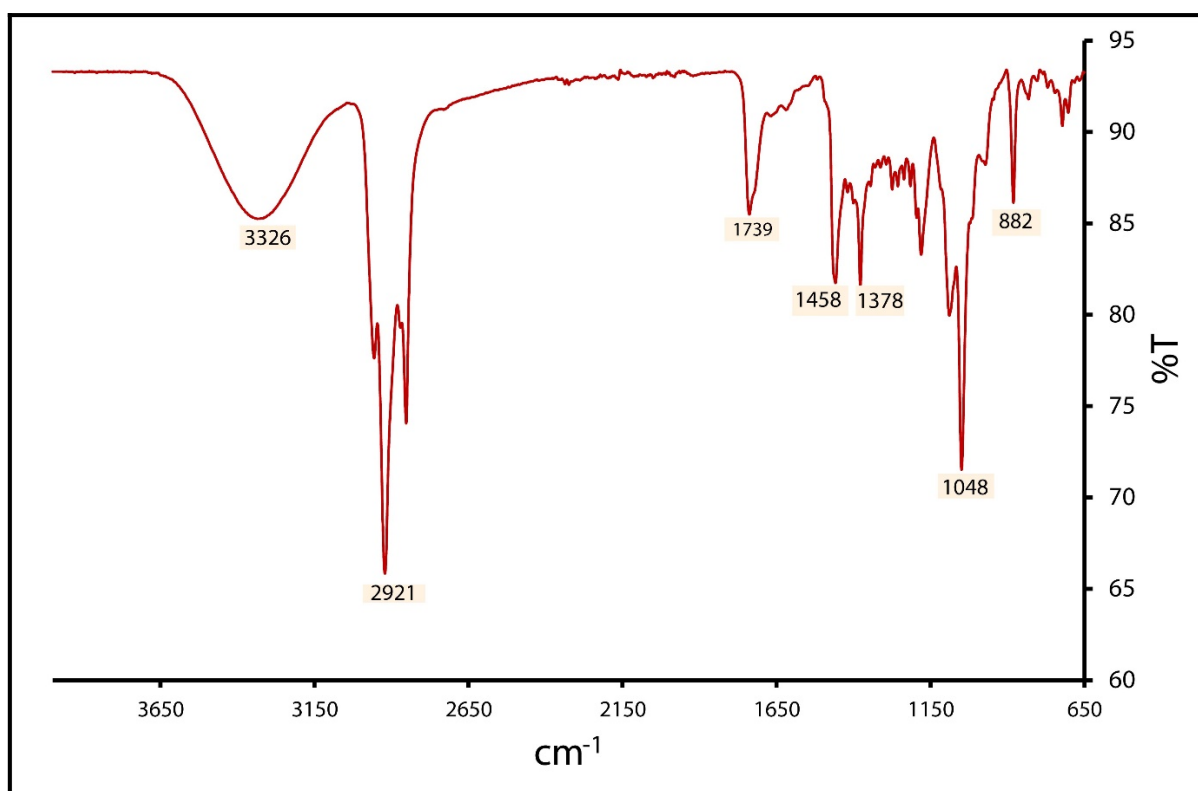


Figure 1: FT-IR spectrum of **PS-2**.

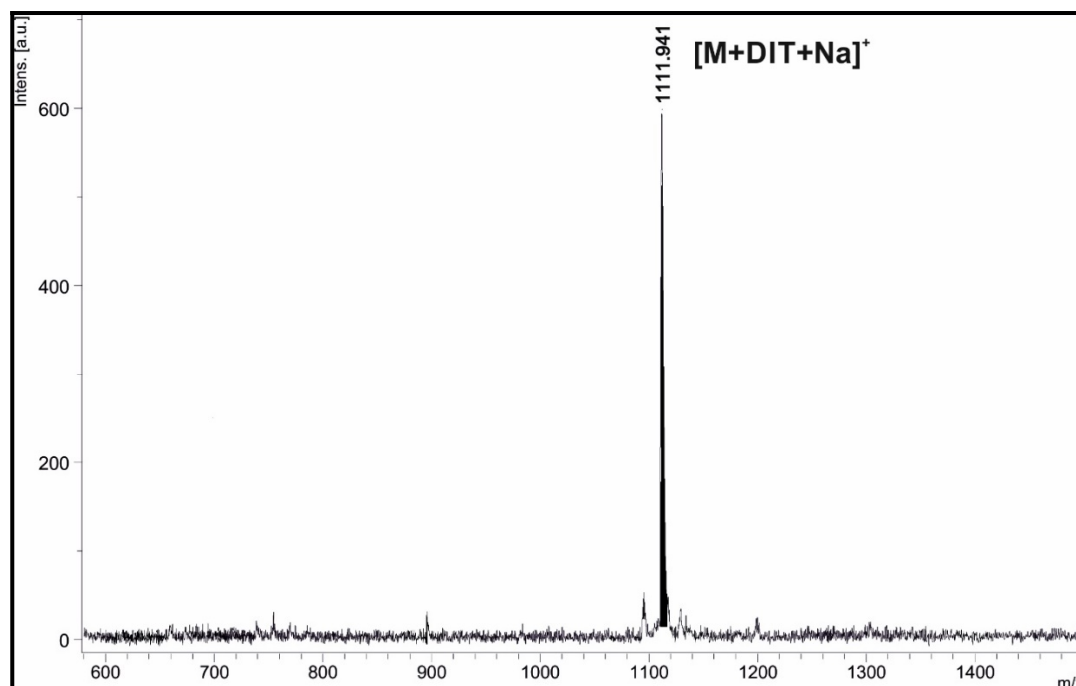


Figure 2: MALDI-TOF mass spectrum of **PS-2**.

The solvent $CDCl_3$ was used to analyze the 1H -NMR spectrum (Figure 3). 1H NMR spectrum for **PS-2**, the NH proton showed up at 6.88 ppm and the aromatic protons showed up at 9.64 and 8.36 ppm. Aliphatic protons ($-CH_3$) showed up in the 1.45 ppm

range. While aliphatic protons ($-O-CH_2$) from **PS-2** showed up 4.16 ppm, aliphatic protons ($-NH-CH_2$) from **PS-2** showed up 3.69 ppm. Results of the 1H NMR spectra confirmed the structure of **PS-2** molecule.

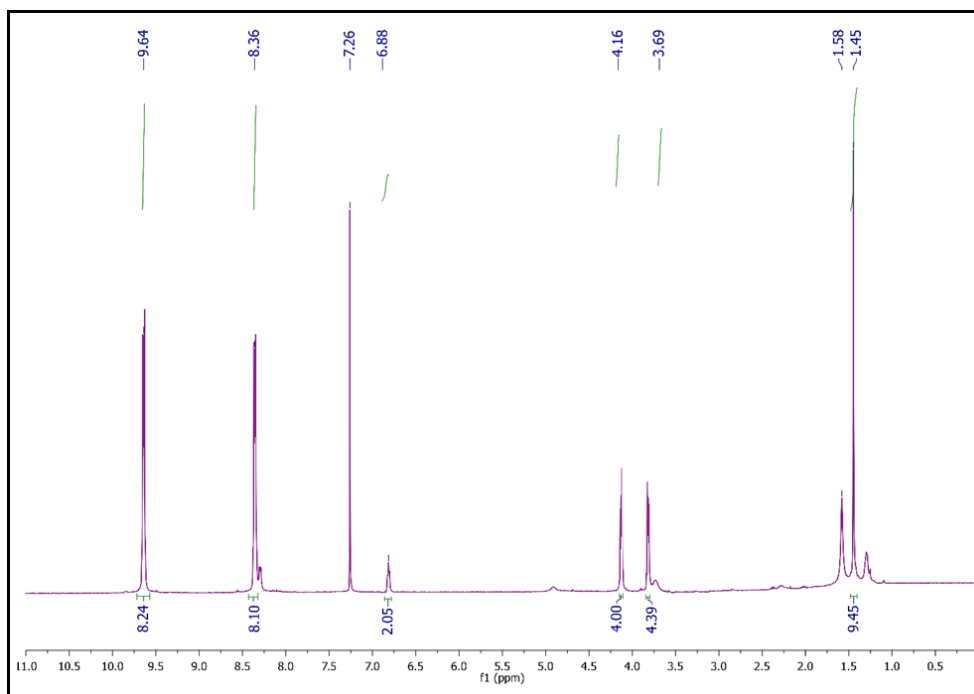


Figure 3: 1H NMR spectrum of **PS-2** in $CDCl_3$.

Electronic Absorption and Aggregation Study in the Ground State

The electronic ground state spectrum of di-axially substituted silicon(IV) phthalocyanine (**PS-2**) was performed in DMSO. It is known that metallo

phthalocyanines have two typical absorption bands, the Q and B bands. These two typical absorption bands (Q and B) are generally observed at 600-750 nm in the visible range of the spectrum and 300-450 nm in the ultraviolet range due to $\pi \rightarrow \pi^*$ transitions.

The aggregation behavior reduces the solubility of the Pc in DMSO and subsequently reduces its performance in a variety of scientific and technological areas. It is therefore important to identify and improve the factors that influence the aggregation behavior of PS. Changing the concentration of Pc, the type of solvent, and the

temperature can change the aggregation as well as the size and position of the substituent. Examining the electronic absorption spectra of **PS-2** is a useful approach to measuring and managing aggregation. For this purpose, the aggregation behavior of **PS-2** was examined at different concentrations (in the range from 1.2×10^{-5} to 2×10^{-6} M) in DMSO to determine the effect of the concentration on the aggregation. Lambert-Beer's law was observed for this compound at these concentrations. Aggregation studies showed that di-axially *N*-Boc ethanolamine substituted silicon(IV) phthalocyanine (**PS-2**) was not aggregated in the studied concentration range in DMSO (Figure 4).

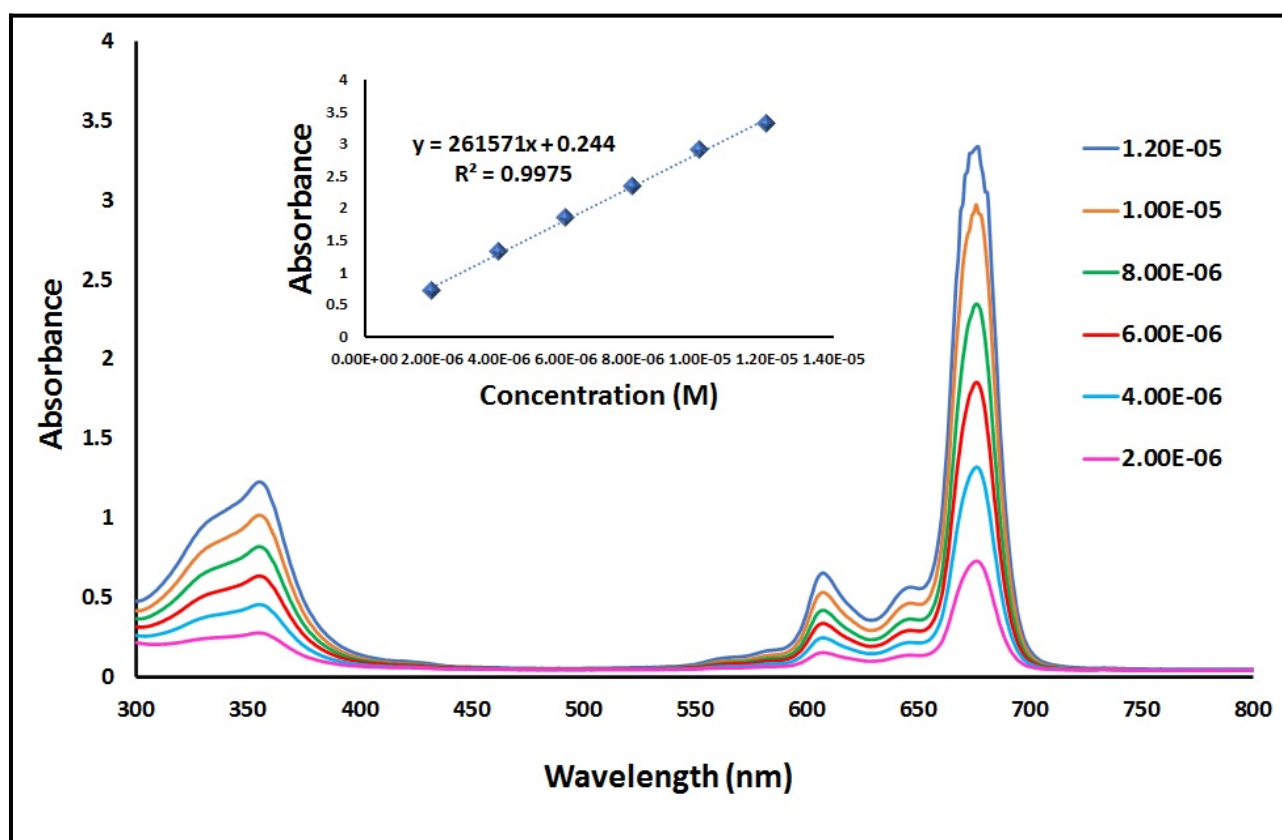


Figure 4: Electronic absorption spectra in the ground state of **PS-2** in DMSO at various concentrations (1.2×10^{-5} to 2×10^{-6} M).

Photochemical Properties (Photodegradation (Φ_{d}) and Singlet Oxygen Quantum Yield (Φ_{1O_2}))

During the photodynamic therapy treatment, the photosensitizer should be stable under the irradiation light. Because it is mandatory to maintain the efficiency of the PS molecule in terms of singlet oxygen production and to keep the PS concentration unchanged.

Photodegradation is the oxidative degradation to determine the stability of PS by light irradiation, and

they are determined by photodegradation quantum yield. In this work, the photodegradation quantum yield of **PS-2** was determined in DMSO (Figure 5). The absorption band of **PS-2** was reduced during the light irradiation. Spectral changes of **PS-2** during the process proved that photodegradation is not a photo-transformation. No new bands were observed in the absorption spectra and only the absorption was decreased. From this result, **PS-2** is moderately stable under the light in DMSO.

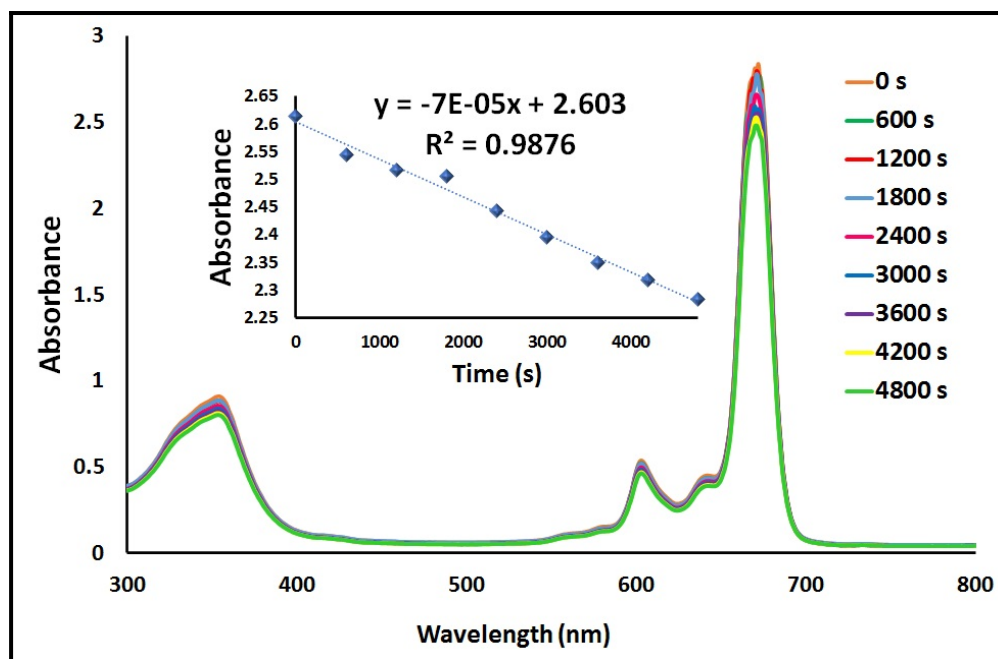


Figure 5: UV-Vis spectral changes of **PS-2** during the determination of the photodegradation quantum yield in DMSO.

The high singlet oxygen production is an important point of photodynamic therapy after the triple combination of light, photosensitizers, and molecular oxygen. Some biological macrosystems (such as lipid membranes, nucleic acids, protein, etc.) can be damaged due to the high reactivity of singlet oxygen and ultimately lead to death of the cell. Energy transfer from the photosensitizer molecule to molecular oxygen occurs *via* singlet oxygen as indicated in the Jablonski's diagram.

The singlet oxygen quantum yield was examined by applying a photochemical method based on the chemical quenching by using DPBF as a singlet oxygen trap. This is the method used for the reduction of the UV-Vis spectrum of the DPBF

absorption at 417 nm (Figure 6). The Φ_{Δ} values of the synthesized **PS-2** and **PS-1** are shown in Table 1. According to the results, it was found that the singlet oxygen generation ability of **PS-2** ($\Phi_{\Delta} = 0.18$) is higher than that of **PS-1** ($\Phi_{\Delta} = 0.15$). In the Φ_{Δ} determination process, the intensity of the Q band is unaffected, so that the electronic absorptions do not change in the ground state. These results indicated that the axial substituents have an impact on singlet oxygen generation for silicon(IV) phthalocyanines. In this study, our goal was to synthesize a new functional silicon(IV) phthalocyanine, this phthalocyanine can be used in PDT after the *N-Boc* group has been deprotected and replaced by new targeted groups.

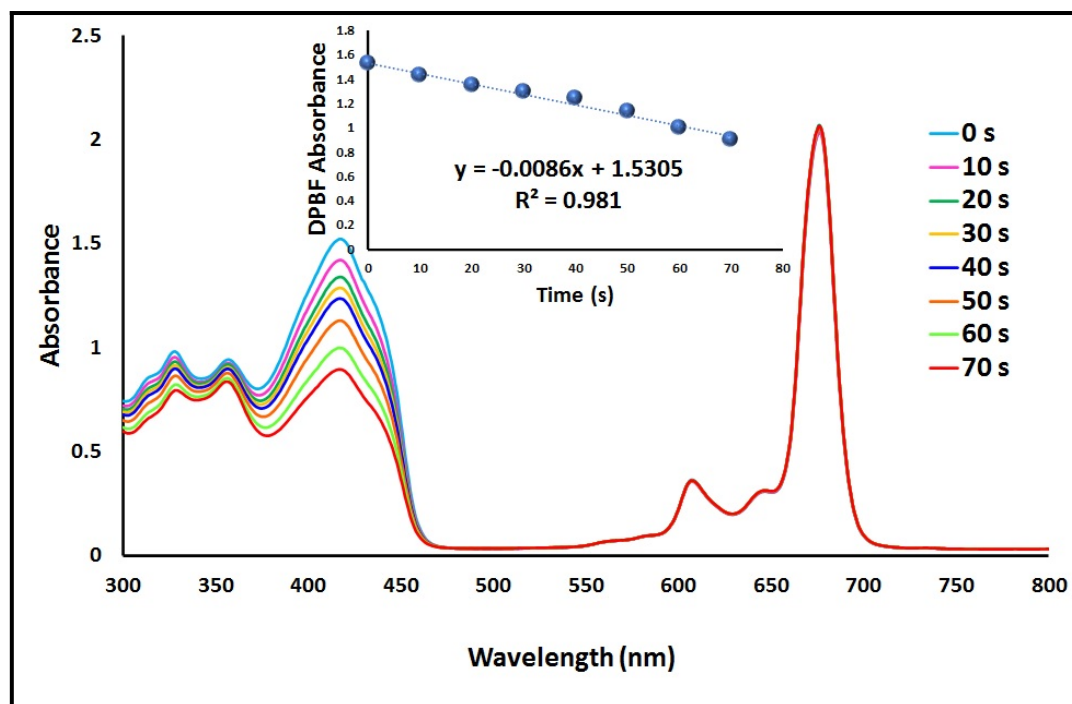


Figure 6: UV-Vis spectral changes of **PS-2** during the determination of the singlet oxygen quantum yield in DMSO.

Table 1: Photochemical data for **PS-2** and **PS-1** in DMSO.

Compound	Q band λ_{\max} , (nm)	$\log I$	Φ_{δ} ($\times 10^{-6}$)	Φ_{Δ}
PS-1	672-701 ^a	4.71-4.47 ^a	-	0.15 ^b
PS-2	676	5.41	7.97	0.18

^aData from reference (19).

^bData from reference (20)

CONCLUSION

In this study, the novel di-axially silicon(IV) phthalocyanine conjugated with the *N*-Boc protecting group was successfully synthesized. Synthesized phthalocyanine (**PS-2**) was characterized with various spectroscopic methods such as FT-IR, mass, ¹H-NMR, and UV-Vis spectroscopy. All data matched the proposed structure. The aggregation behavior of the **PS-2** became with increasing molarity (in the range from 1.2×10^{-5} to 2×10^{-6} M) in DMSO carried out. As the concentration increases, the absorbance increases directly to a stable value, and no new band was observed. Therefore, the non-aggregated behavior of the **PS-2** suggests that PDT applications in DMSO are useful. The photodegradation and the singlet oxygen quantum yield of **PS-2** were measured to examine the PDT ability. The singlet oxygen quantum yield of **PS-2** was slightly higher than the **PS-1**. For **PS-2**, during the determination of photodegradation quantum yield, no new bands were observed in the absorption spectra and only the absorption was decreased. In our future work, after the *N*-Boc group has been deprotected, this

functional silicon phthalocyanine could be used as a targeted photosensitizer if some specific targets were added. As a result, a new functional di-axially substituted silicon(IV) phthalocyanine has been successfully synthesized for use as a pre-drug in photodynamic therapy.

ACKNOWLEDGEMENTS

The authors thank Meltem Göksel for her contribution to the preparation of this publication.

REFERENCES

1. Anonymous. Cancer [Internet]. WHO. 2021 [cited 2022 Mar 19]. <URL>.
2. Wayteck L, Breckpot K, Demeester J, De Smedt SC, Raemdonck K. A personalized view on cancer immunotherapy. *Cancer Letters*. 2014 Sep;352(1):113-25. <DOI>.
3. Kübler AC. Photodynamic therapy. *Medical Laser Application*. 2005 May;20(1):37-45. <DOI>.
4. Yurt F, Ocakoglu K, Ince M, Colak SG, Er O, Soyulu HM, et al. Photodynamic therapy and nuclear imaging activities

- of zinc phthalocyanine-integrated TiO₂ nanoparticles in breast and cervical tumors. *Chem Biol Drug Des.* 2018 Mar;91(3):789–96. <DOI>.
5. Juzeniene A, Juzenas P, Iani V, Moan J. Topical Application of 5-Aminolevulinic Acid and its Methyl ester, Hexylester and Octylester Derivatives: Considerations for Dosimetry in Mouse Skin Model. *Photochemistry and Photobiology.* 2007 May 1;76(3):329–34. <DOI>.
6. Ogunsipe A, Chen J-Y, Nyokong T. Photophysical and photochemical studies of zinc(II) phthalocyanine derivatives—effects of substituents and solvents. *New J Chem.* 2004;28(7):822–7. <DOI>.
7. Kessel D, Oleinick NL. Photodynamic Therapy and Cell Death Pathways. In: Gomer CJ, editor. *Photodynamic Therapy* [Internet]. Totowa, NJ: Humana Press; 2010 [cited 2022 Mar 19]. p. 35–46. (Methods in Molecular Biology; vol. 635). <URL>.
8. Lo P-C, Rodríguez-Morgade MS, Pandey RK, Ng DKP, Torres T, Dumoulin F. The unique features and promises of phthalocyanines as advanced photosensitizers for photodynamic therapy of cancer. *Chem Soc Rev.* 2020;49(4):1041–56. <DOI>.
9. Ekineker G, Göksel M. Synthesis of both peripheral and non-peripheral substituted metal-free phthalocyanines and characterization. *Tetrahedron.* 2020 Jan;76(5):130878. <DOI>.
10. Göksel M, Durmuş M, Biyiklioglu Z. Synthesis and photodynamic activities of novel silicon(IV) phthalocyanines axially substituted with water soluble groups against HeLa cancer cell line. *Dalton Trans.* 2021;50(7):2570–84. <DOI>.
11. Tarhouni M, Durand D, Önal E, Aggad D, İsci Ü, Ekineker G, et al. Triphenylphosphonium-substituted phthalocyanine: Design, synthetic strategy, photophysical properties and photodynamic activity. *J Porphyrins Phthalocyanines.* 2018 Jul;22(07):552–61. <DOI>.
12. Bartlett MA, Mark K, Sundermeyer J. Synthesis, spectroscopy and singlet oxygen quantum yield of a non-aggregating hexadecamethyl-substituted phthalocyanine silicon(IV) derivative. *Inorganic Chemistry Communications.* 2018 Dec;98:41–3. <DOI>.
13. Barut B, Demirbaş Ü, Özel A, Kantekin H. Novel water soluble morpholine substituted Zn(II) phthalocyanine: Synthesis, characterization, DNA/BSA binding, DNA photocleavage and topoisomerase I inhibition. *International Journal of Biological Macromolecules.* 2017 Dec;105:499–508. <DOI>.
14. Skupin-Mrugalska P, Szczolko W, Gierlich P, Konopka K, Goslinski T, Mielcarek J, et al. Physicochemical properties of liposome-incorporated 2-(morpholin-4-yl)ethoxy phthalocyanines and their photodynamic activity against oral cancer cells. *Journal of Photochemistry and Photobiology A: Chemistry.* 2018 Feb;353:445–57. <DOI>.
15. Lowery MK, Starshak AJ, Esposito JN, Krueger PC, Kenney ME. Dichloro(phthalocyanino)silicon. *Inorg Chem.* 1965 Jan;4(1):128–128. <DOI>.
16. Derrin D, Armarego W, Perrin D. *Purification of Laboratory Chemicals.* 1980.
17. Yanık H, Aydın D, Durmuş M, Ahsen V. Peripheral and non-peripheral tetrasubstituted aluminium, gallium and indium phthalocyanines: Synthesis, photophysics and photochemistry. *Journal of Photochemistry and Photobiology A: Chemistry.* 2009 Jul;206(1):18–26. <DOI>.
18. Spiller W, Kliesch H, Wöhrle D, Hackbarth S, Röder B, Schnurpfeil G. Singlet Oxygen Quantum Yields of Different Photosensitizers in Polar Solvents and Micellar Solutions. *J Porphyrins Phthalocyanines.* 1998 Mar;02(02):145–58. <DOI>.
19. Gülmez AD, Göksel M, Durmuş M. Silicon(IV) phthalocyanine-biotin conjugates: Synthesis, photophysical properties and *in vitro* biological activity for photodynamic therapy. *J Porphyrins Phthalocyanines.* 2017 Jul;21(07n08):547–54. <DOI>.
20. Atmaca GY, Dizman C, Eren T, Erdoğan A. Novel axially carborane-cage substituted silicon phthalocyanine photosensitizer; synthesis, characterization and photophysical properties. *Spectrochimica Acta Part A: Molecular and Biomolecular Spectroscopy.* 2015 Feb;137:244–9. <DOI>.



Cyclization Reactions of Non-Conjugate Ynones with Propargyl Amine in the Presence of a Catalyst

Volkan TAŞDEMİR^{1*} 

¹Van Yüzüncü Yıl University, Muradiye Vocational School, Van, 65080, Turkey

Abstract: In this study, acetate derivatives were obtained from the reaction of acetophenones using diethyl carbonate. The acidic proton of CH₂ moiety was abstracted using a suitable base and α-propargyl-β-ketoester (non-conjugated ynone) derivatives **3a-c** were obtained from the reaction of the acetate derivatives with propargyl bromide. By removing the ester group of α-propargyl-β-ketoester derivatives under suitable conditions, α-propargyl acetophenones (non-conjugated ynone) **4a-c** were obtained. In this study, 6 different unconjugated ynone derivatives were synthesized as starting material with yield in a range of 60-95%. Cyclization reactions with propargyl amine in the presence of three different unconjugated ynone derivatives, metal catalysts were investigated. The synthesis of propargyl pyrroles **7a-c** having substituents on C-2 and C-5 was completed.

Keywords: Cyclization, propargyl amine, pyrrole, unconjugated ynone.

Submitted: January 28, 2022. **Accepted:** March 22, 2022.

Cite this: Taşdemir V. Cyclization Reactions of Non-Conjugate Ynones with Propargyl Amine in the Presence of a Catalyst. JOTCSA. 2022;9(2):553-70.

DOI: <https://doi.org/10.18596/jotcsa.1064488>.

***Corresponding author. E-mail:** volkantasdemir@yyu.edu.tr.

INTRODUCTION

Pyrrolic systems, which are in the class of five-membered heterocyclic compounds containing a single nitrogen atom, are bioactive compounds that can be synthesized both from natural products and by synthetic means (1-3). Pyrrole ring containing compounds are used in material chemistry (4), in natural products (5,6), dyes and as bioactive entity (7,8), it has anti-allergic, cholesterol-lowering, antidepressant, anti-inflammatory (9), antidiabetic, antimicrobial (10), antifungal, antiviral, anticonvulsant, antihyperlipidemic, and antitumor (11) properties (12,13). Numerous methods have been developed and continue to be developed for the synthesis of nitrogen-containing heterocyclic compounds. In recent years, great importance has been given to the development of new methods for the synthesis of substituted pyrroles (14). We can cite alkyne groups among the most important groups because of their easy modifications and electronic properties (15). Alkynes allow the

synthesis of molecules of different modifications with a wide variety of reactions such as oxidation (16), reduction (17), and nucleophilic addition (18,19).

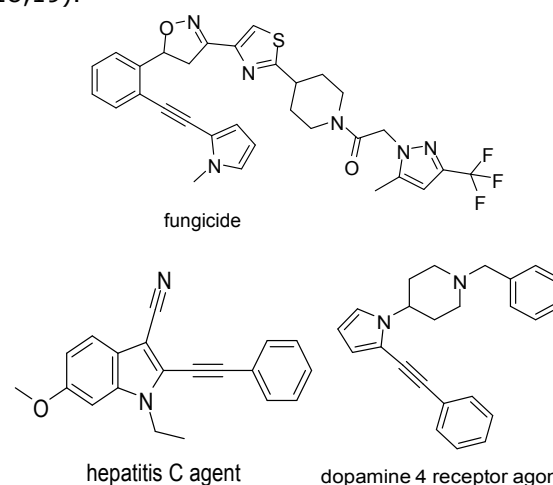


Figure 1: Activity of some compounds containing alkyne group attached to the pyrrole ring.

The presence of propargyl pyrrole compounds in structures such as dopamine 4 receptor agonist (20), fungicide, hepatitis C agent, as shown in Figure 1, increases the interest in new pyrrolic propargyl derivatives and in recent years, the production of metal-catalyzed alkylated pyrrolic systems has attracted a lot of attention (21,22). In the literature, generally, pyrrolic propargyl systems have been synthesized either by removing the NH proton with a base or by binding to the N-protected pyrrolic system at the propargyl ortho and/or meta position (23-26). In these studies, the synthesis of substituted pyrrolic derivatives was carried out, generally starting from the ynone derivative molecule. Recently, ynones, known as alkynones and also referred to as conjugated ynones, are attracting attention as important starting compounds. Ynones are compounds that contain an alkyne group directly attached to a carbonyl group in their structure (27,28). Although conjugated ynone compounds have been used as starting compounds in the synthesis of many heterocycles in the literature, α propargyl acetophenone compounds, which we can express as unconjugated ynone compounds, have not been studied much in the literature (29). In this study, the synthesis of pyrrole propargyl derivatives as a result of metal-catalyzed reaction of unconjugated ynone derivatives (α propargyl acetophenone) and propargyl amine compound as starting compound was investigated.

EXPERIMENTAL SECTION

Materials

All chemicals and solvents were commercially obtained from Sigma-Aldrich with analytical quality. The solutions were distilled and dried with suitable agents. All syntheses were carried out at normal atmospheric conditions. An Electrothermal Gallenkamp apparatus was used to determine the melting points. A Q Exactive High Performance Liquid Chromatography and High Resolution Mass Spectrometer (LC-MS/MS) was used to record the mass spectra of all compounds. $^1\text{H-NMR}$ and $^{13}\text{C-NMR}$ spectra were recorded using a 400 MHz Agilent using TMS (tetramethylsilane) as the internal standard. All experiments were followed by TLC (thin layer chromatography) using DC Alufolien Kieselgel 60 F254 and a Camag TLC lamp (254/366 nm).

General Procedure for the Synthesis of Acetate Derivatives

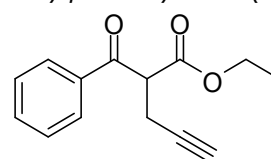
1 mmol of 4-methoxyacetophenone derivative was added into a 50 mL balloon containing 10 mL of DMF and 5 mmol of NaH was added. After 45 minutes, 1.2 mmol diethyl carbonate was added and refluxed. With TLC method, the reaction was observed to end after 24 hours. The crude product was extracted (ethyl acetate/water) and the product

was purified by column chromatography with ethyl acetate/n-hexane (1:5).

General procedure for the synthesis of (α -propargyl- β -ketoester)propargyl acetophenone ethyl ester (non-conjugated ynone) derivatives (3a-c)(29-31)

1 mmol (5 mL) ethylbenzoyl acetate was placed in a 50 mL flask, and 1.3 mmol (0.76 g) metallic sodium was added at 0 °C. After the sodium metal was finished in 10 minutes, 1.3 mmol (3.95 mL) of propargyl bromide was added and mixed. It was observed that the reaction ended after 24 hours by TLC method. The crude product was evaporated by filtration. Purification was done with ethyl acetate - n-hexane (1/5) as the mobile phase.

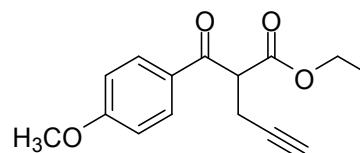
R/S ethyl 2-benzoylpent-4-ynoate (3a)



Yield; 85%, Color: Yellow, appearance: Liquid.

$^1\text{H NMR}$ (400 MHz, CDCl_3) δ = 8.02-7.99 (m, 2H, Ar-H), 7.59-7.55 (m, 1H, Ar-H), 7.48-7.43 (m, 2H, Ar-H), 4.57-4.53 (t, J = 7.39 Hz, 1H, CH), 4.16-4.09 (qd, J = 1.26, 7.10 Hz, 2H, OCH_2), 2.89-2.83 (ddd, J = 2.65, 7.39, 16.18 Hz, 2H, CH_2), 1.97-1.96 (t, J = 2.65 Hz, 1H, CH), 1.15-1.11 (td, J = 2.23, 7.10 Hz, 3H, CH_3). $^{13}\text{C NMR}$ (100 MHz, CDCl_3) δ = 193.6, 193.2, 170.4, 168.2, 135.8, 135.1, 133.8, 133.1, 129.5, 128.8, 128.7, 128.6, 128.3, 128.0, 80.6, 78.3, 72.4, 70.5, 70.4, 62.3, 61.8, 59.8, 53.1, 23.5, 19.9, 18.3, 13.9, 13.8. LC-MS-MS Anal.Calcd. for $\text{C}_{14}\text{H}_{14}\text{O}_3$ [M^+H]: 231.10157, Found 231.10162.

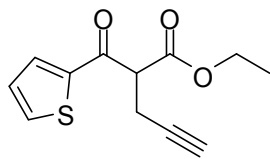
R/S ethyl 2-(4-methoxybenzoyl)pent-4-ynoate (3b)



Yield; 85%, Color: Yellow, appearance: liquid.

$^1\text{H NMR}$ (400 MHz, CDCl_3) δ = 8.03-8.01 (m, A part of AA'BB' system, 2H, Ar-H), 6.96-6.94 (m, B part of AA'BB' system, 2H, Ar-H), 4.53-4.50 (m, 1H, CH), 4.18-4.13 (m, 2H, OCH_2), 3.87 (s, 3H, OCH_3), 2.93-2.87 (m, 2H, CH_2), 1.97 (t, J = 2.67 Hz, 1H, CH), 1.20-1.16 (m, 3H, CH_3). $^{13}\text{C NMR}$ (100 MHz, CDCl_3) δ = 191.5, 168.5, 164.1, 131.3, 113.9, 80.8, 78.5, 72.2, 70.2, 61.7, 55.5, 52.9, 23.7, 18.4, 13.9. LC-MS-MS Anal.Calcd. for $\text{C}_{15}\text{H}_{17}\text{O}_4$ [M^+H]: 261.11214, Found 261.11282.

R/S ethyl 2-(thiophene-2-carbonyl)pent-4-ynoate (3c)



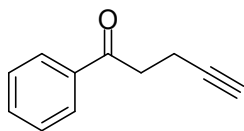
Yield; 90%, Color: Brown, appearance: Gel.

$^1\text{H NMR}$ (400 MHz, CDCl_3) δ = 7.86 (d, J = 1.27, 3.62 Hz, 1H, Ar-H), 7.71-7.69 (m, 1H, Ar-H), 7.15-7.13 (m, 1H, Ar-H), 4.38 (t, J = 7.50 Hz, 1H, CH), 4.18-4.12 (m, 2H, OCH_2), 2.94-2.77 (m, 2H, CH_2), 1.97-1.96 (m, 1H, CH), 1.19-1.15 (m, 3H, CH_3). $^{13}\text{C NMR}$ (100 MHz, CDCl_3) δ = 185.7, 167.9, 142.9, 135.4, 133.7, 128.4, 80.4, 70.5, 61.9, 54.3, 18.3, 13.9.

General Procedure for the Synthesis of Propargyl Acetophenone (Non-Conjugated Ynone) Derivatives (4a-c) (29-31)

12 mL of 10% NaOH solution by mass was added to the crude product and refluxed. It was observed that the reaction ended after 8 hours by TLC method. The crude product was brought to room temperature and the pH was arranged to 4 by adding HCl. It was extracted with diethyl ether and re-extracted with NaHCO_3 solution. It was dried with MgSO_4 and evaporated. The product was purified with ethyl acetate - n-hexane (1/5) as the mobile phase.

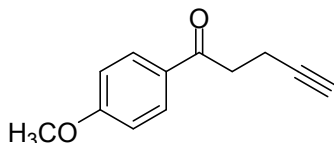
1-phenylpent-4-yn-1-one (4a)(26)



Yield; 60%, Color: White, appearance: Solid. M.P:72-75°C

$^1\text{H NMR}$ (400 MHz, CDCl_3) δ = 7.97-7.95 (m, 2H, Ar-H), 7.59-7.54 (m, 1H, Ar-H), 7.48-7.44 (m, 2H, Ar-H), 3.26-3.22 (m, 2H, CH_2), 2.65-2.60 (m, 2H, CH_2), 1.98 (t, J = 2.68 Hz, 1H, CH). $^{13}\text{C NMR}$ (100 MHz, CDCl_3) δ = 197.6, 136.4, 133.3, 128.6, 128.0, 83.3, 68.8, 37.5, 13.2. LC-MS-MS Anal.Calcd. for $\text{C}_{11}\text{H}_{10}\text{O}$ [M^+H]: 159.08044, Found 159.08058.

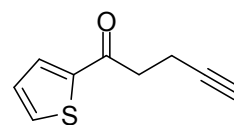
1-(4-methoxyphenyl)pent-4-yn-1-one (4b) (26)



Yield; 65%, Color: White, appearance: Solid. M.P:85-87°C

$^1\text{H NMR}$ (400 MHz, CDCl_3) δ = 7.94-7.91 (m, A part of AA'BB' system, 2H, Ar-H), 6.93-6.90 (m, B part of AA'BB' system, 2H, Ar-H), 3.84 (dd, J = 3.00, 4.70 Hz, 3H, OCH_3), 3.19-3.15 (m, 2H, CH_2), 2.62-2.57 (m, 2H, CH_2), 2.01-1.96 (m, 1H, CH). $^{13}\text{C NMR}$ (100 MHz, CDCl_3) δ = 196.1, 163.6, 130.3, 113.8, 83.5, 68.7, 55.4, 37.1, 13.3. LC-MS-MS Anal.Calcd. for $\text{C}_{12}\text{H}_{12}\text{O}_2\text{Na}$ [M^+Na]: 211.07295, Found 211.07208.

1-(thiophen-2-yl)pent-4-yn-1-one(4c) (26)



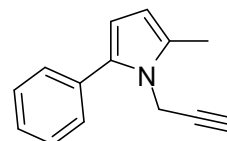
Yield; 60%, Color: Brown, appearance: Gel.

$^1\text{H NMR}$ (400 MHz, CDCl_3) δ = 7.70-7.68 (m, 1H, Ar-H), 7.62-7.60 (m, 1H, Ar-H), 7.10-7.08 (m, 1H, Ar-H), 3.14-3.10 (m, 2H, CH_2), 2.59-2.54 (m, 2H, CH_2), 1.97-1.95 (m, 1H, CH). $^{13}\text{C NMR}$ (100 MHz, CDCl_3) δ = 190.6, 143.6, 133.9, 132.1, 128.2, 83.0, 69.1, 38.0, 13.4.

General Procedure for the Synthesis of Propargyl Pyrrole Derivatives (7a-c)

1 mmol of 4a-c compound was dissolved in 2 mL of ethanol and 3 mmol of propargyl amine was added. The mixture was refluxed after adding a catalytic amount of AuCl_3 . It was observed that the reaction ended after 24 hours by TLC method. The crude product was evaporated by filtration. The reaction product was purified by column chromatography in which the mobile phase was ethyl acetate - n-hexane (1/5).

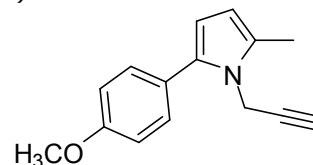
2-methyl-5-phenyl-1-(prop-2-yn-1-yl)-1H-pyrrole (7a)



Yield; 85%, Color: Brown, appearance: Gel.

$^1\text{H NMR}$ (400 MHz, CDCl_3) δ = 7.49-7.47 (m, 2H, Ar-H), 7.43-7.39 (m, 2H, Ar-H), 7.33-7.28 (m, 1H, Ar-H), 6.15 (t, J = 3.0 Hz, 1H, CH), 5.99 (s, 1H, CH), 4.56 (t, J = 2.55 Hz, 2H, CH_2), 2.41(d, J = 2.01 Hz, 3H, CH_3), 2.38(dd, J = 2.55, 5.31 Hz, 1H, CH). $^{13}\text{C NMR}$ (100 MHz, CDCl_3) δ = 128.6, 128.5, 126.8, 107.9, 107.2, 79.5, 72.6, 34.2, 12.4. LC-MS-MS Anal.Calcd. for $\text{C}_{14}\text{H}_{13}\text{N}$ [M^+H]: 196.11208, Found 196.11255.

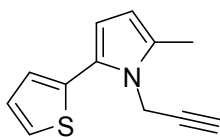
2-(4-methoxyphenyl)-5-methyl-1-(prop-2-yn-1-yl)-1H-pyrrole(7b)



Yield; 50%, Color: White, appearance: Gel.

$^1\text{H NMR}$ (400 MHz, CDCl_3) δ = 7.41-7.39 (m, A part of AA'BB' system, 2H, Ar-H), 6.97-6.94 (m, B part of AA'BB' system, 2H, Ar-H), 6.07-6.06 (m, 1H, CH), 5.96 (s, 1H, CH), 4.52 (d, J = 2.24 Hz, 2H, CH_2), 3.84 (d, J = 1.79 Hz, 3H, OCH_3), 2.39 (d, J = 1.40 Hz, 3H, CH_3), 2.36 (d, J = 2.24 Hz, 1H, CH). $^{13}\text{C NMR}$ (100 MHz, CDCl_3) δ = 158.7, 133.7, 130.1, 129.6, 126.0, 113.9, 107.2, 106.9, 79.6, 72.4, 55.3, 34.0, 12.4. LC-MS-MS Anal.Calcd. for $\text{C}_{15}\text{H}_{15}\text{NO}$ [M^+H]: 226.12264, Found 226.12415.

2-methyl-1-(prop-2-yn-1-yl)-5-(thiophen-2-yl)-1H-pyrrole(7c)



Yield; 60%, Color: Brown, appearance: Gel.

^1H NMR (400 MHz, CDCl_3) δ = 7.28-7.26 (m, 1H, Ar-H), 7.15-7.14 (m, 1H, Ar-H), 7.10-7.07 (m, 1H, Ar-H), 6.23 (d, J = 2.61 Hz, 1H, CH), 5.97 (d, J = 1.38 Hz, 1H, CH), 4.64 (d, J = 1.43 Hz, 2H, CH_2), 2.38 (s,

3H, CH_3), 2.36-2.35 (m, 3H, CH). ^{13}C NMR (100 MHz, CDCl_3) δ = 134.9, 130.7, 127.5, 125.8, 125.3, 124.9, 109.1, 107.4, 79.1, 72.6, 33.9, 12.4. LC-MS-MS Anal. Calcd. for $\text{C}_{12}\text{H}_{11}\text{NS}$ [M^+H]: 202.06850, Found 202.06989.

RESULTS AND DISCUSSION

Molecules 3 and 4, which are unconjugated ynone derivatives, were obtained in several steps (Figure 2).

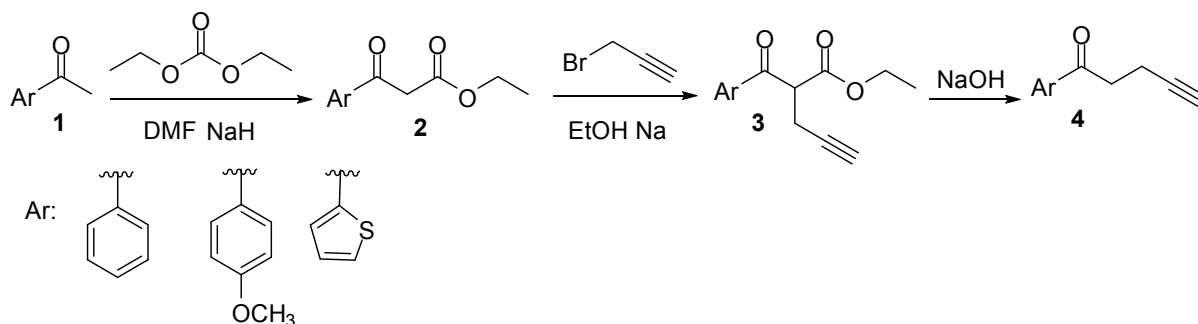
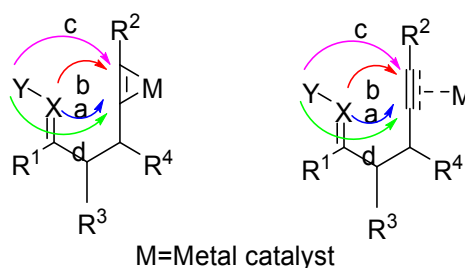


Figure 2: Synthesis of unconjugated ynone compounds.

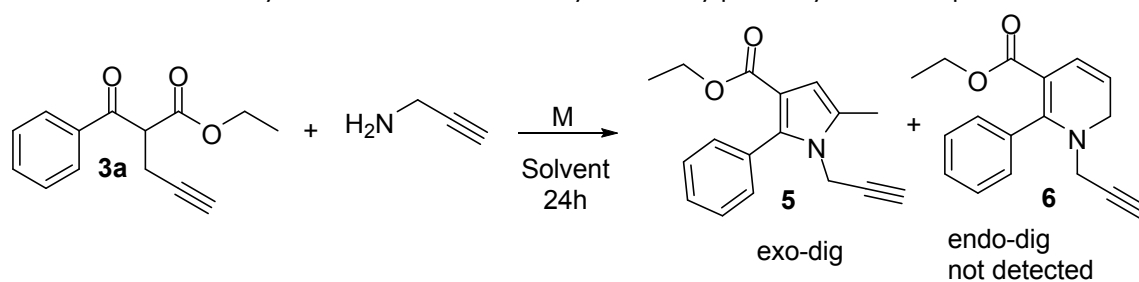
Firstly, as shown in Figure 2, ethyl acetate derivatives 2 were obtained from acetophenone derivative compounds by removing one of the protons in the methyl carbon with sodium hydride (NaH) and reacting with diethyl carbonate. Then, a propargyl acetophenone ethyl esters 3 were obtained from the reaction of ethyl acetate derivatives with propargyl bromide by removing one of the acidic CH_2 protons in the presence of metallic sodium (Na). It is obvious that the synthesis of compounds 3a-c give chiral molecules. However, the reaction will take place in a racemic mixture because of non-stereoselectivity. Finally, the synthesis of a propargyl acetophenone derivatives 4 was carried out by removing the ester part in the compound. Cyclization reactions of ynones 3 and 4 with propargyl amine with various metal catalysts in different solvent were investigated. Possible cyclization reactions are shown in Figure 3. As it is known, a wide research area has emerged in the literature regarding the formation of more than one possible product (endo-dig or exo-dig) or selective cyclization product in alkyne cyclizations (32-35). The reason for this is that the nucleophilic atom in the carbonyl group can attack both atoms of the alkyne group. In such cases, the metal catalyst chosen usually allows a regioselective reaction to proceed.



M=Metal catalyst

Figure 3: Cyclization of alkyne group compounds with metallic catalyst.

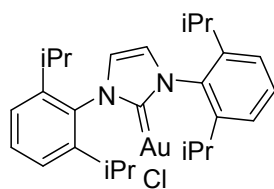
When the possible mechanism of the reaction is examined in the light of this information, X and/or Y atoms in the carbonyl group can attack the inner or outer carbon atom of the alkyne group in the presence of metal catalysts. If the X or Y atom attacks the inner carbon atom (path a and d), there will be exo-dig closure, and if it attacks the outer carbon atom (path b and c), there will be endo-dig closure (Figure 3) (36). Therefore, many different reactions are likely to occur. With both the examples in the literature and the experience we have gained from our studies, we can say that their regioselective properties will depend on the substituents in the ynone skeleton and/or metal catalysts. In this context, cyclization reactions of ynone 3 with propargyl amine in metals and solvent environments shown in Table 1 were investigated.

Table 1: Cyclization reactions of ethyl 2-benzoylpent-4-ynoate compound.

Compound	Solvent	Catalyst	Temperature	Result	
1	3a	EtOH	AuCl ₃	RT	nd
2	3a	EtOH	AuCl ₃	Reflux	nd
3	3a	EtOH	p-toluenesulfonic acid	Reflux	nd
4	3a	PrOH	CuI	Reflux	nd
5	3a	PrOH	AuCl ₃	Reflux	nd
6	3a	EtOH	AgOTf	Reflux	nd
7	3a	PrOH	Au(L)*	Reflux	nd
8	3a	PrOH	Pd(OAc) ₂	Reflux	nd
9	3a	EtOH	InCl ₃	Reflux	nd

nd: No reaction, the starting material was recovered.

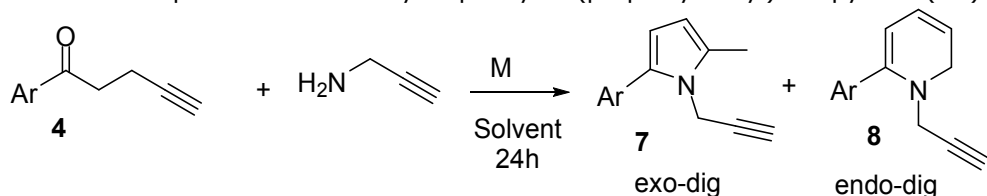
*



Au(L)

Reactions 1 to 9 were first carried out at room temperature. When it was understood that there was the starting product in the reactions controlled by TLC, no product was observed as a result of reacting the molecule 3a with different solvents in the presence of the catalyst for 24 hours in the reactions controlled by TLC again by increasing the temperature. When the reaction medium was examined, only the starting compound was obtained. In this case, it can be considered that the metal catalysts used form a complex with the 1,3-

dicarbonyl structure in the starting compound and this complex is more dominant despite activating the alkyne group, therefore the reaction does not proceed. Then, the reactions of the other starting compound a propargyl acetophenone derivative and propargyl amine were investigated. The pyrrole propargyl derivatives were obtained in the cyclization reactions performed with the starting compound ynone 4 under the reaction conditions shown in Table 2, under different reaction conditions.

Table 2: Preparation of 2-methyl-5-phenyl-1-(prop-2-yn-1-yl)-1H-pyrrole (**7a**).

Compound	Solvent	Catalyst	Temperature	Result	
1	4	EtOH	AuCl ₃	RT	nd
2	4	EtOH	AuCl ₃	Reflux	7a 95%
3	4	EtOH	p-toluenesulfonic acid	Reflux	7a 80%
4	4	EtOH	InCl ₃	Reflux	7a 15%
5	4	EtOH	CuI	Reflux	nd
6	4	EtOH	Pd(OAc) ₂	Reflux	nd

nd: No reaction, the starting material was recovered.

Cyclization reactions of compound 4a-c using *p*-toluenesulfonic acid were screened. However, only compound 4a gave the cyclic product. So, we have decided to use AuCl₃ for further cyclization reactions. The pyrrole derivatives **7a-c** shown in Figure 4 were obtained with a good yield from the

reaction of the starting compound **4a-c** and propargyl amine under the catalytic effect of AuCl₃. When we have checked the reaction media, we did not see any sign of endo-dig cyclization which is represented as compound **8** in Table 2.

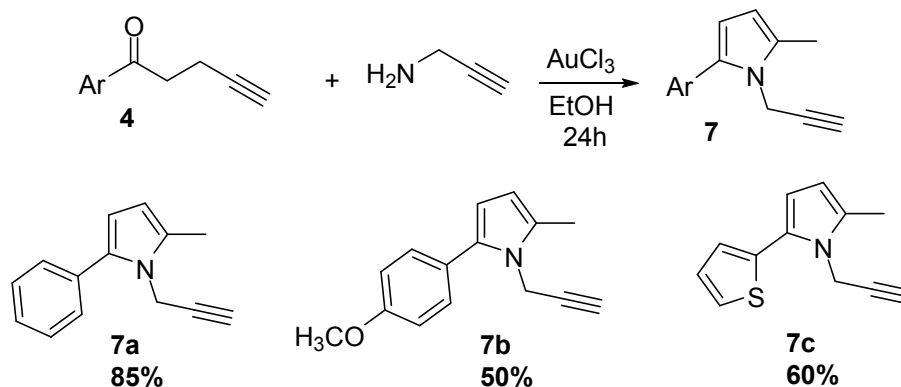


Figure 4: Obtained compounds **7a-c**.

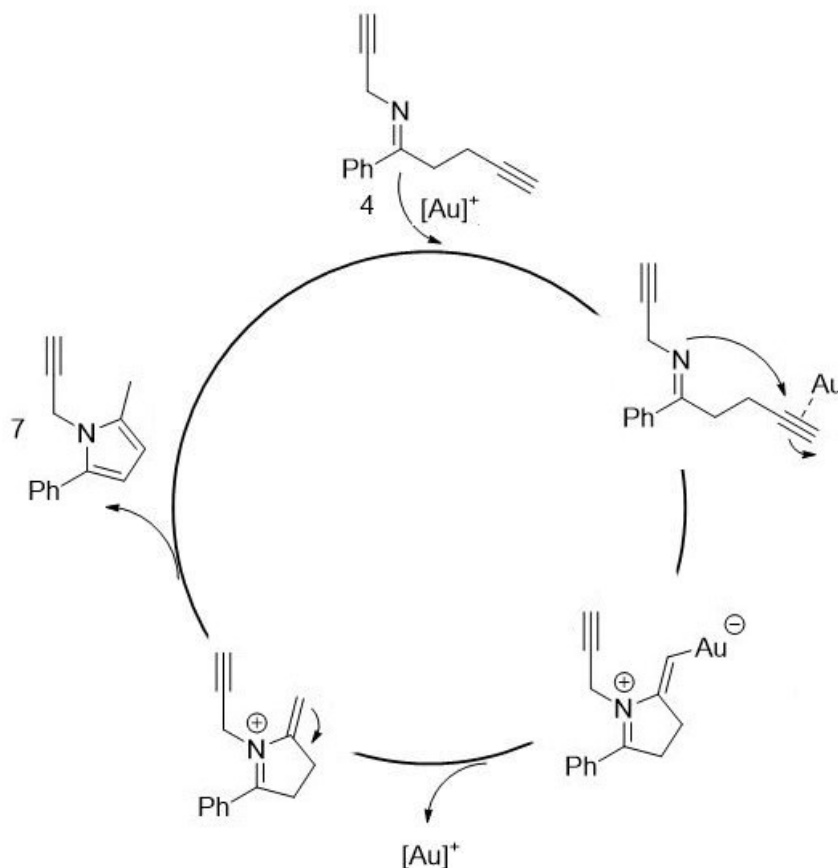


Figure 5: Proposed reaction mechanism of 2-methyl-5-phenyl-1-(prop-2-yn-1-yl)-1H-pyrrole (**7a**).

When the proposed reaction mechanism is examined in Figure 5, it can be said that the metal catalyst AuCl₃ activates the alkyne group, and the imine nitrogen in the imine propargyl group attached to the carbonyl group attacks the inner carbon atom of the activated alkyne group, and the reaction proceeds and becomes cyclic to pyrrole

propargyl derivatives with a quintuple exo-dig closure. When the structure characterization of 2-methyl-5-phenyl-1-(prop-2-yn-1-yl)-1H-pyrrole (**7a**) is examined by NMR spectrum, protons resonating at 6.15 ppm and 5.99 ppm in the ¹H-NMR spectrum indicate pyrrole ring protons, -CH₂ protons coming as a triplet at 4.56 ppm and -CH protons resonating

as a doublet at 2.38 ppm indicate alkyne group protons and protons resonating at 2.41 ppm indicate pyrrole ring methyl protons. When the ^{13}C -NMR spectrum is examined, it is seen that the pyrrole C_3 and C_4 carbons resonate at 107.9 and 107.2 ppm, the alkyne group carbons resonate at 79.4, 72.6 and 34.2 ppm, respectively, and the methyl group attached to the pyrrole ring resonates at 12.4 ppm.

CONCLUSION

In this study, the synthesis of 1,3-diketo esters from acetophenone derivative compounds was carried out and from these derivatives, 6 different unconjugated ynone derivatives were synthesized as starting compounds. Cyclization reactions of unconjugated ynone derivatives were investigated using metal catalysts. In the presence of metal catalysts, 3 different pyrrole propargyl derivatives were obtained as a result of cyclization reactions of unconjugated ynone derivatives and propargyl amine compound in a single step.

CONFLICT OF INTEREST

There is no conflict of interest.

ACKNOWLEDGMENTS

The author thanks to Science Research and Applied Center in Van Yüzüncü Yil University for their research facilities.

SUPPORTING INFORMATION

^1H -NMR, ^{13}C -NMR, spectrum and HRMS data are provided in the Supplementary Material section of this article.

REFERENCES

- Sari O, Seybek AF, Kaya S, Menges N, Erdem SS, Balci M. Mechanistic Insights into the Reaction of *N*-Propargylated Pyrrole- and Indole-Carbaldehyde with Ammonia, Alkyl Amines, and Branched Amines: A Synthetic and Theoretical Investigation. *Eur J Org Chem.* 2019 Sep;2019(31-32):5261-74. [<DOI>](#).
- Özer MS, Menges N, Keskin S, Şahin E, Balci M. Synthesis of Pyrrole-Fused *C*, *N*-Cyclic Azomethine Imines and Pyrazolopyrrolopyrazines: Analysis of Their Aromaticity Using Nucleus-Independent Chemical Shifts Values. *Org Lett.* 2016 Feb 5;18(3):408-11. [<DOI>](#).
- Taskaya S, Menges N, Balci M. Gold-catalyzed formation of pyrrolo- and indolo-oxazin-1-one derivatives: The key structure of some marine natural products. *Beilstein J Org Chem.* 2015 May 28;11:897-905. [<DOI>](#).
- Krzyszewski M, Gryko D, Gryko DT. The Tetraarylpyrrolo[3,2-*b*]pyrroles—From Serendipitous Discovery to Promising Heterocyclic Optoelectronic Materials. *Acc Chem Res.* 2017 Sep 19;50(9):2334-45. [<DOI>](#).
- Domagala A, Jarosz T, Lapkowski M. Living on pyrrolic foundations – Advances in natural and artificial bioactive pyrrole derivatives. *Eur J Med Chem.* 2015 Jul;100:176-87. [<DOI>](#).
- Khajuria R, Dham S, Kapoor KK. Active methylenes in the synthesis of a pyrrole motif: an imperative structural unit of pharmaceuticals, natural products and optoelectronic materials. *RSC Adv.* 2016;6(43):37039-66. [<DOI>](#).
- Fürstner A. Chemistry and Biology of Roseophilin and the Prodigiosin Alkaloids: A Survey of the Last 2500 Years. *Angew Chem Int Ed.* 2003 Aug 11;42(31):3582-603. [<DOI>](#).
- Williamson NR, Fineran PC, Gristwood T, Chawrai SR, Leeper FJ, Salmond GP. Anticancer and immunosuppressive properties of bacterial prodiginines. *Future Microbiol.* 2007 Dec;2(6):605-18. [<DOI>](#).
- Wilkerson WW, Copeland RA, Covington M, Trzaskos JM. Antiinflammatory 4,5-Diarylpyrroles. 2. Activity as a Function of Cyclooxygenase-2 Inhibition. *J Med Chem.* 1995 Sep;38(20):3895-901. [<DOI>](#).
- Rawat P, Singh RN, Ranjan A, Gautam A, Trivedi S, Kumar M. Study of antimicrobial and antioxidant activities of pyrrole-chalcones. *J Mol Struct.* 2021 Mar;1228:129483. [<DOI>](#).
- Lee H, Lee J, Lee S, Shin Y, Jung W, Kim J-H, et al. A novel class of highly potent, selective, and non-peptidic inhibitor of ras farnesyltransferase (FTase). *Bioorg Med Chem Lett.* 2001 Dec;11(23):3069-72. [<DOI>](#).
- Ahmad S, Alam O, Naim MohdJ, Shaquiquzzaman M, Alam MM, Iqbal M. Pyrrole: An insight into recent pharmacological advances with structure activity relationship. *Eur J Med Chem.* 2018 Sep;157:527-61. [<DOI>](#).
- Gholap SS. Pyrrole: An emerging scaffold for construction of valuable therapeutic agents. *Eur J Med Chem.* 2016 Mar;110:13-31. [<DOI>](#).
- Yang H-B, Selander N. Divergent Iron-Catalyzed Coupling of *O*-Acyloximes with Silyl Enol Ethers. *Chem - Eur J.* 2017 Feb 3;23(8):1779-83. [<DOI>](#).
- Brand J, Charpentier J, Waser J. Direct Alkynylation of Indole and Pyrrole Heterocycles. *Angew Chem Int Ed.* 2009 Nov 23;48(49):9346-9. [<DOI>](#).
- Ren W, Xia Y, Ji S-J, Zhang Y, Wan X, Zhao J. Wacker-Type Oxidation of Alkynes into 1,2-Diketones Using Molecular Oxygen. *Org Lett.* 2009 Apr 16;11(8):1841-4. [<DOI>](#).
- Chernichenko K, Madarász Á, Pápai I, Nieger M, Leskelä M, Repo T. A frustrated-Lewis-pair approach to catalytic reduction of alkynes to cis-alkenes. *Nat Chem.* 2013 Aug;5(8):718-23. [<DOI>](#).
- Chen L, Chen K, Zhu S. Transition-Metal-Catalyzed Intramolecular Nucleophilic Addition of Carbonyl Groups to Alkynes. *Chem.* 2018 Jun;4(6):1208-62. [<DOI>](#).

19. Trost BM, Li C-J, editors. Modern alkyne chemistry: catalytic and atom-economic transformations. Weinheim: Wiley-VCH; 2015. 402 p. ISBN: 978-3-527-33505-3.
20. Haubmann C, Hübner H, Gmeiner P. Piperidinyppyroles: Design, synthesis and binding properties of novel and selective dopamine D4 receptor ligands. *Bioorg Med Chem Lett*. 1999 Nov;9(21):3143-6. [<DOI>](#).
21. Brachet E, Belmont P. Palladium-Catalyzed Regioselective Alkynylation of Pyrroles and Azoles under Mild Conditions: Application to the Synthesis of a Dopamine D-4 Receptor Agonist. *J Org Chem*. 2015 Aug 7;80(15):7519-29. [<DOI>](#).
22. Bellina F, La Manna M, Rosadoni E. Undirected, Selective Csp²-H Alkynylation of Five-membered Heteroarenes. *Curr Org Chem*. 2021 Oct 22;25(18):2116-41. [<DOI>](#).
23. Galindo MA, Hannant J, Harrington RW, Clegg W, Horrocks BR, Pike AR, et al. Pyrrolyl-, 2-(2-thienyl)pyrrolyl- and 2,5-bis(2-thienyl)pyrrolyl-nucleosides: synthesis, molecular and electronic structure, and redox behaviour of C5-thymidine derivatives. *Org Biomol Chem*. 2011;9(5):1555. [<DOI>](#).
24. Menges N, Sari O, Abdullayev Y, Erdem SS, Balci M. Design and Synthesis of Pyrrolotriazepine Derivatives: An Experimental and Computational Study. *J Org Chem*. 2013 Jun 7;78(11):5184-95. [<DOI>](#).
25. Huo X, Chen X, Yu L, Zhang C, Zeng L, Zhu H, et al. Transition-metal-free and facile synthesis of 3-alkynylpyrrole-2,4-dicarboxylates from methylene isocyanides and propionaldehyde. *New J Chem*. 2021;45(36):16430-3. [<DOI>](#).
26. Taşdemir V, Kuzu B, Tan M, Genç H, Menges N. Copper-Catalyzed Synthesis of Fused Imidazopyrazine N-Oxide Skeletons. *Synlett*. 2019 Feb;30(03):307-10. [<DOI>](#).
27. Götzinger AC, Theßeling FA, Hoppe C, Müller TJJ. One-Pot Coupling-Coupling-Cyclocondensation Synthesis of Fluorescent Pyrazoles. *J Org Chem*. 2016 Nov 4;81(21):10328-38. [<DOI>](#).
28. Nájera C, Sydnes LK, Yus M. Conjugated Ynones in Organic Synthesis. *Chem Rev*. 2019 Oct 23;119(20):11110-244. [<DOI>](#).
29. Taşdemir V, Menges N. Gold-catalyzed Cyclization of Non-conjugated Ynone-oxime Derivatives: Incorporation of Solvent Molecule. *Asian J Org Chem*. 2020 Dec;9(12):2108-11. [<DOI>](#).
30. Bräse S, Wortal nee Nüske H, Frank D, Vidović D, de Meijere A. Intramolecular Heck Couplings and Cycloisomerizations of Bromodienes and Enynes with 1',1'-Disubstituted Methylene-cyclopropane Terminators: Efficient Syntheses of [3]Dendralenes: Efficient Syntheses of [3]Dendralenes. *Eur J Org Chem*. 2005 Oct;2005(19):4167-78. [<DOI>](#).
31. Wu TR, Chong JM. Ligand-Catalyzed Asymmetric Alkynylboration of Enones: A New Paradigm for Asymmetric Synthesis Using Organoboranes. *J Am Chem Soc*. 2005 Mar 1;127(10):3244-5. [<DOI>](#).
32. Vatanserver EC, Kılıç K, Özer MS, Koza G, Menges N, Balci M. Intermolecular heterocyclization of alkynones with 2-mercaptoacetaldehyde under metal-free conditions: synthesis of 2,3-disubstituted thiophenes. *Tetrahedron Lett*. 2015 Sep;56(40):5386-9. [<DOI>](#).
33. Naoe S, Saito T, Uchiyama M, Oishi S, Fujii N, Ohno H. Direct Construction of Fused Indoles by Gold-Catalyzed Cascade Cyclization of Conjugated Diynes. *Org Lett*. 2015 Apr 3;17(7):1774-7. [<DOI>](#).
34. Dutta S, Mallick RK, Prasad R, Gandon V, Sahoo AK. Alkyne Versus Ynamide Reactivity: Regioselective Radical Cyclization of Yne-Ynamides. *Angew Chem Int Ed*. 2019 Feb 18;58(8):2289-94. [<DOI>](#).
35. Aggarwal T, Kumar S, Verma AK. Iodine-mediated synthesis of heterocycles via electrophilic cyclization of alkynes. *Org Biomol Chem*. 2016;14(32):7639-53. [<DOI>](#).
36. Balci M. Recent advances in the synthesis of fused heterocycles with new skeletons via alkyne cyclization. *Tetrahedron Lett*. 2020 Jun;61(24):151994. [<DOI>](#).

Supplementary material

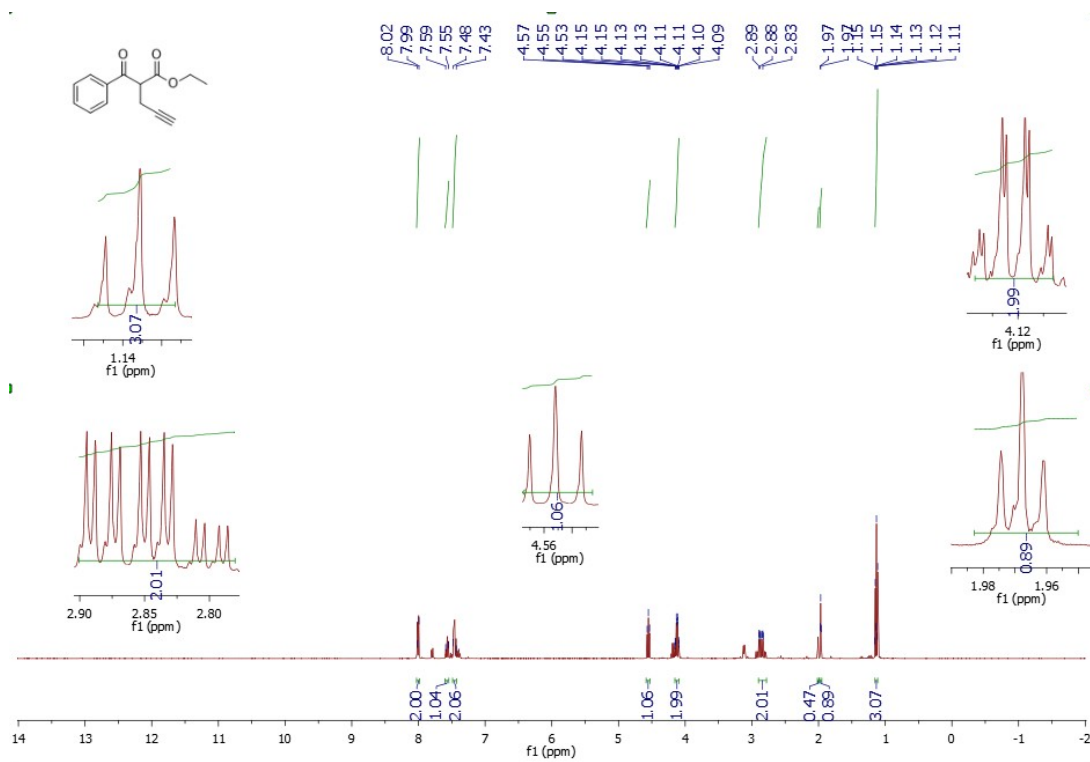
Cyclization Reactions of Non-Conjugate Ynonees with Propargyl Amine in the Presence of a Catalyst

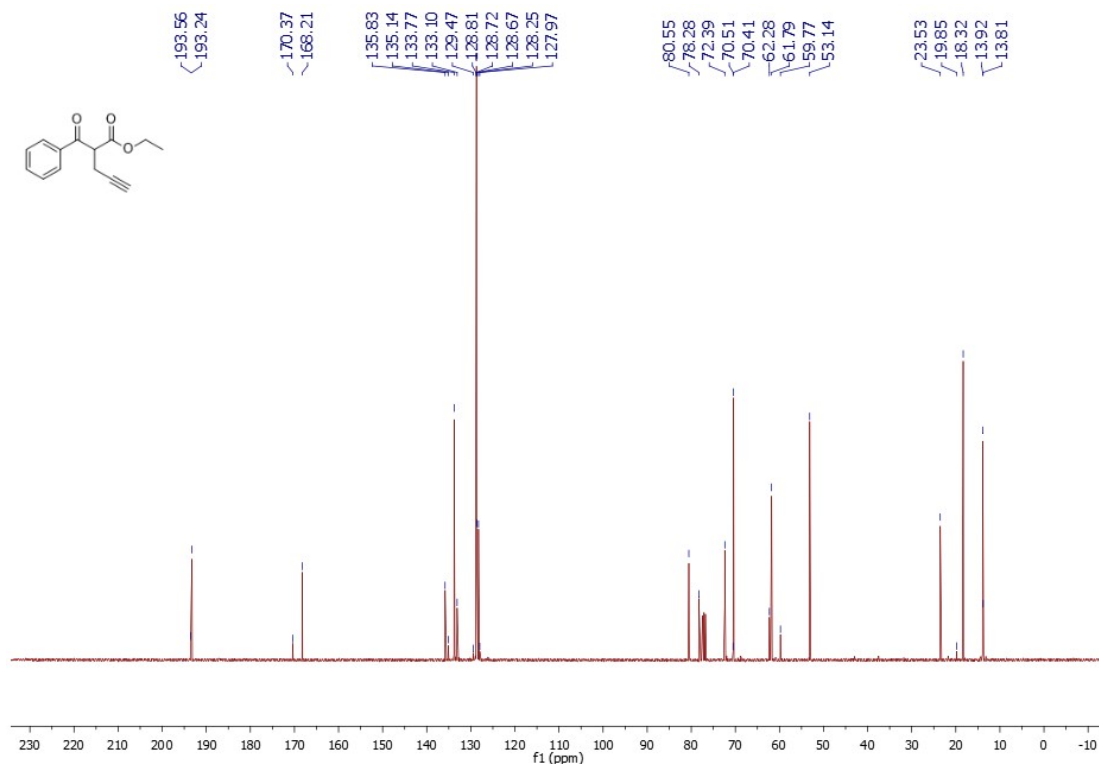
Volkan TAŞDEMİR^{1*}

Spectra

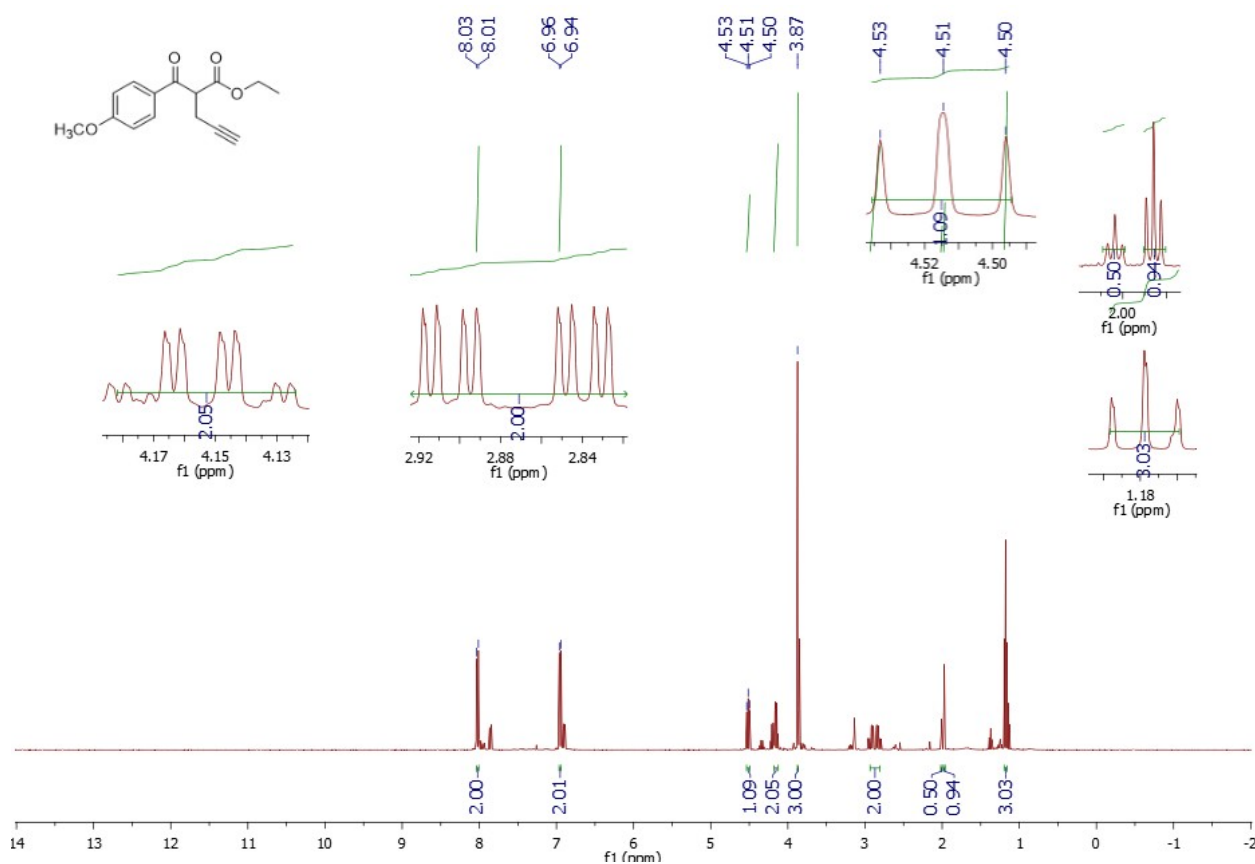
¹H-NMR, ¹³C-NMR spectra were taken with an Agilent 400 MHz (¹³C-NMR: 100 MHz) and mass spectra were taken by a ThermoScientific brand LC-MS / MS.

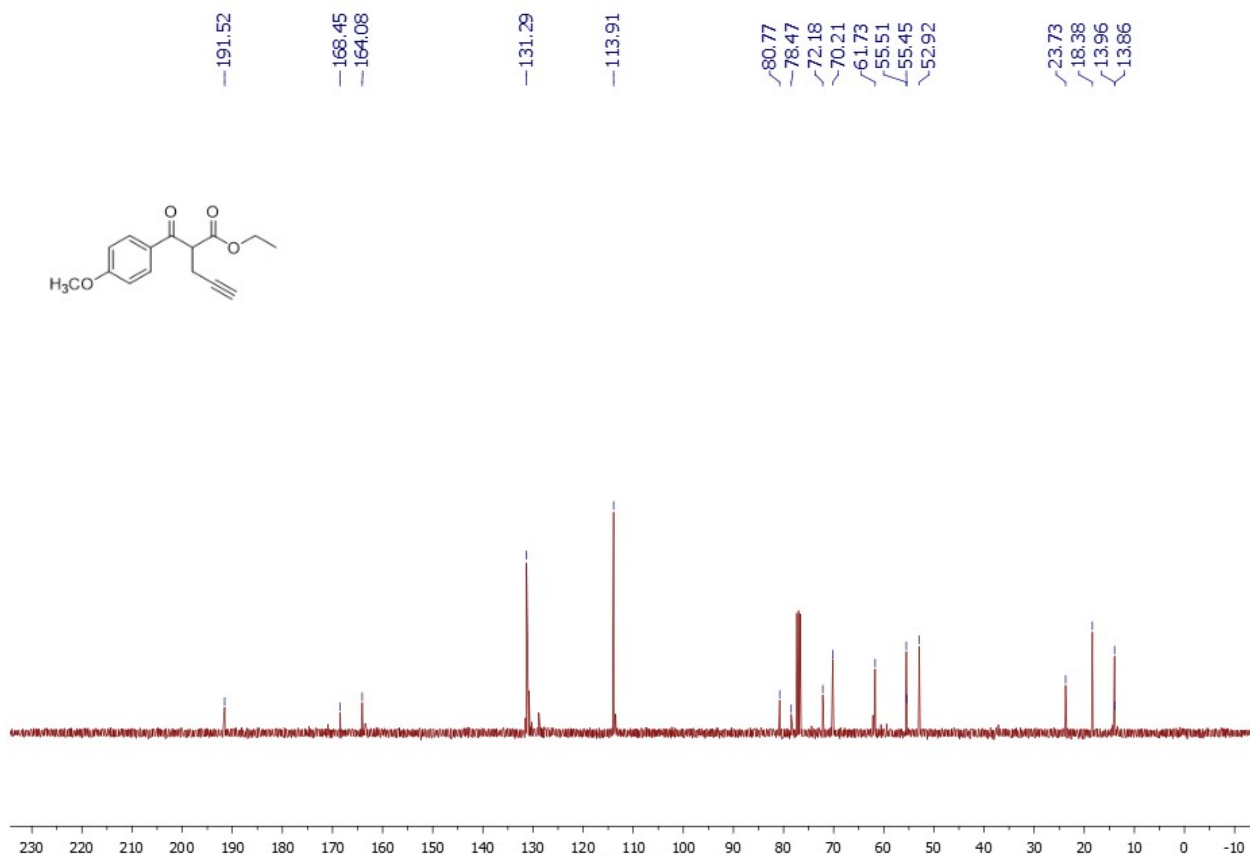
Ethyl 2-benzoylpent-4-ynoate (3a)



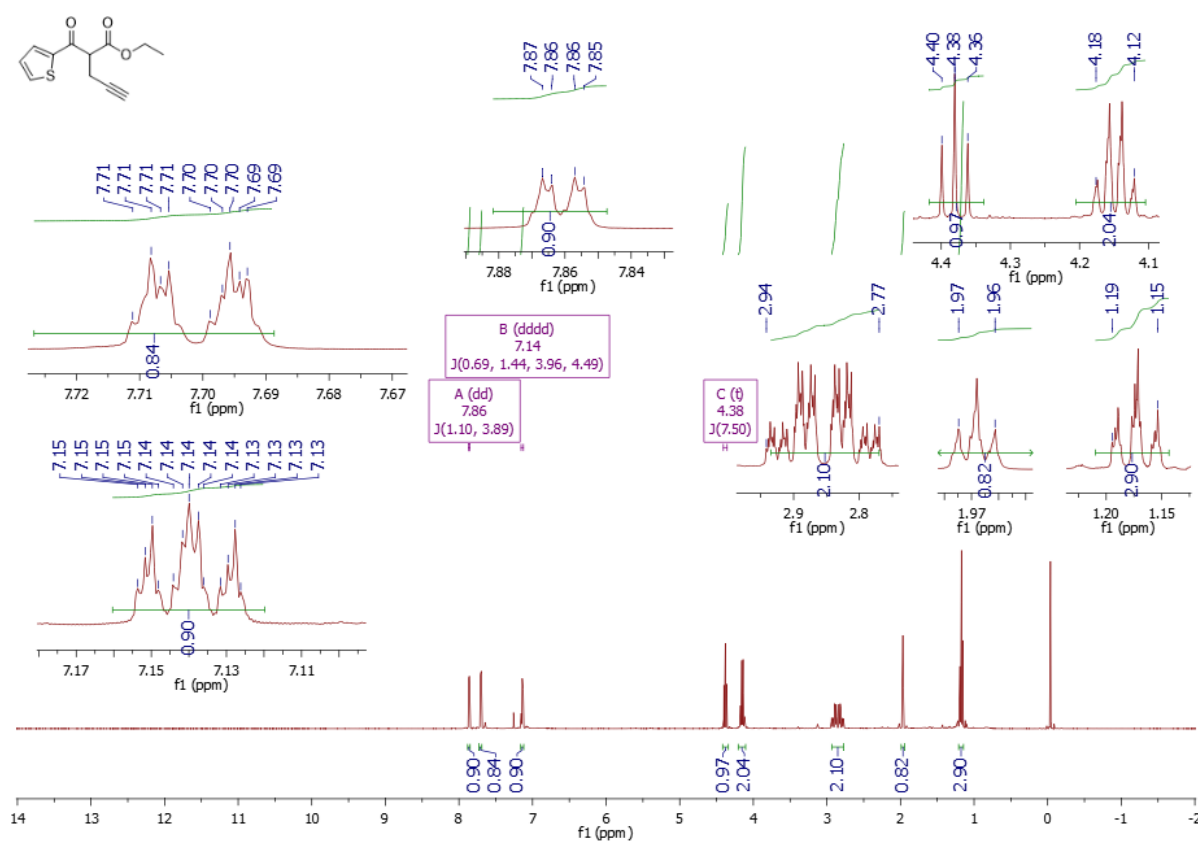


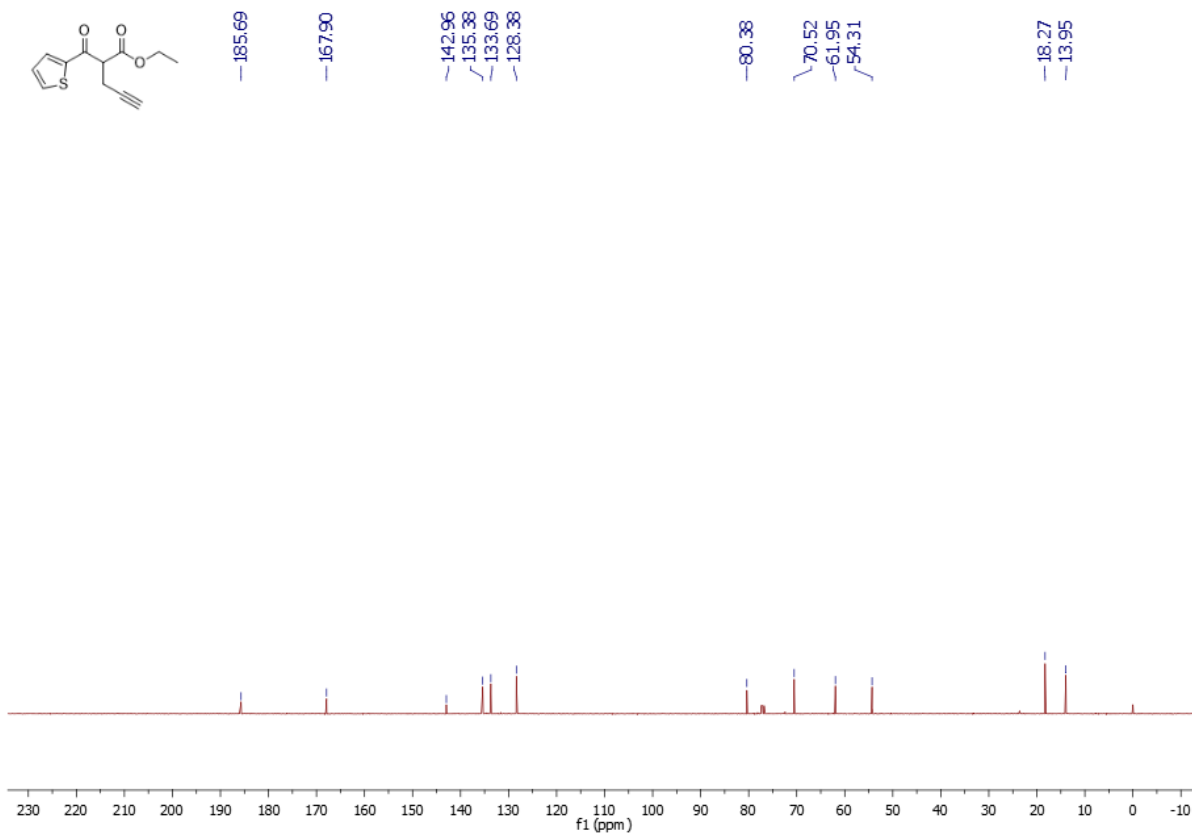
Ethyl 2-(4-methoxybenzoyl)pent-4-ynoate(3b)



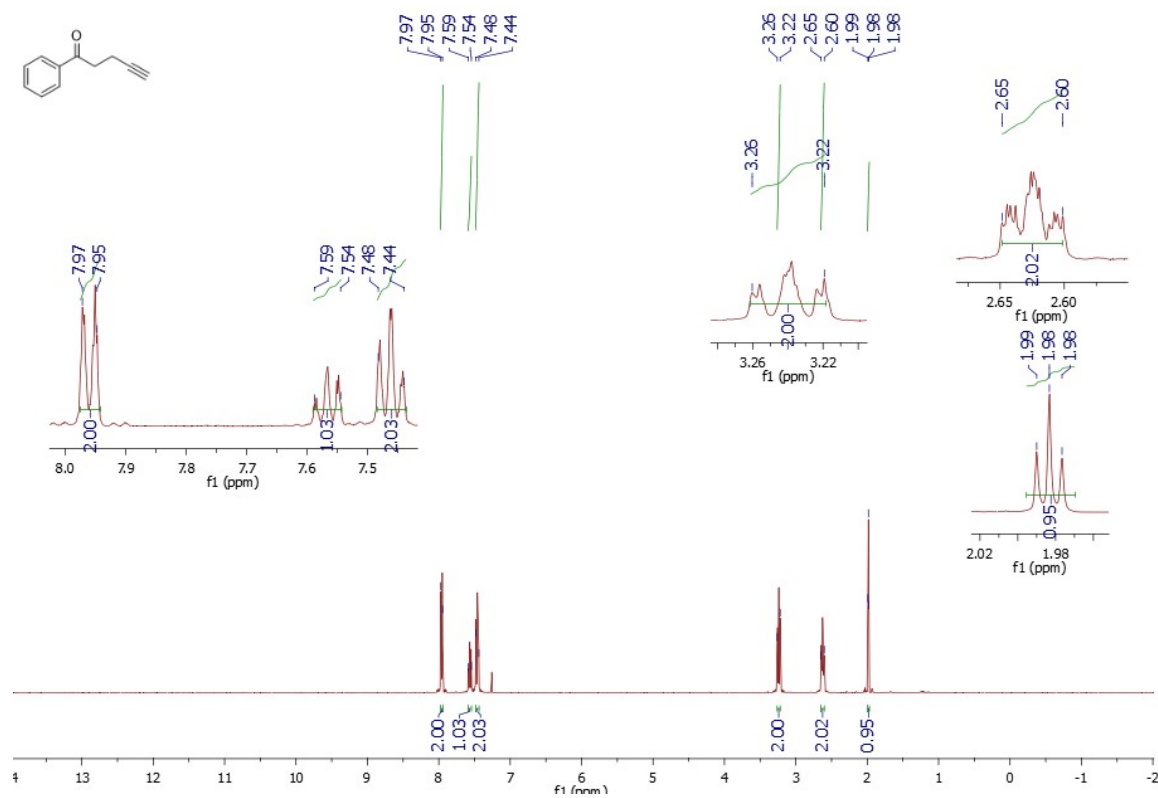


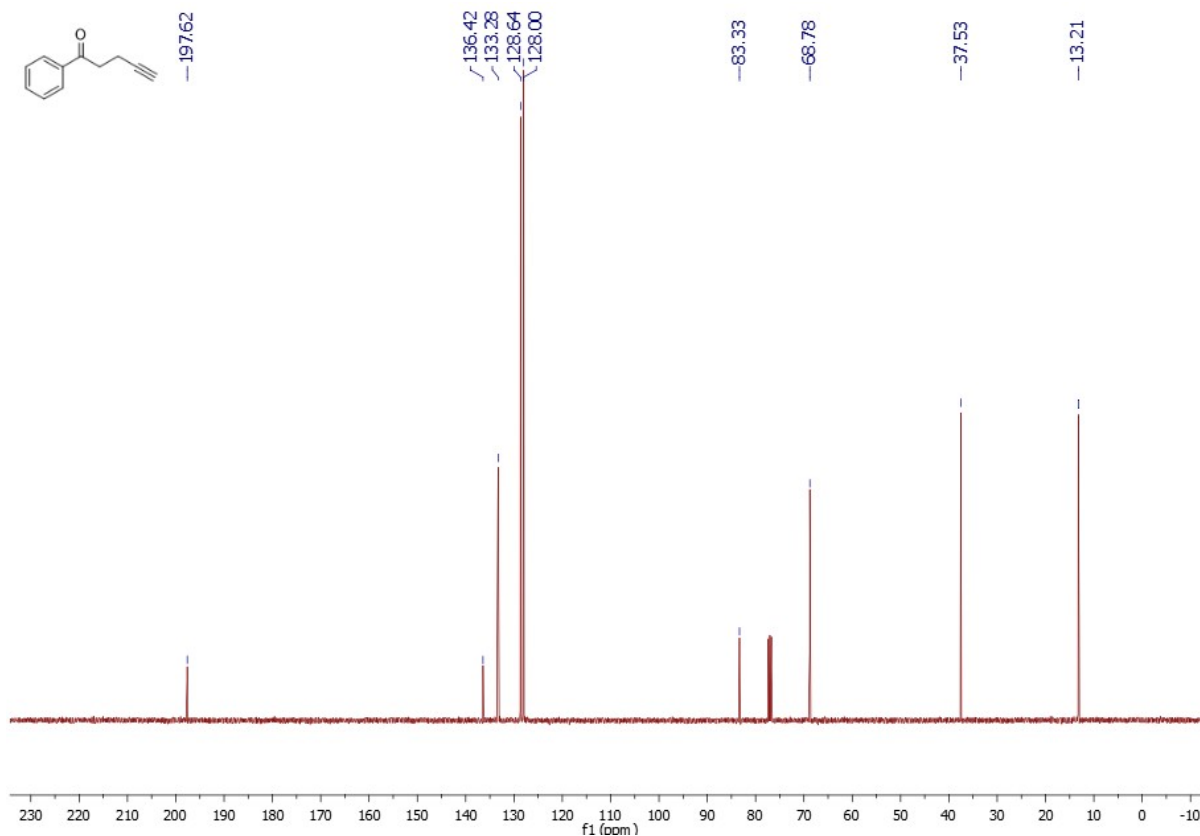
Ethyl 2-(thiophene-2-carbonyl)pent-4-ynoate(3c)



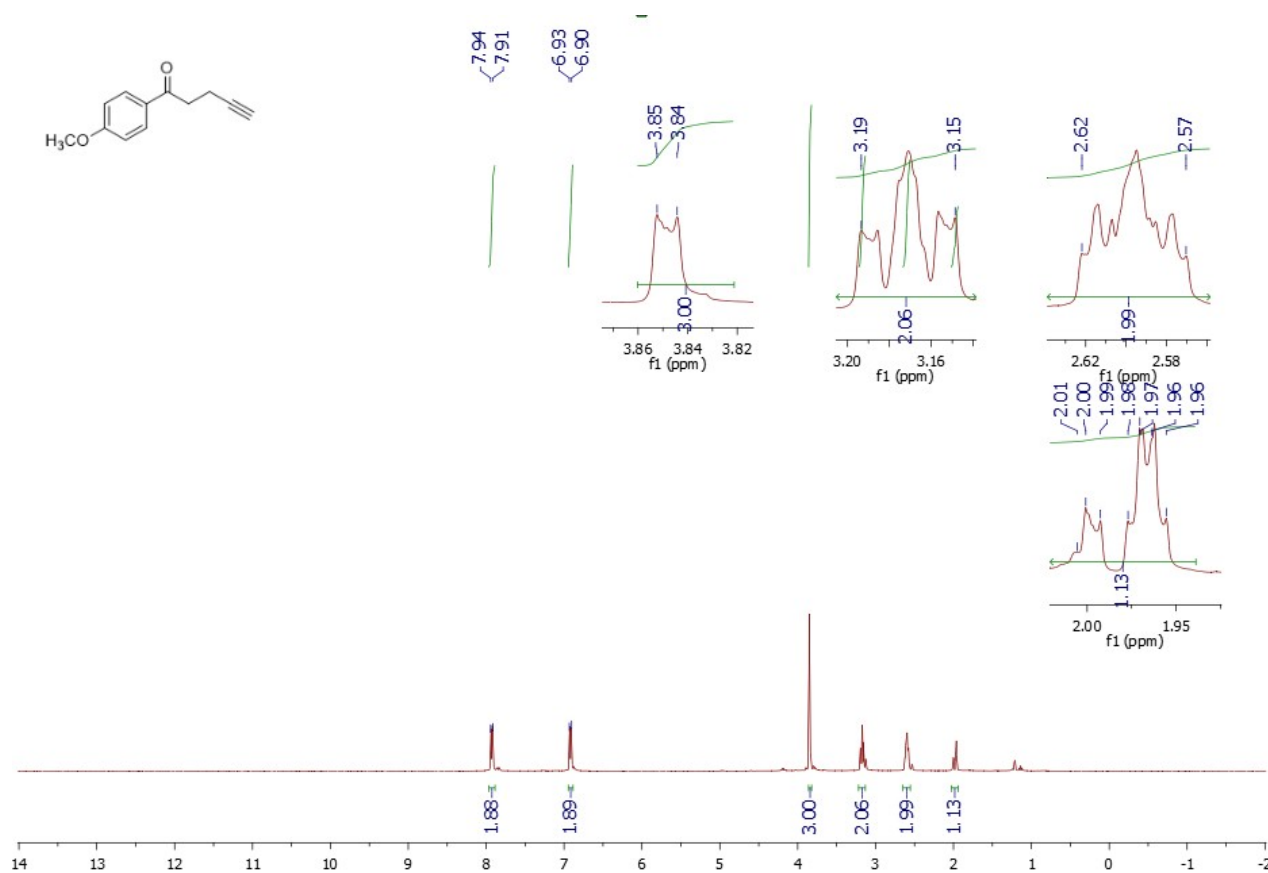


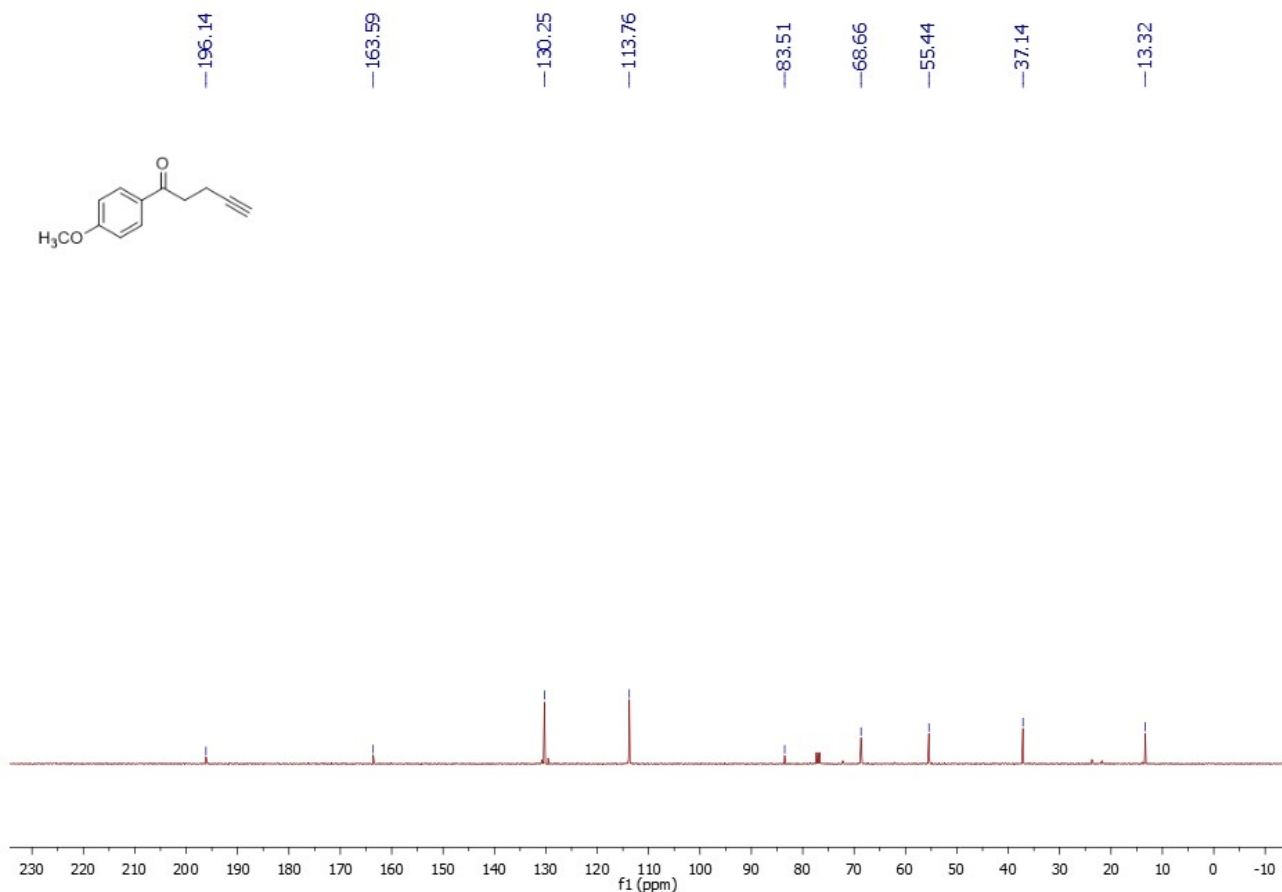
1-Phenylpent-4-yn-1-one (4a)



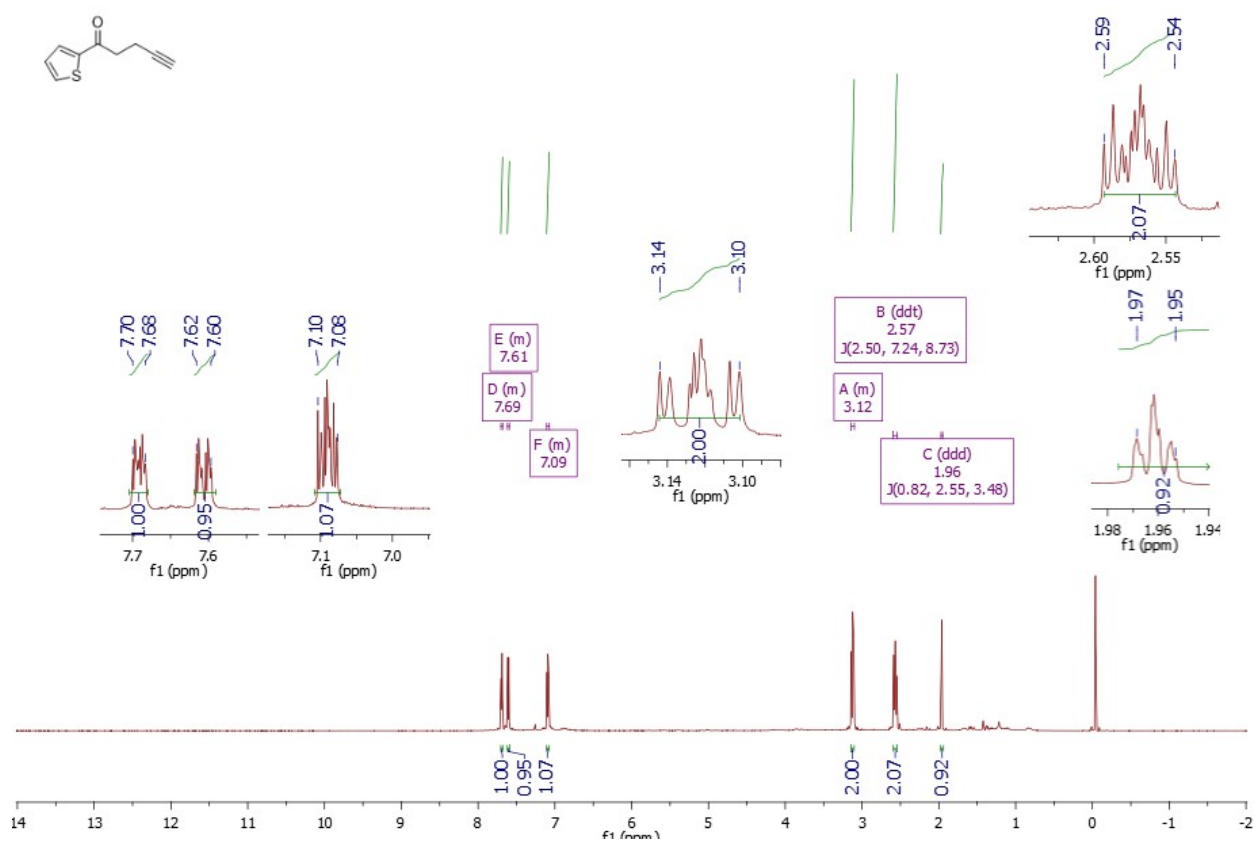


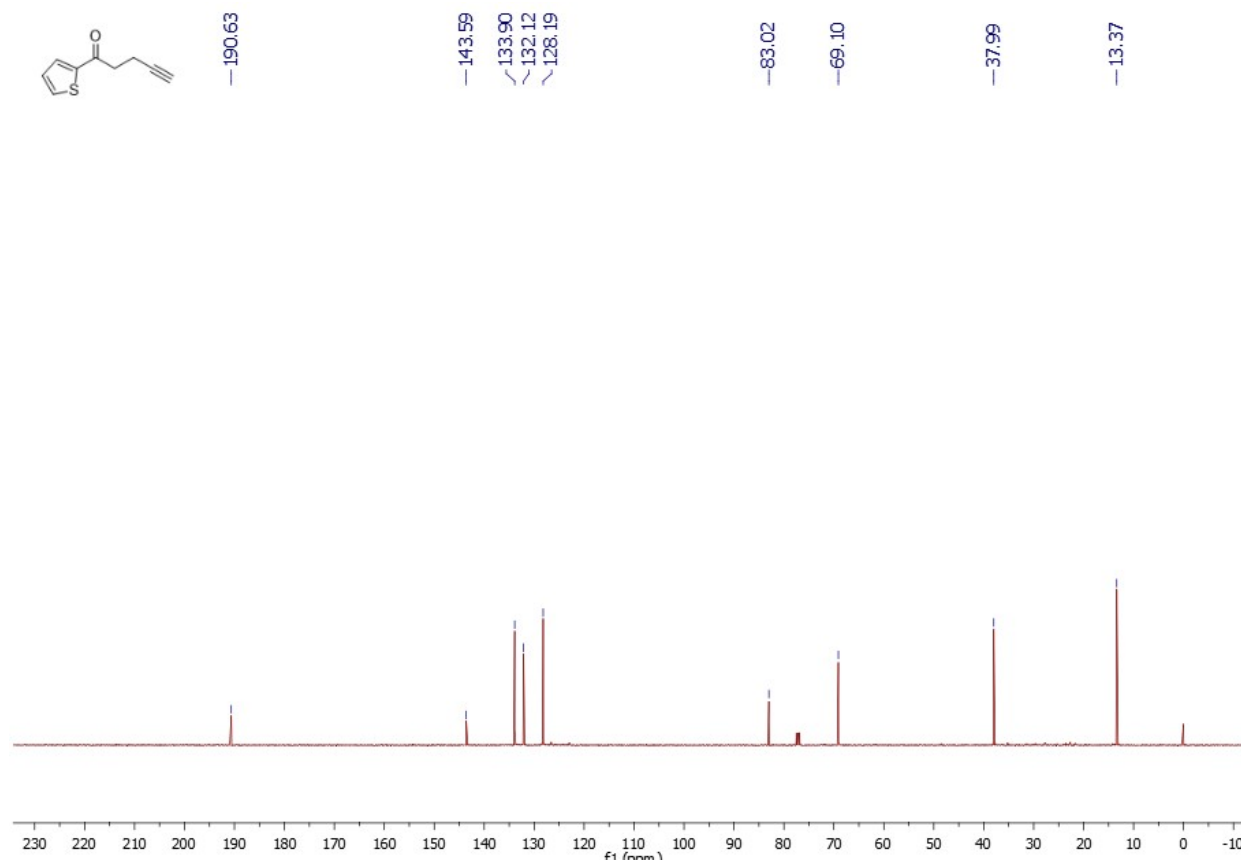
1-(4-Methoxyphenyl)pent-4-yn-1-one (4b)



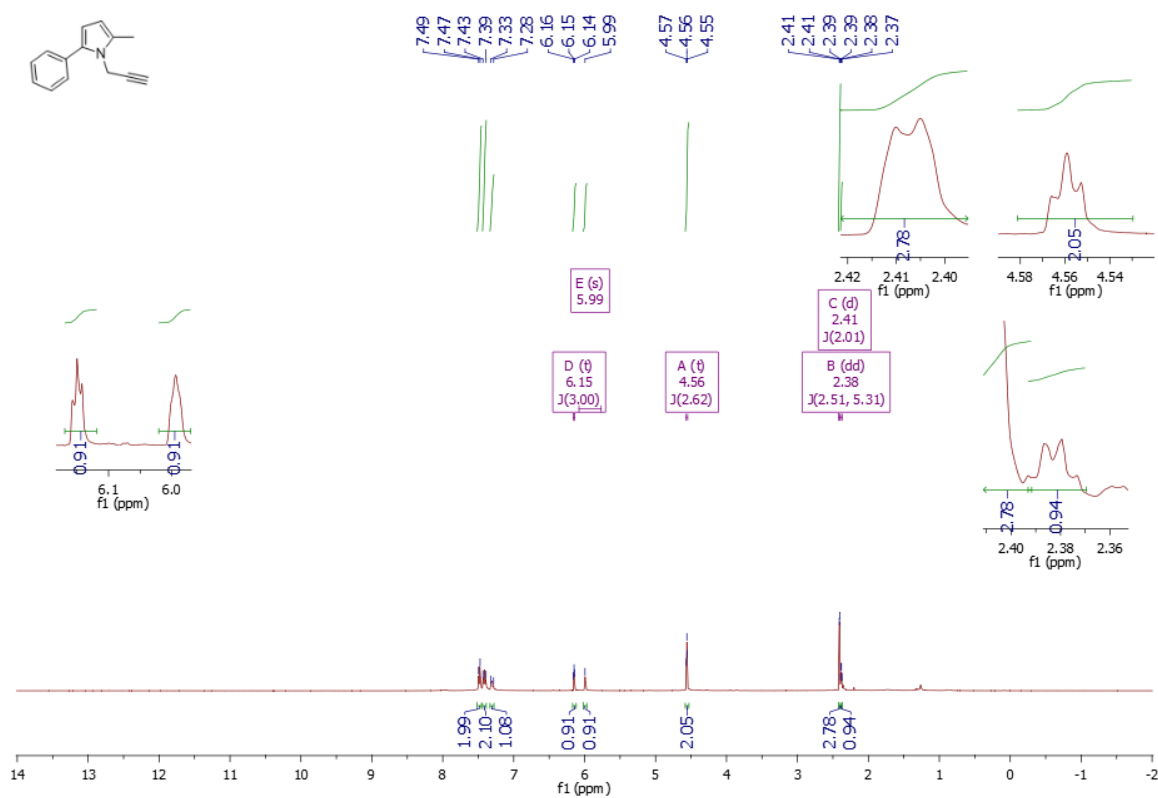


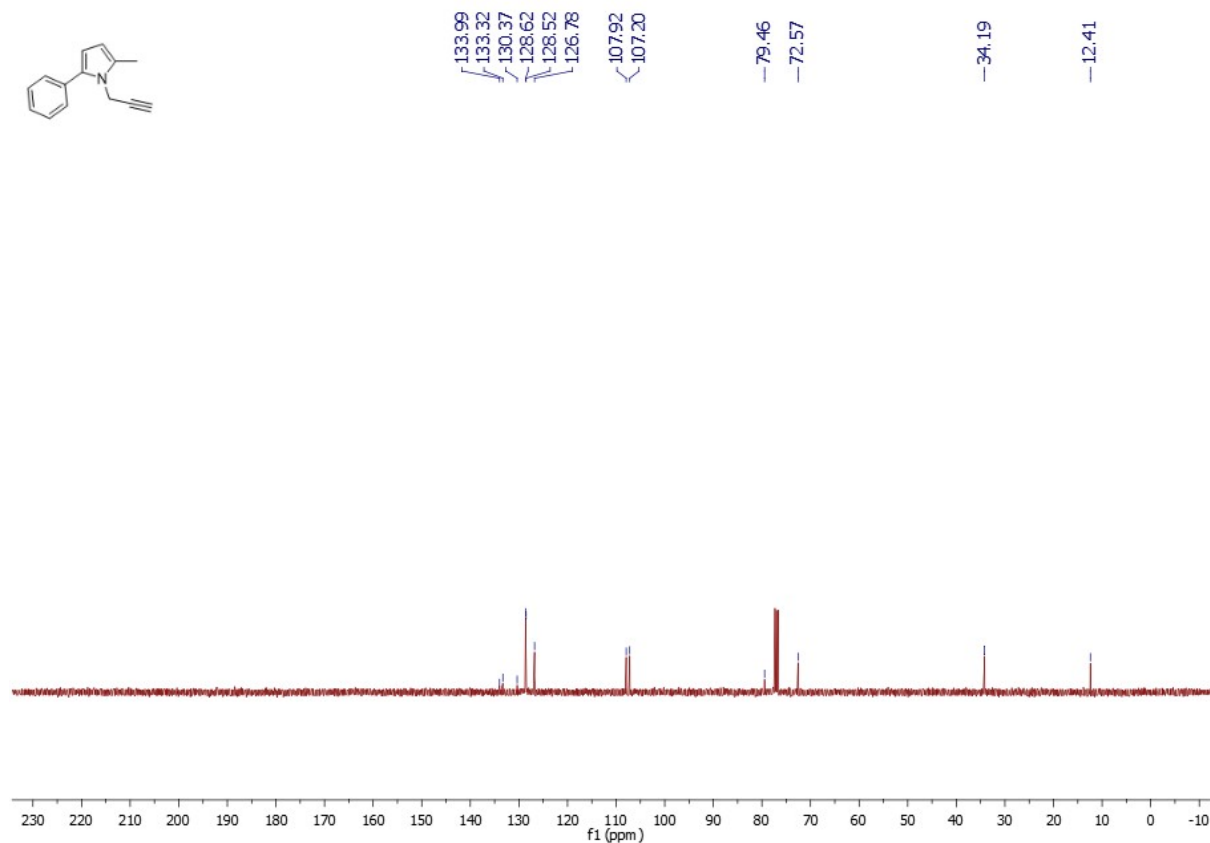
1-(Thiophen-2-yl)pent-4-yn-1-one (4c)



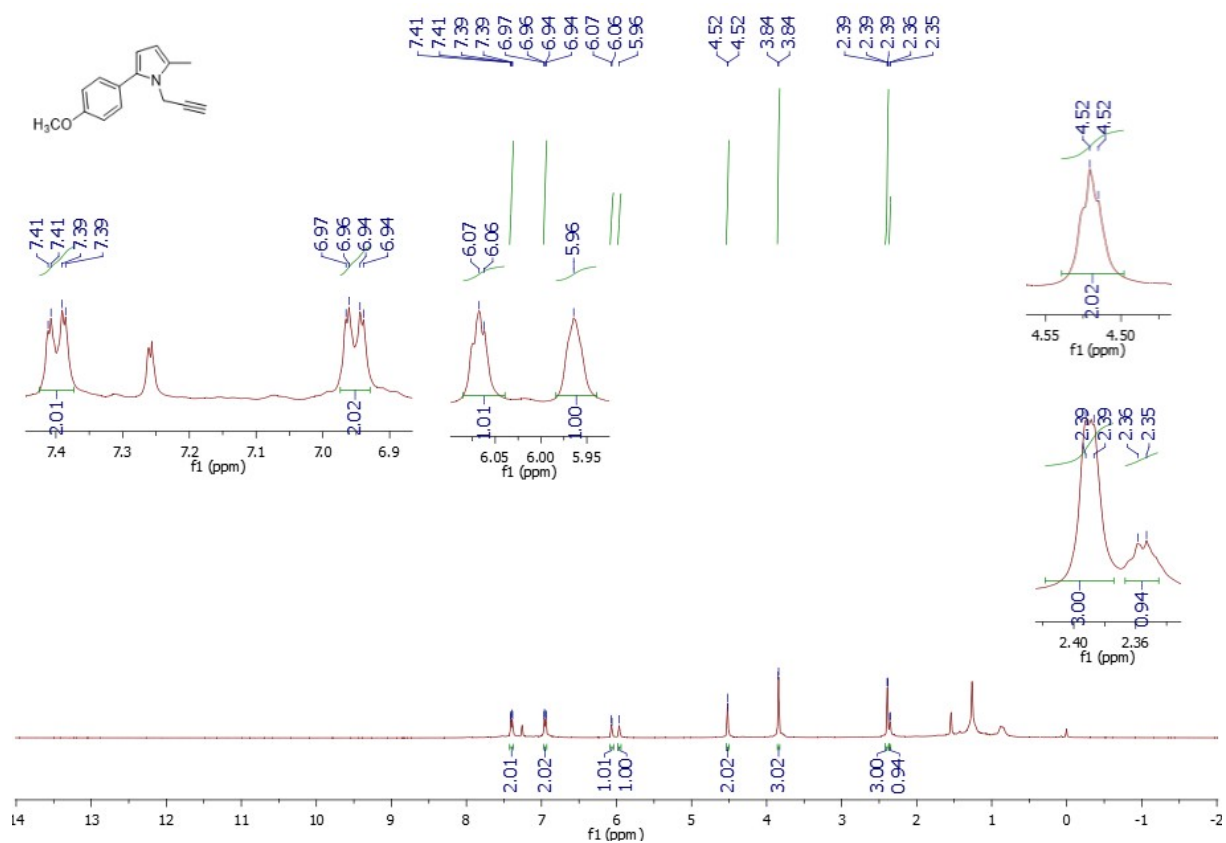


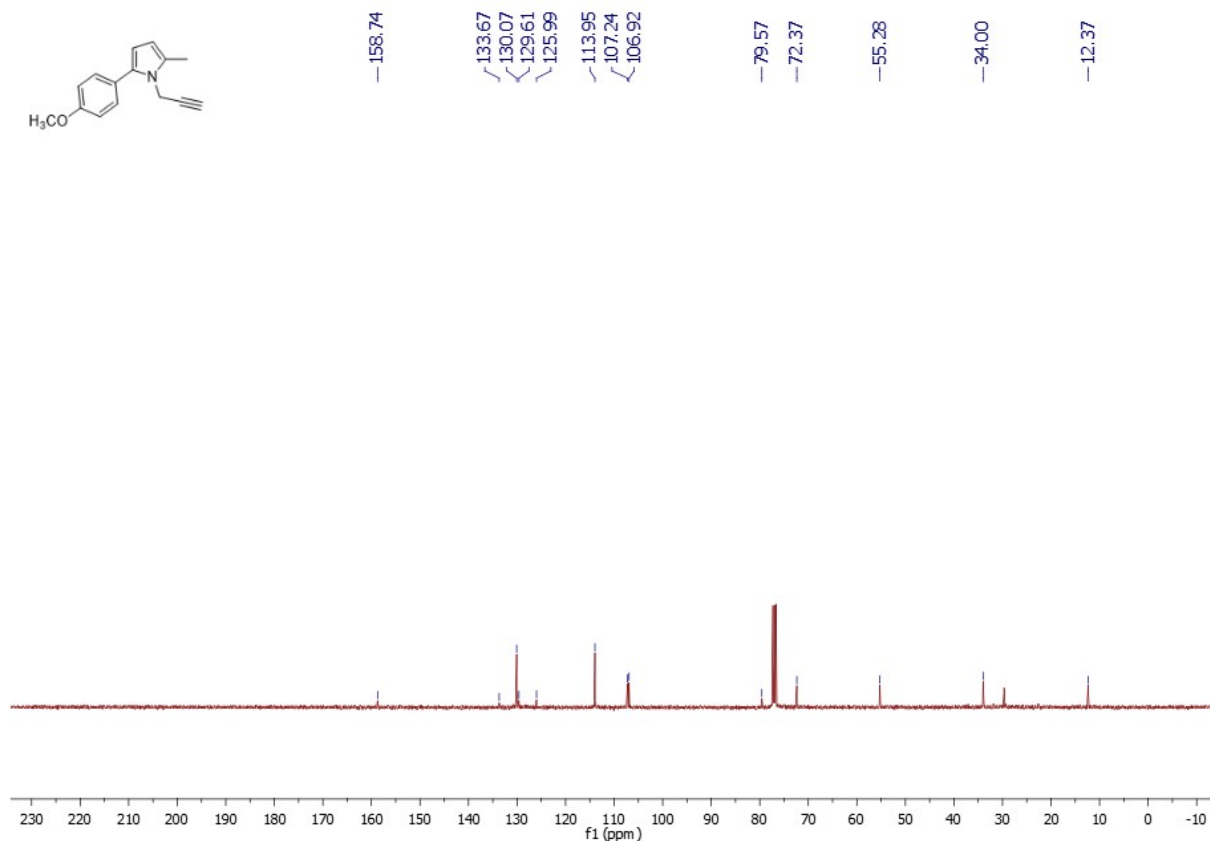
2-Methyl-5-phenyl-1-(prop-2-yn-1-yl)-1H-pyrrole (7a)



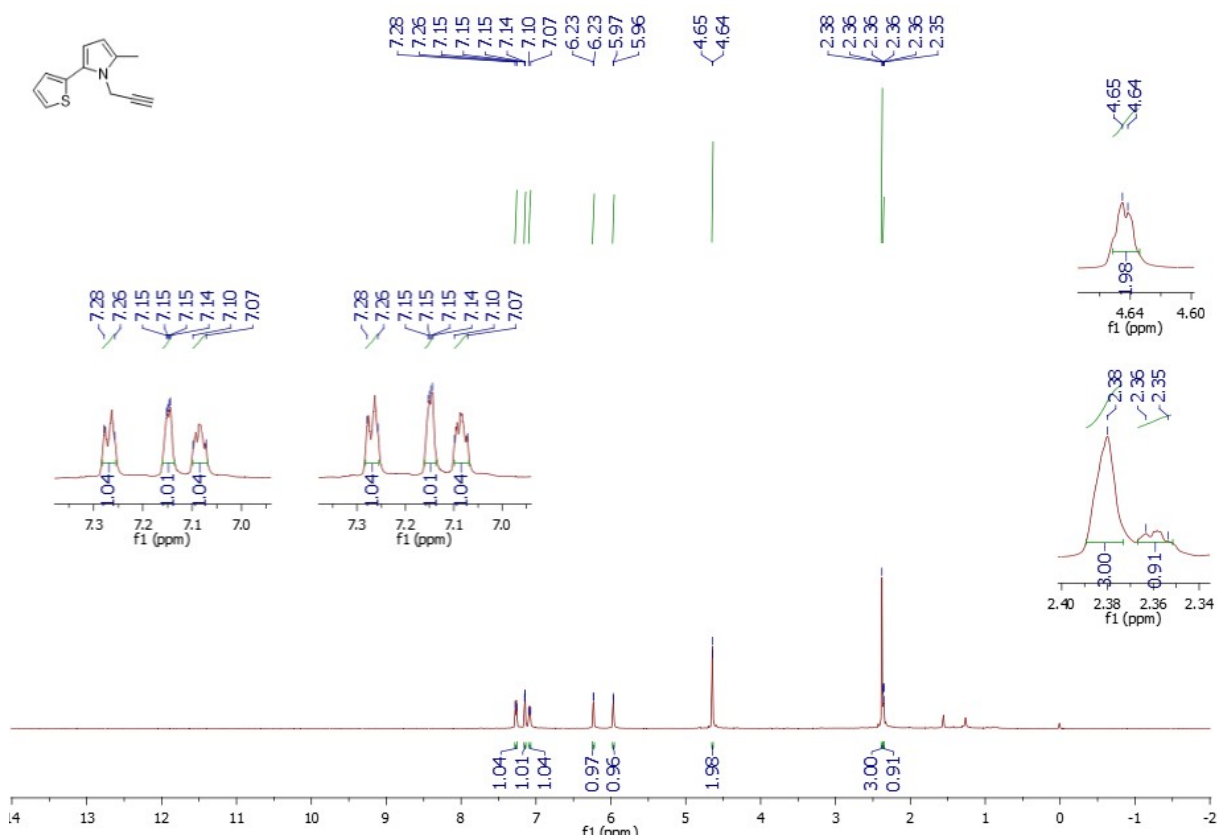


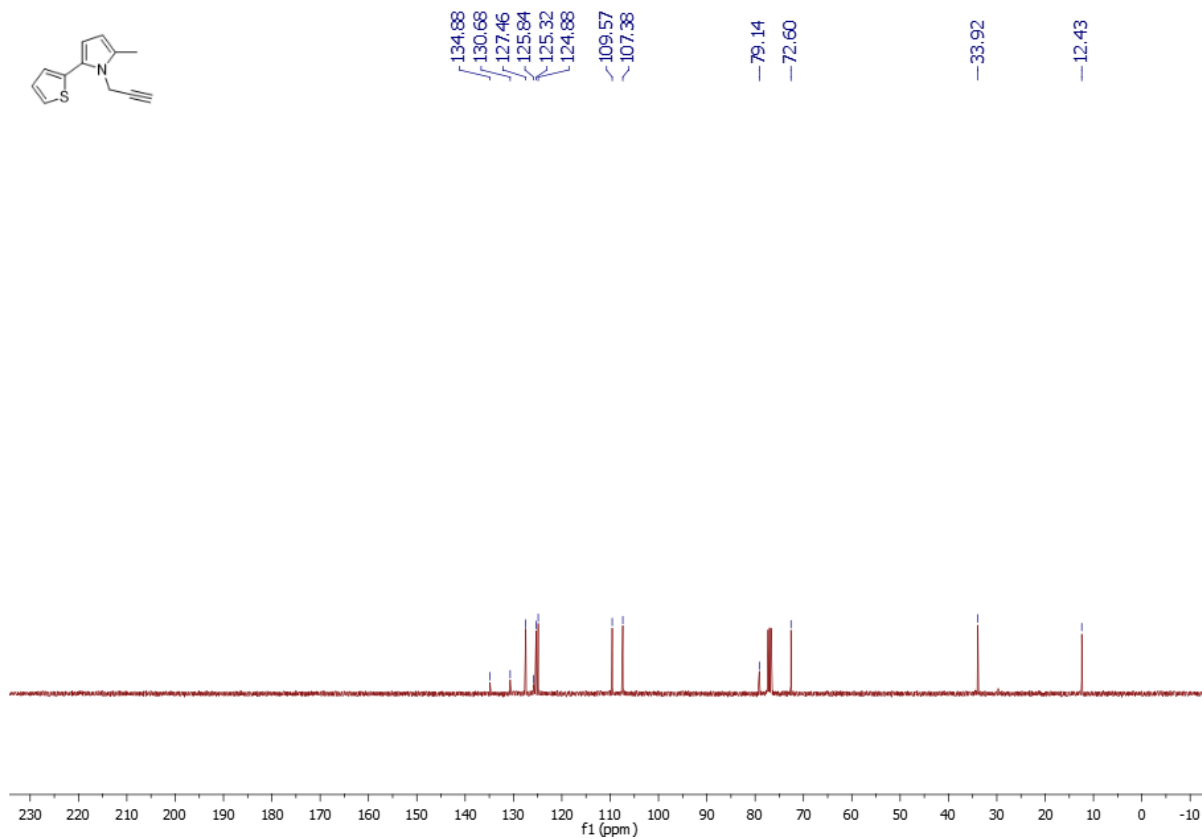
2-(4-Methoxyphenyl)-5-methyl-1-(prop-2-yn-1-yl)-1H-pyrrole (7b)





2-Methyl-1-(prop-2-yn-1-yl)-5-(thiophen-2-yl)-1H-pyrrole (7c)







Studies on Graft Copolymerization of Acrylic Acid onto Acetylated Cellulose from Maize Cob

Aliyu Danmusa Mohammed* and Aisha Kabir Ahmed

Department of Chemistry, Umaru Musa Yar'adua University, PMB 2218, Katsina, Katsina State, Nigeria

Abstract: Acrylic acid was grafted onto cellulose acetate using ceric ammonium nitrate (CAN) initiator at varying temperatures (30, 40, 50, 60, 70, and 80 °C) and reaction period of 2-6 hours. Grafting parameters like grafting yield (GY), grafting efficiency (GE) and total conversion of monomer to polymer (TC) were evaluated at different reaction conditions such as temperature, time, monomer and initiator concentration. The homopolymer was removed from the reaction mixture using Soxhlet extraction. The graft copolymer of cellulose acetate produced at 70 °C after 3 hours had the highest GY of 85%. The products were characterized by Fourier-transform infrared spectroscopy (FTIR), Scanning electron microscopy (SEM) and X-ray diffraction (XRD) analyses.

Keywords: Acrylic acid, cellulose, graft copolymerization, grafting yield, maize cob,

Submitted: January 06, 2022. **Accepted:** March 26, 2022.

Cite this: Mohammed AD, Ahmed AK. Studies on Graft Copolymerization of Acrylic Acid onto Acetylated Cellulose from Maize Cob. JOTCSA. 2022;9(2):571-8.

DOI: <https://doi.org/10.18596/jotcsa.1052157>.

***Corresponding author. Email:** aly27moh27@gmail.com. Tel: +2348032334889.

INTRODUCTION

Cellulose is the most abundant naturally occurring and renewable biopolymer in the world. It is also one of the most promising raw materials due to its availability and low cost. It is a linear polysaccharide which consists of β -D-glucopyranose units joined by β -1, 4 glycosidic linkages (1,2,3). In one repeating unit of the cellulose molecule, there is one methylol and two hydroxyl groups as functional groups (4,5).

Graft copolymerization is a commonly used method for the modification of polymer surfaces and is a vital technique employed in improving the physical and chemical properties of polymers. Chemical modification of natural polymers is normally carried out so as to produce materials with properties that are not found in starting material. In other words, it aims to produce materials with improved properties (6).

The idea of chemical modification of cellulose is to introduce functional groups into the cellulose backbone, usually achieved by substituting the

protons in the hydroxyl groups of cellulose to a varying extent. In which we can have mono, di, and tri-substituted products as shown in Figure 1.

Cellulose grafted with acrylic acid or acrylamide are hydrophilic in nature. Thus, they have a high water absorption capacity. These properties have made them suitably used as body fluid absorbents as well as in medical applications (7). The grafting of water soluble vinyl monomers onto amine-treated cotton fiber produces a graft copolymer with enhanced moisture sorption ability that can be used in athletic wear. Cellulose graft copolymers obtained by grafting vinyl monomers with functional groups such as acrylamide, acrylic acid, and acrylonitrile have been used in the adsorption of hazardous pollutants such as dyes or heavy metals from aqueous solution (8,9,10).

Depending on the chemical structure of the monomer grafted onto cellulose, graft copolymers gain new properties such as water absorption, improved elasticity, hydrophilic or hydrophobic character, ion-exchange and dye adsorption

capabilities, heat resistance, thermosensitivity, pH sensitivity, antibacterial effect, resistance to microbiological attack, etc. (11,12).

Gurdag *et al.* (1997) (13) reported the grafting of acrylic acid onto cellulose using ceric ammonium nitrate (CAN) initiator in aqueous nitric acid solution at 30, 50, 70, and 90 °C, respectively. During the reaction period of 30-180 minutes, about 45% of the AA was polymerized at 90 °C. After 180 minutes, the maximum grafting yield was obtained at 30°C, which has the highest water retention capacity. Hiltunen *et al.* (2011) (14) have reported the preparation of cellulose-graft-polyacrylamide and cellulose-graft-poly (N,N-dimethylacrylamide) copolymers by single-electron transfer living radical polymerization (SET-LRP) using DMSO as solvent.

According to some reports, maize is one of the world's most widely planted crops, which accounts for around 800 million tons every year, and for every 100 kg of maize grain, 18 kg is the cob (15). Ordinarily, maize cobs are often discarded after harvest as unwanted residues in the environment.

In this work, however, extracted cellulose from the residual waste (maize cob) is acetylated before grafting with acrylic acid. The grafting parameters of the copolymerization reaction are studied. Acetylation of polysaccharides before graft copolymerization produces a copolymer with a comb-like structure that is able to retain aqueous substances several times their weight (16). Chemical modification of such materials could find applications in waste water treatment, superabsorbents, etc (16). The samples being used in this work are abundant waste from the plant's harvest in different parts of the world. The environmental concern over hazardous and toxic materials in waste water treatment would suitably encourage the use of ecofriendly materials made from cellulose for important applications.

EXPERIMENTAL

Materials and Methods

The maize cob is an agricultural waste obtained from farms in Katsina State, Nigeria. Acrylic acid, ceric ammonium nitrate, sodium hydroxide, sodium hypochlorite, hydroquinone, potassium hydroxide, pyridine, and acetic anhydride were obtained from Sigma Aldrich.

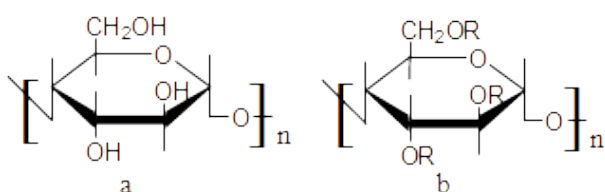


Figure 1: (a) Cellulose and (b) Substituted cellulose.

Delignification and Extraction of Cellulose from Maize Cob

The procedure reported by Azubuike and Okhimifen (16) was used with little modification. The maize cob was crushed to a finer size and 25 g was treated with an aqueous solution of sodium hydroxide (250 cm³, 2% w/v) in a stainless steel vessel immersed in a water bath at 100°C for 3h. Further digestion was carried out with an aqueous solution of sodium hydroxide (200 cm³, 17.5 %w/v) for 1 h at 80 °C. After washing with distilled water, the remaining solid was filtered and dried in an oven at 60 °C for 16 h.

Bleaching of Extracted Cellulose

The extracted cellulose was bleached with an aqueous solution of sodium hypochlorite (62 cm³, 3.2 %w/v) in a stainless steel vessel at 40 °C for 1.5 h. The bleached sample was thoroughly washed with distilled water until a neutral pH was obtained. The sample was then filtered and dried in an oven at 60 °C for 16 h. The dried product was milled and sieved through a mesh (500 µm) and further dried at 60 °C for 1 h. It was then stored in a tightly closed container.

Acetylation of Extracted Cellulose

Cellulose (5 g) was dried in an oven for 24 h at 50 °C and mixed with pyridine (40 g). After stirring for 5 minutes, acetic anhydride (20 g) was added to the mixture, and the temperature was increased to 100 °C within 15 minutes and held for 150 minutes. The final product was precipitated in ethanol and the white acetylated product was dried and ground to a finer size before testing (15). Equation (1) was used to determine the degree of substitution of the samples (17).

$$Ds = \frac{162(Db)}{4300 - 42 - (Db)} \quad (\text{Eq. 1})$$

Where *Db* is the percentage of acetyl group = (value for blank – value for sample)
DS = degree of substitution

Grafting of Acrylic Acid onto Acetylated Cellulose

The cellulose acetate (1.25 g) was poured into 150 mL distilled water in a 250 cm³ three-necked round-bottom flask equipped with magnetic stirrer, temperature controlled oil bath, reflux condenser, and nitrogen inlet. Different amounts of CAN (0.3–0.8 g), followed by addition of acrylic acid (AA) (1.25–2.0 cm³) were used. The reaction was carried out in a nitrogen atmosphere for 2–6 h at varying temperatures of 30–80 °C and terminated by the addition of hydroquinone. The product was poured into cold distilled water with stirring and kept overnight at ambient temperature. It was then filtered, washed with distilled water, dried at 50 °C and weighed. The product was extracted with

acetone using soxhlet extraction technique to remove the homopolymer. The grafted sample was dried at 60 °C to a constant weight. Grafting Yield (%GY), Grafting Efficiency (%GE) and Total Conversion (%TC) were obtained as follows: (18).

$$GY\% = \frac{W3 - W1}{W1 \times 100} \quad (\text{Eq. 2})$$

$$GE\% = \frac{W2 - W1}{W4 \times 100} \quad (\text{Eq. 3})$$

$$TC\% = \frac{W3 - W1}{W2 - W1 \times 100} \quad (\text{Eq. 4})$$

Where W1 is the weight of original cellulose acetate (CA) before reaction; W2 is the weight of grafted CA before extraction; W3 is the weight of grafted product after extraction, and W4 is the weight of monomer charged.

Grafting Parameters

Effect of Time

Table 2 shows that the grafting parameters (% GY, %GE, and %TC) increase with reaction time and then decrease at higher reaction times. This is due to an increase in the number of free radicals on the CA backbone, resulting in high number of reactive sites that interact with monomers there by increasing the grafting parameters. At longer reaction times, however, the three parameters decrease because of the high tendency of free radical coupling, leading to an increase in the rate of termination (16).

Effect of Temperature

Grafting reaction was carried out by varying the temperature from 30 to 80 °C, and the result is given in Table 2. It was observed that %GY of the AA grafted product increases with an increase in temperature. However, at 70 °C and above, the increase in temperature causes a decrease in the % GY. The trend could be due to a higher rate of free radical chain termination at higher temperatures and times. The grafting efficiency comparatively

RESULTS AND DISCUSSION

The crude biomass, apart from cellulose, contains other components. Table 1 shows the composition of each component in the crude biomass.

Acetyl content

Equation (1) was used to determine the acetyl content of the modified cellulose and was found to be 28.24% as indicated in Table 1 (3).

Table 1: Chemical Composition of Maize Cob.

Component	wt (%)
Hemicellulose	40.44
Cellulose	25.56
Lignin	34.00
Acetyl content	28.24

increases with rise in temperature, the trend, however, changes after 60 °C; an increase in temperature at a shorter reaction time favors high GE, but decreases at longer time of reaction. This may be due to the high tendency to increase the chain length of the graft copolymers over a longer time rather than increasing the reaction sites. A similar trend is observed in total conversion yield (16).

Homopolymer Formation

The variation of homopolymer formation was also investigated at different reaction times and temperatures and the results are given in Table 2. Graft copolymerization via free radical technique basically leads to homopolymerization as a side reaction. From the results, it can be observed that homopolymers are being formed along with the copolymers. Homopolymer formation is reported at higher reaction time and reaction temperature to some extent. The highest amount of homopolymer (0.54 g) is obtained at 60°C, at a 2 h reaction time. However, at higher temperatures, the homopolymer amount decreases even at a longer time of reaction.

Table 2: Effect of time and temperature on the grafting parameters.

SN	Temp (°C)	Sample Code	Time (h)	Wt of HP(g)	%GY	%GE	%TC
1	30	CA-g-PAA-01	2	0.09	12.80	64.00	12.08
2		CA-g-PAA-02	3	0.10	15.20	65.52	14.01
3		CA-g-PAA-03	4	0.11	16.00	64.52	14.98
4		CA-g-PAA-04	5	0.06	21.60	81.82	15.94
5		CA-g-PAA-05	6	0.05	24.00	85.71	16.91
6	40	CA-g-PAA-06	2	0.25	12.00	37.50	19.32
7		CA-g-PAA-07	3	0.26	15.20	42.22	21.74
8		CA-g-PAA-08	4	0.22	20.00	53.19	22.71
9		CA-g-PAA-09	5	0.20	24.00	60.00	24.15
10		CA-g-PAA-10	6	0.15	32.00	72.73	26.57
11	50	CA-g-PAA-11	2	0.15	22.40	65.12	20.77
12		CA-g-PAA-12	3	0.14	23.60	66.84	24.98
13		CA-g-PAA-13	4	0.31	25.80	69.04	25.71
14		CA-g-PAA-14	5	0.34	26.00	71.04	26.09
15		CA-g-PAA-15	6	0.30	29.00	75.45	26.57
16	60	CA-g-PAA-16	2	0.54	3.20	6.90	28.02
17		CA-g-PAA-17	3	0.05	36.00	90.00	24.15
18		CA-g-PAA-18	4	0.10	60.00	88.24	41.06
19		CA-g-PAA-19	5	0.17	58.40	81.11	43.48
20		CA-g-PAA-20	6	0.33	59.20	69.16	51.69
21	70	CA-g-PAA-21	2	0.19	85.60	84.92	24.12
22		CA-g-PAA-22	3	0.12	77.60	88.99	47.66
23		CA-g-PAA-23	4	0.08	72.80	91.92	54.83
24		CA-g-PAA-24	5	0.40	24.80	43.66	58.30
25		CA-g-PAA-25	6	0.20	24.00	60.00	60.87
26	80	CA-g-PAA-26	2	0.11	11.20	56.00	12.08
27		CA-g-PAA-27	3	0.06	11.20	57.00	13.66
28		CA-g-PAA-28	4	0.18	10.60	28.00	17.08
29		CA-g-PAA-29	5	0.40	7.00	27.27	26.57
30		CA-g-PAA-30	6	0.30	6.00	21.00	36.23

Effect of Initiator Concentration

The effect of initiator concentration was also investigated and is presented in Table 3. The initiator concentration is varied from 0.55 to 0.918 mmolL⁻¹ at constant AA conc. (11.72 mmolL⁻¹), at 30 °C and a varied time of 2-6 h.

The rate of reaction increases with an increase in initiator concentration because of the increase in the number of free radicals generated on the CA backbone. This results in the increase in the rate of monomer conversion. The rate of reaction rises and then decreases at higher initiator concentration due to initial homopolymerization which occurs at longer reaction time and also decreases the mobility of monomer in the viscous grafted polymer solution (19).

At higher reaction time, however, the monomers tend to decompose, which decreases the number of reactive sites created and, therefore, the percentage grafting and grafting efficiency fall. The termination of growing copolymer radicals was dominated over propagation with CAN concentration, leading to a decrease in %GY. This is due to the difficulty in hydrogen abstraction from the substrate. The decrease in grafting parameters (%GY and %GE) at high CAN concentration could be due to the formation of more initiating radicals and consequently increase their changes to participate in either primary or secondary recombination with each other, or may react with the propagating polymer radicals, which could contribute to termination (20).

Table 3: Variation of CAN concentration at constant temperature 30 °C and AA concentration 11.72 mmol.

SN	CAN Conc. (mmol)	Time (h)	Wt of HP(g)	%GY	%GE	%TC
1	0.55	2	0.15	20.00	62.50	19.32
2		3	0.06	18.40	79.31	14.01
3		4	0.10	16.80	67.74	14.98
4		5	0.14	15.20	57.58	15.94
5		6	0.26	7.20	25.71	16.91
6	0.916	2	0.50	0.00	0.00	24.15
7		3	0.46	14.40	28.13	30.92
8		4	0.10	28.00	77.78	21.74
9		5	0.07	28.00	83.33	20.29
10		6	0.04	19.20	85.71	13.53

CHARACTERIZATION

FTIR Analysis

Figure 2 shows the FTIR spectra of the extracted cellulose, acetylated cellulose and grafted cellulose acetate. Stretching vibration at 3324 cm⁻¹ is due to OH stretching vibration in the cellulose molecules; C-H stretching vibration is observed at 2908 cm⁻¹ while the C-O-C stretching band is observed at 1029 cm⁻¹.

The acetylated cellulose was observed to have the following absorption peaks; absorption peak at 1741

cm⁻¹ due to C=O stretching vibration of the acetyl group present on the cellulose backbone.

In the grafted product, however, there is an observed shift of OH stretching mode from 3324 to 3342 cm⁻¹ and a shift in the C=O stretching peaks from 1741 cm⁻¹ of the acetylated product to 1718 cm⁻¹ of the graft copolymer. The changes above have shown that cellulose has been successfully transformed from its native form to an acetylated product and then to a graft copolymer with acrylic acid.

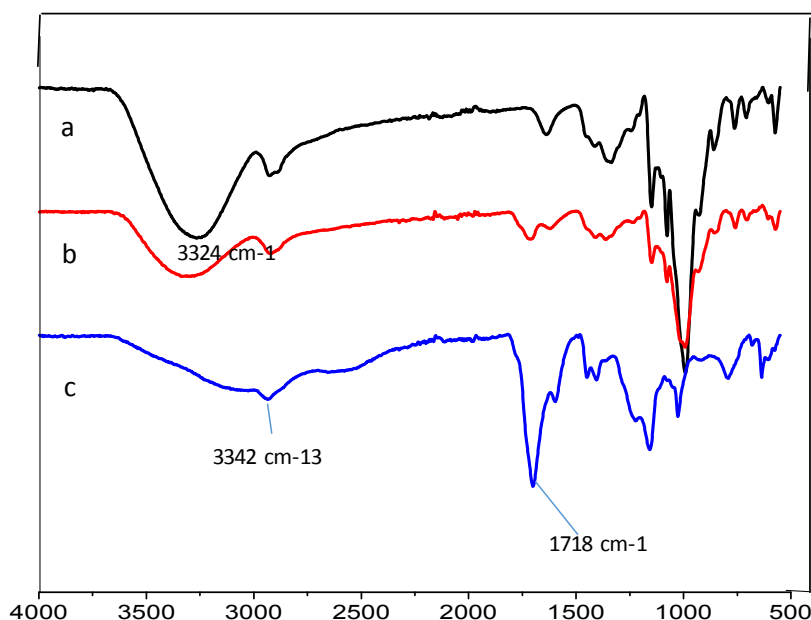


Figure 2: FTIR spectral data of (a) extracted cellulose, (b) acetylated cellulose and (c) CA-g-PAA.

Scanning Electron Microscopy (SEM) Analysis

The surface morphologies of extracted cellulose, CA, and CA-g-PAA are shown in Figure 3 (a-c). The

surface morphology showed some variations due to chemical modifications. Pure cellulose in Figure 3 (a) showed a rough surface and irregular shapes of

varied particles. The cellulose ester in Figure 4 (b) showed a varied morphology with small pores and a relatively rough surface. However, in the graft copolymer, Figure 3 (c), the surface morphology

showed many pores and thick-coated rough surface, which confirmed the grafting of AA onto acetylated cellulose.

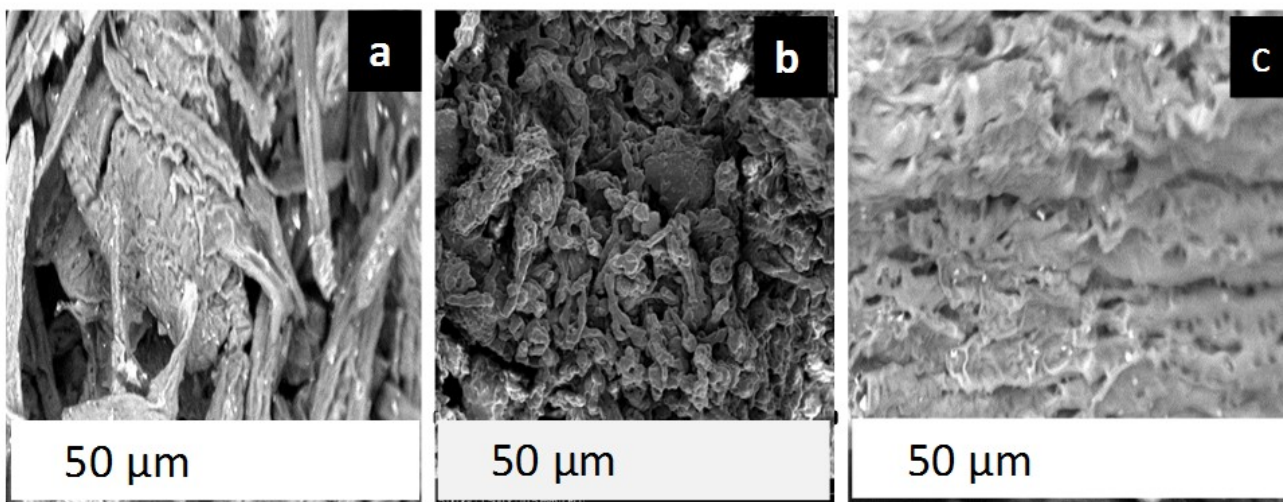


Figure 3: SEM image of (a) extracted cellulose (b) acetylated cellulose, and (c) CA-g-PAA.

X-ray diffraction (XRD) analysis

Structural changes were studied in the cellulose and the modified cellulose samples using X-ray diffraction technique. Figure 4 shows the XRD results of the samples; in the extracted cellulose, two responses were noticed at $2\theta=15.7^\circ$ or 22° and 30° . These indicate that the cellulose is a semi-crystalline material (17). Other responses at 18° and 21° in the modified samples, and with disappearance of intensive peak at 30° , showing that the crystallinity of the cellulose decreases after chemical modification (17).

On grafting the acetate fiber, a new response was observed with different intensities and was accompanied by a decrease in the relative degree of crystallinity (Figure 4). This could be explained on the basis that grafting causes disturbance in the crystalline region of the cellulose and increases the intensity of the amorphous region. As the degree of grafting increases, the amorphous regions become predominant and overshadow the crystalline feature on the cellulose material. This is evidence of the formation of a new material.

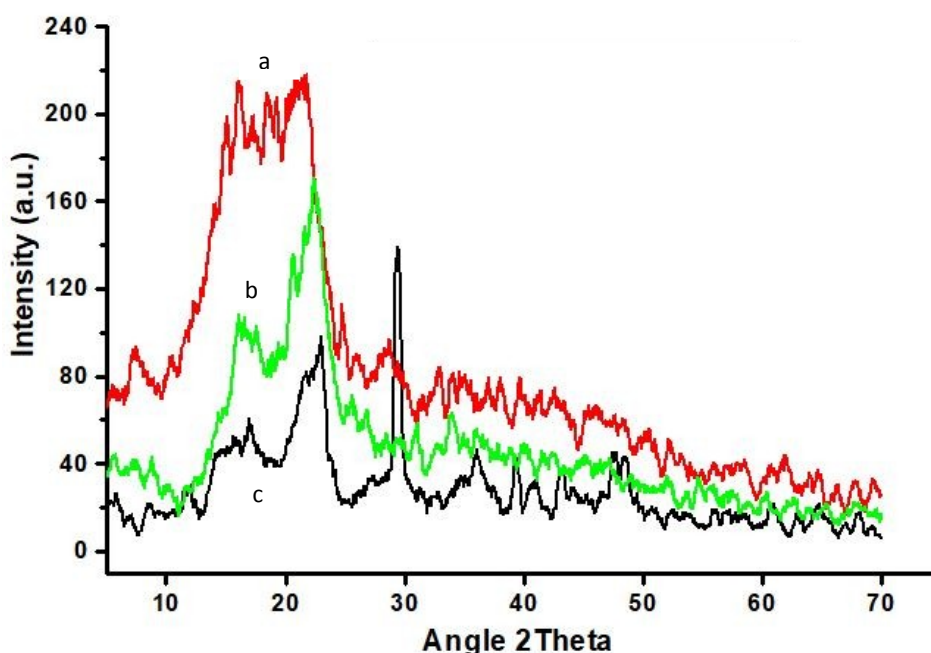


Figure 4: XRD Spectra of (a) cellulose, (b) CA, and (c) CA-g-PAA.

CONCLUSION

Cellulose extracts have been successfully modified through acetylation and grafting by free radical polymerization. The optimum condition for the maximum degree of grafting obtained at 70 °C after 180 min is (85%). Monomer conversion increases as reaction temperature increases, and grafting yield decreases as reaction temperature decreases, and higher temperature favour grafting more than homopolymerization. Samples' characterization using FTIR, SEM and XRD confirmed a successful modification of the starting material. The characterization of the samples has shown that there are structural changes of cellulose molecules after the modification.

ACKNOWLEDGEMENTS

The authors are grateful to The Department of Chemistry, Umaru Musa Yar'adua University Katsina, Katsina State, Nigeria.

REFERENCES

- Gürdağ G, Sarmad S. Cellulose Graft Copolymers: Synthesis, Properties, and Applications. In: Kalia S, Sabaa MW, editors. Polysaccharide Based Graft Copolymers [Internet]. Berlin, Heidelberg: Springer Berlin Heidelberg; 2013 [cited 2022 Apr 5]. p. 15–57. <URL>.
- Eyley S, Thielemans W. Surface modification of cellulose nanocrystals. *Nanoscale*. 2014;6(14):7764–79. <DOI>.
- Bezerra RDS, Teixeira PRS, Teixeira ASNM, Eiras C, Osajima JA, Filho ECS. Chemical Functionalization of Cellulosic Materials — Main Reactions and Applications in the Contaminants Removal of Aqueous Medium. In: Poletto M, Ornaghi HL, editors. Cellulose - Fundamental Aspects and Current Trends [Internet]. InTech; 2015 [cited 2022 Apr 5]. <URL>.
- Ibrahim I (Al-K, Al-Obaidi YM, Hussin SM. Removal of Methylene Blue Using Cellulose Nanocrystal Synthesized from Cotton by Ultrasonic Technique. *Chemical Science International Journal*. 2015;9(3):1–7. <URL>.
- Wojnárovits L, Földvály CsM, Takács E. Radiation-induced grafting of cellulose for adsorption of hazardous water pollutants: A review. *Radiation Physics and Chemistry*. 2010 Aug;79(8):848–62. <DOI>.
- Richardson S, Gorton L. Characterisation of the substituent distribution in starch and cellulose derivatives. *Analytica Chimica Acta*. 2003 Nov;497(1–2):27–65. <DOI>.
- Toledano-Thompson T, Loría-Bastarrachea MI, Aguilar-Vega MJ. Characterization of henequen cellulose microfibers treated with an epoxide and grafted with poly(acrylic acid). *Carbohydrate Polymers*. 2005 Oct;62(1):67–73. <DOI>.
- Coskun M, Temüz MM. Grafting studies onto cellulose by atom-transfer radical polymerization: Grafting studies onto cellulose by ATRP. *Polym Int*. 2005 Feb;54(2):342–7. <DOI>.
- Bhattacharya A. Grafting: a versatile means to modify polymers Techniques, factors and applications. *Progress in Polymer Science*. 2004 Aug;29(8):767–814. <DOI>.
- Liu S, Sun G. Radical graft functional modification of cellulose with allyl monomers: Chemistry and structure characterization. *Carbohydrate Polymers*. 2008 Mar 7;71(4):614–25. <DOI>.
- Chauhan GS, Mahajan S, Guleria LK. Polymers from renewable resources: sorption of Cu²⁺ ions by cellulose graft copolymers. *Desalination*. 2000 Sep;130(1):85–8. <DOI>.
- Fanta GF, Doane W. Grafted starches, modified starches: properties and uses. Wutzburg O, editor. Boca Raton: CRC Press; 1986.
- Gurdag G, Yasar M, Gurkaynak MA. Graft copolymerization of acrylic acid on cellulose: Reaction kinetics of copolymerization. *J Appl Polym Sci*. 1997 Oct 31;66(5):929–34. <DOI>.
- Hiltunen MS, Raula J, Maunu SL. Tailoring of water-soluble cellulose-*g*- copolymers in homogeneous medium using single-electron-transfer living radical polymerization: Tailoring of cellulose-*g*-copolymers using SET-LRP. *Polym Int*. 2011 Sep;60(9):1370–9. <DOI>.
- Scatolino MV, Silva DW, Mendes RF, Mendes LM. Use of maize cob for production of particleboard. *Ciênc agrotec*. 2013 Aug;37(4):330–7. <DOI>.
- Mohammed A. Effect of cross-linking on grafting and super absorbency of Acryloylated starch. *Nigerian Journal of Textiles*. 2016;2:73–84.
- Azubuikwe CP, Okhamafe AO. Physicochemical, spectroscopic and thermal properties of microcrystalline cellulose derived from corn cobs. *Int J Recycling Org Waste Agric*. 2012;1(1):9. <DOI>.
- Ogawa K, Hirai I, Shimasaki C, Yoshimura T, Ono S, Rengakuji S, et al. Simple Determination Method of Degree of Substitution for Starch Acetate. *BCSJ*. 1999 Dec;72(12):2785–90. <DOI>.
- Fernández MJ, Casinos I, Guzmán GM. Grafting of a vinyl acetate/methyl acrylate mixture onto cellulose. Effect of temperature and nature of substrate. *Makromol Chem*. 1990 Jun;191(6):1287–99. <DOI>.
- Mondal MdIH, Uraki Y, Ubukata M, Itoyama K. Graft polymerization of vinyl monomers onto cotton fibres pretreated with amines: Mechanical property and moisture sorption. *Cellulose*. 2008 Aug;15(4):581–92. <DOI>.
- Okieimen EF, Ebhoaye JE. Grafting Acrylic Acid Monomer on Cellulosic Materials. *Journal of Macromolecular Science: Part A - Chemistry*. 1986 Mar;23(3):349–53. <DOI>.



Adsorption Studies of Radionuclides by Turkish Minerals: A Review

Süleyman İnan*¹  and Ümran Hiçsönmez² 

¹Ege University, Institute of Nuclear Sciences, Izmir, 35100, Turkey

²Manisa Celal Bayar University, Department of Chemistry, Manisa, Turkey

Abstract: Hazardous radionuclides are produced during normal operation of nuclear power plants and research facilities. They can also be spread to the environment due to fallout from nuclear accidents and nuclear weapon tests. The removal of hazardous radionuclides and the safe management of radioactive waste are of vital necessity. Natural minerals have been widely used for the removal of heavy metals and radionuclides because of their low cost, high capacity, and radiation resistance properties. Turkey has abundant natural mineral deposits. These deposits include clinoptilolite, bentonite, montmorillonite, kaolinite, vermiculite, illite, red clay, sepiolite, diatomite, perlite, and volcanic tuff. Within the scope of this review, Turkish minerals were classified as three main groups: zeolites, clay minerals, and other minerals. The review consists of sections on the general properties of natural minerals such as zeolites and clays, the characteristics of Turkish minerals, and the adsorption performance of these minerals against some radionuclide ions (Sr, Cs, U, Th and Po).

Keywords: Adsorption, radionuclide, clay, zeolite, Turkish mineral

Submitted: February 16, 2022. **Accepted:** March 31, 2022.

Cite this: İnan S, Hiçsönmez Ü. Adsorption Studies of Radionuclides by Turkish Minerals: A Review. JOTCSA. 2022;9(2):579-600.

DOI: <https://doi.org/10.18596/jotcsa.1074651>.

***Corresponding author. E-mail:** suleyman.inan@ege.edu.tr.

INTRODUCTION

Nuclear power plants play a key role in meeting the increasing energy demand with continuous energy generation as a base load source. Liquid radioactive waste (LRW) is generated as a result of the operation, repair, and disposal activities of nuclear power plants. Removal of radionuclides from the LRW is required prior to discharge. Developments and improvements are ongoing for the safe management of radioactive waste. On the other hand, dangerous radionuclides can be released into the environment as a result of nuclear weapons tests and radiological accidents (1). ¹³⁷Cs and ⁹⁰Sr are fission products that are generated during the splitting of uranium atoms in reactor core. These radioisotopes are the major sources of heat and radiation in high-level waste (2). The half life of ⁹⁰Sr is about 30 years. It tends to accumulate in human bones and is considered one of the most hazardous

pollutants (3). Uranium emerges as a pollutant in the environment as a result of activities from nuclear fuel cycle, use of coal, and processing of depleted uranium munitions. In addition, groundwater seeps can occur with natural erosion of igneous rocks and ore bodies (4).

Thorium is more abundant than uranium in the earth's crust. Even trace amounts of this toxic and dangerous radionuclide pose a threat to human physiology and other biological systems and can cause various diseases (5). Activities such as nuclear fuel reprocessing and exploitation of thorium-containing ores can also contribute to thorium concentrate (6). Thorium is stable at ambient temperature and therefore has low toxicity (7). However, due to the risk of thorium-containing liquid wastes to leak to the surface and mix with groundwater, this situation raises concerns for environmental safety.

Polonium is an important isotope from the uranium series (8,9). When absorbed in large quantities, even low concentrations make it one of the most dangerous radionuclides (10). ^{210}Po is a high energy (5.304 MeV) alpha emitter. It is effectively biomagnified by phytoplankton and zooplankton in the aquatic environment and enters the marine food chain (10–12).

The adsorption process is one of the most efficient methods for the treatment and removal of inorganic or organic pollutants and radionuclides from polluted water and wastewater (13). Natural sorbents such as zeolites and clay minerals are widely used in water purification processes due to their frequent occurrence in nature, low cost as compared with synthetic materials, and remarkable properties with respect to adsorption, ion exchange, and filtration. They have been employed for the removal of heavy metals and radionuclides, owing to their relatively large surface area and high adsorption capacity (14–18).

Today, sepiolite, diatomite, zeolite, industrial sand, dolomite, talc, wollastonite, kyanite, perlite, and calcite are also commercially produced in Turkey (19). Among these minerals, particularly zeolites and clay minerals have a key role in the adsorption processes. A program for the establishment and operation of a nuclear power plant in Turkey has been initiated, and the process continues with determination. The first unit of the nuclear power plant, which is under construction in Mersin Akkuyu, is expected to produce energy in 2023 (20). For this reason, it has become compulsory for Turkey to carry out necessary studies on the control and safe management of radioactive waste.

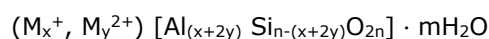
In this context, the objective of this study is to investigate the removal of the activity of radioactive waste with natural minerals obtained from deposits in various regions of Turkey. We focused on the adsorption of radionuclides such as strontium, cesium, uranium, thorium, and polonium by zeolites, clay minerals, and other minerals of Turkey. We present data in terms of adsorption conditions, kinetics, isotherm and thermodynamic studies. This review is a preliminary study on the

usability of natural minerals in Turkey in the removal of some hazardous radionuclides found in radioactive wastes from energy production in nuclear power plants built in Turkey's nuclear program or that may occur as a result of radiation accidents.

TYPES OF NATURAL MINERALS

Zeolites and Properties

Zeolite minerals are crystalline, hydrated aluminosilicates of alkali and alkaline earth cations. They are characterized by reversible hydration/dehydration abilities and exchangeable cations in their structure. Zeolite minerals have aroused interest due to their ion exchange, adsorption, and molecular sieve properties as well as their geographically widespread abundance and have been used in a wide range of applications (21). The general formula for natural zeolites has been proposed as follows (22):



where M^+ denotes monovalent cations with stoichiometry x , and M^{2+} denotes divalent cations with stoichiometry y . M^+ and M^{2+} are the exchangeable cations. Al and Si are the structural cations. They form the framework of the structure together with oxygen. The value of m is the number of water molecules in the structure.

Clinoptilolite is the most abundant naturally occurring zeolite among more than 40 zeolite species with a solid microporous structure (23,24). It is composed of a three-dimensional structure consisting of AlO_4 and SiO_4 tetrahedral bonded together by a common oxygen atom. The micropores in the structure are narrow enough to allow the entry and exchange of cations and water molecules (25). This ability is based on the replacement of SiO_4 by AlO_4^- . By this way, a negative charge is formed and this has to be balanced by exchangeable cations such as Na^+ , K^+ , Ca^{2+} and Mg^{2+} (26). The formation of 3D crystalline structure of zeolite from primary building units (PBU) and secondary building units (SBU) along with the channels in the structure are shown in Figure 1.

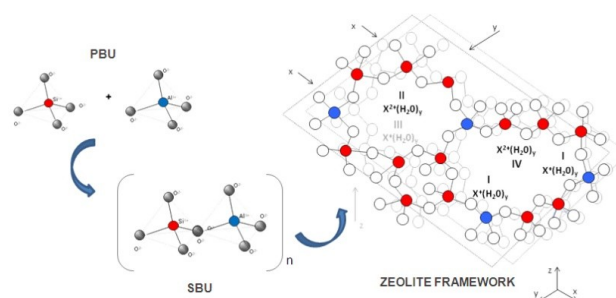


Figure 1: The structure of natural zeolite-clinoptilolite (The represented structure has been used from ref. (27)).

Natural zeolites have been investigated for their potential use in the treatment of nuclear wastewaters, municipal and industrial wastewaters (28–31), and acid mine drainage waters (32) due to their selectivity for specific cations such as Cs^+ ,

Sr^{2+} , and NH_4^+ . Their potential use in the remediation of sites contaminated with fission products such as ^{90}Sr and $^{135, 137}\text{Cs}$ (33–35) has also been studied. The adsorption of radionuclide ions in zeolite structure can be depicted as in Figure 2.

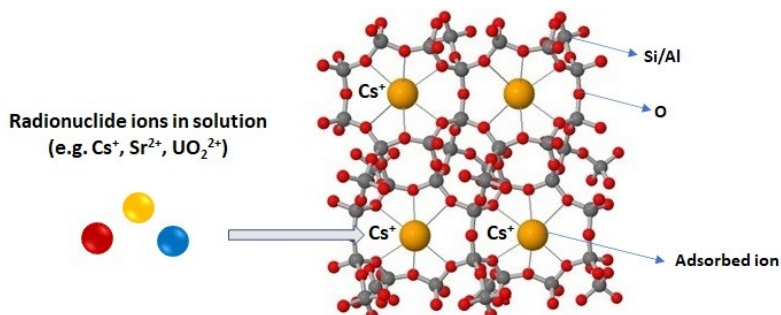


Figure 2: A simplified illustration of radionuclide adsorption in zeolite structure (The illustration has been adapted and modified from ref. (36)).

Clay Minerals and Properties

Clays are hydrous aluminosilicate structures. They consist of mixtures of fine grained clay minerals, crystals of other minerals, and metal oxides (37). Clays are classified into groups such as smectites (montmorillonite, saponite), mica (illite), kaolinite, vermiculite, serpentine, pyrophyllite (talc), and sepiolite (38). Grim (1962) was the first to propose the classification and naming of clay minerals in 1962 (39). Grim (1962) stated that the most significant groups of clay minerals are montmorillonite, kaolinite, and illite. Clays and clay minerals have high specific surface areas and porous structure. This results in interactions with dissolved species caused by electrostatic repulsion, crystallinity, and adsorption/ion exchange reactions (40).

Kaolinite has a chemical formula of $\text{Al}_2\text{Si}_2\text{O}_5(\text{OH})_4$ and is composed of Al_2O_3 (39.53%), SiO_2 (46.53%), and H_2O (13.94%), theoretically. Kaolinite has a 1:1 layered structure consisting of a tetrahedral SiO_4 sheet and an octahedral sheet containing Al^{3+} as the cation. Hydroxyl groups located above and below the two Al atoms form a central hexagonal structure in a single plane. Although the surface charge of kaolinite is neutral, it has a small net negative charge at the fractured edges of the crystals (41,42). Kaolinite is used in the paper, ceramics, pharmaceutical, and cosmetic industries (43,44). In addition, the use of kaolinite in water treatment is increasing rapidly. With the release of H^+ ions from the layered structure in acidic solutions, heavy metal ions are adsorbed (45).

Bentonite has an aluminum phyllosilicate structure mainly composed of montmorillonite. It is a sedimentary rock consisting of clay, with a smectite structure. Na^+ , Ca^{2+} and Li^+ ions are located between its layers. The octahedral and tetrahedral sheets are in such a combination that a single layer is formed by the edges of the tetrahedra in each silica sheet and one of the hydroxyl layers in the octahedral sheet. Montmorillonites are smectite clays and are abundant in the environment. They have a chemical formula of $(\text{Na}, \text{Ca})_{0.33} (\text{Al}, \text{Mg})_2\text{Si}_4\text{O}_{10}(\text{OH})_2 \cdot n\text{H}_2\text{O}$ and are comprised of plate-shaped particles with an average diameter of approximately $1 \mu\text{m}$ (46). In the structure, the octahedral aluminum layer in the center was surrounded by two tetrahedral silica layers. Interactions between the sheets generally take place via $-\text{OH}$ groups in the octahedral layer and the edges of the tetrahedral layer. Montmorillonite tends to swell due to lattice expansion caused by polar molecules such as water. In addition, interlamellar gap may be unbalanced due to cation exchange between the silicate sheets (47).

Figure 3 shows a diagram of the structure of Na-montmorillonite and the adsorption mechanism of metal ions. Si^{4+} cations in the tetrahedral layer and Al^{3+} cations in the octahedral layer are replaced by lower valence cations. As a result, a negative charge is formed. Ions such as Sr^{2+} , Cs^+ , UO_2^{2+} , Th^{4+} are adsorbed by replacing exchangeable ions between tetrahedral layers and forming ion pairs with negative charge centers. Also, adsorption may occur as the complexation of metal cations on Na-montmorillonite surface (48,49).

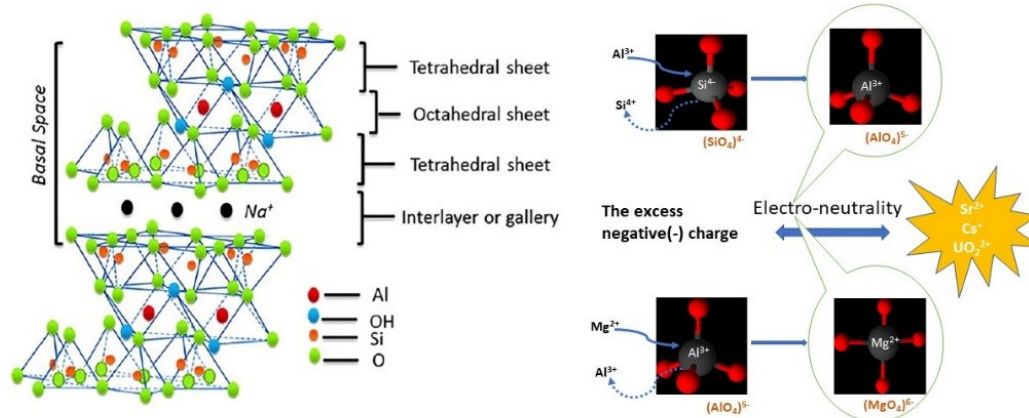


Figure 3: A general illustration of radionuclide adsorption onto Na-montmorillonite (adapted and modified from ref. (50)).

Vermiculite is a common clay mineral. It has a 2:1 aluminosilicate structure composed of a tetrahedral layer of silica and two layers of $\text{MgO}_2(\text{OH})_4$ octahedra. Silicon is partially substituted by aluminum, and it forms a stable mica. The lack of positive charge in the parallel layers is compensated by cations in the interlayer space such as K^+ , Na^+ , Ca^{2+} , and Mg^{2+} . The structure formed by combining two layers in this way is called a 2:1 layered silicate structure (51,52).

Other Minerals

Perlite is an acidic volcanic glass. It expands with heat and becomes lighter and porous. Perlite rocks may differ from each other in terms of color and structural properties. Changes in the color of raw perlite can be observed from transparent light gray to bright black. In its expanded form, the color turns completely white. Perlite contains 2.5% water in its hydrated glassy silica structure, and this feature makes it stable. When perlite is suddenly heated in the range of 750-1200°C, it expands with the effect of the steam formed and aggregates into glassy particles. When it expands up to 20 times its original volume, the product known as expanded perlite is obtained. Properties that make expanded perlite commercially important include low density in small volume, physical flexibility, chemical stability, low sound permeability, and fire resistance. Perlite is used in many areas in construction, agriculture, and industry. It is used as an additive, facilitating the cementing process, as a filling material in packaging and in removing water pollution (53).

Diatomite is used as an industrial raw material. Diatomite is a rock consisting of clay, sand, volcanic ash, and other organic remains, as well as diatom skeletons, a single-celled algae species living at shallow (0-35m) depths, where photosynthesis occurs intensively in fresh and saltwater reservoirs located in regions with high volcanic activity. Diatom skeletons contain $\text{SiO}_2 \cdot n\text{H}_2\text{O}$. Diatomites are resistant to many chemicals, but are affected by

strong bases at high temperatures. Diatomites, whose whiteness can go up to 90% depending on their content, find the opportunity to be used in many different areas of industry with their features such as low densities, moderate refractoriness, high absorption capacities, friability to small grain size, and high surface area value. The usage areas of diatomite products can be listed in order of importance as follows: filter aid material, filling material, insulation (heat, sound, electricity) material, adsorbent, catalyst carrier, light building material, refractory material, silica source, and regulator in fertilizers (54).

Volcanic tuff is used to express consolidated pyroclastic rocks. These rocks react with water and zeolite can be formed by the transformation of volcanic glass (55). It is extensively used as a growth substrate for plants (56). The sorption behavior of volcanic tuffs is explained by the uptake of cations on their porous surfaces, which are connected to each other by channels. This makes tuffs an important alternative material with high selectivity for many heavy metals, toxic cations (57,58) and radionuclides (59,60) in wastewater treatment.

NATURAL MINERALS OF TURKEY

Zeolites

Important zeolite formations in our country consist of clinoptilolite, chabasite, mordenite, erionite, and analcime minerals (61). Turkey's zeolite deposits are mainly composed of clinoptilolite ores and are estimated to be around 50 billion tons. Significant clinoptilolite reserves can be found in the Balıkesir-Bigadiç and Manisa-Gördes deposits. The clinoptilolite reserve identified in the Bigadiç-Balıkesir deposit is approximately 500 million tons (62). Analcime deposits are widely distributed in Bahçecik, Gölpazarı, Göynük, Polatlı, Mülk, Oğlakçı, Aşağı, Mallıhan, Kalecik, Çandır, Şabanözü, Hasavaz regions. There are clinoptilolite, chabasite,

mordenite, and erionite deposits in the Kapadokya region (61).

Elemental composition of zeolites may differ according to the deposit. Table 1 provides data on the chemical composition of various types of Turkish zeolites (63–65). Results show that zeolites are

composed of silica and alumina as major constituents, iron(III) oxide, calcium oxide, magnesium oxide, sodium oxide, potassium oxide and titania as minor constituents. The loss on ignition values is relatively low, and this indicates less carbon and higher mineral content.

Table 1: Chemical composition of Turkish zeolites.

Zeolite	Elemental composition (weight, %)										Ref.
	SiO ₂	Al ₂ O ₃	Fe ₂ O ₃	TiO ₂	CaO	MgO	Na ₂ O	K ₂ O	H ₂ O	Ignition loss, %	
Manisa-Gördes	69.31	13.11	1.31	-	2.07	1.13	0.52	2.83	6.88	-	(63)
Balıkesir-Bigadiç	77.96	13.17	1.06	0.08	3.80	1.53	0.16	2.20	-	-	(64)
Kütahya	67.25	14.20	1.00	0.35	2.80	1.45	0.15	5.20	-	6.95	(62)
Çanakkale-Biga	70.00	12.85	0.75	0.07	2.60	1.65	0.90	4.30	-	6.24	(65)
Çankırı-Çorum	64.85	13.70	1.01	0.30	3.30	1.00	5.50	1.00	-	9.66	(65)

Clay Minerals

The most commonly used Turkish clay minerals in adsorption studies of radionuclides are bentonite, montmorillonite, kaolinite, and sepiolite. Illite, red clay, and vermiculite are among the other clays studied.

As mentioned earlier, montmorillonite is classified under smectite group and it is the major component of bentonite. Bentonite shows stratification in an irregular manner within the magmatic rocks and volcanic units in Turkey. In the market, bentonite is sold in raw, milled bulk, and bagged and activated forms. It is known in our country as drilling, packaging, medicine, filling, casting, and bleaching types of (66). As of 2019, Turkey's bentonite reserves (proven+probable) are 370 million tons (67). Bentonite pitches in Turkey are in Biga peninsula, Gelibolu peninsula and north, Eskişehir-Ankara regions, Çankırı-Tokat region, Ordu-Trabzon region, Kayseri-Nevşehir-Nigde region and Malatya-Elazığ. There are many bentonite deposits of various sizes in these regions and their immediate surroundings (68).

According to the Republic of Turkey Ministry of Trade report (67), Turkey's probable kaolin reserves are over 100 million tons. Kaolin deposits are located in Balıkesir, Nevşehir, Niğde, Bolu,

Çanakkale and East Black Sea region. In 2017, the total export value of kaolin reached 4 million USD.

Sepiolite is a raw material whose resources are extremely limited in the world compared to other industrial minerals and whose economic deposits are only limited to Spain and Turkey. Although meerschaum type sepiolite is a mineral that has been known for centuries and is one of our traditional export products in our country, scientific research on bedded type sepiolite deposits with sedimentary formation was initiated in 1988 with the projects of the MTA General Directorate. In particular, thanks to the joint technology studies developed with the Japanese Research Institutes, a significant part of the sepiolite deposits in Turkey has been characterized (69). Turkey's industrial and layered types of sepiolite deposits that may be considered economically, are located in Eskişehir, Çanakkale, Bursa, Kütahya and Isparta (70).

Elemental composition of various types of clay minerals (66-71), obtained from Turkish deposits, is shown in Table 2. Montmorillonite, red clay and bentonite contain silica and alumina in major quantities but in addition to these, iron(III) oxide and magnesium oxide are present at major levels in the vermiculite structure. However, sepiolite is composed of only silica and magnesium oxide, with an ignition loss of 13.50%.

Table 2: Chemical composition of Turkish clay minerals.

Clays	Elemental composition (weight, %)									Ref.
	SiO ₂	Al ₂ O ₃	Fe ₂ O ₃	TiO ₂	CaO	MgO	Na ₂ O	K ₂ O	Ignition loss, %	
Kula montmorillonite	67.37	19.74	2.31	0.46	0.38	0.13	2.37	3.38	3.81	(71)
Turgutlu montmorillonite	62.86	14.80	6.20	0.82	2.68	1.63	2.84	2.29	5.66	(71)
Bandırma kaolinite	48.00	36.60	0.92	0.05	0.07	0.3	0.1	2.00	11.96	(72)
Eskişehir red clay	59.10	19.05	6.35	1.03	4.00	1.50	1.50	1.00	6.50	(73)
Eskişehir sepiolite	56.91	0.085	0.043	0.008	1.40	27.25	0.019	0.013	13.50	(74)
Çankiri bentonite	60.32	14.78	4.90	-	3.90	2.20	3.05	1.48	9.20	(75)
Sivas-Yıldızeli vermiculite	36.3	14.8	12.4	2.70	4.20	14.6	0.3	4.80	9.10	(76)

Other Minerals in Turkey

Perlite

The world's largest perlite producers are Turkey, Greece, and the United States, with 41, 26, and 18%, respectively. The perlite reserve in Turkey has the potential to contribute significantly to the economy. It is estimated that the world's perlite reserves are around 8 billion tons (77), and 5.7 billion tons of this amount is in Turkey (Industrial Raw Materials Coordinator Mustafa Kırıkoglu, MİGEM (General Directorate of Mining Affairs), in Turkey). It has been reported that perlite in Turkey contains SiO₂ in the range of 71-75% and Al₂O₃ in the range of 12-18% as main constituents (78).

Diatomite

Turkey's diatomite reserves are generally in the form of beds suitable for open pit production. Before starting the operation, the production method is determined by determining the quality and size through drilling, and production is ensured by excavating and transporting machines. The humidity of the diatomite, whose humidity is up to 50%, is transferred to the facilities by reducing the humidity in the field by open field drying. Mining cost in the production of finished goods is around 10%. In the facilities, production is carried out with appropriate processes selected according to the usage areas of diatomite. Turkey Sugar Factories Inc., In order to obtain filtration products in sugar production, a pilot plant was established in 1974. The plant started production in 1980, and the plant was closed in 1994 as perlite was used instead of diatomite. Diatomite consumption areas are generally defined as 66% filtration industry, 21% filling, 1% insulation, and 12% other uses (54).

Volcanic Tuff

Volcanic tuff deposits are widely distributed in Turkey (79). Tertiary and quaternary-age volcanic

rocks cover approximately 155,000 sq. km of area in the country, including tuffs. Studies were conducted on the geology of the quaternary volcanic centers in eastern Turkey and the chemical and mineralogical compositions of the Tendurek tuffs (80).

ADSORPTIVE REMOVAL OF RADIONUCLIDES BY TURKISH MINERALS

The removal of hazardous metal ions by natural minerals via adsorption technique offers simplicity and low investment cost. Figure 4 demonstrates the basics of experimental procedure used for radionuclide removal using adsorption.

In the adsorption studies of radionuclides using Turkish minerals, mostly zeolite and clay minerals have been reported. However, a few studies have also been carried out with diatomite, volcanic tuff and perlite. The majority of the studies reported in this context have focused on the removal of strontium, cesium, and uranium ions. Studies on thorium and polonium adsorption have also been mentioned. In some of the studies, the inactive isotope of the radionuclide to be removed was used, while in some studies, experiments were carried out by adding radioactive tracers. For this reason, studies may contain differences in terms of experimental steps of batch method, elemental analysis techniques used, and outputs obtained. The main focus is to reveal the adsorption performance of Turkish minerals depending on the effecting parameters such as pH, contact time, radionuclide concentration, and temperature. The data obtained as a result of examining the adsorption isotherms, kinetic and thermodynamic behaviors of minerals are presented.

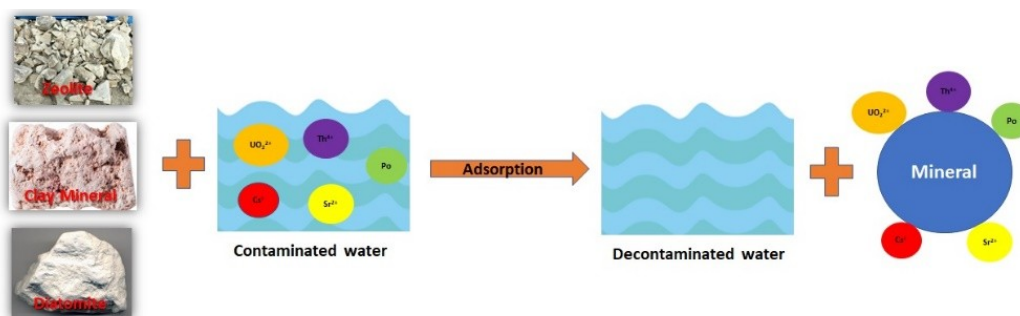


Figure 4: Illustration of adsorption process for the removal of radionuclides from contaminated water using natural minerals as adsorbent.

Adsorption studies by zeolites

Natural zeolites

Manisa-Gördes zeolite is one of the most reported zeolites. There are 18 million tons of natural zeolite reserves in this area. Uranium adsorption onto Manisa-Gördes zeolite was studied by Kilincarslan and Akyil (63). The influence of process parameters such as initial uranium concentration, pH, contact time, and temperature was investigated. The authors reported that they determined the maximum adsorption efficiency at 125 µg/mL when the uranium concentration was increased from 25 to 175 µg/mL. It is also reported that the uranium sorption is strongly pH dependent and is favored by weakly acidic value. Maximum adsorption efficiency was observed at pH 5. The adsorption of UO_2^{2+} ions increased with increasing pH up to pH 5 and then started to decrease at higher pH values. The dominant species in the solution are as follows: free uranyl ion up to pH 6, UO_2OH^+ at pH 5, and $\text{UO}_2(\text{CO}_3)_3^{4-}$ in the range of pH higher than 7. From pH 4 to pH 8, the predominant uranium complex would be the neutral UO_2CO_3^0 (81). Equilibrium was reached within 120 min. The adsorption efficiency of uranium on Manisa-Gördes zeolite was found to be $83 \pm 1.8\%$ at optimum conditions. The adsorption isotherm is used to describe the adsorption process and evaluate the adsorption capacity. It can be defined as the ratio of the metal concentration in the adsorbent phase to the metal concentration in the liquid phase at a given temperature (82). Uranium adsorption behavior of zeolite were best described by the Langmuir adsorption model ($R^2=0.9218$). The data obeying Langmuir isotherm indicate transfer of uranium(VI) from aqueous solution to the surface of zeolite as adsorption and bond formation between uranium(VI) and adsorbent may be chemical in nature. The value of E was calculated as 11.18 kJ/mol from D-R isotherm.

In another study carried out with Manisa-Gördes zeolite, Atun and Bodur (83) investigated Cs sorption using mixtures of zeolite and commercial bentonite in different proportions. ^{137}Cs was spiked as a tracer and experiments were carried out in NaCl solutions of different concentrations. Cs sorption parameters such as K_d , X, and X_m for zeolite were higher than those found for bentonite

at all conditions. The observed $K_d(\text{mix})$ values were smaller than calculated $K_d(\text{mix})$ values except at 1 mol/L NaCl. In the study, it is stated that sorption is achieved by settling 3.45 Å Cs ions in the main channel of the zeolite, which has a cavity size of approximately 3.50 Å. While adsorption in bentonite with decreasing NaCl concentrations was compatible with both Freundlich and D-R isotherms, the situation in zeolite fitted with D-R at all concentrations and Freundlich isotherm at only low concentrations. K_d values increased with increasing zeolite fractions.

Sorption studies of strontium on Manisa clinoptilolite and Sındırgı kaolinite were conducted by Akar et al. (84). Kinetic studies were performed between 5 and 2880 min of contact time. The initial pH of the solution was kept in the pH range of 6.2 to 7.7. The sorption process followed pseudo second order kinetics. Isotherm data were explained well with Freundlich and Dubinin-Radushkevich isotherm models. Clinoptilolite showed a higher strontium sorption capacity than kaolinite. Thermodynamically, the activation energy of Sr^{2+} sorption by clinoptilolite was -18.4 kJ/mol. The sorption process was spontaneous and endothermic at all the studied concentrations, with ΔH° being 9.8 kJ/mol for sorption on clinoptilolite.

Osmanlioğlu (30) focused on the performance of natural zeolite as a sorbent for the disposal of low level liquid waste from Cekmece Waste Processing and Storage Facility (CWPSF). The batch ion-exchange capacities of the five different zeolites (Polatlı-Ankara, Bigadiç-Çanakkale, Saphane-Balıkesir, Gediz-Kütahya) and Gördes-(Manisa) in Turkey were tested for ^{137}Cs , ^{60}Co , ^{90}Sr , and ^{110m}Ag . Gördes zeolite was found to be the most suitable sorbent for LLW for radionuclides. The decontamination factors (DF) of natural zeolites for ^{137}Cs at different pH levels were investigated. It was determined that DF of the natural zeolites is very good for ^{137}Cs at pH is about 10. Stored liquid waste in storage tanks was transferred from the collection tank to the precipitator for developing precipitation strategy. At this stage, natural zeolite (particle size 0.5 mm) has been added from dosage tanks and pH has been increased to 10. Then, after settling of the

sludge, the clarified solution was pumped to decantation tank. With this treatment, a decontamination factor of 430 has been achieved by using 0.5 mm clinoptilolite at 303 K.

Hicsonmez et al. (85) removed ^{209}Po using a natural zeolite mineral from Manisa-Gördes, Turkey. Polonium is one of the most significant isotopes in the uranium series (8,9). It is very dangerous, even at low concentrations, when absorbed in high enough quantities (10). The effect of initial ^{209}Po activity concentration was investigated in the range of 1.85×10^{-10} to 1.85×10^{-9} Ci/mL. The adsorption efficiency slightly increases as the initial polonium activity concentration increases. When the pH of the solutions was increased from 2 to 8, the adsorption removal efficiency of ^{209}Po onto zeolite quickly decreased from 90 to 20%, so pH had an important effect on the adsorption of ^{209}Po . The results demonstrate that adsorption process is rapid and effective. The authors found that the ^{209}Po adsorption efficiency is $90 \pm 2\%$ at optimal experiment conditions (pH<3, 298 K and 40 min of contact time). The adsorption data were compatible with both Freundlich ($R^2=0.92$) and Dubinin-Raduskevich ($R^2=0.92$) isotherms. Freundlich isotherm assumes that the adsorbent surface is coated as multilayers (86). Activation energy (E_a), calculated as 0.1008 J/nmol, indicates that the interaction between polonium and zeolite occurs through physical adsorption. When comparing polonium's K_d values with other minerals, they said that the barrier material has very good performance and selectivity for the adsorption of polonium ions with a K_d value of 4.5×10^2 L/g. The results show that polonium adsorption onto the zeolite is very fast and effective.

Akyuz (65) investigated Cs^+ and Sr^{2+} sorption capacity of zeolite samples obtained from Kütahya, Çanakkale-Biga, Çankırı-Çorum and Manisa-Demirci regions of Anatolia. Na and Ca content of Çorum zeolite is higher than the others, whereas the Si content is less. The natural zeolites (100 mg) had been treated with 0.1 mol/L solutions of Cs^+ and Sr^{2+} chlorides, in bottles at room temperature for one day. Chemical analysis of the washed and dried filtrates was performed on an EDXRF spectrometer. The author has indicated that the Clinoptilolite type zeolite from the deposits of Çankırı-Çorum Basin was the best sorbent for both Cs^+ and Sr^{2+} ions and it can be used for the treatment of radioactive waste water. Chemical analysis also proved the superiority of Çankırı-Çorum clinoptilolite for Cs^+ and Sr^{2+} ions.

Olmez Aytas et al. (64) reported a study dealing with the adsorption of uranium on clinoptilolite-rich zeolite from Bigadiç-Turkey. Before the adsorption studies, clinoptilolite-rich zeolite ($(\text{Na}_6(\text{AlO}_2)_6(\text{SiO}_2)_{30}) \cdot 24\text{H}_2\text{O}$ (Si/Al:5) was treated with 0.1 mol/L HCl at room temperature. The authors compared the U(VI) adsorption capacities of

zeolites in granular (32-48 mesh) and powdered (below 200 mesh) form. The results showed that powdered zeolites exhibited greater adsorption capacities compared with the granular form. Cation exchange capacity was found to be 1.70 mmol of H^+ /g of the natural zeolite. The influence of pH on adsorption was investigated in aqueous solutions from pH 2.0 to 9.0. High adsorption capacity at pH 2 is explained by the displacement of H^+ ions and uranyl ions in the active sites. The adsorption efficiency values decreased with the increase in temperature. Uranium adsorption behavior of zeolite was best described by the Langmuir isotherm model ($R^2=0.967$). In addition, the leachability of uranium has been studied. Zeolite samples were calcined at 873, 1073, 1273, and 1373 K. The leachability of uranium decreased with increasing calcination temperature. The authors stated this situation as an advantage of possible application for the storage of uranium in radioactive wastes.

Yıldız et al. (87) have studied the sorption behavior of Cs^+ ions onto kaolinite (Bozhöyük, Bilecik), bentonite (Çankırı) and zeolite (Bigadiç, Balıkesir). A ^{137}Cs tracer was added to simulated ground water. In all samples, equilibrium was reached in about 2 days at 5°C. Zeolites with crystalline and hydrated aluminosilicates contain regular channels or interlinked voids whose diameters are in the micropore range, depending on the structure type. Because the size of Cs^+ ion is suitable for these channels, the sorption order of cesium ion was found to be zeolite>bentonite>kaolinite. On kaolinite, there are no cations in the interlayer space and only surface bonding of cations occurs. In the adsorption experiments, the higher distribution ratios were obtained with lower Cs^+ concentrations. From the fitting of Freundlich isotherm model, the value of k constant was calculated as 0.8019, 7867, and 0.0916 in the order of bentonite, zeolite, and kaolinite. Desorption studies were performed to check the reversibility of the sorption of Cs^+ on bentonite, zeolite and kaolinite. In all cases, there was no significant activity, indicating that the sorption process was irreversible. From this study, it was suggested that these minerals can be used as backfill materials in geological repositories for the storage of ^{137}Cs containing radioactive wastes.

Modified Zeolites

Yusan and Erenturk (88) prepared PAN/zeolite composite for the adsorption of strontium from aqueous solution. The zeolite was obtained from Manisa-Gördes/Turkey. The percentage of adsorption increased with increasing strontium concentration (25-175 $\mu\text{g}/\text{mL}$) and remained almost constant at 150-175 $\mu\text{g}/\text{mL}$ range. pH tests showed that the adsorption efficiency of Sr(II) on PAN/zeolite increased up to pH 5. The pH of the solution was an effective parameter in Sr adsorption. The uptake of Sr slightly increased with increasing contact time, and 20 min was sufficient

for equilibrium. Various adsorption models were tested and it was found in the following order: Temkin>D-R>Freundlich>Langmuir. According to D-R model, X_m and the mean free energy (E) were determined to be 6.47 mmol/g and 0.91 kJ/mol, respectively.

Akyıl Erenturk and Kılıncarslan Kaygun (89) reported batch sorption studies of ^{210}Po from aqueous solution using the composite zeolite/PAN (Manisa-Gördes, Turkey). In order to work with zeolite in the column, a granular composite adsorbent has been prepared by mixing polyacrylonitrile (PAN) in a flask with reflux as a reactor. The effective parameters such as initial activity concentration of ^{210}Po , pH of the aqueous solution, contact time, and temperature were examined in a column system. Unlike natural zeolite, the highest adsorption levels (66.7%) for zeolite/PAN adsorbent was found between pH 4.0 ± 0.1 and 6.0 ± 0.1 . Adsorption efficiency of ^{210}Po onto composite adsorbent was determined as $75.00 \pm 0.15\%$ in optimum conditions. Experimental equilibrium data was well fitted and found to be in good agreement with the Temkin model. Temkin isotherm explains the interaction between the adsorbent and adsorbate molecules. This model assumes the following conditions: adsorption heat of all molecular interactions is linear rather than logarithmic, and there is a uniform distribution of binding energies (90–92). Adsorption thermodynamics and kinetics of polonium were studied. It was found that the process for ^{210}Po was exothermic.

As can be seen from the above studies, Manisa-Gördes zeolite and its composite were used for the removal of uranium, cesium, strontium, and polonium ions from aqueous solutions. pH of the working solutions had a remarkable effect on the adsorption behaviours. The highest removal efficiencies of uranium and polonium were obtained at pH=5 and at pH<3, respectively. Unlike natural zeolite, the maximum adsorption efficiency of the zeolite based composite for polonium between pH=4-6. In addition, at pH=5, strontium adsorption efficiency was maximized using the same composite.

Due to the affinity of polyacrylonitrile (PAN) for uranium ions, a mineral/polyacrylamidoxime (PAO) with modification of polyacrylonitrile was prepared by Şimşek and Ulusoy (93). They obtained bentonite (B-PAO) and zeolite (Z-PAO) composites. Ion

concentration, temperature, and contact time on the adsorption of Pb^{2+} and UO_2^{2+} were investigated. It has been found that the adsorption capacities of B/Z-PAO composites are higher than those of pure PAO, and their K_L values increase in the order of Z-PAO>B-PAO>PAO for two ions, particularly for U(VI). This situation has been explained by the authors with two effects. Initially, the additional electrostatic force contribution present in the negatively charged Si-O and Al-O minerals of the amidoxime terminals significantly increases the electrostatic attraction for the cations. Consequently, the choice of UO_2^{2+} should probably be related to the high stability of complexes formed with uranyl ions and to the active sites of PAO and/or minerals. On the other hand, it has been determined that the monolayer adsorption capacity of the adsorbents for UO_2^{2+} was lower than that of Pb^{2+} . Because, the required number of chelating amidoxime terminals for UO_2^{2+} (94) was greater than that of Pb^{2+} . 1 mol/L HCl has been used as a regeneration solution. After five sequential treatments, it was observed that there was no change in the B-POA and Z-POA structures, but the PAO gelled completely on the first use. Table 3 summarizes the reported use of Turkish zeolites for radionuclide removal.

Adsorption studies by clay minerals

In this section, kaolinite, montmorillonite, bentonite, sepiolite, illite, red clay, and vermiculite type clay minerals have been reported for the adsorptive removal of various radionuclides.

Strontium sorption studies on kaolinite using radiotracer technique were conducted by Keçeli (95). Kaolinite based clay samples were obtained from Çanakkale-Çan region of Turkey. The composition of the clay was; 90% kaolinite, 9% free quartz, and 1% other impurities such as Na- and K-feldspar. Kinetic and equilibrium studies were performed by batch experiments and adsorption data were evaluated by adsorption efficiency (%), uptake capacity (q) and distribution coefficient (K_d) values. According to Keçeli (95), capacity, affinity, and selectivity results obtained in this study demonstrate that the locally available kaolinite mineral can be successfully used for selective sorption of Sr radionuclides in waste disposal sites.

Data on the effect of temperature on the adsorption of radionuclides with Turkish zeolites, discussed in the text, are given in Table 4.

Table 3: Data on adsorption performance of Turkish zeolites for radionuclide ions.

Adsorbent	Target radionuclide	Metal Concentration	Initial pH	Contact time (min)	Removal efficiency (%)	Ref
Manisa-Gördes zeolite	Uranium	25-175 µg/mL	2-9	5-420	82.9	(63)
Manisa-Gördes zeolite	Cesium	5x10 ⁻⁵ -5x10 ² mol/L	-	420	-	(83)
Manisa clinoptilolite	Strontium	10-500 mg/L	6.2-7.7	5-2880	-	(84)
Manisa-Gördes zeolite	Polonium	-	2-8	40	90.0	(85)
Manisa-Gördes zeolite/PAN	Strontium	25-175 µg/mL	2-8	5-300	84.6	(88)
Manisa-Gördes zeolite/PAN	Polonium	-	4-6	1-180	75.0	(89)
Balıkesir-Bigadiç clinoptilolite-rich zeolite	Uranium	10-100 mg/L	2-9	5-360	88.0	(64)

Table 4: Effect of temperature on the adsorption of radionuclides by Turkish zeolites.

Zeolite	Target radionuclide	Temperature range (K)	Adsorption process	Ref.
Manisa-Gördes zeolite	Uranium	293-323	Endothermic	(63)
Manisa-Gördes zeolite	Polonium	293-323	Endothermic	(85)
Manisa clinoptilolite	Strontium	298-333	Endothermic	(84)
Manisa-Gördes zeolite/PAN	Strontium	293-323	Exothermic	(88)
Manisa-Gördes zeolite/PAN	Polonium	293-323	Endothermic	(89)
Balıkesir-Bigadiç clinoptilolite-rich zeolite	Uranium	293-303	Exothermic	(64)

Erten et al. (96) studied sorption characteristics of Cs⁺ and Sr²⁺ on Reşadiye montmorillonite and Mihaliçcik kaolinite type clays and soil fractions from various regions of Turkey using the batch method. ¹³⁷Cs and ⁹⁰Sr were used as tracers. The initial concentrations ranged from 10⁻⁸ to 10⁻² mol/L. Chemical composition of clay species, water composition, and the properties of the sorbent affect the sorption behaviours of Cs⁺ and Sr²⁺. Equilibrium was reached in 4-7 days for Cs⁺ and 7-11 days for Sr²⁺. K_d values of Mihaliçcik kaolinite for Cs⁺ and Sr²⁺ were obtained to be 200 and 100 mL/g, whereas K_d values of Reşadiye montmorillonite for Cs⁺ and Sr²⁺ were found to be 3500 and 1500 mL/g, respectively. The experimental data reveals that montmorillonite clay adsorbs Cs⁺ and Sr²⁺ much more than kaolinite clay due to their different structural characteristics. The distribution coefficients increased with decreasing grain size, suggesting mainly surface sorption.

In another study, sorption and desorption behaviors of uranyl ion on Turgutlu and Kula montmorillonites

were studied by Akçay and Kurtulmuş (71). The experimental data has shown that pH, solid/aqueous ratio, uranyl concentration, and clay particle dimension could have a significant impact on the sorption of uranium. The influence of contact time was investigated up to 50 h when soil/aqueous ratio, temperature, and pH were kept at 1/2, 293 K and 7.3, respectively. A contact time of 10 h was found sufficient for the establishment of equilibrium. The effect of clay size was examined when the other parameters were kept constant. +0.1 – 0.2 mm dimension range showed the maximum adsorption performance. The effect of initial uranium concentration was studied between 200 and 3000 mg/L. With the increase in the concentration, uranium uptake capacity of both clays increased. Kula clay has higher uranium uptake capacity than Turgutlu clay. pH studies were carried out in acidic (pH=3-6), neutral (pH=7) and basic medium (pH=8-10). In the acidic region, hydrogen ions were competing for cation exchange sites, and uranium uptake was relatively low. A fairly constant retention was observed in the pH range of 4-6, consistent

with the ion-exchange process being dominant. In the basic region, the distribution coefficient demonstrates a gradual increase with pH. The sorption and desorption ability of uranium is defined by the distribution coefficient and Langmuir's affinity constants, which encompass surface retention. The migration of uranium will be reduced, probably due to the formation of hydrolyzed and polymeric species. Diffusion of uranyl ions into the particles probably decreases desorption tendency. The data fitted to the Freundlich equation gave a nonlinear isotherm. The quantities of sorbed and desorbed uranium ions were lower than its theoretical CEC's. This was attributed to a blocking of montmorillonites' CEC by uranium islands sorbed in the interlayer. The experimental results indicate that the montmorillonites studied should be effective components of the buffer and backfill material and lead to eventual immobilization of uranium from solutions.

Kinetic and thermodynamic parameters of Sr^{2+} sorption on Sındırgı kaolinite and Manisa clinoptilolite was investigated by Akar et al. (84). Batch tests were conducted at 25 and 60°C for a contact time range of 5-2880 min. The pH of the solution was kept in the pH range between 6.2 and 7.7. Similar trends were observed for both temperatures. The sorption process followed pseudo second order kinetics, with faster sorption on kaolinite compared to clinoptilolite. Freundlich and Dubinin-Radushkevich isotherm models described data more adequately than Langmuir model. The activation energy of Sr^{2+} sorption by kaolinite was found to be -8.5 kJ/mol. The sorption process was spontaneous and endothermic at all the studied concentrations, with ΔH° being 11.3 kJ/mol for sorption on kaolinite.

Akçay and Kiliç (97) conducted sorption and desorption studies of thorium from aqueous solutions using West Anatolian montmorillonite. The authors stated that the migration of thorium will be reduced, probably due to the formation of hydrolyzed and polymerized species. Moreover, desorption coefficients are higher, probably due to the diffusion of thorium into the particles. The sorption and desorption data were described well by the Freundlich isotherm model. The sorption of thorium on West Anatolian montmorillonite was found to be concentration dependent but nonlinear. Akyüz et al. (73) conducted a study to investigate Cs^+ and Sr^{2+} sorption onto Sivrihisar-Eskişehir red clay samples using EDXRF spectrometry. XRD analysis revealed that red clay is composed of montmorillonite, illite, albite, chlorite, and quartz. For the sorption experiments, cation treated clays were prepared by immersing the natural red-clay samples in Cs^+ and Sr^{2+} bearing solutions with a concentration range of 20-400 mg/L. At low Cs^+ or Sr^{2+} concentrations (20 mg/L) high K_d values were obtained. With the increase in initial metal

concentrations, a decrease in K_d values was determined. When the cation concentration was 120 mg/L, the uptake capacities of Cs^+ and Sr^{2+} were 5.07 and 0.88 mg/g, respectively. The authors stated that the sorption of Cs^+ or Sr^{2+} ions on red-clay is concentration dependent but non-linear. Freundlich equation was the best to explain the relationship between the amount of Cs^+ or Sr^{2+} adsorbed by the red-clay. From the E value of D-R isotherm model, it was found that both Cs^+ and Sr^{2+} sorption were governed by ion-exchange. It was reported that, red clay has high affinity for Cs^+ and Sr^{2+} and it can be considered as a promising material for nuclear waste management.

Bilgin et al. (98) studied the adsorption of strontium on illite type clay as a function of shaking time, the ratio of solution volume to weight of clay, and the concentration of strontium. ^{90}Sr was used as a tracer. Clay samples were collected from Van region in Turkey with a high percentage of illite type clay mixture. 89% of the total Sr^{2+} sorption was attained in the first 10 min. The rapid adsorption reveals that Sr adsorption on illite is an ion exchange process. K_d value decreased with increasing Sr ion concentration. The effect of the initial volume of solution to that of solid (V/m) was studied for 10^{-4} mol/L initial Sr^{2+} concentration. Initially, the K_d value increased strongly with increasing V/m up to V/m=250, whereafter a plateau region was reached. When all of the available sorption sites are covered with strontium, a further increase in the V/m ratio does not appreciably change the K_d value. the variation of the K_d value with Sr loading was investigated. The adsorption experiments were carried out using the batch method and initial Sr^{2+} ion concentrations ranged from 10^{-6} to 10^{-1} mol/L. The authors reported that, Sr is adsorbed predominantly by an ion exchange mechanism in the low Sr loadings. The shapes of the curves suggest the existence of at least two types of adsorption, one taking place at high and the other at low Sr ion concentrations. The influence of Ca^{2+} and Ba^{2+} cations on Sr adsorption was also studied. In the binary Sr-Ba system, strontium uptake capacity was 211.2 mg/g. These effects are correlated with the ionic radii of alkaline earth ions present in the solution. The Freundlich and Dubinin Radushkevich (D-R) isotherms have been applied to the data and the parameters of the isotherm equations were calculated. It was found that the experimental data fit both isotherm models well.

Donat and Aytas (75) prepared algae (*Ulva sp.*)-Na bentonite composite adsorbent for the separation of U(VI) from aqueous media. Dry and powdered algae were mixed with Na bentonite. The mixture was contacted with deionized water and then mixed to ensure homogeneity. The resulting paste was heated and dried. It was reported that the wetting and drying steps are significant to maintain the maximum contact between algae and Na-bentonite.

The influence of selected parameters such as pH, U(VI) concentration, temperature, and contact time was investigated. The influence of pH on U(VI) adsorption was studied in the pH range of 2-9. The change in solution pH affects both the surface properties of adsorbent and species in the solution. It was reported that maximum U(IV) adsorption efficiency was found at pH 3 and the uranium was in the form of UO_2^{2+} . The sorption of U(VI) was examined as a function of U(VI) concentration in the range of 10-175 mg/L. It was reported that the adsorption efficiency increased with the increase in concentration up to 125 mg/L and then a decrease was observed. Sorption isotherm data fitted Freundlich and D-R isotherm well. The effect of contact time on adsorption was studied between 7.5 and 240 min. It was determined that the sorption process was very fast and the maximum adsorption efficiency was reached within minutes. 15 min was selected as the optimum contact time. At this point, the adsorption efficiency of U(VI) was $78\% \pm 1.2$. Thermodynamic studies were conducted between 293 and 343 K. It was found that adsorption of uranium is endothermic, spontaneous, and more favorable at higher temperatures.

Donat (74) investigated the adsorption of U(VI) from aqueous solution onto Eskişehir sepiolite by batch method. The effect of contact time was examined in the range of 15-1440 min, and 92% of the U(VI) ions were adsorbed in the first 240 min. Solution pH was investigated between pH=2.0-9.0 and sepiolite has a maximum sorption efficiency at pH 3.0. This can be explained by the presence of free UO_2^{2+} ions in the solution. The influence of U(VI) concentration was studied in the range of 100-500 mg/L and maximum U(VI) sorption capacity of sepiolite was found to be 34.61 mg/g. The sorption data fitted Langmuir isotherm well. Thermodynamic parameters indicated the exothermic heat of adsorption and the feasibility of the process. It has been stated by the author that sepiolite has the potential to replace activated carbon because it is cheap and abundant.

Eskişehir sepiolite has also been tested for the removal of Th(IV) from aqueous solution by Esen Erden and Donat (99). The influence of contact time, initial pH, Th(IV) concentration and temperature were examined using one factor at a time approach. The adsorption of Th(IV) was rapid in the initial stages and equilibrium was established in 45 min. Th(IV) removal efficiency (%) sharply increased between pH 2 and 3. Above pH 3.5, the uptake of Th(IV) decreased. It is known that when pH is >4 , Th(IV) ions precipitate as $Th(OH)_4$ due to the low solubility ($K_{sp}=2.0 \times 10^{-45}$) (100). The authors mentioned that the formation of strong surface complexes is the mechanism responsible for the sorption rather than ion exchange. Removal efficiency was 61.81% when the initial Th(IV) concentration was 40 mg/L. Langmuir isotherm

demonstrated slightly better fit to the adsorption data than Freundlich and D-R isotherms with a monolayer Th(IV) capacity of 49.91 mg/g. The effect of temperature was studied in the range of 293-323 K. A positive value of ΔH° indicated an endothermic process. The spontaneity of Th(IV) adsorption could be explained by negative ΔG° values.

Bayülken et al. (101) conducted a study for the investigation of Cs^+ adsorption by Çankırı-Şabanözü bentonite, Manisa-Gördes zeolite, Eskişehir-Sivrihisar sepiolite, and Balıkesir-Sındırgı, Düvertepe kaolinite. The effects of Cs^+ concentration, pH, contact time, and temperature on the adsorption were examined using ^{137}Cs radiotracer method. Bentonite was shown to exhibit the highest capacity and sorption affinity towards Cs^+ . The best fits for adsorption isotherms were with Freundlich and D-R models. The second order rate constant of cesium sorption was the highest for kaolinite among the clays. Cs^+ adsorption proceeds essentially by ion exchange and partly by specific adsorption mechanisms. The results showed that especially bentonite and zeolite can be used as effective barrier materials for sorptive hindrance of an expanding Cs^+ radioisotope plume.

Akalın et al. (76) investigated the cesium adsorption performance of raw vermiculite obtained from Sivas-Yıldızeli region of Turkey. Experiments were carried out with nonradioactive Cs^+ ($CsCl$). Results demonstrated that adsorbed Cs^+ ions gradually increased with the increasing adsorbent dosage and did not depend on contact time. The percentage of adsorbed Cs^+ ions at equilibrium increased with increasing pH up to pH 9.2. Maximum adsorption capacity (Q_{max}) was determined as 29.67 mg/g and 8.037 L/g from Langmuir and Freundlich isotherm models, respectively. Thereby, the adsorption process has both chemical and physical characters. In addition, the adsorption process is fitted to Temkin isotherm model. Cesium adsorption was investigated in the presence of K^+ ion and the amount of Cs^+ adsorbed at equilibrium was found to be 16.22 mg/g.

In another study, Tekdal (102) investigated the decontamination of low-level radioactive wastes containing ^{137}Cs radioisotope by using clay minerals. K_d is a parameter used to determine the ratio of ions adsorbed to the solid to the ions in the liquid phase (103). The results of these experiments were used to calculate the K_d values for the adsorption of cesium on clay minerals. In order to prepare the artificial waste solution, the ^{137}Cs isotope was provided by the Çekmece Nuclear Research Center, Health Physics Department. Five different clay samples were used as waste-retention material. These samples were collected from; No.2: Çukurova region, No.3: Konya region, No.7: Söğüt region, No.10: Söğütlü region, No.19: Çınar-Diyarbakır

region. The adsorption capacities of clay samples were determined by radiometric method. For this purpose, column inlet and outlet activity measurements were made by gamma spectrometry. In all experiments, background and sample counting times were counted by taking 5 mL samples. The K_d values for clay samples are calculated to be 48.15 mL/g for sample No.2, 642.59 mL/g for sample No.10, 52.46 mg/g for sample No.7, 513.27 mL/g for sample No.19, and 380.92 mL/g for sample No.3. According to these findings, samples No.10, 19 and 3 are clay samples with the highest activity adsorbents. IR analyzes have shown that these clays are smectite group clay minerals. The selectivity of the smectite group clay minerals for ^{137}Cs is due to the fact that the odd and divalent ions in the wick change with the Cs^+ ion in addition to physical adsorption. Additionally, the Cs^+ ion is large in ionic mobility, as it has the smallest hydrate radius (2.28 Å) and the number of hydrides (~ 9.9) in group I ions. For this reason, the ion exchanger is held in great force (Coulomb Force) by the material. The results of this study revealed that clay minerals have significant radioactivity retention capacities. This situation brings to mind the concern that clay deposits in Turkey may be used for radioactive waste storage and may threaten human health. Table 5 summarizes the reported use of Turkish clay minerals for radionuclide removal.

Adsorption studies by other minerals

Talip et al. (104) used expanded perlite for the removal of thorium ions from aqueous solution. The expanded perlite samples are the most economical commercial products and were provided by Eti Mine Works Perlite (İzmir, Turkey). Before adsorption tests, expanded perlite samples were mechanically washed in water for 24 h and used without chemical treatment. It was suggested that adsorption of thorium is mainly affected by the surface hydroxyl groups of the perlite. Silicon atoms on the surface are bonded to oxygen by forming a tetrahedral structure. They attach to monovalent hydroxyl groups and form silanol groups. Silanol and hydrous oxide groups on the surface are responsible for adsorption (105). The effects of particle size, solution pH, initial thorium concentration, contact time, V/m ratio, and temperature on the adsorption of thorium using expanded perlite were investigated. There was no significant effect of particle size on the adsorption. The adsorption efficiency (%) has been found to be strongly influenced by pH and thorium concentration. The adsorption of thorium onto expanded perlite was investigated from pH 2 to 7 at 303 K and efficiency increased from 20% to over 80% with the increase in pH from pH 3 to 5. This behaviour was explained by the adsorption of positively charged Th(IV) hydrolysis products. The influence of Th(IV) concentration was examined from 25 to 250 mg/L. After 50 mg/L Th(IV) concentration, the adsorption have been sharply decreased. The adsorption

equilibrium was established within 60 min at pH 4.5. Results indicated that the temperature had a minor effect on the adsorption of thorium by expanded perlite. Maximum adsorption efficiency of Th(IV) onto expanded perlite was determined as $84 \pm 4\%$. The adsorption isotherm was best modeled by Langmuir isotherm. The negative value of ΔG° indicates the spontaneous and the negative value of ΔH° shows the exothermic nature of the process. This study showed that expanded perlite can be used as an efficient adsorbent material for the adsorption of thorium from contaminated aqueous solutions, due to its high adsorption capacity, low cost, and ready availability.

Yusan et al. (106) reported a study using calcined and flux calcined diatomites for the adsorption of Th(IV) ions from radioactive waste. Diatomite samples were obtained from Turkish Sugar Factories Inc., Etimesgut-Ankara, Turkey. SiO_2 content of calcined and flux calcined diatomite were 92.68 and 89.81%, respectively. The removal of Th(IV) was affected by the alteration of solution pH. At pH 4.0, Th(IV) adsorption efficiency was maximum to be 99%. Above pH 4.0, the decrease in adsorption efficiency was observed due to hydrolyzation of Th(IV). Within 20 min of contact time, 98% and 89% of Th(IV) ions were adsorbed by calcined and flux calcined diatomites, respectively. The influence of initial concentration on Th(IV) uptake was studied between 25 and 150 mg/L. The adsorption data was well described by Freundlich isotherm for both adsorbents. The effect of temperature was investigated in the range of 288-328 K. ΔH° values for calcined and flux calcined diatomites were obtained as 35.99 kJ/mol and 23.62 kJ/mol, respectively. These values indicate the physical nature of the adsorption. The negative values of ΔG° demonstrate the spontaneity of the removal process. Sorption kinetic studies were carried out to determine the possible adsorption mechanism. The authors mentioned that kinetic data fitted pseudo-second order equation better, suggesting that the rate-limiting step is chemical adsorption.

The removal of uranium from aqueous solutions with diatomite samples supplied from the same origin was investigated by Ölmez Aytaş et al. (107). Calcination and flux calcination (with Na_2CO_3 at 1650 °C) were applied to samples to improve their mechanical properties. As a result of the preliminary tests, it was determined that the sample coded as No. 2 (Flux calcined) had the highest uranium capacity (94.82 mg/g). Further studies were performed using No. 2 (Flux calcined) sample. Adsorption efficiency of uranium was examined as a function of pH in the range of 2-7, a contact time of 24h at 303 K. Up to pH=5, authors observed a slight increase in the uranium uptake. However, uptake values decreased in the pH range of 6-7. This behaviour may be explained by the presence of UO_2^{2+} below pH 5 and stable carbonate complexes

around pH 7. Within 15 min of contact time, maximum adsorption efficiency was 77% at pH 5. 97% of uranium adsorption. A decrease in the adsorption percentage of uranium was observed with the increase in temperature from 298 to 333 K. The authors suggest that the adsorption mechanism was physisorption. Langmuir isotherm model was used to describe the equilibrium between uranium and diatomite. Monolayer capacity of the adsorbent was calculated as 38.58 mg/g for uranium. Diatomite has been reported to be an inexpensive, high-affinity adsorbent for the removal of uranium from waste solutions from uranium refining and mining.

Yusan et al. (92) investigated uranium sorption on volcanic tuff collected from the deposits located at the Tendürek, Eastern Turkey. The effects of solution pH, contact time, initial uranium concentration, and temperature were investigated one factor at a time. The effect of pH was examined between 2.0 and 9.0. Other parameters were kept constant as follows: initial concentration; 100 mg/L, temperature; 303 K, and contact time; 2 h. The

maximum removal efficiency of U(VI) was found to be 69% at pH 5.0. Initial U(VI) concentration parameter was studied in the range of 50-250 mg/L while the other parameters were kept constant. The adsorption efficiency increased gradually, up to 95% when the uranium concentration was 75 mg/L. Adsorption isotherm models were utilized to describe the uranium adsorption. Langmuir model was the best to explain adsorption equilibrium data. The maximum monolayer adsorption capacity was calculated as 2.62 mg/g. The effect of temperature on uranium adsorption was examined between 298 and 323 K and thermodynamic parameters were calculated. Adsorption efficiency gradually decreased from 94% to 76% with the increase in temperature from 298 to 323 K. It was reported that the positive value of ΔH° points out that this adsorption process has an endothermic character. Moreover, the decrease in ΔG° values with the increasing temperature indicates that the adsorption process is physisorption. The authors stated that Tendürek volcanic tuff is a naturally abundant material and it has a high capacity for the efficient removal of uranium ions from aqueous solutions.

Table 5: Data on adsorption performance of Turkish clay minerals for radionuclide ions.

Adsorbent	Target radionuclide	Metal Concentration	Initial pH	Contact time	K _d (mL/g)	Removal efficiency (%)	Q (mg/g)	Ref
Reşadiye montmorillonite	Cesium Strontium	10 ⁻⁸ -10 ⁻² mol/L (Cs) 10 ⁻⁸ -10 ⁻² mol/L (Sr)	-	4-7 d (Cs) 7-11 d (Sr)	3500(Cs) 1500(Sr)	-	-	(96)
Kula montmorillonite	Uranium	200-3000 mg/L	7.3	600 min	-	-	-	(71)
Sındırgı kaolinite	Strontium	10-500 mg/L	6.2-7.7	5-2880 min	-	-	-	(84)
Eskişehir red clay	Strontium Cesium	20-400 mg/L	7	1440 min	-	-	-	(73)
Van illite	Strontium	10 ⁻⁶ -10 ⁻¹ mol/L	-	0-60 min	-	-	211.2	(98)
Algae (Ulva sp.)-Na bentonite composite	Uranium	10-175 mg/L	2-9	7.5-240 min	-	78.2	-	(75)
Eskişehir sepiolite	Uranium	100-500 mg/L	2-9	15-1440 min	2400	96.00	34.61	(74)
Eskişehir sepiolite	Thorium	40-150 mg/L	2-5	5-360 min	-	92.90	49.91	(99)
Sivas-Yıldızeli vermiculite	Cesium	100-300 mg/L	3-10	60-480 min	-	87.00	29.67	(76)

Data on the effect of temperature on the adsorption of radionuclides with Turkish clay minerals, discussed in the text, are given in Table 6.

Table 6: Effect of temperature on the adsorption of radionuclides by Turkish clay minerals.

Adsorbent	Target radionuclide	Temperature range (K)	Adsorption process	Ref
Sındırgı kaolinite	Strontium	298-333	Endothermic	(84)
Algae (Ulva sp.)-Na bentonite composite	Uranium	303-333	Endothermic	(75)
Eskişehir sepiolite	Uranium	298-313	Exothermic	(74)
Eskişehir sepiolite	Thorium	293-323	Endothermic	(99)
Sivas-Yıldızeli vermiculite	Cesium	298-323	Exothermic	(76)

CONCLUSION

Nuclear power generation, rare-earth mining, reprocessing, nuclear medicine, and nuclear research are the main sources of radioactive isotopes released into the environment. They are dangerous to human health due to their long half life and solubility in water. This review attempts to cover a wide range of Turkish mineral adsorbents that have been used so far for the removal of radionuclides from aqueous solutions. Based on the literature reviewed, the following concluding remarks can be made:

For Turkish zeolites;

- U(VI) adsorption was investigated using Manisa-Gördes zeolite under varying parameters (pH, initial concentration, temperature, contact time, etc.), and it was determined that alteration of pH was remarkably effective. The adsorption efficiency is 82.9% at the following experimental conditions: U(VI) concentration 125 mg/L, pH=5, contact time=2 h. The process is compatible with the Langmuir model. The E value is 11.18 kJ/mol according to D-R isotherm.

- Manisa-Gördes zeolite is very stable for ^{137}Cs in LLW at pH 10.

- pH is a significant factor for Po removal and the adsorption efficiency is 90% at pH<3 with a 40 min contact time. Freundlich model is the most appropriate for fit of the experimental data, and E value is 0.1008 J/nmol.

- PAN modified zeolite is promising for Sr at pH>5 and E value was calculated as 0.91 kJ/mol from D-R isotherm. However, the composite adsorbent is effective between pH 4-6 for Po at column and E value was found to be 1.7226 J/nmol.

- The clinoptilolite type zeolite from the deposits of Çankırı-Çorum basin was the best sorbent for both Cs and Sr ions.

- The powdered form of Bigadiç zeolite treated with 0.1 mol/L HCl showed better adsorption properties for U(VI) compared to the granular form. Adsorption equilibrium data were well-fitted with Langmuir model. Uptake of U(VI) decreased with increasing calcination temperature.

- Bigadiç zeolites adsorb ^{137}Cs better than bentonite and kaolinite. Experimental adsorption data can be described by Freundlich isotherm.

- The bentonite (B-PAO) and zeolite (Z)-PAO composites were investigated for U(VI). K_L value was found to be higher on (Z)-PAO composite.

For Turkish clay minerals;

- Kaolinite based clay obtained from Çanakkale-Çan region was proposed as a reasonable candidate for the selective adsorption of Sr in waste disposal sites. On the other hand, Reşadiye montmorillonite has higher K_d values for Cs and Sr than Mihalıççık kaolinite depending on structural properties.

- For the sorption of U(VI) ions on Turgutlu and Kula montmorillonites, optimum contact time for the establishment of equilibrium was determined to be 10 h. For both clays, the maximum uptake was achieved with +0.1 -0.2 mm particle size. The increase in U(VI) concentration has a positive effect on uptake capacity. However, Kula clay showed a higher affinity for U(VI) than Turgutlu clay. K_d values of U(VI) increased in basic pH range.

- When Sr adsorption of Sındırgı kaolinite and Manisa clinoptilolite is compared, clinoptilolite shows a higher sorption capacity than kaolinite. The adsorption isotherm was best modeled by Freundlich isotherm.

- West Anatolian montmorillonites and Eskişehir-Sivrihisar red clay have been used for Th and Sr, Cs adsorption, respectively. Adsorption processes using both clays were found to be concentration dependent. Adsorption data was fitted to Freundlich isotherm. The responsible mechanism for the removal of Sr and Cs was found to be ion exchange.

- Sr affinity of Van illite was relatively high, and the maximum removal efficiency (%) was achieved in 10 min. Experimental data was fitted to Freundlich and D-R isotherms. Adsorption occurs via ion exchange in the relatively low Sr concentration range.

- The maximum U(IV) sorption efficiency using algae (*Ulva sp.*)-Na bentonite composite and Eskişehir sepiolite was reported at pH 3. The equilibrium was attained in 15 min for algae (*Ulva sp.*)-Na bentonite, whereas it took 240 min for sepiolite. Sorption isotherm data for modified bentonite fitted Freundlich and D-R isotherm well while for sepiolite it was compatible with Langmuir isotherm.

- Sivas-Yıldızeli vermiculite demonstrated high affinity for Cs^+ in basic medium. Process has both chemical and physical characters.

- The highest K_d for ^{137}Cs in low-level radioactive waste was obtained by Söğüt region clay as 642.59 mL/g.

For other Turkish minerals;

- The use of expanded perlite was suggested as a high capacity and low cost adsorbent material for the removal of Th(IV) ions. The adsorption process has been found to be strongly influenced by pH and Th(IV) concentration. Adsorption equilibrium was established within 60 min at pH 4.5. Maximum adsorption efficiency of Th(IV) onto expanded perlite was determined as $84 \pm 4\%$. Adsorption data are compatible with Langmuir adsorption isotherm.

- Diatomite samples were used for the removal of Th(IV) and U(VI) ions. 99% of Th(IV) ions were adsorbed at pH 4 whereas the maximum adsorption efficiency of U(VI) was 77% at pH 5. Th(IV) adsorption was described well by Freundlich isotherm, however U(VI) adsorption was Langmuir type. 20 and 15 min of contact time were sufficient for the attainment of equilibrium for Th(IV) and U(VI), respectively. For both ions, the adsorption mechanism was physisorption, depending on thermodynamic data.

- Tendürek volcanic tuff is a naturally abundant material and it has a high capacity for the efficient removal of U(VI) ions from aqueous solution. Adsorption efficiency of U(VI) increased gradually up to 95% when the uranium concentration was 75 mg/L. The adsorption data fitted to Langmuir model and maximum monolayer adsorption capacity was found as 2.62 mg/g. Thermodynamic data point out an endothermic process and physisorption mechanism.

Turkish minerals (natural and modified) have been successfully used for the adsorption of Sr, Cs, U, Th and Po from aqueous solution. Adsorption studies on these minerals should be continued for binary or multiple mixtures of hazardous radionuclides, and thus information about their adsorption performance in the case of a mixed solution should be obtained.

We believe that this article will shed light on the studies to be carried out in terms of the immediate supply and use of our own minerals in the event of nuclear pollution caused by both radioactive waste and atmospheric fallout.

CONFLICT OF INTEREST

The authors have no conflicts of interest to declare that are relevant to the content of this article.

REFERENCES

1. Marinin D v, Brown GN. Studies of sorbent/ion-exchange materials for the removal of radioactive strontium from liquid radioactive waste and high hardness groundwaters. *Waste Management*. 2000 Nov;20(7):545-53. [<DOI>](#)
2. Backgrounder On Radioactive Waste | NRC.gov [Internet]. [cited 2022 Feb 14]. [<URL>](#).
3. Radionuclide Basics: Strontium-90 | US EPA [Internet]. [cited 2022 Feb 14]. Available from: [<URL>](#).
4. Cakir P, Inan S, Altas Y. Investigation of strontium and uranium sorption onto zirconium-antimony oxide/polyacrylonitrile (Zr-Sb oxide/PAN) composite using experimental design. *Journal of Hazardous Materials*. 2014 Apr 30;271:108-19. [<DOI>](#)
5. van Horn J, Huang H. Uranium(VI) bio-coordination chemistry from biochemical, solution and protein structural data. *Coordination Chemistry Reviews*. 2006 Apr;250(7-8):765-75. [<DOI>](#)
6. Salinas-Pedroza MG, Olguín MT. Thorium removal from aqueous solutions of Mexican erionite and X zeolite. *Journal of Radioanalytical and Nuclear Chemistry*. 2004;260(1):115-8. [<DOI>](#)
7. Ryabchikov DI, Gol'braikh EK. *The analytical chemistry of Thorium*. Pergamon Press; 1963.
8. Skwarzec B, Bojanowski R. 210Po content in sea water and its accumulation in southern Baltic plankton. *Marine Biology*. 1988 Feb;97(2):301-7.
9. Skwarzec B, Strumińska DI, Boryło A. Radionuclides of 210Po, 234U and 238U in drinking bottled mineral water in Poland. *Journal of Radioanalytical and Nuclear Chemistry*. 2003;256:361-4. [<DOI>](#)
10. Strumińska-Parulska DI, Skwarzec B, Tuszkowska A, Jahnz-Bielawska A, Boryło A. Polonium (210Po), uranium (238U) and plutonium (239+240Pu) in the biggest Polish rivers. *Journal of Radioanalytical and Nuclear Chemistry*. 2010 Nov 19;286(2):373-80. [<DOI>](#)
11. Ug̃ur A, Özden B, Filizok I. Spatial and temporal variability of 210Po and 210Pb in mussels (*Mytilus galloprovincialis*) at the Turkish coast of the Aegean Sea. *Chemosphere*. 2011 May;83(8):1102-7. [<DOI>](#)
12. Waska H, Kim G, Kim GB. Comparison of S, Se, and 210Po accumulation patterns in common squid *Todarodes pacificus* from the Yellow Sea and East/Japan Sea. *Ocean Science Journal*. 2013 Jun 1;48(2):215-24. [<DOI>](#)
13. Singh NB, Nagpal G, Agrawal S, Rachna. Water purification by using Adsorbents: A Review. *Environmental Technology & Innovation*. 2018 Aug;11:187-240. [<DOI>](#)
14. Galamboš M, Suchánek P, Roskopfová O. Sorption of anthropogenic radionuclides on natural and synthetic inorganic sorbents. *Journal of Radioanalytical and Nuclear Chemistry*. 2012 Aug;293(2):613-33. [<DOI>](#)
15. Krajňák A, Viglašová E, Galamboš M, Krivosudský L. Application of HDTMA-intercalated bentonites in water waste treatment for U(VI) removal. *Journal of Radioanalytical and Nuclear Chemistry*. 2017 Dec 1;314(3):2489-99. [<DOI>](#)
16. Osmanlioglu AE. Natural diatomite process for removal of radioactivity from liquid waste. *Applied Radiation and Isotopes*. 2007 Jan;65(1):17-20. [<DOI>](#)
17. Osmanlioglu AE. Immobilization of radioactive borate liquid waste using natural diatomite. *Desalination*

- and Water Treatment. 2016 Jul 8;57(32):15146–53. [<DOI>](#)
18. Kam E, Osmanlioglu AE, Bozkurt A. Migration test column for decontamination of radioactive liquids by using natural tuff. *Desalination and Water Treatment*. 2014 Oct 30;52:6817–21. [<DOI>](#)
19. Republic of Turkey M of E. Mining industry in Turkey [Internet]. 2018 [cited 2021 Sep 14]. [<URL>](#).
20. Akkuyu Nükleer Güç Santrali Projesi - Nükleer Enerji ve Uluslararası Projeler Genel Müdürlüğü - T.C. Enerji ve Tabii Kaynaklar Bakanlığı [Internet]. [cited 2022 Feb 14]. [<URL>](#).
21. Pabalan RT, Bertetti FP. Cation-Exchange Properties of Natural Zeolites. *Reviews in Mineralogy and Geochemistry*. 2001 Jan 1;45(1):453–518. [<DOI>](#)
22. Gottardi G, Galli E. *Natural zeolites*. Berlin: Springer-Verlag; 1985.
23. Wang S, Peng Y. Natural zeolites as effective adsorbents in water and wastewater treatment. *Chemical Engineering Journal*. 2010 Jan 1;156(1):11–24. [<DOI>](#)
24. Polat E, Karaca M, Demir H, Onus AN. Use of natural zeolite (clinoptilolite) in agriculture. *Journal of Fruit and Ornamental Plant Research*. 2004;12:183–9.
25. Englert AH, Rubio J. Characterization and environmental application of a Chilean natural zeolite. *International Journal of Mineral Processing*. 2005 Jan 6;75(1–2):21–9. [<DOI>](#)
26. Weatherley LR, Miladinovic ND. Comparison of the ion exchange uptake of ammonium ion onto New Zealand clinoptilolite and mordenite. *Water Research*. 2004;38(20):4305–12. [<DOI>](#)
27. Margeta K, Zabukovec N, Siljeg M, Farkas A. Natural Zeolites in Water Treatment – How Effective is Their Use. In: *Water Treatment*. InTech; 2013. [<DOI>](#)
28. Pansini M. Natural zeolites as cation exchangers for environmental protection. *Mineralium Deposita*. 1996 Sep;31(6):563–75. [<DOI>](#)
29. Dyer A, Hriljac J, Evans N, Stokes I, Rand P, Kellet S, et al. The use of columns of the zeolite clinoptilolite in the remediation of aqueous nuclear waste streams. *Journal of Radioanalytical and Nuclear Chemistry*. 2018 Dec 1;318(3):2473–91. [<DOI>](#)
30. Osmanlioglu AE. Treatment of radioactive liquid waste by sorption on natural zeolite in Turkey. *Journal of Hazardous Materials*. 2006 Sep 1;137(1):332–5. [<DOI>](#)
31. Nikashina VA, Serova IB, Kats EM, Tikhonov NA, Tokmachev MG, Novgorodov PG. Mathematical modelling of the sorption dynamics of radionuclides by natural clinoptilolite in permeable reactive barriers. *Clay Minerals*. 2011 Jun 9;46(2):233–40. [<DOI>](#)
32. Zamzow MJ, Eichbaum BR, Sandgren KR, Shanks DE. Removal of Heavy Metals and Other Cations from Wastewater Using Zeolites. *Separation Science and Technology*. 1990 Oct;25(13–15):1555–69. [<DOI>](#)
33. Leppert DE. An Oregon cure for Bikini Island? First results from the zeolite immobilization experiment. *Oregon Geology*. 1998;50:140–1.
34. Valcke E, Engels B, Cremers A. The use of zeolites as amendments in radiocaesium- and radiostrontium-contaminated soils: A soil-chemical approach. Part I: Cs-K exchange in clinoptilolite and mordenite. *Zeolites*. 1997 Feb;18(2–3):205–11.
35. Valcke E, Engels B, Cremers A. The use of zeolites as amendments in radiocaesium- and radiostrontium-contaminated soils: A soil-chemical approach. Part II: Sr-Ca exchange in clinoptilolite, mordenite, and zeolite A. *Zeolites*. 1997 Feb;18(2–3):212–7. [<DOI>](#)
36. ChemTube3D. Zeolite-Clinoptilolite [Internet]. [cited 2021 Nov 30]. [<URL>](#).
37. Mockovciakova A, Orolinov Z. Adsorption properties of modified bentonite clay. *Chemine Technologia*. 2009;1:47–50.
38. Shichi T, Takagi K. Clay minerals as photochemical reaction fields. *Journal of Photochemistry and Photobiology C: Photochemistry Reviews*. 2000 Dec;1(2):113–30. [<DOI>](#)
39. Murray HH. *Applied clay mineralogy: occurrences, processing and application of kaolins, bentonites, palygorskite-sepiolite, and common clays*. Elsevier Science; 2006. 0–188 p.
40. Grim RE. *Applied Clay Mineralogy*. New York: McGraw Hill; 1962.
41. Gruner JW. The Crystal Structure of Kaolinite. *Zeitschrift für Kristallographie - Crystalline Materials*. 1932;83(1–6):75–88.
42. Brindley GW, Robinson K. Structure of Kaolinite. *Nature* 1945 156:3970 [Internet]. 1945 [cited 2022 Feb 14];156(3970):661–2. [<URL>](#).
43. Rhim J-W, Park H-M, Ha C-S. Bio-nanocomposites for food packaging applications. *Progress in Polymer Science*. 2013 Oct;38(10–11):1629–52. [<DOI>](#)
44. El-Sherbiny S, Morsy FA, Hassan MS, Mohamed HF. Enhancing Egyptian kaolinite via calcination and dealumination for application in paper coating. *Journal of Coatings Technology and Research*. 2015 Jul 1;12(4):739–49. [<DOI>](#)
45. Bhattacharyya KG, Gupta S sen. Adsorption of a few heavy metals on natural and modified kaolinite and montmorillonite: A review. *Advances in Colloid and Interface Science*. 2008 Aug;140(2):114–31. [<DOI>](#)
46. Frenkel M. Surface acidity of montmorillonites. *Clays and Clay Minerals*. 1974;22((5-6)):435–41.
47. Winchell AN. Montmorillonite. *American Mineralogist*. 1945;30(7-8):510–8.
48. Poernomo H. Sorption and dispersion of strontium radionuclide in the bentonite-quartz-clay as backfill material candidate on radioactive waste repository. *Indonesian Journal of Chemistry*. 2010 Dec 14;10(3):276–84.

49. Seliman AF, Lasheen YF, Youssief MAE, Abo-Aly MM, Shehata FA. Removal of some radionuclides from contaminated solution using natural clay: Bentonite. *Journal of Radioanalytical and Nuclear Chemistry*. 2014;300(3):969-79. [<DOI>](#)
50. Nuruzzaman M, Rahman MM, Liu Y, Naidu R. Nanoencapsulation, Nano-guard for Pesticides: A New Window for Safe Application. *Journal of Agricultural and Food Chemistry*. 2016 Jan 5;64(7):1447-83. [<DOI>](#)
51. Hendricks SB, Jefferson ME. Crystal structure of vermiculites and mixed vermiculite-chlorites. *American Mineralogist*. 1938;23(12):851-62.
52. Shirozu H, Bailey SW. Crystal structure of a 2-layer Mg-vermiculite. *American Mineralogist*. 1966;51(7):1124.
53. General Directorate of Mineral Exploration and Research. Perlite [Internet]. 2021 [cited 2021 Oct 24]. [<URL>](#).
54. General Directorate of Mineral Exploration and Research. Diatomite [Internet]. [cited 2021 Nov 24]. [<URL>](#).
55. Ruggieri F, Marín V, Gimeno D, Fernandez-Turiel JL, García-Valles M, Gutierrez L. Application of zeolitic volcanic rocks for arsenic removal from water. *Engineering Geology*. 2008 Oct 17;101(3-4):245-50.
56. Silber A, Bar-Yosef B, Chen Y. pH-Dependent kinetics of tuff dissolution. *Geoderma*. 1999;93(1-2):125-40.
57. Tachi Y, Shibutani T, Sato H, Yui M. Sorption and diffusion behavior of selenium in tuff. *Journal of Contaminant Hydrology*. 1998 Dec;35(1-3):77-89. [<DOI>](#)
58. Cerjan Stefanović Š, Zabukovec Logar N, Margeta K, Novak Tušar N, Arčon I, Maver K, et al. Structural investigation of Zn²⁺ sorption on clinoptilolite tuff from the Vranjska Banja deposit in Serbia. *Microporous and Mesoporous Materials*. 2007 Oct 1;105(3):251-9. [<DOI>](#)
59. Krestou A, Xenidis A, Pnias D. Mechanism of aqueous uranium (VI) uptake by natural zeolitic tuff. *Minerals Engineering*. 2003 Dec;16(12):1363-70. [<DOI>](#)
60. Humelnicu D, Drochioiu G, Sturza MI, Cecal A, Popa K. Kinetic and thermodynamic aspects of U(VI) and Th(IV) sorption on a zeolitic volcanic tuff. *Journal of Radioanalytical and Nuclear Chemistry*. 2006 Dec;270(3):637-40. [<DOI>](#)
61. Köktürk U. Zeolit Madenciliği ve Çevre Sağlığına Etkileri. 1995;
62. Ataman G, Gündoğdu N. Analcimic zones in the tertiary of Anatolia and their geologic positions. *Sediment Geology*. 1982;31:89-99.
63. Kilincarslan A, Akyil S. Uranium adsorption characteristic and thermodynamic behavior of clinoptilolite zeolite. *Journal of Radioanalytical and Nuclear Chemistry*. 2005 May;264(3):541-8. [<DOI>](#)
64. Aytas SO, Akyil S, Eral M. Adsorption and thermodynamic behavior of uranium on natural zeolite. *Journal of Radioanalytical and Nuclear Chemistry*. 2004;260(1):119-25. [<DOI>](#)
65. Akyüz T. Strontium and cesium sorption of some anatolian zeolites. *Journal of Inclusion Phenomena and Molecular Recognition in Chemistry*. 1996;26(1-3):89-91.
66. DPT. Sekizinci Beş Yıllık Kalkınma Planı, Madencilik Özel İhtisas Komisyonu Raporu, Endüstriyel Hammaddeler Alt Komisyonu Genel Endüstri Mineralleri IV (Bentonit-Barit-Diatomit-Aşındırıcılar) Çalışma Grubu Raporu. Ankara; 2001.
67. Republic of Turkey Ministry of Trade. Mining industry in Turkey [Internet]. 2019 [cited 2021 Sep 14]. [<URL>](#).
68. Yücel BM, Gül Ö. Dünyada ve Türkiye’de bentonit. 2018.
69. General Directorate of Mineral Exploration and Research. Sepiolite [Internet]. 2021 [cited 2021 Oct 10]. [<URL>](#).
70. Can G. Dünya’da ve Türkiye’de sepiyolitik kil . *Jeoloji Mühendisliği Dergisi*. 1992;41:166-70.
71. Akçay H, Kurtulmuş F. Study of uranium sorption and desorption on some Turkish clays. *Journal of Radioanalytical and Nuclear Chemistry Letters*. 1995 Aug;200(6):529-44. [<DOI>](#)
72. Sari A, Tuzen M, Citak D, Soylak M. Equilibrium, kinetic and thermodynamic studies of adsorption of Pb(II) from aqueous solution onto Turkish kaolinite clay. *Journal of Hazardous Materials*. 2007 Oct 22;149(2):283-91. [<DOI>](#)
73. Akyüz T, Akyüz S, Bassari A. The Sorption of Cesium and Strontium Ions onto Red-Clay from Sivrihisar-Eskisehir (Turkey). *Journal of Inclusion Phenomena and Macrocyclic Chemistry*. 2000;38(1/4):337-44. [<DOI>](#)
74. Donat R. The removal of uranium (VI) from aqueous solutions onto natural sepiolite. *Journal of Chemical Thermodynamics*. 2009 Jul;41(7):829-35. [<DOI>](#)
75. Donat R, Aytas S. Adsorption and thermodynamic behavior of uranium(VI) on Ulva sp.-Na bentonite composite adsorbent. *Journal of Radioanalytical and Nuclear Chemistry*. 2005 Jun;265(1):107-14. [<DOI>](#)
76. Akalin HA, Hiçsönmez Ü, Yılmaz H. Removal of cesium from aqueous solution by adsorption onto sivas-yıldızeli (Türkiye) vermiculite: Equilibrium, kinetic and thermodynamic studies. *Journal of the Turkish Chemical Society, Section A: Chemistry*. 2018;5(1):85-116. [<DOI>](#)
77. Gürtürk M, Oztop HF, Hepbasli A. Energy and exergy assessments of a perlite expansion furnace in a plaster plant. *Energy Conversion and Management*. 2013;75:488-97. [<DOI>](#)
78. Uluatam SS. Assessing perlite as a sand substitute in filtration. *Journal / American Water Works Association*. 1991;83(6):70-1. [<DOI>](#)

79. Turanlı L, Uzal B, Bektas F. Effect of material characteristics on the properties of blended cements containing high volumes of natural pozzolans. *Cement and Concrete Research*. 2004 Dec;34(12):2277-82. [<DOI>](#)
80. Yılmaz Y, Güner Y, Şaroğlu F. Geology of the quaternary volcanic centres of the east Anatolia. *Journal of Volcanology and Geothermal Research*. 1998 Oct;85(1-4):173-210. [<DOI>](#)
81. Sorg TJ. Removal of Uranium from Drinking Water by Conventional Treatment Methods. In: Cothorn CR, Rebers PA, editors. *Radon, radium and uranium in drinking water*. Lewis Publishers ; 1991.
82. Ahmadi SJ, Akbari N, Shiri-Yekta Z, Mashhadizadeh MH, Pourmatin A. Adsorption of strontium ions from aqueous solution using hydrous, amorphous MnO₂-ZrO₂ composite: A new inorganic ion exchanger. *Journal of Radioanalytical and Nuclear Chemistry*. 2014;299(3):1701-7. [<DOI>](#)
83. Atun G, Bodur N. Retention of Cs on zeolite, bentonite and their mixtures. *Journal of Radioanalytical and Nuclear Chemistry*. 2002;253(2):275-9. [<DOI>](#)
84. Akar D, Shahwan T, Eroglu AE. Kinetic and thermodynamic investigations of strontium ions retention by natural kaolinite and clinoptilolite minerals. *Radiochimica Acta*. 2005;93(8):477-85. [<DOI>](#)
85. Hicsonmez U, Erenturk SA, Gorgun AU, Aslani MAA. Removal of 209Po from aquatic environment and its equilibrium and thermodynamic parameters. *J Environ Radioact*. 2020 Sep 1;220-221:106280. [<DOI>](#)
86. Başçetin E, Atun G. Adsorptive Removal of Strontium by Binary Mineral Mixtures of Montmorillonite and Zeolite. *Journal of Chemical & Engineering Data*. 2010 Feb 11;55(2):783-8. [<DOI>](#)
87. Yıldız B, Erten HN, Kış M. The sorption behavior of Cs + ion on clay minerals and zeolite in radioactive waste management: Sorption kinetics and thermodynamics. *Journal of Radioanalytical and Nuclear Chemistry*. 2011;288(2):475-83. [<DOI>](#)
88. Yusan S, Erenturk S. Adsorption Characterization of Strontium on PAN/Zeolite Composite Adsorbent. *World Journal of Nuclear Science and Technology*. 2011;01(01):6-12. [<DOI>](#)
89. Erenturk SA, Kaygun AK. Removal of 210Po from aqueous media and its thermodynamics and kinetics. *Journal of Environmental Radioactivity*. 2017 Aug 1;174:3-9. [<DOI>](#)
90. Aharoni C, Tompkins FC. Kinetics of Adsorption and Desorption and the Elovich Equation. *Advances in Catalysis*. 1970;1-49.
91. Hosseini M, Mertens SFL, Ghorbani M, Arshadi MR. Asymmetrical Schiff bases as inhibitors of mild steel corrosion in sulphuric acid media. *Materials Chemistry and Physics*. 2003 Feb;78(3):800-8. [<DOI>](#)
92. Yusan S, Aslani MAA, Turkozu DA, Aycan HA, Aytas S, Akyil S. Adsorption and thermodynamic behaviour of U(VI) on the Tendurek volcanic tuff. *Journal of Radioanalytical and Nuclear Chemistry*. 2010 Jan;283(1):231-8. [<DOI>](#)
93. Şimşek S, Ulusoy U. Uranium and lead adsorption onto bentonite and zeolite modified with polyacrylamidoxime. *Journal of Radioanalytical and Nuclear Chemistry*. 2012 Apr;292(1):41-51. [<DOI>](#)
94. Kabay N, Demircioğlu M, Yaylı S, Günay E, Yüksel M, Sağlam M, et al. Recovery of Uranium from Phosphoric Acid Solutions Using Chelating Ion-Exchange Resins. *Industrial & Engineering Chemistry Research*. 1998 May 1;37(5):1983-90. [<DOI>](#)
95. Keçeli G. Adsorption Kinetics and Equilibria of Strontium onto Kaolinite. *Separation Science and Technology (Philadelphia)*. 2015 Jan 2;50(1):72-80. [<DOI>](#)
96. Erten HN, Aksoyoglu S, Hatipoglu S, Göktürk H. Sorption of Cesium and Strontium on Montmorillonite and Kaolinite. *Radiochimica Acta*. 1988 May 1;44-45(1):147-52. [<DOI>](#)
97. Akçay H, Kiliç S. Sorption and desorption of thorium from aqueous solutions by montmorillonite. *Journal of Radioanalytical and Nuclear Chemistry Letters*. 1996 Feb;212(3):173-85. [<DOI>](#)
98. Bilgin B, Atun G, Keçeli G. Adsorption of strontium on illite. *Journal of Radioanalytical and Nuclear Chemistry*. 2001;250(2):323-8. [<DOI>](#)
99. Erden KE, Donat R. Removal of thorium(IV) from aqueous solutions by natural sepiolite. *Radiochimica Acta*. 2017;105(3):187-96. [<DOI>](#)
100. Neck V, Müller R, Bouby M, Altmaier M, Rothe J, Denecke MA, et al. Solubility of amorphous Th(IV) hydroxide - application of LIBD to determine the solubility product and EXAFS for aqueous speciation. *Radiochimica Acta*. 2002 Sep 1;90(9-11):485-94. [<DOI>](#)
101. Bayülken S, Başçetin E, Güçlü K, Apak R. Investigation and modeling of cesium(I) adsorption by Turkish clays: Bentonite, zeolite, sepiolite, and kaolinite. *Environmental Progress and Sustainable Energy*. 2011 Apr;30(1):70-80. [<DOI>](#)
102. Tekdal M. Decontamination of Liquid Radioactive Wastes Using Clay Minerals. *Cumhuriyet Science Journal*. 2018;39(3):628-34. [<DOI>](#)
103. Kamel N, Navratil J. Migration of 134Cs in unsaturated soils at a site in Egypt. *Journal of Radioanalytical and Nuclear Chemistry*. 2002;254:421-30. [<DOI>](#)
104. Talip Z, Eral M, Hiçsönmez Ü. Adsorption of thorium from aqueous solutions by perlite. *Journal of Environmental Radioactivity*. 2009 Feb;100(2):139-43. [<DOI>](#)
105. Dogan M, Alkan M, Onganer Y. Adsorption of methylene blue from aqueous solution onto perlite. *Water, Air, & Soil Pollution*. 2000;120:229-48. [<DOI>](#)
106. Yusan S, Gok C, Erenturk S, Aytas S. Adsorptive removal of thorium (IV) using calcined and flux calcined diatomite from Turkey: Evaluation of equilibrium, kinetic

İnan S, Hiçsönmez Ü. JOTCSA. 2022; 9(2): 579-600.

REVIEW ARTICLE

and thermodynamic data. Applied Clay Science. 2012 Oct;67-68:106-16. [<DOI>](#)

107. Ölmez Aytaş Ş, Akyil S, Aslani M, Aytekin U. Removal of uranium from aqueous solutions by diatomite (Kieselguhr). Journal of Radioanalytical and Nuclear Chemistry. 1999;240(3):973-6. [<DOI>](#)



Biogas Production from Wheat Straw using Textile Industrial Wastewater by Co-digestion Process: Experimental and Kinetic Study

Punam Rani^{1,2*} , Vinayak Vandan Pathak² , Megha Bansal² 

¹Government College for Women, Faridabad, Haryana, India

²Department of Chemistry, Manav Rachna University, Faridabad, Haryana, India

Abstract: In the present experimental study, anaerobic co-digestion of wheat straw with textile industry wastewater (TIWW) was evaluated for biogas production. Anaerobic digestion systems were operated at ambient temperature (28-30 °C) for 20 days. Five different ratios of wastewater with distilled water were added to wheat straw inoculated with cow dung operating in five digesters. Time-rate derivative models, including Gompertz's model and its related extensions, were used to represent yields. It has been found that the slurry containing wheat straw and cow dung digested with 75% diluted wastewater has the maximum production, while the slurry digested with only wastewater (not diluted with distilled water) has minimum production.

Keywords: Biogas, lignocellulosic biomass, bioenergy, wastewater, co-digestion

Submitted: October 16, 2021. **Accepted:** March 31, 2022.

Cite this: Rani P, Pathak V, Bansal M. Biogas Production from Wheat Straw using Textile Industrial Wastewater by Co-digestion Process: Experimental and Kinetic study. JOTCSA. 2022;9(2):601-12.

DOI: <https://doi.org/10.18596/jotcsa.1009483>.

***Corresponding author. E-mail:** punamchemistrygcw@gmail.com.

INTRODUCTION

The continuous increase in the price of fossil fuels, greenhouse gas emissions and dependency on non-renewable energy has attracted the attention of researchers to explore sustainable and affordable energy resources. Rapid urbanization and industrialization have not only increased the energy demand but also released significant amounts of waste in various forms. Globally, the expected increase in energy demand is by 45-60% by 2030, and currently a major fraction of energy (85%) is accomplished from conventional energy sources (1, 2). The potential of biomass-based energy generation has to be recognized by various researchers who have found it as a reliable and affordable energy resource. A variety of biomass has been used for the production of biofuels depending upon the constituents or the type of bio-energy product depends upon the process applied for this conversion e.g. fermentation results into

bio-ethanol or biodiesel while anaerobic digestion gives biogas production etc. among different bio-energy products, anaerobic digestion for biogas production is preferred over other chemical or biological methods due to its good output/input ratio. Anaerobic digestion (AD) is a biological process in which organic matter is decomposed by an assortment of microbes under oxygen-free conditions and produces biogas (about 50-75% CH₄ and 25-50% CO₂). Till date, a lot of work has been done for improvements in biogas production and is also in continuation. As in the process of anaerobic digestion, a huge amount of water is required for slurry formation, and thus water wastage is a drawback of anaerobic digestion. This can be improved by replacing distilled water with wastewater from various sources. As the living standards of people have been enhanced, this has resulted in the growth of industrialization. Hence, industrialization is increasing day by day, which releases more industrial wastewater (3). The type of

wastewater depends upon the type of industry or the general used process. Industrial wastewater can be categorized as inorganic and organic wastewater. Inorganic wastewater mainly disposed of coal, steel, and metallic industries. Organic wastewater is mainly produced by the pharmaceutical, beverages, and textile industries (4).

The textile wastewater components are determined by the operations performed, type of the fabric, and the chemicals and dyes used. The color of the wastewater and the type of the dyeing material used play very important roles in the component of wastewater (5). The composition of industrial or textile waste varies with the enhanced variety of manufactured products and with the demand of consumers, so today wastewater has a large number of chemicals that need new methods for degradation and consumption in a sustainable manner (6). Most of the wastewater is discharged with no special treatment into ponds and rivers which leaves them highly polluted. This improper management of waste water from industries is the main cause of environmental hazards (7). Increased population demand for more textile products, as well as an increase in the number of textile industries and wastewater, are the main reason for water pollution worldwide. Specially the colored effluents of the textile wastewater breakdown into different chemical products, making the quality of water very harmful for aquatic life and causing eutrophication and perturbations in aquatic life (8). The use of textile wastewater for anaerobic treatment can help in controlling the water pollution (9). For the last few decades, wastewater has taken the attention of many scientists to be used for some other beneficial purposes like extraction of heavy metals, conversion into biofuels etc. Marques et al. (2001) (10) suggested that olive mill wastewater could be converted into 65-70% biogas using piggery effluent without any chemical modification or dilution with water.

As the nature of the synthetic dyes is toxic for each and every type of living beings so it should not be disposed to the water bodies directly. In the process of manufacturing the textile dyeing and printing more than 8000 chemicals are used in different processes. An average-sized textile mill having a production of about 8000 kg of fabric per day uses about 1.6 million liters of water (11). The World Bank estimated that around 20% of industrial water pollution is due to textile dyeing and finishing treatment given to fabric (12). Azo reactive dyes are very common for dyeing cotton fabric. These dyes cannot be treated using activated sludge treatment or other chemical treatment. The process of chemical coagulation and flocculation for adsorption is used to remove the color from the wastewater, but for the removal of the

contaminants, an advanced oxidation process has been developed, but they are not cost effective due to their high consumption of energy so they cannot be applied in general. As a result, there is a need for a simple and effective process that can be used to make the textile wastewater nontoxic. This process must be cost-effective and environmentally safe. Anaerobic digestion is one of the biological treatments of textile wastewater that helps with contaminants' removal (11). Treatment of textile wastewater by using suitable microorganisms and media in up-flow anaerobic fixed bed reactor (UAFB) can remove COD and color up to 81.33% and 86.78%, respectively, at highest loading rate (13). The biogas production of various biomass using this wastewater can be improved as it provides good nutrients to the methane-producing microorganisms. Incorporation of different biomass to generate biogas is called as "co-digestion". This helps optimize the biogas production (14). Different types of biomass can be considered as the best option as they have the large potential due to their abundance of carbohydrates, which can fulfill requirements for biogas generation and could satisfy fuel supply in the future (15, 16). The major problem in the process of conversion of lignocellulosic biomass into bio-fuels is the complex structure of the biomass that restricts the biological and chemical treatments needed to unfasten the poly-carbohydrates into mono-carbohydrates (17). Different countries have different biomass potentials depending upon temperature and other conditions (18). There is a vast variety of organic materials that can be used as a good substrate for biogas production, like agricultural waste, food and vegetable waste, sewage sludge, manure, and municipal waste, etc. (19).

Jijai et al., (20) suggested that enhanced bio-methane production from chicken manure when co-digested with Thai rice noodle wastewater in different ratios proves the effective role of co-digestion in boosting the biogas yield. The effect of phyto-degradation by *Pistia stratiotes* on wastewater of sugar-mill and its special use for biogas production was investigated and observed (21).

As the process of anaerobic digestion has been used for many years all over the world, it is not a new process. However, the important point is that it was processed without proper knowledge of the mechanism of the reaction in it, so it was not known earlier what the role of carbon content in the substrate was for this process to produce the biogas. Now as the chemistry behind the process of anaerobic digestion has become more clear, it helps understand the role of the structure of cellulose hemicelluloses and lignin in conversion into biomethane (22). To understand the process of

anaerobic digestion of any substrate, the fundamental factors are as follows:

1. Providing proper contact between bacteria and carbon containing substrate,
2. Providing sufficient retention time for bacteria, and
3. Providing suitable uniform environment for depolymerization of complex carbohydrates (23). A lot of factors are there which affect the anaerobic digestion process like pH, temperature, retention time, and the nutrients present in slurry (24).

Agricultural wastes are made up of mainly carbohydrates and have a great potential to be converted into bioenergy and other value-added products. So, conversion to biogas is one of these products that gives many environmental benefits. The global production of wheat was 729 Tg in 2014, and it is one of the three most cultivated crops in the world. As the ratio of straw to grain is 1.5, the production of straw is more than one billion tons annually. Thus, wheat straw is a sustainable substrate due to its availability in abundant amount and at low cost (25). Wheat straw biomass is widely used for the production of biogas, hydrogen fuel, bioethanol, and other complementary products like briquette production (26).

In the present study, textile wastewater is used as a solvent for making the slurry from lignocellulosic biomass and inoculums. Lignocellulosic biomass gives better result when integrated with textile wastewater for the production of biogas. The process of biomethanation has been boosted up by the use of textile wastewater.

MATERIALS AND METHODS

Collection and Characterization of Wastewater

TWW was treated with hydrogen peroxide (H₂O₂) and sodium hypochlorite (NaOCl) before discharge to minimize its hazardous effects. To avoid further oxidation and degradation of wastewater constituents, the sample was stored in an air-tight plastic container at 4 °C without the addition of any chemicals. The physio-chemical characteristics of textile wastewater sample were determined in the laboratory as per Standard Methods for the Examination of Water and Wastewater, 21st Edition, American Public Health Association/American Water Works Association/Water Environment Federation, Washington DC, and are reported in Table 1. The characterization of each parameter has been carried out in triplicate.

Table 1: Characteristic of the textile wastewater sample.

S.No.	Parameter	Wastewater sample
1	pH	8.6±0.14
2	COD	1390±3.5
3	BOD(5 days)	760±2.8
4	TDS	3400±8
5	TSS	168±1.8
6	Sulfides	6±0.16
7	Chlorides	78±0.24
8	Nitrates	4.5±0.12
9	Phosphates	5.8±0.11
10	Electrical conductivity	964±3.2
11	Oil & grease	12

*All the values except pH and EC are in mg/L.

Collection and Characterization of Wheat Straw and Cow Dung (inoculum)

Wheat (*Triticum aestivum*) straw for biogas production was collected from agricultural fields located in Faridabad (India). The straw was cut into pieces with a size smaller than 20 mm, prior to its application. Cow dung was used as an inoculum for the source of methanogens, which was collected from a local dairy farm located in the same region. The characterization of feed wheat straw and inoculum has been performed in the laboratory. The characteristics of wheat straw and cow dung are reported in Table 2. Wheat straw and inocula (cow

dung) were analyzed for evaluation of total solids (TS), total-Kjeldahl nitrogen (TKN), pH, and volatile solids (VS). TS was determined by drying in an oven at 100 °C for 48 h. VS content was determined by the mass of sample remaining after heating the dried milled sample at 550 °C for 4 h (27). The TS and VS of the substrate were determined before and after AD by 2540B method (27). The total carbon by Walkley&Black method (28), total nitrogen 4500-C (27), and chemical oxygen demand open reflux method (COD) by 5220B (27) of the substrate were analyzed. The pH value was detected by a digital pH meter (Cph-102).

Table 2: Compositional characterization of substrates.

Parameters	Cow Dung	Wheat straw
pH	6.2±0.12	7.1±0.14
TS%	32.4±0.11	76.4±1.22
VS%	21.2±0.01	86.23±1.35
TKN%	0.23±0.01	0.4±0.01
TOC%	4.75±0.21	8.82±0.22
COD(mgL ⁻¹)	80±1.2	200.0±4.3
C/N ratio	20.7±0.57	46.5±0.78
Celluloses%	19.6±0.16	39.5±0.56
Hemicelluloses%	21.8±0.24	26.8±0.34
Lignin%	1.9±0.14	6.6±0.12

*All the values except pH and C/N are in mg/L.

The wastewater was used at 25%, 50%, and 75% dilutions and at full concentration (100%).

Anaerobic Digestion Experiments

Anaerobic digestion experiments were performed in triplicate at room temperature (25-30 °C). Aspirator glass bottle (1 liter) was used as the bio-reactor. Wheat straw and cow dung were mixed together in 1:1 ratio and the slurry was prepared in proportion of 1:10 by using industrial wastewater diluted with distilled water. This wastewater is used as a top-up volume in collaboration with distilled water in various ratios to improve the biogas production from lignocellulosic biomass, i.e., wheat straw. Experimental setups have been prepared using wastewater and distilled water at 25%+75%, 50%

+50%, 75%+25%, and at 100%+0%, respectively. A control set up was also tested for anaerobic digestion by loading wheat straw, cow dung, and distilled water in 1:10 for the determination of enhancement in biomethane potential of the substrate, which is important to evaluate the exact biomethane potential of wheat straw using industrial wastewater. Basic operating parameters of the digester set-ups are listed in Table 3 below. The slurry from all experimental set-ups was analyzed for physico-chemical characterization as soon as it was prepared and after completion of the experiment.

Table 3: Basic operating parameters of digester set up.

S. No.	Parameters	Particular detail
1	Hydraulic retention time (HRT)	20 days
2	Operating temperature	25-35 °C
3	C/N	20-30
4	Substrate concentration(TS)	76.40%
5	Substrate/inocula ratio	1:1

Liquid Digestate Characterization

After completion of experiments, the digested slurry was collected from the anaerobic digestion reactors and analyzed as per the methods discussed in the section titled "Collection and Characterization of Wheat Straw and Cow Dung (inoculum).

observed using modified Gompertz model. In order to understand the influence of the addition of wastewater instead of simple water (in slurry preparation) on biogas production, a modified Gompertz model was employed to evaluate the cumulative biogas production. (29, 30)

Kinetic Study of Biogas Production

The yield of AD process depends upon the rate of depolymerisation of substrate by the microbes. Thus, the kinetic study of the reaction has been

$$Y(t) = P \exp\{-\exp m P \lambda - 1 + 1\} \quad (1)$$

Where, Y (t) is the cumulative biogas yield (mL) with respect to time t (days), P is the maximum

biogas production potential (mL), μ_m is maximum biogas production rate (mL/day), λ is lag phase (days). All parameters were estimated by using nonlinear curve fitting by using PAST 4.03 statistical software.

Statistics

The anaerobic digestion experiments were performed in triplicate. The statistical calculations, modeling, optimization, and graphical work were performed using Microsoft Excel.

Economic Evaluation of Bioenergy Generation Process

An economic analysis of the experimental yields of the present study has been performed for the biomethane production process in this study. A comparison of different yields from energy recovery of bioenergy generation process and cost-effective combination was observed and analyzed. The evaluation is also compared to other wastewater-bioenergy conversions reported earlier by several researchers (31).

RESULTS AND DISCUSSION

Textile Wastewater Characteristics

The textile sector produces large amount of wastewater with lots of contamination and high pH and COD value. The pH of TWW samples is 8.6, which is alkaline in nature. COD and TOC of sample are appropriate after dilution for growth and activity of microbial population. The characterization of wastewater has been listed in Table 2. Oil and grease are low in value, but there is sufficiently high amount of other water pollutants, i.e., sulfides, chlorides, and phosphates. Total suspended solids and total dissolved solids are 168 and 1360 mg/L, respectively.

Feedstock Characteristics

Table 4: Design of the experimental set ups after preparation of experimental slurry for digestion of wheat straw with cow dung and yields obtained.

Set ups	Wheat straw: cow dung	Dilution of TWW percentage	Distilled Water (mL)	Textile Wastewater (mL)	HRT	Biogas production (mL/kg VS)
A1	1:1	Control	600	0	20 Days	418
A2	1:1	75%	450	150	20 Days	588
A3	1:1	50%	300	300	20 Days	510
A4	1:1	25%	150	450	20 Days	456
A5	1:1	100%	0	600	20 Days	408

Daily biogas production of the anaerobic digesters is shown in Figure 1. It has been found that the slurry

Feedstocks are the most important parameters for designing and operating an anaerobic digester. The initial characteristics of the starting material have an effective role in initiation, process consistency, and bio-energy production during anaerobic digestion. Hence, the target of enhanced biogas production can be achieved. Initial pH of wheat straw was 7.1, while it was 6.2 for cow dung. Table 2 shows the characteristics of raw wheat straw and cow dung. Volatile solid content of wheat straw is very good i.e. 86.73% as compared to cow dung, i.e., 21.6%. The cow dung manure had already undergone the process of digestion, so it had a low value of volatile solids. C/N ratios of inocula used in the study were in between the optimal range of C/N ratio for anaerobic digestion, i.e., 20 to 30, while that of substrate was quite high. The co-digestion of lignocellulosic biomass with animal manure can adjust the C/N of slurry to an appropriate level.

Biogas Yield from Different Experimental Slurries

During the anaerobic digestion of all types of digester slurry, a significant change in all selected physico-chemical parameters was observed. The time course reduction in the selected slurry parameters has been given in Table 6. Among all the five digesting set ups of wheat straw, the highest percent reduction of pH, TS, TOC, VS, COD, TKN, and C/N ratio for 75% dilution of wastewater (SlurryA2) has been encountered at room temperature with maximum biogas production (588 mL). Table 4 shows that biogas production has been increased when the slurry contained distilled water and textile wastewater at 3:1 ratio. As the ratio of wastewater in the slurry increases, the activity of methanogens decreases, thus falling off the production of biogas. The daily and cumulative biogas production of all the digesters is shown in Figures 1 and 2, respectively.

containing wheat straw and cow dung digested with 75% diluted wastewater has maximum production,

while the slurry digested with only wastewater (not diluted with distilled water) has the minimum production.

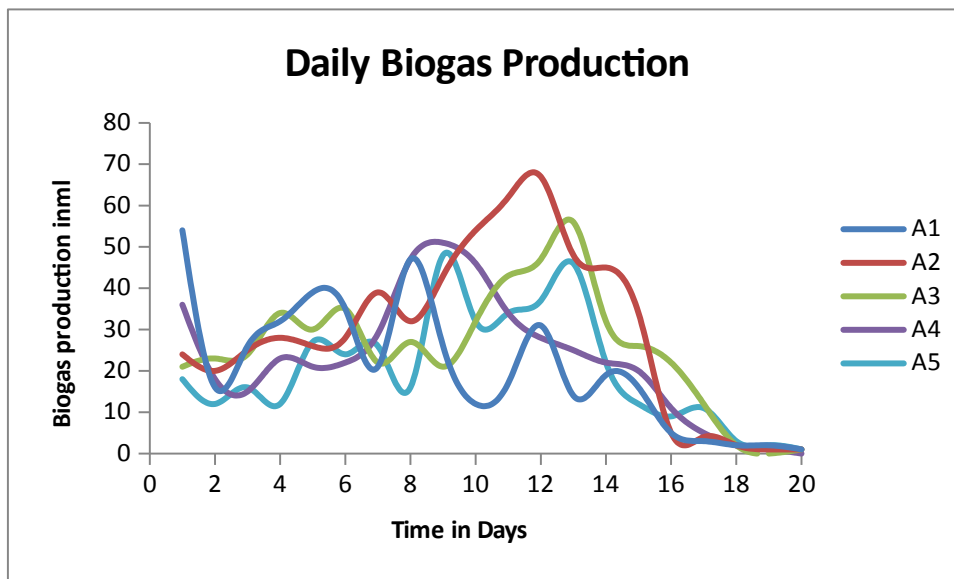


Figure 1: Daily biogas production from different slurries.

Daily and cumulative production showed that 75% dilution of wastewater provides a suitable environment for the bacterial colostr to grow and

procure depolymerization of complex carbohydrates into simple ones and then to methane.

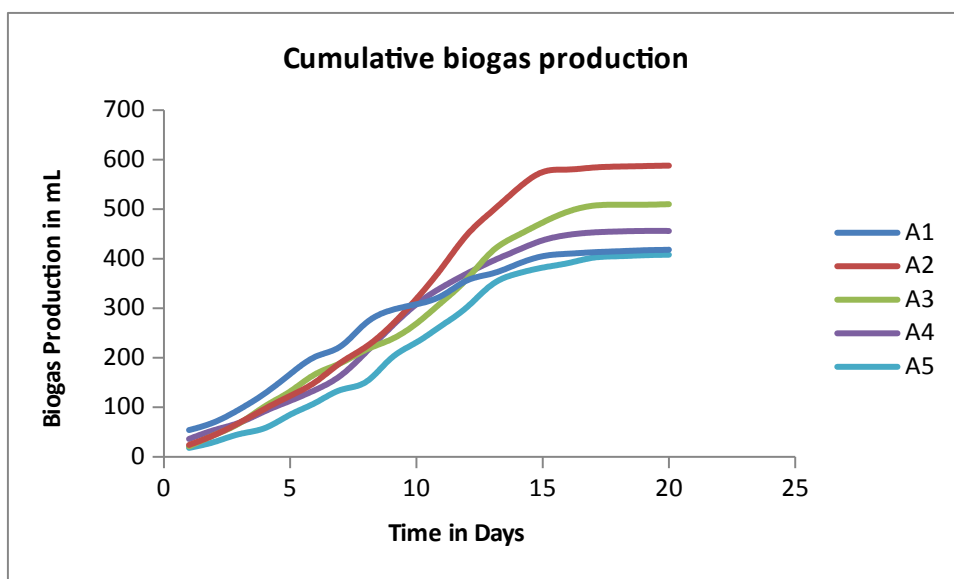


Figure 2: Cumulative biogas production of different slurries.

Effect of Wastewater Composition on Biogas Generation

The ions present in the slurry are crucial parameters as they determine the granulation and stability of the reactor (32). Thus, methanogens perform according to the environment they are provided with. Methanogens need some nutrients that help the working capability of the microbes for methane production (33). The experimental work performed shows that higher concentration of wastewater

lowers the biogas production due to hindrance in methanogens' activity. Also, as the concentration of wastewater remains at appropriate level, it provides proper nutrients to microbes, thus enhances the production of biogas. This can be properly understood by the change in CODs before and after slurry of each sample. Chemical oxygen demand (COD) of any biomass or slurry is calculation of the oxygen equivalent of the organic matter content. Change in COD is amount of oxygen removed by

changing organic compounds to CH₄, a significant amount of CO₂, H₂, and negligible amounts of other gases like H₂S (34). These changes in CODs are shown in Fig 4. The decrease in CODs of all 5 slurry samples are 56.23%, 26.60%, 31.36%, 72.49% and 33.74% respectively. This shows that the maximum decrease in CODs occurs in the digester having a

wastewater concentration of 25%, i.e., sample A2. This can easily come to the fact that accurate ions in limited amount can enhance the potential and activity of methanogens for better performance. Similarly, Manjula and Mahanta (21) showed the effect of the change in CODs in boosting biogas production.

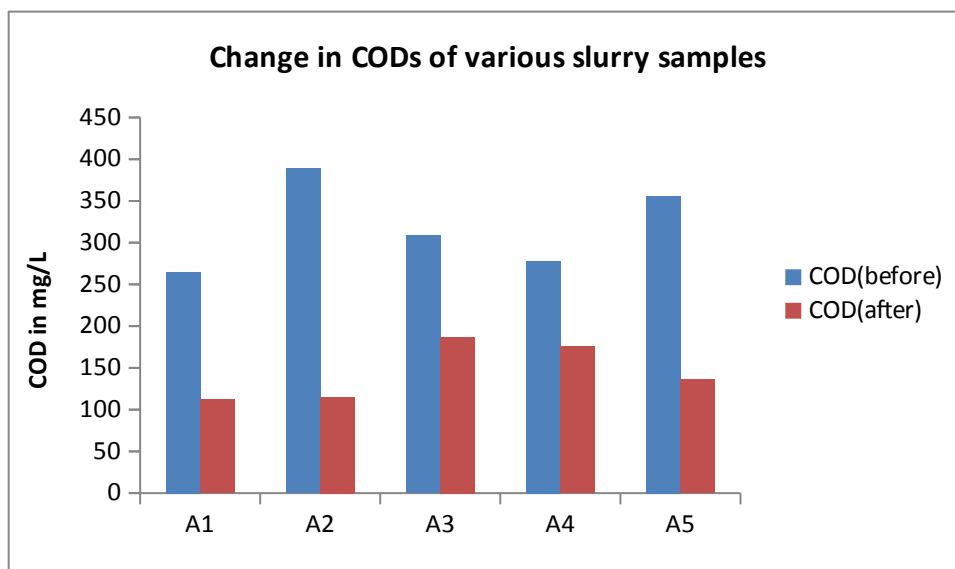


Figure 3: Change in CODs of various slurries samples.

Statistical Analysis of the Results of Experiments

Data were analyzed for means and variances, and statistical significance was determined using non-

linear regression using Excel with a threshold p-value of 0.05. The analysis of samples shows that coefficients and other values are best suited for A2 sample, satisfying the experimental work.

Table 5: Statistical analysis of slurry samples.

Sample	Coefficients	Standard Error	t Stat	P-value	Lower 95%	Upper 95%
A1	68.2	15.80438906	4.315257	0.000417	34.9962108	101.40379
A2	-30.03157895	21.03385729	-1.42777	0.170477	-74.222073	14.158915
A3	-9.105263158	13.21098212	-0.68922	0.499474	-36.860507	18.64998
A4	-22.8	11.0269566	-2.06766	0.053357	-45.966776	0.3667761
A5	-19.25789474	13.43097183	-1.43384	0.168761	-47.475319	8.95953

ANOVA showed a significant difference in biogas yield from A2 slurry as compared to A1 slurry (p < 0.05). This increase in biogas production from A2 slurry might have happened because textile wastewater in appropriate ratio with distilled water has good nutritive value for methanogenic microorganisms. Thus, it would have provided an additional microbial workforce to degrade and convert the available polysaccharides into biogas. CD could have also alleviated the potential toxicity of textile wastewater due to its complex composition containing chelating agents and the ability to enhance the degradation of recalcitrant compounds. Moreover, the C/N ratio of the A2 mixture was also in a particular range, i.e, 21–25.

The values of biogas produced by different set-ups are compared with the predicted values obtained from the statistical analysis of all the experimental yields. This also helps to estimate the result that A2 gives the minimum difference between predicted and experimental yield.

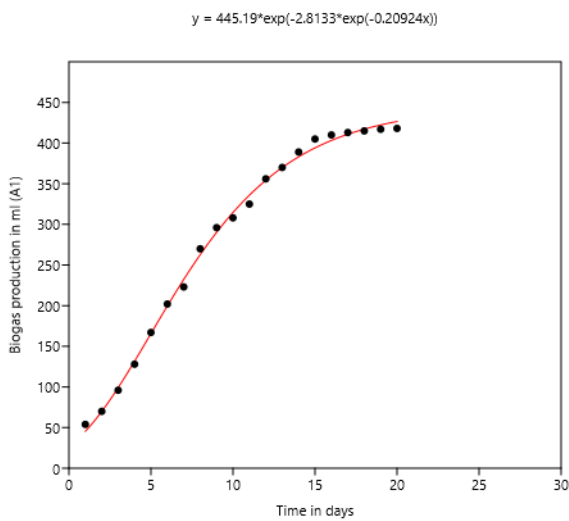
Kinetic Study of Biogas Production Using Modified Gompertz’ Model

It is well known that the action of microbes on substrate for depolymerization of carbohydrates or complex constituents differs in response to the

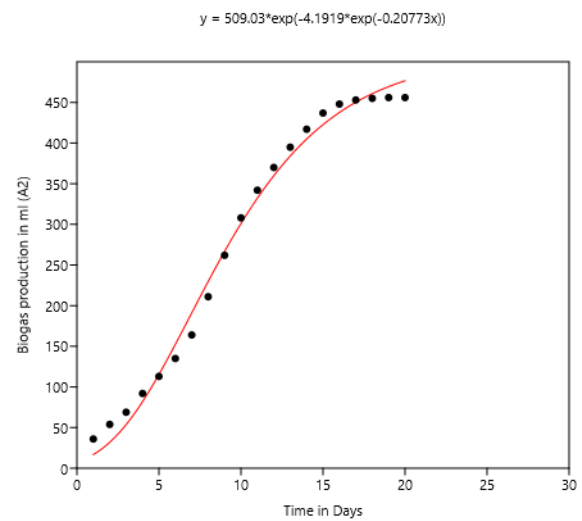
conditions of reactors such as temperature, pH, and nutrient availability. Microbial growth was also analyzed at changing concentrations of wastewater using kinetic study of reacting and found that microbial action is good in 25% and 50% of wastewater in slurry, not much in 75% and was decreased in 100% concentration. Kinetic study of anaerobic digestion revealed that a low concentration of textile wastewater helps in microbial growth and, hence, enhanced biogas production. Also, 25% is the optimum concentration for increasing the yield of anaerobic digestion by

enhancing depolymerization of lignocellulosic biomass, while 100% concentration lowers the production as compared to the control.

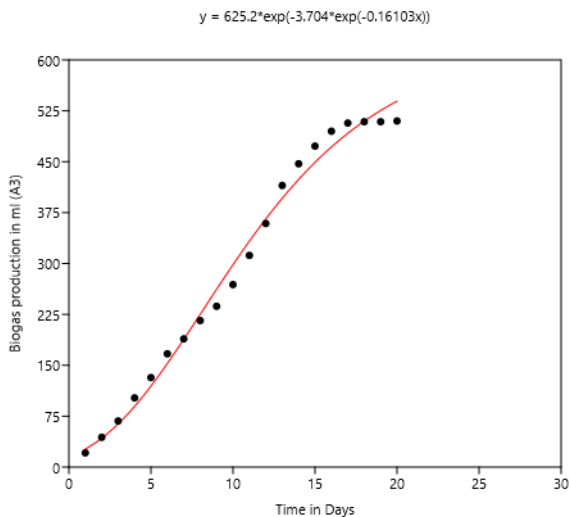
Biogas daily cumulative production data of each test group was fitted best to the modified Gompertz' model. The kinetic parameters of biogas production are shown in Figure 4. This shows that the correlation coefficient for the Gompertz's model was found to be 0.99 for all test groups, which shows a good fit of the model with experimental data.



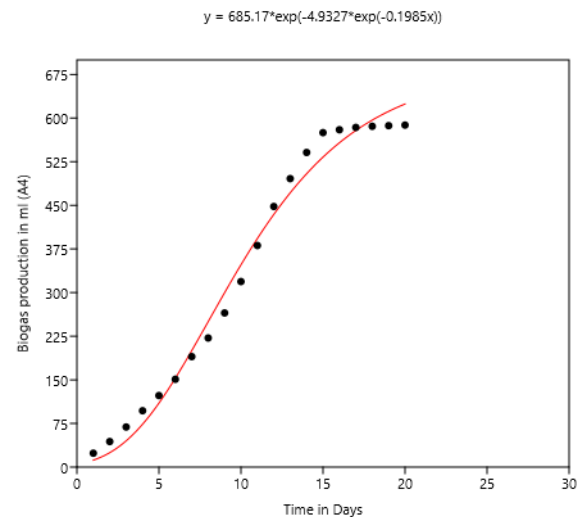
(a)



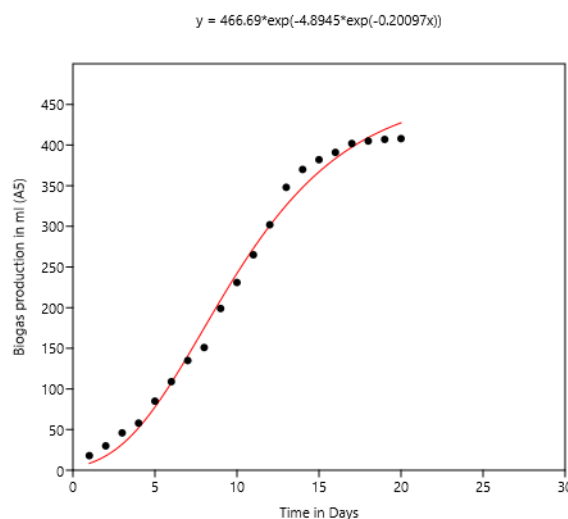
(b)



(c)



(d)



(e)

Figure 4: Kinetics study and predicted biogas production from the slurry.

Economic Analysis of Bioenergy Production Profit and Energy Recovery Capacity

The economic analysis for energy recovery and cost effectiveness has been carried out for biomethane production from textile wastewater. Energy recovery from textile wastewater was measured in terms of the biomethane production that can be generated per unit of substrate utilization and the energy value of the produced energy. The assumption is based on the experimental study, performed by Park et al. (35). Biogas production from slurry A2 is maximum, i.e., 588 mL/kg of VS, which estimates about 60% of methane i.e. 353 mL/kg of VS, as suggested by other researchers (31).

Methane production from slurry containing 25% textile wastewater = 353 mL/kg of VS = 0.35 L/kg of VS

COD of slurry A2 after biomethane production = 115 mg/L

Economic Profit of Methane produced (35) = 0.35 L /kg of VS * 0.57 \$/m³ = 0.2 \$/m³

Pollution Reduction in Textile Wastewater

Textile wastewater has pollutants that can cause a bad effect on aquatic life. Thus, reduction in these pollutants must be made before reviving to water bodies. Anaerobic digestion helps in the reduction of these pollutants. Analysis of pre and post-characterizations of textile wastewater in this study has shown that the chemical moieties that may cause water pollution can enhance the biological activities of microbes.

Table 6: Analysis of pre- and post-characterizations of textile wastewater.

Conc. (%)	25			50			75			100		
	Initial	Final	R*(%)	Initial	Final	R*(%)	Initial	Final	R*(%)	Initial	Final	R*(%)
Chloride	62	38	38.7	65	50	23	78	56	28.2	86	59	31.39
Nitrate	2.4	0.8	66.7	3.6	2	44.4	4	2.4	40	4.4	2.1	52.27
Phosphate	4.2	2	52.4	4.8	2.6	45.8	5.2	3.1	40.3	5.6	4.3	23.2
Sulfate	4.3	1.2	72	5.6	2.3	41	5.8	3.4	41.4	6	4.5	25
COD	1540	854	44.5	1765	1240	29.17	1778	1380	22.38	1840	1540	16.3

Table 6 has shown that the value of chlorides in wastewater reduced by 38.7% after anaerobic digestion in a 25% concentration of slurry. The

results given in table 6 specifically show that pollutants are effectively reduced in all slurry

samples, with the highest level in 25% of the slurry sample.

CONCLUSION

In the present study, the optimization and kinetic modelling of biogas production potential of wheat straw biomass co-digested with cow dung using industrial wastewater was investigated. It has been concluded that with the help of textile wastewater, biogas production can be boosted up. Biogas production by using an appropriate amount of wastewater enhances the depolymerization of polysaccharides by providing proper nutrients to microbes. It has been suggested that an appropriate amount of textile wastewater helps in microbial growth and enhances biogas production. The result in enhanced biodegradability was observed as change in CODs and TOCs before and after of each slurry samples. The economic analysis for energy recovery and cost effectiveness provides a smart approach to use textile wastewater in bioenergy production. A pollution reduction study of the textile wastewater has shown that the use of textile wastewater in biomethane generation helps in the control of water pollution.

CONFLICT OF INTEREST

On behalf of all authors, the corresponding author states that there is no conflict of interest.

ETHICAL STATEMENT

This article does not contain any studies with human participants or animals performed by any of the authors.

ACKNOWLEDGMENTS

Manav Rachna University for financial support and providing all necessary materials and instruments for conducting research.

AUTHOR CONTRIBUTIONS

PR, MB and VVP did the experimental work, experiment design and manuscript editing.

REFERENCES

1. Szreter S. Industrialization and health. *British Medical Bulletin*. 2004 Dec 1;69(1):75–86. [<DOI>](#).
2. Zheng Y, Zhao J, Xu F, Li Y. Pretreatment of lignocellulosic biomass for enhanced biogas production. *Progress in Energy and Combustion Science*. 2014 Jun;42:35–53. [<DOI>](#).
3. Castillo A, Vall P, Garrido-Baserba M, Comas J, Poch M. Selection of industrial (food, drink and milk sector) wastewater treatment technologies: A multi-criteria assessment. *Journal of Cleaner Production*. 2017 Feb;143:180–90. [<DOI>](#).
4. Shi H. Industrial Wastewater Types, Amounts and Effects. In: *Point Sources of Pollution: Local Effects and their Control* [Internet]. China: EOLSS Publications; 2009. p. 1 – 6. [<URL>](#).
5. O'Neill C, Hawkes FR, Esteves SRR, Hawkes DL, Wilcox SJ. Anaerobic and aerobic treatment of a simulated textile effluent. *J Chem Technol Biotechnol*. 1999 Oct;74(10):993–9. [<DOI>](#).
6. Alinsafi A, Evenou F, Abdulkarim EM, Pons MN, Zahraa O, Benhammou A, et al. Treatment of textile industry wastewater by supported photocatalysis. *Dyes and Pigments*. 2007 Jan;74(2):439–45. [<DOI>](#).
7. Nilsson I, Möller A, Mattiasson B, Rubindamayugi MST, Welander U. Decolorization of synthetic and real textile wastewater by the use of white-rot fungi. *Enzyme and Microbial Technology*. 2006 Jan;38(1–2):94–100. [<DOI>](#).
8. Sarayu K, Sandhya S. Current Technologies for Biological Treatment of Textile Wastewater—A Review. *Appl Biochem Biotechnol*. 2012 Jun;167(3):645–61. [<DOI>](#).
9. Nakhate PH, Moradiya KK, Patil HG, Marathe KV, Yadav GD. Case study on sustainability of textile wastewater treatment plant based on lifecycle assessment approach. *Journal of Cleaner Production*. 2020 Feb;245:118929. [<DOI>](#).
10. Marques IP. Anaerobic digestion treatment of olive mill wastewater for effluent re-use in irrigation. *Desalination*. 2001 May;137(1–3):233–9. [<DOI>](#).
11. Kant R. Textile dyeing industry an environmental hazard. *NS*. 2012;04(01):22–6. [<DOI>](#).
12. Georgiou D, Metallinou C, Aivasidis A, Voudrias E, Gimouhopoulos K. Decolorization of azo-reactive dyes and cotton-textile wastewater using anaerobic digestion and acetate-consuming bacteria. *Biochemical Engineering Journal*. 2004 Jul;19(1):75–9. [<DOI>](#).
13. Sandhya S, Swaminathan K. Kinetic analysis of treatment of textile wastewater in hybrid column upflow anaerobic fixed bed reactor. *Chemical Engineering Journal*. 2006 Sep;122(1–2):87–92. [<DOI>](#).
14. Bachmann N, Jansen J la C, Baxter D, Bochmann, G??nther, Montpart N, IEA Bioenergy Programme. Sustainable biogas production in municipal wastewater treatment plants. 2015. ISBN: 978-1-910154-21-2.
15. Liu F, He Y, Wang L. Comparison of calibrations for the determination of soluble solids content and pH of rice vinegars using visible and short-wave near infrared spectroscopy. *Analytica Chimica Acta*. 2008 Mar;610(2):196–204. [<DOI>](#).
16. Rani P, Bansal M, Pathak VV, Ahmad S. Experimental and kinetic studies on co-digestion of agrifood and sewage sludge for biogas production. *Journal of Taibah University for Science*. 2022 Dec 31;16(1):147–54. [<DOI>](#).

17. Davison BH, Parks J, Davis MF, Donohoe BS. Plant Cell Walls: Basics of Structure, Chemistry, Accessibility and the Influence on Conversion. In: Wyman CE, editor. Aqueous Pretreatment of Plant Biomass for Biological and Chemical Conversion to Fuels and Chemicals [Internet]. Chichester, UK: John Wiley & Sons, Ltd; 2013 [cited 2022 Apr 15]. p. 23–38. [<URL>](#).
18. Mushtaq Z, Imran M, Salim-ur-Rehman, Zahoor T, Ahmad RS, Arshad MU. Biochemical perspectives of xylitol extracted from indigenous agricultural by-product mung bean (*vigna radiata*) hulls in a rat model: Biochemical perspectives of xylitol in a rat model. *J Sci Food Agric*. 2014 Mar 30;94(5):969–74. [<DOI>](#).
19. Demirbas MF, Balat M, Balat H. Potential contribution of biomass to the sustainable energy development. *Energy Conversion and Management*. 2009 Jul;50(7):1746–60. [<DOI>](#).
20. Jijai S, Siripatana C. Kinetic Model of Biogas Production from Co-digestion of Thai Rice Noodle Wastewater (Khanomjeen) with Chicken Manure. *Energy Procedia*. 2017 Oct;138:386–92. [<DOI>](#).
21. Kumar V, Singh J, Pathak VV, Ahmad S, Kothari R. Experimental and kinetics study for phytoremediation of sugar mill effluent using water lettuce (*Pistia stratiotes* L.) and its end use for biogas production. *3 Biotech*. 2017 Oct;7(5):330. [<DOI>](#).
22. Neshat SA, Mohammadi M, Najafpour GD, Lahijani P. Anaerobic co-digestion of animal manures and lignocellulosic residues as a potent approach for sustainable biogas production. *Renewable and Sustainable Energy Reviews*. 2017 Nov;79:308–22. [<DOI>](#).
23. Appels L, Baeyens J, Degrève J, Dewil R. Principles and potential of the anaerobic digestion of waste-activated sludge. *Progress in Energy and Combustion Science*. 2008 Dec;34(6):755–81. [<DOI>](#).
24. Parkin GF, Owen WF. Fundamentals of Anaerobic Digestion of Wastewater Sludges. *Journal of Environmental Engineering*. 1986 Oct;112(5):867–920. [<DOI>](#).
25. Mancini G, Papirio S, Lens PNL, Esposito G. Increased biogas production from wheat straw by chemical pretreatments. *Renewable Energy*. 2018 Apr;119:608–14. [<DOI>](#).
26. Kaparaju P, Serrano M, Thomsen AB, Kongjan P, Angelidaki I. Bioethanol, biohydrogen and biogas production from wheat straw in a biorefinery concept. *Bioresource Technology*. 2009 May;100(9):2562–8. [<DOI>](#).
27. Jiang D, Ge X, Zhang Q, Zhou X, Chen Z, Keener H, et al. Comparison of sodium hydroxide and calcium hydroxide pretreatments of giant reed for enhanced enzymatic digestibility and methane production. *Bioresource Technology*. 2017 Nov;244:1150–7. [<DOI>](#).
28. De Vos B, Lettens S, Muys B, Deckers JA. Walkley? Black analysis of forest soil organic carbon: recovery, limitations and uncertainty. *Soil Use & Management*. 2007 Sep;23(3):221–9. [<DOI>](#).
29. Altaş L. Inhibitory effect of heavy metals on methane-producing anaerobic granular sludge. *Journal of Hazardous Materials*. 2009 Mar;162(2–3):1551–6. [<DOI>](#).
30. Lin C. Heavy metal effects on fermentative hydrogen production using natural mixed microflora. *International Journal of Hydrogen Energy*. 2008 Jan;33(2):587–93. [<DOI>](#).
31. Kothari R, Kumar V, Pathak VV, Tyagi VV. Sequential hydrogen and methane production with simultaneous treatment of dairy industry wastewater: Bioenergy profit approach. *International Journal of Hydrogen Energy*. 2017 Feb;42(8):4870–9. [<DOI>](#).
32. Rajeshwari KV, Balakrishnan M, Kansal A, Lata K, Kishore VVN. State-of-the-art of anaerobic digestion technology for industrial wastewater treatment. *Renewable and Sustainable Energy Reviews*. 2000 Jun;4(2):135–56. [<DOI>](#).
33. Murray PA, Zinder SH. Nutritional Requirements of *Methanosarcina* sp. Strain TM-1. *Appl Environ Microbiol*. 1985 Jul;50(1):49–55. [<DOI>](#).
34. Abraham A, Mathew AK, Park H, Choi O, Sindhu R, Parameswaran B, et al. Pretreatment strategies for enhanced biogas production from lignocellulosic biomass. *Bioresource Technology*. 2020 Apr;301:122725. [<DOI>](#).
35. Park J yil, Shiroma R, Al-Haq MI, Zhang Y, Ike M, Arai-Sanoh Y, et al. A novel lime pretreatment for subsequent bioethanol production from rice straw – Calcium capturing by carbonation (CaCCO) process. *Bioresource Technology*. 2010 Sep;101(17):6805–11. [<DOI>](#).



Optoelectronic Parameters of 2-oxo-2-(1-oxo-1*H*-isochromen-3-yl)ethyl methacrylate Compound Thin Film

Adnan Kurt^{1,*} , Murat Koca² 

¹Department of Chemistry, Faculty of Science and Arts, Adiyaman University, Adiyaman, Turkey

²Department of Pharmaceutical Chemistry, Faculty of Pharmacy, Adiyaman University, Adiyaman, Turkey

Abstract: The UV/VIS spectrophotometric scans were obtained to determine the opto-electronic properties of 2-oxo-2-(1-oxo-1*H*-isochromen-3-yl)ethyl methacrylate (other name: 2-(isocoumarin-3-yl)-2-oxoethyl methacrylate) compound thin film. The refractive index of compound at 700 nm was found to be 1.61. The values of the real part of the dielectric constant were higher than those of the imaginary part. The results indicated that the electronic transition responsible for the absorption was the indirect allowed one. The optical band gap constant and the Urbach energy corresponding to the width of the band tails of localized states were calculated to be 3.19 eV and 1.05 eV, respectively. From the results obtained, it is predicted that 2-oxo-2-(1-oxo-1*H*-isochromen-3-yl)ethyl methacrylate (OICEMA) compound can take place in the semiconductor class and play a role in the design of some electro-optic materials.

Keywords: 1*H*-isochromen-1-one, isocoumarin, UV absorptions, optical properties, dispersion parameters

Submitted: November 25, 2021. **Accepted:** April 07, 2022.

Cite this: Kurt A, Koca M. Optoelectronic Parameters of 2-oxo-2-(1-oxo-1*H*-isochromen-3-yl)ethyl methacrylate Compound Thin Film. JOTCSA. 2022;9(2):613–20.

DOI: <https://doi.org/10.18596/jotcsa.1028320>.

***Corresponding author. E-mail:** akurt@adiyaman.edu.tr. Tel: 90416 2233800

INTRODUCTION

Isocoumarins or 1*H*-isochromen-1-ones, are the most important members of the heterocyclic compound class, especially in the natural lactam ring compound group (1). The chemical structure of this compound consists of a lactonic α -pyranone ring fused to the benzene ring at positions 5,6 (2). These compounds form the basis of various biologically and pharmacologically important natural products (3). While isocoumarins and derivatives can be used directly by naturally extracting them from many sources, the synthesis of these compounds has also been carried out by using many different synthetic methods. Some of these commonly used methods are conventional synthetic reactions, microwave-assisted reactions, insertion, cyclization, and bond cleavage reactions, and also transition metal catalyzed reactions (3-6). As a result of the use of isocoumarin derivatives as reagents under different reaction conditions, new types of hetero or carboxylic compounds such as

isocarbostyrils, isoquinolines, and isochromenes have also been synthesized (3,7). Due to their heterocyclic structures, isocoumarins exhibit important biological-pharmacological and chemical properties (2,8).

Due to the π -conjugated bond system in their structures, isocoumarins and derivatives show electrical-optical properties, and thus they may be candidate compounds for optically active materials similar to their coumarin isomers. So, as it is known, studies on the optical properties and application areas of coumarins, which have π -conjugated bonds, are frequently seen in the literature, and some of them show important optoelectronic properties and can be classified as semiconductor materials (9,10). However, the majority of reported studies on isocoumarins are concentrated on their biological or pharmacological effects. But, there are still some publications investigating the photophysical properties of isocoumarins in literature. For example, Elmas and

coworkers designed a novel fluorescent probe based on an isocoumarin compound, 2-amino-4-phenyl-6-(isocoumarin-3-yl) -3-cyanopyridine, for mercury and iron ions and for live cell imaging applications (11). Pirovano and friends reported the synthesis, characterization and photophysical properties of some isocoumarin derivatives-based D-π-A systems (12). In another study, Shoji and coworkers synthesized various benzofurans and isocoumarins with azulene group using intramolecular cyclization reaction of 1-ethynylazulenes. They clarified the structures of molecules by single-crystal XRD analysis and investigated the optical parameters using UV spectroscopy (13). Zamani and friends also synthesized and characterized some novel optically active 3-substituted isocoumarins and 3,4-dihydroisocoumarins containing L-valine and L-leucine moieties (14).

As mentioned above, mostly the biological activities of isocoumarin molecules have been investigated. In addition to these, the synthesis of polymers based isocoumarin molecules has also been encountered in limited numbers in the literature (1,5,15). In this context, some isocoumarin derived polymer/copolymer systems and their various properties have been reported by our research group in previous studies (5,15). Apart from these aforementioned properties of isocoumarins, studies investigating the optical properties of isocoumarin derivatives in detail have not been found within our knowledge of the literature. In order to make a contribution to the existing literature deficiency on the electro-optical properties of isocoumarins or 1H-isochromen-1-ones, herein we aim that UV measurements of 2-oxo-2-(1-oxo-1*H*-isochromen-3-yl)ethyl methacrylate (OICEMA) compound are recorded in the wavelength range of 330 - 700 nm. Some optical parameters are calculated using the related equations available in the literature. From the results obtained, it is predicted that OICEMA compound can take place in the semiconductor class and play a role in the design of some electro-optical materials.

EXPERIMENTAL

Materials

The used solvents, dimethyl sulfoxide (DMSO), tetrahydrofuran (THF), chloroform, and ethanol were purchased from Sigma-Aldrich. In addition, the synthesis of OICEMA compound was achieved again by the reaction of 3-(bromoacetyl)-1*H*-isochromen-1-one and sodium methacrylate in the presence of THF as well as following a series of experimental steps according to our previous studies (5,15). Schematic representation of OICEMA compound was illustrated in Figure 1. The FTIR and ¹H-NMR data are summarized below:

FTIR (cm⁻¹): 1601 (aromatic C=C), 1634 (vinyl C=C), 1708 (acetyl ketone C=O), 1722

(isocoumarin ring C=O), 1741 (methacrylate C=O), 2993–2853 (aliphatic C-H), 3111–3041 (aromatic C-H).

¹H-NMR (DMSO, δppm): 1.95 (vinyl -CH₃), 5.45 (-COOCH₂), 5.82 and 6.17 (vinyl =CH₂), 7.78 - 8.01 (aromatic =CH-), 8.27 (isocoumarin =CH-).

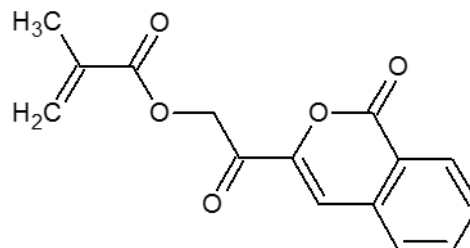


Figure 1: Scheme of OICEMA compound.

Instrumental Techniques

Spectral characterizations were performed with a Perkin Elmer Spectrum 100 FTIR (ATR) spectrometer and a Bruker 300 Mhz Ultrashield TM nuclear magnetic resonance spectrometer. A thin film of compound was prepared with spin coating technique. Therefore, a Laurell WS-400-6NPP-Lite spin coater was used. For this process, 0.025 gram of OICEMA compound was weighed and dissolved in 25 mL of dimethyl sulfoxide and coated onto a glass at the conditions of 5 bar argon gas pressure and 2500 rpm for 25 seconds. The thickness of film was measured to be 2 μm using a digital micrometer supplied by Mitutoyo Corporation Ltd Japan. Then, UV measurements were carried out by a Perkin Elmer Lambda 25 UV/VIS Spectrophotometer (330 - 700 nm).

RESULTS AND DISCUSSION

The spectral characterization of the OICEMA compound was re-achieved with FTIR and ¹H-NMR techniques according to our previous studies (5,15). Figure 2 shows the FTIR spectrum of the compound in which the most characteristic bands are observed at 3111–3041 cm⁻¹ (aromatic C-H), 2993–2853 cm⁻¹ (aliphatic C-H), 1741 cm⁻¹ (methacrylate C=O), 1722 cm⁻¹ (isocoumarin ring C=O), 1708 cm⁻¹ (acetyl ketone C=O), 1634 cm⁻¹ (vinyl C=C), 1601 cm⁻¹ (aromatic C=C).

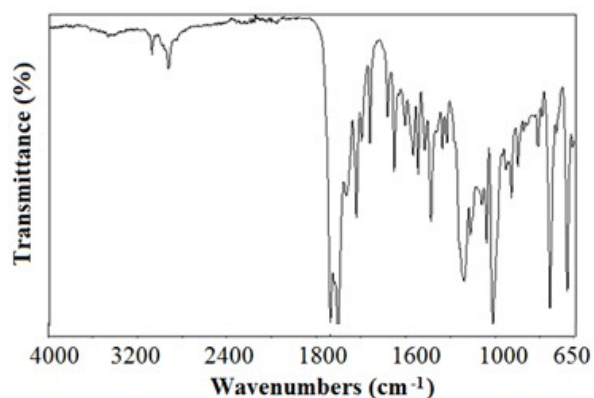


Figure 2: FTIR spectrum of OICEMA compound.

In its $^1\text{H-NMR}$ spectrum (Figure 3), the signal at 8.27 ppm is attributed to the $=\text{CH-}$ proton in the isocoumarin ring. The chemical shifts between 8.01 ppm and 7.78 ppm are due to the aromatic $=\text{CH-}$ protons. Both signals at 6.17 and 5.82 ppm are attributed to vinylic $=\text{CH}_2$ protons. The signal at 5.45 ppm is reasoned by CH_2 protons adjacent to the methacrylate ester and the signal at 1.95 ppm is also due to the $-\text{CH}_3$ protons adjacent to the vinyl group.

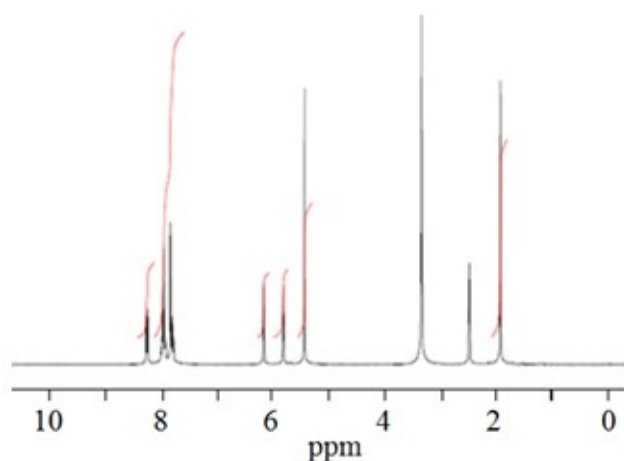


Figure 3: $^1\text{H-NMR}$ spectrum of OICEMA compound.

The optical properties of organic molecules containing multiple n -bonds are reported due to their opto-electronic applications (9,10). In order to determine the optical and electronic properties of molecules, UV-VIS spectroscopy is commonly used (16). Some physical phenomena occur when light passes from an air medium to any dense medium, such as a solid phase. That is, the fractions of incident light are partially reflected, transmitted, or absorbed (16). This situation can be formulated as: $(T + R + A = 1)$ where T: transmittance, R: reflectance, and A: absorbance. Using these values, a different set of optical parameters can be easily obtained.

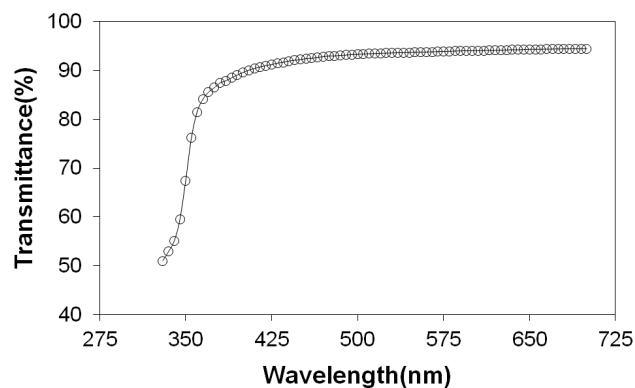


Figure 4: Transmittance spectrum of OICEMA compound.

Therefore, the UV/VIS measurements were obtained between 330 nm and 700 nm for OICEMA compound film. Its transmittance and reflectance spectra were shown in Figures 4 and 5, respectively. Transmittance spectrum was increased depending on the increase in wavelength whereas the reflectance values were decreased. In addition, the results obtained from the UV absorption data showed that the absorption rate in the visible region was less than that of the UV region (17). The absorption exhibited by the OICEMA compound around 330 nm may be reasoned from n - n^* transitions of C=O groups in the molecule (18).

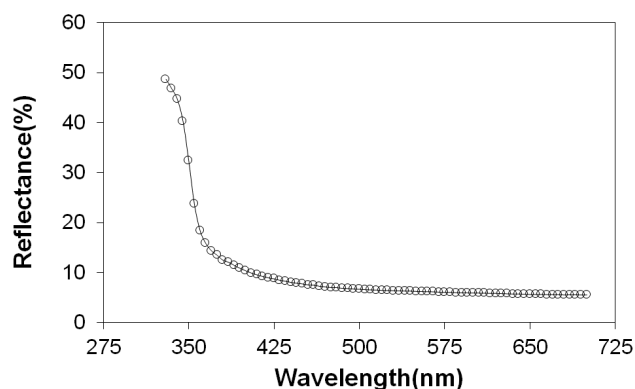


Figure 5: Reflectance spectrum of OICEMA compound.

The refractive index (n) is an important optical parameter and it may be easily determined from the transmittance and reflectance. Therefore, a relationship between these parameters can be explained by the following formula (19):

$$n = \left[\frac{1+R}{1-R} \right] + \left[\frac{4R}{(1-R)^2} - k^2 \right]^{1/2} \quad (1)$$

Where k is the extinction coefficient. This parameter is also obtained as:

$$k = \frac{\alpha \lambda}{4 \pi} \tag{2}$$

Where α is the absorption coefficient and corresponds to the following equation:

$$\alpha = \frac{2.303 A}{d} \tag{3}$$

Where d is the film thickness, and A is the absorbance. Figure 6 shows that the refractive index is inversely related to the wavelength. Depending on the increase in wavelength, a significant decrease in the refractive index was observed. In particular, this decrease is sharper and more pronounced in the UV region, as pointed out by Rodriguez et al (20). Towards the next wavelengths (after about 400 nm) the decreasing rate is slower and reaches an almost constant value. The n value is found to be 1.61 at 700 nm.

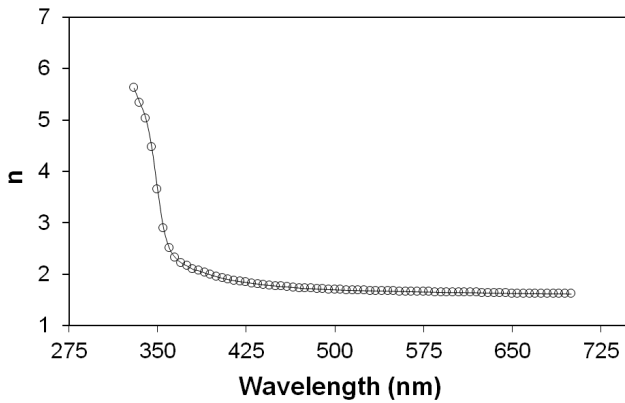


Figure 6: Refractive index dispersion curve of OICEMA compound.

Figure 7 shows the variation of the extinction coefficient with the wavelength. As seen in Figure 7, at the low wavelength range, the decrease in the extinction coefficient is quite evident. However, a stabilization towards higher wavelengths is observed.

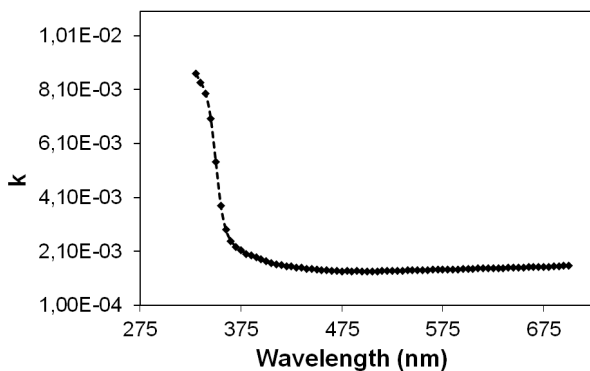


Figure 7: Variation of extinction coefficient (k) as a function of wavelength of OICEMA compound.

The real (ϵ_r) and imaginary (ϵ_i) parts of the dielectric constant are:

$$\epsilon_r = n^2 - k^2 \quad \text{and} \quad \epsilon_i = 2nk \tag{4}$$

The variation of these constants with energy is given in Figure 8. As can be seen from this figure, the imaginary part of dielectric constant is smaller than the real part. The real and imaginary parts values of OICEMA compound were found to be 2.68 and 0.0048 at an energy level of 2 eV, respectively.

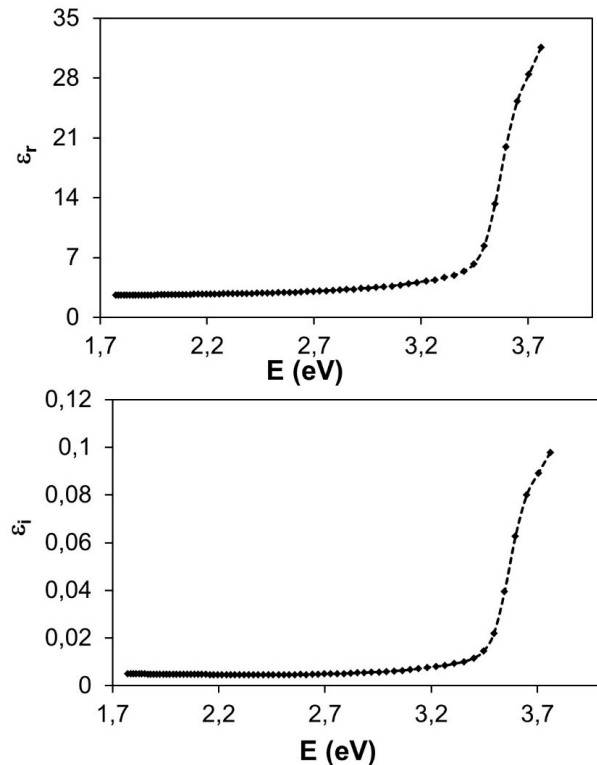


Figure 8: The spectra of real (ϵ_r) and imaginary (ϵ_i) parts of dielectric constant of OICEMA compound.

Dispersion energy parameters are obtained by the Wemple and DrDomenico relationship (21). The relationship between n and single oscillator strength is evaluated according to following relation:

$$n^2(h\nu) = 1 + \frac{E_0 E_d}{E_0^2 - (h\nu)^2} \tag{5}$$

Where E_0 is the single - oscillator energy, E_d is the dispersion energy. E_0 is responsible of the electronic excitations in the compounds and shows the average of the optical band gap. E_d indicates the dispersion energy in the compounds and shows the average strength of interband optical transition (22). Figure 9 shows the plots $(n^2 - 1)^{-1}$ versus $(h\nu)^2$ values. The linear fit of this figure yields a slope equal to $(E_0 E_d)^{-1}$ and an intercept equal to E_0 / E_d . The values of E_0 and E_d for OICEMA compound were

found to be 3.96 eV and 4.33 eV, respectively. These values were also listed in Table 1.

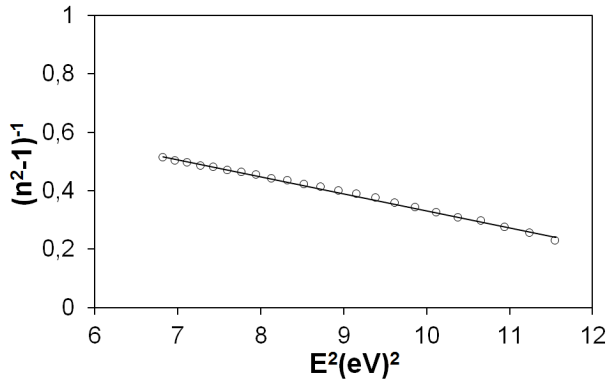


Figure 9: Variation of $(n^2-1)^{-1}$ as a function of E^2 of OICEMA compound.

M_{-1} and M_{-3} moments of the imaginary part of the optical band (21,23) may be defined as: $E_0^2 = M_{-1}/M_{-3}$ and $E_0^2 = (M_{-1})^3/M_{-3}$. Table 1 includes these values. It is noted that M_{-1} value is greater than the M_{-3} when compared to each other.

The single-term Sellmeier relation is used in order to determine the relationship between the refractive index and the wavelength (24):

$$n^2(\lambda) - 1 = \frac{S_0 \lambda_0^2}{1 - (\lambda_0/\lambda)^2} \quad (6)$$

Where λ_0 and S_0 are the average interband oscillator wavelength and oscillator strength, respectively. To determine both parameters, $(n^2-1)^{-1}$ values against λ^{-2} values according to Eq. (6) are plotted. These plots are shown in Figure 10. From the slope and intercept of line, the S_0 and λ_0 values of OICEMA compound are calculated and given in Table 1.

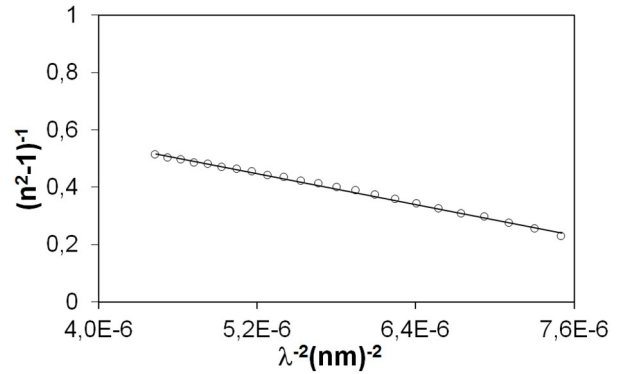


Figure 10: Variation of $(n^2-1)^{-1}$ as a function of $(\lambda)^{-2}$ of OICEMA compound.

In order to understand the interband transition theory of solid state materials, the absorption data at the fundamental edge can be easily analyzed with the following equation (25):

$$(\alpha h\nu) = B(h\nu - E_0)^n \quad (7)$$

Where E_g is the optical band gap, B is a constant, and n is an index that shows the types of electronic transitions. These n values can take different values, like 2, 3, 1/2, and 3/2. Their interpretations are well known in the literature (22). In order to determine the electronic transition type of any material, the value with the best agreement between the n values should be determined. For this, the $(\alpha h\nu)^{1/n}$ values against energy ($h\nu$) values for each n value are plotted and the n value with the best linear regression value is selected. In our work, we achieved the best fit for $n=2$, that is, for indirect allowed transition for OICEMA compound. Accordingly, $(\alpha h\nu)^{1/2}$ versus $(h\nu)$ values were plotted in order to calculate the optical band gap (E_g). This is shown in Figure 11. From the extrapolation of this line, the E_g value was calculated as 3.19 eV.

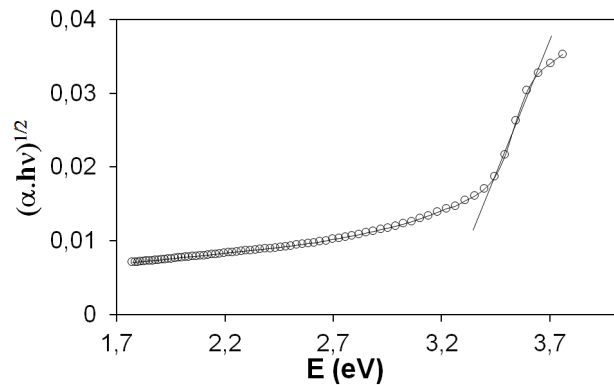


Figure 11: Plot of $(\alpha h\nu)^{1/2}$ vs. E of OICEMA compound.

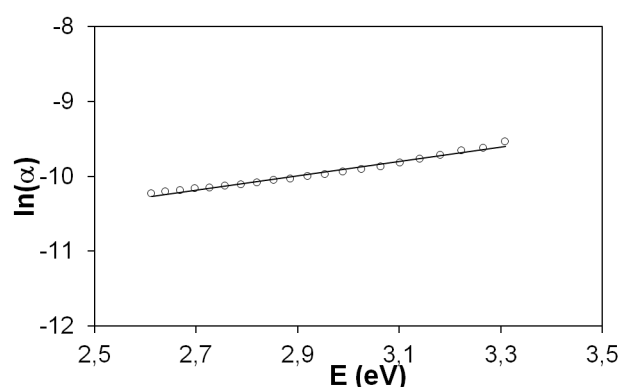
Table 1: Optical parameters of OICEMA compound.

Eu (eV)	Eg (eV)	E ₀ (eV)	E _d (eV)	S ₀ .10 ¹³ (m ⁻²)	λ ₀ (nm)
1.05	3.19	3.96	4.33	1.11	313
M ₋₁	M ₋₃ (eV) ⁻²	β	α ₀	n (700 nm)	T% (700 nm)
1.09	0.07	0.025	2.88.10 ⁻⁶	1.61	94.48

When any material is exposed to a certain UV wavelength, some localized defect states can occur in the band gap. These defect states can trap the excited electrons and prevent their direct transition to the conduction band (26). The tail width of these defect states is defined as the Urbach energy and can be determined by the following general formula (27):

$$\alpha = \alpha_0 \exp\left(\frac{E}{E_u}\right) \quad (8)$$

Where α_0 is a constant, and E_u is the Urbach energy. The slope of the line obtained from the graph of $(\ln \alpha)$ versus energy E (eV) can be used to calculate it. This is shown in Figure 12. The value of Urbach energy was calculated to be 1.05 eV while α_0 constant was 2.88×10^{-6} . In addition, at a constant temperature and in the Urbach tail range, the slope of Figure 10 corresponds to σ/kT . Where k is the Boltzmann constant, and T is the temperature, σ is the steepness parameter. This parameter is temperature dependent and characterizes the broadening of absorption edge. This state is usually caused by electron-phonon interactions (28). The steepness parameter of OICEMA compound is calculated as 0.0245 when T is 298 K.

**Figure 12:** Plot of $\ln \alpha$ vs. E of OICEMA compound.

CONCLUSIONS

The UV measurements of 2-oxo-2-(1-oxo-1*H*-isochromen-3-yl)ethyl methacrylate compound were recorded to determine some optical and dispersion parameters. Transmittance was increased depending on the increase in wavelength, whereas the reflectance values were decreased. The refractive index and wavelength were inversely related, and a significant decrease was observed in

the refractive index with increasing wavelength. The refractive index at 700 nm was 1.61. The real and imaginary part values were found to be 2.68 and 0.0048 at the energy level of 2 eV, respectively. For compounds, the type of electronic transition allowed was the indirect one. The optical band gap constant and the Urbach energy were calculated to be 3.19 eV and 1.05 eV, respectively. These results show that 2-oxo-2-(1-oxo-1*H*-isochromen-3-yl)ethyl methacrylate can take place in the semiconductor class and play a role in the design of some electro-optical materials.

REFERENCES

- Han T, Deng H, Yu CYY, Gui C, Song Z, Kwok RTK, et al. Functional isocoumarin-containing polymers synthesized by rhodium-catalyzed oxidative polycoupling of aryl diacid and internal diyne. *Polym Chem.* 2016;7(14):2501–10. [<DOI>](#).
- Saeed A. Isocoumarins, miraculous natural products blessed with diverse pharmacological activities. *European Journal of Medicinal Chemistry.* 2016 Jun;116:290–317. [<DOI>](#).
- Saikia P, Gogoi S. Isocoumarins: General Aspects and Recent Advances in their Synthesis. *Adv Synth Catal.* 2018 Jun 5;360(11):2063–75. [<DOI>](#).
- Pal S, Chatare V, Pal M. Isocoumarin and Its Derivatives: An Overview on their Synthesis and Applications. *COC.* 2011 Mar 1;15(5):782–800. [<DOI>](#).
- Kurt A, Kılınc İ, Koca M. Preparation of Copolymer Systems of 2-(Isocoumarin-3-yl)-2-oxoethyl Methacrylate with Methyl Methacrylate and Thermal Decomposition Kinetics. *Iran J Sci Technol Trans Sci.* 2020 Aug;44(4):1039–50. [<DOI>](#).
- Koca M, Ertürk AS, Umaz A. Microwave-assisted intermolecular aldol condensation: Efficient one-step synthesis of 3-acetyl isocoumarin and optimization of different reaction conditions. *Arabian Journal of Chemistry.* 2018 May;11(4):538–45. [<DOI>](#).
- Barry RD. Isocoumarins. *Developments since 1950. Chemical Reviews.* 1964;64(3):229–60.
- Tian JF, Li PJ, Li XX, Sun PH, Gao H, Liu XZ, et al. New antibacterial isocoumarin glycosides from a wetland soil derived fungal strain *Metarhizium anisopliae*. *Bioorganic & Medicinal Chemistry Letters.* 2016 Mar;26(5):1391–6. [<DOI>](#).
- Bai Y, Du J, Weng X. Synthesis, characterization, optical properties and theoretical calculations of 6-fluoro coumarin. *Spectrochimica Acta Part A: Molecular and Biomolecular Spectroscopy.* 2014 May;126:14–20. [<DOI>](#).

10. Kurt A, Gündüz B, Koca M. A detailed study on the optical properties of 3-benzoyl-7-hydroxy coumarin compound in different solvents and concentrations. *Maced J Chem Chem Eng*. 2019 Dec 30;38(2):227. [<DOI>](#).
11. Karuk Elmas SN, Dincer ZE, Erturk AS, Bostanci A, Karagoz A, Koca M, et al. A novel fluorescent probe based on isocoumarin for Hg²⁺ and Fe³⁺ ions and its application in live-cell imaging. *Spectrochimica Acta Part A: Molecular and Biomolecular Spectroscopy*. 2020 Jan;224:117402. [<DOI>](#) .
12. Pirovano V, Marchetti M, Carbonaro J, Brambilla E, Rossi E, Ronda L, et al. Synthesis and photophysical properties of isocoumarin-based D-π-A systems. *Dyes and Pigments*. 2020 Feb;173:107917. [<DOI>](#).
13. Shoji T, Tanaka M, Takagaki S, Miura K, Ohta A, Sekiguchi R, et al. Synthesis of azulene-substituted benzofurans and isocoumarins *via* intramolecular cyclization of 1-ethynylazulenes, and their structural and optical properties. *Org Biomol Chem*. 2018;16(3):480–9. [<DOI>](#).
14. Zamani K, Faghihi K, Ebrahimi S. Synthesis of Some Novel Optically Active Isocoumarin and 3,4-Dihydroisocoumarin Containing L-valine and L-leucine Moieties. *Turk J Chem*. 2005;29:171–5. [<URL>](#).
15. Kurt A, Avcı HI, Koca M. Synthesis and characterization of a novel isocoumarin derived polymer and its thermal decomposition kinetics. *Maced J Chem Chem Eng [Internet]*. 2018 Dec 3 [cited 2022 Apr 16];37(2). [<DOI>](#).
16. Aziz SB, Brza MA, Nofal MM, Abdulwahid RT, Hussen SA, Hussein AM, et al. A Comprehensive Review on Optical Properties of Polymer Electrolytes and Composites. *Materials*. 2020 Aug 20;13(17):3675. [<DOI>](#).
17. Rawat A, Mahawar H, Chauhan S, Tanwar A, Singh P. Optical band gap of polyvinylpyrrolidone/polyacrilamide blend thin films. *IJPAP*. 2012;50:100–4. [<URL>](#).
18. Zidan HM, Abu-Elnader M. Structural and optical properties of pure PMMA and metal chloride-doped PMMA films. *Physica B: Condensed Matter*. 2005 Jan;355(1–4):308–17. [<DOI>](#).
19. Atyia H. Influence of deposition temperature on the structural and optical properties of InSbSe₃ films. *Journal of optoelectronics and advanced materials*. 2006;8(4):1359.
20. Rodríguez J, Gómez M, Ederth J, Niklasson GA, Granqvist CG. Thickness dependence of the optical properties of sputter deposited Ti oxide films. *Thin Solid Films*. 2000 Apr;365(1):119–25. [<DOI>](#).
21. Wemple SH, DiDomenico M. Behavior of the Electronic Dielectric Constant in Covalent and Ionic Materials. *Phys Rev B*. 1971 Feb 15;3(4):1338–51. [<DOI>](#).
22. Veena G, Lobo B. Dispersive parameters of oxidized PVA-PVP blend films. *Turkish Journal of Physics*. 2019 Aug 1;43(4):337–54. [<URL>](#).
23. Ammar AH. Studies on some structural and optical properties of Zn_xCd_{1-x}Te thin films. *Applied Surface Science*. 2002 Nov;201(1–4):9–19. [<DOI>](#).
24. DrDomenico M, Wemple SH. Oxygen-Octahedra Ferroelectrics. I. Theory of Electro-optical and Nonlinear optical Effects. *Journal of Applied Physics*. 1969 Feb;40(2):720–34. [<DOI>](#).
25. Tauc J, editor. *Amorphous and Liquid Semiconductors*. New York: Plenum Press; 1974.
26. Akshay VR, Arun B, Mandal G, Vasundhara M. Visible range optical absorption, Urbach energy estimation and paramagnetic response in Cr-doped TiO₂ nanocrystals derived by a sol-gel method. *Phys Chem Chem Phys*. 2019;21(24):12991–3004. [<DOI>](#).
27. Urbach F. The Long-Wavelength Edge of Photographic Sensitivity and of the Electronic Absorption of Solids. *Phys Rev*. 1953 Dec 1;92(5):1324–1324. [<DOI>](#).
28. Abu El-Fadl A, Soltan AS, Shaalan NM. Temperature dependence of the indirect band gap, steepness parameter and related optical constants of [K_x(NH₄)_{1-x}]₂ZnCl₄ mixed crystals. *Optics & Laser Technology*. 2007 Oct;39(7):1310–8. [<DOI>](#).



Enrichment of Magnesite and Usage to Obtain Magnesium Fluoride

Çiğdem Aras¹ , Birsen Demirata Öztürk² , Kevser Sözgen Başkan³ 

¹Istanbul Technical University, Institute of Science and Technology, Istanbul, 34467, Turkey

²Istanbul Technical University, Department of Chemistry, Istanbul, 34467, Turkey

³Istanbul University, Department of Chemistry, Istanbul, 34320, Turkey

Abstract: Magnesium is the sixth most abundant element, constituting 2% of the total mass of the earth's crust. It is a metal that exists only in chemical compounds, and generally in carbonate and oxide forms. The most important mineral forms are magnesite ($MgCO_3$), dolomite ($MgCO_3 \cdot CaCO_3$), and carnallite ($KCl \cdot MgCl_2 \cdot 6H_2O$). Magnesium metal, which is obtained from different sources by various methods, has an important place in the industry. There are approximately 16 billion tons of dolomite and 110 million tons of magnesite reserves in Turkey. The aim of this study is to investigate the use of idle magnesium clay raw material (in Eskişehir) for the production of magnesium fluoride and thus to propose a chemical process for the relevant raw material to the industry. For the experiments, a 10 kg sample was taken and after the whole was ground to 75 μm size, XRF, XRD, and DTA analyzes were performed. As a result of XRF analysis, it contains 44.28% MgO. For XRD analysis, it was determined that it is magnesite with $MgCO_3$ structure, and that it also has dolomite and chlorite group mineral structures. MgF_2 was created by employing HF from the relevant raw material as a result of the study, and it was discovered that the efficiency was higher in the raw magnesite experiments.

Keywords: Enrichment of Magnesite, Calcination of Magnesite, Magnesite.

Submitted: February 08, 2022. **Accepted:** April 06, 2022.

Cite this: Aras Ç, Demirata Öztürk B, Sözgen Başkan K. Enrichment of Magnesite and Usage to Obtain Magnesium Fluoride. JOTCSA. 2022;9(2):621-30.

DOI: <https://doi.org/10.18596/jotcsa.1070017>.

***Corresponding author. E-mail:** cigdemaras@arasglobal.com.tr.

INTRODUCTION

Magnesium is the third most commonly used structural metal after aluminum and iron. It has an important place in today's technology, both as a metal and as a compound. Due to its abundance, light weight, and easy alloying, magnesium metal has great potential for components in the automotive, aerospace, and military industries. While magnesium is expected to be more popular due to its important mechanical properties, it seems to be in the background due to the difficulties in obtaining it. There are six sources of raw materials for the production of magnesium: magnesite, dolomite, bischofite, carnallite, serpentine, and sea water. These sources differ in magnesium content,

production methods, and their origin. Dolomite [$CaMg(CO_3)_2$] and magnesite [$Mg(CO_3)$] are the most widely used Mg metal ores. Magnesite has more Mg content than dolomite, but large magnesite deposits are geographically limited. Magnesite mineral theoretically contains 52.3% CO_2 and 47.7% MgO and it is the primary source for the production of magnesium and its compounds. On the other hand, this mineral almost never occurs pure enough to be used directly in any significant deposit. Its ores contain a variety of gangue minerals, mostly other carbonates, silicates, and oxides (1). World magnesite resources are estimated at over 12 billion tons and are primarily located in China, Russia, North Korea, Australia, Slovakia, Brazil, Turkey, India, and Canada (2).

Although there is a considerable amount of dolomite and magnesite reserves (3;4), magnesium metal was not being produced in Turkey (5) before 2016. Magnesite is generally used instead of its natural state by converting it to MgO by calcining. The calcination of magnesite and the degree of reactivity of the obtained product are technologically important (6). Magnesite that is to be used in the production of metallic magnesium must also be purified by calcining. Thus, the material is enriched in magnesium. Magnesite has a porous structure as it loses CO₂ and H₂O during the calcination process, and the specific gravity of calcined magnesite is between 1.3 and 1.9 g/cm³ (1). Magnesite and magnesite products in the world are evaluated and priced in terms of chemical content, CaO/SiO₂ ratio, bulk density, and crystal structure. Ores containing more than 93.5% MgO on a calcined basis are considered valuable raw materials.

The methods used in the enrichment of magnesite ore can be listed as follows; manual sorting and optical sorting, enrichment with size reduction, heavy medium enrichment, enrichment by electrostatic and magnetic separation, enrichment by hydration, enrichment by calcination, and enrichment by flotation and agglomeration.

The studies were performed using the facilities of Esan Eczacıbaşı Industrial Raw Materials Ind. and Trade Inc.

MATERIALS AND METHODS

Chemicals and Instruments

The following chemical substances of analytical reagent grade were purchased from the corresponding sources. Hydrochloric acid (HCl) and hydrofluoric acid (HF): Merck (Darmstadt, Germany); Lithium tetraborate (Li₂B₄O₇), hydroxylamine hydrochloride (NH₂OH.HCl), and ammonium fluoride (NH₄F): Sigma-Aldrich (Taufkirchen, Germany).

Chemical analysis of the sample was performed with X-Ray Fluorescence (XRF) Spectrometer (Panalytical Axios Model) and structural analysis was performed with X-Ray Diffraction (XRD) instrument (Panalytical X-Pert Pro Model). A differential Thermal Analyzer (DTA) (Orton ST 746 Model) was used for thermal analysis of the sample. Other laboratory equipment used in this study is jaw crusher with tungsten-carbide rim (Retsch BB 100 model), sample divider (20 compartments) (Retsch), tungsten-carbide ring grinder (Retsch-RS 200), precision balance (Mettler Toledo AB 204S model), fan oven (Electro-Mag), ash furnace (max temperature 1200 °C) (Protherm PLF 125 model), grain size device (Malvern Mastersizer 2000 model).

Sample Preparation and Characterization

In this study, a clay containing magnesite, which was obtained from the magnesite quarry of Esan Eczacıbaşı company located in the Alpu region of Eskişehir (Turkey), was used as a magnesium source. The entire clay sample was laid on the sample tray and dried in a 105 °C fan oven for 15 hours. After the sample was dried, it was reduced to 4 mm size by passing it through a tungsten-carbide jaw crusher. All the comminuted material was passed through the sample crusher 3 times and then reassembled. Thus, homogeneous mixing of the crushed material was ensured. According to the information obtained from previous studies, the reaction rate increases as the particle size decreases. For this reason, the entire material was ground to a 75 µm size with a tungsten-carbide grinder at 1200 rpm for 1 min. The entire ground sample was passed through the sample grinder 3 more times and then recombined. Thus, homogeneous mixing of the ground material was ensured. After the final milling, a representative sample of 500 g was taken and used in the experiments.

Loss on ignition of sample

The sample in the glass weighing bottle was dried in an oven at 105 °C for 2 hours. The sample taken out of the oven was taken into a desiccator, cooled to room temperature, and 1 g was weighed with an accuracy of 0.1 mg and placed in a porcelain crucible, which reached a constant weight at 1000 °C. The sample in the porcelain crucible was heated at 1000 °C in an ash furnace for 1 hour. The crucible removed from the ash furnace was transferred to a desiccator, cooled to room temperature, and weighed.

Chemical Analysis with XRF

The sample in the glass weighing bottle was dried in an oven at 105 °C for 2 hours, and after being taken out of the oven, it was taken to the desiccator and cooled to room temperature. 1 g of weight was taken from this sample and after adding 5 g lithium tetraborate, which was kept at 400 °C for 5 hours, the mixture was ground in an agate mortar. The ground mixture was placed in a platinum crucible, and after the lid was closed, it was put into the ash furnace at 1150 °C. At the end of 20 min, the crucible was taken out of the furnace, ammonium iodate was added, and the lid was closed and put back into the furnace at the same temperature. Five minutes later, the crucible was taken off and the content of the crucible was transferred to the lid. The material in the lid was put back into the ashing furnace at 1150 °C and kept at this temperature for 5 min. After 5 min, the lid was taken out and left to cool at room temperature. After cooling, the glassy material on the cover was taken and loaded into the XRF device for analysis under calibration.

Thermal Analysis

The decomposition characteristics of the sample were determined by simultaneous DTA (Differential Thermal Analysis)/TGA (Thermogravimetric Analysis) test using Orton ST 746 instrument. The experimental conditions were continuous heating from room temperature up to 1200°C at a heating rate of 10°C /min, N₂ – gas dynamic atmosphere, and using Alumina as a reference material. The data obtained by thermal analysis is reaction peak temperature and weight loss in the temperature ranges.

Calcination of Sample

Magnesite that is to be used in the production of metallic magnesium must be purified by calcining. Thus, the material will have an enriched magnesium content. It was studied at different temperatures (900-1200 °C) and times (3-5 h) to determine the optimum calcination conditions. Chemical, XRD, and DTA analyses of the products obtained as a result of calcination were performed.

Obtaining Magnesium Fluoride from Magnesite

It was aimed to obtain magnesium fluoride from raw and calcined magnesite material by using HF and NH₄F solutions. As a result of the XRD analysis results made on the samples obtained, it was determined that there was no high rate of MgF₂ (Sellaite) formation as a result of the experiments performed with NH₄F and even high levels of

impurities were formed due to the NH₄F. For this reason, MgF₂ production experiments were carried out using concentrated HF in a polytetrafluoroethylene (PTFE) beaker and the most suitable conditions were determined. In this process, experiments were conducted using different concentrations of HF, and two different experimental methods, called "Drying" and "Filtration", were applied. For this purpose, 10 different experimental sets were prepared. XRD analysis and chemical analysis were applied to the products obtained as a result of the trials. The experimental sets applied using different reagent concentrations and different quantities of raw magnesite and calcined magnesite are summarized in Table 1.

In the drying process, the weighed main material was taken into a PTFE beaker, a certain amount of distilled water and concentrated HF was added to it and mixed for 30 minutes. The mixture was evaporated to dryness on the heating plate, and the residues in the beaker were analyzed.

In the filtration process, the weighed main material was taken into a PTFE beaker, and a certain amount of distilled water and concentrated HF was added to it. The contents of the beaker were filtered through a blue-band filter paper after stirring for 30 minutes. The residue on the filter paper was dried in an oven at 105 °C.

Table 1: The experiment sets prepared to obtain MgF₂.

Experiment No.	Main Material	Material Quantity (g)	Reagent Volume (mL)	Water Volume (mL)	Method Used
1	MgCO ₃	10.415	20	20	Drying
2	MgCO ₃	10.835	20	20	Filtration
3	MgCO ₃	10.021	30	20	Drying
4	MgCO ₃	10.090	30	20	Filtration
5	MgCO ₃	10.053	30	-	Drying
6	MgO	10.060	20	20	Drying
7	MgO	10.036	20	20	Filtration
8	MgO	10.135	30	20	Drying
9	MgO	10.017	30	20	Filtration
10	MgO	10.089	30	-	Drying

RESULTS AND DISCUSSION

Determination of Loss on Ignition and Chemical Analysis

As a result of the analysis performed in the calibrated program by the XRF instrument, it was determined that there was 44.28% MgO in the material. The chemical structure of original sample

and also loss on ignition value is given in the Table 2. When the same sample was analyzed in a semi-quantitative program with the XRF instrument, it was observed that it contained trace amounts of chromium (0.024% Cr₂O₃), nickel (0.0182% NiO), copper (0.0452% CuO), strontium (0.0277% SrO) and barium (0.0545% BaO).

Table 2: Chemical analysis results for the clay containing magnesite.

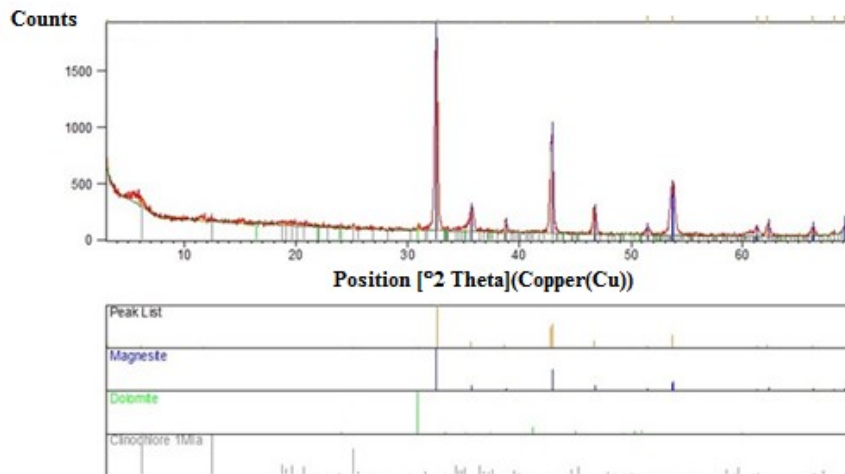
Sample	Content (mass %)								
	LOI*	SiO ₂	Al ₂ O ₃	Fe ₂ O ₃	TiO ₂	CaO	MgO	Na ₂ O	K ₂ O
Clay containing magnesite	44.90	6.90	0.96	0.72	0.10	2.02	44.28	0.01	0.09

*LOI : Loss on ignition

Structural Analysis

In the XRD spectra, peaks of clay minerals can be seen in areas where 2θ is less than 10. When the XRD spectrum of our sample (Fig. 1) was examined, it was thought that it contained chlorite or montmorillonite according to the distance between the layers. The sample was treated with ethylene glycol to examine whether the peak thought to be chlorite was actually a

montmorillonite derivative. As it is known, if a montmorillonite-derived structure is found in the sample, it is expected that the peak, which was around 5 in the XRD analysis performed after the treatment with ethylene glycol, will shift to around 17. However, as a result of the analysis after this process, it was seen that there was no shift in the relevant peak (Fig. 2), and it was thought that this peak belonged to the chlorite derivative.

**Figure 1:** XRD spectra of original sample.

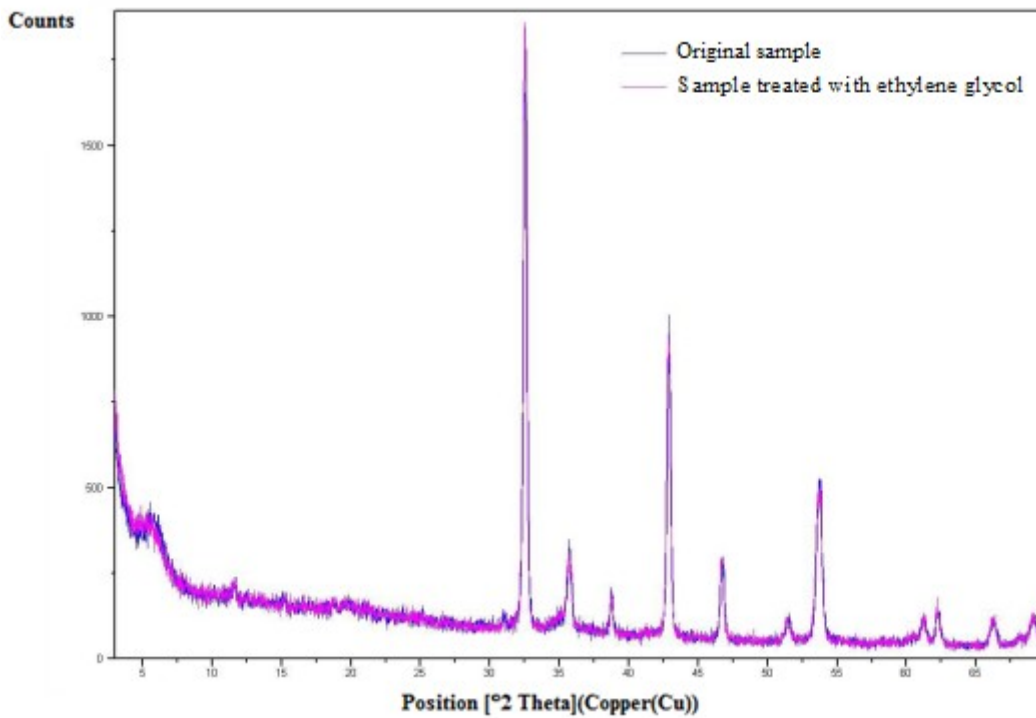


Figure 2: XRD spectra of the original and ethylene glycol treated samples.

Thermal Analysis

The typical DTA/TGA curve of the sample is presented in Fig. 3. It is seen that there is a weight loss in the range of 500-650 °C in the TGA curve, and endothermic peaks occur in the range of 500-700 °C and 800-1000 °C in the DTA curve. The weight loss in the TGA curve indicates the conversion of MgCO₃ to MgO as a result of CO₂

removal. This decomposition is also the cause of the endothermic peak in the DTA curve in the same temperature range. It can be said that the second endothermic peak is caused by the decomposition of CaCO₃ in the dolomite structure by releasing CO₂. The TG thermogram shows a loss of mass of approximately 45%, which is consistent with the determined loss on ignition value (Table 2).

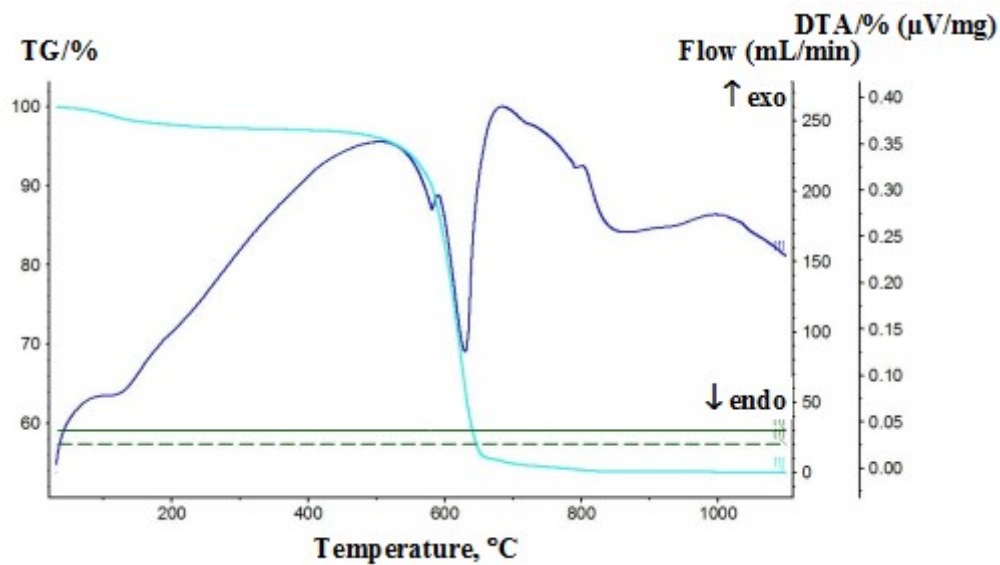


Figure 3: DTA/TGA analysis curves of sample.

Calcination of Sample

In the calcination method, hydrates and carbonates in magnesite are broken down by using high heat. The raw material was subjected to various

calcination processes. The temperature and time parameters of the calcination studies are given in Table 3.

Table 3: Parameters for Calcination.

Sample	Temperature (°C)	Time (Hour)
1	900	3
2	1000	3
3	1000	4
4	1100	3
5	1200	3
6	1200	4
7	1200	5

Chemical analysis, XRD analysis, DTA, and particle size analyses of the products obtained as a result of calcination were performed. It was determined that

as time and temperature increased in the calcination process, the sintering increased and the color of the sample darkened.

Table 4: Chemical analysis results for the calcinated samples.

No	Sample	LOI (%)	SiO ₂ (%)	Al ₂ O ₃ (%)	Fe ₂ O ₃ (%)	TiO ₂ (%)	CaO (%)	MgO (%)	Na ₂ O (%)	K ₂ O (%)
4877-206646	Original	44,90	6,90	0,96	0,72	0,10	2,02	44,28	0,01	0,09
4878-206647	900 °C- 3 hours calcination	0,90	19,30	1,49	1,02	0,15	3,26	73,70	0,01	0,13
4879-206648	1000 °C- 3 hours calcination	0,37	18,15	1,48	1,02	0,15	3,30	75,37	0,01	0,13
4880-206649	1000 °C- 4 hours calcination	0,27	19,05	1,50	1,04	0,14	3,28	74,59	0,01	0,08
4881-206650	1100 °C- 3 hours calcination	0,17	18,35	1,49	1,03	0,15	3,32	75,39	0,01	0,05
4882-206651	1200 °C- 3 hours calcination	0,18	18,50	1,51	1,04	0,15	3,32	75,27	0,01	0,01
4883-206652	1200 °C- 4 hours calcination	0,10	17,75	1,58	1,05	0,15	3,37	75,95	0,01	0,01
4884-206652	1200 °C- 5 hours calcination	0,20	19,00	1,55	1,03	0,16	3,28	74,74	0,01	0,01

When the chemical analysis results of the calcined samples were evaluated, it was decided that 3 hours at 1000 °C was appropriate due to the MgO content of 75.37%. In the same application, the CaO content of the sample was determined as 3.30%.

The loss on ignition analysis gives us information about whether there is a volatile compound in the material. When the results of the chemical analysis were examined, it was determined that the

calcination process performed at 900 °C for 3 hours (Ignition Loss of 0.90%) was not sufficient for the completion of the calcination. It has been determined that the presence of volatile compounds (CO₂ from MgCO₃) still continues in the material and the calcination process has not been completed. However, when the calcination study was performed at 1000 °C for 3 hours and the others were examined, it was seen that there was no significant difference between the chemical analyses.

No	Conditions	Sample No	LOI%
1	900 °C, 3h	4878-206647	0.9
2	1000 °C, 3h	4879-206648	0.37
3	1000 °C, 4h	4880-206649	0.27
4	1100 °C, 3h	4881-206650	0.17
5	1200 °C, 3h	4882-206651	0.18
6	1200 °C, 4h	4883-200652	0.1
7	1200 °C, 5h	4884-206653	0.2

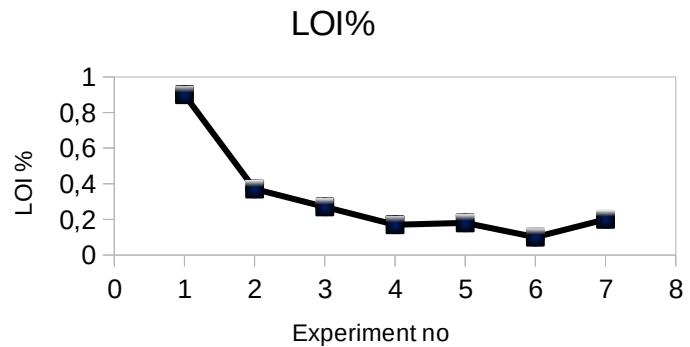


Figure 4: LOI% Values of Calcinated Samples.

It was also observed that different phase formations begin to occur in samples where calcination conditions exceed 1000°C and 3 hours. Phase formation is undesirable because it causes the structure to become more stable and the chemical processes to be applied become more difficult. In this case, 1000 °C temperature and 3 hours are considered suitable as the optimum calcination parameter.

In order to determine whether there are other trace elements in the calcined sample, the sample was analyzed in a semi-quantitative program with the XRF instrument. As a result of the analysis, it was determined that there were traces of chromium, nickel, copper, and strontium in the sample, among other elements.

Obtaining Magnesium Fluoride from Magnesite

In XRD analysis, how pure the material is determined by the height and sharpness of the peak density of the relevant substance. When the XRD spectra of MgF₂ products prepared with the experimental sets given above (Table 1) were examined, two results were obtained:

(i) The yields of the experiments using MgCO₃ as the input material are higher than the experiments using MgO.

(ii) When the main material is the same, the peak intensity of the products obtained by the drying method is higher than the products obtained by the filtration method.

Table 3 shows the peak intensity values derived from XRD examination of the products acquired as a result of the applications listed in Table 1.

Table 5: Peak intensity values of sellaite products obtained by using raw and calcined magnesite.

Experiment No.	Main Material	Method Used	Sellaite peak intensity
1	MgCO ₃	Drying	384
2	MgCO ₃	Filtration	379
3	MgCO ₃	Drying	332
4	MgCO ₃	Filtration	285
5	MgCO ₃	Drying	319
6	MgO	Drying	225
7	MgO	Filtration	133
8	MgO	Drying	242
9	MgO	Filtration	106
10	MgO	Drying	210

All the peaks seen in the XRD spectrum (Fig. 5) of the product obtained as a result of experiment No. 1 in Table 1 are the main and side peaks of the sellaite mineral (MgF₂) expected to be obtained.

There is no impurity. Figure 6 also shows the XRD spectrum of the product (experiment No. 2) with the second highest peak intensity, which was obtained as a result of the filtration process.

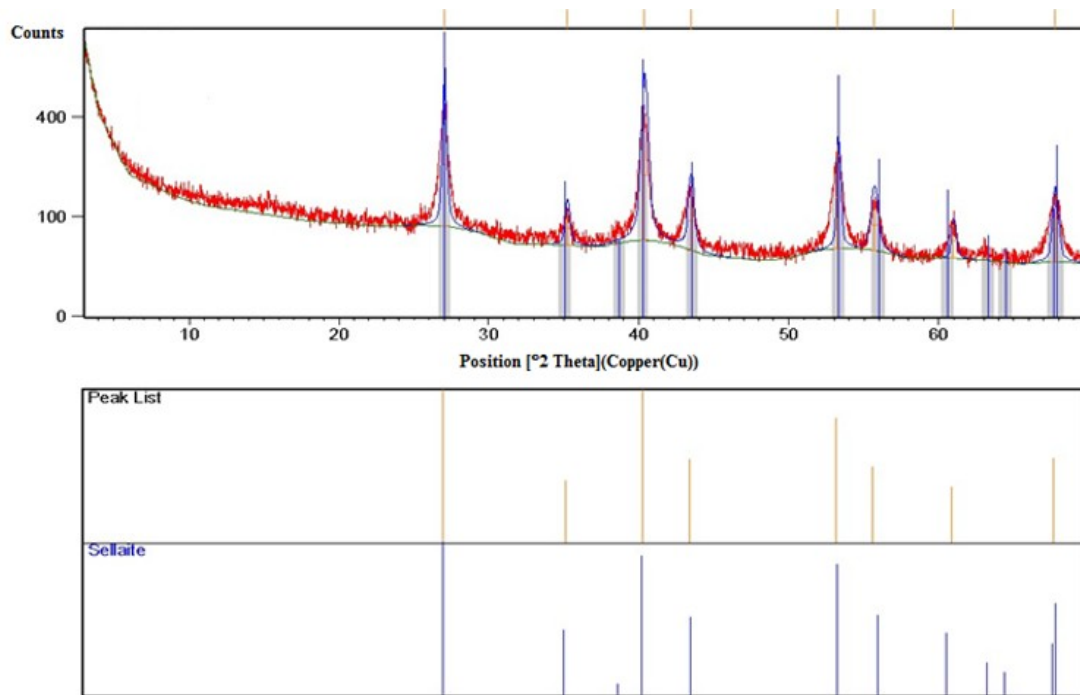


Figure 5: XRD spectrum of sellaite obtained experiment no 1.

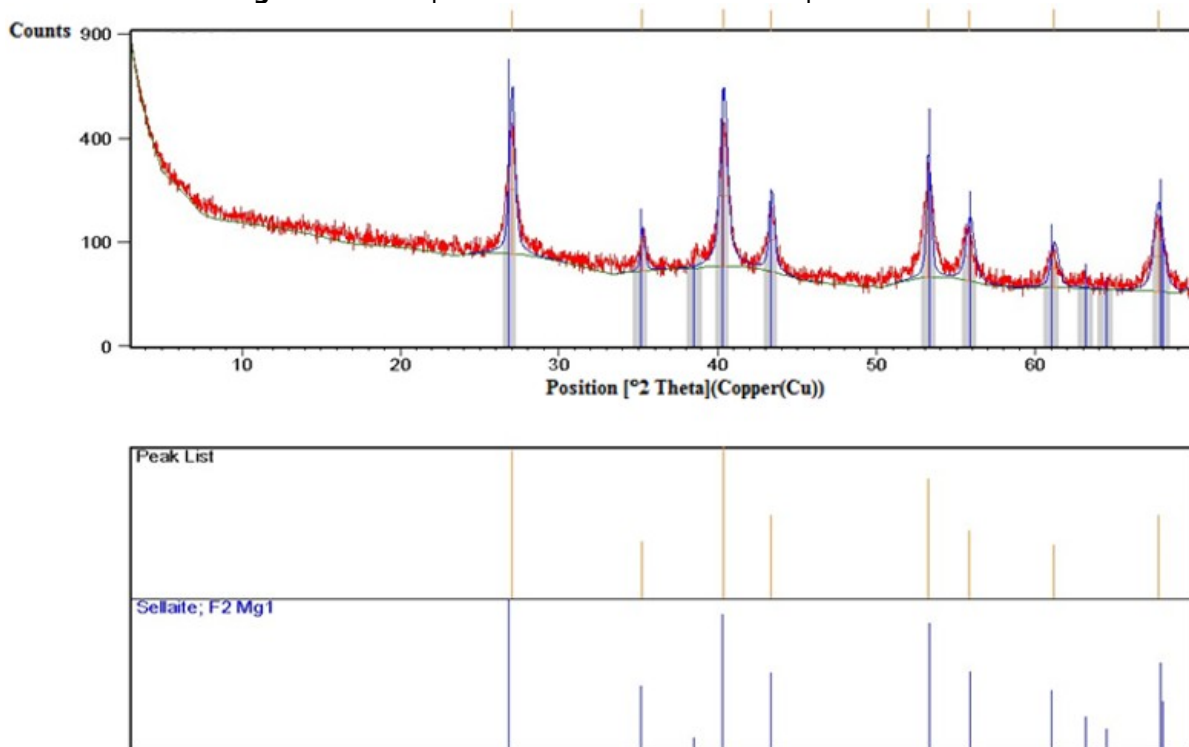


Figure 6: XRD spectrum of sellaite obtained experiment no 2.

The sellaite formed by employing raw magnesite as the main material and the drying technique has the maximum peak intensity value, as shown by the XRD spectra and data in Table 5.

CONCLUSION

The obtained results of experiments employing HF and raw magnesite or calcined magnesite to obtain MgF_2 revealed that raw magnesite had a better productivity than calcined magnesite. As a result, in production processes that do not need heat

processing, it is not necessary to calcinate the material.

CONFLICT OF INTEREST

The authors declare that they have no conflict of interest.

ACKNOWLEDGMENTS

We kindly thank Esan Eczacıbaşı Industrial Raw Materials Ind. and Trade Inc.

REFERENCES

1. Gence N. Enrichment Of Magnesite Ore. Eskişehir Osmangazi Üniversitesi Mühendislik ve Mimarlık Fakültesi Dergisi. 2001 Dec 31;14(2):1-10. [<URL>](#).

2. Wilson I, Ebner F. The World of magnesite. Ind Minerals. 2006;462:54-9.

3. Yucel O, Yiğit S, Derin B. Production of Magnesium Metal from Turkish Calcined Dolomite Using Vacuum Silicothermic Reduction Method. MSF. 2005 Jul;488-489:39-42. [<DOI>](#).

4. Gunay A, Karadag D, Tosun I, Ozturk M. Use of magnesit as a magnesium source for ammonium removal from leachate. Journal of Hazardous Materials. 2008 Aug;156(1-3):619-23. [<DOI>](#).

5. Demiray Y, Yücel O. Production and Refining of Magnesium Metal from Turkey Originating Dolomite. High Temperature Materials and Processes [Internet]. 2012 Jan 6 [cited 2022 Apr 18];31(3). [<DOI>](#).

6. Demir F, Dönmez B, Okur H, Sevim F. Calcination Kinetic of Magnesite from Thermogravimetric Data. Chemical Engineering Research and Design. 2003 Jul;81(6):618-22. [<DOI>](#).

